SULFUR CYCLING IN THE SOUTHERN CASCADE ARC: IMPLICATIONS FOR THE

SULFUR CONTENT, METAL CONTENT, AND OXIDATION STATE OF ARC

MAGMAS

by

MICHELLE JEAN MUTH

A DISSERTATION

Presented to the Department of Earth Sciences
and the Division of Graduate Studies of the University of Oregon
in partial fulfillment of the requirements
for the degree of
Doctor of Philosophy

September 2021

DISSERTATION APPROVAL PAGE

Student: Michelle Jean Muth

Title: Sulfur Cycling in the Southern Cascade Arc: Implications for the Sulfur Content, Metal Content, and Oxidation State of Arc Magmas

This dissertation has been accepted and approved in partial fulfillment of the requirements for the Doctor of Philosophy degree in the Department of Earth Sciences by:

Prof. Paul J. Wallace   Chairperson/Advisor
Prof. James M. Watkins   Core Member
Prof. Mark H. Reed   Core Member
Prof. Michael D. Pluth   Institutional Representative

and

Andrew Karduna   Interim Vice Provost for Graduate Studies

Original approval signatures are on file with the University of Oregon Division of Graduate Studies.

Degree awarded September 2021

DISSERTATION ABSTRACT

Michelle Jean Muth

Doctor of Philosophy

Department of Earth Sciences

September 2021

Title: Sulfur Cycling in the Southern Cascade Arc: Implications for the Sulfur Content, Metal Content, and Oxidation State of Arc Magmas

The behavior of sulfur (S) in volcanic arcs is of fundamental importance to a wide range of geologically and societally relevant processes. Despite this, the influence of subduction on the sulfur content of primitive arc magmas is poorly understood. This is partially because sulfur behavior in arc magmas is challenging to characterize; sulfur is present in two different valence states within silicate melts, and partitions into multiple phases (sulfide, anhydrite, silicate melt, gas). In this work, I address these challenges through the study of high-Mg melt inclusions. The first portion of this dissertation carries out a detailed investigation on the behavior of sulfur within six mafic cinder cones in the southern Cascade Arc. This investigation focuses on the close connections between magma sulfur content, oxidation state, and metal content. Comparisons of δ^{34}S, S and Fe valence state, and melt S content measured within the same suite of inclusions demonstrate that the influence of oxidized slab-derived sulfur in the sub-arc mantle is linked to increases in the oxidation state of arc magmas. In the second portion of this work, applying this framework to metal concentrations in Lassen magmas shows that Pb is dominantly derived from the subducting slab, whereas Mo, Zn, W, and Sn show no clear subduction-related enrichments. Variations in Cu contents between cinder cones are controlled by a combination of ambient mantle heterogeneity and modern subduction influence. In the third portion of this dissertation, I consider arc magma sulfur behavior in a global context through a compilation of published melt inclusion data spanning 115 volcanoes and 29 arc segments. Correlations between S and Cl in these melt inclusions indicate that S is partially derived from the subducting slab. Using models of sulfur content at sulfide saturation, I show that 90% of arc magmas have sulfur contents requiring conditions more oxidizing

than the QFM (quartz-fayalite-magnetite) buffer. Collectively, these three chapters demonstrate that subduction strongly influences the sulfur content of arc magmas, and that the transfer of sulfur from the subducting slab into the mantle source of arc magmas can be an important control on both the oxidation state and metal content of primitive arc magmas. This dissertation includes previously published and unpublished co-authored material.

CURRICULUM VITAE

NAME OF AUTHOR: Michelle J. Muth

GRADUATE AND UNDERGRADUATE SCHOOLS ATTENDED:

    University of Oregon, Eugene
    Rice University, Houston

DEGREES AWARDED:

    Doctor of Philosophy, Earth Sciences, 2021, University of Oregon
    Bachelor of Science, Earth Science, 2015, Rice University

AREAS OF SPECIAL INTEREST:

    Igneous Petrology
    High Temperature Geochemistry
    Volcanology

PROFESSIONAL EXPERIENCE:

    Graduate Researcher, University of Oregon, 2016-2021

    Geoscientist, AECOM Philadelphia Area Remediation Group, 2015-2016

    Undergraduate Researcher, Rice University, 2013-2015

GRANTS, AWARDS, AND HONORS:

    Research Recognition Award, University of Oregon, 2021

    User Beamtime Award, Argonne National Laboratory, 2019

    Warren DuPre Smith Research Award, University of Oregon, 2019

    Geology Emeritus Research Award, University of Oregon, 2018

    Graduate Research Fellowship, National Science Foundation, 2017

    First Year Graduate Student Fellowship, University of Oregon, 2016

    Eugen Merten Memorial Prize in Geology and Geophysics, Rice University, 2013

PUBLICATIONS:

Muth, M. J., Wallace, P.J. (2021). Slab-derived sulfate generates oxidized basaltic magmas in the southern Cascade Arc (California, USA). Geology.

Muth, M., Duncan M. S., Dasgupta, R. (2020). The Effect of Variable Na/K on CO_2 Solubility in Slab-Derived Rhyolitic Melts. Carbon in Earth's Interior AGU Monograph, 195-208.

Frahm, E., Feinberg, J. M., Schmidt-Magee, B. A., Wilkinson, K., Gasparyan, B., Yeritsyan, B., Karapetian, S., Meliksetian, K., **Muth, M.,** and Adler D. S. (2014). Sourcing geochemically identical obsidian: multiscalar magnetic variations in the Gutansar volcanic complex and implications for Palaeolithic research in Armenia, Journal of Archaeological Science, 47, 164-178.

ACKNOWLEDGMENTS

It has been an incredible privilege to spend the last few years contributing to our knowledge of the natural world. I am extremely grateful to everyone who helped me accomplish this goal. First, I would like to thank my advisor, Dr. Paul Wallace. During my time in graduate school his patience, generosity, intellect, and depth of knowledge allowed me to learn and grow as a scientist while pursuing ideas I was passionate about. It has been an honor and pleasure to work with him, and his commitment to scientific mentorship is something I hope to carry into my own career.

My committee members have been an extremely valuable source of support and feedback during the development of these projects. I would like to thank Dr. Jim Watkins for helping me gain confidence in applying numerical models to geochemical problems. I would like to thank Dr. Mark Reed for introducing me to the world of aqueous geochemistry and the thermodynamic tools that can be used to explore it, and for helping me understand porphyry ore deposits from multiple perspectives. I would also like to thank my external committee member Dr. Mike Pluth for his time and support.

The vibrant and collegial atmosphere of the UO Department of Earth Sciences brought a lot of joy and intellectual excitement into my PhD experience. I would like to thank the department faculty for sharing their passion, knowledge, and excitement, and for fostering a supportive and collaborative departmental culture. My time at UO was made immeasurably richer by the wisdom and brilliance of my peers. I am grateful for everyone I have gotten to know in the Department of Earth Sciences, in a Community for Minorities in STEM, and in Inclusion and Diversity in Earth and Atmospheric Sciences.

For my family

TABLE OF CONTENTS

LIST OF FIGURES

CHAPTER I

INTRODUCTION

The movement of sulfur through subduction zones is of fundamental importance to a wide range of geologically and societally relevant processes. In Earth's crust, the behavior of sulfur in arc magmas determines the fate of many ore-forming metals. At active volcanoes, the outgassing of sulfur has both regional and global climate impacts and is an important tool for monitoring volcanic activity. In the mantle wedge beneath volcanic arcs, the flux of sulfur from the down-going plate into the mantle wedge within subduction zones has the potential to affect the redox evolution of arc magmas and Earth's mantle. Because there is controversy concerning the origins of arc magma oxidations state, understanding the effect of subduction on the behavior of sulfur in arc magmas, and how these processes influence the oxidation state and metal content of arc magmas, is essential.

Because it is present in silicate melts in two different valence states, S^{6+} and S^{2-}, the behavior of sulfur in arc magmas is complex. Depending on magmatic conditions, sulfur can partition into a combination of sulfide phases, anhydrite, gas, and silicate melt. Despite this complexity, there are clear lines of evidence that suggest subduction may strongly influence the behavior of sulfur. Sulfur in arc magmas is commonly present in higher concentrations and isotopically heavy compared to mid-ocean ridge basalts (MORB), which suggests sulfur in arcs may be partially derived from the subducting slab. Arc magmas are also more oxidized than MORB, and measurements of $Fe^{3+}/\Sigma Fe$ in arc glasses suggest this oxidized signature is linked to the influence of slab-derived materials. This elevated oxidation state strongly influences the behavior of sulfur in magmas, and slab-derived S^{6+} has the potential to be a powerful oxidizing agent in the mantle wedge.

However, many uncertainties remain around the origins and behavior of sulfur in arc magmas. For example, although these observations suggest large differences in the behavior of sulfur between arcs and mid-ocean ridges, chalcophile elements such as Cu are commonly present in similar concentrations in primitive arc magmas and in MORB. Additionally, although sulfur concentrations and isotopes in arc magmas are consistent

with the influence of sulfur derived from the subducting slab, the source of sulfur within the subducting slab, as well as the oxidation state of the sulfur released during slab melting or dehydration, is debated. These complications suggest that sulfur in arc magmas may be influenced by a range of subduction-related processes.

This dissertation uses the geochemistry of silicate melt inclusions hosted in high-Mg olivine to tease apart these processes. The crystal hosts of melt inclusions shield them from late-stage and eruptive magmatic processes, and allow us to characterize the composition of primitive, relatively undegassed silicate melts. The central goal that ties each chapter together within this dissertation is to understand how slab-derived materials influence the sulfur content, oxidation state, and metal content of arc magmas.

In Chapter II, I use measurements of $\delta^{34}S$, S and Fe valence state, and sulfur concentrations within olivine-hosted melt inclusions from mafic cinder cones in the southern Cascade Arc to trace the origins and behavior of sulfur within arc magmas. These measurements are compared to estimates for the sulfur isotopic composition of the downgoing plate at Lassen, and with combined mantle melting and S-Fe redox equilibrium models. I use these comparisons to show that Lassen magma sulfur contents are influenced by the transfer of oxidized, isotopically heavy sulfur from the subducting plate. Models developed here show that this slab-derived sulfate can drive increases in the oxidation state of arc magmas. However, an extremely sulfur-rich slab material or a more complex, multistage process of oxidation is required.

In Chapter III, I build on insights from Chapter II to understand the behavior of ore-forming metals in subduction zones. I measure the abundance of Cu, Mo, Zn, Pb, W, and Sn in melt inclusions to understand how arc magma metal contents are influenced by sulfur-rich slab-derived material. I find that the Mo, Zn, and Sn contents of Lassen magmas are similar to MORB and are relatively unaffected by subduction, whereas slab melts enrich Lassen cinder cone magmas in Pb. The Cu contents of Lassen magmas are broadly similar to MORB but differ from one cinder cone to another. I develop mantle melting models to compare to constraints inferred from melt inclusion $\delta^{34}S$, S, and S and Fe valance state and show that Lassen Cu contents are controlled by a combination of ambient mantle heterogeneity and subduction-related mass transfer of sulfur into the mantle wedge.

In Chapter IV, I expand the scope of study to consider the behavior of sulfur in primitive arc magmas globally. I compiled published melt inclusion data from 29 arc segments, together with new data from the Cascades to determine the key controls on primitive arc magma S contents, including the role of mantle oxidation state. I find that sulfur in arc magmas is partially derived from the subducting plate. Using models of sulfur content at sulfide saturation, I find that most arc magmas have S contents requiring oxygen fugacity higher than that of MORB. These findings, along with the conclusions from my work on the southern Cascades, demonstrate that the mantle source for arc magmas in oxidized, and that sulfur cycling in arcs is closely linked to the oxidized nature of arc magmas.

CHAPTER II

SLAB-DERIVED SULFATE GENERATES OXIDIZED BASALTIC MAGMAS IN THE SOUTHERN CASCADE ARC

This chapter has been published in *Geology* as of June 2021. I am lead author on the paper, which involved sample preparation, analysis, synthesis of all data, modeling and writing the manuscript. Paul Wallace (University of Oregon) assisted with data interpretation and feedback on manuscript drafts.

1. Introduction

Over long timescales, recycling of redox-sensitive sulfur (S) in subduction zones is likely a key control on the oxidation state of Earth's mantle (Evans 2012). The redox state of arc magmas also strongly affects their chemical evolution and the creation of porphyry ore deposits (Richards, 2015). In arc magmas S is present both as sulfide (S^{2-}), the dominant species in mid-ocean ridge basalt (MORB), and as the oxidized species sulfate (S^{6+}). Trace element systematics suggest that arc magmas become oxidized and S^{6+}-dominated during differentiation (Lee et al., 2010; Tang et al., 2018). In contrast, data from mantle xenoliths and from redox state measured in silicate glasses (Kelley and Cottrell, 2009; Brounce et al., 2014; Bénard et al., 2018; Birner et al., 2017) suggest oxidized magmas form when oxidized materials from the downgoing slab rise into the sub-arc mantle wedge.

Independent of this debate, $\delta^{34}S$ values measured in arc glasses and volcanic gases suggest that some S is derived from seawater sulfate released during slab dehydration (Alt et al., 1993; Bénard et al., 2018). Although mantle melts contain much less S than Fe, one mole of slab-derived S^{6+} can potentially oxidize 8 moles of Fe^{2+}. Whether this S^{6+}-driven oxidation occurs in arcs is difficult to test because it requires integrating the mass transfer of S and electron budget of S and Fe into models of magma formation.

Olivine-hosted melt inclusions (MI) provide a means to study melts minimally affected by degassing. We measured the composition of MI hosted in Mg-rich olivine from tephra of six mafic cinder cones in Lassen Volcanic Area, CA. This region has hundreds of mafic vents that have been variably influenced by slab-derived material in

their mantle source (Borg et al., 1997). Lassen sits at the southern end of the Cascadia subduction zone, which has a hotter thermal structure than most arcs (Syracuse et al., 2010). H_2O in Lassen magmas is likely derived from dehydration of hydrated mantle lithosphere in the subducting Gorda microplate, with the released fluid fluxing into overlying oceanic crust where it induces slab melting (Walowski et al., 2015, 2016). Here we build on this framework, constraining the mass balance and source of S in Lassen magmas using microanalysis of $\delta^{34}S$, S, and Sr/Nd in the same MI for which we constrain electron balance using $S^{6+}/\sum S$ and $Fe^{3+}/\sum Fe$ values measured via XANES spectroscopy (see Supplementary Text for details of all analytical methods).

2. Slab-derived sulfur

Arc magmas commonly contain more S than MORB, regardless of subducted plate thermal structure (Fig. 1). After corrections for post-entrapment crystallization average MI S contents for Lassen cinder cones range from 990 ± 160 ppm (cinder cone BBL), similar to primitive MORB values, to $1,960 \pm 470$ ppm (cinder cone BRM). Within each cone MI do not show signs of S degassing (Fig. DR 4b, DR12). To compare conditions of melting that generated magmas at each cone, we calculate primary magma compositions through olivine addition back to equilibrium with Fo_{90} olivine. Primary magma S contents thus calculated range from 790 to 1,940 ppm (Fig. DR12, see Supp. Text).

To assess the influence of slab-derived S on Lassen primary magma S contents, we compare S/Dy to Sr/Nd. Sr and Nd, and S and Dy, respectively, have similar incompatibility during mantle melting in the presence of immiscible sulfides and during olivine-only fractional crystallization (Saal et al., 2002, Walowski et al., 2016). This means increases in Sr and/or S relative to Nd and Dy can indicate addition of slab material to the mantle source. Increases in S/Dy can also indicate more oxidized melting conditions, which increase the maximum S content of sulfide-saturated melts.
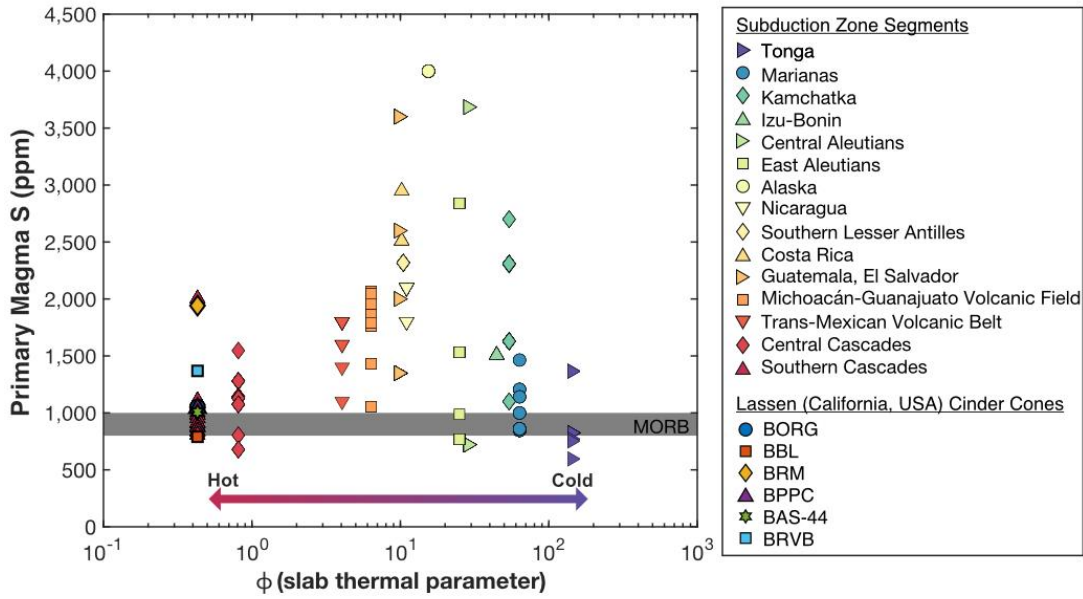
Figure 1. Calculated primary magma S concentrations for arc volcanoes compared to slab thermal parameter (Syracuse et al., 2010; Ruscitto et al., 2012). Primary MORB S reference values (Ding and Dasgupta, 2017) shown for comparison.

S/Dy correlates with Sr/Nd at Lassen (Fig. 2d). If we make a simplifying assumption that relationships between S/Dy and Sr/Nd are linear, a regression including an averaged value for MORB data yields $R^2 = 0.69$, p-value = 0.02. We note that cinder cone BRVB is an outlier within this correlation and attribute this to pre-existing enrichments in Nd within the sub-arc mantle prior to modern subduction (see Supp. Text, Fig. DR14, DR15). Correlations with Sr rather than Sr/Nd are stronger, with no outliers (Fig. DR14), but we have chosen to retain Sr/Nd for modeling slab additions beneath Lassen for consistency with previous work (e.g. Walowski et al., 2016) and to reduce complications related to mantle melt fraction in our interpretations.

Correlations in Figures 2 and DR14 require variable slab addition of S to the mantle source and/or a variably oxidized mantle. With regard to the latter, MORB-source mantle that becomes oxidized without S addition does not contain enough S to generate the high S magmas at Lassen (Fig. DR13). An alternative is that magmas at each cinder cone become variably oxidized and S-enriched during deep crustal differentiation. Theoretically, melt Fe^{3+} enrichment caused by magma recharge and garnet crystallization could increase $S^{6+}/\sum S$ and cause assimilation of sulfide cumulates in the lower crust (e.g.

6

Lee and Tang, 2020). However, Lassen cinder cones are fed by small, short-lived crustal magmatic systems, and high-Mg MI used here formed during early crystallization. Lassen magmas also do not show the strong HREE depletions expected from significant garnet fractionation (Walowski et al., 2016).
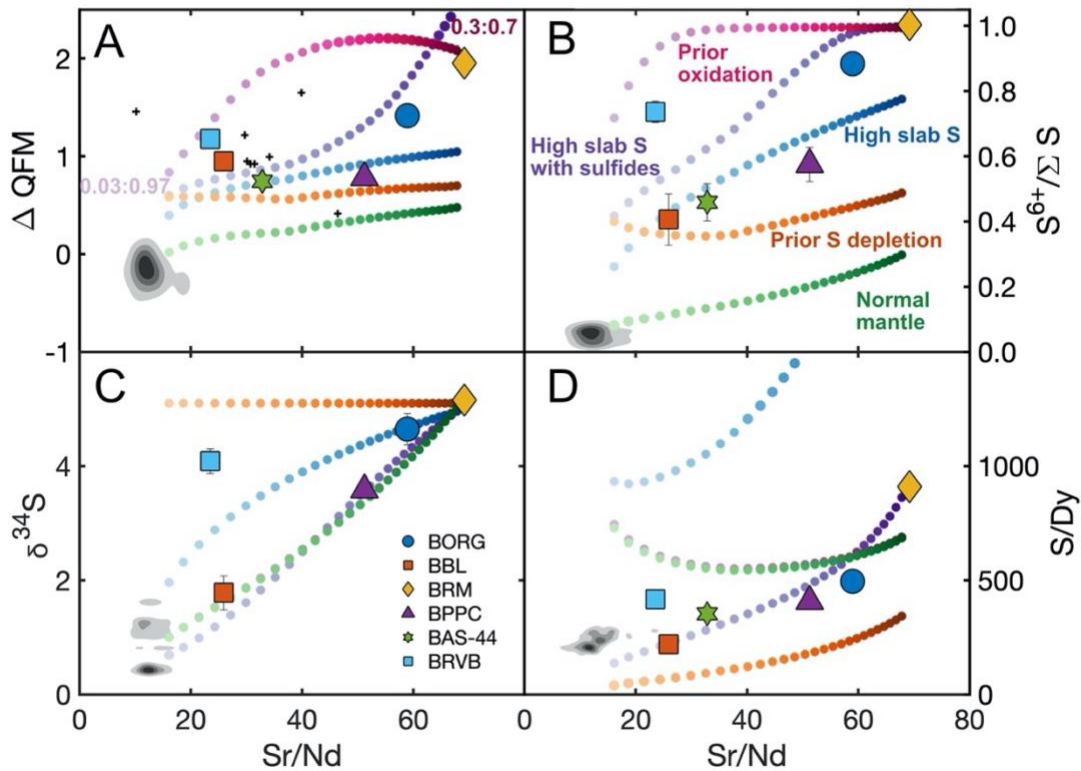
Figure 2. Primary magma compositions for the Lassen region based on melt inclusion data (large symbols) compared to model melt compositions (small circles). Error bars in (b) and (c) represent standard error of the mean. Each set of colored circles represents one modeled scenario, and each individual circle represents the modeled melt at peak mantle wedge temperature, calculated for a specific melt:rock ratio, as labelled in panel a. 'Normal Mantle' and 'Prior Oxidation' models have the same values in c and d. See text and Figure DR3 for model details. Small crosses are oxygen fugacity estimates using spinel-olivine oxybarometry for other Lassen cinder cones (Clynne and Borg, 1997; Ballhaus et al., 1991). MORB compositions (Table DR13) shown in gray density contours for comparison.

We therefore interpret correlations between S/Dy and Sr/Nd (Fig. 2d) to indicate that a large portion of S in Lassen magmas is sourced from the subducting slab. H_2O and Cl in Lassen magmas show similar patterns, indicating that S, Cl, and H_2O are all sourced

primarily from the downgoing plate (Fig. DR16, Walowski et al., 2016), consistent with volatiles in arcs globally (Ruscitto et al., 2012).

3. Sulfur isotopes

Because S/Dy can vary as a function of oxidation state during mantle melting, S isotope ratios ($\delta^{34}S$) measured in MI provide an essential additional constraint on slab-to-mantle mass transfer of S. $\delta^{34}S$ values for Lassen magmas (1.8 ± 0.7 ‰ to 5.2 ± 0.3 ‰) correlate with Sr/Nd in a similar way to S/Dy ($R^2 = 0.68$, p-value = 0.04; Fig. 2c). This requires variable addition of high-$\delta^{34}S$ sulfur into a MORB-like mantle source ($\delta^{34}S = 0.6$ ‰; see Supp. Text). To compare $\delta^{34}S$ in Lassen magmas to $\delta^{34}S$ in slab lithologies, we calculate bulk $\delta^{34}S$ in the downgoing slab at Lassen using constraints from geophysical data and drill cores (Fig. 3, see Supp. Text). Our estimate includes sediments, volcanic and gabbroic sections of altered oceanic crust (AOC) and 2 km of partially hydrated lithospheric mantle. Bulk $\delta^{34}S$ estimated for the slab beneath Lassen is -6.7±2.9 ‰, with uncertainty based on S content in each section. Sediment contribution to the slab-derived component in Lassen magmas is small (Walowski et al., 2016). If we exclude sediment, bulk slab $\delta^{34}S$ is 1.1±0.5 ‰, still lower than $\delta^{34}S$ in the most S-rich Lassen cinder cone ($\delta^{34}S = 5.2$ ‰) and indistinguishable from MORB ($\delta^{34}S = 0.6$ ‰).

Elevated $\delta^{34}S$ in Lassen magmas relative to estimates for the bulk downgoing slab (Figs. 2, 3) could be most readily explained if seawater sulfate in downgoing hydrated lithospheric mantle or AOC is transported into the sub-arc mantle more effectively than sulfur from primary sulfides in downgoing AOC. Heterogeneity in sulfide $\delta^{34}S$ within exhumed high-pressure rocks suggest sulfides do not equilibrate efficiently at slab surface temperatures (Walters et al., 2019). If this is the case, then $\delta^{34}S$-enriched fluids from hydrated lithospheric mantle (e.g. Alt et al., 2012) that flush overlying oceanic crust and cause partial melting would have a disproportionate effect on slab melt $\delta^{34}S$. Alternatively, if equilibrium conditions prevail, slab sulfur may inherit high $\delta^{34}S$ from isotopic fractionation during slab melting. An S^{6+} dominated slab melt in equilibrium with MORB-like sulfides ($\delta^{34}S = 0$ ‰) would have $\delta^{34}S = 5.7$-6.9 ‰ (Miyoshi et al., 1984) at 750-850 °C (Walowski et al., 2015), whereas an S^{2-} dominated slab would undergo little fractionation. For partial melt of oceanic crust to be dominated by S^{6+}

requires that fluids derived from underlying hydrated mantle lithosphere are relatively
oxidized (e.g. Debret and Sverjensky, 2017; Maurice et al., 2020, Evans and Frost, 2021).
Therefore, while assumptions about equilibrium or non-equilibrium $\delta^{34}S$ behavior in
AOC have different implications for the precise source of slab S, both indicate the release
of oxidized, S^{6+} dominated melt from the slab into the mantle wedge.
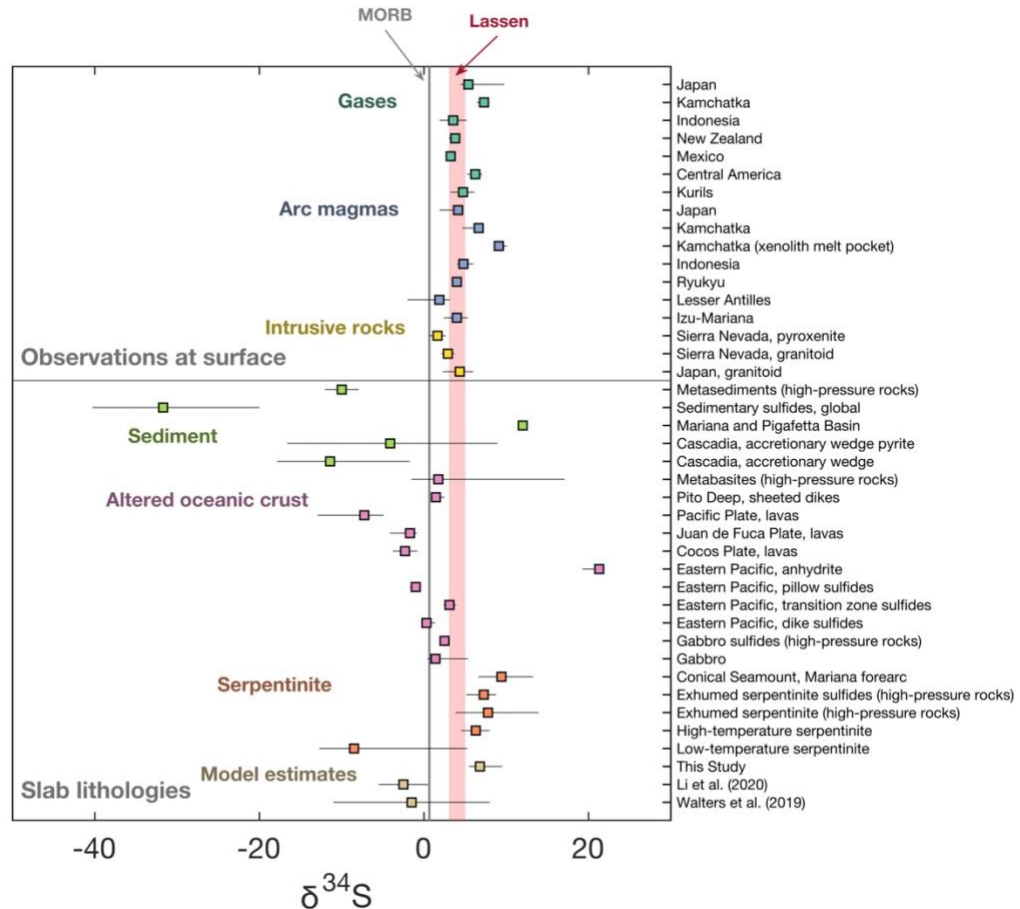
Figure 3. $\delta^{34}S$ values for arc volcanoes, drill cores, exhumed rocks, and slab-fluid/melt
models (Table DR11). Symbols show average, upper and lower quartiles for each data
set. All data are for whole rock S unless otherwise specified. Arc extrusive rocks ('Arc
Magmas') include basalt and basaltic andesite compositions. Average MORB $\delta^{34}S$ and
the upper and lower quartile of Lassen MI $\delta^{34}S$ shown for comparison.

$\delta^{34}S$ values of Lassen MI are similar to $\delta^{34}S$ measured at arcs globally (Fig. 3).
High temperature gases, low-S submarine glasses, and degassed scoria samples all have
$\delta^{34}S$ similar to the minimally degassed MI measured here. This suggests that degassing at
arcs has a relatively small effect on melt $\delta^{34}S$ values. Considering the wide range of

sediment $\delta^{34}S$ compositions (Fig. 3), slab temperatures (Syracuse et al., 2010), and slab-material fluxes (Ruscitto et al., 2012) estimated for arcs, similarities in $\delta^{34}S$ of magmas from different arcs suggest that the addition of slab-derived, oxidized S to the sub-arc mantle at Lassen is common to other subduction zones.

4. Influence of slab-derived sulfur on the oxidation state of Lassen magmas

Lassen primary magma oxygen fugacities (f_{O2}), calculated from $Fe^{3+}/\sum Fe$ measured in MI, range from QFM+0.8 to QFM+2.0 (Fig. 2a; see Supp. Text). Like S and $\delta^{34}S$, f_{O2} correlates with Sr/Nd ($R^2 = 0.61$, p-value = 0.04 for ΔQFM, $R^2 = 0.68$, p-value = 0.02 for $S^{6+}/\sum S$), suggesting that slab-derived S^{6+} has a causal link to oxidized magmas. Both $Fe^{3+}/\sum Fe$ and $S^{6+}/\sum S$ are elevated relative to MORB. This requires that as slab-derived, hydrous, silicic melt causes flux melting of the mantle wedge (Walowski et al., 2015), a portion of slab-derived S^{6+} is reduced to oxidize Fe^{2+}, as there is an equilibrium relationship between melt $Fe^{3+}/\sum Fe$ and $S^{6+}/\sum S$ involving redox exchange between S and Fe (e.g. Nash et al., 2019). Therefore, to assess whether slab-derived S^{6+} causes arc magmas to be more oxidized than MORB, the coupled redox budget of S and Fe must be considered.

To model the redox budget, we combine pMELTS melting models (Ghiorso et al., 2002), redox equilibrium between S and Fe, and electron balance calculations. This model (see Supp. Text for details) approximates the reaction and transport of silicic, hydrous slab melts rising into the inverted thermal gradient of the mantle wedge (Sisson and Kelemen, 2018). Coupled redox balance calculations track changes in $Fe^{3+}/\sum Fe$ and $S^{6+}/\sum S$ during reactions of S^{6+}-rich slab-derived melts with more reduced mantle peridotite. Importantly, the coupled redox balance shows that slab S^{6+} is much less effective at generating oxidized basaltic magmas than predicted when only the relationship between f_{O2} and $S^{6+}/\sum S$ is considered (Klimm et al., 2012).

In our initial model, we assume a slab melt with 1,500 ppm S^{6+} based on a 950°C, 3 GPa partial melting experiment of oxidized, fluid-saturated, S-rich basalt (Jégo and Dasgupta, 2014), and initial mantle peridotite S^{2-} content of 150 ppm based on MORB-source mantle (Ding and Dasgupta, 2017). In this scenario, slab S^{6+} drives clear increases in the f_{O2} and $S^{6+}/\sum S$ of mantle melts but does not predict Lassen f_{O2}, S/Dy, or $S^{6+}/\sum S$

values (green curve, Fig. 2). Given this result, we also modeled the same scenario but assumed 10,000 ppm S^{6+} in slab melt. This model overestimates the S content of Lassen magmas but reproduces all but the highest Lassen f_{O2} and $S^{6+}/\sum S$ values (blue curve in Fig. 2). Given that this modeling approach seems to require unreasonably high slab melt S^{6+} concentrations, we explored three more complex model scenarios.

In the first more complex scenario, melts remain saturated in an immiscible sulfide phase as they react with peridotite. This model scenario creates more oxidizing melts but requires very S-rich slab melt (8,000 ppm) to reproduce the highest f_{O2} and $S^{6+}/\sum S$ values (purple curve in Fig. 2). The second more complex scenario is that the sub-arc mantle experienced S extraction during previous melting events. However, if we assume 1,500 ppm S^{6+} in slab melt and 0 ppm S^{2-} in mantle peridotite, the model cannot reproduce higher f_{O2} and S/Dy values or the correlation between Sr/Nd and $\delta^{34}S$ (orange curve in Fig. 2). The third more complex scenario is that the sub-arc mantle experienced multiple stages of oxidation, consistent with oxygen isotope data for Lassen magmas (Underwood and Clynne, 2017) and other arcs (Auer et al., 2009). This model fails to reproduce the entire range of Lassen compositions with a single, uniform period of prior oxidation (pink curve in Fig. 3), indicating that a more localized and/or multi-stage process is required.

Models developed here show that transfer of slab-derived sulfate to the mantle wedge has a clear effect on the f_{O2} of arc magmas and requires slab melts with $\delta^{34}S = 5.2$-9.5 ‰ to match measured $\delta^{34}S$ values (Figs. 2, 3, 4). These models highlight the importance of resolving sensitivity of S and Fe redox exchange to pressure, temperature, melt composition, including dissolved H_2O, and potential quenching effects (e.g. Matjuschkin et al., 2016; O'Neill, 2021). While these uncertainties are unlikely to alter bulk electron exchange in our models significantly compared to the overall effect of S^{6+} addition, they limit how modelling outcomes considered here can be included in models of S behavior during mantle melting.
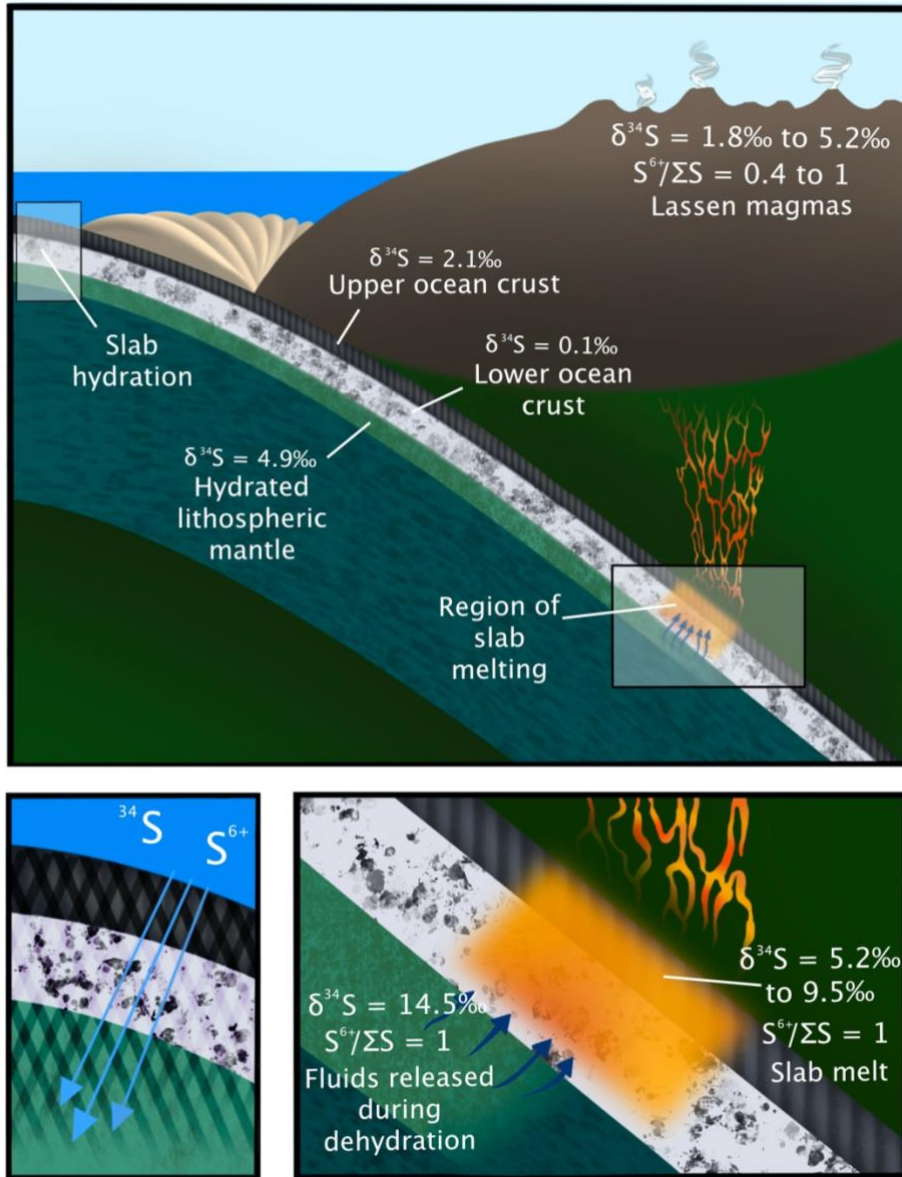
Figure 4. Conceptual model for the generation of sulfur-rich oxidized magmas in the Southern Cascades arc. High $\delta^{34}S$ seawater sulfate (e.g. Alt et al., 2012) becomes incorporated into altered oceanic crust (subdivided into upper crust with volcanic rocks/sheeted dikes, and lower crust with gabbros) and hydrated mantle lithosphere during hydrothermal activity near the ridge crest and later faulting of oceanic crust. When the hydrated mantle lithosphere dehydrates, oxidized fluids rise into overlying oceanic crust, generating high $\delta^{34}S$, sulfate-dominated, hydrous slab melts. These slab melts rise up through the inverted thermal gradient of the mantle wedge, reacting with mantle peridotite to form oxidized, S-rich, high $\delta^{34}S$ basaltic magmas.

A striking feature of our data set is that Lassen magma $\delta^{34}S$ and f_{O2} values are similar to those measured in the Marianas (Fig. DR6, Alt et al., 1993; Brounce et al., 2014) and other arcs globally (Fig. 3, Cottrell et al., 2020) even though the Cascade arc is a near global endmember in terms of young slab age and temperature, which strongly affect slab dehydration and melting (Walowski et al., 2015). This shared similarity in $\delta^{34}S$ and f_{O2} points to a common source of S, either sulfate derived from hydrated mantle lithosphere or AOC-hosted sulfides oxidized by fluids rising up from the hydrated mantle lithosphere, or both (Fig. 4). Our results show that transfer of slab-derived S^{6+} into sub-arc mantle above subducted plates can explain both elevated $\delta^{34}S$ values and f_{O2} of basaltic arc magmas globally.

5. Bridge

In the preceding chapter (II), I used measurements of $\delta^{34}S$, S and Fe valence state, and S contents in olivine-hosted melt inclusions to demonstrate the influence of oxidizing, isotopically heavy, slab-derived sulfur in increasing the S content and oxidation state of Lassen magmas. In chapter III, I combine these insights with measurements of ore-forming metal concentrations (Cu, Zn, Mo, Pb, W, Sn) in the same set of melt inclusions, in order to understand how variations in mantle sulfur content, mantle oxidation state, ambient mantle heterogeneity, and modern subduction all influence the metal content of Lassen magmas.

CHAPTER III

THE INFLUENCE OF SLAB-DERIVED SULFUR ON THE METAL CONTENTS OF MAGMAS IN THE SOUTHERN CASCADE ARC

This chapter is in preparation for submission to *Earth and Planetary Science Letters*. I am lead author on the paper, which involved sample preparation, analysis, synthesis of all data, modeling and writing the manuscript. Paul Wallace (University of Oregon) assisted with data interpretation and feedback on manuscript drafts.

1.0 Introduction

The behavior of Cu in subduction zones is critical to the formation of porphyry Cu deposits (Sillitoe, 2010; Wilkinson, 2013; Richards, 2015; Lee and Tang, 2020), which contain ~60% of the world's copper reserves (John et al., 2010). Most porphyry deposits are found within groups of porphyry stocks formed by fluids exsolved from crystallizing intermediate to felsic calc-alkaline magmas (John et al., 2010; Sillitoe, 2010). They are usually emplaced in the shallow crust, which means their deeper magmatic plumbing system is not simultaneously exposed at the Earth's surface. However, distinct geochemical characteristics shared among fertile deposits (Loucks, 2014) and the commonly observed spatial and temporal association of fertile deposits (Sillitoe, 2010) suggests that more deep-seated magmatic processes may influence their formation. The geochemistry of mantle-derived magmas may affect ore-forming processes by either 'setting the stage' for how arc plutons evolve (e.g. Chiaradia 2020), or by recharging more evolved magma bodies from below (Audétat and Pettke, 2006; Chambefort et al., 2008; Cao et al., 2018a, 2018b; Li et al., 2019). There is also evidence to suggest that hydrous, Cu-sulfide-bearing cumulates from prior magmatism can be remobilized in late stage and/or post subduction settings (Richards, 2009; Lee and Tang, 2020).

While there are several features of mafic magmas that can affect the formation of porphyry Cu deposits, the importance of each is debated (Wilkinson, 2013; Richards, 2015; Rezeau and Jagoutz, 2020). Mass balance considerations suggest that arc magmas do not require atypical enrichments in Cu to form deposits (Cline and Bodnar, 1991). However, the extent to which unusually Cu-enriched magmas affect the Cu content of porphyry

deposits (e.g. Core et al., 2006), and the extent to which the early saturation of Cu-bearing sulfides affects magma fertility (e.g. Du and Audétat, 2020) is debated. Likewise, it is unclear to what extent magma sulfate content (Chambefort et al., 2008; Hutchinson and Dilles, 2019), oxidation state (Grondahl and Zajacz, 2017), H_2O content (Chiaradia 2020; Rezeau and Jagoutz, 2020), and magma emplacement rate (Korges et al., 2020) influence the formation of porphyry deposits. Importantly, in arc settings these factors likely co-vary. Therefore, to tie our knowledge of arc magma petrogenesis into the formation of porphyry ore deposits, variations in arc magma Cu content need to be understood in the context of other key compositional features.

The Cu contents of arc magmas are broadly similar to MORB (Lee et al., 2012; Rezeau and Jagoutz, 2020; Barber et al., 2021), but studies at individual arcs show the Cu content of primitive magmas vary (De Hoog et al., 2001; Timm et al., 2012; Jenner et al., 2012; Mironov and Portnyagin, 2018; Leath, 2019), even within a single arc segment (Jenner et al., 2012; Leath, 2019). The behavior of Cu has the potential to vary widely between arcs because its behavior is sensitive to the stability of Cu-bearing sulfide phases. The melt sulfur content at which magmas become saturated in these sulfides, commonly referred to as the total dissolved sulfur content at sulfide saturation ($SCSS^T$), is sensitive to melt oxygen fugacity, which affects the proportion of sulfur in silicate melts as S^{6+} relative to S^{2-} (Jugo et al., 2010). Whereas calculated oxygen fugacity using measured $Fe^{3+}/\sum Fe$ in arc glasses (Kelley and Cottrell, 2009; Brounce et al., 2014), direct measurements of $S^{6+}/\sum S$ in melt inclusions (Muth and Wallace, 2021), and elevated S contents in magmas (Ruscitto et al., 2012; Wallace and Edmonds, 2011) all demonstrate that some S is present as S^{6+} in arc magmas, the effects of pressure, temperature, and composition on silicate melt $S^{6+}/\sum S$ are unclear (Matjuschkin et al., 2016; Nash et al., 2019; O'Neill, 2021).

In arc magmas, Cu behavior during early crystallization varies. In more strongly tholeiitic magmas, either in arcs or back-arcs, Cu commonly behaves incompatibly during the first stages of crystallization (Jenner et al., 2010; Keith et al., 2017; Rezeau and Jagoutz, 2020). In these magmas, the eventual precipitation of phases like magnetite may reduce the melt FeO content and/or melt f_{O2} via Fe^{3+} sequestration. These decreases in melt f_{O2} and/or FeO lower $SCSS^T$, which can cause the silicate melt to become

saturated in sulfides. These sulfide saturation in turn causes Cu to switch to compatible behavior (Jenner et al., 2010, 2012, 2015; Valetich et al., 2019). In contrast, in many calc-alkaline arc magmas Cu behaves compatibly during most of crystallization. This compatible behavior is caused by an overall Fe-depletion trend in calc-alkaline magmas, which drives melts towards lower $SCSS^T$ and therefore towards higher proportions of precipitated sulfides (Rezeau and Jagoutz, 2020). However, the importance of specific crystallizing phases such as amphibole (Barber et al., 2021), and garnet (Lee and Tang, 2020) in driving this Fe-depletion trend and associated decreases in $SCSS^T$ is debated. Others have additionally proposed that early magnetite crystallization in calc-alkaline magmas can decrease both melt fO_2 and melt FeO content, drastically decreasing melt $SCSS^T$ in a manner similar to that proposed for more tholeiitic magmas (Chiaradia, 2013).

The variable influence of slab-derived material in the source regions for individual mafic cinder cones in the Lassen region makes it an ideal location to test how subduction influences the Cu content of mafic arc magmas. Previous work used geodynamic modelling and isotope, volatile and trace element systematics to demonstrate that the presence of slab-derived material in the sub-arc mantle beneath Lassen drives differences in the H_2O content and Cl content of primitive arc magmas (Walowski et al., 2015, 2016). Similarly, direct measurements of $\delta^{34}S$ and S and Fe valence state in melt inclusions show that this subduction influence also increases the S content and oxidation state of primitive magmas (Muth and Wallace, 2021). Here we report the metal contents of Lassen melt inclusions from the same set of samples, combining the prior constraints with new melt inclusion data to investigate how subduction zone processes affect the behavior of Cu and other metals (Pb, Zn, Mo, Sn, W) in the Lassen region.
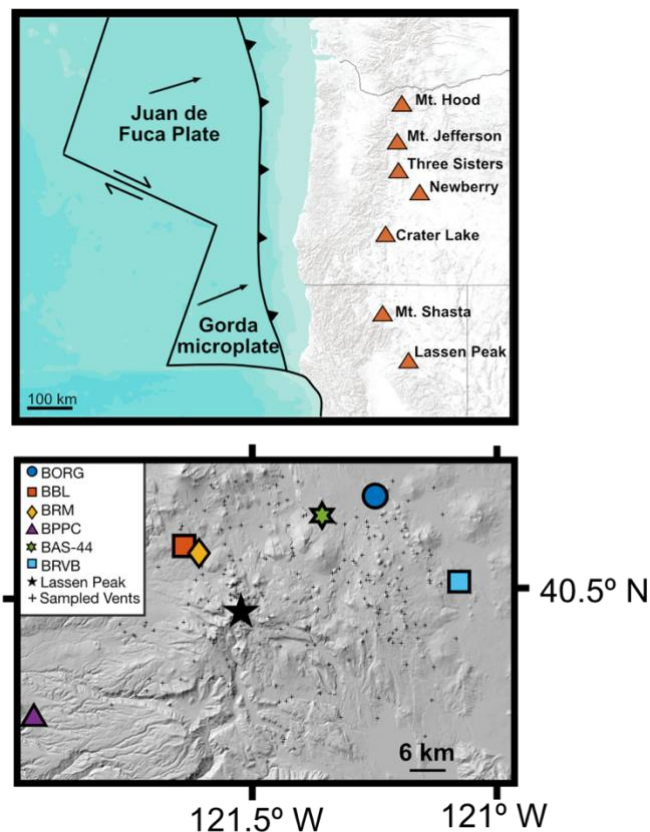
Figure 1. (Top) Map of the southern portion of the Cascade Arc, where major peaks are highlighted with red triangles. (Bottom) Map of the Lassen region showing the location of the cinder cones sampled for this study (large colored symbols), Lassen Peak (black star), and previously sampled vents (small black crosses).

2.0 Geologic Setting

The Lassen region is located in the southern end of the Cascade Arc. The Gorda micro-plate subducting at the trench is relatively young (Fig. 1, 6-9 Ma, Wilson, 2002), and the subducting slab beneath Lassen is hotter than most arcs (Syracuse et al., 2010; Walowski et al., 2015). The southern Cascades contains numerous mafic vents in addition to four more evolved silicic edifices, including Lassen Peak (Guffanti et al., 1990). While volcanism in the region is driven primarily by subduction, the local tectonic environment also has an influence. The Basin and Range province to the east of Lassen impinges on the Lassen area and likely exerts some control on vent locations (Guffanti et al., 1990). Lassen is underlain by a combination of Cenozoic volcanic rocks, Sierra Nevada intrusions (Berge and Stauber, 1987; Blakely et al., 1997), and accreted terranes (Dickinsin, 2008). Trace element and isotope systematics (Borg et al., 1997, 2002;

17

Walowski et al., 2016; Mullen et al., 2017; Underwood and Clynne, 2017) in addition to evidence from Cr-spinel compositions (Borg et al., 2002) and magma volatile contents (Walowski et al., 2015, 2016; Muth and Wallace, 2021) are all consistent with the combined effects of prior mantle heterogeneity and modern subduction influence on mafic magma compositions in the region.

3.0 Methods

3.1 Analytical approach

Olivine-hosted melt inclusions from the tephra of each cinder cone were selected for analysis. The tephra samples used here were a combination of tephra samples used in the study of Walowski et al. (2016) and newly collected samples from sampling locations nearby the original location. These newly collected tephra samples are labeled with the prefix "MM-L17" in supplemental tables. Inclusions that contained quench or daughter crystals, were intersected by cracks in the host crystal prior to sectioning (some inclusions developed cracks during preparation) or contained anomalously large or multiple vapor bubbles were not selected. Some inclusions contain a small ($\sim$2-10 μm) immiscible sulfide bleb, which likely formed post-entrapment, or a co-trapped spinel crystal.

Melt inclusions were analyzed on a Thermo-Nicolet Nexus 670 FT-IR spectrometer interfaced with a Contiuum IR microscope. H_2O concentrations were calculated from IR peak absorbance values using the Beer-Lambert Law. Doubly intersected melt inclusion wafers were prepared to be very thin to avoid host contamination during Fe XANES analysis (Muth and Wallace, 2021). Because of this, the CO_3^{2-} doublet normally used to quantify CO_2 concentration in basaltic glasses could not be deconvolved from interference fringes and therefore was not used. H_2O concentration was determined using the 3570 cm^{-1} OH$^-$ peak with absorption coefficient ε = 63 from Dixon et al. (1995). Thickness was determined using the interference fringe method (e.g. Wysoczanski and Tani, 2006) calculated using the Spectragryph software package (Menges, 2020). Hydrous densities were determined by iteration between calculated glass densities (Luhr, 2001) and Beer-Lambert calculations.

18

Most electron microprobe analyses (EPMA) were conducted using a Cameca SX-100 equipped with five wavelength dispersive spectrometers in the CAMCOR facility at the University of Oregon with a 15 kV accelerating voltage. A subset of olivine analyses were conducted on a JXA-8530FPlus HyperProbe Electron Probe Microanalyzer at the Smithsonian Institution with a 15 kV accelerating voltage. Analytical conditions varied slightly between sessions. Sample current, beam size, and counting times used during each session are given in Muth and Wallace (2021). Effects of element migration in glasses were corrected by performing linear regressions to time zero on Na, K, Al, and Si counts (Hanson et al., 1996; Morgan and London, 1996, 2005). Individual analyses for both olivine and glass are averages of 3-5 analyzed spots. S Kα peak positions used for sulfur analyses were determined based on average $S^{6+}/\Sigma S$ measured by XANES for each cinder cone and the relative offset between S Kα peak locations determined for troilite and anhydrite standards.

Melt inclusions and host olivines were analyzed for a suite of trace elements using Laser Ablation Inductively Coupled Mass Spectrometry (LA-ICPMS) during two different sessions. During the first session in June 2017, melt inclusions were analyzed on the Photon Machines Analyte G2 135 nm ArF "fast" excimer laser system at Oregon State University, using a 40 μm or 50 μm diameter spot size with a 5 Hz pulse rate. Measured trace element concentrations were determined by reference to GSE-1G glass as a calibration standard and using ^{43}Ca as an internal standard. BHVO-2G, BCR-2G, and GSD-1G glasses were also analyzed to monitor accuracy and precision. During the second session in February 2020, melt inclusions and host olivine were analyzed on a Thermo Scientific iCAP RQ and Photon Machines Analyte G2 193 nm ArF excimer laser at Oregon State University, using a 30 μm, 40 μm or 50 μm diameter spot size with a 15 Hz pulse rate. Measured trace element concentrations were determined by reference to NIST 612 glass as a calibration standard for most elements (see below) using ^{43}Ca as an internal standard for glass analyses, and ^{29}Si as an internal standard for olivine analyses. BCR-2G, GSD-1G, and BIR-1G glasses were also analyzed to monitor accuracy and precision.

Comparisons between measured and reference values (Jochum et al., 2007) on external check standards are shown in Supplementary Figure 1 for analyzed metals. Zn

and Pb analyses processed using NIST 612 as a reference standard yielded high concentrations relative to reference values. For these elements BIR-1G was chosen as the reference standard instead. Time-resolved ablation patterns were checked carefully for spikes indicating the ablation of metal-bearing daughter phases within inclusions, and any spikes were screened from processing. Dy concentrations measured during the 2017 session were scattered, with large uncertainties, and were excluded from the data presented here. During the 2017 session, a subset of analyses intersected melt inclusion vapor bubbles. During the 2020 session, higher sensitivity enabled us to choose ablation spots that avoided the ablation of vapor bubbles.

3.2 Primary magma estimates

To estimate primary melt composition at Lassen, the compositions of a subset of melt inclusions above a specified MgO content from each cone were averaged and used to calculate reverse olivine crystallization until each composition was in equilibrium with Fo_{90}. The MgO content used at each cinder cone was determined using MgO and Al_2O_3 bivariate plots, to avoid including melt inclusions whose compositions may have been affected by plagioclase fractionation before entrapment. For most inclusions, an MgO cutoff value was used to select the most primitive inclusions while still retaining enough inclusion compositions for a representative compositional average. For some cinder cones, there is scatter in the Al_2O_3 content in more evolved inclusions, which may represent variable plagioclase fractionation. In these cases, the MgO content was chosen so that these more scattered compositions were avoided. The average high-Mg compositions calculated for each cinder cone were used as a starting composition for reverse crystallization models. All reverse crystallization models were calculated using Petrolog3 at 5 kbar, using the Danyushevsky (2001) olivine temperature model and the Toplis (2005) K_d model. The S, Cl, H_2O, and trace element composition of primary magmas were calculated by diluting each element by the same amount that K_2O was diluted in the reverse crystallization models.
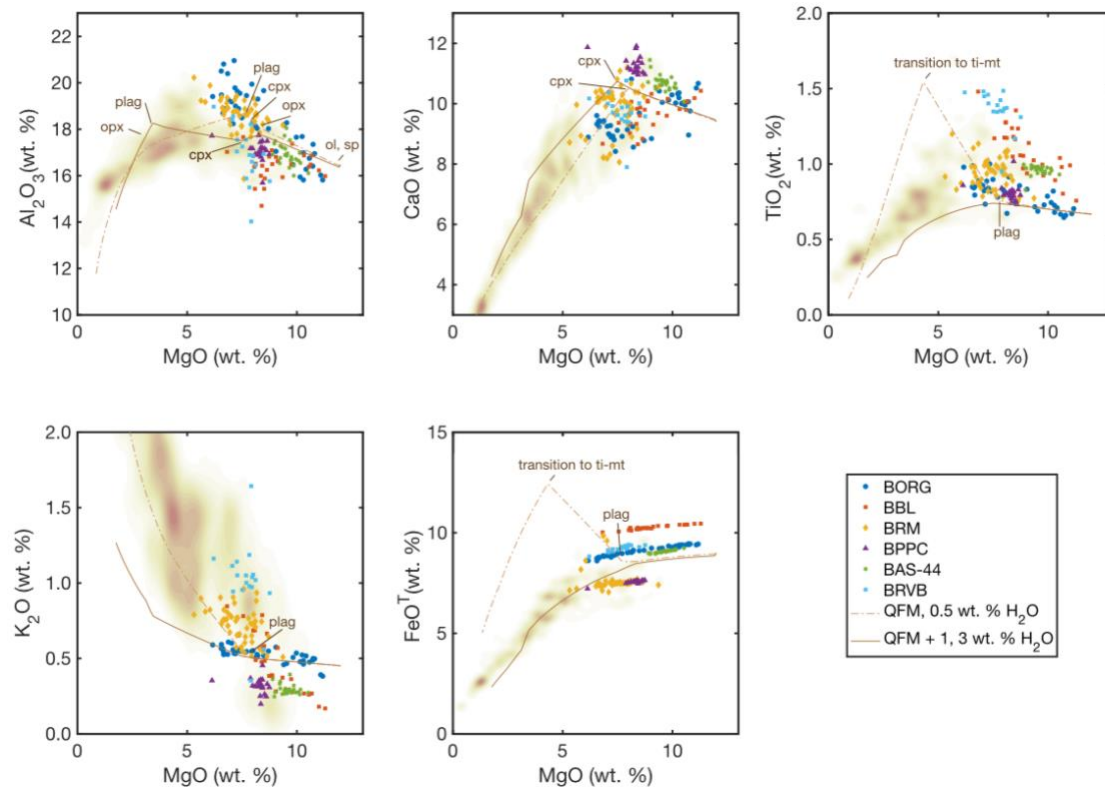
Figure 2. PEC-corrected Lassen melt inclusion compositions from current study and Walowski et al. (2016) from each cinder cone (colored circles) compared to Lassen whole rock compositions (beige density contour, Clynne et al., 2008) and MELTS fractional crystallization models. MELTS crystallization models were calculated at 400 MPa using estimated BORG primary magma as the starting composition. All mineral-in reactions are shown in the top left panel and selected key mineral-in reactions are shown in each panel.

4.0 Results

4.1 Major and trace elements

Host olivine forsterite contents range from Fo_{80} to Fo_{90}, with an average of Fo_{86}. Individual melt inclusion analyses were corrected for post-entrapment crystallization (PEC) and Fe-Mg re-equilibration using Petrolog3 (Danyushevsky and Plechov, 2011). Bulk rock data for each cinder cone studied here is limited, making it difficult to estimate initial FeO^T content for melt inclusions. To circumvent this, forward models of olivine crystallization were calculated using Petrolog3 at 5 kbar. Oxygen fugacity conditions are based on average calculated f_{O2} from measured $Fe^{3+}/\Sigma Fe$ data (Muth and Wallace 2021) and H_2O is based on average melt inclusion values. These olivine-only crystallization models are consistent with whole rock data from other mafic vents at Lassen (e.g. Borg et

al., 1997), which indicate that high-Mg Lassen magmas crystallize along an Fe-depletion trend consistent with olivine (+minor Cr-spinel) crystallization, and little to no contribution from plagioclase, pyroxene, or titanomagnetite crystallization.

For forward olivine crystallization models of each cinder cone, whole rock data with the highest FeO^T content were chosen as starting compositions. For cinder cones that have little (BBL) or no (BRM) bulk rock data, we used a composition based on average analyzed melt inclusions from each cinder cone and the 90th percentile value of measured melt inclusion FeO^T concentration. To estimate FeO^T concentration of each melt inclusion prior to Fe-Mg reequilibration, equilibrium olivine forsterite content was calculated for each melt inclusion composition. The FeO^T value from the forward olivine crystallization model for a given cinder cone that matched this olivine forsterite content was taken as the initial melt FeO^T. We emphasize that the choice of FeO^T value for correcting the melt inclusions from a given cone mainly affects the corrected MgO and FeO^T values and has only a small effect on other major and trace elements.

Melt inclusion compositions were then corrected for PEC and Fe-Mg reequilibration using Petrolog3, with our estimated initial melt FeO^T concentrations as input values. For the Petrolog calculations, the olivine temperature model used was Danyushevsky (2001), with Toplis (2005) used for olivine K_d. All reverse olivine crystallization calculations were performed using f_{O2} values calculated from Fe XANES data as described above for each cinder cone. If melt inclusions did not have measured H_2O contents, average H_2O contents from each cinder cone were used. A subset of inclusions from cinder cone BRM did not show evidence for Fe loss, so we instead calculated simple reverse olivine crystallization using Petrolog3 to correct for post-entrapment crystallization. For all inclusions, the S, Cl, and trace element concentrations for the Petrolog-corrected compositions were calculated by diluting each element's analyzed concentration by the same amount that K_2O was diluted. For consistency all measured melt inclusion compositions reported in (Walowski et al., 2016) have been corrected for PEC-and Fe-Mg re-equilibration in the same manner. For convenience we refer to all compositions that have been corrected for both PEC and Fe-Mg re-equilibration as 'PEC-corrected'.

Corrected melt inclusion compositions have 48-53 wt. % SiO_2, 6-11 wt. % MgO, and 0.18 – 1.11 wt. % K_2O. Melt inclusion compositions are similar to the major element compositions of whole rock analyses from other vents in the region but only overlap with the most primitive whole rock compositions (Fig. 2). K_2O contents in high MgO inclusions vary widely among cinder cones. Cinder cones BAS-44, BPPC, and BRVB contain a relatively restricted set of compositions, while cinder cones BORG, BRM, and BBL contain a range of compositions (Fig. 2, 3). Cinder cone BORG shows large increases in Al_2O_3, K_2O, and decreases in CaO with decreasing MgO. Cinder cone BBL shows relatively steady Al_2O_3 contents, strong increases in K_2O and TiO_2, and decreasing CaO with decreasing MgO.
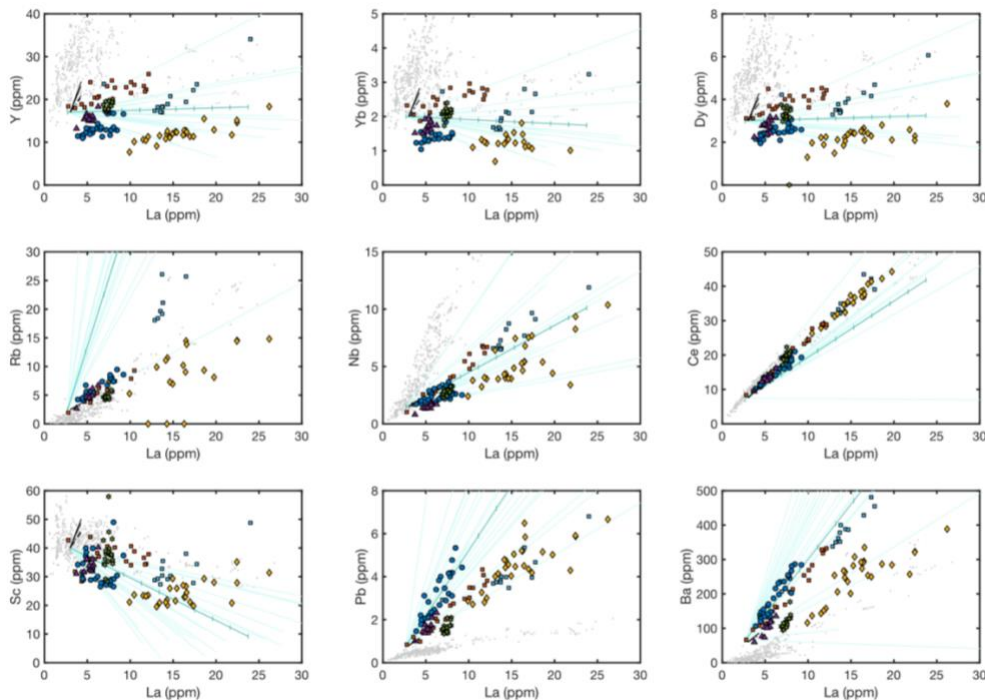
Figure 3. PEC-corrected Lassen melt inclusion compositions from current study and Walowski et al. (2016) from each cinder cone (colored circles) compared to MORB glasses (gray circles, Jenner et al., 2012). Each symbol represents one analyzed inclusion. Fractional crystallization models assuming 0 to 30 % crystallization shown for olivine (solid line), 20 % olivine and 80 % amphibole (short dashed line), and 90 % olivine and 10 % garnet (long dashed line). Thin blue lines show mixing calculations between a representative Lassen primitive magma composition and measured samples of northern Sierra Nevada batholith (Cecil et al., 2012). Thick line shows mixing calculated with the averaged composition of all samples. Tick marks represent 10 % mixing intervals.

4.2 Volatile elements

Lassen melt inclusions contain an average S content of 1400 ± 600 ppm, similar to the range of values measured in melt inclusions from Central Oregon (Ruscitto et al., 2010). H_2O, Cl, and S co-vary among cinder cones as demonstrated in previous work at Lassen (Walowski et al., 2016; Muth and Wallace, 2021).
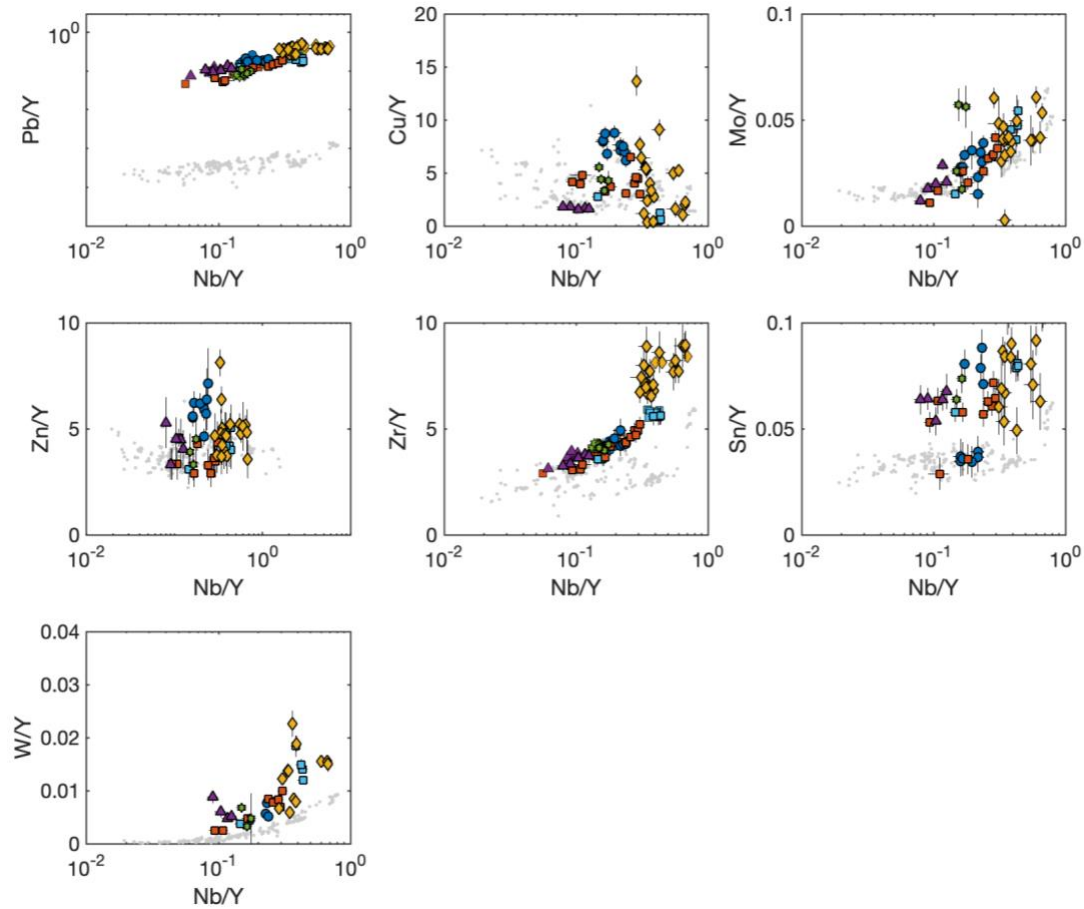
Figure 4. Lassen melt inclusion compositions from current study and Walowski et al. (2016) from each cinder cone. Error bars represent propagated analytical standard error. MORB glass compositions (gray circles, Jenner et al., 2012) shown for comparison.
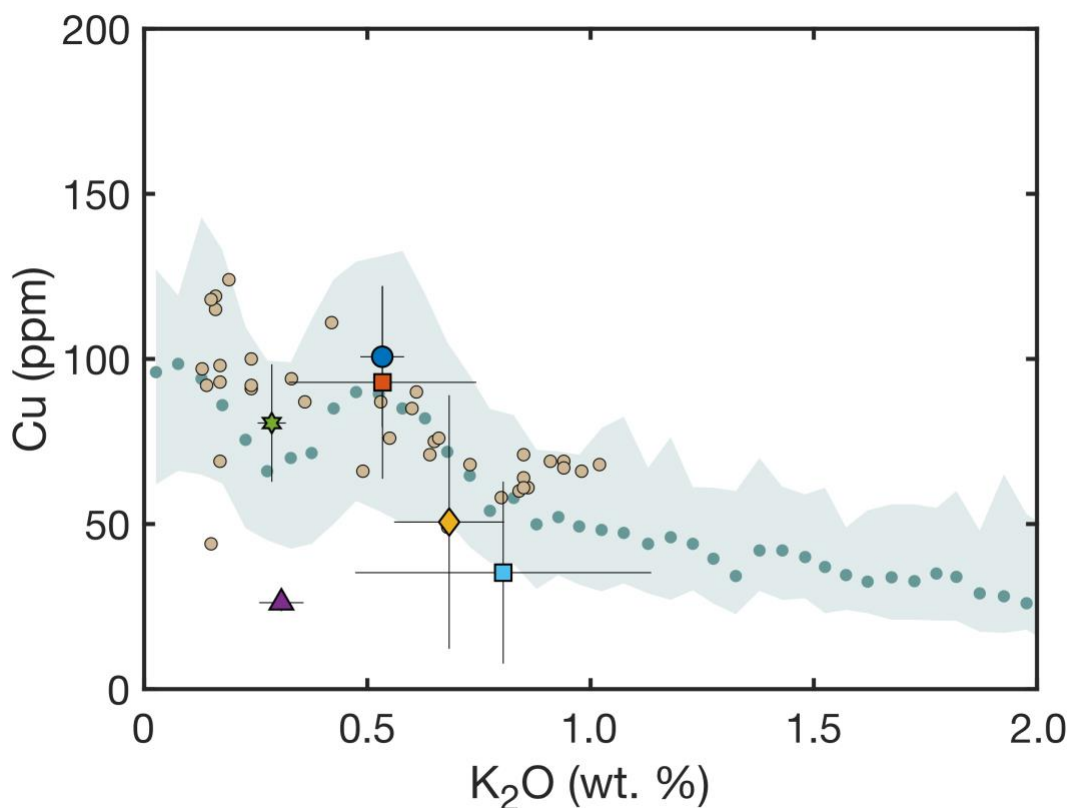
Figure 5. Average analyzed Cu contents in melt inclusions from each cinder cone plotted against K_2O. Error bars represent 2σ standard deviation from calculated average. Beige circles are whole rock analyses from primitive (MgO > 8 wt. %) Lassen samples (Clynne et al., 2008). Blue circles are median compositions of primitive whole rock analyses from arcs globally (Barber et al., 2021) binned by 0.05 wt. % K_2O increments. Shaded regions represent upper and lower quartiles within each bin.

4.3 Metal contents

PEC-corrected Cu concentrations of Lassen melt inclusions vary from 4 to 324 ppm, with an average concentration of 92 ppm (Fig. S2). Zn concentrations vary from 40 to 199 ppm with an average of 77 ppm. Mo concentrations vary from 0.15 to 1.20 ppm with an average of 0.53 ppm. W concentrations range from 0.04 to 0.40 ppm, with an average of 0.10 ppm. Pb concentrations range from 1.0 to 6.7 ppm, with an average of 3.4 ppm. The concentrations of most metals are similar or only slightly elevated compared to those of MORB (Fig. 4). In contrast, Pb shows clear elevations relative to MORB in all cinder cones. Cu contents measured in melt inclusions are consistent with primitive Lassen whole rock data, except for cinder cones BPPC and BRVB where Cu contents are

slightly lower. Whole rock data and inclusion compositions from Lassen show a wide range of Cu contents at low K_2O content, and an inverse correlation between Cu and K_2O (Fig. 5).

Roughly 25% of melt inclusions contain a visible sulfide bleb ranging from 2-12 μm in diameter, typically less than 0.1 volume % of the MI. These sulfide blebs are quenched immiscible sulfide liquids (e.g. Patten et al., 2012). They are most common in cinder cones BRVB and BBL but are present in all cinder cones except for BRM and BPPC. They are found most commonly in inclusions with relatively low analyzed FeO^T (Fig. 6). Olivine phenocrysts occasionally contain sulfide inclusions or melt inclusions dominated by large, obviously co-trapped sulfide blebs. However, these olivine-hosted sulfide inclusions are rare and have only been observed in cinder cone BORG and BRVB. It therefore seems most probable that the small sulfide blebs formed after entrapment during simultaneous cooling, Fe-loss caused by Fe-Mg re-equilibration, and PEC-driven S enrichment.

Although the quenched sulfide liquids make up only a small proportion of the inclusion volume, they can host a large proportion of the inclusion Cu. Depending on inclusion size and initial Cu content, a 5-10 μm diameter sulfide bleb formed after entrapment can easily extract over 100 ppm Cu from the co-existing melt (Fig. S3). Nevertheless, there are no clear depletions in Cu within inclusions that contain sulfide and no relationship between analyzed melt inclusion FeO^T content and Cu content (Fig. S4), as would be expected if sulfides grew and sequestered Cu during Fe-loss from the inclusion. This suggests that some other mechanism is at play in controlling the Cu content of melt inclusions. At temperatures relevant to melt inclusion storage (1100 °C), Cu can diffuse through olivine host crystals on the timescales of months to years (Audétat et al., 2018). Lassen melt inclusions show a clear inverse correlation between analyzed FeO^T and olivine host forsterite content (Fig. S5), which indicates near complete inclusion Fe-Mg equilibration with the olivine host ('Trend 1' of Danyushevsky et al., 2000). This Fe-Mg equilibration process also requires months to several years for melt inclusions of the size analyzed here (Danyushevsky et al., 2000). Therefore, it is likely that melt inclusion Cu contents have diffusively re-equilibrated with the external melt during Fe-Mg re-equilibration and the formation of daughter sulfide liquids. The $SCSS^T$

values of melt inclusions are unlikely to have changed drastically during final ascent and eruption, and Cu diffuses through olivine too slowly to respond to any potential changes in external melt Cu content during ascent and eruption (Audétat et al., 2018). We therefore take analyzed melt inclusion Cu values as representative of the stored melt prior to eruption.
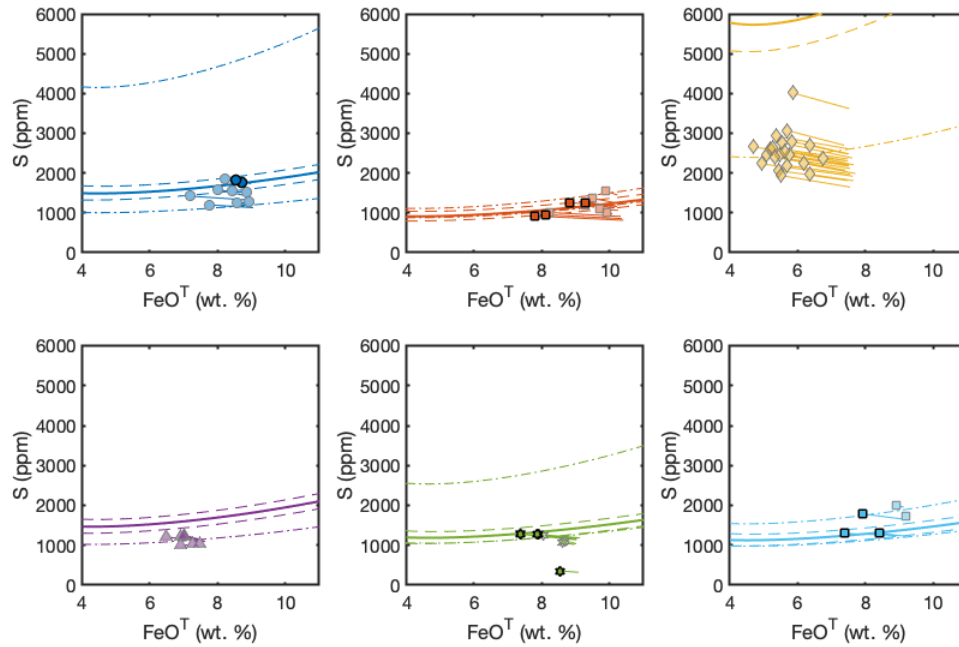
Figure 6. Analyzed S and FeO^T contents of Lassen melt inclusions that have available petrographic data. Light symbols are melt inclusions without sulfides, and dark symbols are inclusions with sulfides. Lines from each symbol show the S and FeO^T content of the inclusion composition corrected for PEC and Fe-Mg re-equilibration. Colored curves represent $SCSS^T$ calculated using the model of Smythe et al. (2017), with the H_2O dependence of Liu et al. (2021) and the oxygen fugacity dependence of Jugo et al. (2010). For each cinder cone $SCSS^T$ was calculated using the average melt inclusion composition, average calculated storage temperature (Sugawara 2000), average oxygen fugacity calculated via measured $Fe^{3+}/\sum Fe$ within melt inclusions from each cinder cone, and pressure estimates based on melt inclusion H_2O and CO_2 barometry of BORG and BRVB (Aster et al., 2016). Short, dashed lines represent $SCSS^T$ calculated using ± one standard deviation of average oxygen fugacity at each cinder cone, and long, dashed lines represent $SCSS^T$ calculated using ± 50 °C.

Cu contents of host olivine phenocrysts are similar to estimates based on the olivine partitioning model of Portnyagin et al. (2017, Fig. S2). However, melt inclusions from BRVB and BRM both show a large range of melt Cu contents at a relatively constant olivine Cu content, forming an upper limit near values based on the partitioning

model of Portnyagin et al. (2017). These patterns raise the question of whether post-entrapment processes have taken MI out of equilibrium with their olivine host. One post-entrapment mechanism that can affect measured glass Cu concentrations is rapid changes to the stability of sulfides in the inclusion. Sulfide stability can decrease with decreasing melt H_2O, temperature, or f_{O2} (Jugo et al., 2010; Smythe et al., 2017; Liu et al., 2021). Cu also becomes more compatible in sulfide with decreasing temperatures (Kiseeva and Wood, 2015). Each of these properties can equilibrate rapidly in olivine (Portnyagin et al., 2008; Gaetani et al., 2012; Humphreys et al., in review). Therefore, rapid equilibration of a melt inclusion with an external melt that is cooling, losing H_2O, or changing f_{O2} can redistribute Cu between melt and sulfide before melt Cu content re-equilibrates with host olivine and external melt. Many of the inclusions with high Cu contents relative to their olivine hosts have anomalous trace element compositions that suggest the influence of crustal assimilation, as discussed in the next section, indicating that some more complex pre- or post-entrapment processes may be influencing their Cu contents. These anomalous inclusions are not included in primary magma calculations and their metal contents are not shown in main text figures. A portion of inclusions in BRVB contain a sulfide, and D/H measured in melt inclusions from BRVB show clear evidence for partial H^+ diffusive reequilibration (Walowski et al., 2015). This rapid decrease in silicate melt H_2O and associated decrease in $SCCS^T$ may explain the array toward low Cu values in BRVB inclusions.

However, post-entrapment changes in sulfide stability cannot explain changes in BRM melt inclusion Cu contents, which trend toward lower melt Cu values but do not contain any visible sulfide blebs. An alternative explanation is that Cu partitioned into the inclusion vapor bubble, because vapor bubbles can change in composition over very short timescales due to diffusive H^+ loss from the MI. Cu vapor bubble partitioning has been documented in quartz-hosted inclusions (e.g. Lowenstern et al., 1991) although experiments in intermediate magmas at oxidizing conditions suggest Cu vapor partitioning is minimal in more mafic magmas (Zajacz et al., 2012). Melt inclusions from BRM do not contain visible precipitates on bubble walls (e.g. Kamenetsky and Kamenetsky, 2010; Wieser et al., 2020) and Cu contents do not correlate with melt H_2O contents, Cl contents, S contents, vapor bubble diameters, or inclusion diameters. Laser

ablation analyses that intersected vapor bubbles similarly do not show Cu spikes indicating the ablation of Cu-bearing precipitates. We cannot definitively rule out vapor bubble Cu partitioning based on these observations alone, however we note that the general patterns in Cu concentrations among cinder cones are consistent between melt inclusion and host olivine.

5.0 Discussion

5.1 Compositional variations at individual cinder cones

Although melt inclusion compositions at Lassen cinder cones are generally consistent with the olivine-dominated fractionation trends of high-Mg whole rock data, individual cinder cones show a range of behavior (Fig. 2). Here we focus on BORG and BBL, which show the most coherent major and trace element trends, and we use estimated BORG primary magma as a starting composition to model fractional crystallization paths using Rhyolite MELTS (Gualda et al., 2012), for comparison with Lassen melt inclusion and whole rock data. BORG melt inclusion Al_2O_3 and TiO_2 contents increase over the crystallization interval, indicating little to no crystallization of plagioclase or titanomagnetite. CaO in more evolved inclusions decreases with decreasing MgO content, indicating the influence of clinopyroxene. Rhyolite MELTS models run at 400 MPa, 3 wt. % H_2O, and at QFM +1 provide an adequate fit to most melt inclusion data, except for clinopyroxene stability, which MELTS underpredicts relative to the natural data set. Decreasing CaO contents may indicate early clinopyroxene crystallization at depth, which has been reproduced experimentally in hydrous basaltic compositions at 700-900 MPa (Blatter et al., 2013). MELTS predicts an increase in spinel Al content at ~8 wt. % MgO which moderates the melt Al_2O_3 increases relative to olivine only crystallization. However, BORG melt inclusions show a stronger increase in Al_2O_3 content than predicted by MELTS, despite good agreement with incompatible elements K_2O and TiO_2, suggesting that any crystallizing spinel phase was closer to chromite in composition.

BBL shows moderate increases in Al_2O_3 with decreasing MgO. However, there is also scatter to low Al_2O_3 values, suggesting plagioclase crystallization. This early precipitation of plagioclase is not reproducible in MELTS even varying pressure down to

200 MPa and H$_2$O content down to 0.1 %. Similar to clinopyroxene, periods of high-pressure storage may drive earlier plagioclase crystallization (Villiger et al., 2004). However, although strong increases in K$_2$O and TiO$_2$ at BBL with decreasing MgO are broadly consistent with plagioclase crystallization, these increases require extremely high (~50-70 %) degrees of crystallization.

Inclusions from cinder cones BAS-44, BRVB, BRM and BPPC do not span enough of a compositional range to identify clear patterns. Cinder cones BAS-44 and BPPC are both consistent with a low-K parent magma, whereas BRVB and BRM are more enriched in K$_2$O and TiO$_2$.

Early crystallization of clinopyroxene and plagioclase may signal the influence of high-pressure differentiation, consistent with high (~700 MPa) pressure fractionation observed in high Mg basaltic andesites in the same region (Hollyday et al., 2020), although melt inclusion thermobarometry on inclusions from BORG and BRVB indicate most melt inclusions from these cinder cones have more shallow entrapment depths (Aster et al., 2016). Inclusions from some cinder cones show slight TiO$_2$ depletions relative to K$_2$O, although this may be due to fractionation during mantle melting (Fig. 7).
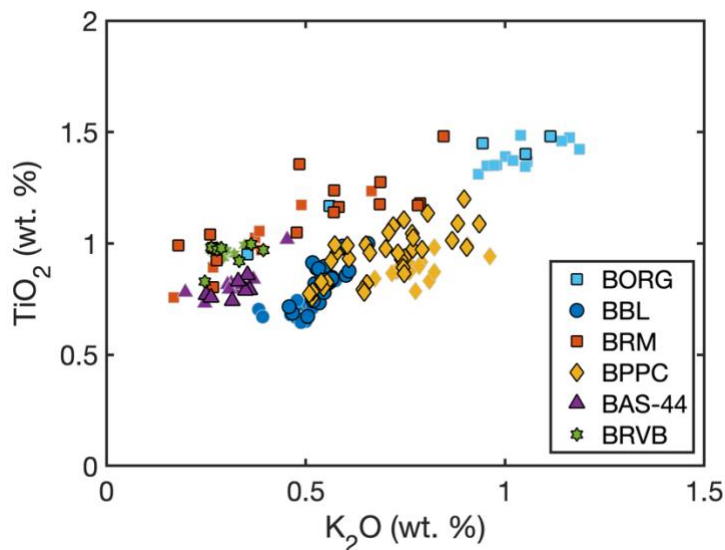
Figure 7. PEC-corrected Lassen melt inclusion compositions from each cinder cone. Inclusion compositions from Walowski et al. (2016) shown in gray outlined symbols. Each symbol represents one analyzed inclusion.

The trace element systematics at Lassen cinder cones are variable (Fig. 8), and some (BBL) show a large range in trace element concentrations (Fig. 3). Some cinder

cones are elevated in Dy/Yb compared to MORB (Fig. 9), which suggests that garnet fractionation may have played some part in petrogenesis, consistent with previous work demonstrating that that HREE trends are likely inherited from garnet-present slab melting (Walowski et al. 2016). Generating HREE trends via garnet or amphibole crystallization requires unrealistically high (> 50 %) degrees of crystallization and cannot consistently reproduce fractionation between different HREE elements. Lack of garnet or amphibole crystallization is consistent with phase stability considerations. Melt inclusion entrapment temperature estimates based on the thermometer of Sugawara (2000) range from 1089 to 1256 °C, with an average of 1178°C. In contrast, even at high (> 400 MPa) pressures amphibole is not stable above 1050 °C (Krawczynski et al., 2012; Blatter et al., 2013; Nandedkar et al., 2014; Waters et al., 2020). In magmas with modest H_2O contents like those at Lassen (Walowski et al., 2015, 2016), amphibole stability will be shifted toward even lower temperatures. H_2O enhances the thermal stability of garnet, but garnet has not been observed at pressures relevant to crystallization in experiments above ~1050 °C (Müntener and Ulmer, 2006; Alonso-Perez et al., 2009; Ulmer et al., 2018).

To assess the impact of crustal assimilation we calculate mixing between Lassen cinder cones and measured northern Sierra Nevada granite compositions, as assimilation of northern Sierra Nevada granite exerts a major control on the composition of lavas and tephra at Cinder Cone, near Mount Lassen (Walowski et al., 2019). The majority of melt inclusions studied here show no evidence for crustal assimilation. However, a more evolved set of inclusions in cinder cone BORG show enrichment in Ba and Pb and depletions in Sc and Nb that are consistent with ~10 % assimilation of granitic host rock (Fig. 7). These high Ba, low Nb inclusions also have Cu contents that are anomalously high compared to other melt inclusions and the whole rock record. (Fig. S6). Because this work focuses on the generation and early crystallization of mantle-derived melts, these anomalous compositions are excluded from calculations of primary magma estimates and their metal contents are not included in main text figures.

5.2 Mantle melting beneath the Lassen region

Comparisons between calculated primary melt compositions at each cinder cone (see Methods) and mantle melting models show that cinder cones at Lassen require

enriched ambient mantle sources relative to depleted MORB-source mantle (DMM, Fig. 8). Here we define the ambient mantle composition as the composition of the mantle prior to modern subduction (Turner et al., 2017). For trace elements that are dominated by mantle rather than slab contributions (e.g. Pearce and Peate, 1995), primary melts are reproduced by ambient mantle source compositions intermediate between DMM and the average enriched mantle source estimated for the central Oregon Cascades (Ruscitto et al., 2010). The latter enriched mantle source is similar in composition to the mantle sources of ocean island basalts (OIB) and is therefore referred to as 'OIB-like'. This is consistent with spinel compositions (Clynne and Borg, 1997), trace elements (Borg et al., 1997), and isotope systematics (Underwood and Clynne, 2017; Borg et al., 2002; Walowski et al., 2016), which indicate Lassen magmas formed from a mantle source affected by variable degrees of depletion/enrichment. We follow the approach of Borg et al. (1997) and model the ambient mantle source for Lassen cinder cones using mixtures of MORB-source mantle (DMM; Workman and Hart, 2005) and an enriched OIB-like mantle source (Ruscitto et al., 2010). Batch melting is calculated using mineral modal proportions as described in Walowski et al. (2016) and mineral melt partition coefficients as described in Venugopal et al. (2020). We find that two distinct mantle compositions calculated using DMM mixed with 15% and 70% of OIB-like mantle reproduces the range of Lassen primary magmas well. Primary magmas for cinder cones BBL, BORG, BAS-44, and BPPC are all reproduced well by melting of a 15% OIB-like source mantle, while BRM and BRVB require a 70% OIB-like source mantle.

We conclude that the variations in incompatible element concentrations and HREE systematics in Lassen magmas that cannot be reproduced by crystallization (Fig. 3) instead represent variable partial melting of a heterogeneous ambient mantle (Fig. 8, 9). This is consistent with melt inclusions suites in MORB (Sobolev and Shimizu, 1993; Schiano, 2003; Laubier et al., 2007), Iceland (MacLennan 2008), and arcs (Iveson et al., 2021) that show melt inclusions may capture melts representing more variable melt batches prior to later mixing and homogenization. Lassen melt inclusions from each cinder cone studied here overlap with measured trace element and isotope whole rock compositions measured in the same cinder cone (Walowski et al., 2015). This overlap is consistent with the mixing and homogenization of small magma batches generated via

variable melt fractions and from variable mantle sources to form the pre-eruptive magmas at each cone. We note however that because Cu in olivine-hosted melt inclusions can diffusively equilibrate with the surrounding melt on the timescales of months to years (Audétat et al., 2018), inclusion Cu contents may not capture this pre-mixing variation.
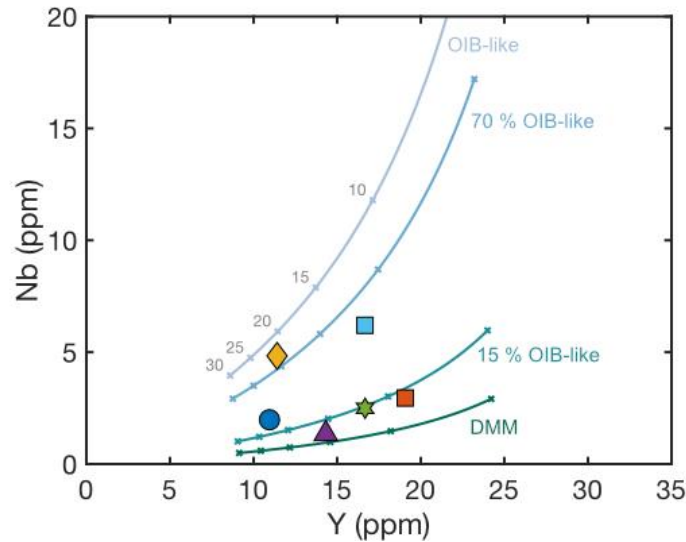
Figure 8. Calculated Lassen primary magma compositions compared to batch melting models of an OIB-like enriched mantle composition (light purple), DMM (dark green) and two intermediate mantle compositions (70 % enriched mantle, light blue; 15 % enriched mantle, dark blue). Labeled tick marks represent modeled melt fraction. Mantle compositions are described in detail in the text.
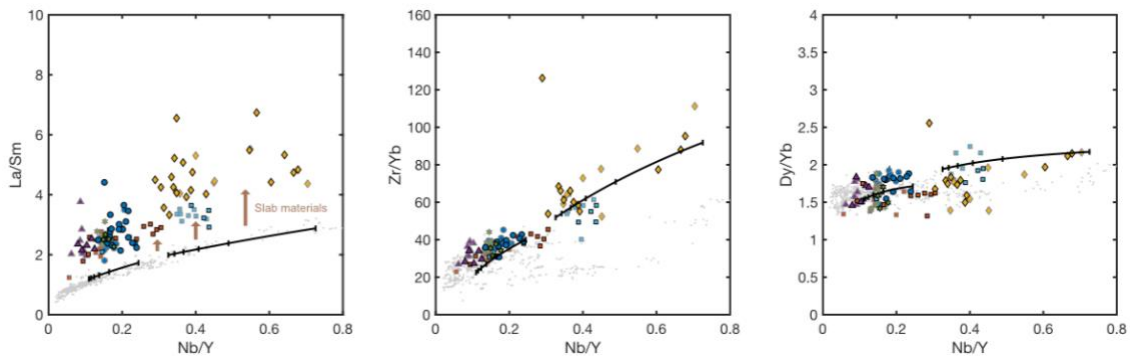
Figure 9. Lassen melt inclusion compositions from the current study and Walowski et al. (2016) from each cinder cone. Each symbol represents one analyzed inclusion. Black lines show 5 to 30 % batch melting of two distinct mantle compositions as described in the text, and each tick mark represents 5 % melt increments. MORB glasses shown for comparison in gray circles (Jenner et al., 2012).

33

Separate from ambient mantle heterogeneity, there is a modern subduction influence at Lassen shown most clearly through variation in the Sr content of primary magmas (Fig. 10, 11; Borg et al., 1997, 2002; Walowski et al., 2016). The combined effects of ambient mantle heterogeneity and modern subduction-component addition are consistent with observations in other continental arc regions (e.g. Iveson et al., 2021; Turner et al., 2017). The influence of modern subduction in the mantle source of each cinder cone drives increases in the H_2O, Cl, S content and oxidation state of Lassen primary magmas (Fig. 11; Walowski et al., 2015, 2016; Muth and Wallace, 2021). Combined melting and Fe-S redox equillibrium calculations suggest this enrichment in S and oxidation state may require a more complex, multi-stage process, consistent with the presence of ambient mantle heterogeneities (Muth and Wallace, 2021).
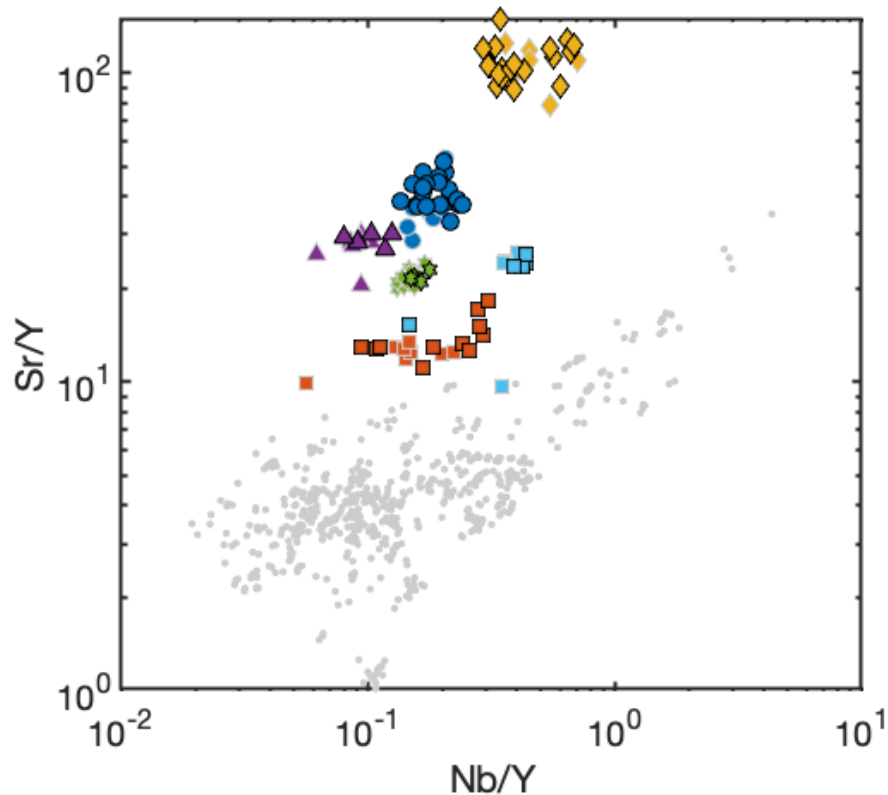
Figure 10. Lassen melt inclusion compositions from Walowski et al. (2016) and current study from each cinder cone. Each symbol represents one analyzed inclusion. MORB glasses (gray circles, Jenner et al., 2012) shown for comparison.
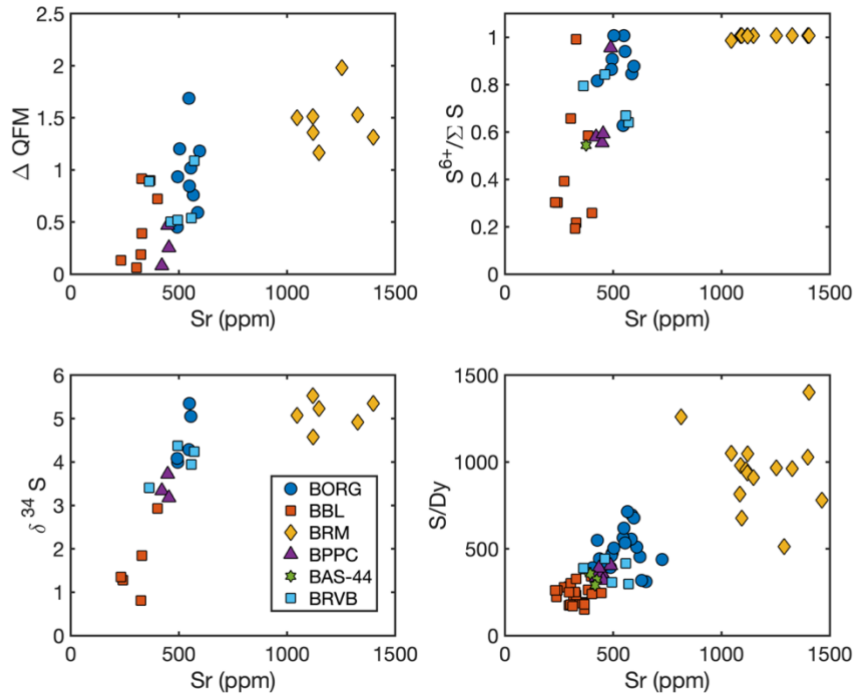
Figure 11. PEC-corrected Sr concentrations in Lassen melt inclusions plotted against oxygen fugacity values, $S^{6+}/\sum S$ values, $\delta^{34}S$ and S/Dy as reported in Muth and Wallace (2021). Each symbol represents one analyzed inclusion.

5.3 Sulfide stability during mantle melting and early crustal storage

Whereas REE concentrations in Lassen primary magmas can be estimated using reverse olivine crystallization calculations alone, estimating the concentration of chalcophile elements in primary magmas also depends closely on the stability of sulfide during mantle melting and early crustal storage. There is a demonstrated inverse pressure effect on $SCSS^T$, which means that sulfide-saturated melts that ascend from the mantle into the crust can become sulfide-undersaturated if ascent is close to adiabatic (Mavrogenes and O'Neill 1999). However, this pressure effect is offset to some extent by decreasing temperature and changing melt composition, both of which decrease $SCSS^T$ (Smythe et al., 2017). To assess whether mantle melts precipitated sulfides between mantle melting and melt inclusion entrapment, we compare conditions of mantle melting and melt inclusion entrapment to $SCSS^T$ models calculated at QFM, using the average PEC-corrected inclusion compositions and primary melt compositions of cinder cone BORG as an example (Fig. 12). We choose to calculate values at QFM to provide a

simple comparison between P-T conditions but note that magmas beneath most cinder cones at Lassen are more oxidized and would therefore have a higher calculated $SCSS^T$. To calculate $SCSS^T$, we combine the model of Smythe et al. (2017) with the H_2O dependence described in Liu et al. (2021), as well as the oxygen fugacity dependence described in Jugo et al. (2010). We assume sulfide liquid XFeS = 0.85 based on the composition of quenched sulfide liquids measured in basalts and basaltic andesites from Ecuador (Georgatou et al., 2018) and consistent with magmatic sulfides in igneous rocks within the New Hebrides, Tonga, and Kermadec arc segments (Keith et al., 2017). BORG parental melts could have precipitated 100-200 ppm S between segregation of the melt from the last-equilibrated mantle source and melt inclusion entrapment in the crust, corresponding to ~130 ppm Cu sequestration in sulfide depending on the initial melt S and Cu content (Kiseeva and Wood, 2015). However, this is a maximum estimate- in Lassen magmas, which contain a significant proportion of melt S^{6+}, the effect of pressure on S-Fe redox equilibrium may outweigh the temperature and compositional effects on SCSS (Matjuschkin et al., 2016; Rezeau and Jagoutz, 2020).

To assess how close Lassen magmas were to sulfide saturation during early crystallization and melt inclusion entrapment, we compare petrographic observations of melt inclusions, $SCSS^T$ models, and analyzed melt inclusion S contents. Approximately 25% of the melt inclusions studied here contain small, quenched sulfide liquids that likely formed in the inclusions after entrapment. These co-existing sulfide and silicate liquids are a useful natural experiment, as they represent a natural, sulfide-saturated silicate melt that we can accurately characterize using analyzed glass compositions. To take advantage of this, we calculate $SCSS^T$ using the model formulation as described above, again assuming sulfide liquid XFeS = 0.85 (Georgatou et al, 2018). S concentrations measured in melt inclusions containing quenched sulfides agree well with predicted $SCSS^T$ values (Fig. 6). This good agreement adds confidence that our chosen $SCSS^T$ model performs well for Lassen magmas at crustal conditions.
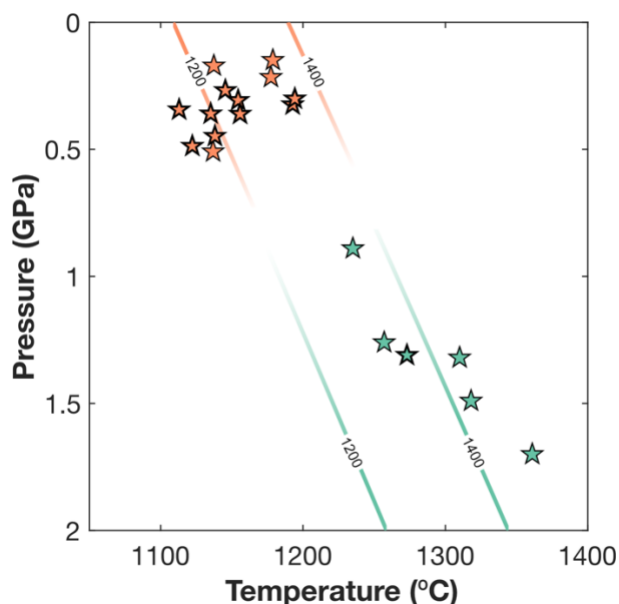
Figure 12. Estimated conditions of Lassen magmas during last melt equilibration in the mantle (green stars) and melt inclusion entrapment (orange stars). Symbols with thick outlines represent P-T estimates for inclusions from BORG, while thin outlined symbols represent P-T estimates for inclusions from other cinder cones. Pressures of entrapment were calculated using the VesiCal thermodynamic engine (Iacovino et al., in press) and the MagmaSat solubility model (Ghiorso and Gualda, 2015) based on corrected melt inclusion H_2O and CO_2 values reported in Aster et al. (2016) from cinder cones BORG and BRVB. Temperature of entrapment calculated via the hydrous thermometer of Sugawara (2000). Pressure and temperature of mantle melt equilibration for Lassen primary magmas calculated via the thermobarometer of Lee et al. (2009). Green contours show calculated $SCSS^T$ values in ppm based on estimated BORG primary magma composition as described in the text. Orange contours show calculated $SCSS^T$ using the same model with average PEC-corrected melt inclusion compositions from BORG.

Sulfides within melt inclusions indicate that mafic magmas at Lassen were near or at sulfide saturation during early crystallization and melt inclusion entrapment. To assess how far entrapped melts were from sulfide saturation, we compare melt inclusion compositions that have been corrected for PEC and Fe-Mg reequilibration to the same $SCSS^T$ models described above (Fig. 6). Offsets between analyzed and corrected melt inclusion compositions illustrate the combined effect of S enrichment and Fe-loss that occurs during PEC and Fe-Mg re-equilibration. Comparisons between analyzed and corrected compositions show that many sulfides within inclusions could have formed during melt inclusion cooling, S enrichment and Fe loss. Differences in $SCSS^T$ between

analyzed and corrected compositions represent the maximum distance from sulfide saturation for entrapped silicate melts.

To add another constraint on the distance from sulfide saturation for entrapped silicate melts, we use the measured diameter of quenched sulfide liquids and host melt inclusions to estimate the relative volume of the sulfide and the total inclusion. We make the simplifying assumption that the sulfide liquid and melt inclusion are both a perfect sphere and use the density of each phase (Mungall and Su, 2005), the analyzed sulfur content of the glass, and the stoichiometric S content of a simple sulfide liquid (FeS) to calculate the amount of sulfur hosted in the sulfide.

For melt inclusions from BAS-44, the difference between calculated $SCSS^T$ at average entrapment conditions (1516 ppm) and average calculated $SCSS^T$ for low FeO^T analyzed compositions (1271 ppm) is 245 ppm. This means that if the melts were sulfide saturated on entrapment, all changes in melt S content during post-entrapment processes would be accommodated by a sulfide phase, and sulfides would contain ~245 ppm S. Mass balance calculations based on measured sulfide and melt inclusion diameters indicate that sulfides hold 165 ± 43 ppm S, where uncertainty is the standard deviation of the calculated average. This comparison suggests that melts at BAS-44 were approximately 80 ppm S away from sulfide saturation upon entrapment.

Sulfide sizes are more variable in BBL, with an average of 199 ± 160 ppm S, so we take two melt inclusions, BBL-5 44 and BBL-5 47, with low analyzed FeO^T and similar analyzed S concentration as examples. The sulfide in BBL-5 47 contains 26 ppm S, and the sulfide in BBL-5 44 contains 250 ppm. In comparison, the average difference between calculated $SCSS^T$ at entrapment (1372 ppm) and calculated $SCSS^T$ for analyzed compositions (1137 ppm) is 235 ppm. This suggests that one inclusion was ~200 ppm S away from sulfide saturation upon entrapment, while the other was likely sulfide saturated. Variations in S content are consistent with the wide range of trace element compositions at BBL (Fig. 3).

One inclusion from cinder cone BRVB contains a large sulfide bleb with an estimated 1052 ppm S, far more sulfur than can be sequestered by typical post-entrapment processes as detailed above. The combined glass and sulfide S content is also much higher than S contents of other melt inclusions from BRVB. These observations

indicate that this was likely a primary sulfide that was co-trapped with silicate melt when the melt inclusion formed. No other large sulfides are observed in olivine from BRVB, in melt inclusions or hosted directly in olivine. The average difference between calculated $SCSS^T$ at entrapment (1400 ppm) and calculated $SCSS^T$ for analyzed compositions in low FeO^T inclusions (1274 ppm) at BRVB is 126 ppm. However, D/H ratios in melt inclusions from BRVB show clear evidence for diffusive loss of up to 2 wt. % H_2O (Walowski et al., 2015). Melt inclusions from BRVB with sulfides contain an average analyzed H_2O content of 0.6 wt. %, whereas melt inclusions without sulfides contain an average analyzed H_2O content of 2.0 wt. %. This difference in H_2O content corresponds to a 194 ppm S shift in $SCSS^T$. Taking this H_2O difference into account, an updated $SCSS^T$ value for entrapment is 1594 ppm, and the difference between $SCSS^T$ calculated for entrapment and analyzed compositions is 326 ppm S. Sulfides in BRVB inclusions contain 135 ± 77 ppm S, which suggests BRVB melt inclusions were ~190 ppm S away from sulfide saturation during entrapment.

The other three Lassen cinder cones (BORG, BRM, BPPC) were likely further away from sulfide saturation during entrapment. At BORG, the two inclusions containing sulfides have anomalous compositions likely affected by crustal assimilation (Fig. S4, S6). Sulfur contents from most other BORG inclusions are below predicted $SCSS^T$ values and do not contain visible sulfides (Fig. 6), which suggests that BORG magmas were not close to sulfide saturation upon entrapment. Melt inclusions from BRM and BPPC have S contents below predicted $SCSS^T$ values and inclusions also do not contain sulfides.

Collectively, these observations suggest Lassen magmas at BBL, BRVB, and BAS-44 were within 200-300 ppm S of $SCSS^T$ during entrapment, and inclusions from cinder cones BORG, BRM, BPPC were more strongly sulfide undersaturated. Comparisons between sulfide sizes and $SCSS^T$ models in BBL, BRVB, and BAS-44 suggest that most inclusions from these cinder cones were sulfide undersaturated upon entrapment, except for a small subset of larger inclusion-hosted sulfides in cinder cones BBL and BRVB. A period of early, sulfide-undersaturated, olivine-dominated crystallization is consistent with an inventory of sulfides hosted in arc basalt and basaltic andesites in Ecuador, where sulfide inclusions were found within host phenocrysts in a

wide variety of volcanic rocks spanning basalts to andesites, except for mafic volcanic rocks containing only olivine phenocrysts (Georgatou et al, 2018).

5.4 Metal contents of Lassen magmas

Most metal concentrations show limited or small (Sn, W, Zn) evidence for mobility except for Pb, which shows clear elevations relative to MORB (Fig. 3,4,13). This pattern of limited metal mobility of Sn, W, and Mo, and high mobility of Pb is consistent with the work of Noll et al. (1996) comparing metal contents in several arcs globally, where it is suggested that complexing with reduced aqueous species such as H_2S and OH^- may enhance Pb mobility in slab-derived fluids. Measured Pb contents in meta-basalts from exhumed slabs also suggest that most Pb is hosted in silicate minerals and is therefore relatively insensitive to sulfide stability (Walters et al., 2021), making it more likely to be removed from the slab during periods of dehydration and/or slab melting. Since the study of Noll et al. (1996) the resolution of Mo and W measurements have improved, and Mo and W enrichments have been found in some arc magmas with high sediment influence (König et al., 2008, 2010). This mobility may depend on the composition of slab fluids (König et al., 2008; Bali et al., 2012) and/or the stability of rutile within the slab (Bali et al., 2012). Although measured concentrations of metals in exhumed meta-basalts suggest Zn may be expelled into the sub-arc mantle (Walters et al., 2021), Zn is not enriched in Lassen magmas. This inconsistency may be due to sequestration of Zn in the lower oceanic crust (Jenner, 2017) or low solubility in slab-derived fluids (Kogiso et al., 1997), although Zn mobility may be higher in slab-derived melts (Canil et al., 2017).

Measurements of Cu concentrations in exhumed meta-basalts suggest that most, if not all slab Cu is hosted in sulfides in contrast to Pb which is hosted dominantly in silicates (Walters et al., 2021), and would be completely released during sulfide destabilization during slab dehydration or melting. Trace element systematics in the Mariana back-arc suggest Cu is partially derived from the subducting slab (Stolper and Newman 1994). Cu mobility is not necessarily inconsistent with the lack of clear correlations between magma Cu and Sr at Lassen, because mantle sulfide saturation may mask small mantle Cu enrichments. However, a lack of slab-derived Cu enrichment is

consistent with Cu contents measured in mantle xenoliths, which are rarely elevated relative to the primitive upper mantle (Lorand and Luguet, 2016), even for xenoliths that are strongly metasomatized (Luhr and Aranda-Gómez, 1997). Cu isotope ratios measured in arc basalts also do not show evidence for metasomatic Cu enrichments related to slab-derived fluids (Wang et al., 2019). These observations suggest that either slab-derived fluids and melts are not efficient carriers of Cu compared to the relatively high Cu (20-30 ppm) content of mantle peridotite, or that sulfide is present as a residual phase in altered oceanic crust during slab dehydration and melting, consistent with thermodynamic models of the Cascadia subducting slab (Walters et al., 2020). We note that the presence of sulfide in the subducting slab does not preclude the presence of S^{6+}-rich slab melts (e.g. Jugo et al., 2010).
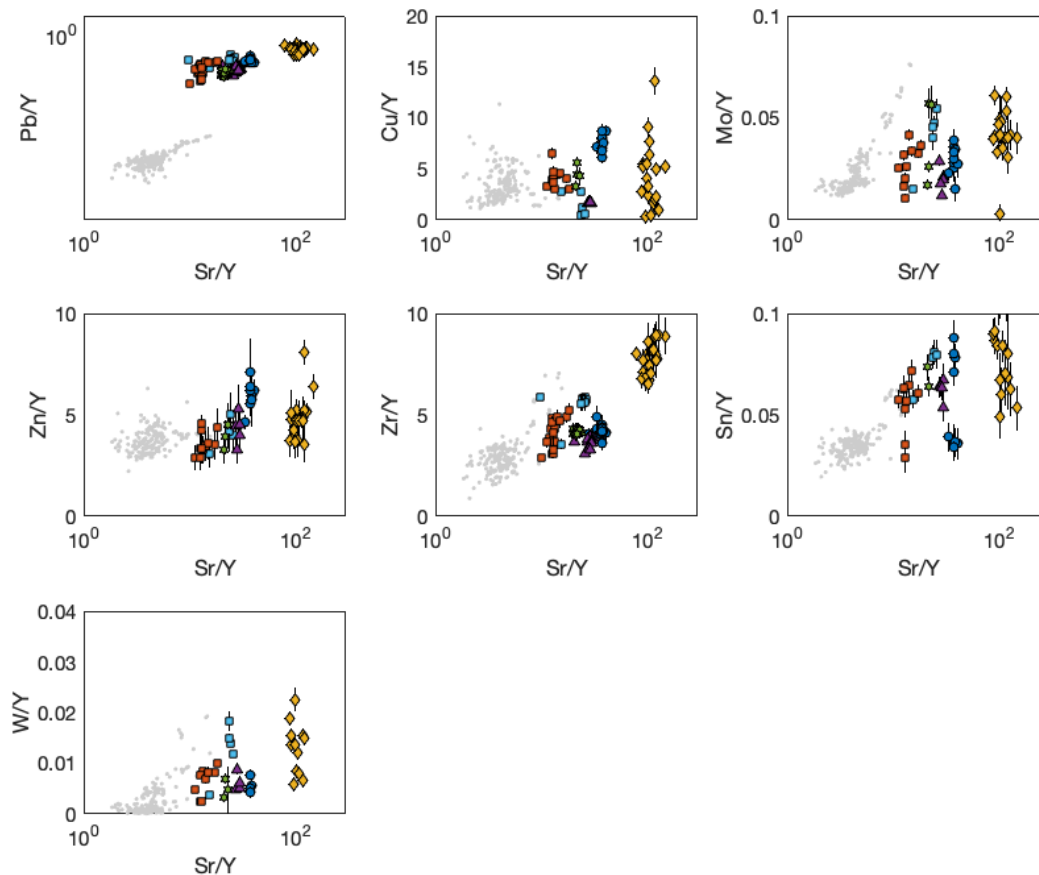
Figure 13. Lassen melt inclusion compositions from Walowski et al. (2016) and current study from each cinder cone. Error bars represent propagated analytical standard error. MORB glasses (gray circles, Jenner et al., 2012) shown for comparison.

5.5 The effect of subduction on Lassen primary magma Cu

Lassen magmas show clear variations in Cu but do not show straightforward relationships with trace element indicators of mantle enrichment or slab-derived components (Fig. 3, 14). This suggests a more complex mantle melting scenario during which the behavior of Cu is moderated by an immiscible sulfide phase (Lee et al., 2012) regardless of the extent of depletion or enrichment of the mantle wedge. This decoupled behavior between Cu and other trace elements has been documented in MORB (Sun et al., 2020) and ocean island basalts (Wieser et al., 2020). Sulfide stability during melting depends heavily on the oxidation state of the mantle and the amount of sulfur present. Both of these parameters are influenced by the addition of slab-derived materials at Lassen (Fig. 11).

To assess how variations in mantle Cu, S and f_{O_2} moderate the Cu content of Lassen magmas, we model the stability of sulfide during aggregate near fractional melting using the framework of Lee et al. (2012) and Sun et al. (2020). To calculate the proportion of sulfide present we calculate $SCSS^T$ for each estimated primary melt using the model of Smythe et al. (2017) with the H_2O dependence described in Liu et al. (2021) in combination with the oxygen fugacity dependence described in Jugo et al. (2010). All models are calculated at 1.6 GPa and 1300 °C, consistent with estimates for conditions of last mantle melt re-equillibration for Lassen magmas (Fig. 12). This is the same model formulation used to calculate sulfide saturation during crustal storage (Fig. 6). We use the mineral-melt partition coefficients of Sun et al. (2020) for Cu and the partition coefficients reported in Venugopal et al. (2020) for Y, combined with mantle mineral modal proportions from Walowski et al. (2016). Consistent with the Lassen mantle heterogeneity discussed previously, we use a moderately enriched composition to calculate cinder cone BRM and BRVB and a slightly enriched mantle source to calculate the source for all other cinder cones. See mantle melting discussion above for detailed mantle source descriptions. Sulfide liquid – silicate melt Cu partitioning is calculated using the average temperature and composition of Lassen primary magmas and the model of Kiseeva and Wood (2015).

For each cinder cone, minimization schemes were run to find the best model fit to Cu and Y primary magma concentrations for a range of assumed mantle f_{O_2} and mantle

Cu contents, while varying mantle S content (Fig. S7-S12). This modelling approach allows us to generate an array of combinations of mantle f_{O2}, mantle Cu, and mantle S contents that can reproduce Cu and Y primary magma values for each cinder cone. We can compare these model outputs to a series of external constraints to determine which model combinations are most realistic.

The first external constraint is the estimated sulfur contents of primary melts. Primary melt sulfur content helps constrain both mantle S content and mantle f_{O2}, because calculated $SCSS^T$ varies solely as a function of mantle f_{O2} within models for a given cinder cone. The second external constraint is primary magma oxygen fugacity calculated from measured $Fe^{3+}/\sum Fe$ (Muth and Wallace, 2021). For the third constraint, we assume that the mantle source beneath each cinder cone is similar to estimates for the Cu content of MORB-source mantle (30 ppm Cu; Wang and Becker, 2015; Salters and Stracke, 2014) and that slab-derived Cu is negligible. The fourth constraint uses sulfur isotope ratios ($\delta^{34}S$) measured in the same suite of inclusions (Muth and Wallace 2021) to estimate the relative amount of slab-derived sulfur present beneath each of the other cinder cones. First, we use the best fit mantle S content at BBL and an assumed initial mantle S content of 170 ppm (Saal et al., 2002; Ding and Dasgupta, 2017; Sun et al., 2020) and $\delta^{34}S$ = 0.6 ‰ based on MORB source mantle (Muth and Wallace, 2021) to calculate slab melt $\delta^{34}S$ = 9.5 ‰. This value is consistent with previous estimates of slab melt $\delta^{34}S$ based on more detailed mantle melting calculations (Muth and Wallace, 2021). We then use this slab melt $\delta^{34}S$ value and the same pre-subduction source to calculate the mantle sulfur content beneath each other cinder cone. Cinder cone BAS-44 melt inclusions have no measured $\delta^{34}S$ values, and so melt $\delta^{34}S$ was approximated using a linear regression between $\delta^{34}S$ and primary magma S in other cinder cones.
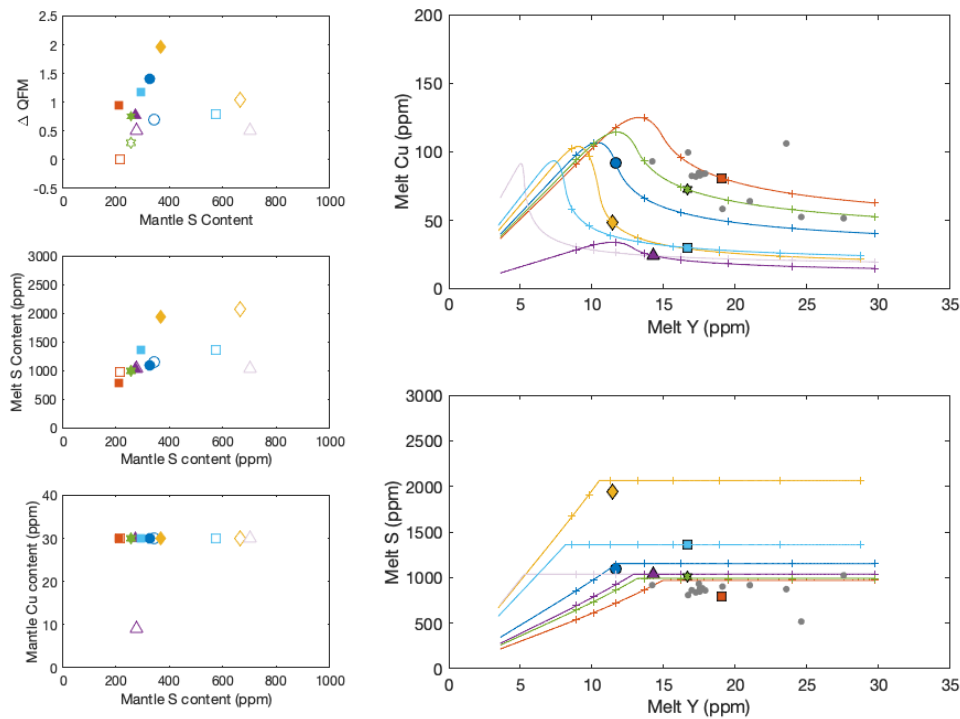
Figure 14. (Right) Modeled Cu behavior during mantle melting compared to calculated Lassen primary magma compositions. Tick marks represent melt fractions from 5 to 40 % in 5 % increments. Gray dots are primitive mid-ocean ridge basalt compositions (Jenner et al., 2012). (Left) Model input parameters (open symbols) compared to external constraints based on literature and melt inclusion data (filled symbols). See text for details.

Figure 14 shows model outputs for the series of models that best match external constraints. A mantle source with Cu contents similar to MORB-source mantle and variably increasing mantle S and f_{O2} contents can reproduce observed Lassen melt Cu contents for all cinder cones except for BPPC. Mantle S contents inferred from melt $\delta^{34}S$ are in good agreement for cinder cones BBL, BAS-44, and BORG. Mantle S contents inferred from $\delta^{34}S$ for cinder cones BRVB and BRM are systematically lower than mantle S content required to match measured Cu contents. This may be due to uncertainty in the Y content of the enriched mantle source for BRVB and BRM, which affects melt fraction estimates, or may indicate some heterogeneity in initial mantle $\delta^{34}S$ prior to modern subduction influence. Both scenarios are consistent with the influence of some prior metasomatism and/or sediment addition (Fig. 8, 9). Despite this offset, there is

44

good agreement in the relative difference in model inputs and inferred values of mantle S content between BRM and BRVB.

Although models can reproduce co-variations between mantle source f_{O2} and mantle S content calculated using melt inclusion compositions, Lassen primary magma S contents based on melt inclusion data require f_{O2} conditions that are systematically lower than primary magma f_{O2} calculated from melt inclusion $Fe^{3+}/\sum Fe$. The $SCSS^T$ vs. relative f_{O2} calibration we use is based on 200 MPa experiments on hydrous basalt compositions and performs well when predicting $SCSS^T$ at entrapment conditions based on measured melt inclusion $Fe^{3+}/\sum Fe$ (Fig. 6). Therefore, this offset at melting pressures (~1.6 GPa) required by the model results described above suggests that the $SCSS^T$ vs. relative f_{O2} relationship shifts towards lower $SCSS^T$ values at a given f_{O2} as pressure increases. This is consistent with experiments on hydrous trachyandesite melts (Matjuschkin et al., 2016), although the offset shown here is smaller than the predicted offset based on their experiments, suggesting that composition and/or temperature may also play a role in driving $SCSS^T$ vs. relative f_{O2} relationships.

In contrast to the other five cinder cones, BPPC magmas require a mantle source with either a high sulfur concentration, which keeps a high proportion of sulfide stable, or a mantle Cu content distinctly lower than that of MORB. Based on $\delta^{34}S$ comparisons, BPPC mantle S content is unlikely to be unusually high compared to other cinder cones. This conclusion is consistent with the depleted mantle source at BPPC inferred from Nb/Y values (Fig. 8, 9), and with its moderate Sr/Y values (Fig. 13), volatile contents and measured oxidation state (Fig. 11; Walowski et al., 2016; Muth and Wallace, 2021). A more likely scenario is that the mantle source of BPPC is depleted in Cu relative to MORB source mantle. This is consistent with previous work at Lassen which suggests that the mantle source beneath the forearc regions has been affected by prior melt extraction (Borg et al., 1997, 2002; Clynne and Borg, 1997). BPPC is located more towards the forearc than the other cones studied here, within a region noted for its low-K magmas (Bullen and Clynne, 1990).

Low Cu magmas have been observed in other regions of the Cascade Arc. For example, LKOT-like Park Butte basalts erupted from a vent on the flanks of Mt. Baker have substantially lower Cu contents than basalts from other vents in the region (Moore

and DeBari, 2012). More generally, boninites commonly have extremely low Cu contents compared to typical arc magmas (Hamlyn et al., 1985), and high magnesium andesites have Cu contents systematically lower than that of most arc calc-alkaline basalts and basaltic andesites (Rezeau and Jagoutz, 2020). Submarine glasses sampled from the Havre Trough and Kermadec arc vary widely in their Cu contents in ways that broadly co-vary with indicators of mantle source fertility in addition to subduction influence, where glasses with the lowest Cu contents are sourced from the most depleted mantle (Leath, 2019).

Although more primitive (MgO > 8 wt. %) whole rock samples at Lassen have higher Cu concentrations than BPPC (Fig. 5), scatter towards low Cu values in low K compositions suggest there are some mafic vents at Lassen that are sourced from low-Cu depleted mantle. Interestingly, aside from a subset of low-K, low-Cu compositions similar to BPPC, both melt inclusion and whole rock data show a negative correlation between Cu and K_2O that spans too large a range to be explained by crystallization alone. This inverse correlation is consistent with the modeling above, where high-K magmas strongly influenced by subduction have higher proportions of sulfide present during mantle melting and therefore retain more Cu in peridotite residue. This mantle Cu sequestration occurs despite increases in melt S content and oxygen fugacity (Fig. 11), because mass addition of sulfur to the mantle wedge outweighs increases in mantle oxidation state. Primitive (MgO > 8 wt. %) whole rock compositions from arcs globally (Barber et al., 2021) likewise show a general inverse relationship between Cu and K_2O, with scatter towards low Cu contents at low K_2O. This consistency between Lassen and global arc Cu trends suggests that decreases in melt Cu caused by the addition of slab-derived sulfur to the sub-arc mantle may be a common occurrence within other arcs.

6.0 Conclusions

The Cu and Pb contents of Lassen magmas are influenced by a combination of ambient mantle heterogeneity and modern subduction influence, whereas Mo, Zn, Sn and W concentrations are similar to or only slightly elevated compared to MORB and show no systematic variations. Pb is strongly elevated relative to MORB in Lassen magmas and increases with the addition of slab-derived material to the sub-arc mantle. In contrast,

Cu responds to subduction influence indirectly via changes in sulfide stability, such that mantle sources with larger proportions of slab-derived sulfur generate primary melts with lower melt Cu contents. Cinder cone BPPC has low Cu contents relative to most mafic vents in the Lassen region due to prior extraction of Cu from the mantle source combined with the addition of slab-derived sulfur. The inverse relationship between mantle enrichment by subduction process and primitive magma Cu contents, as well as variations in the Cu content of magmas from more depleted source regions, is also reflected in the whole rock record at Lassen and in many arc rocks globally. These patterns demonstrate that (1) ambient mantle heterogeneity, (2) variations in the proportions of slab-derived sulfur delivered to the mantle, and (3) consequent effects on mantle oxygen fugacity during melting can influence the Cu content of primary arc magmas.

7.0 Bridge

In the previous Chapter (III), I investigated controls on the metal content of arc magmas in the southern Cascade Arc using measured concentrations of Cu, Zn, Mo, Pb, W, and Sn and combined this new data set with constraints on mantle sulfur content and oxidation state from Chapter II. In Chapter IV, I consider processes discussed in Chapters II and III from a global perspective by compiling a data set of published melt inclusion compositions from 29 arcs segments, investigating the relationships between arc magma sulfur content, arc magma oxidation state, and the influence of slab-derived materials.

CHAPTER IV

INSIGHTS INTO VOLATILE CYCLING AND ARC MAGMA OXIDATION STATE FROM GLOBAL SULFUR TRENDS

This chapter is planned for submission to *Earth and Planetary Science Letters*. I am lead author on the paper, which involved sample preparation, analysis, synthesis of all data, modeling and writing the manuscript. Paul Wallace (University of Oregon) assisted with data interpretation and feedback on manuscript drafts.

1.0 Introduction

The sulfur concentration in arc magmas is an integrated result of processes occurring at depth, including slab devolatilization, mantle melting, crystallization, and degassing (Wallace and Edmonds, 2011). These processes are all closely linked to each other such that the dynamics of mantle melting likely affect the behavior of sulfur during storage and evolution within the crust (Lee et al., 2012; Richards, 2015). Globally, many arc magmas have S contents that are elevated relative to mid-ocean ridge basalts (MORB), which suggests that subduction processes play an important role in controlling the S content of arc magmas. However, the precise connection between subduction and elevated sulfur contents is unclear.

Sulfur enters subduction zones via the subducting plate and is present in seafloor sediments, primary MORB sulfides, hydrothermally altered ocean crust (Alt, 1995; Li et al., 2020; Walters et al., 2019), and serpentinized lithospheric mantle (Alt et al., 2013; Debret et al., 2017). Sulfur is also likely present in sub-arc mantle wedge peridotite prior to subduction in the form of sulfide phases, similar to MORB-source mantle. The pathways that slab sulfur takes between subduction and eruption at volcanic arcs can affect which phases sulfur enters (silicate melt, sulfides, vapor) and the valence state of sulfur (S^{2-}, S^{4+}, S^{6+}). These differences in sulfur behavior affect the fate of many ore-forming metals (Jenner et al., 2012; Lee et al., 2012; Richards, 2015), the long-term redox budget of Earth's mantle (Evans and Tomkins, 2011; Brounce et al., 2019), and the sulfur degassing that is commonly used to monitor volcanic activity (Fiege et al., 2014).

During interactions between materials derived from the subducting slab and peridotite in the mantle wedge, the sulfur contents of mantle melts are sensitive to three key factors. One is the sulfur content of the mantle source prior to any input from slab-derived materials. The mantle source beneath arcs is variable in isotopic and trace element composition, ranging from variably depleted MORB-like mantle sources to those more similar to the source of ocean island basalts (Iveson et al., 2021; Turner et al., 2017). The processes that formed these ambient mantle heterogeneities likely also created variations in the sulfur content of the sub-arc mantle. The second is the mass addition of slab-derived material into the mantle source of arc magmas. Experimental evidence suggests that slab-derived melts and fluids can transfer significant amounts of sulfur into the mantle wedge (Jégo and Dasgupta, 2014), consistent with high S contents found in inclusions within ultra-high-pressure eclogite-facies metamorphic suites (Ferrando et al., 2005). The third factor is mantle oxidation state. Globally, arc magmas are oxidized relative to mid-ocean ridge basalts, and measured $Fe^{3+}/\sum Fe$ in silicate glasses (Brounce et al., 2014; Kelley and Cottrell, 2009) suggest that the mantle source for arc magmas is oxidized via the input of slab-derived materials in the mantle wedge. Variations in the oxidation state of the mantle wedge have the potential to change the solubility of sulfur in silicate melts during mantle melting, driving enrichments in the sulfur contents of primary magmas (Jugo et al., 2010; Muth and Wallace, 2021). Importantly, these three factors do not necessarily vary independently of each other. Combined geochemical and geodynamic models predict the transport of oxidized sulfur into the mantle wedge as slab-derived melts (Canil and Fellows, 2017) or fluids (Tomkins and Evans, 2015; Walters et al., 2020) at sub-arc depths, although these predictions require that the subducting slab is sufficiently oxidized (Evans and Frost, 2021; Li et al., 2020). This oxidized sulfur can increase the oxygen fugacity of the mantle wedge and the melts that form within it (Muth and Wallace 2021).

The challenge is to unravel how strongly these three factors, mantle heterogeneity, slab-derived sulfur, mantle oxidation state, influence the sulfur content of arc magmas. A major obstacle to doing this is that sulfur, like other volatile elements, is lost to the gas phase during the shallow storage and eruption of arc magmas. There are several ways to work around this challenge. One method is to use the partitioning

behavior of chalcophile elements such as Cu to track the behavior of sulfur indirectly (Lee et al., 2012; Jenner et al., 2012; Barber et al., 2021). This approach has the advantage of relying less on finding undegassed arc samples and can be sensitive to subtle changes in sulfide phase behavior. However, whereas this method is extremely sensitive to the stability of sulfides, it cannot directly constrain the amount of sulfur dissolved in silicate melts. Similarly, although sulfur isotopes measured in submarine glasses, volcanic gas, and whole rock samples provide valuable information about the sources of sulfur in subduction zones, S contents in most of these samples have been affected by partial or complete degassing (Alt et al., 1993; J. C.M. De Hoog et al., 2001; Kagoshima et al., 2015).

Melt inclusion data allows for a direct determination of sulfur concentration in arc magmas, making it an excellent complement to other approaches. Melt inclusions are tiny, quenched parcels of minimally degassed silicate melts. Measuring the sulfur content and major element compositions of melt inclusions allows us to estimate the sulfur content of primitive arc magmas directly. In this study, we combine measured sulfur contents of melt inclusions with trace elements and major elements to constrain the sulfur content of the mantle source for subduction zone magmas, the characteristics of slab-derived sulfur in arc magmas, and the oxidation state of the mantle source needed to generate the sulfur content observed at each arc. To investigate the global-scale controls on arc magmatic sulfur, we compiled published melt inclusion data sets from 115 volcanoes within 29 subduction zone segments.

2.0 Methods

The goal of this effort was to compile the compositions of melt inclusions from the most primitive, least-degassed arc magmas. To this end, we only used olivine-hosted melt inclusions (MI), because olivine is the liquidus phase (+Cr-spinel) in most arc magmas. To take advantage of all available data and assess a full range of subduction-related processes we include arc front and non-arc front volcanoes, but we exclude volcanoes that do not show a clear subduction-related signature (e.g. elevated volatile contents, light rare earth element enrichment). We used inclusion compositions where either negligible evidence for post-entrapment crystallization (PEC) and Fe-Mg re-

equilibration were found, or compositions that had been screened and/or corrected for both processes by the original authors. However, there are several sources of uncertainty that affect the interpretations of melt inclusion S data even in early-trapped inclusions. Uncertainties in the data presented here and the steps we took to mitigate them are described below. We also highlight that although primitive melt S contents inferred from melt inclusions can carry uncertainties, each complication would skew our compiled data set toward lower S values. In other words, despite uncertainties in analysis and interpretation of melt inclusion S contents, our data set provides a robust lower limit to primitive melt S contents.

Most S concentrations reported in the compiled data set were measured using electron probe micro-analysis (EPMA). The accuracy of such measurements depends on knowledge of the oxidation state of sulfur in the silicate glass. The position of the S Kα peak used to measure sulfur concentration shifts according to the oxidation state of S in silicate glasses, and in arc glasses this means that the S Kα peak is commonly different than those for commonly used standards like barite, pyrite, or pyrrhotite (Carroll and Rutherford, 1988; Wallace and Carmichael, 1994). Failure to place the spectrometer position correctly results in measured S concentrations that are typically up to 10-15% too low, and the error can be higher depending on the instrument setup (Muth et al., in prep).

Another process that could affect interpretations of published S data is post-entrapment partitioning of S into a vapor or sulfide phase. Sulfur-bearing precipitates have sometimes been observed in the vapor bubbles of melt inclusions (e.g. Schiavi et al., 2020; Venugopal et al., 2020; Wieser et al., 2020; Kamenetsky and Kamenetsky, 2010). However, S concentrations measured in homogenized arc melt inclusions from Seguam and Fuego are indistinguishable from pre-homogenized measured S concentrations (Rasmussen et al., 2020). This comparison suggests that S partitioning into melt inclusion vapor bubbles during post entrapment processes is small, and that most measured glass S contents are representative of the silicate melt during inclusion entrapment. Quenched immiscible sulfide liquids are also occasionally found in melt inclusions. These sulfide blebs likely form due to Fe-Mg reequilibration after melt inclusion entrapment. Sulfides are more likely to form in high Mg inclusions, which commonly undergo larger extents

51

of PEC and Fe-Mg reequilibration relative to more evolved inclusions (Danyushevsky et al., 2000).

To minimize bias in the melt inclusion data from degassing or sulfide precipitation, we only use samples with S/K_2O ratios in the upper quartile within each volcano. The S/K_2O ratio has been shown to be a valuable tracer of S loss during crystallization (e.g. Johnson et al., 2010; Spilliaert et al., 2006), and is sensitive to both S sequestration in sulfides and in a vapor phase.

To consider the behavior of sulfur during mantle melting and to make direct comparisons between melt inclusions trapped during different stages of crystallization, we calculate a primary magma composition for each volcano within each arc segment. For each inclusion from the upper quartile of S/K_2O values at each volcano, we use reverse crystallization models to calculate melts in equilibrium with Fo_{90} olivine (Fig. S2). If the H_2O contents of melt inclusions are not reported, we use the average H_2O content of other melt inclusions from the same volcano, or if this information is not available, from the same arc segment. We make the additional assumption that olivine has dominated the crystallization behavior at each volcano. This is consistent with the lack of any clear Al_2O_3 depletions in the data set from each volcano, although some more evolved inclusions show scattered Al_2O_3 trends that may indicate some influence of plagioclase fractionation. We calculate reverse olivine crystallization with the program Petrolog3, using the model of Danyushevsky (2001) for olivine crystallization temperature and the model of Toplis (2005) to calculate olivine K_d values. Both models are chosen because they account for the effect of dissolved H_2O in the melt. We assume a constant $Fe^{3+}/\sum Fe = 0.2$, based on estimates of $Fe^{3+}/\sum Fe$ in primary magmas at arcs (Muth and Wallace, 2021, Brounce et al., 2014).

Melt H_2O concentration and melt $Fe^{3+}/\sum Fe$ both affect modeled olivine-melt partitioning behavior. The effect of H_2O is relatively small. Taking Fuego MI 127-1 as an example, varying initial melt inclusion H_2O concentration from 1 to 5 wt. % results in a shift from 27.1 to 27.7 % reverse crystallization to obtain compositions in equilibrium with olivine Fo_{90}. Varying $Fe^{3+}/\sum Fe$ from 0.15 (close to MORB values) to 0.25 (roughly the upper limit of $Fe^{3+}/\sum Fe$ estimates for primary arc compositions) results in a shift from 29.2 to 24.1 % crystallization. We therefore take our crystallization calculations as

accurate to ~5 % absolute crystallization, although there is likely some additional uncertainty caused by small proportions of plagioclase or clinopyroxene crystallization in more evolved compositions. There is a subset of inclusions with high FeO^T concentrations that result in high MgO (> 18 wt. %) primary magmas. It may be that these compositions were significantly affected by the crystallization of phases other than olivine such as plagioclase or clinopyroxene. Alternatively, these may be compositions that formed in equilibrium with a more refractory mantle residue (Fig. S2; Parman and Grove, 2004; Schmidt and Jagoutz, 2017).

To calculate the S, Cl, and trace element composition of each inclusion, we assume that each behaves as a perfectly incompatible element, and we dilute each according to the percent K_2O dilution from the calculations above (Fig. S2). Because magmas may undergo some degree of sulfide precipitation and/or sulfur degassing prior to inclusion entrapment, we again emphasize that the primary magma S contents calculated here are minimum estimates.

The thermal parameter ($\Phi = t*v*\sin\theta$), where t is age, v is speed, and θ is angle, is traditionally used as an indicator of slab temperature. Slab thermal parameter values for each arc segment were taken from Syracuse et al. (2010). We note that the Aeolian Islands are included within the Calabria arc segment.

3.0 Results

The final filtered data set contains data from 659 melt inclusions. The data set spans 29 arc segments and 115 volcanoes. Most inclusions are low to medium-K calc-alkaline basalts (Fig. 1). Average PEC-corrected MI sulfur contents for each arc segment range from 594 ± 241 ppm (Mariana Forearc) to $5,022 \pm 795$ ppm (Ecuador; Fig. 2). Average calculated primary magma sulfur contents calculated for each arc range from 466 ± 220 ppm to $4,264 \pm 819$ ppm. Arcs where the subducted plate has a higher thermal parameter (colder slabs) generally have thinner (oceanic) overlying crust (Fig. 3), whereas arcs with lower thermal parameter (hotter slab) generally have thicker (continental) overlying crust. This association means that variations in arc geochemistry attributed to slab temperature may instead be caused by crustal thickness, and that the reverse may also occur. Sulfur contents are elevated relative to those measured in mid-

ocean ridge basalts, across a range of both host olivine forsterite content (Fig. 2) and subduction zone slab thermal parameter (Fig. 4).
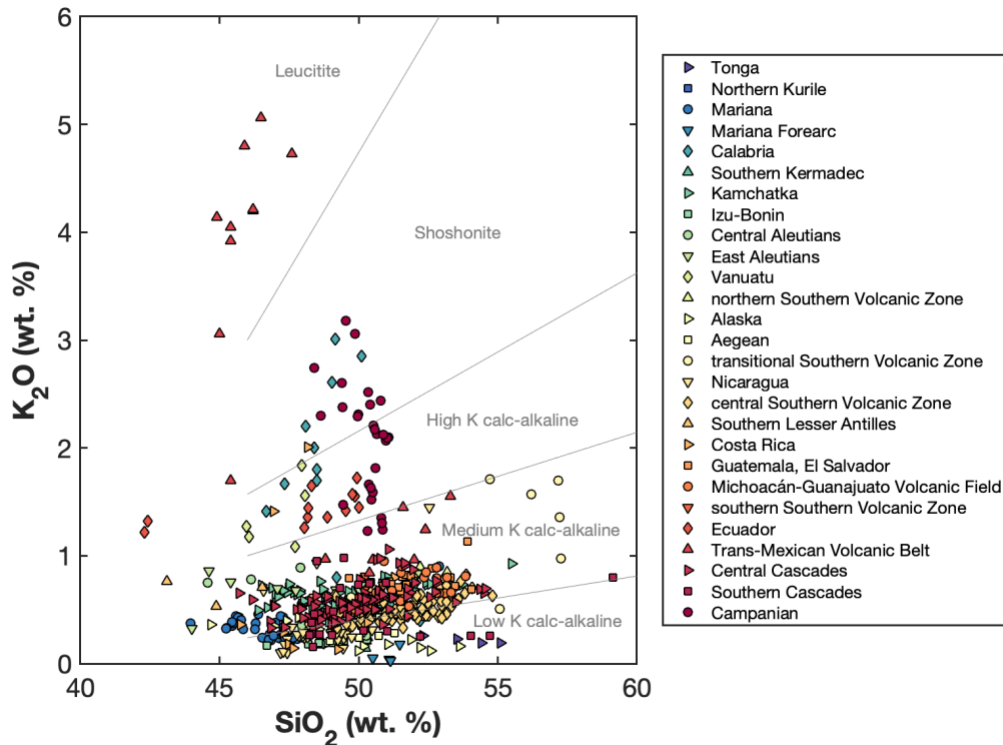
Figure 1. PEC-corrected compositions of compiled melt inclusions. Each symbol represents one melt inclusion. Each symbol type represents one subduction zone segment. Compositional boundaries after Vigoroux et al. (2008).

4.0 Discussion

4.1 Controls on the sulfur contents of arc magmas

There are three key potential controls on the sulfur content of primary arc magmas. The first is the composition of the mantle source prior to modern subduction. If sulfur is added or removed from the mantle source during previous melt/fluid infiltration or melt extraction, this can influence the sulfur content of magmas generated during modern subduction. The second factor is the addition of slab-derived sulfur to the sub-arc mantle source, which increases the sulfur content of the mantle source during melting. The third factor is sulfide saturation. If the mantle is saturated in sulfide during melting, this will limit the sulfur content of the melt at the total dissolved sulfur content at sulfide saturation ($SCSS^T$). Because $SCSS^T$ is strongly controlled by f_{O2}, the sulfur content of arc magmas is likely to be sensitive to the oxidation state during mantle wedge melting.
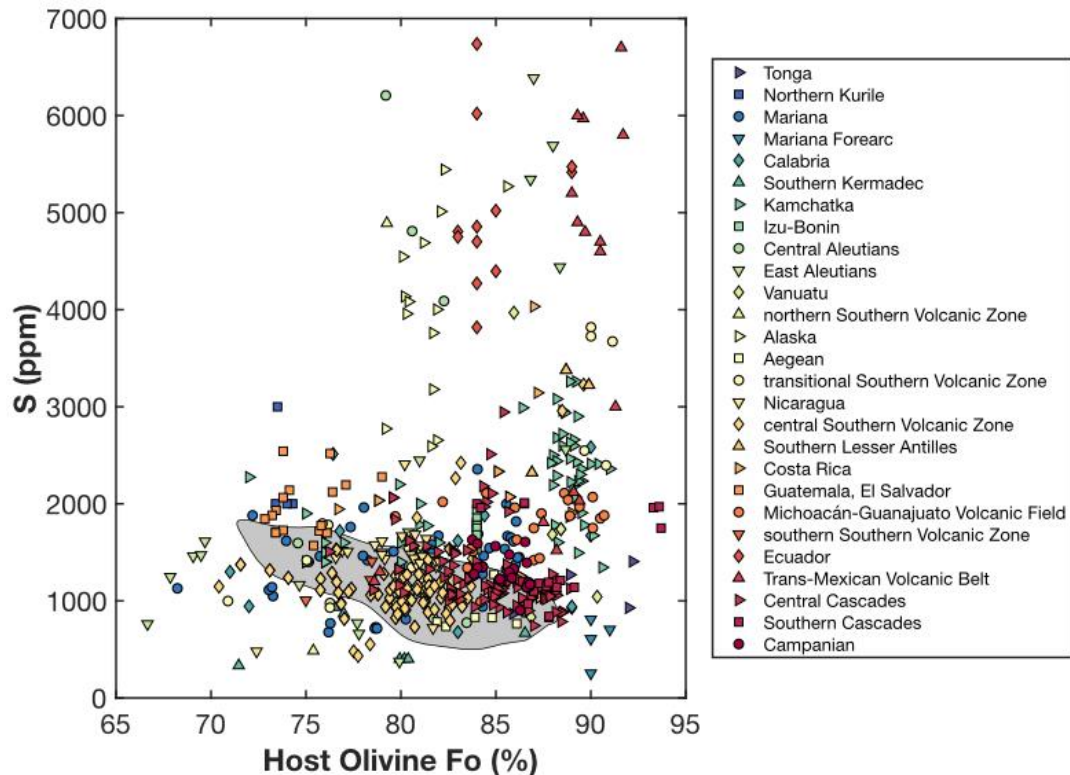
Figure 2. PEC-corrected compositions of compiled melt inclusions plotted as a function of host olivine forsterite content. Each symbol represents one melt inclusion. Each symbol type represents one subduction zone segment. Shaded field represents MORB data (Jenner et al., 2012).

A first step towards investigating the importance of each control is to determine whether primary magmas require elevated sulfur contents in their mantle source. This is a complex question because the "source" is likely a hybrid of mantle wedge peridotite and slab components, and the latter could be introduced either at some earlier time (metasomatism) or in conjunction with and as the causative force for mantle wedge melting. As a first step, we use simple batch melting models to calculate the minimum mantle sulfur content required to generate primary melt sulfur concentrations. As a simplifying assumption we assume that the mantle is sulfide free. We use partition coefficients from Callegaro et al. (2020) with mineral modal proportions approximating those of spinel lherzolite (Ol:53, Opx:30, Cpx:12, Sp:5). We assume a melt fraction of 15%, consistent with melt fraction estimates for arcs based on trace element concentrations (Pearce and Parkinson, 1993; Till, 2017). This calculation shows that arc

magmas require mantle source sulfur contents ranging from 31 to 1011 ppm S (Fig. S3).

Varying melt fraction to 10 and 20 % shifts this range to 21-676 ppm S and 40-1345 ppm

S, respectively. In contrast, estimates for MORB-source mantle range from 100-300 ppm

S (Ding and Dasgupta, 2017; Saal et al., 2002; Sun et al., 2020). Importantly this

calculation is a minimum estimate because sulfur may behave more compatibly during

sulfide-saturated mantle melting. These calculations therefore indicate that any model

used to explain the S contents of arc magmas globally must involve source (mantle plus

slab component) sulfur contents that are higher in many cases than those in the MORB

source. In the following sections, we discuss the effects of mantle wedge composition,

addition of slab components, and mantle oxidation state in controlling the sulfur content

of primary arc magmas.
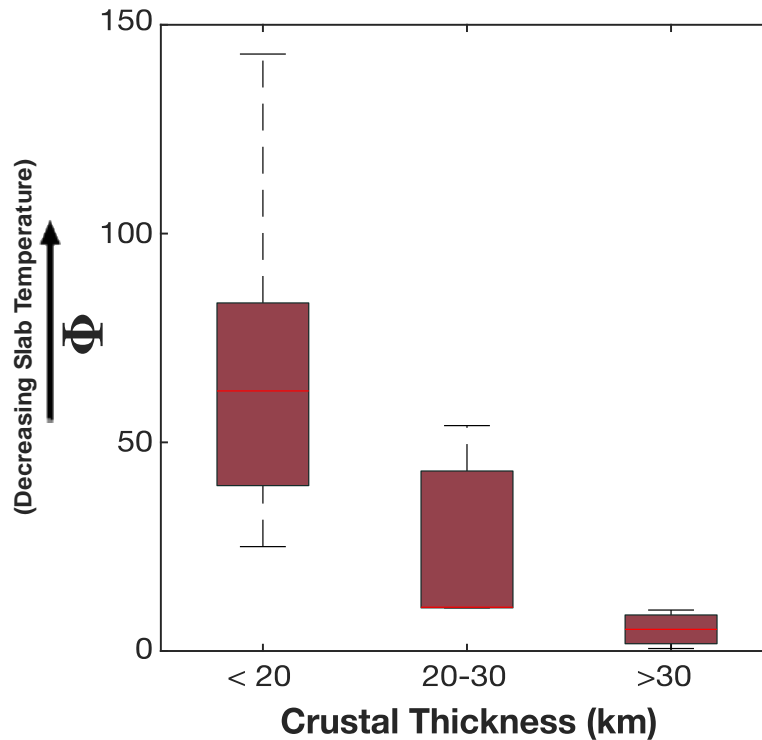
Figure 3. Comparisons between average crustal thickness and slab thermal parameter for each subduction zone segment. Boxes bound the upper and lower quartile of a given bin, red bars are the median value, and thin lines are the range of values.
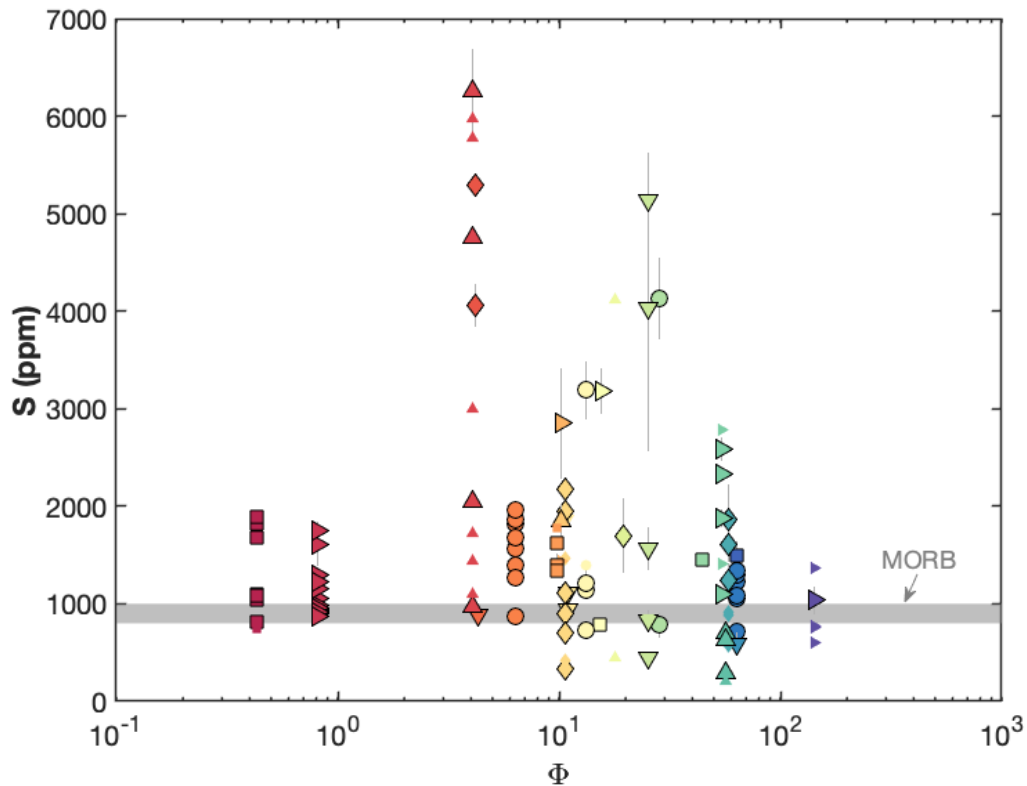
Figure 4. Primary magma compositions of volcanoes plotted as a function of slab thermal parameter (Φ). Symbols as in Figure 1. Small symbols represent compositions calculated using only one melt inclusion. Error bars represent uncertainty in primary magma compositions, calculated using the standard deviation for each volcano data set. Gray bar represents primary MORB reference values (Ding and Dasgupta 2017).

4.1.1 Mantle source

One important control on arc magma S contents is the initial S budget of the mantle prior to modern subduction influence. It has been estimated that the S contents of E-DMM and D-DMM (enriched and depleted mantle, respectively, compared to average depleted MORB mantle) vary from 165 to 100 ppm (Shimizu et al., 2016). Ocean island basalt (OIB) sulfur and copper systematics suggest the sulfur content of OIB mantle sources are variable (Ding and Dasgupta, 2018). Many arc magmas in continental arcs show evidence for the influence of an enriched component in the mantle wedge (Gómez Tuena et al., 2003; Heydolph et al., 2012; Iveson et al., 2021; Johnson et al., 2009; Leeman et al., 1990), perhaps due to the incorporation of components of subcontinental lithospheric mantle within the asthenospheric mantle source (Turner et al., 2017). In

contrast, the mantle sources for island arcs are commonly more depleted than those of continental arcs, and in some cases are even more depleted than DMM (Ewart and Hawkesworth, 1987; Hochstaedter et al., 2000; Woodhead et al., 1993; Pearce and Peate, 1995).

Because S is dominantly hosted in sulfide phases in mantle peridotite and not in silicate minerals (Callegaro et al., 2020), mantle S concentration may become decoupled from rare earth element (REE) enrichment/depletion trends. In extreme cases, chalcophile element depletions have been linked to melt percolation events with high melt/rock ratios that destabilize mantle sulfides (Ackerman et al., 2009; Büchl et al., 2002; Lee, 2002; Lorand and Luguet, 2016), sometimes despite associated REE enrichment (Ackerman et al., 2009). However, mantle peridotites generally show positive correlations between peridotite fertility indices (such as Al_2O_3) and S and Cu concentrations, suggesting that the sulfur content of peridotites is dominantly controlled by previous melting events (Lorand and Luguet, 2016; Wang and Becker, 2015).

To investigate whether variations in arc magma sulfur content are related to heterogeneity in the sub-arc mantle source prior to modern subduction influence, we compare Nb/Y to S/Dy (Fig. 5). High S/Dy values indicate increases in the S content of magmas due to higher concentrations of S in the mantle source and/or more oxidized melting conditions (Muth and Wallace, 2021, Saal et al., 2002). S/Dy ratios in arc magmas are almost all higher than MORB, whereas Nb/Y contents of arc magmas, which indicate the extent of depletion or enrichment of the source, span the range of values observed in MORB. Consistent with previous work as discussed above, intraoceanic arcs, which tend to overlie colder subducting slabs, commonly have more depleted mantle sources, whereas continental arcs, which tend to overlie hotter subducting slabs, commonly have more enriched mantle sources. Arc magmas show no systematic variations between S/Dy and Nb/Y, indicating that S enrichment in arc magmas is not dominantly controlled by prior enrichment or depletion of the mantle source. Chlorine and H_2O show stronger enrichments in colder-slab arcs, suggesting that ambient mantle heterogeneity may have a moderate effect on Cl and H_2O contents in arcs. However, it may be that this link is due to the overall association between cold-slab arcs and the more

depleted mantle common in island arcs, such that the effect of added slab components on magmatic Cl and H_2O contents is more pronounced (Fig. 3; Ruscitto et al., 2012).
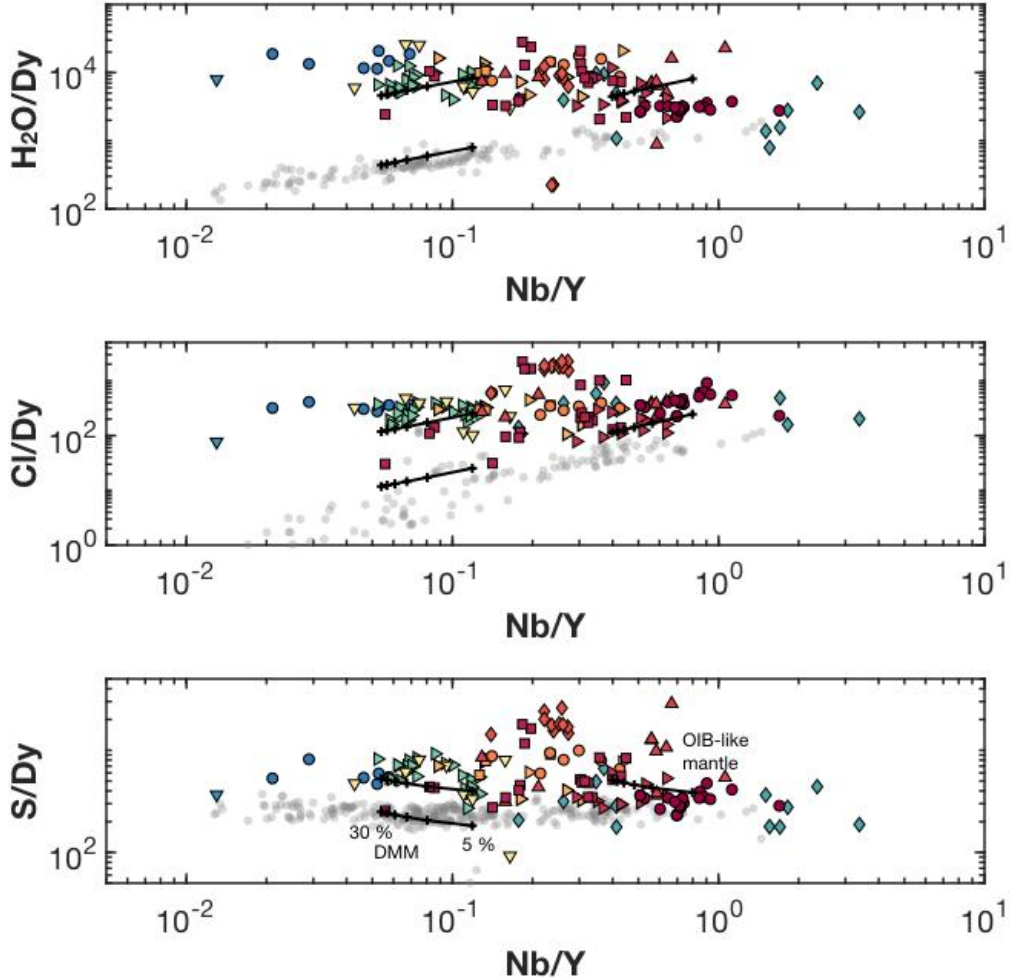
Figure 5. PEC-corrected melt inclusion compositions of volcanoes within each arc. Each symbol represents one analyzed inclusion. Symbols as in Figure 1. Small gray symbols are MORB compositions (Jenner et al., 2012, Shimizu et al., 2016). MORB Cl contents were filtered to exclude those affected by seawater assimilation (Cl/K < 0.08). Three batch melting curves are shown for comparison. The first is based on DMM (Workman and Hart 2005) for trace elements and Pacific Upper Plate source (Shimizu et al., 2016) for volatile elements. The second is based on DMM for trace elements with the addition of 154 ppm S, 45 ppm Cl, and 1809 ppm H_2O in the mantle source. The third is an enriched, OIB-like mantle source composition based on the inferred composition of enriched mantle in the Central Oregon portion of the Cascade arc (Ruscitto et al., 2010) and volatile contents based on the same volatile-enriched DMM mantle source used for the second curve described above. Tick marks on each model curve represent percent melt fraction.

4.1.2 Slab derived materials

The lack of any clear relationships between S/Dy and proxies for mantle enrichment ore depletion in arc magmas suggests that pre-subduction mantle source composition is not the dominant control on arc magma sulfur contents. Here we consider whether the mass transfer of sulfur from the subducting slab into the overlying mantle wedge is a strong control on the sulfur content of arc magmas. There is evidence for slab-derived mass transfer of sulfur in the heavy sulfur isotope ratios commonly measured in arc glasses and volcanic gases (Alt et al., 1993; Bénard et al., 2018; Gurenko, 2021; Muth and Wallace, 2021), which suggest the input of isotopically heavy seawater-derived sulfur in the sulfur budget of arc magmas. Experiments and thermodynamic models also indicate that slab-derived melts and fluids can release and carry a significant amount of sulfur (Jégo and Dasgupta, 2014; Tomkins and Evans 2015; Walters et al., 2020).
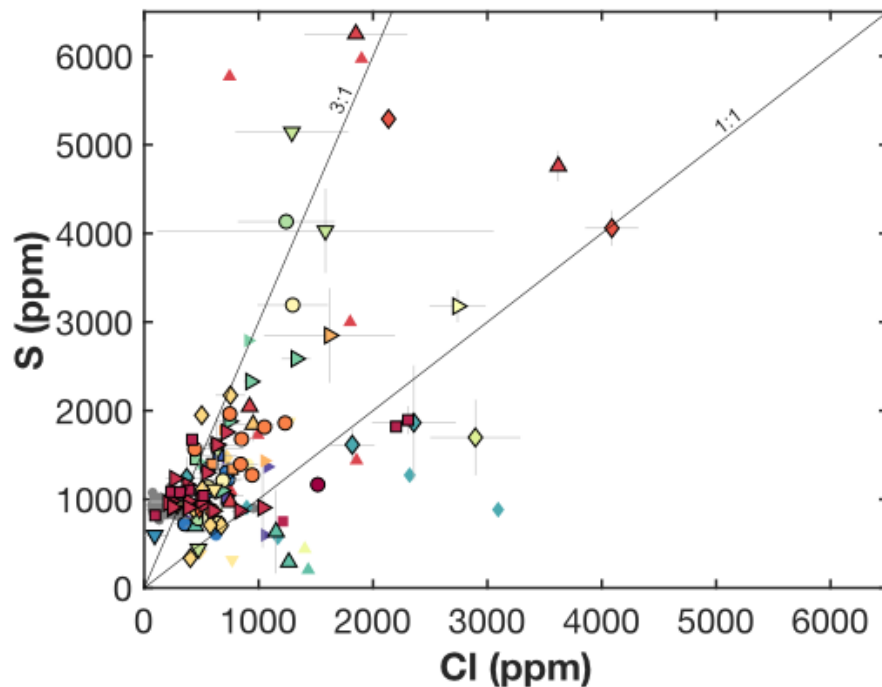
Figure 6. S and Cl contents of primary magma compositions of volcanoes within each arc. Symbols as in Figure 1. Small symbols represent compositions calculated using only one melt inclusion. Error bars represent uncertainty in primary magma compositions, calculated using the standard error of the mean for each volcano data set. Small gray symbols are unaltered (Cl/K < 0.08) MORB compositions (Jenner et al., 2012). Thin lines are 1:1 and 3:1 ratio shown for comparison.

One way to assess the mass transfer of S is by comparing S to Cl. Chlorine is elevated in arc magmas relative to MORB and is derived from the subducting slab (Ruscitto et al., 2012). This comparison is valuable because chlorine is very soluble in basaltic melts and degasses strongly only at relatively low (<100 MPa) pressure (Thomas and Wood, 2021; Webster et al., 2015), in contrast to sulfur, which may be lost to degassing or to sulfide formation, especially in more evolved magmas. Chlorine also has straightforward melting behavior in the mantle, and enrichments in chlorine have been demonstrably linked to slab inputs beneath arcs (Barnes et al., 2009; Ruscitto et al., 2012) and back-arcs (Kent and Elliot, 2002). Primary magma S and Cl estimates for arc magmas correlate both within and across arcs in a roughly 1:1 ratio with an upper limit of 3:1, although there is considerable scatter. If we assume that both elements behave incompatibly during mantle melting, this suggests that the sulfur and chlorine contents of slab-derived melts or fluids are of the same order of magnitude beneath the majority of arcs. This is broadly consistent with slab melting experiments focusing on both sulfur and chlorine (Jégo and Dasgupta, 2014; Van den Bleeken and Koga, 2015), and estimates for the chlorine and sulfur content of slab-derived aqueous fluids (Jégo and Dasgupta, 2014; Wallace, 2005). Many of the volcanoes with high Cl/S relative to other volcanoes have atypical melt compositions; high-Mg andesites (Mt. Shasta), nepheline normative (Puñalica), or high-K to shoshonitic (Apaxtepec, Procida Island, Ustica, Aoba Island). In these cases, prior metasomatism in the mantle (Vigouroux et al., 2008), or unusually large proportions of slab-derived materials (Kelemen et al., 2003) may create mantle sources with higher concentrations of chlorine.

To study the relationship between slab-derived materials and magma S contents more directly, we compare the ratio S/Dy to Sr/Y as an indicator of slab-derived material (Fig. 7). For these global comparisons we do not include volcanoes from the Calabria segment, because atypical geodynamic interactions in that region complicate the interpretation of trace element data (De Astis et al., 2003; Faccenna et al., 2005). Although there is considerable scatter, the relationship between S and Cl, and S/Dy and Sr/Y, show some variation with differences in slab temperature.
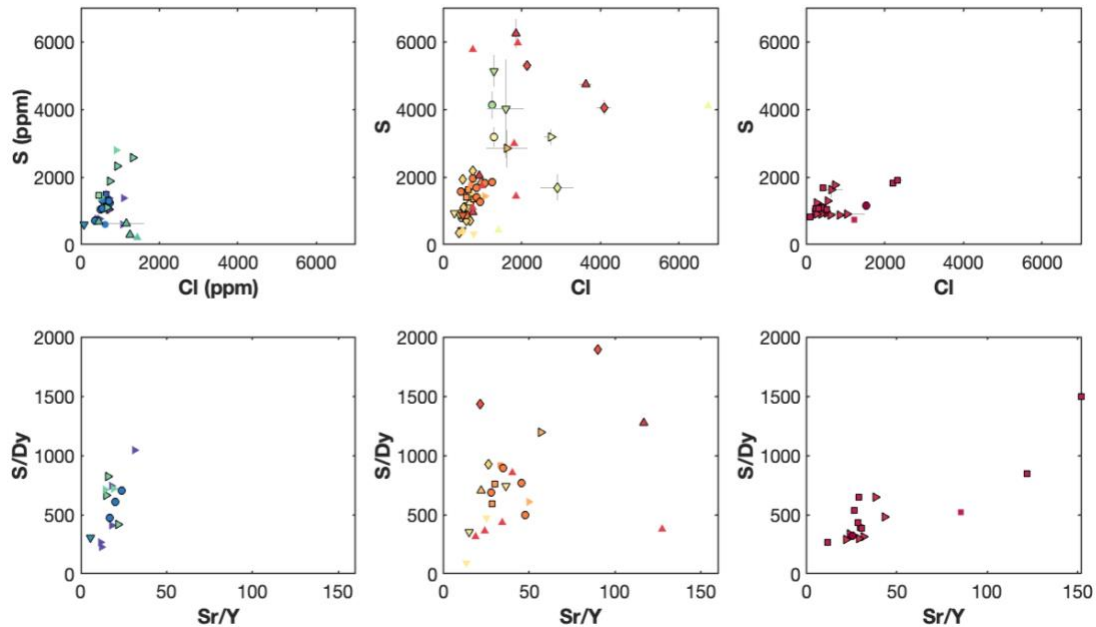
Figure 7. Average primary magma composition for volcanoes from each arc shown for cold arcs ($\Phi > 40$, left), intermediate temperature arcs ($1 < \Phi < 40$, middle), and warm arcs ($\Phi < 1$, right). Error bars represent uncertainty in primary magma compositions, calculated using the standard error of the mean for each volcano data set. Symbols as in Figure 1.

Inverse modelling of arc magma compositions suggests that global variations in slab-derived volatiles in arc magmas are strongly influenced by the temperature of the subducting slab (Ruscitto et al., 2012). At 6-14 kbar, anhydrite-saturated fluids contain higher sulfur contents at higher temperature (Newton and Manning, 2005). The same relationship has been observed in experiments on slab-derived melts, although it is not clear whether this effect holds in slab-derived fluids (Jégo and Dasgupta, 2014). Despite these observations, the highest primary magma S contents are in intermediate slab-temperature arcs, not the hottest arcs. It may be that these subduction zones represent a thermal 'sweet spot', where aqueous fluids, which can dissolve more sulfur than slab melts (Ferrando et al., 2005; Jégo and Dasgupta, 2014), are released simultaneously with slab melts into the mantle wedge. Sulfur speciation may also play a role in driving these differences. Slab dehydration models that incorporate sulfur predict a release of oxidized sulfur during the blueschist to eclogite transition (Tomkins and Evans, 2015; Walters et al., 2020). For arcs with hotter subducted plates, the oceanic crust beneath the arc has

likely already been affected by the shallower release of oxidized sulfur (e.g. Walowski et al., 2015) and as a result release sulfur that is more reduced. These differences in sulfur oxidation state may change the solubility of sulfur in slab melts and fluids and may also affect how much sulfur mantle melts can hold, as discussed in more detail below.

4.1.3 Oxygen fugacity

In addition to the mass transfer of S into the mantle wedge, S/Dy is sensitive to the oxidation state of the mantle wedge during melting, because the total dissolved S content at sulfide saturation ($SCSS^T$) is extremely sensitive to f_{O_2} (Jugo et al., 2010). We can quantify this relationship by calculating a minimum f_{O_2} for magmas using the measured S contents in melt inclusions. At reducing conditions, the $SCSS^T$ is controlled mainly by temperature, pressure, melt FeO and H_2O content, and sulfide composition (Fortin et al., 2015; Liu et al., 2021; Smythe et al., 2017). However, at oxidizing conditions, where S^{6+} becomes stable, f_{O_2} is commonly a dominant control (Jugo et al., 2010). The mantle wedge sources for arc magmas have a specific ratio of Fe^{3+} to Fe^{2+}, which correspond to certain f_{O_2} values. This ratio and corresponding f_{O_2} value in the mantle wedge beneath each arc depends on the composition of the mantle source prior to subduction influence, and the composition of the slab components added. To model the effect of variable f_{O_2} on $SCSS^T$, we combine existing models of $SCSS^T$ for reducing conditions (Smythe et al., 2017), with the H_2O effect described in Liu et al. (2021), and with an f_{O_2} dependence based on experimental data (Fig. 8; Jugo et al., 2010).

This combined model is used to calculate the f_{O_2} of each melt inclusion composition assuming the melt is sulfide saturated. We calculate the pre-eruptive temperature of melt inclusions using the model of Danyushevsky (2001) and assume 500 MPa pressure. For H_2O content we use either measured H_2O values or average values from the same volcano if melt inclusion H_2O was not measured. We assume $X_{FeS} = 0.85$ in the sulfide phase, consistent with the measured compositions of magmatic sulfides in arc rocks (Georgatou et al., 2018; Keith et al., 2017). The 68% confidence interval of the modelled f_{O_2} based on these model assumptions was calculated using a Monte Carlo approach for n = 10,000 iterations. Input parameters were randomly generated assuming a normal distribution and a specified one standard deviation(σ), where $\sigma_T = 100$ °, $\sigma_P = 0.1$

GPa, σ_{H2O} = 0.5 wt. %, σ_{XFeS} = 0.1, σ_S = 15 %, and σ = 5 % for all other melt oxides. The resulting error distribution was also propagated through the mean estimate for each volcano using the Monte Carlo approach for n = 10,000 iterations.
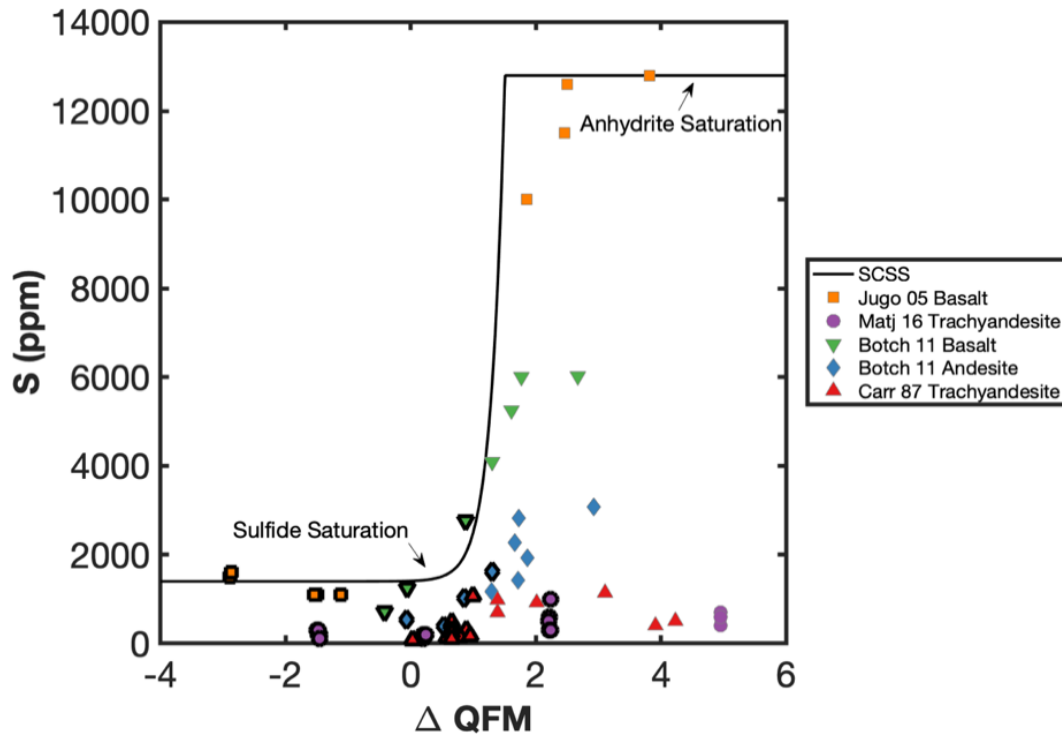
Figure 8. Sulfur solubility - oxygen fugacity relationship used to calculate the minimum oxygen fugacity of melt inclusion sulfur contents (Jugo et al. 2010). Sulfur content at sulfide and anhydrite saturation is based on the experiments of Jugo et al. (2005). Measured sulfur content of experimental glasses created with variable melt compositions, pressures and temperatures shown for comparison (Jugo et al., 2005, Matjuschkin et al., 2016, Botcharnikov et al. 2011, Carroll and Rutherford 1987). Thick black outlined symbols are experiments saturated in a sulfide phase.

The results of these calculations show that 90% of arc volcanoes require conditions more oxidizing than QFM (Quartz-Fayalite-Magnetite; Fig. 9, S4). Minimum f_{O2} estimates calculated via this approach are consistent with f_{O2} calculated using measured $Fe^{3+}/\Sigma Fe$ in melt inclusions (Fig. S5). Degassing, assimilation, and the crystallization of Fe^{2+}-rich phases can all theoretically change the f_{O2} of magmas after mantle melting and before inclusion entrapment. However, typical arc magma crystallization models indicate that fractional crystallization drives only modest increases in magma f_{O2}, and there is little experimental or natural data to suggest that degassing at

depth drives large increases in magma f_{O2} at arcs (Kelley and Cottrell, 2012). Although garnet crystallization or more complex magma recharge scenarios can theoretically drive increases in Fe^{3+}, this Fe^{3+} increase requires protracted periods of crystallization that are inconsistent with the high S contents of high-Mg inclusions in the global data compilation (Fig. 2). Assimilation of oxidized crustal material (anhydrite-rich veins or hydrothermally altered rocks) could simultaneously cause both local enrichment of sulfur and magma oxidation (e.g. Kamenetsky et al., 2017), but it is unlikely this process would occur in the majority of high-Mg melt compositions represented by melt inclusions in the global dataset.
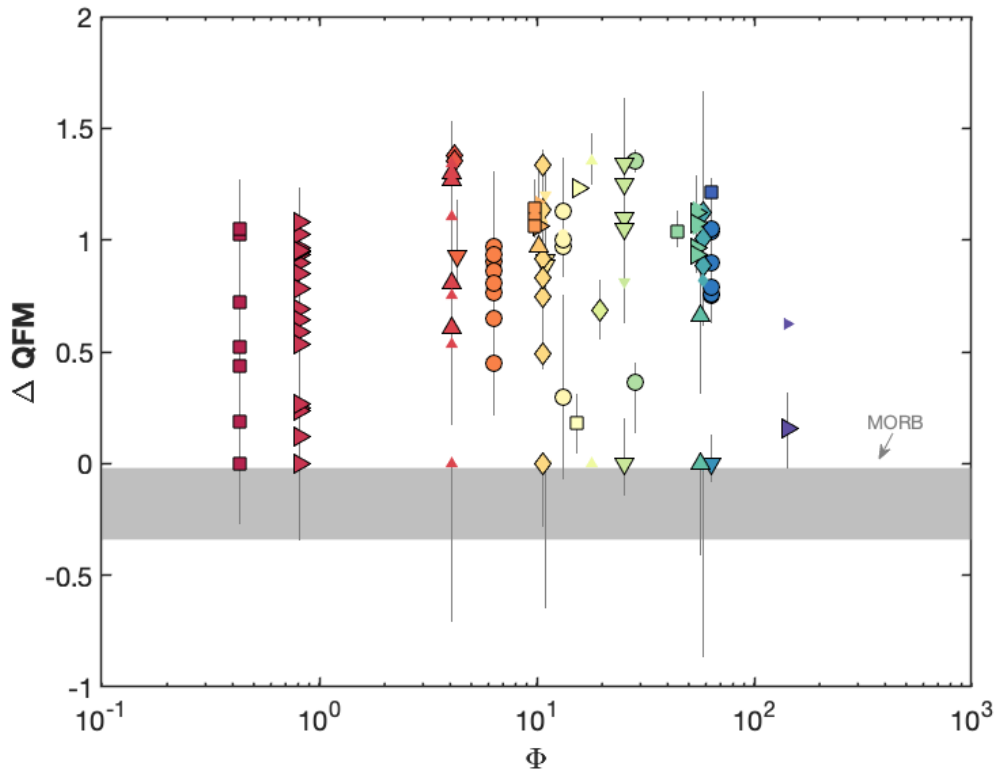
Figure 9. Mean minimum oxygen fugacity of magmas beneath volcanoes calculated using PEC-corrected melt inclusion sulfur contents. Error bars represent propagated uncertainty as described in the text. Symbols as in Figure 1. Oxygen fugacity of MORB shown for comparison in gray bar (Cottrell et al., 2011, Zhang et al., 2018).

4.2 Slab-derived sulfur and arc magma f_{O2}

The relatively consistent range in arc magma S contents may also be linked to the broadly consistent f_{O2} across arcs (Fig. 10; Cottrell et al., 2020). The relationship between magma S content and f_{O2} holds true even when comparing S/Dy (Fig. 10), which during

sulfide-saturated melting does not vary strongly with melt fraction. The observed correlation between Nb/Y and f_{O2} therefore suggests that the addition of S-rich slab-derived material is linked to increased f_{O2}. This is consistent with evidence that elevated magma oxidation state is directly linked to slab-derived material in the Mariana Arc (Brounce et al., 2014; Kelley and Cottrell, 2012, 2009), and that slab-derived S^{6+} in the Cascade Arc is linked to elevated magma f_{O2} (Muth and Wallace, 2021).
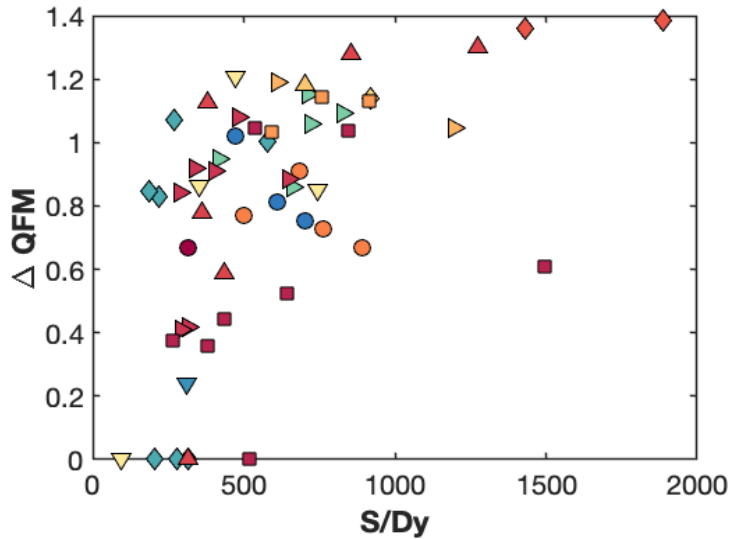
Figure 10. Average calculated minimum f_{O2} based on measured sulfur contents in melt inclusions, plotted as a function of primary magma S/Dy for volcanos from each arc segment. Symbols as in Figure 1.

Slab-derived S^{6+} can be an effective oxidizing agent in the mantle wedge, but its effect is muted to some extent because of the high concentrations of Fe^{2+} in mantle wedge peridotite. To test how equilibrium between S and Fe redox state affects the relationship between slab-derived S^{6+} and arc magma f_{O2}, we do a simple calculation of S^{6+} addition into a basaltic melt with the composition of N-MORB (Gale et al., 2013), using a modified version of the S-Fe redox equilibrium model of Nash et al. (2019) as described in Muth and Wallace (2021). This titration calculation tracks both the mass balance of S and Fe and the redox exchange between S and Fe. After the first ~1,500 ppm S^{6+} addition to a MORB-like mantle melt, during which the melt becomes increasingly S^{6+}-dominated, the S-Fe equilibrium shifts less drastically in response to further S^{6+} addition. This smaller shift means that S^{6+} addition becomes less efficient at increasing melt $Fe^{3+}/\Sigma Fe$ (Fig. 11). A more realistic calculation can be achieved by combining these

types of redox equilibrium calculations with MELTS-based mantle melting models (Muth and Wallace 2021). The results of such model calculations show the same drop-off is present (Figure 11; Muth and Wallace 2021). This waning effect of S^{6+} addition could explain why f_{O2} values across arcs cover a broadly similar range, despite a wide range of slab thermal conditions and primary magma S contents (Fig. 4, 9).
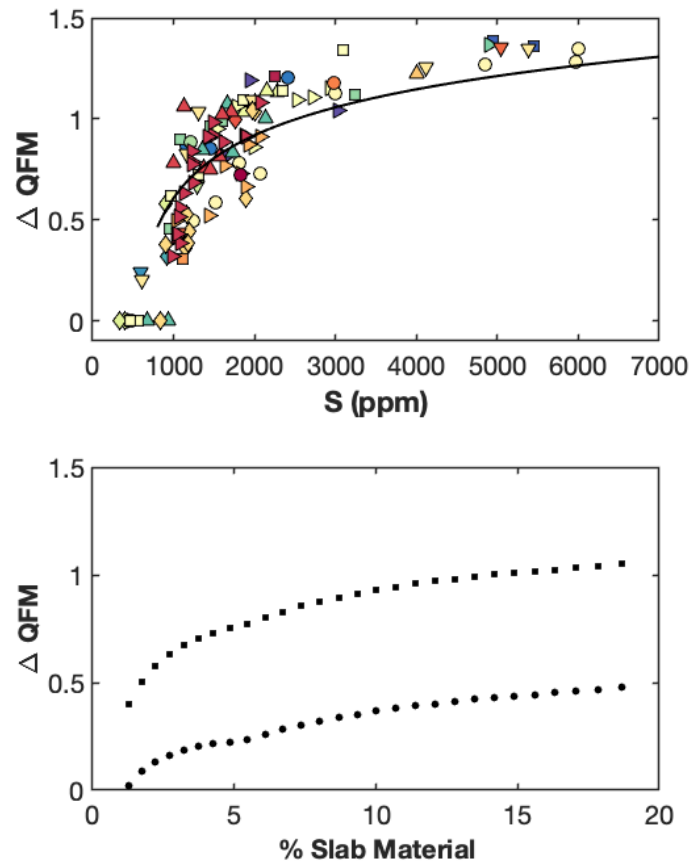
Figure 11. (Top) Mean minimum f_{O2} calculated for the magmas at each volcano shown as a function of primary magma S content. The black line shows the effect of S^{6+} titration into N-MORB composition at 1150 °C. (Bottom) Calculated oxygen fugacity of mantle melts at peak mantle wedge temperature with variable proportions of slab melt containing 1,500 (circles) or 10,000 (squares) ppm S.

4.3 Slab-derived sulfur and porphyry Cu deposits

The behavior of sulfur and its close relationship to f_{O2} is important to the formation of porphyry ore deposits. There has been some debate as to whether high LREE/HREE ratios of volcanic rocks from ore-forming magmas stem from variations in primary magma composition or from crustal storage (Barber et al., 2021; Lee and Tang,

2020; Mungall, 2002). Previous work has used the association of adakite-like (e.g. high Sr/Y, high La/Yb) signatures and fertile deposits to argue for slab-derived melts in arc magmas as a key driver of fertile ore deposits (Mungall, 2002), primarily due to the capacity of slab melts to carry Fe^{3+} into the mantle wedge. Muth and Wallace (2021) show that slab-derived melts can influence mantle melt f_{O2}, but that it is likely the transport of S^{6+}, not Fe^{3+}, that drives most of this change, given that slab melts are likely relatively Fe-poor and andesitic to dacitic in composition (e.g. Jégo and Dasgupta 2014). High LREE/HREE ratios within ore-forming magmas may also be due to fractionation of amphibole, and possibly phases such as garnet and titanite (Richards and Kerrich, 2007). It is uncertain which of these two processes is the dominant driver of the association between ore deposits and high LREE/HREE ratios associated with fertile Cu deposits.

Here we revisit the connection between slab melts and porphyry Cu deposits. Correlations between Sr/Y and S/Dy suggest that 'adakite-like' magmas are more oxidized and sulfur rich. The highest Sr/Y and S/Dy magma in the data compilation is a high-Mg andesite from Mt. Shasta, which has been interpreted as forming by high degrees of melting of a depleted mantle wedge caused by addition of slab-derived fluids (Grove et al., 2003; Ruscitto et al., 2010). Models of formation of high-Mg andesites in other regions likewise usually require high proportions of slab-derived materials (Kelemen et al., 2003; Yogodzinski et al., 2014). Interestingly, high-Mg andesites have relatively low Cu contents compared to many arc magmas, which has been previously attributed to sulfide sequestration during melt transport in a depleted mantle (Rezeau and Jagoutz, 2020). Another explanation based on the high S/Dy contents of these magmas is that these magmas contain a higher proportion of sulfur-rich, slab-derived melts than typical calc-alkaline basalts. As shown in the previous section, due to Fe-S redox equilibrium, the efficiency of slab-derived sulfate in oxidizing mantle melts may drop off significantly after the range of S and f_{O2} typical of many primitive arc basalts. Therefore, even if slab-derived S is present as S^{6+}, increasing slab-derived S addition to the mantle may still stabilize more sulfide in the mantle wedge. These sulfides may then sequester more Cu and drive depletions in the Cu content of arc magmas.

Although high-Mg andesites may have low Cu contents compared to more typical arc basalts, they commonly are relatively rich in S and Cl and have S/Dy concentrations

indicative of an oxidized, S-rich mantle source. High-S, oxidized magmas may be more likely to precipitate anhydrite during crustal storage, providing an easily remobilized source of sulfur for more shallow crustal magmas during periods of magma recharge (Chambefort et al., 2008; Hutchinson and Dilles, 2019). Although high-Mg andesites are uncommon as volcanic rocks at the surface, it may be that these magmas and their differentiates make up a greater proportion of plutons at depth (Kelemen et al., 2003).

Crystallization within the crust can be another way to produce the HREE depletions observed in association with many porphyry Cu deposits. While the high Sr/Y melt inclusions studied here formed relatively early during crystallization, source plutons for porphyry deposits are commonly intermediate to felsic in composition and have therefore likely undergone a substantial amount of hornblende, garnet, and/or accessory phase (e.g. titanite) crystallization (Richards, 2011). However, although hornblende crystallization is a viable explanation for the genetic relationship with HREE depleted magmas and ore deposits, typical arc magmas, even those that contain hornblende, commonly do not show the strong HREE depletions that are found in magmas associated with ore deposits (e.g. Bachmann et al., 2005). In contrast, high-Sr/Y, high-Mg andesites may contain more H_2O and be more likely to stall and precipitate large amounts of hornblende in the crust, which would reinforce pre-existing HREE depletion. High pressure experiments also suggest that high-Mg andesites at high pressure crystallize a greater proportion of amphibole than high-Mg basalts (Ulmer et al., 2018). High-Mg andesites may therefore reconcile evidence for extensive amphibole crystallization in ore-forming magmas (Barber et al., 2021) with the scarcity of amphibole directly observed in calc-alkaline basalts.

4.4 Slab-derived sulfur and sulfur degassing

The mass addition of sulfur to the sub-arc mantle and the oxidizing potential of slab-derived sulfate can drive increases in the bulk S content, f_{O2}, and S/H_2O ratio of mantle melts that feed eruptible magma bodies. These parameters also strongly influence the amount of sulfur that partitions into the vapor phase during magma storage in the crust (Burgisser and Scaillet, 2007; Scaillet and Pichavant, 2005), which is an important consideration for the prediction and interpretation of volcanic gas fluxes (Aiuppa et al.,

2019; Shinohara, 2008; Wallace and Edmonds, 2011). The results of this work show, for example, that although the S content and f_{O_2} of primitive arc magmas are broadly consistent, intermediate temperature arcs tend to have magmas that extend to higher S contents.

The findings of our study also highlight that the cycling of sulfur is a function of both slab-derived sulfur mass transfer and elevated mantle f_{O_2}, and that these two factors are likely linked (e.g., Muth and Wallace, 2021; Walters et al., 2020; Brounce et al., 2014). If the sub-arc mantle is sulfide saturated, S may be somewhat decoupled from the cycling of other incompatible elements from the slab to the surface, including other volatiles such as CO_2 and Cl (Aiuppa et al., 2019; Robidoux et al., 2017). In this case, interpretations of S contents in arc magmas and models for crustal degassing require considerations of both the sulfur content and oxidation state of the sub-arc mantle source. However, as shown here, correlations between S and Cl (Fig. 6), and f_{O_2} and S/Dy (Fig. 10), suggest f_{O_2}, primitive magma S and primitive magma Cl concentrations will broadly co-vary between most arcs.

5.0 Conclusions

We have compiled olivine-hosted melt inclusion compositional data from 29 subduction zone segments and 115 volcanoes and have used this data to estimate primary magma sulfur contents at each volcano. We find that S concentrations in primary magmas from each arc range from 466 ± 220 ppm to 4,264 ± 819 ppm. Melt S/Dy does not correlate with indicators of mantle enrichment such as Nb/Y, showing that the enrichment or depletion of the mantle source before the addition of subduction-derived components is not a strong control on magma S concentration. Instead, S/Dy correlates with proxies for slab-derived components such as Sr/Y. We conclude from these observations that addition of slab-derived sulfur plays an important role in determining the S contents of arc magmas, consistent with correlations between primary magma S and Cl content.

To quantify the role of oxygen fugacity in controlling arc magma S concentrations, we calculate the minimum f_{O_2} needed during melting to match the sulfur contents of primary magmas from each volcano. We find that 90% of primary arc

magmas require f_{O_2} greater than QFM, and the data require minimum relative f_{O_2} values up to QFM + 1.4. Correlations between S/Dy and relative f_{O_2} suggest slab-derived S and f_{O_2} are related. This link has implications for processes such as porphyry ore deposit formation and volcanic degassing. In magmas associated with porphyry Cu deposits, high Sr/Y ratios may signal high-S, oxidizing magmas. These magmas may be related to high-Mg andesites that erupt less commonly than high-Mg basalts but are more likely abundant as intrusive rocks and may therefore explain the high Sr/Y signature of magma bodies associated with porphyry deposits compared to most arc volcanic rocks. During magma storage in the crust, the degassing behavior of S and its relationship to other slab-derived volatiles depends on how the mass transfer of sulfur into the mantle is tied to the f_{O_2}, Cl, and H_2O content of primary magmas. These applications demonstrate that variations in the behavior of slab-derived sulfur and its close connection to magma oxidation state is an important consideration for a range of arc magmatic processes.

CHAPTER V

DISSERTATION SUMMARY

This dissertation examines the origins and behavior of sulfur in volcanic arcs. Using the measured compositions of olivine-hosted melt inclusions, I investigate how the transfer of sulfur from the subducting plate into the mantle source for arc magmas influences the sulfur content, metal content, and oxidation state of arc magmas. In Chapters II and III, I combine measurements of major element and trace element composition, S isotope ratios, S and Fe valence state, and ore-forming metal concentrations to build a detailed and self-consistent model of sulfur behavior in the southern Cascade Arc. In Chapter IV, I expand my geographic consideration of the same topics, and use published melt inclusion compositions to examine the causes and implications of sulfur in magmas in subduction zones globally.

In Chapter II correlations between magma sulfur contents, sulfur isotope ratios, and magma oxidation state demonstrate that sulfur in the southern Cascade Arc is partially derived from the subducting slab. Using comparisons between sulfur isotope ratios of subducting lithologies and those measured in Lassen inclusions I show that slab-derived sulfur is oxidized. I then use a combined mantle melting and electron budget calculation to show that oxidized, slab-derived sulfur can generate the elevated sulfur contents observed in arc magmas, but that this requires either extremely S-rich slab melts, or a multi-stage process of oxidation.

In Chapter III, I apply insights gained within Chapter II to investigate the behavior of ore-forming metals within the southern Cascade Arc. I show that Mo, Sn, Zn, and W are relatively unaffected by the influence of slab-derived materials, whereas Pb is strongly enriched in arc magmas via the mass transfer of Pb from the subducting slab. I compare mantle melting models of Cu behavior to external constraints on mantle S content and mantle oxidation state to show that Lassen magma Cu contents are controlled by a combination of ambient mantle heterogeneity and modern subduction influence.

In Chapter IV, I use the framework developed within Chapter II and III to consider the behavior of sulfur in arc magmas globally. I use a compilation of olivine-hosted melt inclusions from 29 arc segments to characterize the S contents of primitive

magmas from 115 volcanoes. I use comparisons between S and slab-derived elements such as Cl and Sr to show that S in arc magmas is partially sourced from the subducting slab. I also compare primitive S contents at arc volcanoes to oxygen fugacity-dependent sulfur solubility models and find that 90% of arc magmas require conditions more oxidizing than QFM.

APPENDICES

APPENDIX A

CHAPTER II SUPPLEMENTARY INFORMATION AND FIGURES

Appendix A Supplementary Text

Analytical methods

Olivine-hosted melt inclusions from the tephra of each cinder cone were selected for analysis. Inclusions that contained quench or daughter crystals, were intersected by cracks in the host crystal prior to sectioning (some inclusions developed cracks during preparation) or contained anomalously large or multiple vapor bubbles were not selected. Some inclusions contain a small (~3-5 µm) immiscible sulfide bleb or a co-trapped spinel crystal. Inclusions that contained a sulfide bleb were not selected for SIMS analysis. Representative photomicrographs are shown in Figure S1, and inclusion petrographic data is provided in Supplementary Table S1.

Melt inclusions were analyzed on a Thermo-Nicolet Nexus 670 FT-IR spectrometer interfaced with a Contiuum IR microscope. H_2O concentrations were calculated from IR peak absorbance values using the Beer-Lambert Law. Doubly polished melt inclusion wafers were prepared to be very thin to avoid host contamination during Fe XANES analysis. Because of this, the CO_3^{2-} doublet normally used to quantify CO_2 in basaltic glasses could not be deconvolved from interference fringes and therefore was not used. H_2O concentration was determined using the 3570 cm^{-1} OH^- peak with absorption coefficient $\varepsilon = 63$ from Dixon et al. (1995). Thickness was determined using the interference fringe method (e.g. Wysoczanski and Tani, 2006) calculated using the Spectragryph software package (Menges, 2020). Hydrous densities were determined by iteration between calculated glass densities (Luhr, 2001) and Beer-Lambert calculations.

$S^{6+}/\Sigma S$ and $Fe^{3+}/\Sigma Fe$ values were calculated using S and Fe XANES spectra acquired at the Advanced Photon Source (APS) at Argonne National Laboratory. Fe XANES measurements were made in fluorescence mode at APS on December 7-9, 2018 and June 14-17, 2019, using an incident photon flux of ~3 x 10^9 photons/s and 10x10 µm spot. To identify and correct for beam-induced oxidation (Cottrell et al., 2018), multiple rapid pre-edge scans (82s in length) were taken over the energy range 7092-7144 eV before a longer full energy range scan (352s) from 7012-7355 eV. The pre-edge scans were fit following the peak-fitting convention of Cottrell et al. (2009) using the Larch XAS viewer software package (Newville, 2013). Linear regressions to time zero of centroid values for consecutive rapid pre-edge scans were calculated for each sample, and each calculated value at time zero was taken as the corrected centroid value. The average 1 standard error of fit for corrected centroid value in each rapid scan is 0.03 eV. The average 1 standard error of regression for corrected centroid values is 0.04 eV. These corrected centroid values were then used to calculate $Fe^{3+}/\Sigma Fe$ using the calibration of Zhang et al. (2018). An example of this regression is shown in Figure S2. Full details and discussion of this correction approach are described in Lerner et al. (in review).

The energy offset between our basaltic glass measurements and those used in the Fe XANES calibration of Cottrell et al. (2009) was determined by comparing the Fe pre-edge centroid position of basaltic reference glass LW_0 (Cottrell et al., 2009, 2018; Zhang et al., 2018) from the Smithsonian Institution. The split of LW_0 glass analyzed here is embedded in the mount NMNH 118279/IGSN NHB007V34, and is the same specimen as found in the mount with catalog number NMNH 117393/IGSN NHB0073V8 (both available by request from the Smithsonian Institution). The pre-edge centroid position of LW_0 was measured by Cottrell et al. (2009) to have an energy of 7112.30 eV using the beamline configuration they described at the National Synchrotron Light Source (Brookhaven National Laboratory), whereas the pre-edge centroid position of LW_0 measured during our Fe XANES session was 7111.98 eV. Therefore when calculating Fe valences of basaltic glasses, energy shifts of +0.32 eV were applied to Fe pre-edge centroid positions to provide consistency with centroid values measured for LW_0 in Cottrell et al. (2009).

S XANES measurements were conducted on October 18-20, 2019. Incident beam flux ranged from $\sim 1 \times 10^9$ to 4×10^{10} photons/sec for S XANES analyses. To avoid the ingrowth of S^{4+} during beam exposure (Wilke et al., 2008), we used a 50x50 μm or 20x20 μm defocused beam, and used an analysis time of 0.5 seconds per step bin for rapid scans over the 2437-2622 eV energy range with total durations of 154 seconds. Analyses using a 50x50 μm beam induced very little S^{4+} ingrowth but often the beam was too large to analyze inclusions without some crystal host in the beam path. Partitioning data (Callegaro et al., 2020) and analyses on host crystals indicate the S content of olivine is negligible compared to the S content of S-rich (>500 ppm S) melt inclusions. Therefore, we used a 50x50 μm beam to analyze most inclusions, despite some small overlap with the olivine host. However, for smaller inclusions, where a 50x50 μm beam would have intersected a significant amount of olivine, weakening the signal from the glass, a 20x20 μm beam was used. In these cases, we observed a small ingrowth of S^{4+} that was corrected using the approach and correction factor described in Lerner et al. (in review). The applied correction in these samples is always 10 % or less (Supplementary Table S5). In many analyses, the 50x50 μm beam used for S XANES analyses overlapped with the 10x10 μm area affected by previous Fe XANES analyses. However, within these analyses, we do not observe any evidence for beam damage such as ingrowth of S^{4+} glass species (e.g. Wilke et al., 2008). $S^{6+}/\Sigma S$ was quantified using the fitting method and calibration detailed in Lerner et al. (in review). Detailed information about both measurement setup and correction procedures used for S and Fe XANES are presented in Lerner et al. (in review).

Most electron microprobe analyses (EPMA) were conducted using a Cameca SX-100 equipped with five wavelength dispersive spectrometers in the CAMCOR facility at the University of Oregon with a 15 kV accelerating voltage. A subset of olivine analyses were conducted on a JXA-8530FPlus HyperProbe Electron Probe Microanalyzer at the Smithsonian Institution with a 15 kV accelerating voltage. Analytical conditions varied slightly between sessions. See Table S8 for sample current, beam size, and counting times used during each session. Effects of element migration were corrected by performing linear regressions to time zero on Na, K, Al, and Si counts (Hanson et al., 1996; Morgan and London, 1996, 2005). Individual analyses for both olivine and glass are averages of 3-5 analyzed spots.

Analyses of ^{32}S and ^{34}S in individual melt inclusions were performed on a CAMECA IMS 1280 ion probe at the Northeast National Ion Microprobe Facility at Woods Hole Oceanographic Institution over a five day period in November 2019. The analyses were carried out using 10 kV $^{133}Cs^+$ primary beam of 0.3 nA current. The beam was rastered across a 20x20 µm area for a pre-sputtering period of 60 seconds, then rastered across a 10x10 µm area for analysis. Count times were 4s for ^{32}S and 10s for ^{34}S. Wait times were 2s for ^{32}S and ^{34}S. Standards were run at the beginning of the analytical week-long session. VG-2 MORB glass was also embedded in each mount and was used as an internal run standard. No instrument drift was detected over the course of the session. We used several external standards to calculate instrument mass fractionation (IMF), encompassing a range of $S^{6+}/\sum S$ and H_2O contents. Compositional information and reference values for each standard are reported in Table S7. Comparisons between reference values and measured values for all external calibration standard glasses are shown in Figure S3.

Melt inclusions were analyzed for a suite of trace elements using Laser Ablation Inductively Coupled Mass Spectrometry (LA-ICPMS) during two different sessions. During the first session in June 2017, melt inclusions were analyzed on the Photon Machines Analyte G2 135 nm ArF "fast" excimer laser system at Oregon State University, using a 40 µm or 50 µm diameter spot size with a 5 Hz pulse rate. Measured trace element concentrations were determined by reference to GSE-1G glass as a calibration standard and using ^{43}Ca as an internal standard. BHVO-2G, BCR-2G, and GSD-1G glasses were also analyzed to monitor accuracy and precision. During the second session in February 2020, melt inclusions were analyzed on a Thermo Scientific iCAP RQ and Photon Machines Analyte G2 193 nm ArF excimer laser at Oregon State University, using a 30 µm, 40 µm or 50 µm diameter spot size with a 15 Hz pulse rate. Measured trace element concentrations were determined by reference to NIST 612 glass as a calibration standard and using ^{43}Ca as an internal standard. BCR-2G, GSD-1G, and BIR-1G glasses were also analyzed to monitor accuracy and precision.

Post-entrapment crystallization and Fe-Mg diffusive reequilibration corrections

Individual melt inclusion analyses were corrected for post-entrapment crystallization (PEC) and Fe-Mg re-equilibration using Petrolog3 (Danyushevsky and Plechov, 2011). Bulk rock data for each cinder cone studied here is limited, making it difficult to estimate initial FeO^T content for melt inclusions. To circumvent this, forward models of olivine crystallization were calculated using Petrolog3 at 5 kbar. Detailed model inputs are listed in Table S9. Oxygen fugacity conditions are based on average calculated f_{O2} from Fe XANES data (Table S5), and H_2O is based on average melt inclusion values. These olivine-only crystallization models are consistent with whole rock data from other mafic vents at Lassen (e.g. Borg 1997), which indicate that high-Mg Lassen magmas crystallize along an Fe-depletion trend consistent with olivine (+minor Cr-spinel) crystallization, and little to no contribution from plagioclase, pyroxene, or titanomagnetite crystallization.

For forward olivine crystallization models of each cinder cone, whole rock data with the highest FeO^T content were chosen as starting compositions. For cinder cones that have little (BBL) or no (BRM) bulk rock data, we used a composition based on

average analyzed melt inclusions (MI) from each cinder cone and the 90th percentile value of measured MI FeO^T concentration. To estimate FeO^T concentration of each melt inclusion prior to Fe-Mg reequilibration, equilibrium olivine forsterite content was calculated for each MI composition. The FeO^T value from the forward olivine crystallization model for a given cinder cone that matched this olivine forsterite content was taken as the initial melt FeO^T. We emphasize that the choice of FeO^T value for correcting the melt inclusions from a given cone mainly affects the corrected MgO and FeO^T values and has only a small effect on other major and trace elements.

Melt inclusion compositions were then corrected for PEC and Fe-Mg reequilibration using Petrolog3, with our estimated initial melt FeO^T concentrations as input values. For the Petrolog calculations, the olivine temperature model used was Danyushevsky (2001), with Toplis used (2005) for olivine K_d. All reverse olivine crystallization calculations were performed using f_{O2} values from Fe XANES data as described above for each cinder cone. If melt inclusions did not have measured H_2O contents, average H_2O contents from each cinder cone were used, as listed in Table S9. A subset of inclusions from cinder cone BBL did not show evidence for Fe loss, so we instead calculated simple reverse olivine crystallization using Petrolog3 to correct for post-entrapment crystallization. For all inclusions, the S, Cl, and trace element concentrations for the Petrolog-corrected compositions were calculated by diluting each element's analyzed concentration by the same amount that K_2O was diluted.

We do not see any systematic changes in $Fe^{3+}/\Sigma Fe$ measured in melt inclusions as a function of H_2O concentration (which varies as a result of post-entrapment diffusive loss), consistent with experimental results (Gaetani et al., 2012), natural datasets (Hartley et al., 2017), and calculations of available redox pairs (Danyuschevksy et al., 2002) that suggest rapid reequilibration of melt inclusion redox state with external melt even during post-entrapment diffusive H loss (Figure S4d). For this reason, we assume that redox reequilibration is more rapid than post-entrapment crystallization and therefore do not change melt $Fe^{3+}/\Sigma Fe$ during PEC corrections.

Primary magma estimates

See Ruscitto et al. (2012) for a detailed description of primary magma estimates at arc segments other than Lassen. Primary magma estimates based on melt inclusion data showing obvious S degassing signals (e.g. decreasing S with increasing K_2O) have been removed from the original compilation.

To estimate primary melt composition at Lassen, the composition of a subset of melt inclusions above a specified MgO content were averaged and used to calculate reverse olivine crystallization until each composition was in equilibrium with Fo$_{90}$. The MgO content used at each cinder cone was determined using MgO and Al_2O_3 bivariate plots, to avoid including melt inclusions whose compositions may have been affected by plagioclase fractionation before entrapment. For most inclusions, an MgO cutoff value was used in order to select the most primitive inclusions while still retaining enough inclusion compositions for a representative compositional average. Within some cinder cones, there is some scatter in the Al_2O_3 content in more evolved inclusions, suggesting the potential influence of plagioclase fractionation. In these cases, the MgO content was chosen so that these more scattered compositions were avoided. The average high-Mg

compositions calculated for each cinder cone were used as a starting composition for reverse crystallization models. All reverse crystallization models were calculated using Petrolog3 at 5 kbar, using the Danyushevsky (2001) olivine temperature model and the Toplis (2005) K_d model. Specific conditions used for models of each cinder cone are listed in Table S9. The S, Cl, H_2O, and trace element composition of primary magmas were calculated by diluting each element by the same amount that K_2O was diluted in the reverse crystallization models.

The average measured $Fe^{3+}/\sum Fe$ in melt inclusions from each cinder cone is taken as the primary magma $Fe^{3+}/\sum Fe$ for that cinder cone. This average and average $S^{6+}/\sum S$ are calculated only with XANES data that has major element concentrations measured in the same inclusion, with the exception of BAS-44 inclusions which have limited associated XANES data. We take this simplified approach to avoid introducing uncertainties in the behavior of magma oxygen fugacity during early crystallization because the magmas are in a range of ΔQFM values where oxidation of S^{2-} to S^{6+} would likely play a role in moderating any increase in Fe^{3+} as a result of olivine-only crystallization. Because the data studied here were measured in relatively high Mg inclusions, the choice of assumption about melt $Fe^{3+}/\sum Fe$ evolution during early olivine-only crystallization would change primary magma $Fe^{3+}/\sum Fe$ values by ~0.03 at the most. These $Fe^{3+}/\sum Fe$ values and melt compositions were used to calculate primary melt f_{O2} relative to the QFM buffer using the calibration of Kress and Carmichael (1991) and Frost (1991) at 1.6 GPa, 1400 °C. Calculated primary magma compositions for each cinder cone are provided in Table S6.

Slab sulfur $\delta^{34}S$ budget

To estimate the bulk $\delta^{34}S$ value of the subducted oceanic lithosphere beneath the Lassen region, we divide the downgoing plate into three sections; sediments, altered oceanic crust (AOC), and hydrated mantle lithosphere. In oceanic sediments, $\delta^{34}S$ values depend heavily on the variable influence of microbially-mediated sulfur reduction (Jørgensen et al., 2019). The bacteria communities that drive sulfur reduction need nutrient-rich water to thrive. For this reason, sediments in ocean basins may experience little sulfur reduction and remain S^{6+} dominated and isotopically heavy. Cascadia, in contrast, is located on the coast of a continent in a bacterially productive area. Therefore, the sediments are isotopically light and S^{2-} dominated (Fig. 3), although a large proportion of this S^{2-} is often re-oxidized during continued microbial activity. For sediment sulfur budget estimates, thickness values are taken from Gorda plate sediment thickness calculated from seismic data (Gulick et al., 2002), and $\delta^{34}S$ values are taken from bulk $\delta^{34}S$ measured at the Cascadia margin (Turner et al., 2018). Although these $\delta^{34}S$ measurements are only made in shallow (< 20 mbsf) sediments, the nutrient-rich Cascadia margin likely creates similar microbial environments through the length of the sediment package (Jørgensen et al., 2019). We therefore take these measurements as representative values.

Sulfur in altered oceanic crust (AOC) includes primary sulfides inherited from crustal formation and sulfur deposited during hydrothermal alteration. Hydrothermal circulation, which affects the upper oceanic crust much more strongly than lower crust, alters pre-existing sulfides and deposits seawater sulfate as anhydrite with the isotopically

heavy δ^{34}S of seawater (Alt, 1995). It is uncertain whether this anhydrite remains in the slab until sub-arc slab dehydration (Tomkins and Evans, 2015) or is removed from the slab during the earliest stages of subduction and porewater exsolution (Walters et al., 2019). The composition of AOC used to calculate bulk δ^{34}S is based on Ocean Drilling Program drill cores Hole 504B in the eastern Pacific for the volcanic section and 735B from the Indian Ocean for the gabbroic section (Alt, 1995). Ridge spreading rate, eruption style, plate age, and sediment deposition rate can all influence the sulfur content and bulk δ^{34}S of AOC (Alt et al., 2010; Alt and Shanks, 2011). Drill core from Hole 1256D (15 Ma), for example, contains older AOC more heavily influenced by low temperature alteration on ridge flanks than core from Hole 504B (5.9 Ma). This alteration and associated microbial sulfate reduction shifted the bulk δ^{34}S of the analyzed 800 m section to -6 ‰ (Alt and Shanks, 2011). The oceanic crust that subducted beneath the Lassen region may also have been affected by microbial sulfate reduction and therefore have been shifted toward more negative δ^{34}S values relative to Hole 504B. However, because the age of the crust subducting beneath Lassen (6-9 Ma, Wilson, 2002) is comparable to the age of crust at Hole 504B we take measured values at 504B as the most applicable values for Lassen. We additionally note that basalts in 3.5 Ma ocean crust on the eastern flank of the Juan de Fuca ridge have an average δ^{34}S similar to that of Hole 504B (-2.8‰, Ono et. al, 2012), which also suggests that 504B is a suitable analog.

The lithosphere underlying oceanic crust can become serpentinized near the ridge axis during high temperature alteration as fluid circulates near igneous bodies or by low temperature alteration during shearing and faulting on ridge flanks (Alt et al., 2013; Rouméjon and Cannat, 2014). In Cascadia and many modern subduction zones, the downgoing plates are generated at intermediate and fast-spreading ridges, where these processes play a smaller role (e.g., Schwarzenbach et al., 2016). The underlying mantle lithosphere can also become serpentinized during slab bending and faulting outboard of the subduction zone, where seawater penetrates through the oceanic crust and hydrates the underlying lithosphere, incorporating seawater sulfate (Alt et al., 2013). S^{6+} in serpentinite may be hosted directly in the structure of serpentine (Debret et al., 2017).

Offshore of Lassen, the crust of the Gorda microplate is young and warm and is overlain by a thick sediment package. All of these factors likely limit the extent of serpentinization, as shown at the nearby Juan de Fuca plate (Canales et al., 2017). Unlike the Juan de Fuca plate, however, the Gorda microplate is extensively faulted which may lead to more serpentinization, though whether the subducted portion of the plate that is now beneath the Lassen region experienced such faulting is not known (Wilson, 2002). Calculations of H_2O cycling in the Lassen region indicate that only a modest amount of lithosphere hydration is needed to generate observed H_2O contents in Lassen magmas (Walowski et al., 2015). This modest hydration may be difficult to detect using seismic data. To constrain the S content and δ^{34}S value of serpentinized subducted lithosphere that is beneath the Lassen region, we use Hess Deep as an analog (Alt et al., 2013). Estimates for extent of serpentinization at Hess Deep are ~10 wt. %, similar to estimates for the mantle lithosphere beneath Lassen (~15 wt. %; Walowski et al., 2015). Hess Deep and other serpentinites often contain a high proportion of S^{6+} despite containing no visible anhydrite, consistent with the incorporation of S^{6+} into the mineral structure of serpentine (Debret et al., 2017). Based on Walowski et al. (2015) we assume a 2-km

section of partially hydrated mantle lithosphere. See Table S12 for compiled S content and $\delta^{34}S$ values used to calculate the composition of the bulk slab beneath Lassen.

Modeling of slab-derived melt interactions with peridotite in the mantle wedge

This model is intended to approximate hydrous melting in the mantle (the "double" flux- melting model of Walowski et al., (2015, 2016)), wherein a hydrous slab-derived melt percolates up through the inverted thermal gradient of the mantle wedge, equilibrating with mantle peridotite as it rises. To start, a S^{6+} dominated slab melt equilibrates with the mantle wedge at a specified melt:rock ratio. This equilibrated melt then rises and equilibrates with fresh peridotite along a specified sub-arc mantle P-T path. We describe here the base model used in this paper ('Normal Mantle'), then describe variations on the model as discussed in the main text. The model begins by using pMELTS models (Ghiorso et al., 2002; Antoschechkina and Ghiorso, 2018) to calculate equilibrium between a hydrous slab melt and mantle peridotite at a specified temperature and pressure above the slab interface and a specified starting melt:rock ratio. Slab melt major element composition is the average melt composition from 2.8 GPa MORB partial melting experiments (Sisson and Kelemen, 2018) and contain 5 wt. % H_2O. Mantle peridotite is a partially depleted source comprised of 60% spinel lherzolite (Bulk DMM; Workman and Hart, 2005) and 40% harzburgite (Falloon and Danyushevsky, 2000). At Lassen, spinel compositions (Clynne and Borg, 1997), whole rock trace element compositions (Borg et al., 1997, 2002), and measured volatile contents (Walowski et al., 2016) are all consistent with the variable influence of slab-derived materials in the mantle source of each cinder cone. To approximate this process, models are run using melt:rock ratios ranging from 0.03:0.97 to 0.3:0.7. Because pMELTS calibration data is limited at oxidizing conditions relevant to arcs, we calculate all melting phase equilibria at QFM instead.

After phase equilibrium and equilibrated major element melt composition are calculated in pMELTS, melt trace element concentrations are calculated using specified mineral-melt partition coefficients and using mineral modal proportions as described in Walowski et al. (2016). S^{6+}, S^{2-}, and Fe^{3+} are all treated as trace elements, whereas melt Fe^{2+} is calculated from mass balance using pMELTS melt FeO^T output. Trace element composition for initial source mantle is taken from DMM (Workman and Hart, 2005). Mantle peridotite Fe_2O_3 content is taken as 0.3 wt. %, consistent with previous estimates for the MORB source mantle (Canil et al., 1994; Cottrell and Kelley, 2011). Mantle peridotite S content is 150 ppm, based on previous estimates for the MORB mantle source (Saal et al., 2002; Ding and Dasgupta, 2017). Unless otherwise specified we assume all mantle peridotite S is present as S^{2-}. Slab melt trace element composition was calculated following the methods of Walowski et al. (2016), calculating a 5% partial melt of Gorda MORB (Davis et al., 2008) via batch melting using 900 °C, 4 GPa partition coefficients from Kessel et al. (2005). Slab melt $Fe^{3+}/\sum Fe$ was calculated using the calibration of Kress and Carmichael (1991) at QFM+2. We assume 1,500 ppm S^{6+} in the slab melt based on experiments of fluid-saturated, anhydrite-saturated MORB partial melting at 950 °C and 3 GPa (Jégo and Dasgupta, 2014). Trace element compositions of the slab melt and the mantle peridotite are mixed according to the specified melt:rock ratio to calculate the mantle source composition.

Equilibrium melt trace element compositions are then calculated via batch melting equations, using trace element partition coefficients from Eiler et al. (2000) for Sr, Nd, and Dy and from Callegaro et al. (2020) for S. We assume bulk $D^{Fe2O3} = 0.2$. This value is the upper end of the range estimated based on xenolith data (Canil et al., 1994) and is consistent with experimental estimates (Mallmann and O'Neill, 2009). We do not take into account changes in Fe^{3+} partitioning during mantle melting (e.g. Davis and Cottrell, 2018), but note that these uncertainties are secondary relative to the effect of S^{6+} addition (Fig. S5).

Once the melt composition is calculated, we calculate the relative proportion of S^{6+}, S^{2-}, Fe^{2+} and Fe^{3+} using an equilibrium relationship modified from O'Neill (2021) and Nash et al. (2019). This step is critical to the model, as models that assume all S^{6+} is reduced to oxidize Fe^{2+} (Klimm et al., 2012) can overestimate the oxidizing effect of S^{6+} on $Fe^{3+}/\sum Fe$ and calculated f_{O2}. However, we recognize that our modeling approach is still an oversimplification, because our results do not maintain redox equilibrium between the melt and the surrounding peridotite during each equilibration step. Rather, our approach seeks to approximate a reactive transport process (e.g., Sisson and Kelemen, 2018) in which basaltic melt components from the peridotite are "titrated" into a slab-derived melt that interacts with peridotite as it rises upwards through the inverted temperature gradient in the mantle wedge.

Current models for the redox equilibrium relationship between Fe and S species (Nash et al., 2019; O'Neill, 2021) have focused on the effect of temperature, but at present, the separate effects of temperature, pressure, and melt H_2O content are poorly constrained by experimental data. The limited experimental data available suggest that increasing pressure shifts melts to lower $S^{6+}/\sum S$ at a constant relative f_{O2} (Matjuschkin et al., 2016), consistent with thermodynamic analysis (Moretti and Baker, 2008). Given current uncertainties, we adopted the temperature dependence of reaction for the Fe-S redox equilibrium from O'Neill (2021) based on 1 bar data, but we empirically adjusted the constant in the expression for log K of reaction such that the resulting equation fits our measured $S^{6+}/\sum S$ and $Fe^{3+}/\sum Fe$ values for Lassen melt inclusions and similar data for MORB glasses and comes closer to predicting the 200 MPa, 1050°C experimental data of Jugo (2010) on hydrous basaltic compositions (Fig. S6). The equation calculated in this manner is log K = -2863/T + 7.2 for the reaction $8Fe^{3+} + S^{2-} = S^{6+} + 8Fe^{2+}$. This is the relationship that we used to calculate melt $S^{6+}/\sum S$ and $Fe^{3+}/\sum Fe$ at each model step. A simplified calculation demonstrating this relationship for an initially dacitic slab melt that has mantle-derived basaltic melt added is shown in Figure S7.

In each model step, melt $\delta^{34}S$ is calculated via mass balance between the ascending melt and mantle peridotite. We assume initial mantle peridotite $\delta^{34}S = 0.6$ ‰ based on the average of previously measured MORB $\delta^{34}S$ values (Kanehira et al., 1973; Sakai et al., 1982; Chaussidon et al., 1991; Alt et al., 1993). We use model outputs to constrain $\delta^{34}S$ of the initial slab-derived melt by modifying the slab $\delta^{34}S$ mixing endmember value to provide a best fit to the data set for Lassen primary melt compositions.

We note that there has been debate about the correct MORB $\delta^{34}S$ value (Labidi et al., 2012). Some authors argue that many basaltic glass $\delta^{34}S$ values that were measured using the Kiba reagent for extraction are inaccurate, and they propose that mean $\delta^{34}S$ of MORB is -0.91 ± 0.50 ‰, ~1-2 ‰ lower than many previous estimates made using the

Kiba method. The majority of the calibration glasses used in our SIMS calibration were measured using the Kiba method and are consistent with MORB values of $\delta^{34}S = 0.6$ ‰. Calculated sulfur isotope SIMS instrument mass fractionation values during our analytical session are consistent between standards (Fig. S3). This indicates that the Kiba reagent yields consistent results across different samples and suggests complete sulfur extraction from glasses, as reported in other calibrations (Fiege et al., 2014). This means that changes to the reference values of our calibration standards would change the calculated $\delta^{34}S$ in our melt inclusions by a fixed amount across all samples but would not change comparisons between them. We additionally note that analyses of MORB glass VG-2, used as a secondary standard during our SIMS run, yield $\delta^{34}S = 0.6 \pm 0.1$‰, consistent with values of MORB measured via Kiba extraction. We therefore also use MORB $\delta^{34}S$ values measured using the Kiba reagent in our modelling and discussion to maintain internal consistency. However, we provide our raw measured $^{34}S/^{32}S$ values (Table S4) for authors who may wish to re-process our data set using alternative $\delta^{34}S$ values for our chosen calibration standards.

After calculating the mantle-equilibrated major and trace element composition of the melt, and its S-Fe redox and $\delta^{34}S$ values at a given model step, that melt is extracted and re-equilibrated with fresh mantle peridotite using the same specified melt:rock ratio at a different pressure and temperature as in Sisson and Kelemen (2018). This repeated melt/peridotite equilibration and melt extraction continues in 0.2 GPa increments along a hypothetical P-T path up through the mantle wedge. The pressures for the P-T path are based on a geodynamic model of the Lassen area (Walowski et al., 2015) and mantle wedge P-T paths used in Sisson and Kelemen (2018), tuned to match major element compositions of Lassen primary magmas (Fig. S5). We note that in each model, peak P-T conditions are ~50°C hotter than the estimated temperature of last equilibration calculated via thermobarometry (Walowski et al., 2016; Till, 2017), but that this is consistent with the well documented overstabilization of clinopyroxene in pMELTS in comparison to experiments (Ghiorso et al., 2002). See Table S10 for a summary of all base model inputs and Figures S5,8,9 for representative model outputs. In addition to models based on the assumptions detailed above, we modeled several variations, as detailed below and shown schematically in Figure S10.

We note that this melting model does not account for pre-existing trace element heterogeneity in the mantle wedge, although mantle enrichments in trace elements such as Rb, Ba, K, and Cs unrelated to modern subduction influence have been documented at Lassen. This enrichment is more prevalent toward the back-arc and may be due to prior terrane accretion or bulk sediment addition (Walowski et al., 2016, Borg et al., 1997). Cinder cone BRVB, located more towards the back-arc relative to other cones studied here, shows clear elevations in Nd relative to Sr (Fig. S15), that are consistent with this prior enrichment. These enrichments complicate interpretations of Sr/Nd in BRVB primary magmas (Fig. 2). Simple comparisons against Sr yield relationships that are more consistent across all cinder cones, including BRVB (Fig. S14). However, within melting models, Sr concentrations are sensitive to melt fraction in addition to slab melt addition. Therefore, although we compare models to Sr/Nd values, we note that Sr/Nd values in BRVB primary magmas likely underestimate the degree of slab melt addition relative to other cinder cones.

Model Cases

Normal mantle

As described above, in this scenario we combine constraints from MORB-source mantle estimates and from slab partial melting experiments. We assume 1,500 ppm S^{6+} in the slab melt and assume 150 ppm S^{2-} and 0.3 wt. % Fe_2O_3 in the mantle source.

No S in slab melt

To test our model assumptions in a simplified case, we calculate melting assuming 0 ppm sulfur in the slab melt. This base model can reproduce MORB S and Fe data fairly well, though it should be noted that the major element composition and dissolved H_2O of the model melts differ from MORB because of the slab melt contribution. In calculations that assume a high slab melt:peridotite ratio (i.e. more slab-derived H_2O in the mantle wedge), high melt fractions dilute melt Fe^{3+} and lead to slightly lower $S^{6+}/\sum S$ and ΔQFM values than are found in MORB. This model is shown in Figure S11.

High S in slab melt

In this scenario we increase the amount of S^{6+} in the melt from 1,500 ppm S^{6+} to 10,000 ppm S^{6+}. This is much higher than values found in relevant experimental melts (Jégo and Dasgupta, 2014), but we note that slab melting experiments that constrain anhydrite-saturated slab partial melting are limited. These models also do not consider high temperature aqueous or super-critical slab-derived fluids, which can contain substantially higher S concentrations than slab melts (Jégo and Dasgupta, 2014; Ferrando et al., 2005) but may be present in different proportions relative to mantle peridotite during melting than the slab melts considered here.

High S in slab melt (melts precipitate sulfide that is sequestered in mantle)

In this scenario we increase the amount of S^{6+} in the melt from 1,500 ppm S^{6+} to 8,000 ppm S^{6+} and assume that all melts are sulfide saturated. This is consistent with evidence from arc copper systematics (Lee et al., 2012) that many arc magmas are sulfide-saturated during mantle melting. To calculate this effect of immiscible sulfide saturation on melt redox state, we calculate the sulfur content at sulfide saturation (SCSS) at each model step, then remove the excess dissolved sulfur from the melt into a separate sulfide reservoir that remains in the mantle as a residual phase.

To calculate SCSS, we assume that all Lassen magmas are sulfide saturated during mantle melting and that primary magma S contents reflect the SCSS of mantle melting conditions. To this end, we create an empirical SCSS model using a linear regression of Lassen primary magma sulfur content and relative f_{O2}. To account for the effect of sulfide sequestration in the redox balance calculations, we calculate the amount of sulfur hosted in sulfide at each equilibration step by subtracting calculated SCSS from the modeled melt S content. This excess sulfur is then subtracted from the total S^{2-} of the melt, and S-Fe redox equilibrium is recalculated, assuming that the subtracted S^{2-} is no longer in contact with the melt. As the melt ascends along the P-T path, the continuous removal of S^{2-} from the silicate melt becomes an electron sink, producing higher melt $S^{6+}/\sum S$ and $Fe^{3+}/\sum Fe$ at a given model step than models with no sulfide removal.

83

<u>Prior mantle S depletion</u>

We consider here the case where prior metasomatism and/or melt extraction has completely stripped the mantle peridotite of S^{2-}, so that any S^{6+} addition into the mantle would oxidize magmas more efficiently. Relationships between depleted mantle source regions and more oxidized magmas have been proposed previously in the Cascade arc (Rowe et al., 2009), and are consistent with evidence from chromian spinel compositions, which suggest that the Lassen region has a variably depleted mantle source (Clynne and Borg, 1997). In this scenario, mantle peridotite S content is 0 ppm. Peridotite xenoliths entrained in continental alkaline basalts are often depleted in S relative to orogenic peridotites, and many researchers attribute this depletion to prior melt extraction events (e.g., Lorand and Luguet, 2016). Although this process likely involves a complex interplay between melt extraction and the saturation of immiscible sulfides during melt transport, here we model the extreme case as a point of comparison, assuming all sulfur has been completely removed before we introduce the slab melt, as in the other models above.

<u>Prior mantle oxidation (metasomatism or melt infiltration)</u>

We consider here the case where prior metasomatism or melt infiltration has oxidized the mantle by enriching it in Fe^{3+}. The southern Cascades arc is built on a region with a complex history of terrane accretion, and the modern arc may inherit some enrichments related to these accretion events, prior metasomatism, and/or the effects of Sierra Nevada magmatism. To consider this case, we assume 1.2 wt. % Fe_2O_3 in the mantle source, based on the Fe^{3+} content needed to reproduce $Fe^{3+}/\sum Fe$ and $S^{6+}/\sum S$ values in cinder cone BRM, which has the most oxidized primary magma. It is likely that the mantle S content and $S^{6+}/\sum S$ would also have been modified during prior metasomatism, but we have ignored this for simplicity and to model an endmember case of more oxidized mantle.

<u>Appendix A References Cited</u>

Alt, J.C., Shanks, W.C., and Jackson, M.C., 1993, Cycling of sulfur in subduction zones: The geochemistry of sulfur in the Mariana Island Arc and back-arc trough: Earth and Planetary Science Letters, v. 119, p. 477–494, https://doi.org/10.1016/0012-821X(93)90057-G.

Alt, J.C., 1995, Sulfur isotopic profile through the oceanic crust: sulfur mobility and seawater-crustal sulfur exchange during hydrothermal alteration: Geology, v. 23, p. 585–588, https://doi.org/10.1130/0091-7613(1995)023<0585:SIPTTO>2.3.CO;2.

Alt, J.C., Laverne, C., Coggon, R.M., Teagle, D.A.H., Banerjee, N.R., Morgan, S., Smith-Duque, C.E., Harris, M., and Galli, L., 2010, Subsurface structure of a submarine hydrothermal system in ocean crust formed at the East Pacific Rise, ODP/IODP Site 1256: Geochemistry, Geophysics, Geosystems, v. 11, p. 1–28, https://doi.org/10.1029/2010GC003144.

Alt, J.C., and Shanks, W.C., 2011, Microbial sulfate reduction and the sulfur budget for a complete section of altered oceanic basalts, IODP Hole 1256D (eastern Pacific): Earth and Planetary Science Letters, v. 310, p. 73–83,

https://doi.org/10.1016/j.epsl.2011.07.027.

Alt, J.C., Schwarzenbach, E.M., Früh-Green, G.L., Shanks, W.C., Bernasconi, S.M., Garrido, C.J., Crispini, L., Gaggero, L., Padrón-Navarta, J.A., and Marchesi, C., 2013, The role of serpentinites in cycling of carbon and sulfur: Seafloor serpentinization and subduction metamorphism: Lithos, v. 178, p. 40–54, https://doi.org/10.1016/j.lithos.2012.12.006.

Antoschechkina, P.M., and Ghiorso, M.S., 2018, MELTS for MATLAB: A new Educational and Research Tool for Computational Thermodynamics: Abstract ED44B-23 presented at 2018 Fall Meeting, AGU, Washington, D.C., 10–14 December.

Borg, L.E., Clynne, M.A., and Bullen, T.D., 1997, The variable role of slab-derived fluids in the generation of a suite of primitive calc-alkaline lavas from the Southernmost Cascades, California: Canadian Mineralogist, v. 35, p. 425–452.

Borg, L.E., Blichert-Toft, J., and Clynne, M.A., 2002, Ancient and modern subduction zone contributions to the mantle sources of lavas from the Lassen region of California inferred from Lu-Hf isotopic systematics: Journal of Petrology, v. 43, p. 705–723, https://doi.org/10.1093/petrology/43.4.705.

Brounce, M.N., Kelley, K.A., and Cottrell, E., 2014, Variations in $Fe^{3+}/\Sigma Fe$ of Mariana Arc Basalts and Mantle Wedge fO₂: Journal of Petrology, v. 55, p. 2514–2536, https://doi.org/10.1093/petrology/egu065.

Callegaro, S., Geraki, K., Marzoli, A., de Min, A., Maneta, V., and Baker, and D.R., 2020, The quintet completed: the partitioning of sulfur between nominally volatile-free minerals and silicate melts: American Mineralogist, v. 105, p. 697–707, https://doi.org/10.2138/am-2020-7188.

Canales, J.P., Carbotte, S.M., Nedimovic, M.R., and Carton, H., 2017, Dry Juan de Fuca slab revealed by quantification of water entering Cascadia subduction zone: Nature Geoscience, v. 10, p. 864–870, https://doi.org/10.1038/NGEO3050.

Canil, D., O'Neill, H.S.C., Pearson, D.G., Rudnick, R.L., McDonough, W.F., and Carswell, D.A., 1994, Ferric iron in peridotites and mantle oxidation states: Earth and Planetary Science Letters, v. 123, p. 205–220, https://doi.org/10.1016/0012-821X(94)90268-2.

Chaussidon, M., Sheppard, S.M.F., Michard, A., Recherches, C. De, and Vandoeuvre-les-nancy, F., 1991, Hydrogen, sulphur and neodymium isotope variations in the mantle beneath the EPR at 12°50'N: Stable Isotope Geochemistry: A Tribute to Samuel Epstein, v. 15, p. 325–337.

Clynne, M.A., and Borg, L.E., 1997, Olivine and chromian spinel in primitive calc-alkaline and tholeiitic lavas from the southernmost cascade range, California: A reflection of relative fertility of the source: Canadian Mineralogist, v. 35, p. 453–472.

Cottrell, E., Kelley, K.A., Lanzirotti, A., and Fischer, R.A., 2009, High-precision determination of iron oxidation state in silicate glasses using XANES: Chemical Geology, v. 268, p. 167–179, https://doi.org/10.1016/j.chemgeo.2009.08.008.

Cottrell, E., and Kelley, K.A., 2011, The oxidation state of Fe in MORB glasses and the oxygen fugacity of the upper mantle: Earth and Planetary Science Letters, v. 305, p. 270–282, https://doi.org/10.1016/j.epsl.2011.03.014.

Cottrell, E., Lanzirotti, A., Mysen, B., Birner, S., Kelley, K.A., Botcharnikov, R., Davis,

F.A., and Newville, M., 2018, A Mössbauer-based XANES calibration for hydrous basalt glasses reveals radiation-induced oxidation of Fe: American Mineralogist, v. 103, p. 489–501, https://doi.org/10.2138/am-2018-6268.

Danyushevsky, L. V., and Plechov, P., 2011, Petrolog3: Integrated software for modeling crystallization processes: Geochemistry, Geophysics, Geosystems, v. 12, https://doi.org/10.1029/2011GC003516.

Danyushevsky, L.V., 2001, The effect of small amounts of H_2O on crystallisation of mid-ocean ridge and backarc basin magmas: Journal of Volcanology and Geothermal Research, v. 110, no. 3, p. 265-280, https://doi.org/10.1016/S0377-0273(01)00213-X.

Danyushevsky, L. V., McNeill, A.W., Sobolev, A.V., 2002, Experimental and petrological studies of melt inclusions in phenocrysts from mantle-derived magmas: an overview of techniques, advantages and complications: Chemical Geology, v. 183, p. 5-24, https://doi.org/10.1016/S0009-2541(01)00369-2.

Davis, A.S., Clague, D.A., Cousens, B.L., Keaten, R., and Paduan, J.B., 2008, Geochemistry of basalt from the North Gorda segment of the Gorda Ridge: Evolution toward ultraslow spreading ridge lavas due to decreasing magma supply: Geochemistry, Geophysics, Geosystems, v. 9, https://doi.org/10.1029/2007GC001775.

Davis, F.A., and Cottrell, E., 2018, Experimental investigation of basalt and peridotite oxybarometers: Implications for spinel thermodynamic models and Fe^{3+} compatibility during generation of upper mantle melts: American Mineralogist, v. 103, p. 1056–1067, https://doi.org/10.2138/am-2018-6280.

Debret, B., Andreani, M., Delacour, A., Rouméjon, S., Trcera, N., and Williams, H., 2017, Assessing sulfur redox state and distribution in abyssal serpentinites using XANES spectroscopy: Earth and Planetary Science Letters, v. 466, p. 1–11, https://doi.org/10.1016/j.epsl.2017.02.029.

Ding, S., and Dasgupta, R., 2017, The fate of sulfide during decompression melting of peridotite – implications for sulfur inventory of the MORB-source depleted upper mantle: Earth and Planetary Science Letters, v. 459, p. 183–195, https://doi.org/10.1016/j.epsl.2016.11.020.

Dixon, J., Stolper, E.M., and Holloway, J.R., 1995, An Experimental Study of Water and Carbon Dioxide Solubilities in Mid-Ocean Ridge Basaltic Liquids. Part I: Calibration and Solubility Models: Journal of Petrology, v. 36, p. 1607–1631.

Eiler, J.M., Crawford, A., Elliott, T., Farley, K.A., Valley, J.W., and Stolper, E.M., 2000, Oxygen isotope geochemistry of oceanic-arc lavas: Journal of Petrology, v. 41, p. 229–256, https://doi.org/10.1093/petrology/41.2.229.

Falloon, T.J., and Danyushevsky, L. V, 2000, Melting of Refractory Mantle at 1.5, 2 and 2.5 GPa under Anhydrous and H_2O-undersaturated Conditions : Implications for the Petrogenesis of High-Ca Boninites and the Influence of Subduction Components on Mantle Melting: Journal of Petrology, v. 41, p. 257–283.

Ferrando, S., Frezzotti, M. L., Dallai, L., Compagnoni, R., 2005, Multiphase solid inclusions in UHP rocks (Su-Lu, China): Remnants of supercritical silicate-rich aqueous fluids released during continental subduction: Chemical Geology, v. 223, p. 68-81, https://doi:10.1016/j.chemgeo.2005.01.029.

Fiege, A., Holtz, F., Shimizu, N., Mandeville, C.W., Behrens, H., and Knipping, J.L.,

2014, Sulfur isotope fractionation between fluid and andesitic melt: An experimental study: Geochimica et Cosmochimica Acta, v. 142, p. 501–521, https://doi.org/10.1016/j.gca.2014.07.015.

Frost, B., 1991, Introduction to oxygen fugacity and its petrologic importance: Reviews in Mineralogy and Geochemistry, v. 25, p. 1–10.

Gaetani, G.A., O'Leary, J.A., Shimizu, N., Bucholz, C.E., and Newville, M., 2012, Rapid reequilibration of H_2O and oxygen fugacity in olivine-hosted melt inclusions: Geology, v. 40, p. 915–918, https://doi.org/10.1130/G32992.1.

Ghiorso, M.S., Hirschmann, M.M., Reiners, P.W., and Kress, V.C., 2002, The pMELTS: A revision of MELTS for improved calculation of phase relations and major element partitioning related to partial melting of the mantle to 3 GPa: Geochemistry, Geophysics, Geosystems, v. 3, p. 1–35, https://doi.org/10.1029/2001gc000217.

Gulick, S.P.S., Meltzer, A.S., Henstock, T.J., and Levander, A., 2002, Internal deformation of the southern Gorda plate: Fragmentattion of a weak plate near the Mendocino triple junction: Geology, v. 29, p. 691–694, https://doi.org/10.1130/0091-7613(2001)029<0691:IDOTSG>2.0.CO;2.

Hanson, B., Delano, J.W., and Lindstrom, D.J., 1996, High-precision analysis of hydrous rhyolitic glass inclusions in quartz phenocrysts using the electron microprobe and INAA: American Mineralogist, v. 81, p. 1249–1262, https://doi.org/10.2138/am-1996-9-1023.

Hartley, M.E., Shorttle, O., Maclennan, J., Moussallam, Y., Edmonds, M., 2017, Olivine-hosted melt inclusions as an archive of redox heterogeneity in magmatic systems: Earth and Planetary Science Letters, v. 479, p. 192-205, https://doi.org/10.1016/j.epsl.2017.09.029.

Jégo, S., and Dasgupta, R., 2014, The fate of sulfur during fluid-present melting of subducting basaltic crust at variable oxygen fugacity: Journal of Petrology, v. 55, p. 1019–1050, https://doi.org/10.1093/petrology/egu016.

Jenner, F.E., and O'Neill, H.S.C., 2012, Analysis of 60 elements in 616 ocean floor basaltic glasses: Geochemistry, Geophysics, Geosystems, v. 13, https://doi.org/10.1029/2011GC004009.

Jørgensen, B.B., Findlay, A.J., and Pellerin, A., 2019, The biogeochemical sulfur cycle of marine sediments: Frontiers in Microbiology, v. 10, https://doi.org/10.3389/fmicb.2019.00849.

Klaus Peter Jochum, Uwe Nohl, Kirstin Herwig, Esin Lammel, Brigitte Stoll, Albrecht W. Hofmann

Jugo, P.J., Wilke, M., and Botcharnikov, R.E., 2010, Sulfur K-edge XANES analysis of natural and synthetic basaltic glasses: Implications for S speciation and S content as function of oxygen fugacity: Geochimica et Cosmochimica Acta, v. 74, p. 5926–5938, https://doi.org/10.1016/j.gca.2010.07.022.

Kanehira, K., Yui, S., Sakai, H., and Sasaki, A., 1973, Sulphide globules and sulphur isotope ratios in the abyssal tholeiite from the Mid-Atlantic Ridge near 30° N latitutde: Geochemical Journal, v. 7, p. 89–96.

Kessel, R., Schmidt, M.W., Ulmer, P., and Pettke, T., 2005, Trace element signature of subduction-zone fluids, melts and supercritical liquids at 120-180 km depth: Nature, v. 437, p. 724–727, https://doi.org/10.1038/nature03971.

Klimm, K., Kohn, S.C., and Botcharnikov, R.E., 2012, The dissolution mechanism of

sulphur in hydrous silicate melts. II: Solubility and speciation of sulphur in hydrous silicate melts as a function of fO$_2$: Chemical Geology, v. 322–323, p. 250–267, https://doi.org/10.1016/j.chemgeo.2012.04.028.

Kress, V.C., and Carmichael, S.E., 1991, The compressibility of silicate liquids containing Fe$_2$O$_3$ and the effect of composition, temperature, oxygen fugacity and pressure on their redox states: Contribution to Mineralogy and Petrology, v. 108, p. 82–92.

Labidi, J., Cartigny, P., Birck, J.L., Assayag, N., and Bourrand, J.J., 2012, Determination of multiple sulfur isotopes in glasses: A reappraisal of the MORB δ^{34}S: Chemical Geology, v. 334, p. 189–198, https://doi.org/10.1016/j.chemgeo.2012.10.028.

Lee, C.-T.A., Luffi, P., Chin, E.J., Bouchet, R., Dasgupta, R., Morton, D.M., Le Roux, V., Yin, Q.Z., and Jin, D., 2012, Copper systematics in arc magmas and implications for crust-mantle differentiation: Science, v. 335, p. 64–66, https://doi.org/10.1126/science.1217313.

Lerner, A.H., Muth, M.J., Wallace, P.J., Lanzirotti, A., Newville, M., Gaetani, G. A., Chowdhury, P., Dasgupta, R., In Review, Improving the reliability of Fe- and S-XANES measurements in silicate glasses: correcting beam damage and identifying Fe-oxide nanolites in hydrous and anhydrous melt inclusions: Chemical Geology.

Lorand, J.P., and Luguet, A., 2016, Chalcophile and siderophile elements in mantle rocks: Trace elements controlled by trace minerals: Reviews in Mineralogy and Geochemistry, v. 81, p. 441–488, https://doi.org/10.2138/rmg.2016.81.08.

Luhr, J.F., 2001, Glass inclusions and melt volatile contents at Parícutin volcano, Mexico: Contributions to Mineralogy and Petrology, v. 142, p. 261–283, https://doi.org/10.1007/s004100100293.

Mallmann, G., and O'Neill, H.S.C., 2009, The crystal/melt partitioning of V during mantle melting as a function of oxygen fugacity compared with some other elements (Al, P, Ca, Sc, Ti, Cr, Fe, Ga, Y, Zr and Nb): Journal of Petrology, v. 50, p. 1765–1794, https://doi.org/10.1093/petrology/egp053.

Matjuschkin, V., Blundy, J.D., and Brooker, R.A., 2016, The effect of pressure on sulphur speciation in mid- to deep-crustal arc magmas and implications for the formation of porphyry copper deposits: Contributions to Mineralogy and Petrology, v. 171, https://doi.org/10.1007/s00410-016-1274-4.

Menges, F., 2020, Spectragryph - optical spectroscopy software:Version 1.2.14.

Moretti, R., and Baker, D.R., 2008, Modeling the interplay of fO$_2$ and fS$_2$ along the FeS-silicate melt equilibrium: Chemical Geology, v. 256, p. 286–298, https://doi.org/10.1016/j.chemgeo.2008.06.055.

Morgan, G.B., and London, D., 2005, Effect of current density on the electron microprobe analysis of alkali aluminosilicate glasses: American Mineralogist, v. 90, p. 1131–1138, https://doi.org/10.2138/am.2005.1769.

Morgan, G.B., and London, D., 1996, Optimizing the electron microprobe analysis of hydrous alkali aluminosilicate glasses: American Mineralogist, v. 81, p. 1176–1185, https://doi.org/10.2138/am-1996-9-1016.

Nash, W.M., Smythe, D.J., and Wood, B.J., 2019, Compositional and temperature effects on sulfur speciation and solubility in silicate melts: Earth and Planetary Science Letters, v. 507, p. 187–198, https://doi.org/10.1016/j.epsl.2018.12.006.

Newville, M., 2013, Larch: An Analysis Package For XAFS and Related Spectroscopies:

Journal of Physics: Conference Series, v. 430, p. 012007, https://doi.org/10.1088/1742-6596/430/1/012007.

O'Neill, H.S., 2021, Comment on 'Compositional and temperature effects on sulfur speciation and solubility in silicate melts' by Nash et al. [Earth and Planetary Science Letters 507, 187–198, 2019]: Earth and Planetary Science Letters, v. 560, p. 116769, https://doi.org/10.1016/j.epsl.2021.116843.

Ono, S., Keller, N.S., Rouxel, O., Alt, J.C., 2012. Sulfur-33 constraints on the origin of secondary pyrite in altered oceanic basement: Geochim. Cosmochim. Acta v. 87, p. 323–340, https://doi.org/10.1016/j.gca.2012.04.016.

Rouméjon, S., and Cannat, M., 2014, Serpentinization of mantle-derived peridotites at mid-ocean ridges: Mesh texture development in the context of tectonic exhumation: Geochemistry, Geophysics, Geosystems, v. 15, p. 2354–2379, https://doi.org/10.1002/2013GC005148.

Rowe, M.C., Kent, A.J.R., and Nielsen, R.L., 2009, Subduction influence on oxygen fugacity and trace and volatile elements in basalts across the cascade volcanic arc: Journal of Petrology, v. 50, p. 61–91, https://doi.org/10.1093/petrology/egn072.

Ruscitto, D.M., Wallace, P.J., Cooper, L.B., and Plank, T., 2012, Global variations in H_2O/Ce: 2. Relationships to arc magma geochemistry and volatile fluxes: Geochemistry Geophysics Geosystems, v. 13, Q03025, https://doi.org/10.1029/2011GC003887.

Saal, A.E., Hauri, E.H., Langmuir, C.H., and Perfit, M.R., 2002, Vapour undersaturation in primitive mid-ocean-ridge basalt and the volatile content of earth's upper mantle: Nature, v. 419, p. 451–455, https://doi.org/10.1038/nature01073.

Sakai, H., Casadevall, T.J., and Moore, J.G., 1982, Chemistry and isotope ratios of sulfur in basalts and volcanic gases at Kilauea volcano, Hawaii: Geochimica et Cosmochimica Acta, v. 46, p. 729–738, https://doi.org/10.1016/0016-7037(82)90024-2.

Schwarzenbach, E.M., Gill, B.C., Gazel, E., and Madrigal, P., 2016, Sulfur and carbon geochemistry of the Santa Elena peridotites : Comparing oceanic and continental processes during peridotite alteration: Lithos, v. 252–253, p. 92–108, https://doi.org/10.1016/j.lithos.2016.02.017.

Sisson, T.W., and Kelemen, P.B., 2018, Near-solidus melts of MORB + 4 wt% H_2O at 0.8–2.8 GPa applied to issues of subduction magmatism and continent formation: Contributions to Mineralogy and Petrology, v. 173, p. 1–23, https://doi.org/10.1007/s00410-018-1494-x.

Till, C.B., 2017, A Review and Update of Mantle Thermobarometry for Primitive Arc Magmas: American Mineralogist, v. 102, p. 931–947.

Tomkins, A.G., and Evans, K.A., 2015, Separate zones of sulfate and sulfide release from subducted mafic oceanic crust: Earth and Planetary Science Letters, v. 428, p. 73–83, https://doi.org/10.1016/j.epsl.2015.07.028.

Toplis, M.J., 2005, The thermodynamics of iron and magnesium partitioning between olivine and liquid: Criteria for assessing and predicting equilibrium in natural and experimental systems: Contributions to Mineralogy and Petrology, v. 149, p. 22–39, https://doi.org/10.1007/s00410-004-0629-4.

Turner, S.C., 2018, Tracking Sulfur Diagenesis in Methane Rich Marine Sediments on the Cascadia Margin: Comparing Sulfur Isotopes of Bulk Sediment and Chromium Reducible Sulfur: University of New Hampshire, 1188 p., https://scholars.unh.edu/thesis/1188/.

Wallace, P.J., and Carmichael, I.S.E., 1994, S speciation in submarine basaltic glasses as determined by measurements of SKα X-ray wavelength shifts: American Mineralogist, v. 79, p. 161–167.

Walowski, K.J., Wallace, P.J., Clynne, M.A., Rasmussen, D.J., and Weis, D., 2016, Slab melting and magma formation beneath the southern Cascade arc: Earth and Planetary Science Letters, v. 446, p. 100–112, https://doi.org/10.1016/j.epsl.2016.03.044.

Walowski, K.J., Wallace, P.J., Hauri, E.H., Wada, I., and Clynne, M.A., 2015, Slab melting beneath the Cascade Arc driven by dehydration of altered oceanic peridotite: Nature Geoscience, v. 8, p. 404–409, https://doi.org/10.1038/ngeo2417.

Walters, J.B., Cruz-Uribe, A.M., and Marschall, H.R., 2019, Isotopic Compositions of Sulfides in Exhumed High-Pressure Terranes: Implications for Sulfur Cycling in Subduction Zones: Geochemistry, Geophysics, Geosystems, v. 20, p. 3347–3374, https://doi.org/10.1029/2019GC008374.

Wilke, M., Jugo, P.J., Klimm, K., Susini, J., Botcharnikov, R., Kohn, S.C., and Janousch, M., 2008, The origin of S^{4+} detected in silicate glasses by XANES: American Mineralogist, v. 93, p. 235–240, https://doi.org/10.2138/am.2008.2765.

Wilson, D.S., 2002, The Juan de Fuca plate and slab: Isochron structure and Cenozoic plate motions: U.S. Geological Survey Open-File Report 02–328, 9-12 p., 0-607-99675-7.

Workman, R.K., and Hart, S.R., 2005, Major and trace element composition of the depleted MORB mantle (DMM): Earth and Planetary Science Letters, v. 231, p. 53–72, https://doi.org/10.1016/j.epsl.2004.12.005.

Wysoczanski, R., and Tani, K., 2006, Spectroscopic FTIR imaging of water species in silicic volcanic glasses and melt inclusions: An example from the Izu-Bonin arc: Journal of Volcanology and Geothermal Research, v. 156, p. 302–314, https://doi.org/10.1016/j.jvolgeores.2006.03.024.

Zhang, H.L., Cottrell, E., Solheid, P.A., Kelley, K.A., and Hirschmann, M.M., 2018, Determination of $Fe^{3+}/\Sigma Fe$ of XANES basaltic glass standards by Mössbauer spectroscopy and its application to the oxidation state of iron in MORB: Chemical Geology, v. 479, p. 166–175, https://doi.org/10.1016/j.chemgeo.2018.01.006.
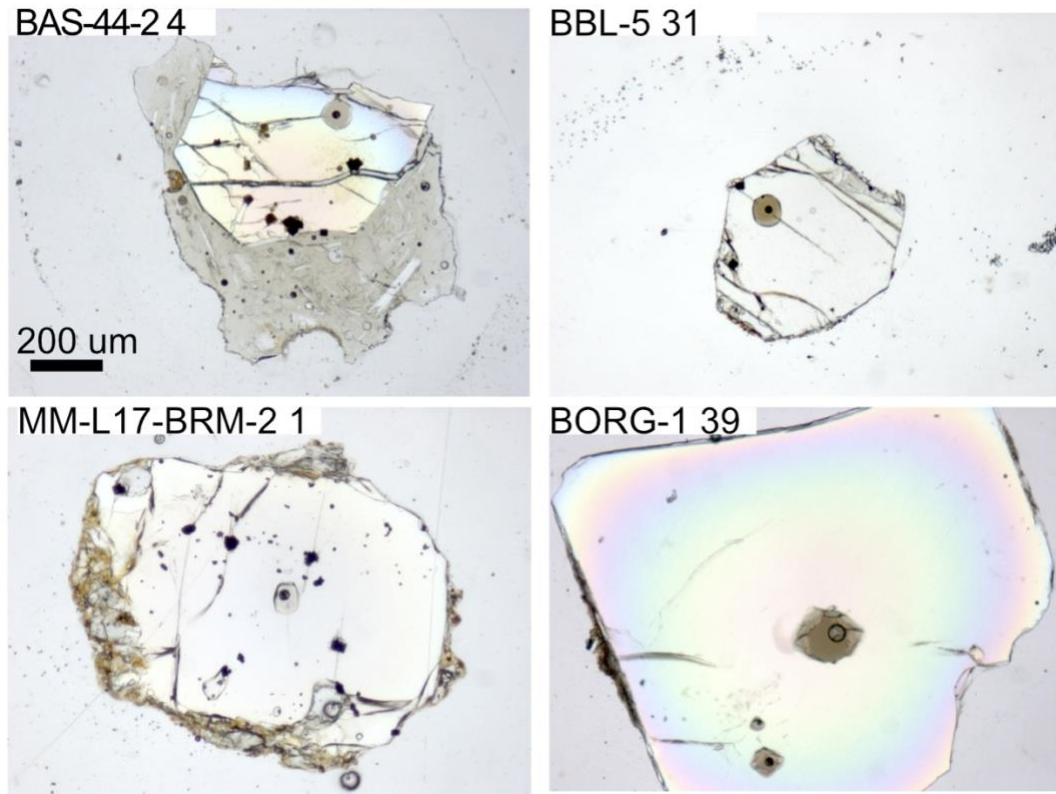
Figure S1. Photomicrographs of representative melt inclusions. Labels denote the name of each cinder cone and melt inclusion number. Each inclusion shown contains a vapor bubble, and inclusion BBL-5 31 contains a small sulfide bleb. Note that cracks intersecting the inclusions shown here formed during sample preparation and were not present during sample selection.
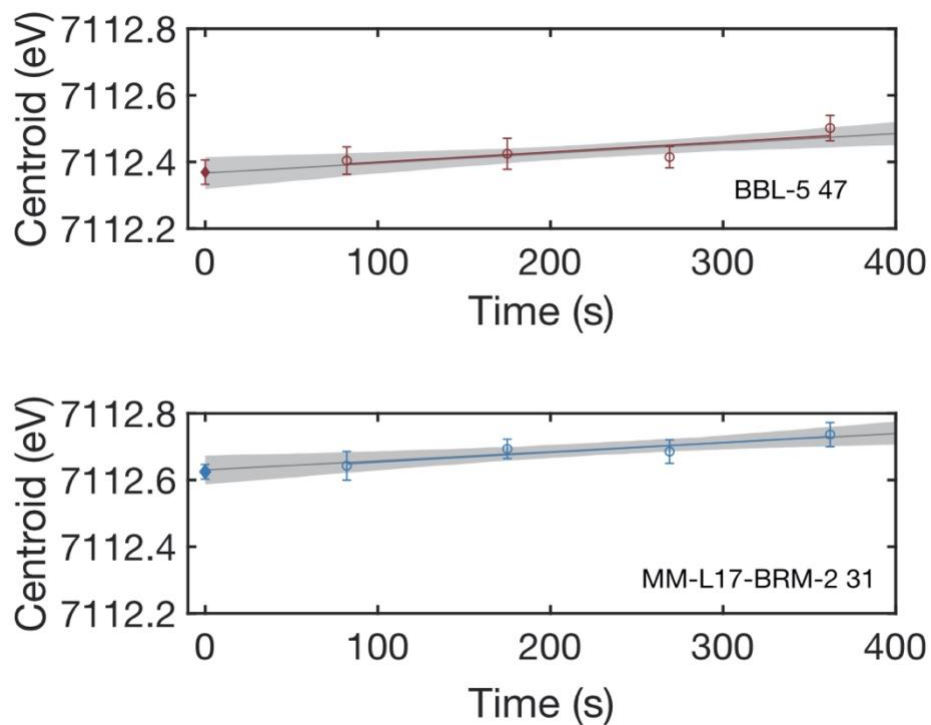
Figure S2. Fe Kα pre-edge centroid positions calculated from repeated rapid scans of natural melt inclusions. Circles represent the centroid values calculated from one pre-edge scan. Error bars represent ±1 standard error for individual centroid fits. Colored lines are linear regressions through measured centroid values from 82 to 362 s. Diamonds at t = 0 s are the intercept of each linear regression to the centroid time series and are taken to be the beam damage-corrected initial centroid position. Error bars on corrected initial centroid positions represent ±1 SE of the time series linear regression. Gray bands show ±1 standard deviation non-simultaneous prediction bounds for the linear fit function calculated using a Monte Carlo approach. Figure adapted from Lerner et al. (in review).
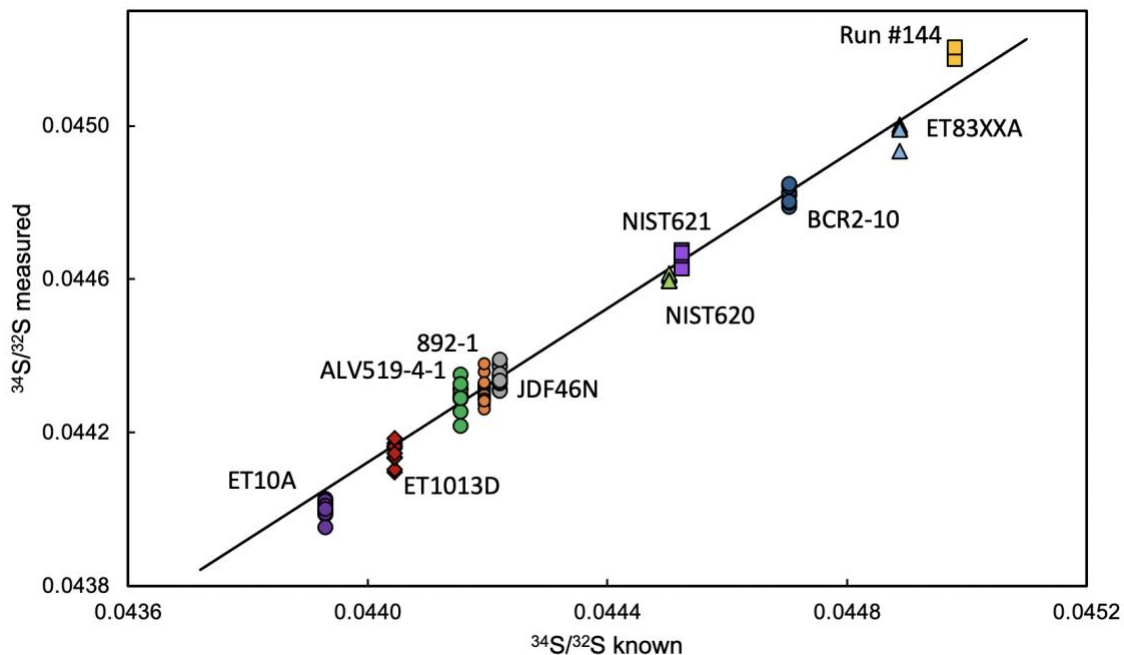
Figure S3. Measured and known glass standard $^{34}S/^{32}S$ values used to calculate instrument mass fractionation (IMF) during the 2019 sulfur SIMS session at Woods Hole Oceanographic Institution. IMF was calculated for individual analyses using the known and measured $^{34}S/^{32}S$ values of each calibration standard. The average calculated IMF from analyses on standards was used to calculate $^{34}S/^{32}S$ values of each unknown. This average calculated IMF is shown as a black line. See Tables S4 and S7 for the SIMS full data set and detailed information on standards.
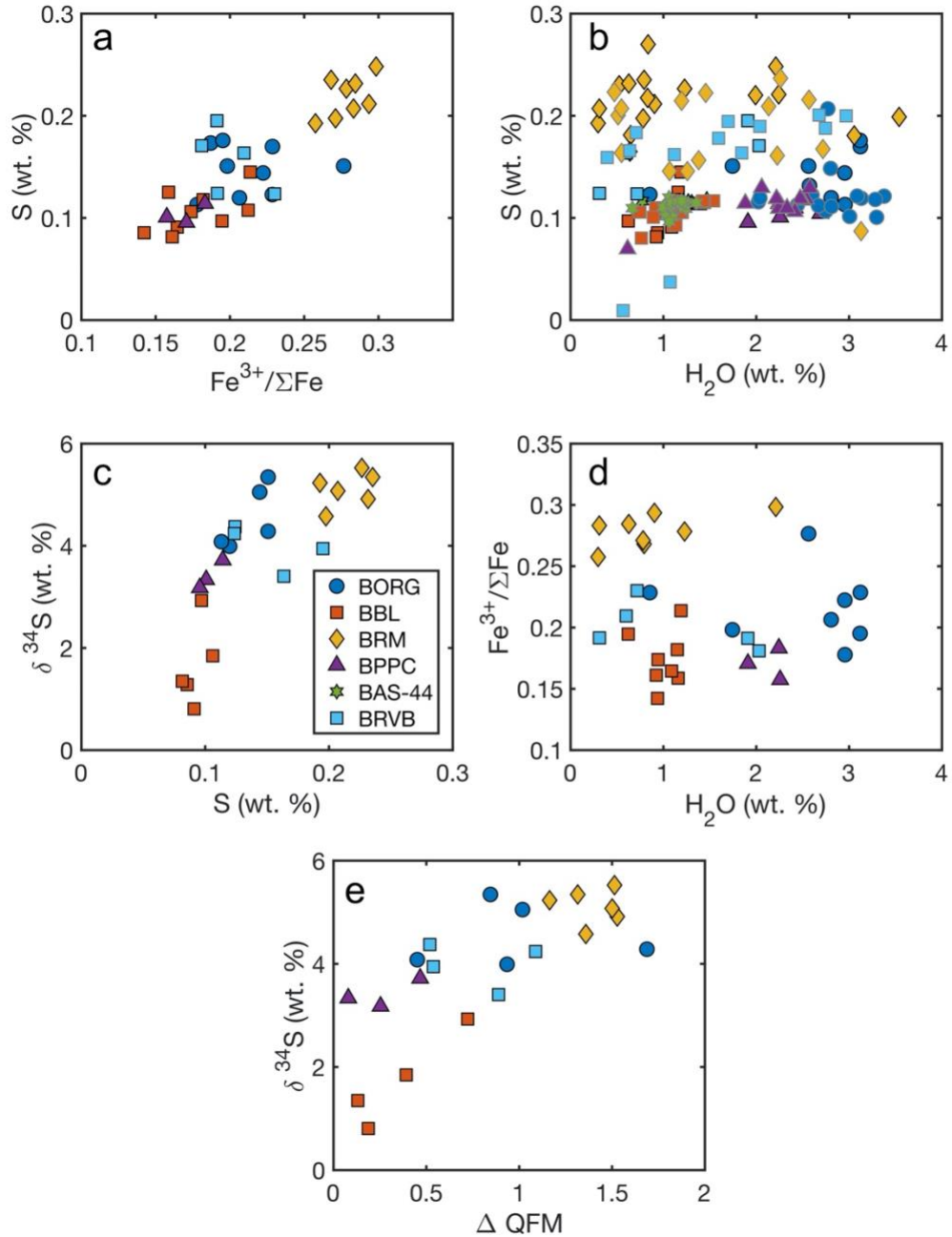
Figure S4. PEC-corrected melt inclusion compositions calculated for inclusions at each cinder cone. Each symbol represents one analyzed inclusion. Symbols with gray outlines represent data from Walowski et al. (2016).
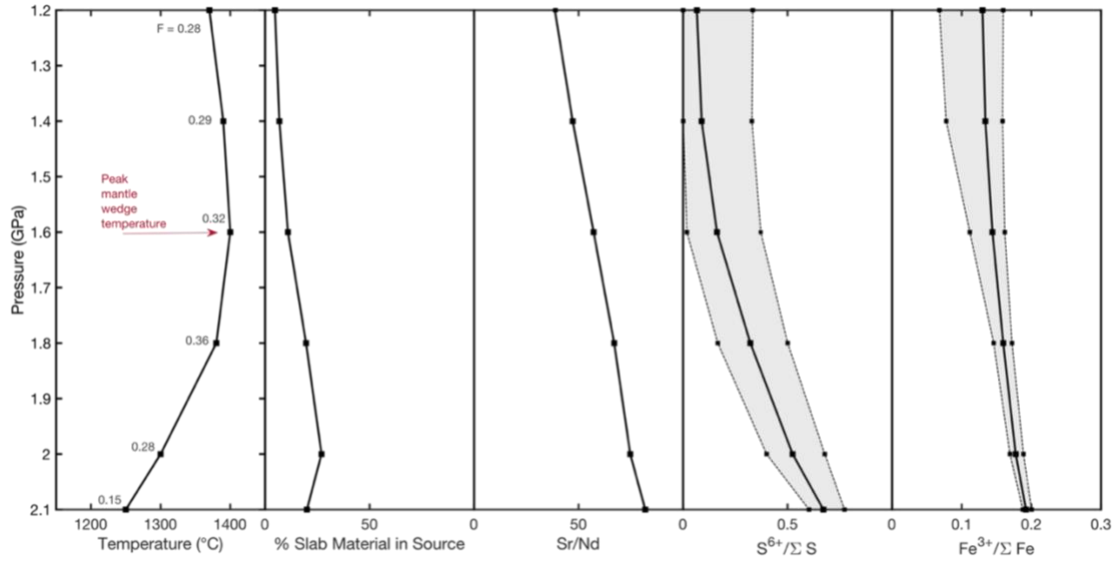
Figure S5. Model output for a 'Normal Mantle' melting case, assuming a melt:rock ratio of 0.2:0.8 during each melt extraction step at successively lower pressure. Tick marks in left panel are labeled with equilibrium melt fraction at each step. Gray error envelope shows melt compositions modeled using $D^{Fe2O3} = 0.05$ and $D^{Fe2O3} = 0.5$ for comparison.
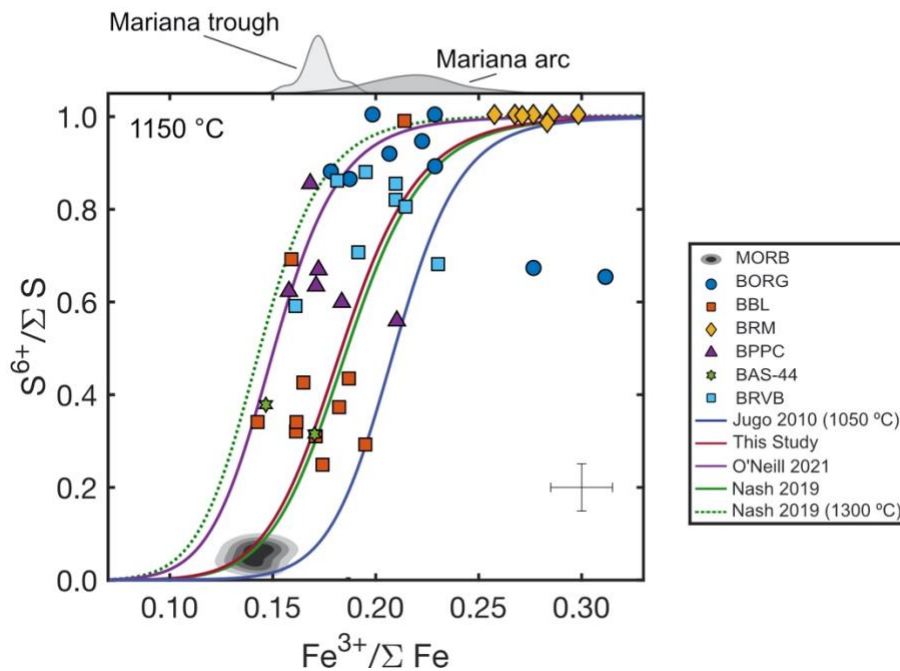
Figure S6. Measured $S^{6+}/\sum S$ and $Fe^{3+}/\sum Fe$ in Lassen melt inclusions (symbols), compared to $Fe^{3+}/\sum Fe$ values measured in melt inclusions and submarine glasses from the Mariana Arc (Brounce et al., 2014). Reported Mariana $Fe^{3+}/\sum Fe$ values have been recalculated using the updated Fe XANES calibration of (Zhang et al., 2018, Brounce, M., Written Comm., 2021). Average uncertainty for Lassen data shown in lower right. Measured MORB values in gray contoured area are shown for comparison (Wallace and Carmichael, 1994; Jugo et al., 2010; Zhang et al., 2018; Lerner et al., in review). Curves show several modeled S-Fe redox relationships. The model of Jugo et al. (2010) is calculated for average Lassen analyzed melt inclusion compositions. The three curves calculated for 1150 °C are for (1) the relationship from this study as discussed previously, (2) the weighted 1 bar model from O'Neill (2021), and (3) the much more strongly temperature dependent model of Nash et al. (2019). Shown for comparison is the experimental calibration for basaltic compositions at 200 MPa, 1050°C from Jugo et al. (2010) and a calculated curve at 1300°C from Nash et al. (2019).
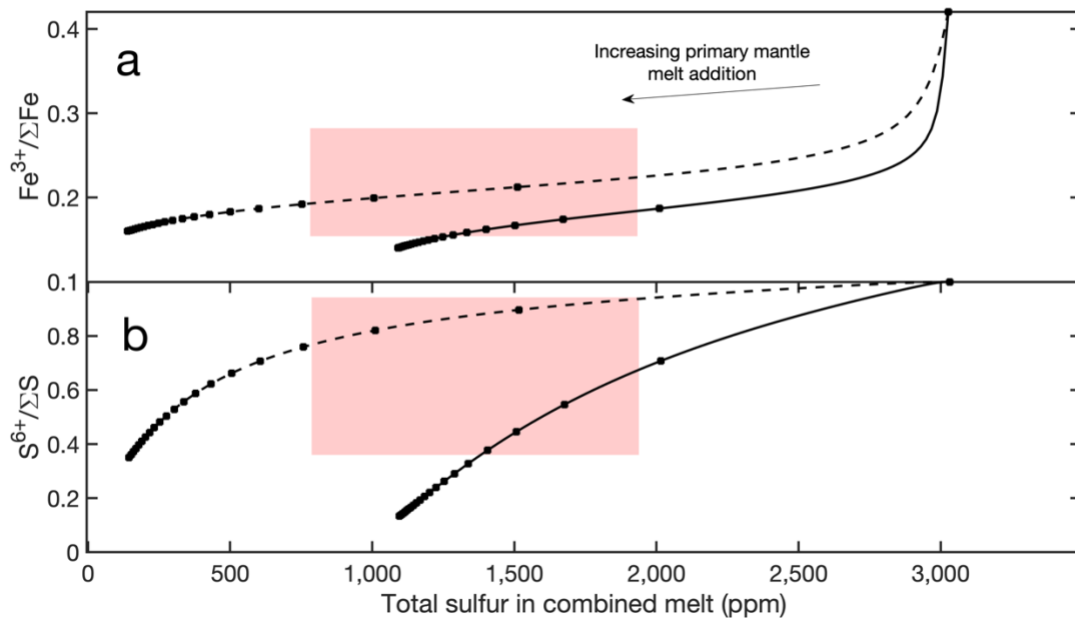
Figure S7. Variations in silicate melt $Fe^{3+}/\sum Fe$ (a) and $S^{6+}/\sum S$ (b) during the addition of primary mantle melt containing 1,000 ppm (solid line) or 0 ppm S^{2-} (dashed line) into 100 g of a dacitic slab melt containing 3,000 ppm S^{6+}. Results are plotted as a function of melt total sulfur content. Circles mark each 100 g increment of primary melt addition. Sulfur and iron redox equilibria calculated at 1400 °C using the model of O'Neill (2021) modified as described in the Supplementary Text. Range of Lassen primary magma compositions are highlighted in red for comparison. The addition of S^{6+} to the primary mantle melt creates clear increases in $Fe^{3+}/\sum Fe$ and $S^{6+}/\sum S$. However, this S^{6+} addition cannot reproduce the full range of primary magma $Fe^{3+}/\sum Fe$ at Lassen.
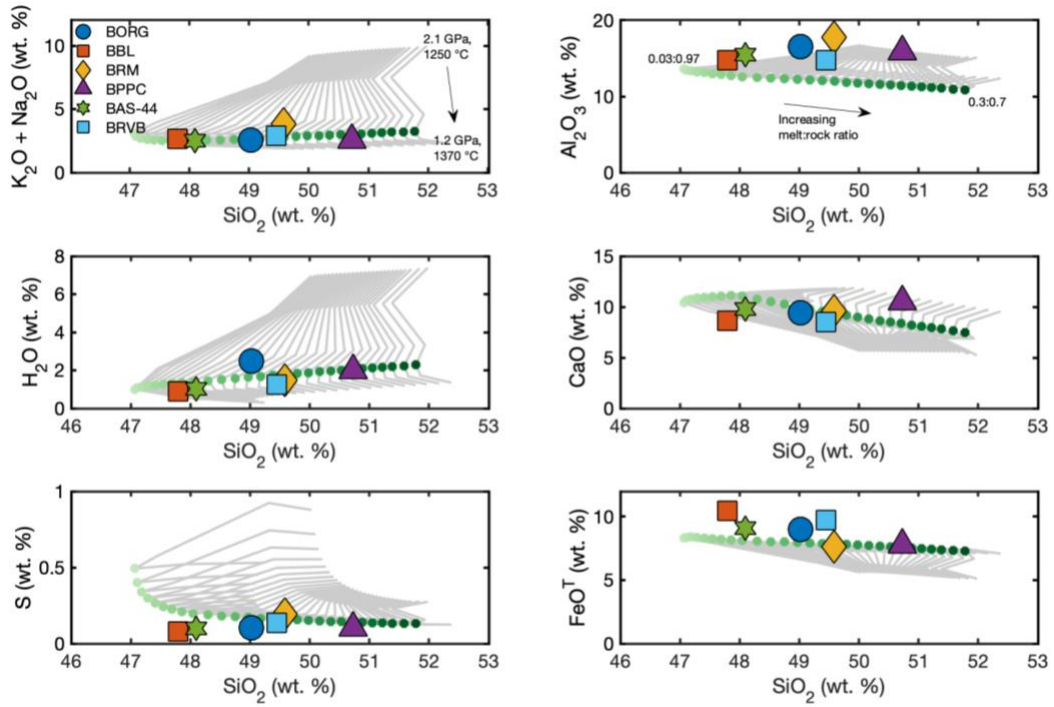
Figure S8. Mantle-equilibrated melt compositions for a 'Normal Mantle' model case. Each curve represents one melting model assuming a separate melt:rock ratio, varying from 0.03:0.97 (light green) to 0.3:0.7 (dark green). Maximum temperature of each run (1400 °C, 1.6 GPa) marked with colored circles, as in Figure 2.
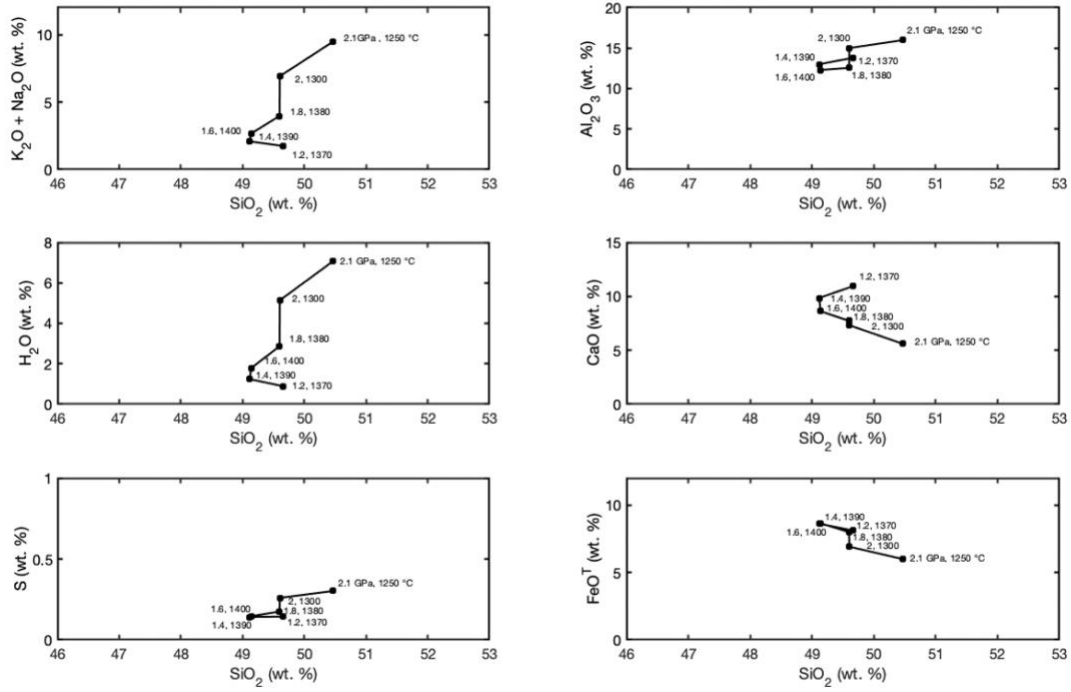
Figure S9. Mantle-equilibrated melt compositions for a 'Normal Mantle' melting case, assuming a melt:rock ratio of 0.2:0.8 during each melt extraction step at successively lower pressure. Pressure and temperature of equilibration is marked for each model step.
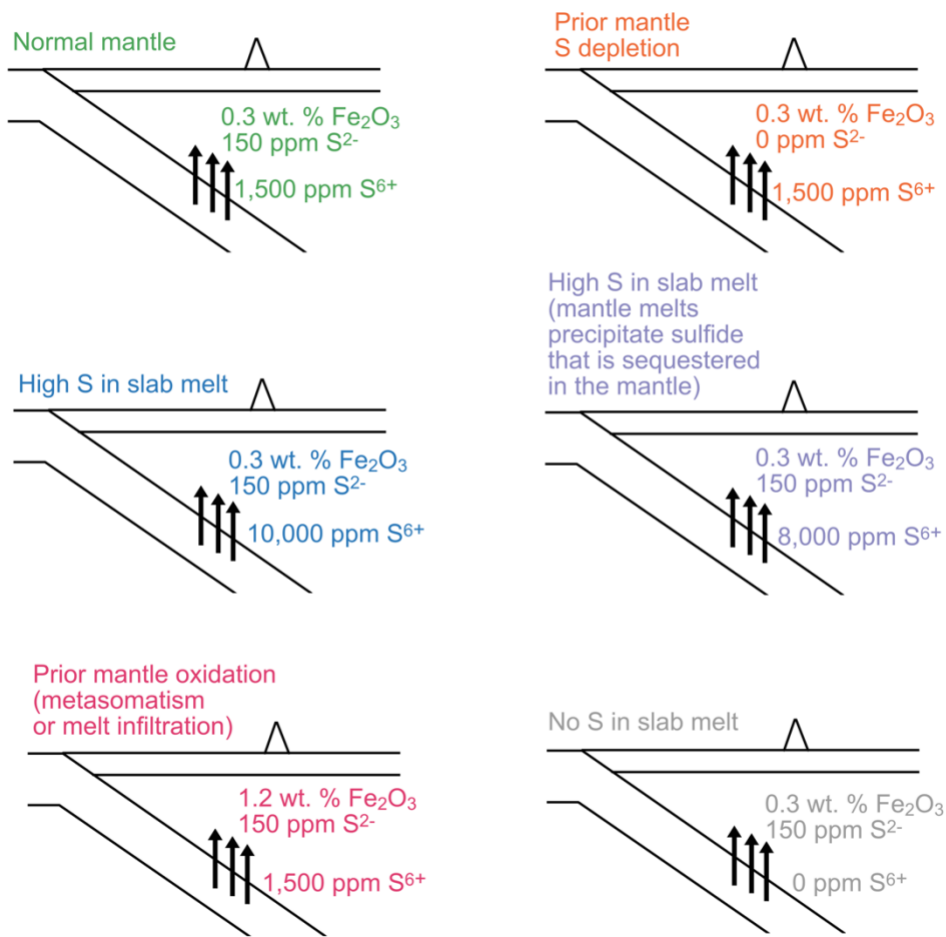
Figure S10. Summary of model scenarios, illustrating variation in slab melt S content and mantle S and Fe_2O_3 content between each model run. Colors correspond to those used in Figure 2.
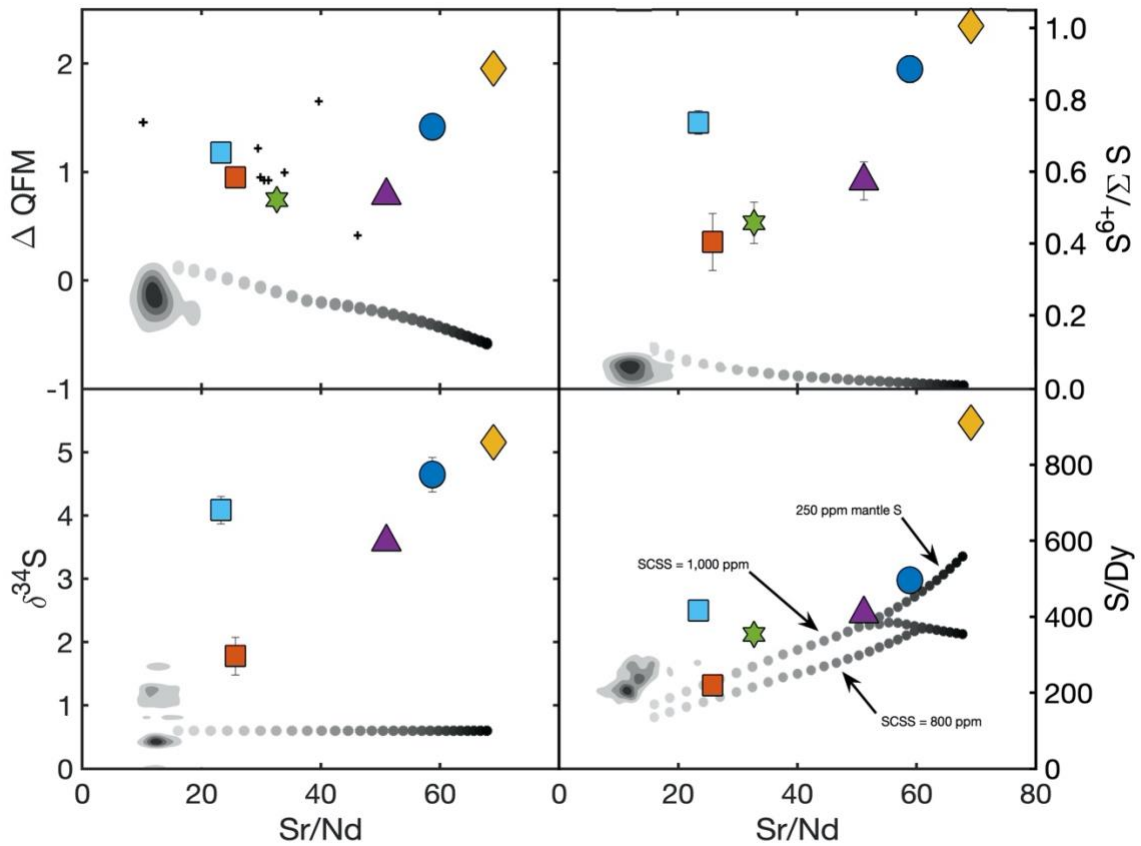
Figure S11. Primary magma compositions at cinder cones in the Lassen region (large symbols) compared to model melt compositions assuming 0 ppm S in the slab melt (small colored circles), 150 ppm S in the mantle source, and sulfur content at sulfide saturation (SCSS) values of 800 and 1,000 ppm. The change in slope for the SCSS = 1,000 ppm curve marks the point where mantle melts become sulfide undersaturated because of high melt fractions. If the mantle source concentration is increased to 250 ppm, sulfide undersaturation does not occur even at high melt fractions. Each set of gray circles represents one modeled scenario, and each individual circle represents the modeled melt at peak mantle wedge temperature, calculated for a specific melt:rock ratio.
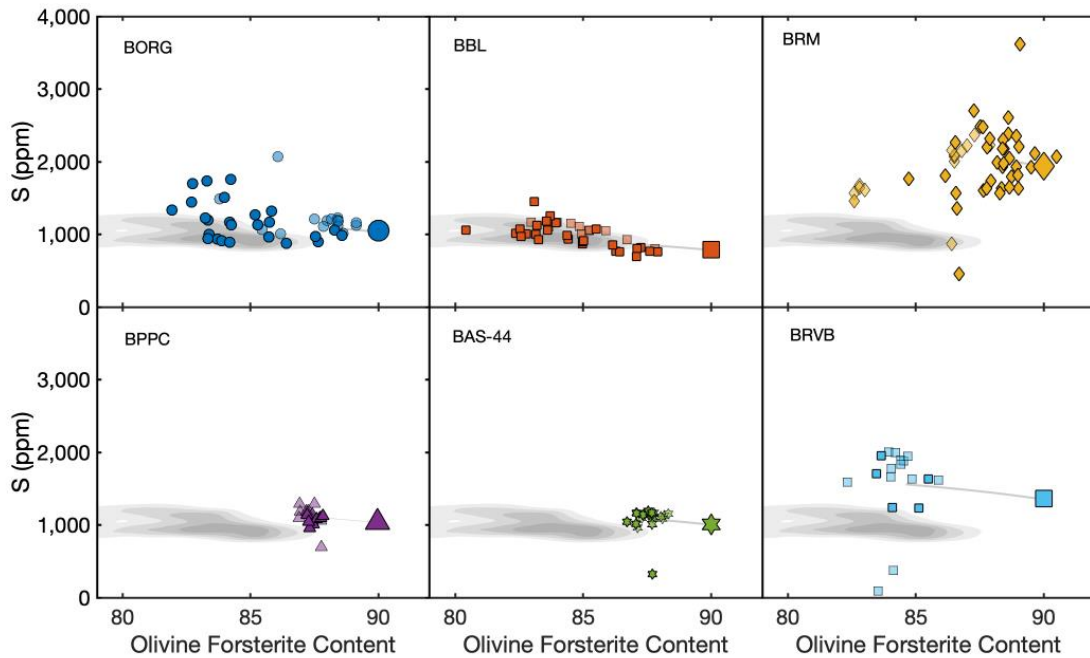
Figure S12. Sulfur concentrations in individual silicate melt inclusions (small symbols) from six cinder cones in Lassen Volcanic area, corrected for post-entrapment crystallization and Fe-Mg reequilibration, plotted against the forsterite content of their olivine hosts. Light colored symbols represent values from previous studies (Walowski et al., 2016). Large symbols show the composition of primary magmas estimated for each cinder cone. Gray lines show reverse crystallization calculations used to estimate each primary magma composition. MORB sulfur data (Jenner and O'Neill, 2012) plotted as a function of calculated equilibrium olivine forsterite content (Toplis, 2005) shown for comparison in gray density contours. Average sulfur concentrations vary between cinder cones. Only a few melt inclusions show low S values that might result from degassing-related sulfur loss before inclusion entrapment.
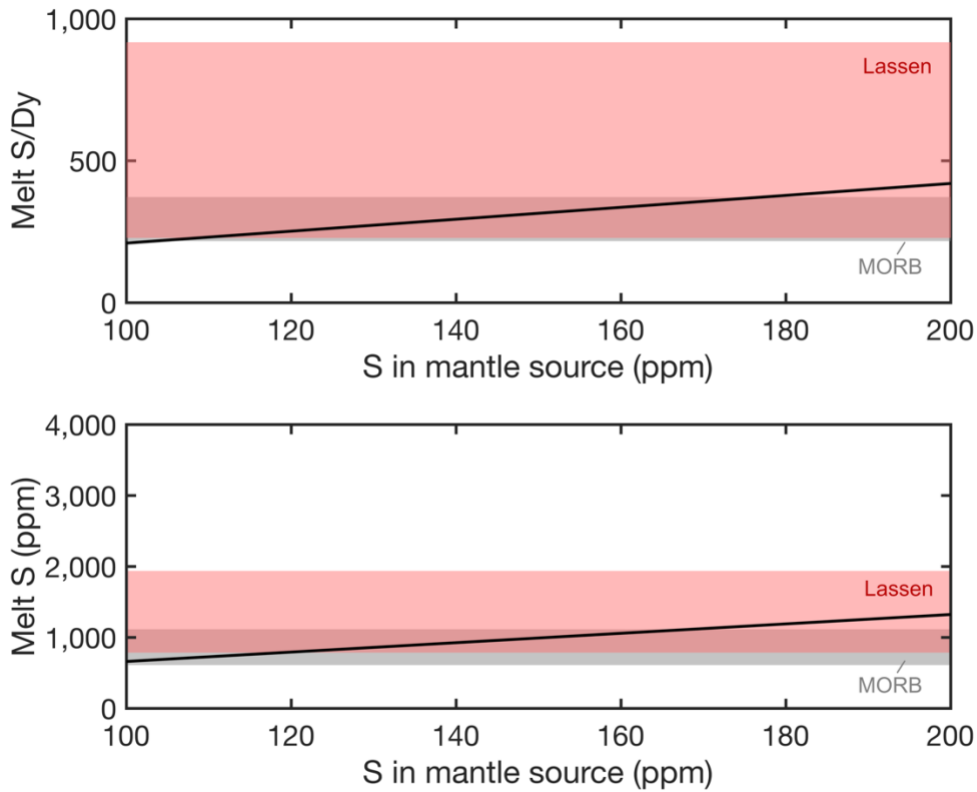
Figure S13. Melt S and S/Dy calculated using batch melting models. Black lines show melt S or S/Dy calculated as a function of mantle source S content, assuming: (1) 15% partial melting, (2) all sulfur is dissolved in the silicate melt due to high melt $S^{6+}/\sum S$, and (3) no immiscible sulfide phases are present. Bulk partition coefficients for S and Dy are the same as those used in Lassen mantle melting models. Gray field represents MORB S and S/Dy (Jenner and O'Neill, 2012) filtered for primitive melt compositions (equilibrium olivine Fo > 0.85). Red field shows the range of Lassen primary magma values. Mantle melting cannot reproduce the entire range of S and S/Dy values observed in Lassen primary magmas using MORB-source values (e.g. 111-170 ppm S, Saal et al., 2002) for mantle source sulfur content.
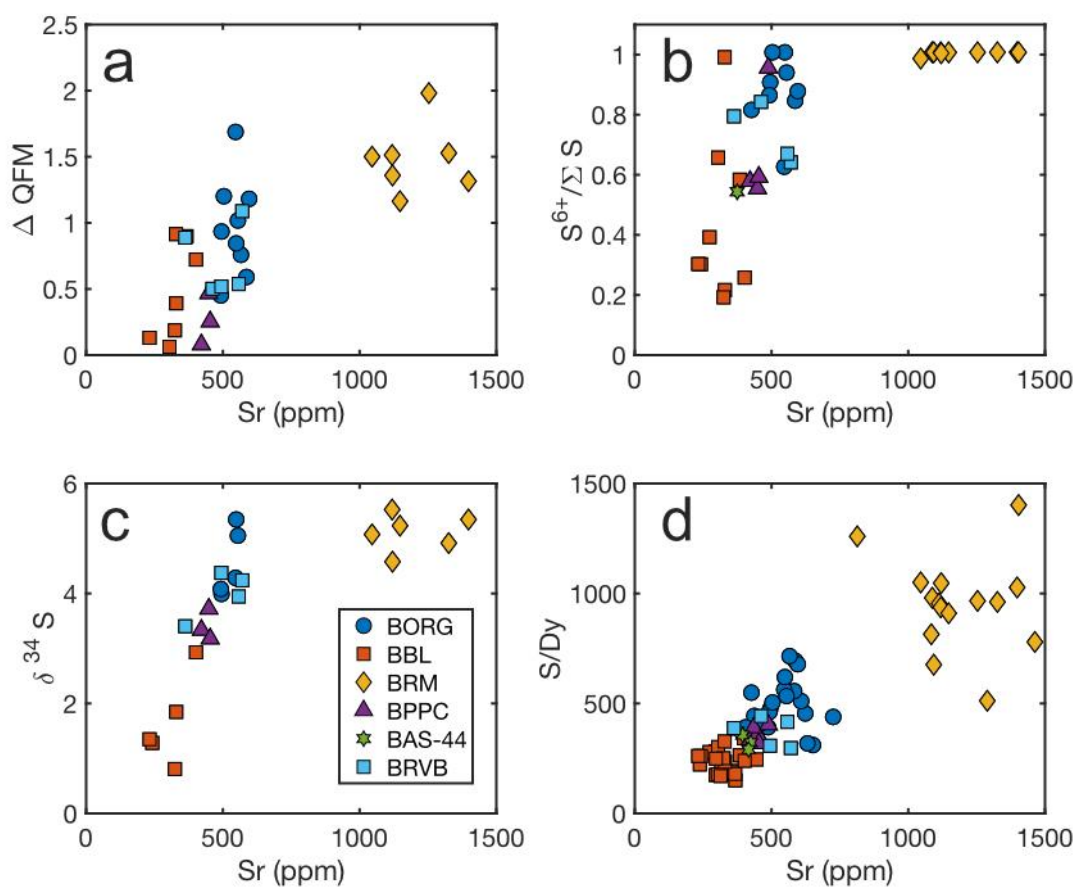
Figure S14. PEC-corrected melt inclusion Sr concentrations plotted against (a) melt inclusion relative oxygen fugacity, (b) measured $S^{6+}/\sum S$, (c) measured $\delta^{34}S$, and (d) measured S/Dy. Each symbol represents one analyzed inclusion. Oxygen fugacity calculated using analyzed melt inclusion compositions at 400 MPa, 1150 °C.
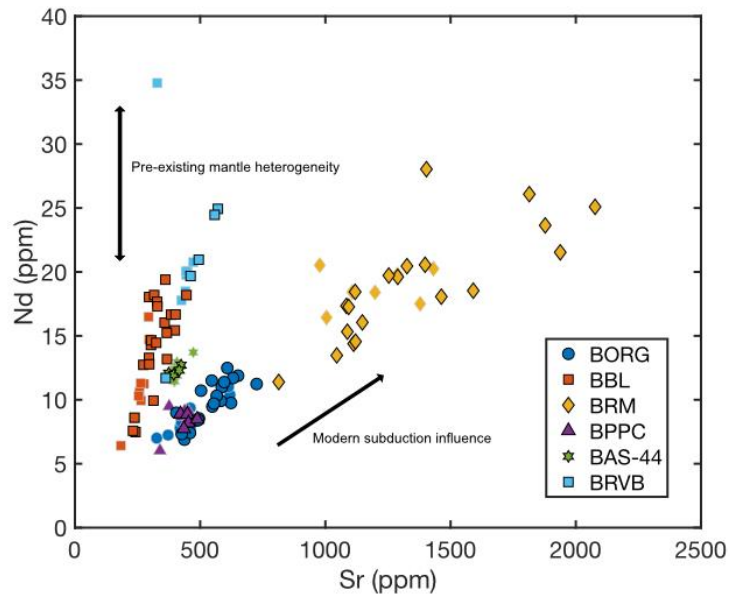
Figure S15. PEC-corrected melt inclusion compositions calculated for each cinder cone. Each symbol represents one analyzed inclusion. Inclusion compositions with gray outlines are data from Walowski et al., (2016). Arrows denote the influence of pre-existing mantle heterogeneity in the sub-arc mantle source and the influence of modern slab-derived materials.
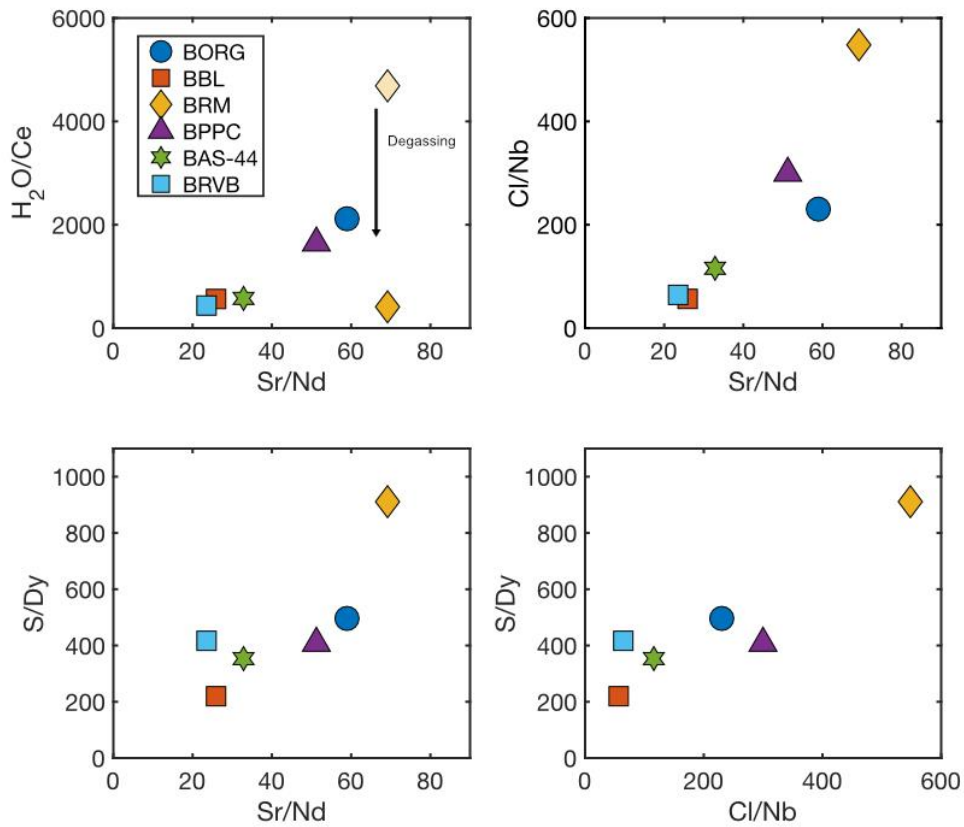
Figure S16. Calculated primary magma compositions for each cinder cone at Lassen. For cinder cone BRM, melts trapped as inclusions experienced H_2O degassing prior to entrapment and/or diffusive H loss post-entrapment, causing them to deviate from the overall H_2O/Ce trend (Walowski et al., 2016). Light colored symbol for BRM represents degassing-corrected H_2O/Ce value based on a linear extrapolation of the H_2O/Ce vs. Cl/Nb correlation for other cinder cones.

Table S1. Analyzed Major element and trace element melt inclusion data. Major elements values and standard deviation calculated from the average of 3-5 analysis spots. H_2O uncertainty represents propogated error calculated with standard devation of 2-4 sample thickness and absorbance peak height measurements. Trace elements measured via LA-ICPMS. Uncertainty represents standard error including uncertainty in calibration standard. Major elements, S, Cl, and H_2O reported in wt. %. Trace elements reported in ppm.

Cinder Cone	Tephra Sample	Inclusion	Minimum Inclusion Width (μm)	Maxmimum Inclusion Width (μm)	Vapor bubble?	Vapor bubble Diameter* (μm)	Oxide in MI?	Sulfide in MI?	Date Analyzed EPMA	SiO_2	1 s. d.	TiO_2	1 s. d.	Al_2O_3	1 s. d.	FeO^T	1 s. d.
BAS-44	BAS-44-2	1	54	58	yes	12	no	no	7/31/18	48.47	0.26	0.84	0.04	17.63	0.06	7.85	0.16
BAS-44	BAS-44-2	10	36	40	yes	8	no	yes	7/31/18	48.14	0.52	1.01	0.04	18.25	0.06	8.31	0.21
BAS-44	BAS-44-2	2	52	91	yes	19	yes	yes	7/31/18	48.34	1.65	1.01	0.03	17.58	0.16	7.14	0.31
BAS-44	BAS-44-2	4	84	86	yes	22	yes	yes	7/23/18	48.86	0.41	1.04	0.03	18.26	0.29	7.15	0.45
BAS-44	BAS-44-2	5	55	66	yes	14	no	yes	7/23/18	47.49	2.34	0.98	0.12	17.63	0.12	7.61	0.19
BAS-44	BAS-44-2	6	62	98	yes	19	yes	yes	7/23/18	47.58	0.23	1.02	0.07	18.45	0.82	7.68	0.46
BAS-44	BAS-44-2	7a	36	66	no	n.r.	no	no	7/23/18	49.86	0.83	0.94	0.07	16.89	0.20	8.45	0.21
BAS-44	BAS-44-2	7b	46	58	no	n.r.	no	no	7/23/18	48.32	2.08	0.99	0.02	16.80	0.12	8.39	0.21
BBL	BBL-5	11	137	163	yes	29	yes	n.r.	6/12/17	47.97	0.04	1.22	0.00	17.00	0.16	9.90	0.05
BBL	BBL-5	14	106	109	yes	23	n.r.	n.r.	6/12/17	48.41	0.31	1.68	0.05	16.14	0.21	9.40	0.07
BBL	BBL-5	15	54	61	n.r.	n.r.	n.r.	n.r.	6/12/17	48.66	0.14	1.50	0.03	15.71	0.07	10.48	0.10
BBL	BBL-5	17	47	66	yes	12	n.r.	n.r.	6/12/17	48.10	0.17	1.09	0.03	18.34	0.18	7.46	0.14
BBL	BBL-5	18	51	65	n.r.	n.r.	n.r.	n.r.	6/12/17	48.75	0.16	1.49	0.02	16.07	0.29	9.77	0.15
BBL	BBL-5	19	103	87	yes	17	n.r.	n.r.	6/12/17	47.71	0.05	1.15	0.03	18.37	0.14	7.71	0.10
BBL	BBL-5	20	57	87	yes	19	n.r.	n.r.	6/12/17	47.97	0.24	1.29	0.03	17.64	0.63	9.51	0.10
BBL	BBL-5	21A	50	61	yes	11	n.r.	n.r.	6/12/17	48.18	0.41	1.44	0.04	17.23	0.56	8.98	0.06
BBL	BBL-5	21B	29	36	n.r.	n.r.	n.r.	n.r.	6/12/17	48.44	0.20	1.49	0.04	17.66	0.41	9.22	0.11
BBL	BBL-5	22	55	76	yes	10	yes	yes	6/12/17	48.11	0.24	1.15	0.04	18.00	0.43	7.93	0.15
BBL	BBL-5	23	112	72	yes	15	n.r.	n.r.	6/12/17	48.06	0.15	1.33	0.02	17.23	0.27	8.85	0.06
BBL	BBL-5	30	43	54	n.r.	n.r.	n.r.	n.r.	6/12/17	49.12	0.25	1.17	0.04	17.17	0.15	9.03	0.10
BBL	BBL-5	31	88	88	yes	21	no	yes	7/31/18	49.96	0.89	1.23	0.05	15.94	0.17	8.56	0.22
BBL	BBL-5	32	46	68	no	n.r.	no	no	7/31/18	49.93	0.68	1.27	0.10	16.76	0.40	9.23	0.30
BBL	BBL-5	33	50	73	yes	15	no	no	7/23/18	49.22	0.83	1.29	0.03	16.75	0.12	9.61	0.42
BBL	BBL-5	34	66	70	n.r.	n.r.	no	yes	7/31/18	51.67	1.88	1.12	0.02	15.42	0.08	9.14	0.19
BBL	BBL-5	43	84	99	no	n.r.	no	no	11/14/19	49.59	0.31	1.25	0.04	16.66	0.31	9.49	0.42
BBL	BBL-5	44	46	50	yes	15	yes	yes	11/14/19	48.50	0.39	0.98	0.04	18.78	0.16	7.93	0.39
BBL	BBL-5	46	57	68	yes	17	yes	no	11/14/19	48.84	0.37	1.18	0.00	17.54	0.11	7.96	0.18
BBL	BBL-5	47	156	199	yes	30	yes	yes	11/14/19	49.02	0.27	0.94	0.02	18.90	0.50	7.71	0.18
BBL	BBL-5	49	87	124	yes	23	no	no	11/14/19	49.42	0.27	1.17	0.03	18.14	0.09	9.79	0.21
BBL	BBL-5	3	41	58	yes	7	n.r.	n.r.	6/12/17	48.13	0.37	1.14	0.06	18.53	0.35	7.20	0.13
BBL	BBL-5	4	62	79	yes	15	n.r.	yes	6/12/17	48.53	0.61	1.20	0.09	18.94	0.42	7.01	0.33
BBL	BBL-5	5	44	52	n.r.	n.r.	n.r.	n.r.	6/12/17	48.59	0.51	1.39	0.03	16.13	0.40	11.50	0.20
BBL	BBL-5	6	97	105	yes	23	n.r.	n.r.	6/12/17	48.58	0.46	1.37	0.02	16.41	0.20	9.39	0.14
BBL	BBL-5	7	44	69	n.r.	n.r.	n.r.	n.r.	6/12/17	47.64	0.39	1.13	0.04	18.03	0.21	7.42	0.04
BORG	BORG-1	2	148	199	yes	50	n.r.	n.r.	6/5/17	47.68	0.38	0.77	0.00	20.18	0.29	8.72	0.05
BORG	BORG-1	3	84	117	yes	21	n.r.	n.r.	6/5/17	48.28	0.15	0.91	0.04	20.89	0.23	7.77	0.13
BORG	BORG-1	8	207	226	yes	61	n.r.	yes	6/5/17	47.35	0.46	0.73	0.03	20.83	0.24	8.15	0.06
BORG	BORG-1	9	154	174	yes	41	yes	n.r.	6/5/17	49.05	0.71	0.91	0.02	20.43	0.28	5.97	0.09
BORG	BORG-1	10	182	292	yes	73	n.r.	n.r.	6/5/17	49.86	0.28	0.90	0.02	20.13	0.69	7.60	0.10
BORG	BORG-1	11	87	94	yes	25	n.r.	n.r.	6/5/17	50.59	0.11	0.90	0.02	22.45	0.22	6.71	0.15
BORG	BORG-1	12	80	92	yes	36	n.r.	n.r.	6/5/17	49.70	0.33	0.85	0.04	20.27	0.42	8.49	0.11
BORG	BORG-1	13	312	327	yes	58	n.r.	n.r.	6/5/17	47.28	0.05	0.90	0.03	20.97	0.53	9.32	0.08
BORG	BORG-1	14	108	127	yes	34	n.r.	n.r.	6/5/17	48.67	0.61	0.75	0.03	19.96	0.21	6.74	0.14
BORG	BORG-1	15	105	128	yes	32	n.r.	n.r.	6/5/17	50.62	0.29	0.98	0.03	19.43	0.63	9.08	0.11
BORG	BORG-1	18	81	114	yes	15	yes	n.r.	6/5/17	46.57	1.13	0.08	0.00	23.10	0.18	8.33	0.19
BORG	BORG-1	19	101	127	yes	25	n.r.	n.r.	6/5/17	49.65	1.24	0.91	0.01	21.84	1.64	4.09	0.13
BORG	BORG-1	20	103	131	n.r.	n.r.	n.r.	n.r.	6/5/17	48.81	0.23	0.99	0.01	20.90	0.70	7.90	0.16
BORG	BORG-1	21	166	179	yes	41	n.r.	n.r.	6/5/17	48.03	0.73	0.80	0.02	21.21	0.66	6.69	0.32
BORG	BORG-1	22	113	142	yes	33	n.r.	n.r.	6/5/17	47.25	0.16	0.91	0.04	19.62	0.20	6.23	0.07
BORG	BORG-1	23	132	139	n.r.	n.r.	n.r.	n.r.	6/5/17	48.13	1.38	0.84	0.05	20.30	2.61	8.20	1.03
BORG	BORG-1	24	159	178	yes	40	n.r.	n.r.	6/5/17	48.67	0.18	0.83	0.02	19.77	0.52	7.87	0.13
BORG	BORG-1	25	91	145	yes	39	n.r.	n.r.	6/5/17	49.16	0.02	0.78	0.04	19.83	0.27	7.11	0.04
BORG	BORG-1	31	117	142	yes	n.r.	no	no	11/14/19	48.87	0.45	0.96	0.01	18.13	0.22	8.51	0.36
BORG	BORG-1	35	79	105	yes	30	yes	no	7/31/18	49.11	1.56	0.81	0.03	17.97	0.06	7.75	0.40
BORG	BORG-1	37	154	175	yes	43	no	yes	7/23/18	47.87	0.92	0.80	0.01	17.80	0.17	8.17	0.42
BORG	BORG-1	38	119	156	yes	n.r.	no	yes	7/23/18	48.49	1.52	0.87	0.01	17.91	0.13	8.11	0.20
BORG	BORG-1	40	108	106	yes	12	no	no	11/14/19	48.46	0.19	0.85	0.07	18.68	0.84	8.19	0.50
BORG	BORG-1	42	92	157	yes	33	no	no	11/14/19	47.95	0.38	0.80	0.02	17.91	0.20	7.34	0.17
BORG	BORG-1	43	156	182	yes	36	no	no	11/14/19	48.95	0.18	0.85	0.01	18.20	0.22	8.10	0.37
BORG	BORG-1	44	120	124	yes	37	no	no	11/14/19	48.99	0.30	0.85	0.01	18.86	0.09	7.53	0.20
BORG	BORG-1	45	73	103	yes	26	no	no	11/14/19	48.39	0.19	0.95	0.01	18.72	0.97	8.58	0.40
BORG	MM-L17-BORG-1	1	80	95	no	23	no	no	11/14/19	48.47	0.37	0.68	0.02	18.31	0.11	6.85	0.41
BORG	MM-L17-BORG-1	2	128	146	yes	43	yes	no	11/14/19	46.51	0.58	0.04	0.01	20.12	0.29	8.05	0.25
BPPC	MM-L17-BPPC-4	13	68	80	yes	21	no	no	11/14/19	49.61	0.42	0.77	0.02	17.03	0.43	7.23	0.31
BPPC	MM-L17-BPPC-4	14	59	72	yes	14	no	no	11/14/19	50.45	0.50	0.79	0.04	17.78	0.24	6.83	0.16
BPPC	MM-L17-BPPC-4	15	81	91	yes	19	yes	no	11/14/19	50.25	0.38	0.73	0.01	16.74	0.11	6.65	0.35
BPPC	MM-L17-BPPC-4	2	69	73	yes	n.r.	yes	no	7/31/18	48.73	1.53	0.77	0.01	17.45	0.12	6.13	0.10
BPPC	MM-L17-BPPC-4	3	72	81	yes	21	no	yes	7/23/18	50.50	1.35	0.80	0.02	16.52	0.01	7.02	0.13
BPPC	MM-L17-BPPC-4	4	68	92	yes	17	yes	no	7/31/18	48.99	0.31	0.83	0.00	17.48	0.36	6.56	0.27
BPPC	MM-L17-BPPC-4	5	50	59	yes	12	no	no	7/31/18	50.06	1.61	0.78	0.02	17.67	0.21	6.75	0.16
BRM	BRM-1	14	34	48	yes	21	n.r.	n.r.	6/5/17	49.46	#N/A	1.06	#N/A	20.25	#N/A	5.89	#N/A
BRM	BRM-1	16	80	120	yes	44	yes	Sulfide n.r.	6/5/17	50.46	0.18	1.07	0.03	19.27	0.54	5.90	0.02
BRM	BRM-1	17	64	109	yes	32	n.r.	n.r.	6/5/17	50.05	0.42	0.98	0.58	18.95	0.58	5.83	0.07
BRM	BRM-1	18	37	52	yes	22	n.r.	n.r.	6/5/17	47.82	0.28	1.14	0.04	19.50	0.74	5.74	0.12
BRM	BRM-1	19	51	81	yes	25	n.r.	n.r.	6/5/17	49.99	0.15	1.04	0.03	19.77	0.28	6.99	0.06
BRM	BRM-1	22	57	63	yes	23	n.r.	n.r.	6/5/17	49.85	0.63	1.03	0.01	19.48	0.28	6.00	0.25
BRM	BRM-1	23	n.r.	n.r.	n.r.	n.r.	n.r.	n.r.	6/5/17	48.72	0.21	1.15	0.03	18.43	0.31	4.51	0.02
BRM	BRM-1	24	58	70	yes	19	n.r.	n.r.	6/5/17	55.52	0.37	1.97	0.08	14.40	0.16	6.67	0.03
BRM	BRM-1	25	66	88	yes	26	yes	n.r.	6/5/17	48.90	0.20	1.05	0.05	20.01	0.36	6.60	0.06
BRM	BRM-1	30	87	126	yes	32	no	no	7/31/18	51.28	1.40	0.84	0.00	18.24	0.13	6.07	0.25
BRM	BRM-1	34	57	83	yes	25	yes	no	7/23/18	49.52	0.67	1.00	0.01	20.07	0.30	6.25	0.23
BRM	BRM-1	35	44	55	no	n.r.	yes	no	7/23/18	48.22	0.02	0.98	0.04	19.34	0.54	5.24	0.21
BRM	BRM-1	36	43	48	yes	17	yes	no	7/31/18	51.28	1.48	1.06	0.01	19.58	0.08	4.59	0.01
BRM	BRM-1	39	39	90	yes	15	yes	no	7/31/18	51.14	1.41	0.97	0.04	18.66	0.16	5.96	0.41
BRM	BRM-1	40	33	47	yes	16	yes	no	7/23/18	49.54	0.40	1.04	0.01	20.01	0.12	5.63	0.07
BRM	BRM-1	41	56	104	yes	26	yes	no	7/31/18	49.16	0.83	0.85	0.02	18.68	0.22	5.47	0.04

107

Table S1. (continued)

Cinder Cone	Tephra Sample	Inclusion	Minimum Inclusion Width (μm)	Maxmimum Inclusion Width (μm)	Vapor bubble?	Vapor bubble Diameter* (μm)	Oxide in MI?	Sulfide in MI?	Date Analyzed EPMA	SiO_2	1 s. d.	TiO_2	1 s. d.	Al_2O_3	1 s. d.	FeO^T	1 s. d.
BRM	BRM-1	2	55	62	yes	21	yes	n.r.	6/5/17	50.23	0.03	1.03	0.04	19.97	0.29	5.46	0.16
BRM	BRM-1	3	81	103	yes	33	yes	n.r.	6/5/17	50.41	0.34	1.03	0.02	19.94	0.47	5.74	0.13
BRM	BRM-1	5	49	72	yes	19	yes	n.r.	6/5/17	48.92	0.51	1.17	0.03	19.90	0.62	5.41	0.09
BRM	BRM-1	6	42	54	yes	20	n.r.	n.r.	6/5/17	48.37	0.31	1.04	0.03	20.29	1.14	6.91	0.25
BRM	BRM-1	7	45	67	n.r.	n.r.	n.r.	n.r.	6/5/17	49.79	0.72	1.17	0.11	20.03	1.02	6.49	0.59
BRM	BRM-1	8	50	68	yes	20	n.r.	n.r.	6/5/17	49.12	0.19	1.21	0.02	20.76	0.39	5.79	0.22
BRM	MM-L17-BRM-2	1	71	89	yes	28	yes	no	7/23/18	48.63	0.53	0.82	0.04	20.04	0.10	4.90	0.04
BRM	MM-L17-BRM-2	10	70	84	yes	30	yes	n.r.	7/23/18	48.62	1.40	1.21	0.12	20.64	0.07	5.48	0.27
BRM	MM-L17-BRM-2	13	65	112	yes	33	n.r.	n.r.	7/23/18	48.87	1.07	1.13	0.08	20.24	0.06	5.22	0.07
BRM	MM-L17-BRM-2	14	43	64	yes	18	yes	n.r.	7/23/18	49.26	1.81	0.85	0.02	19.96	0.08	5.33	0.16
BRM	MM-L17-BRM-2	16	38	52	yes	n.r.	n.r.	n.r.	7/23/18	48.42	0.76	0.87	0.08	19.75	0.32	4.91	0.24
BRM	MM-L17-BRM-2	17	44	81	yes	20	yes	n.r.	7/23/18	48.87	1.11	0.85	0.01	20.42	0.21	5.30	0.22
BRM	MM-L17-BRM-2	18	80	87	yes	32	yes	n.r.	7/23/18	50.10	0.76	0.96	0.04	20.68	0.09	5.36	0.16
BRM	MM-L17-BRM-2	24	77	133	yes	41	no	no	11/14/19	49.55	0.36	1.00	0.03	19.60	0.17	6.61	0.28
BRM	MM-L17-BRM-2	25	70	144	yes	38	no	no	11/14/19	48.86	0.25	1.08	0.04	20.48	0.37	5.49	0.14
BRM	MM-L17-BRM-2	26	81	109	yes	41	yes	no	11/14/19	49.27	0.33	1.07	0.03	21.26	0.34	5.18	0.23
BRM	MM-L17-BRM-2	29	71	100	yes	34	yes	no	11/14/19	49.98	0.43	0.87	0.02	20.46	0.17	4.83	0.42
BRM	MM-L17-BRM-2	31	92	115	yes	36	yes	no	11/14/19	49.30	0.17	0.85	0.02	19.98	0.49	5.20	0.37
BRM	MM-L17-BRM-2	32	68	82	yes	92	no	no	11/14/19	49.15	0.08	0.89	0.03	20.71	0.85	5.60	0.12
BRM	MM-L17-BRM-2	8	76	288	yes	50	yes	no	7/23/18	46.63	1.12	1.11	0.00	20.18	0.19	5.61	0.13
BRVB	MM-L17-BRVB-2	10	80	83	yes	n.r.	yes	no	11/14/19	48.59	0.32	1.36	0.02	17.02	0.55	8.89	0.28
BRVB	MM-L17-BRVB-2	2	72	70	yes	17	no	yes	11/14/19	49.48	0.19	1.19	0.02	17.25	0.30	7.64	0.04
BRVB	MM-L17-BRVB-2	4	55	66	yes	19	no	yes	11/14/19	48.27	0.52	1.49	0.01	19.09	0.26	8.32	0.11
BRVB	MM-L17-BRVB-2	6	55	62	yes	n.r.	no	yes	11/14/19	48.97	0.51	0.97	0.02	18.57	0.38	7.26	0.32
BRVB	MM-L17-BRVB-2	7	21	61	yes	70	no	no	11/14/19	47.72	0.57	1.49	0.01	18.52	0.22	8.72	0.47

Table S1. (continued)

Cinder Cone	Tephra Sample	Inclusion	MnO	1 s. d.	MgO	1 s. d.	CaO	1 s. d.	Na₂O	1 s. d.	K₂O	1 s. d.	P₂O₅	1 s. d.	S	1 s. d.	Cl	1 s. d.	H₂O	1 s. d.	Olivine Host Fo %
BAS-44	BAS-44-2	1	0.12	0.02	7.94	0.05	11.61	0.08	2.64	0.08	0.25	0.03	0.14	0.02	0.12	0.01	0.03	0.00	0.76	0.01	87.09
BAS-44	BAS-44-2	10	0.15	0.01	7.16	0.21	10.83	0.05	2.87	0.13	0.41	0.04	0.19	0.00	0.03	0.00	0.04	0.00	1.44	0.09	87.70
BAS-44	BAS-44-2	2	0.14	0.01	7.82	0.08	11.17	0.14	2.93	0.12	0.28	0.03	0.18	0.02	0.13	0.01	0.04	0.00	1.44	0.09	87.55
BAS-44	BAS-44-2	4	0.13	0.01	6.84	0.90	11.42	0.34	2.91	0.41	0.28	0.04	0.20	0.04	0.12	0.00	0.04	0.00	1.14	0.03	87.33
BAS-44	BAS-44-2	5	0.12	0.01	7.57	0.18	11.31	0.13	2.78	0.12	0.28	0.02	0.17	0.00	0.12	0.00	0.04	0.00	1.27	0.01	87.09
BAS-44	BAS-44-2	6	0.14	0.02	7.43	1.13	11.41	0.10	3.12	0.28	0.30	0.01	0.17	0.02	0.12	0.01	0.05	0.00	1.25	0.03	87.68
BAS-44	BAS-44-2	7a	0.16	0.00	7.77	0.10	10.79	0.10	2.76	0.13	0.34	0.03	0.16	0.04	0.11	0.01	0.04	0.00	0.51	0.72	87.06
BAS-44	BAS-44-2	7b	0.15	0.01	7.66	0.04	10.64	0.12	2.87	0.17	0.36	0.02	0.17	0.01	0.11	0.00	0.04	0.00	n. a.	n. a.	86.70
BBL	BBL-5	11	0.18	0.01	6.56	0.02	9.23	0.01	3.58	0.09	0.72	0.00	0.28	0.02	0.10	0.00	0.03	0.00	n. a.	n. a.	82.37
BBL	BBL-5	14	0.15	0.01	6.60	0.02	8.30	0.69	4.35	0.09	0.83	0.01	0.34	0.02	0.10	0.00	0.03	0.00	n. a.	n. a.	82.77
BBL	BBL-5	15	0.18	0.02	6.67	0.19	8.29	0.79	3.82	0.10	0.65	0.06	0.31	0.02	0.11	0.00	0.03	0.00	n. a.	n. a.	82.53
BBL	BBL-5	17	0.12	0.01	6.73	0.07	10.97	0.12	3.29	0.06	0.33	0.02	0.14	0.00	0.09	0.00	0.02	0.00	n. a.	n. a.	87.91
BBL	BBL-5	18	0.18	0.00	6.75	0.05	8.76	0.05	3.88	0.14	0.76	0.02	0.30	0.01	0.10	0.00	0.03	0.00	n. a.	n. a.	83.16
BBL	BBL-5	19	0.13	0.01	6.95	0.01	9.86	0.81	3.22	0.13	0.33	0.00	0.19	0.02	0.08	0.00	0.02	0.00	n. a.	n. a.	86.28
BBL	BBL-5	20	0.16	0.01	6.52	0.03	9.13	0.70	3.46	0.16	0.64	0.03	0.29	0.02	0.09	0.00	0.03	0.00	n. a.	n. a.	83.25
BBL	BBL-5	21A	0.15	0.02	6.82	0.32	8.99	0.84	3.78	0.09	0.61	0.01	0.28	0.02	0.09	0.00	0.02	0.00	n. a.	n. a.	84.96
BBL	BBL-5	21B	0.15	0.01	6.69	0.45	9.25	0.64	3.81	0.18	0.60	0.01	0.31	0.02	0.09	0.00	0.03	0.00	n. a.	n. a.	84.96
BBL	BBL-5	22	0.12	0.01	6.21	0.36	11.08	0.08	3.12	0.01	0.30	0.00	0.15	0.00	0.09	0.00	0.02	0.01	n. a.	n. a.	86.42
BBL	BBL-5	23	0.15	0.02	6.71	0.04	9.95	0.08	3.45	0.05	0.50	0.02	0.22	0.01	0.10	0.00	0.02	0.00	n. a.	n. a.	84.42
BBL	BBL-5	30	0.17	0.01	6.25	0.07	9.54	0.18	3.41	0.14	0.73	0.05	0.31	0.03	0.12	0.01	0.05	0.00	n. a.	n. a.	85.51
BBL	BBL-5	31	0.16	0.01	6.76	0.08	9.95	0.18	3.49	0.08	0.55	0.04	0.22	0.02	0.12	0.01	0.04	0.00	1.15	0.03	83.94
BBL	BBL-5	32	0.17	0.02	5.49	0.52	9.81	0.05	3.62	0.26	0.62	0.03	0.28	0.02	0.13	0.01	0.04	0.00	1.24	0.11	83.71
BBL	BBL-5	33	0.17	0.01	6.03	0.15	9.21	0.17	3.70	0.21	0.72	0.10	0.33	0.03	0.15	0.01	0.04	0.00	1.23	0.11	83.08
BBL	BBL-5	34	0.16	0.02	6.32	0.15	10.35	0.14	3.39	0.19	0.47	0.02	0.21	0.01	0.12	0.00	0.03	0.00	1.21	0.03	83.57
BBL	BBL-5	43	0.19	0.00	7.12	0.04	8.81	0.07	3.56	0.27	0.79	0.04	0.28	0.02	0.11	0.00	0.04	0.00	0.97	0.00	83.61
BBL	BBL-5	44	0.14	0.00	7.26	0.06	11.03	0.13	2.78	0.10	0.28	0.00	0.11	0.01	0.09	0.00	0.02	0.00	1.02	0.08	86.16
BBL	BBL-5	46	0.17	0.00	7.03	0.04	9.77	0.06	3.26	0.29	0.64	0.02	0.25	0.00	0.10	0.00	0.03	0.00	1.17	0.00	85.01
BBL	BBL-5	47	0.14	0.00	7.74	0.08	11.25	0.02	2.99	0.23	0.26	0.02	0.10	0.02	0.09	0.00	0.02	0.01	1.03	0.06	87.24
BBL	BBL-5	49	0.18	0.00	6.06	0.20	9.55	0.08	3.38	0.19	0.77	0.02	0.28	0.01	0.10	0.00	0.03	0.00	0.64	0.01	82.56
BBL	BBL-5	3	0.13	0.01	6.17	0.15	10.97	0.76	3.23	0.04	0.27	0.01	0.16	0.03	0.09	0.00	0.01	0.00	n. a.	n. a.	87.10
BBL	BBL-5	4	0.13	0.02	5.35	0.61	11.58	0.09	3.29	0.38	0.31	0.04	0.15	0.01	0.08	0.00	0.02	0.00	n. a.	n. a.	87.08
BBL	BBL-5	5	0.18	0.04	6.16	0.11	8.25	0.77	3.72	0.14	0.79	0.04	0.30	0.03	0.10	0.00	0.03	0.00	n. a.	n. a.	80.43
BBL	BBL-5	6	0.16	0.02	5.94	0.13	10.24	0.09	3.75	0.02	0.52	0.02	0.23	0.01	0.10	0.00	0.02	0.00	n. a.	n. a.	84.37
BBL	BBL-5	7	0.13	0.01	7.02	0.20	11.30	0.03	3.10	0.08	0.23	0.02	0.12	0.00	0.09	0.00	0.01	0.00	n. a.	n. a.	87.59
BORG	BORG-1	2	0.14	0.01	6.59	0.07	9.15	0.76	3.57	0.09	0.51	0.02	0.08	0.02	0.10	0.00	0.05	0.00	n. a.	n. a.	83.38
BORG	BORG-1	3	0.12	0.01	5.50	0.31	9.63	0.79	4.07	0.08	0.54	0.02	0.08	0.02	0.09	0.00	0.05	0.00	n. a.	n. a.	83.72
BORG	BORG-1	8	0.15	0.02	6.71	0.08	8.91	0.71	4.02	0.12	0.53	0.02	0.13	0.02	0.12	0.00	0.04	0.00	n. a.	n. a.	84.19
BORG	BORG-1	9	0.09	0.01	5.39	0.04	11.91	0.18	3.54	0.03	0.62	0.04	0.11	0.01	0.12	0.00	0.07	0.01	n. a.	n. a.	88.29
BORG	BORG-1	10	0.14	0.02	5.23	0.40	9.71	0.04	4.35	0.31	0.63	0.03	0.11	0.00	0.09	0.00	0.04	0.00	n. a.	n. a.	83.88
BORG	BORG-1	11	0.10	0.01	3.15	0.05	10.29	0.02	5.11	0.16	0.63	0.03	0.11	0.01	0.14	0.00	0.04	0.00	n. a.	n. a.	85.18
BORG	BORG-1	12	0.13	0.00	5.52	0.47	8.73	0.71	4.34	0.24	0.57	0.02	0.11	0.02	0.12	0.00	0.04	0.00	n. a.	n. a.	84.25
BORG	BORG-1	13	0.16	0.00	8.46	0.03	10.56	0.84	1.34	0.05	0.06	0.00	-0.02	0.03	0.01	0.00	0.00	0.00	n. a.	n. a.	85.19
BORG	BORG-1	14	0.11	0.01	6.50	0.37	10.97	0.08	3.19	0.07	0.51	0.02	0.07	0.00	0.10	0.00	0.05	0.00	n. a.	n. a.	87.64
BORG	BORG-1	15	0.13	0.01	6.11	0.44	8.90	0.28	4.51	0.17	0.59	0.04	0.12	0.02	0.13	0.01	0.05	0.00	n. a.	n. a.	81.93
BORG	BORG-1	18	0.15	0.01	3.82	0.03	12.46	0.23	1.48	0.10	0.05	0.00	0.00	0.01	0.00	0.00	0.00	0.00	n. a.	n. a.	83.34
BORG	BORG-1	19	0.13	0.01	7.82	0.32	10.01	0.32	4.49	0.40	0.60	0.03	0.08	0.01	0.10	0.00	0.05	0.00	n. a.	n. a.	85.72
BORG	BORG-1	20	0.13	0.01	4.78	0.09	9.27	0.12	4.66	0.04	0.56	0.01	0.11	0.01	0.12	0.00	0.04	0.00	n. a.	n. a.	85.75
BORG	BORG-1	21	0.10	0.02	5.57	0.63	10.45	0.03	3.53	0.15	0.56	0.05	0.08	0.01	0.09	0.00	0.04	0.00	n. a.	n. a.	86.41
BORG	BORG-1	22	0.11	0.02	6.01	0.14	11.46	0.11	3.31	0.17	0.58	0.02	0.11	0.02	0.11	0.00	0.06	0.00	n. a.	n. a.	88.57
BORG	BORG-1	23	0.12	0.02	6.47	3.46	9.51	1.08	3.98	0.44	0.56	0.05	0.09	0.01	0.09	0.01	0.05	0.01	n. a.	n. a.	83.33
BORG	BORG-1	24	0.13	0.01	6.87	0.26	9.27	0.09	3.79	0.19	0.56	0.02	0.10	0.00	0.09	0.00	0.04	0.00	n. a.	n. a.	84.18
BORG	BORG-1	25	0.12	0.00	6.82	0.21	11.36	0.09	2.95	0.02	0.50	0.02	0.07	0.00	0.10	0.00	0.06	0.00	n. a.	n. a.	87.54
BORG	BORG-1	31	0.15	0.00	7.02	0.06	8.45	0.03	2.84	0.14	0.63	0.04	0.15	0.01	0.15	0.00	0.06	0.00	2.46	0.09	83.97
BORG	BORG-1	35	0.13	0.00	5.56	0.23	8.87	0.01	3.39	0.12	0.55	0.07	0.16	0.02	0.18	0.00	0.05	0.00	n. a.	n. a.	83.29
BORG	BORG-1	37	0.13	0.02	6.21	0.36	8.70	0.02	3.37	0.22	0.51	0.03	0.16	0.01	0.17	0.01	0.05	0.00	2.94	0.06	82.75
BORG	BORG-1	38	0.14	0.01	6.75	0.09	8.83	0.11	3.19	0.17	0.53	0.01	0.14	0.04	0.17	0.00	0.05	0.00	3.02	0.00	84.23
BORG	BORG-1	40	0.14	0.01	6.10	1.18	9.15	0.10	2.99	0.36	0.59	0.07	0.12	0.00	0.12	0.01	0.06	0.00	2.72	0.03	83.33
BORG	BORG-1	42	0.13	0.00	7.19	0.10	9.42	0.09	3.00	0.16	0.54	0.05	0.10	0.01	0.11	0.00	0.05	0.00	2.89	0.39	85.29
BORG	BORG-1	43	0.14	0.01	7.27	0.03	8.52	0.01	3.15	0.27	0.51	0.01	0.11	0.01	0.15	0.00	0.06	0.00	1.67	0.01	83.98
BORG	BORG-1	44	0.14	0.01	3.75	0.04	9.48	0.04	3.47	0.06	0.57	0.02	0.10	0.00	0.15	0.00	0.05	0.00	2.98	0.02	82.70
BORG	BORG-1	45	0.15	0.00	5.98	1.18	8.96	0.06	3.39	0.33	0.57	0.05	0.12	0.02	0.12	0.01	0.05	0.00	0.82	1.43	83.23
BORG	MM-L17-BORG-1	1	0.13	0.01	6.86	0.20	10.93	0.08	2.46	0.14	0.51	0.05	0.08	0.01	0.14	0.00	0.06	0.00	2.60	0.05	85.82
BORG	MM-L17-BORG-1	2	0.16	0.01	7.85	0.08	11.89	0.04	1.01	0.19	0.05	0.01	0.00	0.01	0.00	0.00	0.00	0.00	1.07	1.85	86.37
BPPC	MM-L17-BPPC-4	13	0.14	0.00	7.94	0.05	10.79	0.04	2.51	0.13	0.35	0.03	0.09	0.01	0.10	0.00	0.04	0.00	2.23	0.12	87.50
BPPC	MM-L17-BPPC-4	14	0.14	0.01	7.04	0.08	11.06	0.07	2.54	0.35	0.35	0.01	0.08	0.01	0.12	0.01	0.04	0.00	2.23	0.07	87.24
BPPC	MM-L17-BPPC-4	15	0.14	0.01	7.53	0.15	11.03	0.08	2.44	0.17	0.31	0.01	0.09	0.01	0.10	0.00	0.04	0.00	1.87	0.10	87.35
BPPC	MM-L17-BPPC-4	2	0.12	0.01	6.28	0.29	11.84	0.13	2.56	0.03	0.25	0.01	0.11	0.00	0.11	0.00	0.06	0.00	n. a.	n. a.	87.60
BPPC	MM-L17-BPPC-4	3	0.14	0.01	7.43	0.20	11.07	0.09	2.56	0.04	0.33	0.01	0.12	0.01	0.10	0.01	0.05	0.00	2.67	0.01	87.31
BPPC	MM-L17-BPPC-4	4	0.10	0.01	6.72	0.30	11.03	0.09	2.73	0.10	0.33	0.01	0.13	0.01	0.12	0.00	0.06	0.00	2.35	0.05	87.77
BPPC	MM-L17-BPPC-4	5	0.14	0.02	5.76	0.12	11.89	0.09	2.65	0.09	0.27	0.04	0.09	0.01	0.11	0.00	0.07	0.00	1.34	n. a.	87.86
BRM	BRM-1	14	0.08	#N/A	4.29	#N/A	11.18	#N/A	4.39	#N/A	0.76	#N/A	0.26	#N/A	0.24	#N/A	0.34	#N/A	n. a.	n. a.	88.45
BRM	BRM-1	16	0.08	0.01	4.79	0.04	10.31	0.09	4.64	0.15	0.70	0.02	0.22	0.01	0.18	0.00	0.27	0.00	n. a.	n. a.	88.34
BRM	BRM-1	17	0.08	0.01	5.48	0.19	9.85	0.08	4.69	0.19	0.64	0.03	0.19	0.01	0.17	0.00	0.25	0.00	n. a.	n. a.	88.29
BRM	BRM-1	18	0.09	0.01	5.28	0.14	10.31	0.10	4.30	0.23	0.98	0.04	0.31	0.00	0.21	0.00	0.27	0.00	n. a.	n. a.	88.93
BRM	BRM-1	19	0.09	0.02	4.66	0.03	8.54	0.72	4.36	0.12	0.89	0.06	0.23	0.02	0.14	0.00	0.25	0.01	n. a.	n. a.	86.61
BRM	BRM-1	22	0.09	0.00	3.97	0.39	10.50	0.05	5.27	0.21	0.62	0.07	0.21	0.02	0.19	0.00	0.29	0.00	n. a.	n. a.	87.93
BRM	BRM-1	23	0.09	0.00	7.51	0.11	9.55	0.86	4.58	0.19	0.86	0.02	0.30	0.03	0.17	0.00	0.23	0.00	n. a.	n. a.	84.73
BRM	BRM-1	24	0.09	0.02	3.78	0.08	7.21	0.02	4.37	0.04	1.81	0.04	0.48	0.01	0.05	0.00	0.36	0.01	n. a.	n. a.	86.70
BRM	BRM-1	25	0.09	0.02	6.45	0.34	10.68	0.04	4.85	0.01	0.64	0.04	0.24	0.01	0.21	0.01	0.32	0.00	n. a.	n. a.	88.39
BRM	BRM-1	30	0.10	0.02	4.94	0.33	8.82	0.06	3.95	0.09	0.67	0.05	0.20	0.02	0.19	0.00	0.30	0.00	3.13	0.06	86.16
BRM	BRM-1	34	0.09	0.01	4.12	0.15	10.83	0.14	4.50	0.16	0.80	0.04	0.26	0.02	0.27	0.00	0.33	0.00	2.36	0.19	87.51
BRM	BRM-1	35	0.07	0.01	4.63	0.21	10.31	0.06	4.32	0.09	0.78	0.00	0.28	0.01	0.26	0.00	0.35	0.00	n. a.	n. a.	88.61
BRM	BRM-1	36	0.06	0.02	4.39	0.01	11.11	0.02	4.08	0.38	0.81	0.00	0.30	0.03	0.26	0.00	0.41	0.00	0.58	0.00	88.40
BRM	BRM-1	39	0.09	0.01	4.08	0.15	9.98	0.06	4.05	0.11	0.81	0.02	0.27	0.02	0.22	0.01	0.32	0.01	3.85	0.05	88.17
BRM	BRM-1	40	0.07	0.02	3.93	0.36	10.84	0.19	3.89	0.07	0.82	0.02	0.31	0.01	0.27	0.00	0.34	0.00	2.05	0.06	87.62
BRM	BRM-1	41	0.08	0.02	5.11	0.21	11.13	0.19	3.42	0.23	0.57	0.05	0.19	0.01	0.23	0.01	0.32	0.01	2.05	0.06	87.79

Table S1. (continued)

Cinder Cone	Tephra Sample	Inclusion	MnO	1 s. d.	MgO	1 s. d.	CaO	1 s. d.	Na$_2$O	1 s. d.	K$_2$O	1 s. d.	P$_2$O$_5$	1 s. d.	S	1 s. d.	Cl	1 s. d.	H$_2$O	1 s. d.	Olivine Host Fo %
BRM	BRM-1	2	0.07	0.02	3.55	0.24	11.62	0.90	4.32	0.02	0.63	0.03	0.22	0.02	0.18	0.00	0.27	0.00	n. a.	n. a.	89.02
BRM	BRM-1	3	0.08	0.00	4.49	0.03	10.35	0.07	4.74	0.08	0.71	0.01	0.21	0.01	0.17	0.00	0.27	0.01	n. a.	n. a.	87.64
BRM	BRM-1	5	0.07	0.01	4.42	0.12	10.84	0.04	4.62	0.09	0.78	0.02	0.28	0.01	0.20	0.00	0.31	0.00	n. a.	n. a.	88.74
BRM	BRM-1	6	0.07	0.02	3.88	0.43	10.86	0.04	4.21	0.18	0.60	0.03	0.24	0.03	0.17	0.00	0.27	0.00	n. a.	n. a.	87.77
BRM	BRM-1	7	0.11	0.02	3.61	0.90	10.79	0.33	4.51	0.46	0.79	0.08	0.27	0.01	0.17	0.00	0.27	0.01	n. a.	n. a.	86.57
BRM	BRM-1	8	0.07	0.01	2.82	0.36	9.89	0.68	5.07	0.07	0.98	0.14	0.27	0.02	0.23	0.01	0.33	0.00	n. a.	n. a.	88.66
BRM	MM-L17-BRM-2	1	0.07	0.01	5.17	0.05	11.50	0.05	4.06	0.18	0.56	0.04	0.19	0.01	0.24	0.01	0.38	0.00	0.98	0.00	89.64
BRM	MM-L17-BRM-2	10	0.08	0.01	3.42	0.02	10.85	0.07	4.50	0.23	0.86	0.02	0.31	0.04	0.30	0.00	0.26	0.00	0.89	0.03	87.27
BRM	MM-L17-BRM-2	13	0.09	0.01	4.74	0.06	10.92	0.15	4.63	0.16	0.83	0.04	0.37	0.02	0.29	0.00	0.34	0.00	n. a.	n. a.	88.62
BRM	MM-L17-BRM-2	14	0.07	0.01	4.63	0.03	11.37	0.08	4.30	0.01	0.69	0.02	0.20	0.02	0.24	0.00	0.30	0.00	0.89	0.01	88.40
BRM	MM-L17-BRM-2	16	0.09	0.03	3.93	0.07	11.25	0.02	3.94	0.21	0.59	0.03	0.25	0.01	0.25	0.00	0.27	0.00	2.43	0.11	89.04
BRM	MM-L17-BRM-2	17	0.09	0.02	4.57	0.12	12.14	0.11	3.84	0.43	0.56	0.03	0.21	0.02	0.20	0.01	0.29	0.00	0.70	0.04	88.98
BRM	MM-L17-BRM-2	18	0.09	0.02	3.42	0.25	10.77	0.17	4.19	0.15	0.83	0.06	0.23	0.03	0.19	0.00	0.26	0.00	0.71	0.03	88.65
BRM	MM-L17-BRM-2	24	0.10	0.01	5.27	0.08	10.58	0.03	3.87	0.31	0.92	0.04	0.26	0.00	0.23	0.01	0.24	0.00	1.25	0.01	86.55
BRM	MM-L17-BRM-2	25	0.08	0.01	5.05	0.10	10.82	0.04	4.02	0.13	0.81	0.04	0.27	0.01	0.25	0.00	0.33	0.01	0.66	0.04	87.89
BRM	MM-L17-BRM-2	26	0.08	0.00	4.88	0.07	10.98	0.06	4.25	0.16	0.87	0.09	0.28	0.00	0.26	0.00	0.35	0.01	0.87	0.02	88.92
BRM	MM-L17-BRM-2	29	0.07	0.00	5.00	0.03	11.40	0.03	4.05	0.24	0.72	0.01	0.18	0.01	0.22	0.00	0.28	0.00	0.33	0.01	89.51
BRM	MM-L17-BRM-2	31	0.08	0.00	5.53	0.20	11.60	0.04	3.67	0.28	0.56	0.03	0.17	0.00	0.23	0.00	0.28	0.00	0.34	0.60	90.49
BRM	MM-L17-BRM-2	32	0.09	0.01	4.94	0.08	11.93	0.05	3.80	0.09	0.58	0.03	0.20	0.01	0.22	0.00	0.27	0.00	0.84	0.05	88.42
BRM	MM-L17-BRM-2	8	0.08	0.00	4.79	0.00	11.29	0.03	4.33	0.22	0.75	0.10	0.33	0.03	0.38	0.01	0.37	0.00	4.30	0.11	89.06
BRVB	MM-L17-BRVB-2	10	0.15	0.00	6.95	0.06	9.41	0.02	2.90	0.23	1.02	0.03	0.28	0.00	0.17	0.00	0.05	0.00	1.97	0.01	83.46
BRVB	MM-L17-BRVB-2	2	0.13	0.01	6.97	0.16	10.20	0.11	2.57	0.05	0.57	0.02	0.15	0.00	0.17	0.01	0.02	0.00	0.61	1.06	85.50
BRVB	MM-L17-BRVB-2	4	0.15	0.01	5.73	0.05	10.67	0.03	3.54	0.10	0.97	0.03	0.33	0.01	0.13	0.00	0.05	0.00	0.32	0.01	84.09
BRVB	MM-L17-BRVB-2	6	0.14	0.00	7.61	0.03	10.98	0.01	3.01	0.09	0.36	0.03	0.16	0.00	0.13	0.00	0.03	0.00	0.73	0.06	85.11
BRVB	MM-L17-BRVB-2	7	0.15	0.00	5.92	0.10	10.06	0.14	3.57	0.18	1.12	0.02	0.33	0.01	0.20	0.01	0.07	0.00	1.92	0.05	83.66

Table S1. (continued)

Cinder Cone	Tephra Sample	Inclusion	Li	s. e.	B	s. e.	Sc	s. e.	V	s. e.	Rb	s. e.	Sr	s. e.	Y	s. e.	Zr	s. e.	Nb	s. e.
BAS-44	BAS-44-2	1	n. a.	n. a.	n. a.	n. a.	n. a.	n. a.	n. a.	n. a.	n. a.	n. a.	n. a.	n. a.	n. a.	n. a.	n. a.	n. a.	n. a.	n. a.
BAS-44	BAS-44-2	10	n. a.	n. a.	n. a.	n. a.	n. a.	n. a.	n. a.	n. a.	n. a.	n. a.	n. a.	n. a.	n. a.	n. a.	n. a.	n. a.	n. a.	n. a.
BAS-44	BAS-44-2	2	n. a.	n. a.	n. a.	n. a.	30.36	3.01	196.85	27.52	n. a.	n. a.	401.19	10.74	18.36	1.08	75.81	5.61	2.84	0.22
BAS-44	BAS-44-2	4	n. a.	n. a.	n. a.	n. a.	31.88	3.20	222.42	6.65	n. a.	n. a.	430.87	5.60	18.76	1.06	79.88	4.43	3.33	0.25
BAS-44	BAS-44-2	5	n. a.	n. a.	n. a.	n. a.	37.58	3.70	214.50	4.05	n. a.	n. a.	445.71	2.82	21.10	1.14	83.85	4.59	3.46	0.28
BAS-44	BAS-44-2	6	n. a.	n. a.	n. a.	n. a.	n. a.	n. a.	n. a.	n. a.	n. a.	n. a.	n. a.	n. a.	n. a.	n. a.	n. a.	n. a.	n. a.	n. a.
BAS-44	BAS-44-2	7a	n. a.	n. a.	n. a.	n. a.	35.90	3.59	210.63	4.48	n. a.	n. a.	432.60	6.00	19.92	1.08	81.45	4.47	2.97	0.24
BAS-44	BAS-44-2	7b	n. a.	n. a.	n. a.	n. a.	n. a.	n. a.	n. a.	n. a.	n. a.	n. a.	n. a.	n. a.	n. a.	n. a.	n. a.	n. a.	n. a.	n. a.
BBL	BBL-5	11	10.87	1.59	3.71	1.38	35.77	1.47	212.51	11.13	11.71	0.25	405.10	6.29	18.50	1.60	101.53	7.47	5.76	0.55
BBL	BBL-5	14	8.41	1.18	3.02	1.16	42.48	1.69	255.53	13.57	13.27	0.35	305.18	8.62	30.87	2.29	137.78	10.36	6.43	0.66
BBL	BBL-5	15	10.47	1.52	4.95	1.86	51.28	2.73	311.08	17.22	12.92	0.37	363.62	8.58	30.19	2.46	133.86	11.47	6.45	0.64
BBL	BBL-5	17	9.65	1.40	2.26	0.99	55.25	2.31	339.21	18.52	6.72	0.28	432.46	10.74	33.97	2.62	106.60	8.31	2.66	0.34
BBL	BBL-5	18	10.21	1.46	3.05	1.20	44.73	1.83	230.41	12.18	12.17	0.22	326.15	5.58	25.13	2.31	123.99	9.40	6.44	0.62
BBL	BBL-5	19	7.30	1.04	0.37	0.38	31.38	1.39	205.76	11.30	4.51	0.22	265.44	5.30	21.22	1.60	75.49	5.60	2.45	0.27
BBL	BBL-5	20	11.70	1.90	4.40	1.70	47.80	2.60	301.70	16.40	13.40	0.30	460.30	9.90	23.80	2.30	123.00	10.80	6.50	0.70
BBL	BBL-5	21A	9.80	1.72	3.62	1.48	46.21	2.89	341.21	18.26	12.35	0.56	382.44	10.32	24.75	2.96	109.26	11.38	5.89	0.61
BBL	BBL-5	21B	9.32	1.53	3.63	1.43	44.90	2.42	299.84	15.22	10.57	0.31	324.96	17.00	23.79	2.72	120.69	12.86	5.89	0.58
BBL	BBL-5	22	n. a.	n. a.	n. a.	n. a.	n. a.	n. a.	n. a.	n. a.	n. a.	n. a.	n. a.	n. a.	n. a.	n. a.	n. a.	n. a.	n. a.	n. a.
BBL	BBL-5	23	10.48	1.58	2.80	1.07	40.95	1.84	293.40	18.25	8.20	0.20	313.52	6.23	24.44	1.85	91.60	6.91	4.11	0.41
BBL	BBL-5	30	15.16	2.36	4.51	2.39	41.03	1.70	194.72	3.61	12.68	0.28	403.72	9.49	28.21	2.47	122.37	15.20	6.44	0.82
BBL	BBL-5	31	n. a.	n. a.	n. a.	n. a.	39.65	3.89	228.75	4.69	n. a.	n. a.	290.43	4.18	25.95	1.46	94.76	5.92	4.29	0.34
BBL	BBL-5	32	n. a.	n. a.	n. a.	n. a.	38.17	3.75	199.68	3.72	n. a.	n. a.	329.01	2.52	24.67	1.34	107.08	5.81	5.90	0.45
BBL	BBL-5	33	n. a.	n. a.	n. a.	n. a.	39.74	3.90	220.76	4.54	n. a.	n. a.	344.96	2.81	27.22	1.52	125.64	7.10	7.04	0.54
BBL	BBL-5	34	n. a.	n. a.	n. a.	n. a.	n. a.	n. a.	n. a.	n. a.	n. a.	n. a.	n. a.	n. a.	n. a.	n. a.	n. a.	n. a.	n. a.	n. a.
BBL	BBL-5	43	n. a.	n. a.	n. a.	n. a.	38.02	3.73	199.67	2.17	n. a.	n. a.	342.09	6.44	24.01	1.31	118.48	6.42	7.06	0.53
BBL	BBL-5	44	n. a.	n. a.	n. a.	n. a.	31.27	3.12	202.12	3.72	n. a.	n. a.	267.48	3.31	20.87	1.19	64.72	3.62	2.26	0.17
BBL	BBL-5	46	n. a.	n. a.	n. a.	n. a.	37.00	3.62	219.52	6.26	n. a.	n. a.	352.83	6.06	23.39	1.29	109.60	5.92	6.64	0.51
BBL	BBL-5	47	n. a.	n. a.	n. a.	n. a.	35.99	3.54	204.01	2.64	n. a.	n. a.	262.59	1.59	20.36	1.08	62.32	3.29	1.91	0.15
BBL	BBL-5	49	n. a.	n. a.	n. a.	n. a.	35.52	3.56	218.75	3.89	n. a.	n. a.	416.17	2.70	22.65	1.20	117.96	6.27	6.91	0.52
BBL	BBL-5	3	n. a.	n. a.	n. a.	n. a.	n. a.	n. a.	n. a.	n. a.	n. a.	n. a.	n. a.	n. a.	n. a.	n. a.	n. a.	n. a.	n. a.	n. a.
BBL	BBL-5	4	n. a.	n. a.	n. a.	n. a.	n. a.	n. a.	n. a.	n. a.	n. a.	n. a.	n. a.	n. a.	n. a.	n. a.	n. a.	n. a.	n. a.	n. a.
BBL	BBL-5	5	n. a.	n. a.	n. a.	n. a.	n. a.	n. a.	n. a.	n. a.	n. a.	n. a.	n. a.	n. a.	n. a.	n. a.	n. a.	n. a.	n. a.	n. a.
BBL	BBL-5	6	10.75	1.58	2.72	1.11	42.99	1.68	271.14	16.02	7.97	0.23	317.15	4.86	24.30	1.94	100.95	7.69	4.42	0.43
BBL	BBL-5	7	11.40	1.70	2.40	1.40	50.80	2.20	375.60	19.50	4.30	0.20	362.90	7.70	27.80	2.60	92.00	8.50	3.10	0.50
BORG	BORG-1	2	n. a.	n. a.	n. a.	n. a.	n. a.	n. a.	n. a.	n. a.	n. a.	n. a.	n. a.	n. a.	n. a.	n. a.	n. a.	n. a.	n. a.	n. a.
BORG	BORG-1	3	n. a.	n. a.	n. a.	n. a.	n. a.	n. a.	n. a.	n. a.	n. a.	n. a.	n. a.	n. a.	n. a.	n. a.	n. a.	n. a.	n. a.	n. a.
BORG	BORG-1	8	n. a.	n. a.	n. a.	n. a.	n. a.	n. a.	n. a.	n. a.	n. a.	n. a.	n. a.	n. a.	n. a.	n. a.	n. a.	n. a.	n. a.	n. a.
BORG	BORG-1	9	n. a.	n. a.	n. a.	n. a.	n. a.	n. a.	n. a.	n. a.	n. a.	n. a.	n. a.	n. a.	n. a.	n. a.	n. a.	n. a.	n. a.	n. a.
BORG	BORG-1	10	n. a.	n. a.	n. a.	n. a.	n. a.	n. a.	n. a.	n. a.	n. a.	n. a.	n. a.	n. a.	n. a.	n. a.	n. a.	n. a.	n. a.	n. a.
BORG	BORG-1	11	6.80	1.00	4.70	1.80	33.40	1.60	261.20	13.80	9.30	0.40	715.70	14.50	14.90	1.20	61.40	4.60	2.50	0.30
BORG	BORG-1	12	6.32	1.06	5.74	2.26	39.20	2.03	278.90	14.47	9.01	0.21	760.81	16.13	17.40	1.40	70.48	5.55	2.64	0.27
BORG	BORG-1	13	n. a.	n. a.	n. a.	n. a.	n. a.	n. a.	n. a.	n. a.	n. a.	n. a.	n. a.	n. a.	n. a.	n. a.	n. a.	n. a.	n. a.	n. a.
BORG	BORG-1	14	6.99	1.01	2.68	1.07	35.18	1.52	268.70	17.48	4.97	0.10	487.96	7.94	12.97	1.00	53.39	4.05	2.07	0.20
BORG	BORG-1	15	8.00	1.10	6.70	2.50	30.20	1.70	254.30	14.90	9.40	0.40	604.20	10.80	12.70	1.00	61.80	5.10	2.60	0.30
BORG	BORG-1	18	n. a.	n. a.	n. a.	n. a.	n. a.	n. a.	n. a.	n. a.	n. a.	n. a.	n. a.	n. a.	n. a.	n. a.	n. a.	n. a.	n. a.	n. a.
BORG	BORG-1	19	7.40	1.10	3.80	1.40	35.40	1.60	253.20	14.50	5.10	0.10	533.60	10.70	14.40	1.10	51.90	4.00	2.30	0.20
BORG	BORG-1	20	7.20	1.00	4.90	1.80	30.70	1.40	243.80	15.60	8.10	0.20	640.40	9.40	12.40	1.10	53.10	4.00	2.50	0.30
BORG	BORG-1	21	5.47	0.78	2.65	1.03	32.09	1.93	252.48	14.38	4.99	0.18	508.41	8.71	12.43	0.94	51.19	3.86	2.07	0.20
BORG	BORG-1	22	6.58	0.98	4.19	1.65	37.54	1.49	271.57	15.43	6.22	0.12	467.93	8.20	14.11	1.15	69.47	5.35	3.06	0.31
BORG	BORG-1	23	n. a.	n. a.	n. a.	n. a.	n. a.	n. a.	n. a.	n. a.	n. a.	n. a.	n. a.	n. a.	n. a.	n. a.	n. a.	n. a.	n. a.	n. a.
BORG	BORG-1	24	8.35	1.20	4.17	1.91	38.55	1.94	307.75	15.89	8.15	0.29	664.56	16.76	17.22	1.53	72.45	6.09	3.73	0.37
BORG	BORG-1	25	11.42	1.82	4.20	1.74	53.92	2.40	429.98	21.93	8.13	0.30	694.76	26.80	18.44	1.39	83.54	6.63	3.61	0.41
BORG	BORG-1	31	n. a.	n. a.	n. a.	n. a.	29.21	2.87	205.34	3.61	n. a.	n. a.	547.31	4.19	13.07	0.69	62.69	3.34	2.75	0.21
BORG	BORG-1	35	n. a.	n. a.	n. a.	n. a.	28.21	2.79	219.27	22.59	n. a.	n. a.	611.22	5.18	13.35	0.72	56.64	3.04	2.56	0.19
BORG	BORG-1	37	n. a.	n. a.	n. a.	n. a.	26.64	2.63	218.22	22.45	n. a.	n. a.	598.25	3.57	13.56	0.74	56.93	3.22	2.59	0.20
BORG	BORG-1	38	n. a.	n. a.	n. a.	n. a.	27.59	2.72	187.59	3.70	n. a.	n. a.	575.75	7.31	13.09	0.73	50.41	2.83	2.24	0.17
BORG	BORG-1	40	n. a.	n. a.	n. a.	n. a.	29.65	2.92	211.16	2.77	n. a.	n. a.	502.63	8.38	13.32	0.78	58.11	3.36	3.11	0.24
BORG	BORG-1	42	n. a.	n. a.	n. a.	n. a.	29.85	2.93	215.68	2.53	n. a.	n. a.	509.03	5.63	13.08	0.71	55.86	2.99	2.98	0.23
BORG	BORG-1	43	n. a.	n. a.	n. a.	n. a.	26.47	2.59	184.92	1.91	n. a.	n. a.	547.75	5.25	12.92	0.68	52.17	2.79	2.15	0.16
BORG	BORG-1	44	n. a.	n. a.	n. a.	n. a.	32.20	3.16	229.18	3.52	n. a.	n. a.	594.34	16.29	15.35	0.84	56.69	3.03	2.07	0.18
BORG	BORG-1	45	n. a.	n. a.	n. a.	n. a.	27.96	2.91	223.05	2.49	n. a.	n. a.	504.38	7.09	13.53	0.94	57.99	3.22	3.24	0.24
BORG	MM-L17-BORG-1	1	n. a.	n. a.	n. a.	n. a.	31.42	3.13	109.89	1.38	n. a.	n. a.	450.79	4.11	12.14	0.79	50.46	2.71	2.09	0.17
BORG	MM-L17-BORG-1	2	n. a.	n. a.	n. a.	n. a.	27.94	2.75	126.47	13.02	n. a.	n. a.	586.52	4.33	1.24	0.08	1.57	0.10	0.07	0.01
BPPC	MM-L17-BPPC-4	13	n. a.	n. a.	n. a.	n. a.	34.39	3.39	229.41	23.55	n. a.	n. a.	423.71	4.50	15.66	0.83	59.40	3.21	1.83	0.14
BPPC	MM-L17-BPPC-4	14	n. a.	n. a.	n. a.	n. a.	32.89	3.37	253.51	26.24	n. a.	n. a.	463.15	8.03	15.42	1.07	57.27	3.56	1.93	0.16
BPPC	MM-L17-BPPC-4	15	n. a.	n. a.	n. a.	n. a.	33.15	3.26	222.63	23.28	n. a.	n. a.	463.74	10.34	15.33	0.88	55.68	3.23	1.59	0.14
BPPC	MM-L17-BPPC-4	2	n. a.	n. a.	n. a.	n. a.	33.52	3.31	218.58	3.91	n. a.	n. a.	459.54	12.21	16.27	0.90	54.42	3.14	1.47	0.12
BPPC	MM-L17-BPPC-4	3	n. a.	n. a.	n. a.	n. a.	n. a.	n. a.	n. a.	n. a.	n. a.	n. a.	n. a.	n. a.	n. a.	n. a.	n. a.	n. a.	n. a.	n. a.
BPPC	MM-L17-BPPC-4	4	n. a.	n. a.	n. a.	n. a.	n. a.	n. a.	n. a.	n. a.	n. a.	n. a.	n. a.	n. a.	n. a.	n. a.	n. a.	n. a.	n. a.	n. a.
BPPC	MM-L17-BPPC-4	5	n. a.	n. a.	n. a.	n. a.	38.80	3.85	226.76	5.22	n. a.	n. a.	522.41	4.84	17.80	0.99	57.90	3.12	1.42	0.12
BRM	BRM-1	14	n. a.	n. a.	n. a.	n. a.	n. a.	n. a.	n. a.	n. a.	n. a.	n. a.	n. a.	n. a.	n. a.	n. a.	n. a.	n. a.	n. a.	n. a.
BRM	BRM-1	16	n. a.	n. a.	n. a.	n. a.	n. a.	n. a.	n. a.	n. a.	n. a.	n. a.	n. a.	n. a.	n. a.	n. a.	n. a.	n. a.	n. a.	n. a.
BRM	BRM-1	17	7.67	1.12	4.55	1.70	31.70	1.86	292.84	14.68	10.11	0.45	1720.19	42.82	16.75	1.40	119.26	9.18	5.83	0.58
BRM	BRM-1	18	n. a.	n. a.	n. a.	n. a.	n. a.	n. a.	n. a.	n. a.	n. a.	n. a.	n. a.	n. a.	n. a.	n. a.	n. a.	n. a.	n. a.	n. a.
BRM	BRM-1	19	5.35	1.22	4.17	1.71	28.18	1.56	224.81	14.42	15.29	0.63	1362.67	48.84	13.41	1.10	115.34	9.59	5.74	0.58
BRM	BRM-1	22	9.18	1.53	3.01	1.26	30.87	1.63	345.69	22.65	8.95	0.28	2135.02	55.18	14.21	1.11	126.25	9.36	4.86	0.53
BRM	BRM-1	23	n. a.	n. a.	n. a.	n. a.	n. a.	n. a.	n. a.	n. a.	n. a.	n. a.	n. a.	n. a.	n. a.	n. a.	n. a.	n. a.	n. a.	n. a.
BRM	BRM-1	24	18.60	2.80	8.00	3.00	30.00	1.60	350.00	17.50	23.00	0.40	734.40	18.10	20.70	1.80	175.50	13.10	12.80	1.30
BRM	BRM-1	25	8.80	1.30	3.00	1.20	32.00	1.50	250.50	17.60	7.60	0.20	1595.40	28.70	13.10	1.00	104.50	7.80	4.30	0.50
BRM	BRM-1	30	23.43	2.30	n. a.	n. a.	177.33	3.86	1160.96	8.58	12.80	0.71	90.89	4.92	4.28	0.33				
BRM	BRM-1	34	n. a.	n. a.	n. a.	n. a.	24.94	2.48	196.18	5.11	n. a.	n. a.	1364.11	19.99	13.85	0.77	106.60	5.77	5.06	0.39
BRM	BRM-1	35	n. a.	n. a.	n. a.	n. a.	n. a.	n. a.	n. a.	n. a.	n. a.	n. a.	n. a.	n. a.	n. a.	n. a.	n. a.	n. a.	n. a.	n. a.
BRM	BRM-1	36	n. a.	n. a.	n. a.	n. a.	n. a.	n. a.	n. a.	n. a.	n. a.	n. a.	n. a.	n. a.	n. a.	n. a.	n. a.	n. a.	n. a.	n. a.
BRM	BRM-1	39	n. a.	n. a.	n. a.	n. a.	n. a.	n. a.	n. a.	n. a.	n. a.	n. a.	n. a.	n. a.	n. a.	n. a.	n. a.	n. a.	n. a.	n. a.
BRM	BRM-1	40	n. a.	n. a.	n. a.	n. a.	n. a.	n. a.	n. a.	n. a.	n. a.	n. a.	n. a.	n. a.	n. a.	n. a.	n. a.	n. a.	n. a.	n. a.
BRM	BRM-1	41	n. a.	n. a.	n. a.	n. a.	25.39	2.49	200.59	3.63	n. a.	n. a.	1173.64	10.26	12.18	0.65	80.92	4.37	4.24	0.33

Table S1. (continued)

Cinder Cone	Tephra Sample	Inclusion	Li	s. e.	B	s. e.	Sc	s. e.	V	s. e.	Rb	s. e.	Sr	s. e.	Y	s. e.	Zr	s. e.	Nb	s. e.
BRM	BRM-1	2	n. a.	n. a.	n. a.	n. a.	n. a.	n. a.	n. a.	n. a.	n. a.	n. a.	n. a.	n. a.	n. a.	n. a.	n. a.	n. a.	n. a.	n. a.
BRM	BRM-1	3	n. a.	n. a.	n. a.	n. a.	n. a.	n. a.	n. a.	n. a.	n. a.	n. a.	n. a.	n. a.	n. a.	n. a.	n. a.	n. a.	n. a.	n. a.
BRM	BRM-1	5	12.03	2.27	1.75	0.76	31.16	1.98	308.97	17.08	16.28	0.71	2099.54	100.51	16.31	1.36	145.21	11.93	10.46	1.19
BRM	BRM-1	6	8.00	1.50	1.50	1.50	22.80	1.70	195.00	12.10	5.70	0.40	878.30	41.20	8.30	0.80	61.60	5.20	2.60	0.40
BRM	BRM-1	7	12.50	1.90	2.50	1.10	33.90	2.20	358.20	25.00	16.00	0.80	2243.10	149.90	19.80	1.70	162.80	16.00	11.20	1.30
BRM	BRM-1	8	8.50	1.70	6.40	3.10	40.40	2.00	318.20	17.50	16.60	0.70	2086.80	65.50	17.40	1.50	133.70	10.50	9.50	0.90
BRM	MM-L17-BRM-2	1	n. a.	n. a.	n. a.	n. a.	26.33	2.61	211.45	4.06	n. a.	n. a.	1251.65	7.90	11.92	0.69	80.05	4.47	3.64	0.28
BRM	MM-L17-BRM-2	10	n. a.	n. a.	n. a.	n. a.	n. a.	n. a.	n. a.	n. a.	n. a.	n. a.	n. a.	n. a.	n. a.	n. a.	n. a.	n. a.	n. a.	n. a.
BRM	MM-L17-BRM-2	13	n. a.	n. a.	n. a.	n. a.	n. a.	n. a.	n. a.	n. a.	n. a.	n. a.	n. a.	n. a.	n. a.	n. a.	n. a.	n. a.	n. a.	n. a.
BRM	MM-L17-BRM-2	14	n. a.	n. a.	n. a.	n. a.	n. a.	n. a.	n. a.	n. a.	n. a.	n. a.	n. a.	n. a.	n. a.	n. a.	n. a.	n. a.	n. a.	n. a.
BRM	MM-L17-BRM-2	16	n. a.	n. a.	n. a.	n. a.	n. a.	n. a.	n. a.	n. a.	n. a.	n. a.	n. a.	n. a.	n. a.	n. a.	n. a.	n. a.	n. a.	n. a.
BRM	MM-L17-BRM-2	17	n. a.	n. a.	n. a.	n. a.	n. a.	n. a.	n. a.	n. a.	n. a.	n. a.	n. a.	n. a.	n. a.	n. a.	n. a.	n. a.	n. a.	n. a.
BRM	MM-L17-BRM-2	18	n. a.	n. a.	n. a.	n. a.	24.65	2.42	198.88	3.57	n. a.	n. a.	1250.41	13.12	14.23	0.77	96.59	5.23	5.57	0.43
BRM	MM-L17-BRM-2	24	n. a.	n. a.	n. a.	n. a.	26.88	2.63	188.35	2.08	n. a.	n. a.	1158.90	10.80	12.77	0.69	98.46	5.20	7.72	0.59
BRM	MM-L17-BRM-2	25	n. a.	n. a.	n. a.	n. a.	22.87	2.26	194.46	2.37	n. a.	n. a.	1431.35	19.97	12.21	0.67	108.07	5.92	8.13	0.61
BRM	MM-L17-BRM-2	26	n. a.	n. a.	n. a.	n. a.	22.09	2.21	184.30	1.92	n. a.	n. a.	1557.82	11.04	12.63	0.69	113.05	6.23	8.56	0.65
BRM	MM-L17-BRM-2	29	n. a.	n. a.	n. a.	n. a.	23.80	2.47	202.09	4.08	n. a.	n. a.	1304.03	14.65	13.11	0.71	91.04	4.89	4.45	0.35
BRM	MM-L17-BRM-2	31	n. a.	n. a.	n. a.	n. a.	26.75	2.66	199.29	2.55	n. a.	n. a.	1181.07	13.93	11.43	0.64	74.60	4.34	4.28	0.34
BRM	MM-L17-BRM-2	32	n. a.	n. a.	n. a.	n. a.	25.44	2.51	217.09	3.75	n. a.	n. a.	1227.00	13.73	11.42	0.68	80.79	4.39	4.42	0.37
BRM	MM-L17-BRM-2	8	n. a.	n. a.	n. a.	n. a.	22.93	2.25	171.43	3.35	n. a.	n. a.	1545.02	27.30	12.90	0.70	140.42	7.58	3.74	0.29
BRVB	MM-L17-BRVB-2	10	n. a.	n. a.	n. a.	n. a.	29.22	2.86	251.91	25.91	n. a.	n. a.	462.66	4.65	18.96	1.01	105.84	5.63	8.26	0.63
BRVB	MM-L17-BRVB-2	2	n. a.	n. a.	n. a.	n. a.	36.51	3.60	276.10	28.40	n. a.	n. a.	383.35	4.74	24.99	1.39	88.91	5.14	3.63	0.28
BRVB	MM-L17-BRVB-2	4	n. a.	n. a.	n. a.	n. a.	31.48	3.10	242.94	2.49	n. a.	n. a.	514.31	3.64	21.59	1.17	120.06	6.39	9.11	0.69
BRVB	MM-L17-BRVB-2	6	n. a.	n. a.	n. a.	n. a.	28.83	2.85	292.18	30.48	n. a.	n. a.	591.87	9.60	22.98	1.27	129.06	7.72	10.02	0.80
BRVB	MM-L17-BRVB-2	7	n. a.	n. a.	n. a.	n. a.	35.37	3.51	308.06	31.68	n. a.	n. a.	573.24	5.59	24.19	1.33	134.90	7.47	9.38	0.77

Table S1. (continued)

Cinder Cone	Tephra Sample	Inclusion	Ba	s. e.	La	s. e.	Ce	s. e.	Nd	s. e.	Sm	s. e.	Dy	s. e.	Yb	s. e.	Pb	s. e.
BAS-44	BAS-44-2	1	n. a.	n. a.	n. a.	n. a.	n. a.	n. a.	n. a.	n. a.	n. a.	n. a.	n. a.	n. a.	n. a.	n. a.	n. a.	n. a.
BAS-44	BAS-44-2	10	n. a.	n. a.	n. a.	n. a.	n. a.	n. a.	n. a.	n. a.	n. a.	n. a.	n. a.	n. a.	n. a.	n. a.	n. a.	n. a.
BAS-44	BAS-44-2	2	114.47	1.91	7.88	0.20	21.08	0.57	12.95	0.30	2.95	0.08	3.40	0.15	2.40	0.15	2.26	0.09
BAS-44	BAS-44-2	4	115.24	2.68	7.78	0.19	21.20	0.67	13.08	0.35	3.43	0.15	3.48	0.19	2.33	0.19	1.91	0.03
BAS-44	BAS-44-2	5	136.41	2.37	8.35	0.18	21.93	0.43	13.35	0.30	3.31	0.10	3.78	0.15	2.22	0.15	2.08	0.07
BAS-44	BAS-44-2	6	n. a.	n. a.	n. a.	n. a.	n. a.	n. a.	n. a.	n. a.	n. a.	n. a.	n. a.	n. a.	n. a.	n. a.	n. a.	n. a.
BAS-44	BAS-44-2	7a	144.20	3.42	8.27	0.15	20.99	0.55	12.79	0.46	3.30	0.19	3.64	0.14	2.29	0.14	2.72	0.08
BAS-44	BAS-44-2	7b	n. a.	n. a.	n. a.	n. a.	n. a.	n. a.	n. a.	n. a.	n. a.	n. a.	n. a.	n. a.	n. a.	n. a.	n. a.	n. a.
BBL	BBL-5	11	314.82	5.14	10.96	0.22	27.95	0.62	15.67	0.34	3.75	0.21	3.02	0.21	2.43	0.13	3.83	0.19
BBL	BBL-5	14	336.73	8.65	12.36	0.36	30.10	0.78	18.58	0.65	4.26	0.11	5.93	0.45	3.30	0.33	3.69	0.14
BBL	BBL-5	15	336.91	10.41	12.67	0.30	30.82	0.60	19.53	0.51	4.44	0.14	5.61	0.23	3.60	0.41	3.68	0.21
BBL	BBL-5	17	190.65	5.51	6.69	0.32	19.13	0.86	15.50	0.54	3.94	0.39	5.96	0.54	3.59	0.24	2.00	0.19
BBL	BBL-5	18	329.36	6.39	11.94	0.46	30.87	0.82	18.74	0.59	5.30	0.54	4.91	0.25	2.62	0.22	3.70	0.24
BBL	BBL-5	19	125.48	2.45	5.40	0.08	13.61	0.43	9.59	0.45	2.72	0.21	3.84	0.15	1.96	0.17	1.33	0.07
BBL	BBL-5	20	350.00	13.10	12.30	0.40	32.20	0.70	18.80	0.90	3.90	0.30	3.90	0.40	2.40	0.30	5.40	0.40
BBL	BBL-5	21A	310.63	11.30	12.49	0.53	28.92	0.57	17.12	0.69	3.67	0.33	4.96	0.39	3.25	0.22	4.29	0.26
BBL	BBL-5	21B	288.08	12.92	10.70	0.58	30.59	0.67	15.29	2.02	4.51	0.24	5.37	0.38	2.86	0.40	3.72	0.24
BBL	BBL-5	22	n. a.	n. a.	n. a.	n. a.	n. a.	n. a.	n. a.	n. a.	n. a.	n. a.	n. a.	n. a.	n. a.	n. a.	n. a.	n. a.
BBL	BBL-5	23	219.71	4.36	8.19	0.18	23.36	1.33	14.08	0.42	3.25	0.12	3.50	0.30	2.03	0.24	2.96	0.11
BBL	BBL-5	30	339.03	9.11	13.42	0.56	35.16	0.81	16.76	1.51	5.03	0.40	6.59	0.45	3.94	0.14	4.63	0.31
BBL	BBL-5	31	218.93	4.20	8.35	0.17	20.99	0.56	13.53	0.53	2.95	0.40	4.43	0.16	3.02	0.16	3.12	0.07
BBL	BBL-5	32	273.97	5.73	10.28	0.20	25.13	0.44	15.82	0.40	4.08	0.11	4.48	0.11	2.82	0.11	3.71	0.11
BBL	BBL-5	33	349.28	5.99	12.75	0.24	30.31	0.60	18.55	0.44	4.33	0.13	4.65	0.20	2.92	0.20	4.61	0.10
BBL	BBL-5	34	n. a.	n. a.	n. a.	n. a.	n. a.	n. a.	n. a.	n. a.	n. a.	n. a.	n. a.	n. a.	n. a.	n. a.	n. a.	n. a.
BBL	BBL-5	43	341.20	5.68	12.04	0.27	29.94	0.49	17.97	0.25	4.24	0.13	4.70	0.14	2.93	0.14	4.90	0.14
BBL	BBL-5	44	118.57	2.60	4.79	0.10	12.55	0.28	8.27	0.35	2.37	0.14	3.62	0.14	2.07	0.14	1.41	0.11
BBL	BBL-5	46	292.18	5.40	10.96	0.18	26.31	0.43	15.72	0.23	4.08	0.09	3.94	0.13	2.99	0.13	4.11	0.09
BBL	BBL-5	47	108.41	2.62	4.04	0.08	10.83	0.35	8.58	0.21	2.26	0.09	3.53	0.15	2.33	0.15	1.46	0.06
BBL	BBL-5	49	329.50	6.60	12.14	0.24	30.06	0.51	17.28	0.53	4.18	0.08	4.20	0.13	2.59	0.13	4.59	0.16
BBL	BBL-5	3	n. a.	n. a.	n. a.	n. a.	n. a.	n. a.	n. a.	n. a.	n. a.	n. a.	n. a.	n. a.	n. a.	n. a.	n. a.	n. a.
BBL	BBL-5	4	n. a.	n. a.	n. a.	n. a.	n. a.	n. a.	n. a.	n. a.	n. a.	n. a.	n. a.	n. a.	n. a.	n. a.	n. a.	n. a.
BBL	BBL-5	5	n. a.	n. a.	n. a.	n. a.	n. a.	n. a.	n. a.	n. a.	n. a.	n. a.	n. a.	n. a.	n. a.	n. a.	n. a.	n. a.
BBL	BBL-5	6	228.55	4.47	8.77	0.23	23.54	0.73	13.66	0.50	3.44	0.31	4.23	0.20	2.19	0.14	2.94	0.15
BBL	BBL-5	7	151.90	5.40	6.20	0.40	16.80	0.40	11.50	0.70	2.40	0.50	5.20	0.80	3.60	0.40	1.60	0.20
BORG	BORG-1	2	n. a.	n. a.	n. a.	n. a.	n. a.	n. a.	n. a.	n. a.	n. a.	n. a.	n. a.	n. a.	n. a.	n. a.	n. a.	n. a.
BORG	BORG-1	3	n. a.	n. a.	n. a.	n. a.	n. a.	n. a.	n. a.	n. a.	n. a.	n. a.	n. a.	n. a.	n. a.	n. a.	n. a.	n. a.
BORG	BORG-1	8	n. a.	n. a.	n. a.	n. a.	n. a.	n. a.	n. a.	n. a.	n. a.	n. a.	n. a.	n. a.	n. a.	n. a.	n. a.	n. a.
BORG	BORG-1	9	n. a.	n. a.	n. a.	n. a.	n. a.	n. a.	n. a.	n. a.	n. a.	n. a.	n. a.	n. a.	n. a.	n. a.	n. a.	n. a.
BORG	BORG-1	10	n. a.	n. a.	n. a.	n. a.	n. a.	n. a.	n. a.	n. a.	n. a.	n. a.	n. a.	n. a.	n. a.	n. a.	n. a.	n. a.
BORG	BORG-1	11	282.10	5.70	9.00	0.20	18.70	0.90	11.20	0.20	2.70	0.30	3.20	0.20	1.30	0.30	4.60	0.20
BORG	BORG-1	12	298.27	8.78	9.66	0.39	20.27	0.36	11.78	0.99	2.19	0.14	2.71	0.21	2.15	0.49	4.64	0.24
BORG	BORG-1	13	n. a.	n. a.	n. a.	n. a.	n. a.	n. a.	n. a.	n. a.	n. a.	n. a.	n. a.	n. a.	n. a.	n. a.	n. a.	n. a.
BORG	BORG-1	14	156.17	3.55	4.91	0.09	13.01	0.48	7.69	0.23	2.06	0.09	2.26	0.11	1.04	0.10	2.46	0.18
BORG	BORG-1	15	284.50	4.80	8.40	0.20	20.90	0.70	12.40	0.20	2.30	0.30	2.60	0.10	1.10	0.10	5.30	0.30
BORG	BORG-1	18	n. a.	n. a.	n. a.	n. a.	n. a.	n. a.	n. a.	n. a.	n. a.	n. a.	n. a.	n. a.	n. a.	n. a.	n. a.	n. a.
BORG	BORG-1	19	182.00	3.40	5.80	0.10	14.70	0.50	9.20	0.40	2.30	0.10	2.70	0.20	1.20	0.20	3.10	0.10
BORG	BORG-1	20	258.10	4.50	7.40	0.20	17.80	0.60	10.90	0.20	2.60	0.20	2.30	0.20	1.00	0.10	4.40	0.40
BORG	BORG-1	21	164.02	4.81	5.02	0.21	12.82	0.31	8.20	0.21	1.83	0.11	2.37	0.14	1.06	0.09	2.15	0.08
BORG	BORG-1	22	154.61	3.02	6.46	0.09	16.57	0.58	10.37	0.29	2.51	0.31	2.90	0.18	1.77	0.07	2.52	0.11
BORG	BORG-1	23	n. a.	n. a.	n. a.	n. a.	n. a.	n. a.	n. a.	n. a.	n. a.	n. a.	n. a.	n. a.	n. a.	n. a.	n. a.	n. a.
BORG	BORG-1	24	257.07	7.84	7.81	0.27	18.88	0.25	12.13	0.48	2.26	0.60	2.94	0.26	1.81	0.29	3.28	0.15
BORG	BORG-1	25	222.97	7.81	8.86	0.24	21.08	0.40	12.88	1.40	4.14	0.29	3.37	0.23	2.28	0.23	3.42	0.22
BORG	BORG-1	31	281.14	5.56	8.09	0.13	18.35	0.34	11.52	0.17	2.61	0.11	2.68	0.07	1.48	0.07	4.69	0.12
BORG	BORG-1	35	265.06	4.65	8.08	0.15	18.04	0.29	11.47	0.30	2.68	0.10	2.60	0.11	1.43	0.11	4.59	0.11
BORG	BORG-1	37	267.76	4.36	8.09	0.15	18.57	0.32	11.43	0.20	2.84	0.12	2.51	0.07	1.53	0.07	4.42	0.23
BORG	BORG-1	38	240.11	3.86	7.32	0.13	16.26	0.29	10.49	0.19	2.55	0.08	2.50	0.07	1.39	0.07	4.18	0.03
BORG	BORG-1	40	190.20	3.75	6.06	0.11	14.30	0.37	8.67	0.43	2.54	0.09	2.56	0.08	1.36	0.08	2.86	0.06
BORG	BORG-1	42	176.15	3.49	5.57	0.08	13.55	0.20	8.70	0.13	2.32	0.05	2.53	0.06	1.37	0.06	2.58	0.05
BORG	BORG-1	43	230.41	3.76	6.51	0.12	15.05	0.22	9.45	0.23	2.51	0.05	2.43	0.05	1.34	0.05	4.30	0.10
BORG	BORG-1	44	231.19	4.45	6.64	0.15	15.04	0.24	10.40	0.15	2.66	0.18	2.89	0.12	1.58	0.12	4.08	0.11
BORG	BORG-1	45	198.88	5.31	6.62	0.14	16.02	0.32	10.73	0.34	2.96	0.15	2.44	0.08	1.49	0.08	3.01	0.09
BORG	MM-L17-BORG-1	1	137.56	2.43	4.68	0.17	11.39	0.27	7.74	0.31	2.02	0.12	2.53	0.11	1.64	0.11	2.12	0.05
BORG	MM-L17-BORG-1	2	20.34	0.44	0.41	0.01	0.91	0.03	0.43	0.04	0.11	0.00	0.12	0.01	0.29	0.01	0.26	0.02
BPPC	MM-L17-BPPC-4	13	122.10	1.88	5.75	0.09	14.26	0.21	8.95	0.16	2.27	0.11	3.01	0.09	1.75	0.09	2.16	0.10
BPPC	MM-L17-BPPC-4	14	122.75	2.07	5.76	0.13	14.98	0.31	9.16	0.16	2.63	0.18	3.29	0.12	1.93	0.12	2.13	0.06
BPPC	MM-L17-BPPC-4	15	112.46	2.22	5.48	0.12	13.80	0.34	8.37	0.14	2.37	0.14	3.07	0.11	2.04	0.11	1.77	0.36
BPPC	MM-L17-BPPC-4	2	81.10	1.64	4.89	0.10	12.91	0.24	8.18	0.28	2.27	0.15	2.93	0.13	1.60	0.13	1.69	0.03
BPPC	MM-L17-BPPC-4	3	n. a.	n. a.	n. a.	n. a.	n. a.	n. a.	n. a.	n. a.	n. a.	n. a.	n. a.	n. a.	n. a.	n. a.	n. a.	n. a.
BPPC	MM-L17-BPPC-4	4	n. a.	n. a.	n. a.	n. a.	n. a.	n. a.	n. a.	n. a.	n. a.	n. a.	n. a.	n. a.	n. a.	n. a.	n. a.	n. a.
BPPC	MM-L17-BPPC-4	5	78.58	1.77	5.26	0.11	14.38	0.31	9.07	0.38	2.24	0.07	2.99	0.10	2.05	0.10	2.11	0.10
BRM	BRM-1	14	n. a.	n. a.	n. a.	n. a.	n. a.	n. a.	n. a.	n. a.	n. a.	n. a.	n. a.	n. a.	n. a.	n. a.	n. a.	n. a.
BRM	BRM-1	16	n. a.	n. a.	n. a.	n. a.	n. a.	n. a.	n. a.	n. a.	n. a.	n. a.	n. a.	n. a.	n. a.	n. a.	n. a.	n. a.
BRM	BRM-1	17	310.15	9.89	20.12	0.33	45.64	0.90	20.04	1.19	3.07	0.17	3.03	0.46	1.13	0.08	5.57	0.23
BRM	BRM-1	18	n. a.	n. a.	n. a.	n. a.	n. a.	n. a.	n. a.	n. a.	n. a.	n. a.	n. a.	n. a.	n. a.	n. a.	n. a.	n. a.
BRM	BRM-1	19	311.71	12.26	17.44	0.70	39.10	1.49	20.73	0.91	4.33	0.30	2.80	0.32	1.05	0.23	4.86	0.51
BRM	BRM-1	22	313.30	12.85	21.78	0.69	48.73	2.54	23.72	1.69	4.17	0.35	2.32	0.16	0.35	0.48	5.53	0.37
BRM	BRM-1	23	n. a.	n. a.	n. a.	n. a.	n. a.	n. a.	n. a.	n. a.	n. a.	n. a.	n. a.	n. a.	n. a.	n. a.	n. a.	n. a.
BRM	BRM-1	24	574.00	15.50	29.70	0.50	65.70	1.00	34.70	0.90	6.00	0.30	4.30	0.20	2.30	0.10	9.80	0.40
BRM	BRM-1	25	219.20	6.50	16.30	0.20	40.70	1.20	19.70	0.60	4.90	0.50	2.70	0.30	0.70	0.10	4.40	0.30
BRM	BRM-1	30	264.99	4.46	15.28	0.27	34.94	0.56	18.57	0.32	3.33	0.09	2.38	0.05	1.33	0.04	5.16	0.09
BRM	BRM-1	34	297.93	5.12	17.72	0.34	40.28	0.82	21.46	0.46	3.49	0.10	2.80	0.11	1.61	0.10	6.34	0.14
BRM	BRM-1	35	n. a.	n. a.	n. a.	n. a.	n. a.	n. a.	n. a.	n. a.	n. a.	n. a.	n. a.	n. a.	n. a.	n. a.	n. a.	n. a.
BRM	BRM-1	36	n. a.	n. a.	n. a.	n. a.	n. a.	n. a.	n. a.	n. a.	n. a.	n. a.	n. a.	n. a.	n. a.	n. a.	n. a.	n. a.
BRM	BRM-1	39	n. a.	n. a.	n. a.	n. a.	n. a.	n. a.	n. a.	n. a.	n. a.	n. a.	n. a.	n. a.	n. a.	n. a.	n. a.	n. a.
BRM	BRM-1	40	n. a.	n. a.	n. a.	n. a.	n. a.	n. a.	n. a.	n. a.	n. a.	n. a.	n. a.	n. a.	n. a.	n. a.	n. a.	n. a.
BRM	BRM-1	41	170.26	2.77	13.03	0.23	30.61	0.57	16.53	0.29	3.21	0.18	2.42	0.08	1.32	0.06	3.49	0.06

Table S1. (continued)

Cinder Cone	Tephra Sample	Inclusion n	Ba	s. e.	La	s. e.	Ce	s. e.	Nd	s. e.	Sm	s. e.	Dy	s. e.	Yb	s. e.	Pb	s. e.
BRM	BRM-1	2	n. a.	n. a.	n. a.	n. a.	n. a.	n. a.	n. a.	n. a.	n. a.	n. a.	n. a.	n. a.	n. a.	n. a.	n. a.	n. a.
BRM	BRM-1	3	n. a.	n. a.	n. a.	n. a.	n. a.	n. a.	n. a.	n. a.	n. a.	n. a.	n. a.	n. a.	n. a.	n. a.	n. a.	n. a.
BRM	BRM-1	5	360.84	19.99	25.10	1.50	60.16	3.06	26.43	1.09	4.71	0.78	2.55	0.37	1.62	0.14	6.56	0.44
BRM	BRM-1	6	125.20	6.80	10.70	0.70	26.30	1.20	12.30	0.70	3.00	0.30	1.40	0.20	1.40	0.40	3.10	0.30
BRM	BRM-1	7	419.30	22.10	28.30	1.90	63.70	3.80	27.10	1.50	4.20	0.30	4.10	0.20	1.90	0.20	7.20	0.40
BRM	BRM-1	8	369.20	12.80	25.80	0.80	59.40	1.60	30.00	1.60	4.70	0.50	2.40	0.10	1.30	0.10	6.80	0.40
BRM	MM-L17-BRM-2	1	160.83	2.92	12.94	0.27	31.34	0.52	16.18	0.35	3.05	0.12	2.49	0.06	1.49	0.06	4.21	0.25
BRM	MM-L17-BRM-2	10	n. a.	n. a.	n. a.	n. a.	n. a.	n. a.	n. a.	n. a.	n. a.	n. a.	n. a.	n. a.	n. a.	n. a.	n. a.	n. a.
BRM	MM-L17-BRM-2	13	n. a.	n. a.	n. a.	n. a.	n. a.	n. a.	n. a.	n. a.	n. a.	n. a.	n. a.	n. a.	n. a.	n. a.	n. a.	n. a.
BRM	MM-L17-BRM-2	14	n. a.	n. a.	n. a.	n. a.	n. a.	n. a.	n. a.	n. a.	n. a.	n. a.	n. a.	n. a.	n. a.	n. a.	n. a.	n. a.
BRM	MM-L17-BRM-2	16	n. a.	n. a.	n. a.	n. a.	n. a.	n. a.	n. a.	n. a.	n. a.	n. a.	n. a.	n. a.	n. a.	n. a.	n. a.	n. a.
BRM	MM-L17-BRM-2	17	n. a.	n. a.	n. a.	n. a.	n. a.	n. a.	n. a.	n. a.	n. a.	n. a.	n. a.	n. a.	n. a.	n. a.	n. a.	n. a.
BRM	MM-L17-BRM-2	18	322.58	6.31	17.46	0.37	40.23	0.74	19.75	0.41	3.68	0.13	2.79	0.09	1.75	0.09	6.49	0.09
BRM	MM-L17-BRM-2	24	318.52	5.40	15.97	0.30	38.01	0.61	19.10	0.40	3.61	0.11	2.50	0.06	1.27	0.06	5.05	0.11
BRM	MM-L17-BRM-2	25	273.93	4.76	18.32	0.33	43.89	0.76	22.08	0.33	3.86	0.08	2.60	0.06	1.23	0.06	5.26	0.10
BRM	MM-L17-BRM-2	26	277.89	4.75	19.35	0.31	46.07	0.74	22.91	0.36	4.00	0.07	2.55	0.11	1.19	0.11	5.21	0.09
BRM	MM-L17-BRM-2	29	233.81	4.47	15.25	0.25	36.31	0.69	18.24	0.36	3.59	0.15	2.41	0.06	1.38	0.06	4.95	0.08
BRM	MM-L17-BRM-2	31	153.97	2.45	11.82	0.37	29.67	0.43	15.22	0.28	3.01	0.18	2.23	0.11	1.24	0.11	3.26	0.06
BRM	MM-L17-BRM-2	32	166.20	3.06	12.96	0.21	31.78	0.49	15.94	0.37	3.12	0.07	2.07	0.10	1.38	0.10	3.45	0.08
BRM	MM-L17-BRM-2	8	283.10	7.45	24.04	0.65	60.37	1.62	30.86	0.88	5.35	0.13	2.84	0.10	1.11	0.10	5.58	0.15
BRVB	MM-L17-BRVB-2	10	388.98	6.94	14.39	0.23	34.60	0.59	19.71	0.49	4.14	0.16	3.86	0.07	2.14	0.07	4.30	0.09
BRVB	MM-L17-BRVB-2	2	218.90	3.84	7.32	0.12	17.71	0.29	12.38	0.25	3.51	0.13	4.46	0.10	2.89	0.10	3.45	0.08
BRVB	MM-L17-BRVB-2	4	402.25	6.27	15.27	0.24	36.57	0.53	21.80	0.44	4.73	0.22	4.19	0.09	2.18	0.09	3.86	0.14
BRVB	MM-L17-BRVB-2	6	498.79	13.85	18.00	0.46	43.73	1.52	25.86	0.63	6.17	0.45	4.31	0.21	2.21	0.21	4.64	0.17
BRVB	MM-L17-BRVB-2	7	467.12	8.76	18.24	0.48	40.15	0.61	25.14	0.67	5.00	0.29	4.81	0.21	2.73	0.21	5.64	0.29

n. a. = not analyzed

n.r. = not recorded

*many bubble diameters reported here have been measured on intersected inclusions and are a minimum value

Table S2. Corrected major element and trace element melt inclusion data. Major element compositions and trace element concentrations have been corrected for post entrapment crystallization and Fe-Mg reequlibration. Major elements, S, Cl, and H2O reported in wt. %. Trace elements reported in ppm.

Cinder Cone	Tephra Sample	Melt Inclusion	SiO$_2$	TiO$_2$	Al$_2$O$_3$	FeO^T	MnO	MgO
BAS-44	BAS-44-2	1	49.16	0.83	17.39	8.94	0.12	8.97
BAS-44	BAS-44-2	10	48.79	0.97	17.53	9.08	0.14	9.68
BAS-44	BAS-44-2	2	49.06	0.97	16.96	9.09	0.13	9.57
BAS-44	BAS-44-2	4	49.19	0.98	17.23	9.02	0.12	9.33
BAS-44	BAS-44-2	5	48.84	0.97	17.49	8.98	0.12	9.01
BAS-44	BAS-44-2	6	48.11	0.98	17.72	9.04	0.13	9.44
BAS-44	BAS-44-2	7a	50.31	0.92	16.54	8.95	0.16	9.22
BAS-44	BAS-44-2	7b	49.76	1.00	16.92	8.99	0.15	8.89
BBL	BBL-5	11	49.52	1.22	17.32	10.15	0.20	7.51
BBL	BBL-5	14	49.98	1.72	16.25	10.10	0.20	7.82
BBL	BBL-5	15	50.58	1.54	16.17	10.18	0.21	7.84
BBL	BBL-5	17	48.02	0.97	16.07	10.51	0.09	11.43
BBL	BBL-5	18	50.02	1.50	16.15	10.22	0.20	8.07
BBL	BBL-5	19	48.55	1.03	17.23	10.36	0.09	10.00
BBL	BBL-5	20	49.34	1.30	17.61	10.10	0.20	7.93
BBL	BBL-5	21A	49.24	1.36	16.68	10.26	0.10	9.08
BBL	BBL-5	21B	48.87	1.44	16.94	10.26	0.19	9.00
BBL	BBL-5	22	48.57	1.10	16.47	10.39	0.09	10.02
BBL	BBL-5	23	49.20	1.27	16.83	10.22	0.10	8.59
BBL	BBL-5	3	48.32	0.98	16.48	10.41	0.09	10.63
BBL	BBL-5	30	49.57	1.12	16.11	10.38	0.19	9.61
BBL	BBL-5	31	50.72	1.16	15.43	10.20	0.19	8.51
BBL	BBL-5	32	50.43	1.24	15.99	10.18	0.19	8.36
BBL	BBL-5	33	50.22	1.27	16.38	10.23	0.20	8.06
BBL	BBL-5	34	51.74	1.05	14.70	10.18	0.19	8.39
BBL	BBL-5	4	48.29	1.04	16.38	10.40	0.09	10.54
BBL	BBL-5	43	50.24	1.18	16.43	10.25	0.20	8.42
BBL	BBL-5	44	48.36	0.92	17.37	10.35	0.09	9.79
BBL	BBL-5	46	49.32	1.14	16.62	10.31	0.19	9.12
BBL	BBL-5	47	48.04	0.80	16.87	10.40	0.09	10.68
BBL	BBL-5	49	49.60	1.17	17.66	10.06	0.20	7.55
BBL	BBL-5	5	50.69	1.48	17.03	10.02	0.21	6.82
BBL	BBL-5	6	49.61	1.36	15.88	10.19	0.19	8.54
BBL	BBL-5	7	47.99	0.99	16.23	10.45	0.09	11.00
BORG	BORG-1	10	49.71	0.86	19.18	8.85	0.13	7.03
BORG	BORG-1	11	48.86	0.78	19.45	8.97	0.09	7.70
BORG	BORG-1	12	49.78	0.82	19.55	8.91	0.13	7.40
BORG	BORG-1	13	48.45	0.09	22.04	8.97	0.17	7.69
BORG	BORG-1	14	48.52	0.69	18.28	9.24	0.10	9.53
BORG	BORG-1	15	50.42	0.98	19.41	8.61	0.13	6.16
BORG	BORG-1	18	48.10	0.08	22.81	8.69	0.15	6.35
BORG	BORG-1	19	48.14	0.83	19.94	9.01	0.12	7.95
BORG	BORG-1	2	48.97	0.79	20.81	8.75	0.14	6.66
BORG	BORG-1	20	48.68	0.91	19.30	9.13	0.12	8.22
BORG	BORG-1	21	48.22	0.74	19.67	9.11	0.09	8.49
BORG	BORG-1	22	47.74	0.82	17.68	9.33	0.10	10.24
BORG	BORG-1	23	48.82	0.85	20.51	8.73	0.12	6.55
BORG	BORG-1	24	49.35	0.83	19.78	8.87	0.13	7.18
BORG	BORG-1	25	48.57	0.72	18.19	9.22	0.11	9.40
BORG	BORG-1	3	48.77	0.89	20.40	8.86	0.12	6.84
BORG	BORG-1	31	50.94	1.00	18.89	8.88	0.16	7.34

Table S2. (continued)

Cinder Cone	Tephra Sample	Melt Inclusion	SiO_2	TiO_2	Al_2O_3	FeO^T	MnO	MgO
BORG	BORG-1	35	51.37	0.82	18.24	8.96	0.13	7.09
BORG	BORG-1	37	50.92	0.85	18.90	8.79	0.14	6.66
BORG	BORG-1	38	50.69	0.90	18.49	8.96	0.14	7.49
BORG	BORG-1	40	50.58	0.88	19.27	8.82	0.14	6.87
BORG	BORG-1	42	50.17	0.82	18.32	9.04	0.13	8.01
BORG	BORG-1	43	50.94	0.89	19.00	8.78	0.15	7.20
BORG	BORG-1	44	51.25	0.84	18.69	8.76	0.14	6.62
BORG	BORG-1	45	50.47	0.99	19.48	8.60	0.16	6.56
BORG	BORG-1	8	48.24	0.73	20.96	8.94	0.15	7.14
BORG	BORG-1	9	48.08	0.79	17.66	9.28	0.08	9.97
BORG	MM-L17-BORG-1	1	49.90	0.67	18.12	9.03	0.13	8.13
BORG	MM-L17-BORG-1	2	48.46	0.04	20.87	8.91	0.17	8.12
BPPC	MM-L17-BPPC-4	13	51.31	0.79	17.49	7.58	0.14	8.43
BPPC	MM-L17-BPPC-4	14	51.34	0.79	17.74	7.57	0.14	8.26
BPPC	MM-L17-BPPC-4	15	51.95	0.74	17.03	7.56	0.14	8.33
BPPC	MM-L17-BPPC-4	2	50.84	0.77	17.44	7.57	0.12	8.33
BPPC	MM-L17-BPPC-4	3	52.66	0.86	17.72	7.22	0.15	6.13
BPPC	MM-L17-BPPC-4	4	50.90	0.83	17.49	7.63	0.10	8.65
BPPC	MM-L17-BPPC-4	5	51.22	0.76	17.16	7.54	0.14	8.52
BRM	BRM-1	14	49.25	0.98	18.66	7.49	0.07	7.72
BRM	BRM-1	16	50.37	0.99	17.91	7.54	0.07	7.94
BRM	BRM-1	17	50.47	0.93	18.02	7.54	0.08	7.96
BRM	BRM-1	18	48.85	1.09	18.61	7.59	0.09	8.17
BRM	BRM-1	19	50.94	1.01	19.26	7.51	0.09	7.15
BRM	BRM-1	2	49.87	0.92	17.86	7.57	0.06	8.30
BRM	BRM-1	22	49.99	0.96	18.12	7.49	0.08	7.48
BRM	BRM-1	23	50.25	1.20	19.23	7.22	0.10	5.63
BRM	BRM-1	24	56.73	1.96	14.31	7.19	0.09	5.55
BRM	BRM-1	25	48.96	0.99	18.87	7.49	0.08	7.63
BRM	BRM-1	3	50.22	0.96	18.57	7.47	0.07	7.39
BRM	BRM-1	30	52.59	0.82	17.80	7.65	0.10	7.27
BRM	BRM-1	34	49.57	0.94	18.80	7.50	0.08	7.21
BRM	BRM-1	35	49.56	0.93	18.33	7.61	0.07	8.08
BRM	BRM-1	36	50.63	0.96	17.68	7.48	0.05	7.90
BRM	BRM-1	39	51.40	0.89	17.15	7.71	0.08	8.39
BRM	BRM-1	40	50.03	0.97	18.75	7.46	0.07	7.31
BRM	BRM-1	41	50.56	0.83	18.15	7.52	0.08	7.48
BRM	BRM-1	5	49.17	1.08	18.35	7.60	0.06	8.04
BRM	BRM-1	6	49.23	0.99	19.40	7.45	0.07	7.23
BRM	BRM-1	7	49.97	1.11	18.93	7.42	0.10	6.60
BRM	BRM-1	8	49.37	1.09	18.69	7.56	0.06	8.15
BRM	MM-L17-BRM-2	1	48.96	0.76	18.46	7.54	0.06	8.64
BRM	MM-L17-BRM-2	10	49.23	1.14	19.36	7.36	0.08	6.83
BRM	MM-L17-BRM-2	13	48.82	1.04	18.70	7.51	0.08	7.80
BRM	MM-L17-BRM-2	14	49.46	0.79	18.61	7.50	0.07	7.65
BRM	MM-L17-BRM-2	16	49.56	0.80	18.22	7.63	0.08	8.45
BRM	MM-L17-BRM-2	17	48.96	0.78	18.85	7.47	0.08	7.93
BRM	MM-L17-BRM-2	18	49.99	0.86	18.62	7.52	0.08	8.10
BRM	MM-L17-BRM-2	24	50.01	0.98	19.25	7.33	0.10	6.51
BRM	MM-L17-BRM-2	25	49.14	1.02	19.44	7.41	0.08	7.26
BRM	MM-L17-BRM-2	26	48.65	0.97	19.34	7.48	0.07	8.03

Table S2. (continued)

Cinder Cone	Tephra Sample	Melt Inclusion	SiO$_2$	TiO$_2$	Al$_2$O$_3$	FeO^T	MnO	MgO
BRM	MM-L17-BRM-2	29	49.37	0.78	18.37	7.60	0.06	8.70
BRM	MM-L17-BRM-2	31	49.20	0.77	18.18	7.40	0.07	9.36
BRM	MM-L17-BRM-2	32	48.91	0.83	19.25	7.53	0.08	7.61
BRM	MM-L17-BRM-2	8	47.67	1.05	19.07	7.52	0.08	8.11
BRVB	MM-L17-BRVB-2	10	50.18	1.40	17.54	9.18	0.15	7.28
BRVB	MM-L17-BRVB-2	2	50.56	1.17	16.94	9.29	0.13	8.49
BRVB	MM-L17-BRVB-2	4	48.47	1.45	18.57	9.02	0.15	7.09
BRVB	MM-L17-BRVB-2	6	49.22	0.95	18.21	9.20	0.14	7.89
BRVB	MM-L17-BRVB-2	7	48.51	1.48	18.42	9.13	0.15	7.06

Table S2. (continued)

Cinder Cone	Tephra Sample	Melt Inclusion	CaO	Na$_2$O	K$_2$O	P$_2$O$_5$	S	Cl	H$_2$O
BAS-44	BAS-44-2	1	11.45	2.60	0.25	0.14	0.12	0.03	0.77
BAS-44	BAS-44-2	10	10.40	2.76	0.39	0.18	0.03	0.04	n. a.
BAS-44	BAS-44-2	2	10.78	2.83	0.27	0.17	0.12	0.04	1.47
BAS-44	BAS-44-2	4	10.77	2.75	0.26	0.19	0.11	0.04	1.16
BAS-44	BAS-44-2	5	11.22	2.76	0.28	0.17	0.12	0.04	1.31
BAS-44	BAS-44-2	6	10.96	3.00	0.29	0.16	0.12	0.04	1.27
BAS-44	BAS-44-2	7a	10.57	2.70	0.33	0.16	0.10	0.04	n. a.
BAS-44	BAS-44-2	7b	10.71	2.89	0.36	0.17	0.10	0.04	n. a.
BBL	BBL-5	11	9.37	3.67	0.71	0.31	0.10	0.03	n. a.
BBL	BBL-5	14	8.38	4.44	0.81	0.30	0.10	0.03	n. a.
BBL	BBL-5	15	8.55	3.91	0.72	0.31	0.11	0.03	n. a.
BBL	BBL-5	17	9.66	2.90	0.26	0.09	0.08	0.02	n. a.
BBL	BBL-5	18	8.83	3.91	0.80	0.30	0.10	0.03	n. a.
BBL	BBL-5	19	9.27	3.00	0.28	0.19	0.08	0.02	n. a.
BBL	BBL-5	20	9.11	3.50	0.60	0.30	0.09	0.03	n. a.
BBL	BBL-5	21A	8.73	3.68	0.58	0.29	0.09	0.02	n. a.
BBL	BBL-5	21B	8.81	3.64	0.57	0.29	0.09	0.03	n. a.
BBL	BBL-5	22	10.16	2.84	0.27	0.09	0.08	0.02	n. a.
BBL	BBL-5	23	9.78	3.33	0.49	0.20	0.09	0.02	n. a.
BBL	BBL-5	3	9.80	2.85	0.27	0.18	0.08	0.01	n. a.
BBL	BBL-5	30	8.90	3.18	0.66	0.28	0.11	0.04	n. a.
BBL	BBL-5	31	9.61	3.40	0.58	0.19	0.12	0.04	1.10
BBL	BBL-5	32	9.33	3.43	0.57	0.29	0.13	0.03	1.16
BBL	BBL-5	33	9.02	3.63	0.69	0.29	0.14	0.04	1.19
BBL	BBL-5	34	9.83	3.25	0.48	0.19	0.12	0.03	1.15
BBL	BBL-5	4	10.06	2.86	0.26	0.09	0.07	0.01	n. a.
BBL	BBL-5	43	8.66	3.54	0.79	0.30	0.11	0.04	0.94
BBL	BBL-5	44	10.16	2.59	0.28	0.09	0.09	0.02	0.94
BBL	BBL-5	46	9.31	3.13	0.57	0.28	0.09	0.03	1.09
BBL	BBL-5	47	10.08	2.68	0.27	0.09	0.08	0.02	0.92
BBL	BBL-5	49	9.37	3.32	0.78	0.29	0.10	0.03	0.62
BBL	BBL-5	5	8.67	3.91	0.85	0.32	0.11	0.04	n. a.
BBL	BBL-5	6	9.88	3.68	0.48	0.19	0.10	0.02	n. a.
BBL	BBL-5	7	10.19	2.79	0.18	0.09	0.08	0.01	n. a.
BORG	BORG-1	10	9.25	4.15	0.60	0.10	0.09	0.04	n. a.
BORG	BORG-1	11	8.92	4.43	0.55	0.10	0.13	0.04	n. a.
BORG	BORG-1	12	8.42	4.18	0.55	0.11	0.11	0.04	n. a.
BORG	BORG-1	13	11.10	1.41	0.06	0.00	0.01	0.00	n. a.
BORG	BORG-1	14	10.05	2.92	0.47	0.06	0.09	0.05	n. a.
BORG	BORG-1	15	8.89	4.51	0.59	0.12	0.13	0.05	n. a.
BORG	BORG-1	18	12.31	1.46	0.05	0.00	0.00	0.00	n. a.
BORG	BORG-1	19	9.14	4.10	0.55	0.07	0.10	0.05	n. a.
BORG	BORG-1	2	9.44	3.68	0.53	0.08	0.10	0.05	n. a.
BORG	BORG-1	20	8.56	4.30	0.52	0.10	0.12	0.04	n. a.
BORG	BORG-1	21	9.69	3.27	0.52	0.07	0.09	0.04	n. a.
BORG	BORG-1	22	10.33	2.98	0.52	0.10	0.10	0.06	n. a.
BORG	BORG-1	23	9.61	4.02	0.57	0.09	0.09	0.05	n. a.
BORG	BORG-1	24	9.28	3.79	0.56	0.10	0.09	0.04	n. a.
BORG	BORG-1	25	10.42	2.71	0.46	0.06	0.10	0.05	n. a.
BORG	BORG-1	3	9.40	3.97	0.53	0.08	0.09	0.05	n. a.
BORG	BORG-1	31	8.80	2.96	0.66	0.16	0.15	0.06	2.56

Table S2. (continued)

Cinder Cone	Tephra Sample	Melt Inclusion	CaO	Na$_2$O	K$_2$O	P$_2$O$_5$	S	Cl	H$_2$O
BORG	BORG-1	35	9.00	3.44	0.56	0.16	0.17	0.05	n. a.
BORG	BORG-1	37	9.24	3.58	0.54	0.17	0.17	0.05	3.12
BORG	BORG-1	38	9.12	3.29	0.55	0.14	0.18	0.05	3.12
BORG	BORG-1	40	9.44	3.08	0.61	0.12	0.12	0.06	2.81
BORG	BORG-1	42	9.63	3.07	0.55	0.10	0.11	0.05	2.96
BORG	BORG-1	43	8.89	3.29	0.53	0.11	0.15	0.06	1.74
BORG	BORG-1	44	9.39	3.44	0.57	0.10	0.14	0.05	2.95
BORG	BORG-1	45	9.32	3.53	0.59	0.13	0.12	0.05	0.85
BORG	BORG-1	8	8.97	4.05	0.53	0.13	0.12	0.04	n. a.
BORG	BORG-1	9	10.29	3.06	0.54	0.10	0.11	0.06	n. a.
BORG	MM-L17-BORG-1	1	10.82	2.43	0.50	0.08	0.13	0.05	2.57
BORG	MM-L17-BORG-1	2	12.33	1.05	0.05	0.00	0.00	0.00	1.11
BPPC	MM-L17-BPPC-4	13	11.08	2.58	0.36	0.09	0.10	0.04	2.26
BPPC	MM-L17-BPPC-4	14	11.04	2.53	0.35	0.08	0.11	0.04	2.24
BPPC	MM-L17-BPPC-4	15	11.22	2.48	0.32	0.09	0.10	0.04	1.91
BPPC	MM-L17-BPPC-4	2	11.84	2.56	0.25	0.11	0.11	0.06	n. a.
BPPC	MM-L17-BPPC-4	3	11.87	2.75	0.35	0.13	0.10	0.05	2.69
BPPC	MM-L17-BPPC-4	4	11.04	2.73	0.33	0.13	0.11	0.06	2.41
BPPC	MM-L17-BPPC-4	5	11.55	2.57	0.26	0.09	0.11	0.07	1.37
BRM	BRM-1	14	10.30	4.05	0.70	0.24	0.22	0.31	n. a.
BRM	BRM-1	16	9.58	4.31	0.65	0.20	0.16	0.25	n. a.
BRM	BRM-1	17	9.37	4.46	0.61	0.18	0.16	0.24	n. a.
BRM	BRM-1	18	9.84	4.10	0.94	0.30	0.19	0.25	n. a.
BRM	BRM-1	19	8.32	4.25	0.87	0.22	0.14	0.24	n. a.
BRM	BRM-1	2	10.39	3.86	0.56	0.20	0.16	0.24	n. a.
BRM	BRM-1	22	9.77	4.90	0.58	0.20	0.17	0.26	n. a.
BRM	BRM-1	23	9.97	4.78	0.90	0.31	0.18	0.23	n. a.
BRM	BRM-1	24	7.16	4.34	1.80	0.48	0.05	0.35	n. a.
BRM	BRM-1	25	10.07	4.57	0.60	0.23	0.19	0.30	n. a.
BRM	BRM-1	3	9.64	4.41	0.66	0.20	0.16	0.25	n. a.
BRM	BRM-1	30	8.61	3.85	0.65	0.20	0.18	0.29	3.05
BRM	BRM-1	34	10.14	4.21	0.75	0.24	0.25	0.31	2.21
BRM	BRM-1	35	9.77	4.09	0.74	0.26	0.24	0.32	n. a.
BRM	BRM-1	36	10.03	3.68	0.73	0.27	0.23	0.36	0.52
BRM	BRM-1	39	9.17	3.72	0.74	0.25	0.20	0.29	3.54
BRM	BRM-1	40	10.16	3.64	0.77	0.29	0.25	0.31	n. a.
BRM	BRM-1	41	10.81	3.32	0.55	0.19	0.22	0.30	1.99
BRM	BRM-1	5	10.00	4.26	0.72	0.26	0.18	0.28	n. a.
BRM	BRM-1	6	10.38	4.03	0.57	0.23	0.16	0.25	n. a.
BRM	BRM-1	7	10.20	4.26	0.75	0.26	0.16	0.26	n. a.
BRM	BRM-1	8	8.90	4.56	0.88	0.24	0.20	0.29	n. a.
BRM	MM-L17-BRM-2	1	10.60	3.74	0.52	0.17	0.21	0.34	0.90
BRM	MM-L17-BRM-2	10	10.18	4.22	0.81	0.29	0.27	0.24	0.83
BRM	MM-L17-BRM-2	13	10.09	4.28	0.77	0.34	0.26	0.31	n. a.
BRM	MM-L17-BRM-2	14	10.60	4.01	0.64	0.19	0.22	0.27	0.83
BRM	MM-L17-BRM-2	16	10.38	3.63	0.54	0.23	0.22	0.24	2.24
BRM	MM-L17-BRM-2	17	11.21	3.54	0.52	0.19	0.18	0.26	0.65
BRM	MM-L17-BRM-2	18	9.70	3.77	0.75	0.21	0.16	0.23	0.64
BRM	MM-L17-BRM-2	24	10.39	3.80	0.90	0.26	0.23	0.23	1.23
BRM	MM-L17-BRM-2	25	10.27	3.82	0.77	0.26	0.23	0.31	0.63
BRM	MM-L17-BRM-2	26	9.99	3.87	0.79	0.26	0.24	0.32	0.79

Table S2. (continued)

Cinder Cone	Tephra Sample	Melt Inclusion	CaO	Na$_2$O	K$_2$O	P$_2$O$_5$	S	Cl	H$_2$O
BRM	MM-L17-BRM-2	29	10.23	3.64	0.65	0.16	0.19	0.24	0.30
BRM	MM-L17-BRM-2	31	10.55	3.34	0.51	0.16	0.21	0.25	0.31
BRM	MM-L17-BRM-2	32	11.09	3.53	0.54	0.19	0.20	0.25	0.78
BRM	MM-L17-BRM-2	8	10.67	4.09	0.71	0.31	0.36	0.35	4.06
BRVB	MM-L17-BRVB-2	10	9.70	2.99	1.05	0.29	0.17	0.05	2.03
BRVB	MM-L17-BRVB-2	2	10.02	2.52	0.56	0.15	0.16	0.02	0.60
BRVB	MM-L17-BRVB-2	4	10.38	3.44	0.94	0.32	0.12	0.05	0.31
BRVB	MM-L17-BRVB-2	6	10.77	2.95	0.35	0.16	0.12	0.03	0.72
BRVB	MM-L17-BRVB-2	7	10.00	3.55	1.11	0.33	0.20	0.07	1.91

Table S2. (continued)

Cinder Cone	Tephra Sample	Melt Inclusion	% olivine	Fo Olivine	Li	B	Sc	V	Rb
BAS-44	BAS-44-2	1	3.4	87.1	n. a.	n. a.	n. a.	n. a.	n. a.
BAS-44	BAS-44-2	10	6.7	87.7	n. a.	n. a.	n. a.	n. a.	n. a.
BAS-44	BAS-44-2	2	6.3	87.5	n. a.	n. a.	28.34	183.72	n. a.
BAS-44	BAS-44-2	4	8.3	87.3	n. a.	n. a.	29.19	203.69	n. a.
BAS-44	BAS-44-2	5	4.4	87.1	n. a.	n. a.	35.75	204.07	n. a.
BAS-44	BAS-44-2	6	6.3	87.7	n. a.	n. a.	n. a.	n. a.	n. a.
BAS-44	BAS-44-2	7a	3.8	87.1	n. a.	n. a.	34.54	202.67	n. a.
BAS-44	BAS-44-2	7b	2.8	86.7	n. a.	n. a.	n. a.	n. a.	n. a.
BBL	BBL-5	11	1.6	82.4	10.70	3.65	35.22	209.24	11.53
BBL	BBL-5	14	2.9	82.8	8.16	2.93	41.24	248.06	12.88
BBL	BBL-5	15	1.1	82.5	10.39	4.92	50.92	308.91	12.83
BBL	BBL-5	17	16.6	87.9	8.21	1.92	46.98	288.38	5.71
BBL	BBL-5	18	3.0	83.2	9.91	2.96	43.41	223.63	11.81
BBL	BBL-5	19	10.6	86.3	6.55	0.33	28.14	184.52	4.05
BBL	BBL-5	20	3.4	83.3	11.32	4.26	46.24	291.86	12.96
BBL	BBL-5	21A	6.6	85.0	9.18	3.39	43.28	319.54	11.57
BBL	BBL-5	21B	6.7	85.0	8.71	3.39	41.94	280.08	9.87
BBL	BBL-5	22	12.7	86.4	n. a.	n. a.	n. a.	n. a.	n. a.
BBL	BBL-5	23	5.6	84.4	9.88	2.64	38.63	276.78	7.73
BBL	BBL-5	3	15.6	87.1	n. a.	n. a.	n. a.	n. a.	n. a.
BBL	BBL-5	30	9.7	85.5	13.78	4.10	37.29	317.54	11.53
BBL	BBL-5	31	5.8	83.9	n. a.	n. a.	37.31	215.27	n. a.
BBL	BBL-5	32	7.8	83.7	n. a.	n. a.	35.35	184.93	n. a.
BBL	BBL-5	33	5.1	83.1	n. a.	n. a.	37.85	210.22	n. a.
BBL	BBL-5	34	6.3	83.6	n. a.	n. a.	n. a.	n. a.	n. a.
BBL	BBL-5	4	18.2	87.1	n. a.	n. a.	n. a.	n. a.	n. a.
BBL	BBL-5	43	3.7	83.6	n. a.	n. a.	36.61	192.25	n. a.
BBL	BBL-5	44	9.6	86.2	n. a.	n. a.	28.37	182.78	n. a.
BBL	BBL-5	46	8.0	85.0	n. a.	n. a.	34.04	201.95	n. a.
BBL	BBL-5	47	11.9	87.2	n. a.	n. a.	31.79	180.21	n. a.
BBL	BBL-5	49	3.6	82.6	n. a.	n. a.	34.28	211.12	n. a.
BBL	BBL-5	5	1.8	80.4	n. a.	n. a.	n. a.	n. a.	n. a.
BBL	BBL-5	6	6.8	84.4	10.06	2.54	40.21	253.63	7.45
BBL	BBL-5	7	14.3	87.6	9.85	2.07	43.90	324.55	3.72
BORG	BORG-1	10	5.7	83.9	n. a.	n. a.	n. a.	n. a.	n. a.
BORG	BORG-1	11	14.0	85.2	5.92	4.09	29.09	227.48	8.10
BORG	BORG-1	12	4.7	84.2	6.02	5.48	37.39	265.97	8.59
BORG	BORG-1	13	2.9	85.2	n. a.	n. a.	n. a.	n. a.	n. a.
BORG	BORG-1	14	10.6	87.6	6.26	2.40	31.51	240.67	4.45
BORG	BORG-1	15	0.4	81.9	8.06	6.75	30.41	256.08	9.47
BORG	BORG-1	18	5.4	83.3	n. a.	n. a.	n. a.	n. a.	n. a.
BORG	BORG-1	19	7.3	85.7	6.75	3.47	32.31	231.13	4.66
BORG	BORG-1	2	0.5	83.4	n. a.	n. a.	n. a.	n. a.	n. a.
BORG	BORG-1	20	9.6	85.7	6.55	4.46	27.93	221.80	7.37
BORG	BORG-1	21	9.9	86.4	4.94	2.40	28.99	228.13	4.51
BORG	BORG-1	22	14.2	88.6	5.69	3.63	32.50	235.15	5.38
BORG	BORG-1	23	0.5	83.3	n. a.	n. a.	n. a.	n. a.	n. a.
BORG	BORG-1	24	1.6	84.2	8.19	4.09	37.79	301.66	7.99
BORG	BORG-1	25	9.2	87.5	10.38	3.82	48.98	390.65	7.39
BORG	BORG-1	3	4.2	83.7	n. a.	n. a.	n. a.	n. a.	n. a.
BORG	BORG-1	31	0.1	84.0	n. a.	n. a.	29.17	205.02	n. a.

Table S2. (continued)

Cinder Cone	Tephra Sample	Melt Inclusion	% olivine	Fo Olivine	Li	B	Sc	V	Rb
BORG	BORG-1	35	3.9	83.3	n. a.	n. a.	27.06	210.36	n. a.
BORG	BORG-1	37	0.2	82.7	n. a.	n. a.	26.53	217.39	n. a.
BORG	BORG-1	38	1.6	84.2	n. a.	n. a.	27.13	184.46	n. a.
BORG	BORG-1	40	1.5	83.3	n. a.	n. a.	29.20	207.99	n. a.
BORG	BORG-1	42	2.8	85.3	n. a.	n. a.	28.88	208.67	n. a.
BORG	BORG-1	43	0.4	84.0	n. a.	n. a.	26.52	185.27	n. a.
BORG	BORG-1	44	7.1	82.7	n. a.	n. a.	30.06	213.98	n. a.
BORG	BORG-1	45	0.3	83.2	n. a.	n. a.	27.91	222.67	n. a.
BORG	BORG-1	8	1.5	84.2	n. a.	n. a.	n. a.	n. a.	n. a.
BORG	BORG-1	9	16.0	88.3	n. a.	n. a.	n. a.	n. a.	n. a.
BORG	MM-L17-BORG-1	1	5.0	85.8	n. a.	n. a.	29.73	103.97	n. a.
BORG	MM-L17-BORG-1	2	0.5	86.4	n. a.	n. a.	27.40	124.03	n. a.
BPPC	MM-L17-BPPC-4	13	0.7	87.5	n. a.	n. a.	34.20	229.41	n. a.
BPPC	MM-L17-BPPC-4	14	3.1	87.2	n. a.	n. a.	31.87	253.51	n. a.
BPPC	MM-L17-BPPC-4	15	2.1	87.3	n. a.	n. a.	32.41	222.63	n. a.
BPPC	MM-L17-BPPC-4	2	5.5	87.6	n. a.	n. a.	31.71	218.58	n. a.
BPPC	MM-L17-BPPC-4	3	3.5	87.3	n. a.	n. a.	n. a.	n. a.	n. a.
BPPC	MM-L17-BPPC-4	4	4.8	87.8	n. a.	n. a.	n. a.	n. a.	n. a.
BPPC	MM-L17-BPPC-4	5	6.8	87.9	n. a.	n. a.	36.28	226.76	n. a.
BRM	BRM-1	14	9.9	88.4	n. a.	n. a.	n. a.	n. a.	n. a.
BRM	BRM-1	16	9.2	88.3	n. a.	n. a.	n. a.	n. a.	n. a.
BRM	BRM-1	17	7.6	88.3	7.09	4.20	29.31	270.76	9.35
BRM	BRM-1	18	8.5	88.9	n. a.	n. a.	n. a.	n. a.	n. a.
BRM	BRM-1	19	5.8	86.6	5.06	3.94	26.65	212.64	14.46
BRM	BRM-1	2	13.7	89.0	n. a.	n. a.	n. a.	n. a.	n. a.
BRM	BRM-1	22	9.7	87.9	8.33	2.73	28.02	313.76	8.12
BRM	BRM-1	23	1.5	84.7	n. a.	n. a.	n. a.	n. a.	n. a.
BRM	BRM-1	24	4.0	86.7	17.87	7.69	28.83	336.35	22.10
BRM	BRM-1	25	7.4	88.4	8.07	2.75	29.35	229.72	6.97
BRM	BRM-1	3	8.7	87.6	n. a.	n. a.	n. a.	n. a.	n. a.
BRM	BRM-1	30	6.6	86.2	n.d.	n.d.	21.88	165.62	0.00
BRM	BRM-1	34	8.4	87.5	n.d.	n.d.	22.92	180.24	0.00
BRM	BRM-1	35	10.4	88.6	n. a.	n. a.	n. a.	n. a.	n. a.
BRM	BRM-1	36	12.0	88.4	n. a.	n. a.	n. a.	n. a.	n. a.
BRM	BRM-1	39	11.8	88.2	n. a.	n. a.	n. a.	n. a.	n. a.
BRM	BRM-1	40	9.7	87.6	n. a.	n. a.	n. a.	n. a.	n. a.
BRM	BRM-1	41	7.3	87.8	n.d.	n.d.	23.53	185.93	0.00
BRM	BRM-1	5	11.0	88.7	10.76	1.57	27.87	276.33	14.56
BRM	BRM-1	6	7.8	87.8	7.41	1.39	21.12	180.64	5.28
BRM	BRM-1	7	7.7	86.6	11.57	2.31	31.39	331.65	14.81
BRM	BRM-1	8	14.4	88.7	7.39	5.56	35.12	276.64	14.43
BRM	MM-L17-BRM-2	1	11.3	89.6	n. a.	n. a.	23.41	188.00	n. a.
BRM	MM-L17-BRM-2	10	9.8	87.3	n. a.	n. a.	n. a.	n. a.	n. a.
BRM	MM-L17-BRM-2	13	9.9	88.6	n. a.	n. a.	n. a.	n. a.	n. a.
BRM	MM-L17-BRM-2	14	9.6	88.4	n. a.	n. a.	n. a.	n. a.	n. a.
BRM	MM-L17-BRM-2	16	13.4	89.0	n. a.	n. a.	n. a.	n. a.	n. a.
BRM	MM-L17-BRM-2	17	10.5	89.0	n. a.	n. a.	n. a.	n. a.	n. a.
BRM	MM-L17-BRM-2	18	13.6	88.7	n. a.	n. a.	21.55	173.87	n. a.
BRM	MM-L17-BRM-2	24	3.4	86.6	n. a.	n. a.	25.95	181.85	n. a.
BRM	MM-L17-BRM-2	25	7.3	87.9	n. a.	n. a.	21.19	180.14	n. a.
BRM	MM-L17-BRM-2	26	10.4	88.9	n. a.	n. a.	19.82	165.40	n. a.

Table S2. (continued)

Cinder Cone	Tephra Sample	Melt Inclusion	% olivine	Fo Olivine	Li	B	Sc	V	Rb
BRM	MM-L17-BRM-2	29	12.5	89.5	n. a.	n. a.	20.95	177.86	n. a.
BRM	MM-L17-BRM-2	31	11.9	90.5	n. a.	n. a.	23.68	176.41	n. a.
BRM	MM-L17-BRM-2	32	8.6	88.4	n. a.	n. a.	23.23	198.23	n. a.
BRM	MM-L17-BRM-2	8	9.4	89.1	n. a.	n. a.	20.83	155.72	n. a.
BRVB	MM-L17-BRVB-2	10	0.2	83.5	n. a.	n. a.	29.17	251.43	n. a.
BRVB	MM-L17-BRVB-2	2	5.2	85.5	n. a.	n. a.	34.53	261.08	n. a.
BRVB	MM-L17-BRVB-2	4	4.0	84.1	n. a.	n. a.	30.25	233.51	n. a.
BRVB	MM-L17-BRVB-2	6	3.1	85.1	n. a.	n. a.	27.80	281.74	n. a.
BRVB	MM-L17-BRVB-2	7	2.7	83.7	n. a.	n. a.	34.42	299.84	n. a.

Table S2. (continued)

Cinder Cone	Tephra Sample	Melt Inclusion	Sr	Y	Zr	Nb	Sn	Ba	La
BAS-44	BAS-44-2	1	n. a.	n. a.	n. a.	n. a.	n. a.	n. a.	n. a.
BAS-44	BAS-44-2	10	n. a.	n. a.	n. a.	n. a.	n. a.	n. a.	n. a.
BAS-44	BAS-44-2	2	374.44	17.13	70.75	2.65	23.46	106.84	7.35
BAS-44	BAS-44-2	4	394.59	17.18	73.15	3.05	1.15	105.53	7.12
BAS-44	BAS-44-2	5	424.04	20.08	79.77	3.29	1.48	129.78	7.94
BAS-44	BAS-44-2	6	n. a.	n. a.	n. a.	n. a.	n. a.	n. a.	n. a.
BAS-44	BAS-44-2	7a	416.25	19.16	78.37	2.85	1.22	138.75	7.96
BAS-44	BAS-44-2	7b	n. a.	n. a.	n. a.	n. a.	n. a.	n. a.	n. a.
BBL	BBL-5	11	398.86	18.21	99.96	5.67	0.79	309.97	10.79
BBL	BBL-5	14	296.26	29.96	133.76	6.24	1.28	326.88	12.00
BBL	BBL-5	15	361.09	29.98	132.93	6.41	1.12	334.56	12.58
BBL	BBL-5	17	367.66	28.88	90.62	2.26	1.24	162.08	5.69
BBL	BBL-5	18	316.55	24.39	120.34	6.25	0.97	319.68	11.59
BBL	BBL-5	19	238.04	19.03	67.70	2.20	0.57	112.53	4.85
BBL	BBL-5	20	445.28	23.02	118.99	6.29	15.48	338.58	11.90
BBL	BBL-5	21A	358.14	23.18	102.32	5.52	1.11	290.90	11.70
BBL	BBL-5	21B	303.55	22.23	112.73	5.50	0.99	269.09	9.99
BBL	BBL-5	22	n. a.	n. a.	n. a.	n. a.	n. a.	n. a.	n. a.
BBL	BBL-5	23	295.77	23.05	86.41	3.88	0.89	207.27	7.73
BBL	BBL-5	3	n. a.	n. a.	n. a.	n. a.	n. a.	n. a.	n. a.
BBL	BBL-5	30	366.92	25.64	111.21	5.85	0.99	308.12	12.20
BBL	BBL-5	31	273.31	24.42	89.18	4.04	1.41	206.03	7.85
BBL	BBL-5	32	304.70	22.84	99.17	5.46	1.30	253.72	9.52
BBL	BBL-5	33	328.49	25.92	119.64	6.70	1.63	332.60	12.14
BBL	BBL-5	34	n. a.	n. a.	n. a.	n. a.	n. a.	n. a.	n. a.
BBL	BBL-5	4	n. a.	n. a.	n. a.	n. a.	n. a.	n. a.	n. a.
BBL	BBL-5	43	329.39	23.12	114.08	6.80	1.49	328.53	11.59
BBL	BBL-5	44	241.88	18.87	58.52	2.04	1.19	107.22	4.33
BBL	BBL-5	46	324.58	21.51	100.82	6.11	1.54	268.79	10.09
BBL	BBL-5	47	231.95	17.98	55.05	1.68	0.96	95.76	3.57
BBL	BBL-5	49	401.66	21.86	113.84	6.67	2.81	318.01	11.72
BBL	BBL-5	5	n. a.	n. a.	n. a.	n. a.	n. a.	n. a.	n. a.
BBL	BBL-5	6	296.67	22.73	94.43	4.14	0.81	213.79	8.21
BBL	BBL-5	7	313.57	24.02	79.50	2.68	0.69	131.25	5.36
BORG	BORG-1	10	n. a.	n. a.	n. a.	n. a.	n. a.	n. a.	n. a.
BORG	BORG-1	11	623.31	12.98	53.47	2.18	0.44	245.69	7.84
BORG	BORG-1	12	725.55	16.59	67.21	2.52	0.45	284.44	9.21
BORG	BORG-1	13	n. a.	n. a.	n. a.	n. a.	n. a.	n. a.	n. a.
BORG	BORG-1	14	437.05	11.62	47.82	1.86	0.43	139.88	4.40
BORG	BORG-1	15	608.44	12.79	62.23	2.62	0.60	286.50	8.46
BORG	BORG-1	18	n. a.	n. a.	n. a.	n. a.	n. a.	n. a.	n. a.
BORG	BORG-1	19	487.08	13.14	47.38	2.10	0.46	166.13	5.29
BORG	BORG-1	2	n. a.	n. a.	n. a.	n. a.	n. a.	n. a.	n. a.
BORG	BORG-1	20	582.60	11.28	48.31	2.27	0.64	234.81	6.73
BORG	BORG-1	21	459.39	11.23	46.25	1.87	0.40	148.20	4.53
BORG	BORG-1	22	405.17	12.22	60.15	2.65	0.48	133.87	5.59
BORG	BORG-1	23	n. a.	n. a.	n. a.	n. a.	n. a.	n. a.	n. a.
BORG	BORG-1	24	651.41	16.88	71.02	3.66	0.62	251.98	7.66
BORG	BORG-1	25	631.40	16.76	75.90	3.28	0.58	202.58	8.05
BORG	BORG-1	3	n. a.	n. a.	n. a.	n. a.	n. a.	n. a.	n. a.
BORG	BORG-1	31	546.46	13.05	62.59	2.74	0.89	280.70	8.08

Table S2. (continued)

Cinder Cone	Tephra Sample	Melt Inclusion	Sr	Y	Zr	Nb	Sn	Ba	La
BORG	BORG-1	35	586.38	12.80	54.34	2.45	1.04	254.29	7.76
BORG	BORG-1	37	595.94	13.51	56.71	2.58	1.09	266.74	8.06
BORG	BORG-1	38	566.15	12.87	49.57	2.20	1.05	236.11	7.19
BORG	BORG-1	40	495.10	13.12	57.24	3.07	1.16	187.35	5.97
BORG	BORG-1	42	492.49	12.65	54.04	2.88	0.99	170.43	5.39
BORG	BORG-1	43	548.80	12.95	52.27	2.15	1.07	230.85	6.53
BORG	BORG-1	44	554.92	14.33	52.93	1.94	1.02	215.86	6.20
BORG	BORG-1	45	503.53	13.51	57.89	3.23	0.96	198.54	6.60
BORG	BORG-1	8	n. a.	n. a.	n. a.	n. a.	n. a.	n. a.	n. a.
BORG	BORG-1	9	n. a.	n. a.	n. a.	n. a.	n. a.	n. a.	n. a.
BORG	MM-L17-BORG-1	1	426.52	11.48	47.75	1.98	0.92	130.15	4.43
BORG	MM-L17-BORG-1	2	575.24	1.22	1.54	0.07	0.32	19.94	0.40
BPPC	MM-L17-BPPC-4	13	421.32	15.57	59.07	1.82	0.99	121.41	5.72
BPPC	MM-L17-BPPC-4	14	448.67	14.94	55.48	1.87	1.01	118.92	5.58
BPPC	MM-L17-BPPC-4	15	453.50	14.99	54.45	1.56	0.80	109.98	5.35
BPPC	MM-L17-BPPC-4	2	434.70	15.39	51.47	1.39	0.99	76.72	4.63
BPPC	MM-L17-BPPC-4	3	n. a.	n. a.	n. a.	n. a.	n. a.	n. a.	n. a.
BPPC	MM-L17-BPPC-4	4	n. a.	n. a.	n. a.	n. a.	n. a.	n. a.	n. a.
BPPC	MM-L17-BPPC-4	5	488.46	16.65	54.14	1.32	1.06	73.47	4.92
BRM	BRM-1	14	n. a.	n. a.	n. a.	n. a.	n. a.	n. a.	n. a.
BRM	BRM-1	16	n. a.	n. a.	n. a.	n. a.	n. a.	n. a.	n. a.
BRM	BRM-1	17	1590.51	15.49	110.27	5.39	1.04	286.77	18.61
BRM	BRM-1	18	n. a.	n. a.	n. a.	n. a.	n. a.	n. a.	n. a.
BRM	BRM-1	19	1288.89	12.68	109.10	5.43	0.62	294.84	16.50
BRM	BRM-1	2	n. a.	n. a.	n. a.	n. a.	n. a.	n. a.	n. a.
BRM	BRM-1	22	1937.83	12.90	114.59	4.41	0.69	284.36	19.77
BRM	BRM-1	23	n. a.	n. a.	n. a.	n. a.	n. a.	n. a.	n. a.
BRM	BRM-1	24	705.76	19.89	168.65	12.30	1.25	551.61	28.54
BRM	BRM-1	25	1463.06	12.01	95.83	3.94	0.83	201.02	14.95
BRM	BRM-1	3	n. a.	n. a.	n. a.	n. a.	n. a.	n. a.	n. a.
BRM	BRM-1	30	1084.25	11.95	84.89	3.99	1.03	247.48	14.27
BRM	BRM-1	34	1253.28	12.73	97.94	4.65	1.32	273.72	16.28
BRM	BRM-1	35	n. a.	n. a.	n. a.	n. a.	n. a.	n. a.	n. a.
BRM	BRM-1	36	n. a.	n. a.	n. a.	n. a.	n. a.	n. a.	n. a.
BRM	BRM-1	39	n. a.	n. a.	n. a.	n. a.	n. a.	n. a.	n. a.
BRM	BRM-1	40	n. a.	n. a.	n. a.	n. a.	n. a.	n. a.	n. a.
BRM	BRM-1	41	1087.81	11.29	75.00	3.93	0.95	157.81	12.08
BRM	BRM-1	5	1877.70	14.59	129.87	9.36	0.91	322.72	22.45
BRM	BRM-1	6	813.61	7.69	57.06	2.41	0.46	115.98	9.91
BRM	BRM-1	7	2076.84	18.33	150.73	10.37	1.30	388.22	26.20
BRM	BRM-1	8	1814.25	15.13	116.24	8.26	1.22	320.98	22.43
BRM	MM-L17-BRM-2	1	1112.82	10.60	71.17	3.23	1.45	142.99	11.51
BRM	MM-L17-BRM-2	10	n. a.	n. a.	n. a.	n. a.	n. a.	n. a.	n. a.
BRM	MM-L17-BRM-2	13	n. a.	n. a.	n. a.	n. a.	n. a.	n. a.	n. a.
BRM	MM-L17-BRM-2	14	n. a.	n. a.	n. a.	n. a.	n. a.	n. a.	n. a.
BRM	MM-L17-BRM-2	16	n. a.	n. a.	n. a.	n. a.	n. a.	n. a.	n. a.
BRM	MM-L17-BRM-2	17	n. a.	n. a.	n. a.	n. a.	n. a.	n. a.	n. a.
BRM	MM-L17-BRM-2	18	1093.19	12.44	84.44	4.87	1.12	282.02	15.27
BRM	MM-L17-BRM-2	24	1118.89	12.33	95.07	7.46	1.13	307.53	15.42
BRM	MM-L17-BRM-2	25	1325.90	11.31	100.11	7.54	1.20	253.75	16.97
BRM	MM-L17-BRM-2	26	1398.14	11.33	101.46	7.68	1.20	249.41	17.37

125

Table S2. (continued)

Cinder Cone	Tephra Sample	Melt Inclusion	Sr	Y	Zr	Nb	Sn	Ba	La
BRM	MM-L17-BRM-2	29	1147.69	11.54	80.12	3.92	1.26	205.78	13.42
BRM	MM-L17-BRM-2	31	1045.50	10.12	66.03	3.79	1.12	136.30	10.46
BRM	MM-L17-BRM-2	32	1120.39	10.43	73.77	4.04	0.87	151.76	11.83
BRM	MM-L17-BRM-2	8	1403.44	11.72	127.55	3.39	2.95	257.16	21.84
BRVB	MM-L17-BRVB-2	10	461.76	18.92	105.64	8.24	1.53	388.23	14.36
BRVB	MM-L17-BRVB-2	2	362.48	23.63	84.07	3.44	1.36	206.99	6.93
BRVB	MM-L17-BRVB-2	4	494.35	20.75	115.40	8.76	1.63	386.63	14.67
BRVB	MM-L17-BRVB-2	6	570.73	22.16	124.45	9.67	1.77	480.98	17.36
BRVB	MM-L17-BRVB-2	7	557.94	23.54	131.30	9.13	2.68	454.66	17.76

Table S2. (continued)

Cinder Cone	Tephra Sample	Melt Inclusion	Ce	Nd	Sm	Dy	Yb	Pb
BAS-44	BAS-44-2	1	n. a.	n. a.	n. a.	n. a.	n. a.	n. a.
BAS-44	BAS-44-2	10	n. a.	n. a.	n. a.	n. a.	n. a.	n. a.
BAS-44	BAS-44-2	2	19.68	12.08	2.75	3.17	2.24	n. a.
BAS-44	BAS-44-2	4	19.42	11.98	3.14	3.19	2.14	1.75
BAS-44	BAS-44-2	5	20.86	12.71	3.15	3.60	2.11	1.98
BAS-44	BAS-44-2	6	n. a.	n. a.	n. a.	n. a.	n. a.	n. a.
BAS-44	BAS-44-2	7a	20.20	12.31	3.18	3.50	2.21	2.61
BAS-44	BAS-44-2	7b	n. a.	n. a.	n. a.	n. a.	n. a.	n. a.
BBL	BBL-5	11	27.52	15.43	3.69	2.97	2.39	3.77
BBL	BBL-5	14	29.22	18.04	4.14	5.75	3.20	3.58
BBL	BBL-5	15	30.60	19.40	4.41	5.57	3.57	3.65
BBL	BBL-5	17	16.26	13.18	3.35	5.07	3.05	1.70
BBL	BBL-5	18	29.96	18.19	5.14	4.76	2.54	3.59
BBL	BBL-5	19	12.21	8.60	2.44	3.44	1.76	1.19
BBL	BBL-5	20	31.15	18.19	3.77	3.77	2.32	5.22
BBL	BBL-5	21A	27.08	16.03	3.44	4.65	3.04	4.02
BBL	BBL-5	21B	28.57	14.28	4.21	5.02	2.67	3.47
BBL	BBL-5	22	n. a.	n. a.	n. a.	n. a.	n. a.	n. a.
BBL	BBL-5	23	22.04	13.28	3.06	3.30	1.92	2.79
BBL	BBL-5	3	n. a.	n. a.	n. a.	n. a.	n. a.	n. a.
BBL	BBL-5	30	31.95	15.23	4.57	5.99	3.58	4.21
BBL	BBL-5	31	19.75	12.73	2.78	4.17	2.84	2.94
BBL	BBL-5	32	23.27	14.65	3.78	4.15	2.61	3.44
BBL	BBL-5	33	28.86	17.66	4.12	4.43	2.78	4.39
BBL	BBL-5	34	n. a.	n. a.	n. a.	n. a.	n. a.	n. a.
BBL	BBL-5	4	n. a.	n. a.	n. a.	n. a.	n. a.	n. a.
BBL	BBL-5	43	28.83	17.30	4.08	4.53	2.82	4.72
BBL	BBL-5	44	11.35	7.48	2.15	3.27	1.87	1.28
BBL	BBL-5	46	24.20	14.46	3.75	3.63	2.75	3.78
BBL	BBL-5	47	9.57	7.58	2.00	3.12	2.06	1.29
BBL	BBL-5	49	29.01	16.68	4.03	4.05	2.50	4.43
BBL	BBL-5	5	n. a.	n. a.	n. a.	n. a.	n. a.	n. a.
BBL	BBL-5	6	22.02	12.78	3.22	3.95	2.05	2.75
BBL	BBL-5	7	14.52	9.94	2.07	4.49	3.11	1.38
BORG	BORG-1	10	n. a.	n. a.	n. a.	n. a.	n. a.	n. a.
BORG	BORG-1	11	16.29	9.75	2.35	2.79	1.13	4.01
BORG	BORG-1	12	19.33	11.23	2.09	2.58	2.05	4.43
BORG	BORG-1	13	n. a.	n. a.	n. a.	n. a.	n. a.	n. a.
BORG	BORG-1	14	11.65	6.88	1.84	2.03	0.93	2.21
BORG	BORG-1	15	21.05	12.49	2.32	2.62	1.11	5.34
BORG	BORG-1	18	n. a.	n. a.	n. a.	n. a.	n. a.	n. a.
BORG	BORG-1	19	13.42	8.40	2.10	2.46	1.10	2.83
BORG	BORG-1	2	n. a.	n. a.	n. a.	n. a.	n. a.	n. a.
BORG	BORG-1	20	16.19	9.92	2.37	2.09	0.91	4.00
BORG	BORG-1	21	11.59	7.41	1.66	2.14	0.96	1.94
BORG	BORG-1	22	14.35	8.98	2.17	2.51	1.54	2.18
BORG	BORG-1	23	n. a.	n. a.	n. a.	n. a.	n. a.	n. a.
BORG	BORG-1	24	18.51	11.89	2.21	2.88	1.77	3.21
BORG	BORG-1	25	19.15	11.70	3.76	3.06	2.07	3.11
BORG	BORG-1	3	n. a.	n. a.	n. a.	n. a.	n. a.	n. a.
BORG	BORG-1	31	18.33	11.50	2.60	2.68	1.48	4.68

Table S2. (continued)

Cinder Cone	Tephra Sample	Melt Inclusion	Ce	Nd	Sm	Dy	Yb	Pb
BORG	BORG-1	35	17.31	11.00	2.57	2.50	1.37	4.40
BORG	BORG-1	37	18.50	11.38	2.83	2.50	1.53	4.40
BORG	BORG-1	38	15.99	10.31	2.51	2.46	1.37	4.11
BORG	BORG-1	40	14.08	8.54	2.50	2.52	1.34	2.82
BORG	BORG-1	42	13.11	8.42	2.25	2.45	1.33	2.49
BORG	BORG-1	43	15.08	9.47	2.52	2.43	1.34	4.30
BORG	BORG-1	44	14.04	9.71	2.49	2.70	1.47	3.81
BORG	BORG-1	45	15.99	10.71	2.96	2.44	1.48	3.00
BORG	BORG-1	8	n. a.	n. a.	n. a.	n. a.	n. a.	n. a.
BORG	BORG-1	9	n. a.	n. a.	n. a.	n. a.	n. a.	n. a.
BORG	MM-L17-BORG-1	1	10.78	7.32	1.91	2.40	1.55	2.01
BORG	MM-L17-BORG-1	2	0.89	0.42	0.11	0.12	0.29	n. a.
BPPC	MM-L17-BPPC-4	13	14.18	8.90	2.26	3.00	1.74	2.14
BPPC	MM-L17-BPPC-4	14	14.51	8.87	2.54	3.19	1.87	2.07
BPPC	MM-L17-BPPC-4	15	13.50	8.19	2.32	3.00	1.99	1.73
BPPC	MM-L17-BPPC-4	2	12.21	7.74	2.15	2.77	1.51	1.60
BPPC	MM-L17-BPPC-4	3	n. a.	n. a.	n. a.	n. a.	n. a.	n. a.
BPPC	MM-L17-BPPC-4	4	n. a.	n. a.	n. a.	n. a.	n. a.	n. a.
BPPC	MM-L17-BPPC-4	5	13.44	8.48	2.09	2.80	1.92	1.97
BRM	BRM-1	14	n. a.	n. a.	n. a.	n. a.	n. a.	n. a.
BRM	BRM-1	16	n. a.	n. a.	n. a.	n. a.	n. a.	n. a.
BRM	BRM-1	17	42.20	18.53	2.84	2.80	1.05	5.15
BRM	BRM-1	18	n. a.	n. a.	n. a.	n. a.	n. a.	n. a.
BRM	BRM-1	19	36.99	19.61	4.10	2.65	0.99	6.49
BRM	BRM-1	2	n. a.	n. a.	n. a.	n. a.	n. a.	n. a.
BRM	BRM-1	22	44.23	21.53	3.79	2.11	0.31	5.02
BRM	BRM-1	23	n. a.	n. a.	n. a.	n. a.	n. a.	n. a.
BRM	BRM-1	24	63.14	33.35	5.77	4.13	2.21	9.42
BRM	BRM-1	25	37.32	18.07	4.49	2.48	0.64	4.04
BRM	BRM-1	3	n. a.	n. a.	n. a.	n. a.	n. a.	n. a.
BRM	BRM-1	30	32.63	17.34	3.11	2.22	1.24	4.82
BRM	BRM-1	34	37.00	19.72	3.21	2.57	1.48	5.82
BRM	BRM-1	35	n. a.	n. a.	n. a.	n. a.	n. a.	n. a.
BRM	BRM-1	36	n. a.	n. a.	n. a.	n. a.	n. a.	n. a.
BRM	BRM-1	39	n. a.	n. a.	n. a.	n. a.	n. a.	n. a.
BRM	BRM-1	40	n. a.	n. a.	n. a.	n. a.	n. a.	n. a.
BRM	BRM-1	41	28.37	15.32	2.98	2.25	1.22	3.23
BRM	BRM-1	5	53.81	23.64	4.21	2.28	1.45	5.87
BRM	BRM-1	6	24.36	11.39	2.78	1.30	1.30	2.87
BRM	BRM-1	7	58.98	25.09	3.89	3.80	1.76	6.67
BRM	BRM-1	8	51.64	26.08	4.09	2.09	1.13	5.91
BRM	MM-L17-BRM-2	1	27.87	14.38	2.71	2.22	1.32	3.74
BRM	MM-L17-BRM-2	10	n. a.	n. a.	n. a.	n. a.	n. a.	n. a.
BRM	MM-L17-BRM-2	13	n. a.	n. a.	n. a.	n. a.	n. a.	n. a.
BRM	MM-L17-BRM-2	14	n. a.	n. a.	n. a.	n. a.	n. a.	n. a.
BRM	MM-L17-BRM-2	16	n. a.	n. a.	n. a.	n. a.	n. a.	n. a.
BRM	MM-L17-BRM-2	17	n. a.	n. a.	n. a.	n. a.	n. a.	n. a.
BRM	MM-L17-BRM-2	18	35.17	17.27	3.21	2.44	1.53	5.68
BRM	MM-L17-BRM-2	24	36.70	18.44	3.49	2.42	1.23	4.88
BRM	MM-L17-BRM-2	25	40.66	20.45	3.58	2.41	1.14	4.87
BRM	MM-L17-BRM-2	26	41.35	20.56	3.59	2.29	1.06	4.68

128

Table S2. (continued)

Cinder Cone	Tephra Sample	Melt Inclusion	Ce	Nd	Sm	Dy	Yb	Pb
BRM	MM-L17-BRM-2	29	31.96	16.05	3.16	2.12	1.21	4.36
BRM	MM-L17-BRM-2	31	26.27	13.47	2.66	1.97	1.10	2.89
BRM	MM-L17-BRM-2	32	29.02	14.56	2.85	1.89	1.26	3.15
BRM	MM-L17-BRM-2	8	54.83	28.04	4.86	2.58	1.01	5.07
BRVB	MM-L17-BRVB-2	10	34.53	19.68	4.13	3.86	2.14	4.30
BRVB	MM-L17-BRVB-2	2	16.74	11.70	3.32	4.22	2.73	3.26
BRVB	MM-L17-BRVB-2	4	35.15	20.96	4.55	4.03	2.10	3.71
BRVB	MM-L17-BRVB-2	6	42.17	24.93	5.95	4.16	2.13	4.48
BRVB	MM-L17-BRVB-2	7	39.07	24.46	4.87	4.69	2.66	5.49

n. a. = not analyzed

n. d. = not detected

Table S3. Major element data for melt inclusion olivine hosts analyzed via EPMA. Values reported in wt. %. Values and standard deviation calculated from the average of 3-5 analysis spots.

Cinder Cone	Tephra Sample	Inclusion	Date Analyzed	SiO$_2$	1 s. d.	Al$_2$O$_3$	1 s. d.	FeO^T	1 s. d.
BAS-44	BAS-44-2	1	8/1/18	40.29	0.31	0.03	0.01	12.02	0.07
BAS-44	BAS-44-2	10	8/1/18	39.93	0.49	0.04	0.00	11.69	0.09
BAS-44	BAS-44-2	2	8/1/18	40.97	0.50	0.05	0.00	11.28	0.08
BAS-44	BAS-44-2	4	8/1/18	38.34	0.27	0.05	0.00	11.82	0.14
BAS-44	BAS-44-2	5	7/25/18	41.08	0.40	0.04	0.00	12.54	0.09
BAS-44	BAS-44-2	6	7/25/18	38.23	0.24	0.04	0.00	11.84	0.12
BAS-44	BAS-44-2	7a	7/25/18	40.26	0.63	0.04	0.00	12.33	0.22
BAS-44	BAS-44-2	7b	8/1/18	41.02	0.26	0.04	0.00	12.64	0.17
BBL	BBL-5	11	6/12/17	39.13	0.18	0.02	0.00	16.03	0.29
BBL	BBL-5	14	6/12/17	39.62	0.22	0.02	0.00	15.89	0.33
BBL	BBL-5	15	6/12/17	39.76	0.44	0.02	0.00	16.07	0.42
BBL	BBL-5	17	11/26/18	40.51	0.23	0.07	0.02	11.77	0.18
BBL	BBL-5	18	11/26/18	38.66	0.28	0.06	0.01	15.75	0.08
BBL	BBL-5	19	11/26/18	39.34	0.36	0.08	0.02	12.77	0.40
BBL	BBL-5	20	11/26/18	39.70	0.26	0.04	0.02	15.74	0.30
BBL	BBL-5	21A	11/26/18	39.36	0.21	0.05	0.01	14.12	0.16
BBL	BBL-5	21B	11/26/18	39.36	0.21	0.05	0.01	14.12	0.16
BBL	BBL-5	22	11/26/18	40.15	0.38	0.06	0.01	12.90	0.51
BBL	BBL-5	23	11/26/18	39.69	0.57	0.04	0.02	14.73	0.27
BBL	BBL-5	30	11/26/18	39.57	0.58	0.05	0.02	13.71	0.21
BBL	BBL-5	30b	8/1/18	38.80	0.07	0.03	0.00	15.57	0.14
BBL	BBL-5	31	8/1/18	39.52	0.55	0.04	0.00	14.70	0.12
BBL	BBL-5	32	8/1/18	39.21	0.22	0.04	0.00	14.62	0.10
BBL	BBL-5	33	7/25/18	38.26	0.66	0.02	0.00	15.68	0.24
BBL	BBL-5	34	8/1/18	40.60	0.64	0.03	0.00	14.91	0.27
BBL	BBL-5	43	2/12/20	39.75	0.15	n. a.	n. a.	15.49	0.82
BBL	BBL-5	44	2/12/20	40.11	0.10	n. a.	n. a.	13.19	0.18
BBL	BBL-5	46	2/12/20	39.75	0.07	n. a.	n. a.	14.16	0.06
BBL	BBL-5	47	2/12/20	40.17	0.06	n. a.	n. a.	12.21	0.10
BBL	BBL-5	49	2/12/20	39.61	0.06	n. a.	n. a.	16.41	0.14
BBL	BBL-5	3	11/26/18	40.63	0.45	0.07	0.02	12.41	0.66
BBL	BBL-5	4	11/26/18	40.25	0.14	0.06	0.03	12.38	0.30
BBL	BBL-5	5	11/26/18	38.82	0.35	0.03	0.02	18.12	0.55
BBL	BBL-5	6	11/26/18	40.40	0.24	0.07	0.02	14.96	0.31
BBL	BBL-5	7	6/12/17	40.15	0.19	0.05	0.00	11.41	0.39
BORG	BORG-1	2	6/5/17	40.09	0.37	0.03	0.01	15.72	0.11
BORG	BORG-1	3	6/5/17	40.65	0.41	0.03	0.00	15.31	0.27
BORG	BORG-1	8	6/5/17	40.20	0.32	0.03	0.00	14.86	0.31
BORG	BORG-1	9	6/5/17	40.63	0.34	0.03	0.00	10.90	0.25
BORG	BORG-1	10	6/5/17	41.23	0.18	0.02	0.00	15.25	0.19
BORG	BORG-1	11	6/5/17	40.93	0.36	0.02	0.01	14.21	0.92
BORG	BORG-1	12	6/5/17	40.77	0.35	0.03	0.00	14.65	0.68
BORG	BORG-1	13	6/5/17	41.72	0.19	0.02	0.01	14.36	1.11
BORG	BORG-1	14	6/5/17	40.40	0.31	0.03	0.00	11.62	0.28
BORG	BORG-1	15	6/5/17	40.53	0.31	0.02	0.00	17.13	0.33
BORG	BORG-1	18	6/5/17	39.24	0.52	0.02	0.01	15.36	0.82
BORG	BORG-1	19	6/5/17	40.57	0.22	0.02	0.01	13.45	1.11
BORG	BORG-1	20	6/5/17	40.25	0.28	0.03	0.01	13.24	1.87

Table S3. (continued)

Cinder Cone	Tephra Sample	Inclusion	Date Analyzed	SiO_2	1 s. d.	Al_2O_3	1 s. d.	FeO^T	1 s. d.
BORG	BORG-1	21	6/5/17	38.72	1.29	0.03	0.00	12.59	0.24
BORG	BORG-1	22	6/5/17	40.16	0.34	0.02	0.00	10.71	0.36
BORG	BORG-1	23	6/5/17	39.65	0.52	0.03	0.01	15.45	0.24
BORG	BORG-1	24	6/5/17	39.79	0.50	0.03	0.00	14.95	0.70
BORG	BORG-1	25	6/5/17	40.36	0.57	0.02	0.01	11.86	0.27
BORG	BORG-1	31	2/12/20	39.72	0.07	n. a.	n. a.	15.13	0.06
BORG	BORG-1	35	8/1/18	39.11	0.85	0.02	0.00	15.56	0.19
BORG	BORG-1	37	8/1/18	39.59	0.93	0.02	0.00	16.17	0.14
BORG	BORG-1	38	7/25/18	39.66	0.32	0.02	0.00	14.82	0.29
BORG	BORG-1	40	2/12/20	39.57	0.03	n. a.	n. a.	15.74	0.15
BORG	BORG-1	42	2/12/20	40.02	n. a.	n. a.	n. a.	14.05	n. a.
BORG	BORG-1	43	2/12/20	39.60	0.22	n. a.	n. a.	15.19	0.10
BORG	BORG-1	44	2/12/20	38.04	2.94	n. a.	n. a.	16.15	0.17
BORG	BORG-1	45	2/12/20	39.44	0.37	n. a.	n. a.	15.79	0.36
BORG	MM-L17-BORG-1	1	2/12/20	40.17	0.26	n. a.	n. a.	13.53	0.45
BORG	MM-L17-BORG-1	2	2/12/20	40.30	0.17	n. a.	n. a.	13.06	1.47
BPPC	MM-L17-BPPC-4	13	2/12/20	40.60	0.09	n. a.	n. a.	12.10	0.11
BPPC	MM-L17-BPPC-4	14	2/12/20	39.78	1.02	n. a.	n. a.	12.24	0.15
BPPC	MM-L17-BPPC-4	15	2/12/20	40.62	0.06	n. a.	n. a.	12.22	0.10
BPPC	MM-L17-BPPC-4	2	7/25/18	40.67	0.43	0.03	0.00	11.44	0.12
BPPC	MM-L17-BPPC-4	3	8/1/18	40.53	0.56	0.03	0.00	11.76	0.16
BPPC	MM-L17-BPPC-4	4	8/1/18	40.37	0.92	0.03	0.01	11.56	0.11
BPPC	MM-L17-BPPC-4	5	8/1/18	38.53	1.61	0.03	0.00	11.34	0.19
BRM	BRM-1	14	11/26/18	41.10	0.40	0.02	0.01	11.46	0.13
BRM	BRM-1	16	11/26/18	41.24	0.44	0.02	0.01	11.59	0.30
BRM	BRM-1	17	11/26/18	40.87	0.36	0.03	0.01	11.45	0.36
BRM	BRM-1	18	11/26/18	40.93	0.70	0.02	0.01	10.95	0.07
BRM	BRM-1	19	11/26/18	40.74	0.42	0.07	0.02	13.21	1.13
BRM	BRM-1	22	11/26/18	41.53	6.44	0.07	0.02	11.74	3.43
BRM	BRM-1	23	11/26/18	39.88	0.68	0.07	0.02	14.80	0.91
BRM	BRM-1	24	11/26/18	40.38	0.28	0.07	0.02	12.93	0.37
BRM	BRM-1	25	11/26/18	40.67	0.35	0.07	0.02	11.49	0.07
BRM	BRM-1	30	8/1/18	40.01	0.68	0.00	0.00	13.01	0.30
BRM	BRM-1	34	7/25/18	40.47	0.47	0.01	0.00	12.23	0.13
BRM	BRM-1	35	7/25/18	39.04	0.26	n. a.	n. a.	10.77	0.12
BRM	BRM-1	36	8/1/18	40.30	0.39	0.01	0.00	10.72	0.05
BRM	BRM-1	39	8/1/18	41.24	0.27	0.01	0.00	10.97	0.07
BRM	BRM-1	40	7/25/18	40.33	0.49	0.01	0.00	11.66	0.06
BRM	BRM-1	41	8/1/18	40.81	0.40	0.01	0.00	10.82	0.25
BRM	BRM-1	2	11/26/18	41.25	0.07	0.07	0.02	10.81	0.21
BRM	BRM-1	3	11/26/18	40.45	0.45	0.07	0.02	12.15	0.36
BRM	BRM-1	5	11/26/18	40.88	0.33	0.07	0.02	11.07	0.85
BRM	BRM-1	6	11/26/18	40.95	0.35	0.07	0.02	11.96	1.45
BRM	BRM-1	7	11/26/18	39.71	0.16	0.07	0.02	13.14	0.76
BRM	BRM-1	8	11/26/18	41.02	0.33	0.07	0.02	11.33	0.02
BRM	MM-L17-BRM-2	1	8/1/18	40.20	0.85	n. a.	n. a.	9.76	0.23
BRM	MM-L17-BRM-2	10	7/25/18	39.43	0.41	0.01	0.00	12.01	0.04
BRM	MM-L17-BRM-2	13	7/25/18	39.10	0.82	0.00	0.00	10.81	0.14

131

Table S3. (continued)

Cinder Cone	Tephra Sample	Inclusion	Date Analyzed	SiO$_2$	1 s. d.	Al$_2$O$_3$	1 s. d.	FeO^T	1 s. d.
BRM	MM-L17-BRM-2	14	7/25/18	39.02	0.13	0.00	0.00	10.79	0.28
BRM	MM-L17-BRM-2	16	8/1/18	41.36	0.40	n. a.	n. a.	10.30	0.03
BRM	MM-L17-BRM-2	17	7/25/18	39.47	0.46	0.00	0.00	10.51	0.39
BRM	MM-L17-BRM-2	18	7/25/18	39.54	0.44	0.00	0.00	10.71	0.10
BRM	MM-L17-BRM-2	24	2/12/20	41.44	0.19	n. a.	n. a.	12.71	0.30
BRM	MM-L17-BRM-2	25	2/12/20	40.38	0.18	n. a.	n. a.	11.61	0.65
BRM	MM-L17-BRM-2	26	2/12/20	41.47	0.06	n. a.	n. a.	10.40	0.17
BRM	MM-L17-BRM-2	29	2/12/20	41.92	0.33	n. a.	n. a.	9.87	0.09
BRM	MM-L17-BRM-2	31	2/12/20	41.05	0.09	n. a.	n. a.	9.30	0.04
BRM	MM-L17-BRM-2	32	2/12/20	41.77	0.20	n. a.	n. a.	10.85	0.43
BRM	MM-L17-BRM-2	8	7/25/18	38.91	0.11	0.00	0.00	10.32	0.08
BRVB	MM-L17-BRVB-2	10	2/12/20	39.68	0.12	n. a.	n. a.	15.61	0.12
BRVB	MM-L17-BRVB-2	2	2/12/20	39.96	0.04	n. a.	n. a.	13.81	0.23
BRVB	MM-L17-BRVB-2	4	2/12/20	39.79	0.04	n. a.	n. a.	15.11	0.17
BRVB	MM-L17-BRVB-2	6	2/12/20	39.99	0.04	n. a.	n. a.	14.16	0.12
BRVB	MM-L17-BRVB-2	7	2/12/20	41.12	0.40	n. a.	n. a.	15.45	0.20

Table S3. (continued)

Cinder Cone	Tephra Sample	Inclusion	MnO	1 s. d.	MgO	1 s. d.	CaO	1 s. d.
BAS-44	BAS-44-2	1	0.19	0.00	45.50	0.14	0.22	0.01
BAS-44	BAS-44-2	10	0.18	0.01	46.78	0.31	0.22	0.00
BAS-44	BAS-44-2	2	0.17	0.01	44.48	0.26	0.21	0.01
BAS-44	BAS-44-2	4	0.18	0.02	45.70	0.12	0.21	0.00
BAS-44	BAS-44-2	5	0.18	0.02	47.44	0.37	0.22	0.00
BAS-44	BAS-44-2	6	0.18	0.01	47.28	0.20	0.22	0.00
BAS-44	BAS-44-2	7a	0.18	0.00	46.57	0.44	0.22	0.00
BAS-44	BAS-44-2	7b	0.20	0.01	46.24	0.50	0.23	0.00
BBL	BBL-5	11	0.27	0.01	42.00	0.31	0.18	0.01
BBL	BBL-5	14	0.28	0.00	42.82	0.17	0.21	0.00
BBL	BBL-5	15	0.27	0.01	42.59	0.46	0.22	0.01
BBL	BBL-5	17	0.19	0.00	48.00	0.93	0.24	0.00
BBL	BBL-5	18	0.27	0.01	43.62	0.45	0.20	0.01
BBL	BBL-5	19	0.21	0.02	45.04	1.10	0.23	0.00
BBL	BBL-5	20	0.27	0.01	43.90	1.20	0.22	0.00
BBL	BBL-5	21A	0.24	0.01	44.76	0.32	0.24	0.00
BBL	BBL-5	21B	0.24	0.01	44.76	0.32	0.24	0.00
BBL	BBL-5	22	0.21	0.01	46.05	0.28	0.22	0.00
BBL	BBL-5	23	0.25	0.01	44.78	0.88	0.22	0.00
BBL	BBL-5	30	0.23	0.02	45.40	0.58	0.22	0.01
BBL	BBL-5	30b	0.24	0.02	43.25	0.24	0.20	0.01
BBL	BBL-5	31	0.24	0.01	43.08	0.63	0.23	0.00
BBL	BBL-5	32	0.23	0.01	42.15	0.55	0.23	0.00
BBL	BBL-5	33	0.25	0.01	43.20	0.33	0.22	0.01
BBL	BBL-5	34	0.25	0.01	42.55	0.56	0.23	0.01
BBL	BBL-5	43	n. a.	n. a.	44.35	0.62	n. a.	n. a.
BBL	BBL-5	44	n. a.	n. a.	46.07	0.51	n. a.	n. a.
BBL	BBL-5	46	n. a.	n. a.	45.04	0.23	n. a.	n. a.
BBL	BBL-5	47	n. a.	n. a.	46.83	0.21	n. a.	n. a.
BBL	BBL-5	49	n. a.	n. a.	43.57	0.15	n. a.	n. a.
BBL	BBL-5	3	0.19	0.00	46.99	0.64	0.23	0.00
BBL	BBL-5	4	0.20	0.01	46.81	0.25	0.22	0.00
BBL	BBL-5	5	0.32	0.01	41.76	0.73	0.22	0.00
BBL	BBL-5	6	0.24	0.00	45.29	0.75	0.23	0.00
BBL	BBL-5	7	0.18	0.01	45.19	0.58	0.22	0.00
BORG	BORG-1	2	0.21	0.01	44.24	1.23	0.15	0.01
BORG	BORG-1	3	0.20	0.01	44.15	0.23	0.15	0.00
BORG	BORG-1	8	0.20	0.01	44.38	0.41	0.14	0.01
BORG	BORG-1	9	0.15	0.01	46.09	0.60	0.16	0.00
BORG	BORG-1	10	0.21	0.00	44.51	0.25	0.14	0.01
BORG	BORG-1	11	0.19	0.01	45.79	0.12	0.14	0.01
BORG	BORG-1	12	0.20	0.01	43.93	0.63	0.14	0.01
BORG	BORG-1	13	0.19	0.01	46.36	1.39	0.15	0.01
BORG	BORG-1	14	0.16	0.00	46.22	0.21	0.15	0.00
BORG	BORG-1	15	0.22	0.01	43.56	0.44	0.13	0.00
BORG	BORG-1	18	0.21	0.01	43.12	0.85	0.14	0.00
BORG	BORG-1	19	0.19	0.01	45.29	0.30	0.15	0.00
BORG	BORG-1	20	0.19	0.02	44.66	1.05	0.14	0.01

Table S3. (continued)

Cinder Cone	Tephra Sample	Inclusion	MnO	1 s. d.	MgO	1 s. d.	CaO	1 s. d.
BORG	BORG-1	21	0.17	0.01	44.88	1.08	0.14	0.02
BORG	BORG-1	22	0.16	0.00	46.57	0.31	0.16	0.00
BORG	BORG-1	23	0.21	0.01	43.34	0.49	0.13	0.01
BORG	BORG-1	24	0.20	0.01	44.62	0.55	0.14	0.00
BORG	BORG-1	25	0.16	0.01	46.74	0.39	0.16	0.00
BORG	BORG-1	31	n. a.	n. a.	44.47	0.05	n. a.	n. a.
BORG	BORG-1	35	0.21	0.01	43.53	0.44	0.14	0.00
BORG	BORG-1	37	0.22	0.01	43.50	0.31	0.14	0.00
BORG	BORG-1	38	0.20	0.02	44.40	0.19	0.14	0.00
BORG	BORG-1	40	n. a.	n. a.	44.15	0.11	n. a.	n. a.
BORG	BORG-1	42	n. a.	n. a.	45.70	n. a.	n. a.	n. a.
BORG	BORG-1	43	n. a.	n. a.	44.67	0.06	n. a.	n. a.
BORG	BORG-1	44	n. a.	n. a.	43.32	0.88	n. a.	n. a.
BORG	BORG-1	45	n. a.	n. a.	43.96	0.29	n. a.	n. a.
BORG	MM-L17-BORG-1	1	n. a.	n. a.	45.92	0.81	n. a.	n. a.
BORG	MM-L17-BORG-1	2	n. a.	n. a.	46.41	1.35	n. a.	n. a.
BPPC	MM-L17-BPPC-4	13	n. a.	n. a.	47.50	0.14	n. a.	n. a.
BPPC	MM-L17-BPPC-4	14	n. a.	n. a.	46.93	0.32	n. a.	n. a.
BPPC	MM-L17-BPPC-4	15	n. a.	n. a.	47.34	0.15	n. a.	n. a.
BPPC	MM-L17-BPPC-4	2	0.18	0.01	45.37	0.29	0.20	0.00
BPPC	MM-L17-BPPC-4	3	0.18	0.01	45.41	0.42	0.20	0.00
BPPC	MM-L17-BPPC-4	4	0.19	0.00	46.54	0.39	0.20	0.01
BPPC	MM-L17-BPPC-4	5	0.18	0.01	46.02	0.79	0.20	0.01
BRM	BRM-1	14	0.16	0.01	49.22	1.01	0.11	0.00
BRM	BRM-1	16	0.17	0.00	49.26	0.25	0.10	0.00
BRM	BRM-1	17	0.16	0.01	48.44	0.40	0.11	0.00
BRM	BRM-1	18	0.15	0.01	49.35	0.75	0.11	0.00
BRM	BRM-1	19	0.20	0.02	47.93	1.18	0.12	0.01
BRM	BRM-1	22	0.17	0.41	48.01	6.93	0.10	0.32
BRM	BRM-1	23	0.21	0.02	46.07	1.04	0.12	0.02
BRM	BRM-1	24	0.19	0.01	47.25	1.16	0.12	0.00
BRM	BRM-1	25	0.16	0.01	49.07	0.47	0.10	0.00
BRM	BRM-1	30	0.17	0.00	45.40	0.14	0.06	0.01
BRM	BRM-1	34	0.17	0.01	48.05	0.43	0.10	0.00
BRM	BRM-1	35	0.16	0.00	47.03	0.15	0.08	0.01
BRM	BRM-1	36	0.15	0.02	45.84	0.38	0.11	0.00
BRM	BRM-1	39	0.15	0.01	45.88	0.26	0.11	0.00
BRM	BRM-1	40	0.16	0.01	46.27	0.34	0.11	0.00
BRM	BRM-1	41	0.16	0.01	43.65	0.13	0.12	0.00
BRM	BRM-1	2	0.16	0.00	49.15	0.36	0.12	0.00
BRM	BRM-1	3	0.18	0.01	48.33	1.45	0.14	0.01
BRM	BRM-1	5	0.16	0.02	48.91	1.01	0.10	0.00
BRM	BRM-1	6	0.18	0.02	48.16	0.60	0.11	0.01
BRM	BRM-1	7	0.21	0.01	47.51	0.75	0.08	0.04
BRM	BRM-1	8	0.16	0.00	49.68	0.72	0.11	0.00
BRM	MM-L17-BRM-2	1	0.14	0.01	47.40	0.38	0.12	0.01
BRM	MM-L17-BRM-2	10	0.16	0.01	46.18	0.11	0.11	0.00
BRM	MM-L17-BRM-2	13	0.13	0.01	47.25	0.34	0.10	0.00

Table S3. (continued)

Cinder Cone	Tephra Sample	Inclusion	MnO	1 s. d.	MgO	1 s. d.	CaO	1 s. d.
BRM	MM-L17-BRM-2	14	0.13	0.01	46.13	0.43	0.11	0.00
BRM	MM-L17-BRM-2	16	0.14	0.01	46.92	0.13	0.10	0.00
BRM	MM-L17-BRM-2	17	0.14	0.00	47.64	0.28	0.11	0.01
BRM	MM-L17-BRM-2	18	0.14	0.00	46.96	0.30	0.10	0.00
BRM	MM-L17-BRM-2	24	n. a.	n. a.	45.90	0.20	n. a.	n. a.
BRM	MM-L17-BRM-2	25	n. a.	n. a.	47.25	0.73	n. a.	n. a.
BRM	MM-L17-BRM-2	26	n. a.	n. a.	46.82	0.11	n. a.	n. a.
BRM	MM-L17-BRM-2	29	n. a.	n. a.	47.24	0.27	n. a.	n. a.
BRM	MM-L17-BRM-2	31	n. a.	n. a.	49.68	0.13	n. a.	n. a.
BRM	MM-L17-BRM-2	32	n. a.	n. a.	46.47	0.36	n. a.	n. a.
BRM	MM-L17-BRM-2	8	0.13	0.00	47.13	0.34	0.09	0.01
BRVB	MM-L17-BRVB-2	10	n. a.	n. a.	44.19	0.12	n. a.	n. a.
BRVB	MM-L17-BRVB-2	2	n. a.	n. a.	45.67	0.03	n. a.	n. a.
BRVB	MM-L17-BRVB-2	4	n. a.	n. a.	44.81	0.02	n. a.	n. a.
BRVB	MM-L17-BRVB-2	6	n. a.	n. a.	45.42	0.09	n. a.	n. a.
BRVB	MM-L17-BRVB-2	7	n. a.	n. a.	44.36	0.44	n. a.	n. a.

n. a. = not analyzed

Table S4a. Measured $^{34}S/^{32}S$ values on standards and calculated α for Instrument Mass Fractionation (IMF) during sulfur SIMS. Each analysis was taken on one analysis point. All reported values have been corrected for deadtime and 32S/34S midpoint calculations.

Analysis	Analysis Date	Measured $^{32}S/^{34}S$	1 RSE	Calculated α (IMF)	Known $^{34}S/^{32}S$
892-1@1.asc	11/19/19	4.4370E-02	5.57E-04	1.0040	4.4195E-02
892-1@2.asc	11/19/19	4.4379E-02	4.75E-04	1.0042	4.4195E-02
892-1@3.asc	11/19/19	4.4359E-02	4.46E-04	1.0037	4.4195E-02
892-1@4.asc	11/19/19	4.4407E-02	4.73E-04	1.0048	4.4195E-02
892-1@5.asc	11/19/19	4.4372E-02	4.30E-04	1.0040	4.4195E-02
892-1@6.asc	11/19/19	4.4364E-02	4.31E-04	1.0038	4.4195E-02
892-1@7.asc	11/19/19	4.4361E-02	3.86E-04	1.0038	4.4195E-02
892-1@8.asc	11/19/19	4.4318E-02	4.63E-04	1.0028	4.4195E-02
892-1@9.asc	11/19/19	4.4343E-02	4.74E-04	1.0034	4.4195E-02
892-1@10.asc	11/19/19	4.4405E-02	4.40E-04	1.0048	4.4195E-02
892-1@11.asc	11/19/19	4.4419E-02	4.10E-04	1.0051	4.4195E-02
892-1@12.asc	11/19/19	4.4388E-02	4.81E-04	1.0044	4.4195E-02
892-1@13.asc	11/19/19	4.4362E-02	5.58E-04	1.0038	4.4195E-02
892-1@14.asc	11/19/19	4.4384E-02	5.61E-04	1.0043	4.4195E-02
892-1@15.asc	11/19/19	4.4386E-02	4.53E-04	1.0043	4.4195E-02
519-4-1@16.asc	11/19/19	4.4290E-02	5.52E-04	1.0031	4.4155E-02
519-4-1@17.asc	11/19/19	4.4298E-02	4.82E-04	1.0032	4.4155E-02
519-4-1@18.asc	11/19/19	4.4312E-02	4.44E-04	1.0036	4.4155E-02
519-4-1@19.asc	11/19/19	4.4286E-02	4.89E-04	1.0030	4.4155E-02
519-4-1@20.asc	11/19/19	4.4314E-02	4.77E-04	1.0036	4.4155E-02
519-4-1@21.asc	11/19/19	4.4350E-02	5.09E-04	1.0044	4.4155E-02
519-4-1@22.asc	11/19/19	4.4254E-02	4.26E-04	1.0022	4.4155E-02
519-4-1@23.asc	11/19/19	4.4217E-02	5.48E-04	1.0014	4.4155E-02
519-4-1@24.asc	11/19/19	4.4289E-02	4.50E-04	1.0030	4.4155E-02
519-4-1@25.asc	11/19/19	4.4325E-02	4.74E-04	1.0039	4.4155E-02
892-1@26.asc	11/19/19	4.4352E-02	3.85E-04	1.0036	4.4195E-02
892-1@27.asc	11/19/19	4.4352E-02	3.96E-04	1.0036	4.4195E-02
ET10A@28.asc	11/19/19	4.3995E-02	4.12E-04	1.0015	4.3930E-02
ET10A@29.asc	11/19/19	4.3986E-02	4.17E-04	1.0013	4.3930E-02
ET10A@30.asc	11/19/19	4.3995E-02	4.09E-04	1.0015	4.3930E-02
ET10A@31.asc	11/19/19	4.4014E-02	5.44E-04	1.0019	4.3930E-02
ET10A@32.asc	11/19/19	4.3988E-02	4.07E-04	1.0013	4.3930E-02
ET10A@33.asc	11/19/19	4.4026E-02	4.57E-04	1.0022	4.3930E-02
ET10A@34.asc	11/19/19	4.3951E-02	4.88E-04	1.0005	4.3930E-02
ET10A@35.asc	11/19/19	4.4021E-02	4.51E-04	1.0021	4.3930E-02
ET10A@36.asc	11/19/19	4.4009E-02	3.31E-04	1.0018	4.3930E-02
ET10A@37.asc	11/19/19	4.3999E-02	3.30E-04	1.0016	4.3930E-02
892-1@38.asc	11/19/19	4.4342E-02	4.78E-04	1.0033	4.4195E-02
892-1@39.asc	11/19/19	4.4331E-02	5.00E-04	1.0031	4.4195E-02
ET13D@40.asc	11/19/19	4.4097E-02	4.34E-04	1.0012	4.4045E-02
ET13D@41.asc	11/19/19	4.4103E-02	4.13E-04	1.0013	4.4045E-02
ET13D@42.asc	11/19/19	4.4134E-02	4.20E-04	1.0020	4.4045E-02
ET13D@43.asc	11/19/19	4.4173E-02	4.55E-04	1.0029	4.4045E-02
ET13D@44.asc	11/19/19	4.4166E-02	4.07E-04	1.0028	4.4045E-02
ET13D@45.asc	11/19/19	4.4136E-02	5.39E-04	1.0021	4.4045E-02
ET13D@46.asc	11/19/19	4.4158E-02	4.66E-04	1.0026	4.4045E-02
ET13D@47.asc	11/20/19	4.4163E-02	4.70E-04	1.0027	4.4045E-02
ET13D@48.asc	11/20/19	4.4185E-02	3.81E-04	1.0032	4.4045E-02
ET13D@49.asc	11/20/19	4.4146E-02	5.12E-04	1.0023	4.4045E-02
892-1@50.asc	11/20/19	4.4341E-02	5.06E-04	1.0033	4.4195E-02
892-1@51.asc	11/20/19	4.4395E-02	4.45E-04	1.0045	4.4195E-02
JDF46N@52.asc	11/20/19	4.4308E-02	5.79E-04	1.0020	4.4221E-02
JDF46N@53.asc	11/20/19	4.4343E-02	4.18E-04	1.0028	4.4221E-02
JDF46N@54.asc	11/20/19	4.4376E-02	6.41E-04	1.0035	4.4221E-02
JDF46N@55.asc	11/20/19	4.4313E-02	4.73E-04	1.0021	4.4221E-02
JDF46N@56.asc	11/20/19	4.4372E-02	4.29E-04	1.0034	4.4221E-02

Table S4a. (continued)

Analysis	Analysis Date	Measured ^{32}S/^{34}S	1 RSE	Calculated α (IMF)	Known ^{34}S/^{32}S
JDF46N@57.asc	11/20/19	4.4372E-02	5.37E-04	1.0034	4.4221E-02
JDF46N@58.asc	11/20/19	4.4348E-02	5.88E-04	1.0029	4.4221E-02
JDF46N@59.asc	11/20/19	4.4329E-02	4.21E-04	1.0024	4.4221E-02
JDF46N@60.asc	11/20/19	4.4308E-02	4.86E-04	1.0020	4.4221E-02
JDF46N@61.asc	11/20/19	4.4389E-02	4.81E-04	1.0038	4.4221E-02
892-1@62.asc	11/20/19	4.4318E-02	5.43E-04	1.0028	4.4195E-02
892-1@63.asc	11/20/19	4.4364E-02	4.33E-04	1.0038	4.4195E-02
BCR2_10@64.asc	11/20/19	4.4820E-02	3.86E-04	1.0026	4.4704E-02
BCR2_10@65.asc	11/20/19	4.4825E-02	3.91E-04	1.0027	4.4704E-02
BCR2_10@66.asc	11/20/19	4.4817E-02	4.08E-04	1.0025	4.4704E-02
BCR2_10@67.asc	11/20/19	4.4787E-02	4.09E-04	1.0019	4.4704E-02
BCR2_10@68.asc	11/20/19	4.4798E-02	4.27E-04	1.0021	4.4704E-02
BCR2_10@69.asc	11/20/19	4.4820E-02	3.57E-04	1.0026	4.4704E-02
BCR2_10@70.asc	11/20/19	4.4827E-02	3.93E-04	1.0028	4.4704E-02
BCR2_10@71.asc	11/20/19	4.4801E-02	3.28E-04	1.0022	4.4704E-02
BCR2_10@72.asc	11/20/19	4.4841E-02	3.15E-04	1.0031	4.4704E-02
BCR2_10@73.asc	11/20/19	4.4847E-02	3.36E-04	1.0032	4.4704E-02
892-1@74.asc	11/20/19	4.4340E-02	4.07E-04	1.0033	4.4195E-02
892-1@75.asc	11/20/19	4.4352E-02	3.62E-04	1.0036	4.4195E-02
892-1@76.asc	11/20/19	4.4304E-02	5.34E-04	1.0025	4.4195E-02
892-1@77.asc	11/20/19	4.4323E-02	5.17E-04	1.0029	4.4195E-02
892-1@78.asc	11/20/19	4.4377E-02	4.78E-04	1.0041	4.4195E-02
892-1@79.asc	11/20/19	4.4370E-02	4.78E-04	1.0040	4.4195E-02
519-4-1@80.asc	11/20/19	4.4290E-02	6.68E-04	1.0031	4.4155E-02
519-4-1@83.asc	11/20/19	4.4251E-02	8.20E-04	1.0022	4.4155E-02
519-4-1@84.asc	11/20/19	4.4241E-02	5.22E-04	1.0019	4.4155E-02
ET10A@85.asc	11/20/19	4.3988E-02	3.96E-04	1.0013	4.3930E-02
ET10A@86.asc	11/20/19	4.3976E-02	4.33E-04	1.0011	4.3930E-02
892-1@87.asc	11/20/19	4.4345E-02	5.32E-04	1.0034	4.4195E-02
ET10A@87.asc	11/20/19	4.3983E-02	3.34E-04	1.0012	4.3930E-02
892-1@88.asc	11/20/19	4.4372E-02	4.03E-04	1.0040	4.4195E-02
892-1_S-iso1@89.asc	11/20/19	4.4358E-02	4.34E-04	1.0037	4.4195E-02
892-1_S-iso1@90.asc	11/20/19	4.4306E-02	4.76E-04	1.0025	4.4195E-02
892-1_S-iso1@91.asc	11/20/19	4.4316E-02	4.95E-04	1.0027	4.4195E-02
892-1_S-iso1@92.asc	11/20/19	4.4273E-02	4.27E-04	1.0018	4.4195E-02
892-1_S-iso1@93.asc	11/20/19	4.4378E-02	3.22E-04	1.0041	4.4195E-02
892-1_S-iso1@94.asc	11/20/19	4.4315E-02	4.47E-04	1.0027	4.4195E-02
NBS621@94.asc	11/20/19	4.4640E-02	8.81E-04	1.0026	4.4525E-02
NBS621@95.asc	11/20/19	4.4675E-02	6.02E-04	1.0034	4.4525E-02
NBS621@96.asc	11/20/19	4.4628E-02	5.51E-04	1.0023	4.4525E-02
NBS621@97.asc	11/20/19	4.4661E-02	6.29E-04	1.0031	4.4525E-02
NBS621@98.asc	11/20/19	4.4667E-02	5.23E-04	1.0032	4.4525E-02
892-1_S-iso1@99.asc	11/20/19	4.4323E-02	4.43E-04	1.0029	4.4195E-02
892-1_S-iso1@100.asc	11/20/19	4.4291E-02	4.14E-04	1.0022	4.4195E-02
NBS620@101.asc	11/20/19	4.4610E-02	3.06E-04	1.0024	4.4503E-02
NBS620@102.asc	11/20/19	4.4595E-02	4.13E-04	1.0021	4.4503E-02
NBS620@103.asc	11/20/19	4.4614E-02	5.62E-04	1.0025	4.4503E-02
NBS620@104.asc	11/20/19	4.4598E-02	2.53E-04	1.0021	4.4503E-02
NBS620@105.asc	11/20/19	4.4595E-02	3.14E-04	1.0021	4.4503E-02
Run144@108.asc	11/20/19	4.5181E-02	2.81E-04	1.0045	4.4981E-02
Run144@109.asc	11/20/19	4.5188E-02	4.37E-04	1.0046	4.4981E-02
Run144@110.asc	11/20/19	4.5174E-02	3.06E-04	1.0043	4.4981E-02
Run144@111.asc	11/20/19	4.5174E-02	3.10E-04	1.0043	4.4981E-02
Run144@112.asc	11/20/19	4.5204E-02	2.43E-04	1.0050	4.4981E-02
892-1_iso1@113.asc	11/20/19	4.4316E-02	4.83E-04	1.0027	4.4195E-02
892-1_iso1@114.asc	11/20/19	4.4318E-02	4.42E-04	1.0028	4.4195E-02
892-1_iso1@120.asc	11/20/19	4.4314E-02	4.93E-04	1.0027	4.4195E-02

Table S4a. (continued)

Analysis	Analysis Date	Measured $^{32}S/^{34}S$	1 RSE	Calculated α (IMF)	Known $^{34}S/^{32}S$
892-1_iso1@121.asc	11/20/19	4.4300E-02	4.70E-04	1.0024	4.4195E-02
JDF46N_iso1@122.asc	11/20/19	4.4327E-02	3.42E-04	1.0024	4.4221E-02
JDF46N_iso1@123.asc	11/20/19	4.4338E-02	2.82E-04	1.0026	4.4221E-02
JDF46N_iso1@124.asc	11/20/19	4.4352E-02	3.47E-04	1.0030	4.4221E-02
JDF46N_iso1@125.asc	11/20/19	4.4329E-02	4.23E-04	1.0024	4.4221E-02
JDF46N_iso1@126.asc	11/20/19	4.4334E-02	2.88E-04	1.0026	4.4221E-02
892-1_iso1@127.asc	11/21/19	4.4325E-02	4.47E-04	1.0029	4.4195E-02
892-1_iso1@128.asc	11/21/19	4.4316E-02	3.43E-04	1.0027	4.4195E-02
83XXA@129.asc	11/21/19	4.5003E-02	4.63E-04	1.0026	4.4888E-02
83XXA@130.asc	11/21/19	4.4995E-02	4.02E-04	1.0024	4.4888E-02
83XXA@131.asc	11/21/19	4.4934E-02	3.52E-04	1.0010	4.4888E-02
83XXA@132.asc	11/21/19	4.4992E-02	4.56E-04	1.0023	4.4888E-02
83XXA@133.asc	11/21/19	4.4991E-02	3.93E-04	1.0023	4.4888E-02
892-1_iso1@134.asc	11/21/19	4.4298E-02	3.19E-04	1.0023	4.4195E-02
892-1_iso1@135.asc	11/21/19	4.4260E-02	4.19E-04	1.0015	4.4195E-02
892-1_Siso1@136.asc	11/21/19	4.4285E-02	4.28E-04	1.0020	4.4195E-02
892-1_Siso1@137.asc	11/21/19	4.4286E-02	4.25E-04	1.0021	4.4195E-02
892-1_Siso1@138.asc	11/21/19	4.4325E-02	4.09E-04	1.0029	4.4195E-02
892-1_Siso1@139.asc	11/21/19	4.4281E-02	4.08E-04	1.0020	4.4195E-02
892-1_Siso1@140.asc	11/21/19	4.4330E-02	5.11E-04	1.0031	4.4195E-02
519-4-1_Siso2_400pA@322.asc	11/24/19	4.4322E-02	4.92E-04	1.0038	4.4155E-02
519-4-1_Siso2_400pA@323.asc	11/24/19	4.4259E-02	3.95E-04	1.0024	4.4155E-02
519-4-1_Siso2_400pA@324.asc	11/24/19	4.4315E-02	4.54E-04	1.0036	4.4155E-02
519-4-1_Siso2_400pA@325.asc	11/24/19	4.4300E-02	4.33E-04	1.0033	4.4155E-02
519-4-1_Siso2_400pA@326.asc	11/24/19	4.4311E-02	3.77E-04	1.0035	4.4155E-02
519-4-1_Siso2_400pA@332.asc	11/24/19	4.4255E-02	3.95E-04	1.0023	4.4155E-02
519-4-1_Siso2_400pA@333.asc	11/24/19	4.4275E-02	5.04E-04	1.0027	4.4155E-02
519-4-1_Siso2_400pA@334.asc	11/24/19	4.4253E-02	4.01E-04	1.0022	4.4155E-02
519-4-1_Siso2_400pA@335.asc	11/24/19	4.4294E-02	3.99E-04	1.0031	4.4155E-02
519-4-1_Siso2_400pA@336.asc	11/24/19	4.4285E-02	4.65E-04	1.0029	4.4155E-02
892-1_Siso2@342.asc	11/24/19	4.4339E-02	6.30E-04	1.0033	4.4195E-02
892-1_Siso2@343.asc	11/24/19	4.4320E-02	5.51E-04	1.0028	4.4195E-02
892-1_Siso2@344.asc	11/24/19	4.4306E-02	4.87E-04	1.0025	4.4195E-02
892-1_Siso2@345.asc	11/24/19	4.4288E-02	4.82E-04	1.0021	4.4195E-02
892-1_Siso2@346.asc	11/24/19	4.4318E-02	5.69E-04	1.0028	4.4195E-02
JDF46N_Siso2@352.asc	11/24/19	4.4321E-02	3.93E-04	1.0023	4.4221E-02
JDF46N_Siso2@353.asc	11/24/19	4.4331E-02	4.37E-04	1.0025	4.4221E-02
JDF46N_Siso2@354.asc	11/24/19	4.4367E-02	3.14E-04	1.0033	4.4221E-02
JDF46N_Siso2@355.asc	11/24/19	4.4295E-02	3.71E-04	1.0017	4.4221E-02
JDF46N_Siso2@356.asc	11/24/19	4.4345E-02	4.12E-04	1.0028	4.4221E-02

Table S4b. Measured and calculated $^{34}S/^{32}S$ values on unkowns. Each analysis was taken on one point. All reported values have been corrected for deadtime and 32S/34S midpoint calculations. δ34S values calculated relative to Vienna-Canyon Diablo Troilite (34S/32S = 0.04416375)

Analysis	Sample Name	Analysis Date	Measured $^{32}S/^{34}S$	RSE	α (IMF)	α 2σ	Sample $^{32}S/^{34}S$	$δ^{34}S$ (‰)	2σ
VG2_LI-2@147.asc	VG2_LI-2	11/21/19	4.4263E-02	4.0186E-04	1.0028	0.00086	4.4138E-02	-0.6	1.2
VG-2_LI-2@149.asc	VG-2_LI-2	11/21/19	4.4289E-02	3.6520E-04	1.0028	0.00086	4.4164E-02	0.0	1.1
VG-2_LI-2@150.asc	VG-2_LI-2	11/21/19	4.4337E-02	4.4193E-04	1.0028	0.00086	4.4212E-02	1.1	1.2
VG-2_LI-2@151.asc	VG-2_LI-2	11/21/19	4.4302E-02	3.4576E-04	1.0028	0.00086	4.4177E-02	0.3	1.1
VG-2_LI-2@152.asc	VG-2_LI-2	11/21/19	4.4307E-02	2.5202E-04	1.0028	0.00086	4.4182E-02	0.4	1.0
VG-2_LI-2@153.asc	VG-2_LI-2	11/21/19	4.4303E-02	3.3733E-04	1.0028	0.00086	4.4178E-02	0.3	1.1
VG-2_LI-1@158.asc	VG-2_LI-1	11/21/19	4.4299E-02	3.9497E-04	1.0028	0.00086	4.4174E-02	0.2	1.2
VG-2_LI-1@159.asc	VG-2_LI-1	11/21/19	4.4295E-02	3.9879E-04	1.0028	0.00086	4.4170E-02	0.1	1.2
VG-2_LI-1@160.asc	VG-2_LI-1	11/21/19	4.4366E-02	4.8694E-04	1.0028	0.00086	4.4240E-02	1.7	1.3
BBL-5_46@161.asc	BBL-5_46	11/21/19	4.4329E-02	8.4970E-04	1.0028	0.00086	4.4204E-02	0.9	1.9
BBL-5_43@162.asc	BBL-5_43	11/21/19	4.4375E-02	5.2976E-04	1.0028	0.00086	4.4249E-02	1.9	1.4
MM-L17-BRM-2_25@163.asc	MM-L17-BRM-2_25	11/21/19	4.4511E-02	2.3809E-04	1.0028	0.00086	4.4385E-02	5.0	1.0
BBL-5_42@164.asc	BBL-5_42	11/21/19	4.4377E-02	4.9529E-04	1.0028	0.00086	4.4251E-02	2.0	1.3
MM-L17-BRM-2_29@165.asc	MM-L17-BRM-2_29	11/21/19	4.4525E-02	2.1499E-04	1.0028	0.00086	4.4399E-02	5.3	1.0
VG-2_LI-1@168.asc	VG-2_LI-1	11/21/19	4.4324E-02	5.3828E-04	1.0028	0.00086	4.4199E-02	0.8	1.4
VG-2_LI-1@169.asc	VG-2_LI-1	11/21/19	4.4372E-02	3.7969E-04	1.0028	0.00086	4.4246E-02	1.9	1.1
BBL-5_44@170.asc	BBL-5_44	11/21/19	4.4350E-02	7.3314E-04	1.0028	0.00086	4.4225E-02	1.4	1.7
BBL-5_49@171.asc	BBL-5_49	11/21/19	4.4423E-02	2.6756E-04	1.0028	0.00086	4.4297E-02	3.0	1.0
MM-L17-BRM-2_32@172.asc	MM-L17-BRM-2_32	11/21/19	4.4496E-02	2.6760E-04	1.0028	0.00086	4.4370E-02	4.7	1.0
MM-L17-BRM-2_24@174.asc	MM-L17-BRM-2_24	11/21/19	4.4538E-02	2.2450E-04	1.0028	0.00086	4.4412E-02	5.6	1.0
VG-2_LI-1@175.asc	VG-2_LI-1	11/21/19	4.4314E-02	4.1014E-04	1.0028	0.00086	4.4189E-02	0.6	1.2
VG-2_LI-1@176.asc	VG-2_LI-1	11/21/19	4.4333E-02	3.6139E-04	1.0028	0.00086	4.4208E-02	1.0	1.1
MM-L17-BRM-2_31@177.asc	MM-L17-BRM-2_31	11/22/19	4.4518E-02	2.9632E-04	1.0028	0.00086	4.4392E-02	5.2	1.0
MM-L17-BRM-2_26@181.asc	MM-L17-BRM-2_26	11/22/19	4.4530E-02	3.2183E-04	1.0028	0.00086	4.4404E-02	5.4	1.1
BORG-1_43@184.asc	BORG-1_43	11/22/19	4.4530E-02	3.6068E-04	1.0028	0.00086	4.4404E-02	5.4	1.1
VG-2_LI-1@185.asc	VG-2_LI-1	11/22/19	4.4382E-02	4.3833E-04	1.0028	0.00086	4.4256E-02	2.1	1.2
VG-2_LI-1@186.asc	VG-2_LI-1	11/22/19	4.4338E-02	4.7058E-04	1.0028	0.00086	4.4213E-02	1.1	1.3
VG-2_LI-1@188.asc	VG-2_LI-1	11/22/19	4.4317E-02	4.3102E-04	1.0028	0.00086	4.4192E-02	0.6	1.2
BBL-5_47@189.asc	BBL-5_47	11/22/19	4.4353E-02	6.0135E-04	1.0028	0.00086	4.4228E-02	1.4	1.5
BORG-1_44@190.asc	BORG-1_44	11/22/19	4.4517E-02	3.6497E-04	1.0028	0.00086	4.4391E-02	5.1	1.1
BORG-1_42@191.asc	BORG-1_42	11/22/19	4.4474E-02	5.2439E-04	1.0028	0.00086	4.4348E-02	4.2	1.4
BORG-1_31@192.asc	BORG-1_31	11/22/19	4.4483E-02	6.5812E-04	1.0028	0.00086	4.4357E-02	4.4	1.6
BORG-1_40@193.asc	BORG-1_40	11/22/19	4.4470E-02	4.1928E-04	1.0028	0.00086	4.4344E-02	4.1	1.2
VG-2_LI-1@194.asc	VG-2_LI-1	11/22/19	4.4314E-02	3.2962E-04	1.0028	0.00086	4.4189E-02	0.6	1.1
VG-2_LI-1@195.asc	VG-2_LI-1	11/22/19	4.4329E-02	3.1795E-04	1.0028	0.00086	4.4204E-02	0.9	1.1
VG-2_LI-1@196.asc	VG-2_LI-1	11/22/19	4.4339E-02	3.6501E-04	1.0028	0.00086	4.4214E-02	1.1	1.1
VG-2_LI-2@200.asc	VG-2_LI-2	11/22/19	4.4325E-02	3.2166E-04	1.0028	0.00086	4.4200E-02	0.8	1.1
VG-2_LI-2@201.asc	VG-2_LI-2	11/22/19	4.4372E-02	3.0234E-04	1.0028	0.00086	4.4246E-02	1.9	1.0
VG-2_LI-2@203.asc	VG-2_LI-2	11/22/19	4.4310E-02	3.3579E-04	1.0028	0.00086	4.4185E-02	0.5	1.1
MM-L17-BPPC-4_13@204.asc	MM-L17-BPPC-4_13	11/22/19	4.4441E-02	3.8287E-04	1.0028	0.00086	4.4315E-02	3.4	1.1
MM-L17-BPPC-4_14@205.asc	MM-L17-BPPC-4_14	11/22/19	4.4458E-02	3.3573E-04	1.0028	0.00086	4.4332E-02	3.8	1.1
MM-L17-BPPC-4_12@206.asc	MM-L17-BPPC-4_12	11/22/19	4.4458E-02	4.1879E-04	1.0028	0.00086	4.4332E-02	3.8	1.2
MM-L17-BPPC-4_15@207.asc	MM-L17-BPPC-4_15	11/22/19	4.4434E-02	4.3680E-04	1.0028	0.00086	4.4308E-02	3.3	1.2
VG-2_LI-1@209.asc	VG-2_LI-1	11/22/19	4.4334E-02	3.4667E-04	1.0028	0.00086	4.4209E-02	1.0	1.1
VG-2_LI-1@210.asc	VG-2_LI-1	11/22/19	4.4288E-02	5.1736E-04	1.0028	0.00086	4.4163E-02	0.0	1.3
BRVB-2_6@211.asc	BRVB-2_6	11/22/19	4.4481E-02	4.6872E-04	1.0028	0.00086	4.4355E-02	4.3	1.3
BRVB-2_7@212.asc	BRVB-2_7	11/22/19	4.4468E-02	2.6266E-04	1.0028	0.00086	4.4342E-02	4.0	1.0
BRVB-2_4@213.asc	BRVB-2_4	11/22/19	4.4487E-02	3.0474E-04	1.0028	0.00086	4.4361E-02	4.5	1.0
BRVB-2_2@214.asc	BRVB-2_2	11/22/19	4.4444E-02	2.4673E-04	1.0028	0.00086	4.4318E-02	3.5	1.0
VG-2_LI-1@215.asc	VG-2_LI-1	11/22/19	4.4314E-02	4.3725E-04	1.0028	0.00086	4.4189E-02	0.6	1.2
VG-2_LI-1@216.asc	VG-2_LI-1	11/22/19	4.4346E-02	4.3272E-04	1.0028	0.00086	4.4221E-02	1.3	1.2
VG-2_LI-1@217.asc	VG-2_LI-1	11/22/19	4.4300E-02	4.7820E-04	1.0028	0.00086	4.4175E-02	0.2	1.3

Table S5. Sulfur and iron speciation calculated via S- and Fe-XANES. Reported centroid value adjusted for use with Zhang 2018 Fe-XANES calibration. See methods for details. Δ QFM and log (fO2) calculated via Kress and Carmichael 1991 and Frost 1991 using melt inclusion EPMA data for major elements at 400 Mpa, 1150 °C. Oxygen fugacity is not calculated for melt inclusions without compositional data. See Lerner et al., in review for S- and Fe-XANES calibration details.

Cinder Cone	Sample	Inclusion	S XANES							Fe XANES			
			IS^{6+}	IS^{4+}	IS^{2-}	$S^{6+}/\Sigma S$	% Correction	Centroid (eV)	Centroid s.e.	$Fe^{3+}/\Sigma Fe$	$Fe^{3+}/\Sigma Fe$ s.e.	log (f_{O_2})	Δ QFM
BAS-44	BAS-44-2	1	7.35	0.42	11.24	0.41	3.41	n. a.	n. a.	n. a.	n. a.	n. a.	n. a.
BAS-44	BAS-44-2	11	4.14	0.01	9.09	0.32	0.24	7112.36	0.05	0.17	0.02	-	-
BAS-44	BAS-44-2	13	5.98	0.08	10.06	0.38	0.84	7112.29	0.05	0.15	0.02	-	-
BAS-44	BAS-44-2	2	9.56	0.24	7.06	0.59	1.05	n. a.	n. a.	n. a.	n. a.	n. a.	n. a.
BAS-44	BAS-44-2	6	11.11	0.17	7.67	0.60	0.60	n. a.	n. a.	n. a.	n. a.	n. a.	n. a.
BAS-44	BAS-44-2	7	n. a.	n. a.	n. a.	n. a.	n. a.	7112.41	0.05	0.19	0.02	-7.89	0.63
BBL	BBL-5	30	n. a.	n. a.	n. a.	n. a.	n. a.	7112.46	0.03	0.21	0.01	-7.69	0.90
BBL	BBL-5	30b	5.06	0.27	3.26	0.63	2.01	n. a.	n. a.	n. a.	n. a.	n. a.	n. a.
BBL	BBL-5	31	3.54	0.00	4.66	0.43	0.00	n. a.	n. a.	n. a.	n. a.	n. a.	n. a.
BBL	BBL-5	32	27.03	0.00	12.19	0.69	0.00	7112.33	0.05	0.16	0.02	-8.53	0.06
BBL	BBL-5	33	9.37	0.00	0.13	0.99	0.00	7112.46	0.04	0.21	0.01	-7.68	0.91
BBL	BBL-5	34	14.99	0.00	25.35	0.37	0.00	7112.39	0.05	0.18	0.02	-8.19	0.40
BBL	BBL-5	35	n. a.	n. a.	n. a.	n. a.	n. a.	7112.34	0.01	0.16	0.01	-	-
BBL	BBL-5	40	11.71	0.00	15.32	0.44	0.00	7112.40	0.01	0.19	0.01	n. a.	n. a.
BBL	BBL-5	41	n. a.	n. a.	n. a.	n. a.	n. a.	7112.38	0.06	0.18	0.02	-	-
BBL	BBL-5	42	3.93	0.29	9.11	0.32	5.00	7112.33	0.07	0.16	0.02	-	-
BBL	BBL-5	43	2.43	0.08	7.65	0.25	2.43	7112.37	0.02	0.17	0.01	-8.20	0.39
BBL	BBL-5	44	4.24	0.13	8.56	0.34	2.08	7112.28	0.03	0.14	0.01	-8.74	-0.15
BBL	BBL-5	45	3.20	0.04	7.27	0.31	0.96	7112.36	0.03	0.17	0.01	-	-
BBL	BBL-5	46	3.47	0.63	5.73	0.43	10.58	7112.34	0.07	0.16	0.03	-8.40	0.19
BBL	BBL-5	47	4.26	0.03	8.35	0.34	0.44	7112.33	0.04	0.16	0.02	-8.46	0.13
BBL	BBL-5	49	3.00	0.00	7.30	0.29	0.02	7112.42	0.04	0.19	0.02	-7.87	0.72
BORG	BORG-1	30	10.02	2.85	7.19	0.66	10.19	7112.69	0.08	0.31	0.04	-	-
BORG	BORG-1	31	10.52	3.03	6.96	0.68	9.76	7112.61	0.06	0.28	0.03	-6.90	1.69
BORG	BORG-1	32	n. a.	n. a.	n. a.	n. a.	n. a.	7112.60	0.04	0.27	0.02	-	-
BORG	BORG-1	35	12.52	0.49	2.11	0.87	0.54	7112.40	0.03	0.19	0.01	-7.99	0.59
BORG	BORG-1	37	14.14	0.38	1.83	0.90	0.30	7112.50	0.02	0.23	0.01	-7.41	1.18
BORG	BORG-1	38	n. a.	n. a.	n. a.	n. a.	n. a.	7112.42	0.02	0.20	0.01	-7.83	0.76
BORG	BORG-1	40	15.51	1.24	1.56	0.92	0.68	7112.45	0.01	0.21	0.01	-7.66	0.93
BORG	BORG-1	41	n. a.	n. a.	n. a.	n. a.	n. a.	7112.47	0.10	0.22	0.04	-	-
BORG	BORG-1	42	10.23	0.31	1.48	0.88	0.38	7112.38	0.06	0.18	0.02	-8.14	0.45
BORG	BORG-1	43	24.69	0.09	0.00	1.01	0.00	7112.43	0.05	0.20	0.02	-7.75	0.84
BORG	BORG-1	44	19.83	0.62	1.25	0.95	0.18	7112.49	0.01	0.22	0.01	-7.57	1.02
BORG	BORG-1	45	15.71	0.44	0.00	1.01	0.00	7112.50	0.02	0.23	0.01	-7.39	1.20
BORG	MM-L17-BORG-2	1	15.32	0.37	3.13	0.84	0.40	n. a.	n. a.	n. a.	n. a.	n. a.	n. a.
BORG	MM-L17-BORG-2	2	14.45	0.40	2.01	0.89	0.33	n. a.	n. a.	n. a.	n. a.	n. a.	n. a.
BORG	MM-L17-BORG-2	3	20.09	1.08	0.13	1.00	0.03	n. a.	n. a.	n. a.	n. a.	n. a.	n. a.
BRM	BRM-1	34	28.26	2.47	0.00	1.01	0.00	7112.66	0.05	0.30	0.02	-6.61	1.98
BRM	BRM-1	35	13.88	0.06	0.00	1.01	0.00	n. a.	n. a.	n. a.	n. a.	n. a.	n. a.
BRM	BRM-1	39	13.73	0.98	17.08	0.47	3.83	n. a.	n. a.	n. a.	n. a.	n. a.	n. a.
BRM	BRM-1	41	5.47	2.47	0.00	1.01	0.00	n. a.	n. a.	n. a.	n. a.	n. a.	n. a.
BRM	MM-L17-BRM-2	14	16.25	0.77	0.00	1.01	0.00	n. a.	n. a.	n. a.	n. a.	n. a.	n. a.
BRM	MM-L17-BRM-2	17	6.92	1.23	2.00	0.81	3.52	n. a.	n. a.	n. a.	n. a.	n. a.	n. a.
BRM	MM-L17-BRM-2	18	15.30	0.89	0.00	1.01	0.00	n. a.	n. a.	n. a.	n. a.	n. a.	n. a.
BRM	MM-L17-BRM-2	23	13.89	0.76	0.00	1.01	0.00	n. a.	n. a.	n. a.	n. a.	n. a.	n. a.
BRM	MM-L17-BRM-2	24	17.50	0.30	0.00	1.01	0.00	7112.61	0.02	0.28	0.01	-7.08	1.51
BRM	MM-L17-BRM-2	25	16.57	0.92	0.00	1.01	0.00	7112.63	0.06	0.29	0.03	-7.06	1.53
BRM	MM-L17-BRM-2	26	13.24	1.03	0.00	1.01	0.00	7112.59	0.03	0.27	0.01	-7.28	1.32
BRM	MM-L17-BRM-2	27	14.28	0.83	0.00	1.01	0.00	7112.59	0.01	0.27	0.01	-	-
BRM	MM-L17-BRM-2	29	15.41	0.95	0.00	1.01	0.00	7112.57	0.03	0.26	0.01	-7.43	1.16
BRM	MM-L17-BRM-2	31	12.19	0.70	0.23	0.99	0.10	7112.62	0.02	0.28	0.01	-7.09	1.50
BRM	MM-L17-BRM-2	32	14.18	0.82	0.04	1.01	0.01	7112.60	0.05	0.27	0.02	-7.23	1.36
BRM	MM-L17-BRM-2	8	21.46	0.60	0.00	1.01	0.00	n. a.	n. a.	n. a.	n. a.	n. a.	n. a.
BPPC	MM-L17-BPPC-4	10	7.27	0.28	3.81	0.67	1.30	7112.36	0.06	0.17	0.02	-	-
BPPC	MM-L17-BPPC-4	11	12.48	1.24	2.43	0.86	1.50	7112.35	0.01	0.17	0.01	-	-
BPPC	MM-L17-BPPC-4	12	4.54	0.46	4.05	0.56	4.58	7112.46	0.05	0.21	0.02	-	-
BPPC	MM-L17-BPPC-4	13	4.07	0.49	2.85	0.62	4.67	7112.32	0.01	0.16	0.00	-8.51	0.08
BPPC	MM-L17-BPPC-4	14	5.65	0.67	4.36	0.60	4.88	7112.39	0.05	0.18	0.02	-8.12	0.47
BPPC	MM-L17-BPPC-4	15	4.08	0.31	2.59	0.64	2.83	7112.33	0.05	0.17	0.02	-8.34	0.25
BPPC	MM-L17-BPPC-4	2a	4.81	0.55	2.91	0.66	3.99	n. a.	n. a.	n. a.	n. a.	n. a.	n. a.
BPPC	MM-L17-BPPC-4	2b	7.65	0.74	0.35	0.97	0.39	n. a.	n. a.	n. a.	n. a.	n. a.	n. a.
BPPC	MM-L17-BPPC-4	5	16.15	1.03	0.79	0.96	0.28	n. a.	n. a.	n. a.	n. a.	n. a.	n. a.
BRVB	MM-L17-BRVB-2	2b	6.20	0.41	1.17	0.86	0.98	7112.45	0.02	0.21	0.01	-7.70	0.89
BRVB	MM-L17-BRVB-2	1	8.45	0.94	6.69	0.59	4.65	7112.33	0.01	0.16	0.00	-	-
BRVB	MM-L17-BRVB-2	10	12.41	0.43	2.14	0.86	0.50	7112.38	0.05	0.18	0.02	-8.09	0.50
BRVB	MM-L17-BRVB-2	2	7.83	0.67	1.93	0.82	1.58	7112.45	0.02	0.21	0.01	-7.70	0.89
BRVB	MM-L17-BRVB-2	4	n. a.	n. a.	n. a.	n. a.	n. a.	7112.41	0.06	0.19	0.02	-8.07	0.52
BRVB	MM-L17-BRVB-2	5a	11.40	0.87	3.07	0.81	1.53	7112.47	0.03	0.21	0.01	-	-
BRVB	MM-L17-BRVB-2	5b	12.95	0.93	3.49	0.81	1.44	n. a.	n. a.	n. a.	n. a.	n. a.	n. a.
BRVB	MM-L17-BRVB-2	6	5.69	0.64	3.06	0.68	3.68	7112.50	0.03	0.23	0.01	-7.50	1.09
BRVB	MM-L17-BRVB-2	7	6.72	0.38	3.01	0.71	1.69	7112.41	0.03	0.19	0.01	-8.05	0.54
BRVB	MM-L17-BRVB-2	9	9.88	0.29	1.44	0.88	0.36	7112.42	0.05	0.19	0.02	-	-

s.e. = standard error

n. a. = not analyzed

140

Table S6. Calculated Lassen primary magma compositions. Δ QFM calculated via Kress and Carmichael 1991 and Frost 1991 using primary magma compositions at 1400 °C, 1.6 Gpa. Major elements, S, Cl, and H2O reported in wt. %. Trace elements reported in ppm.

Cinder Cone	BORG	BBL	BRM	BRVB	BPPC	BAS-44
Δ QFM	1.42	0.95	1.95	1.18	0.78	0.75
$Fe^{3+}/\Sigma Fe$	0.22	0.17	0.28	0.20	0.17	0.17
$S^{6+}/\Sigma S$	0.88	0.41	1.00	0.74	0.58	0.46
$\delta^{34}S$	4.65	1.78	5.16	4.09	3.58	n.a.
SiO_2	49.02	47.80	49.58	49.45	50.72	48.10
TiO_2	0.67	0.92	0.90	1.24	0.75	0.88
Al_2O_3	16.51	14.78	17.78	14.72	15.89	15.45
FeO^T	9.01	10.45	7.65	9.74	7.79	9.11
MnO	0.10	0.10	0.08	0.12	0.12	0.12
MgO	12.01	14.09	9.25	13.35	11.10	12.44
CaO	9.42	8.66	9.59	8.48	10.49	9.78
Na_2O	2.57	2.64	3.82	2.90	2.54	2.53
K_2O	0.45	0.31	0.67	0.88	0.30	0.27
P_2O_5	0.09	0.15	0.22	0.26	0.15	0.15
S	0.10	0.08	0.19	0.14	0.10	0.10
Cl	0.05	0.02	0.26	0.04	0.04	0.03
H_2O	2.50	0.88	1.47	1.26	1.99	1.02
Li	4.9	7.6	8.1	9.6	6.1	5.2
B	2.8	2.2	2.9	19.4	2.2	2.3
Sc	31.4	33.0	23.2	26.9	31.6	34.7
V	230.8	219.9	207.2	219.3	203.1	200.0
Rb	5.3	5.7	10.4	18.0	4.5	4.5
Sr	440.6	252.2	1237.3	395.5	398.6	361.9
Y	11.0	19.1	11.4	16.7	14.3	16.7
Zr	46.5	72.0	89.8	90.9	51.9	69.5
Nb	2.0	3.0	4.8	6.2	1.3	2.5
Ba	139.9	153.0	228.3	321.4	94.4	105.0
La	4.8	6.0	15.1	12.0	4.8	6.7
Ce	11.8	15.6	35.7	28.9	12.1	17.8
Nd	7.5	9.7	17.9	16.8	7.8	11.0
Sm	1.9	2.6	3.2	3.7	2.1	2.6
Dy	2.1	3.6	2.1	3.3	2.5	2.8
Yb	1.2	2.3	1.1	1.8	1.6	1.9
Pb	2.2	1.9	4.5	3.5	1.6	1.5

n.a. = not analyzed.

Table S7. Reference standards used to calcualate Instrument Mass Fraction (IMF) during November 2019 sulfur SIMS analytical session.

Glass Standard	Description	$\delta^{34}S$ (‰)	$^{34}S/^{32}S$	S (ppm)	$S^{6+}/\Sigma S$	H_2O (wt. %)	References
ET10A	Enta basalt	-5.3	4.393E-02	n/a	n/a	n/a	[4]
ET1013D	Enta basalt	-2.7	4.404E-02	n/a	n/a	n/a	[4]
892-1	MORB glass	0.7	4.419E-02	1606	0.06	~0	[1,3]
ALV519-4-1	MORB glass	-0.2	4.415E-02	965	n/a	n/a	[4,4]
JDF46N	MORB glass	1.3	4.422E-02	1121	0.05	0.87*	[1,2,3]
NIST620	synthetic high-Si glass	7.68	4.450E-02	1121	1	0.18*	[1,5]
NIST621	synthetic high-Si glass	8.18	4.453E-02	521	1	0.20*	[1,5]
BCR2-10	Columbia River basalt	12.23	4.470E-02	n/a	n/a	n/a	[4]
ET83XXA	Synthetic Etna basalt glass	16.4	4.489E-02	822	~0	0.91*	[1]
Run #144	Synthetic andesite glass (Anhydrite bearing)	18.5	4.498E-02	1830	~1**	3.55	[1,5]

* Estimated via H_2O by difference based on reported EPMA data

** Reported as $S6+/\Sigma S = 0$ in Fiege 2014. However, we note that this glass is anhydrite saturated, indicating that it is sulfate dominated, as confirmed by communication with C. Mandeville

n/a = information unkown

[1] Fiege, A., Holtz, F., Shimizu, N., Mandeville, C. W., Behrens, H., & Knipping, J. L. (2014). Sulfur isotope fractionation between fluid and andesitic melt: An experimental study. Geochimica et Cosmochimica Acta, 142, 501–521.

[2] Black, B. A., Hauri, E. H., Elkins-Tanton, L. T., & Brown, S. M. (2014). Sulfur isotopic evidence for sources of volatiles in Siberian Traps magmas. Earth and Planetary Science Letters, 394, 58–69.

[3] Gurenko, A. A., Belousov, A. B., Kamenetsky, V. S., & Zelenski, M. E. (2018). Origin of volatiles emitted by Plinian mafic eruptions of the Chikurachki volcano, Kurile arc, Russia: Trace element, boron and sulphur isotope constraints. Chemical Geology, 478, 131–147.

[4] Internal WHOI measurements

[5] C. Mandeville personal communication

Table S8. Analytical conditions used for EPMA. Values in parentheses indicate off-peak counting times. Elements with no listed off-peak times were corrected via MAN corrections.

	Element	Na	Si	Ca	K	Al	Fe	Mg	Cl	Ti	S	Mn	P	Ni	Cr
June 2017 Glass	Count Time (s)	90	60	80	20 (20)	160	160	60	100 (25)	100 (25)	100 (25)	30 (15)	100 (25)	n. a.	n. a.
	Current (nA)	20	20	20	20	20	20	20	50	50	50	20	50	n. a.	n. a.
	Beam Size (10 μm)	10	10	10	10	10	10	10	10	10	10	10	10	10	10
June 2017 Olivine	Count Time (s)	n. a.	30	120	n. a.	160	40	120	n. a.	n. a.	n. a.	120 (15)	n. a.	80 (10)	n. a.
	Current (nA)	n. a.	30	30	n. a.	30	30	30	n. a.	n. a.	n. a.	30	n. a.	30	n. a.
	Beam Size (10 μm)	0	0	0	0	0	0	0	0	0	0	0	0	0	0
August 2018 Glass	Count Time (s)	30	15	40	16 (4)	60	70	180	80 (40)	60 (18)	80 (40)	40 (10)	16 (4)	n. a.	n. a.
	Current (nA)	10	10	10	10	10	10	50	50	50	50	50	10	n. a.	n. a.
	Beam Size (10 μm)	5	5	5	5	5	5	5	5	5	5	5	5	5	5
August 2018 Olivine	Count Time (s)	n. a.	120	80 (16)	n. a.	n. a.	120	150	n. a.	60 (10)	n. a.	n. a.	n. a.	60 (12)	100 (16)
	Current (nA)	n. a.	30	30	n. a.	n. a.	30	30	n. a.	30	n. a.	n. a.	n. a.	30	30
	Beam Size (10 μm)	0	0	0	0	0	0	0	0	0	0	0	0	0	0
November 2018 Olivine	Count Time (s)	n. a.	30	80	n. a.	30	30	90	n. a.	n. a.	n. a.	45 (15)	n. a.	60 (15)	n. a.
	Current (nA)	n. a.	30	30	n. a.	30	30	30	n. a.	n. a.	n. a.	30	n. a.	30	n. a.
	Beam Size (10 μm)	0	0	0	0	0	0	0	0	0	0	0	0	0	0
November 2019 Glass	Count Time (s)	40	30	40	20 (6)	30	30	90	100 (25)	200 (25)	160 (20)	45 (15)	200 (25)	n. a.	n. a.
	Current (nA)	10	10	50	10	10	10	50	50	50	50	50	50	n. a.	n. a.
	Beam Size (10 μm)	10	10	10	10	10	10	10	10	10	10	10	10	10	10
November 2019 Olivine	Count Time (s)	n. a.	30	80	n. a.	n. a.	30	90	n. a.	n. a.	n. a.	45 (15)	n. a.	60 (15)	n. a.
	Current (nA)	30	30	30	30	30	30	30	30	30	30	30	30	30	30
	Beam Size (10 μm)	0	0	0	0	0	0	0	0	0	0	0	0	0	0
February 2020 Olivine	Count Time (s)	n. a.	20 (10)	n. a.	n. a.	n. a.	20 (10)	20 (10)	n. a.	n. a.	n. a.	n. a.	n. a.	20 (10)	n. a.
	Current (nA)	n. a.	40	n. a.	n. a.	n. a.	40	40	n. a.	n. a.	n. a.	n. a.	n. a.	40	n. a.
	Beam Size (10 μm)	0	0	0	0	0	0	0	0	0	0	0	0	0	0

n. a. = not analyzed

Table S9. Model input paramters used to correct for PEC and Fe-Mg re-equillibration in melt inclusions, and to calculate reverse olivine crystallization for primary magma estimates. See supplementary text for details.

<u>PEC and Fe-Mg re-equllibration calculations</u>
Model conditions for forward olivine crystalization model

Cinder Cone	H$_2$O (wt. %)	f_{O2} (Δ QFM)
BRM	1.52	1.5
BORG	3.04	0.9
BAS-44	1.13	0.4
BRVB	1.68	0.5
BPPC	2.22	0.2

Starting composition for forward olivine crystalization model in cinder cone BRM and BBL (wt. %).

Cinder cone	SiO$_2$	TiO$_2$	Al$_2$O$_3$	FeO^T	MnO	MgO	CaO	Na$_2$O	K$_2$O	P$_2$O$_5$	H$_2$O
BRM	50.00	0.90	19.00	7.84	0.10	10.00	9.00	4.00	0.70	0.30	1.52
BBL	49.00	1.40	15.00	10.57	0.17	10.50	9.00	3.50	0.70	0.30	1.21

<u>Primary magma composition calculations</u>
Model conditions for reverse olivine crystalization model, and MgO content used to calculated average melt inclusion compositions for each cinder cone

Cinder Cone	H$_2$O content	f_{O2} (Δ QFM)	MgO cut-off (wt. %)
BRM	1.52	1.5	7.00
BORG	3.04	0.9	8.00
BAS-44	1.13	0.4	8.90
BRVB	1.68	0.5	7.10
BPPC	2.22	0.2	7.90
BBL	1.21	0.2	9.00

Table S10. Initial conditions used for mantle melting model in 'Normal Mantle' melting scenario.

Mantle Melting Source Composition		
Element	Slab Melt	Mantle Peridotite
SiO_2 (wt. %)	54.90	45.67
TiO_2 (wt. %)	0.18	0.11
Al_2O_3 (wt. %)	9.77	2.32
Cr_2O_3 (wt. %)	0.00	0.57
FeO (wt. %)	0.32	6.28
Fe_2O_3 (wt. %)	0.26	0.30
MnO (wt. %)	0.01	0.14
MgO (wt. %)	0.11	42.46
NiO (wt. %)	0.00	0.12
CaO (wt. %)	1.13	1.95
Na_2O (wt. %)	5.42	0.09
K_2O (wt. %)	0.83	0.02
H_2O (wt. %)	5.00	0.00
S^{6+} (ppm)	1500	0
S^{2-} (ppm)	0	150
La (ppm)	29.56	0.192
Ce (ppm)	46.53	0.550
Nd (ppm)	14.02	0.581
Sm (ppm)	1.29	0.239
Eu (ppm)	0.25	0.096
Gd (ppm)	0.44	0.358
Dy (ppm)	0.16	0.505
Er (ppm)	0.05	0.348
Yb (ppm)	0.04	0.365
Ba (ppm)	259.44	0.563
Th (ppm)	1.01	0.008
Y (ppm)	1.13	3.328
Hf (ppm)	1.30	0.157
U (ppm)	0.34	0.003
Pb (ppm)	5.48	0.018
Rb (ppm)	30.69	0.050
Sr (ppm)	1321.66	7.664

Mineral-Melt Partition Coefficients				
Element	Clinopyroxene	Orthopyroxene	Olivine	Spinel
La	0.054	0.00005	0.00003	0.003
Ce	0.09	0.00015	0.0001	0.003
Nd	0.15	0.0005	0.0004	0.005
Sm	0.25	0.0015	0.001	0.0075
Ba	0.00068	0.0001	0.0003	0.0005
Th	0.013	0.0001	0.00005	0.01
U	0.0038	0.0002	0.00002	0.01
Pb	0.008	0.008	0.008	0.008
Sr	0.13	0.0005	0.0015	0.1
Zr	0.123	0.014	0.0007	0.4
Dy	0.4	0.008	0.001	0.008
S^{6+}	0.017	0.002	0.001	0
S^{2-}	0.025	0.007	0.001	0
Fe^{3+}	0.2	0.2	0.2	0.2

P-T Path	
P (Gpa)	T (°C)
2.2	1100
2.1	1250
2.0	1300
1.8	1380
1.6	1400
1.4	1390
1.2	1370

Table S11. Compilation of sulfur isotopes from literature shown in Figure 2.
Full reference details are listed at the bottom of the compilation.

Citation	Location	Type	δ³⁴S (‰)	Citation	Location	Type	δ³⁴S (‰)	Citation	Location	Type	δ³⁴S (‰)
Taran 1995	Kurils	Gas	2.9	Benard 2018	Kamchatka (xenoli	Arc Magma	8.5	Turner 2018	Accretionary Wedg	Sediments	-33.9
Taran 1995	Kurils	Gas	5.9	Benard 2019	Kamchatka (xenoli	Arc Magma	10.1	Turner 2018	Accretionary Wedg	Sediments	-30.9
Taran 1995	Kurils	Gas	3.6	Benard 2020	Kamchatka (xenoli	Arc Magma	9.1	Turner 2018	Accretionary Wedg	Sediments	-28.9
Taran 1995	Kurils	Gas	6.4	Benard 2021	Kamchatka (xenoli	Arc Magma	10.0	Turner 2018	Accretionary Wedg	Sediments	-26.6
Williams 1990	Central America	Gas	0.8	Benard 2022	Kamchatka (xenoli	Arc Magma	11.0	Turner 2018	Accretionary Wedg	Sediments	-25.5
Williams 1990	Central America	Gas	0.8	Benard 2023	Kamchatka (xenoli	Arc Magma	8.5	Turner 2018	Accretionary Wedg	Sediments	-22.5
Williams 1990	Central America	Gas	1.8	Benard 2024	Kamchatka (xenoli	Arc Magma	7.0	Turner 2018	Accretionary Wedg	Sediments	-11.1
Williams 1990	Central America	Gas	2.9	Alt 1993	Izu-Mariana	Arc Magma	1.5	Turner 2018	Accretionary Wedg	Sediments	1.8
Williams 1990	Central America	Gas	3.3	Alt 1993	Izu-Mariana	Arc Magma	5.1	Turner 2018	Accretionary Wedg	Sediments	7.5
Goff 1998	Mexico	Gas	3.1	Alt 1993	Izu-Mariana	Arc Magma	5.5	Turner 2018	Accretionary Wedg	Sediments	-4.3
Goff 1998	Mexico	Gas	2.7	Alt 1993	Izu-Mariana	Arc Magma	0.1	Turner 2018	Accretionary Wedg	Sediments	-2.2
Goff 1998	Mexico	Gas	3.0	Alt 1993	Izu-Mariana	Arc Magma	4.0	Turner 2018	Accretionary Wedg	Sediments	-4.6
Goff 1998	Mexico	Gas	3.5	Alt 1993	Izu-Mariana	Arc Magma	4.0	Turner 2018	Accretionary Wedg	Sediments	-7.3
Goff 1998	Mexico	Gas	2.7	Bouvier 2008	Lesser Antilles	Arc Magma	5.3	Turner 2018	Accretionary Wedg	Sediments	-0.8
Goff 1998	Mexico	Gas	2.3	Bouvier 2008	Lesser Antilles	Arc Magma	-2.5	Turner 2018	Accretionary Wedg	Sediments	1.1
Goff 1998	Mexico	Gas	1.5	Bouvier 2008	Lesser Antilles	Arc Magma	2.3	Turner 2018	Accretionary Wedg	Sediments	-1.8
Goff 1998	Mexico	Gas	2.5	Bouvier 2008	Lesser Antilles	Arc Magma	-2.5	Turner 2018	Accretionary Wedg	Sediments	-1.6
Goff 1998	Mexico	Gas	3.0	Bouvier 2008	Lesser Antilles	Arc Magma	1.2	Turner 2018	Accretionary Wedg	Sediments	-26.1
Goff 1998	Mexico	Gas	6.5	Bouvier 2008	Lesser Antilles	Arc Magma	7.0	Turner 2018	Accretionary Wedg	Sediments	-15.6
Goff 1998	Mexico	Gas	3.9	Bouvier 2008	Lesser Antilles	Arc Magma	-9.0	Turner 2018	Accretionary Wedg	Sediments	-1.4
Goff 1998	Mexico	Gas	3.4	Bouvier 2008	Lesser Antilles	Arc Magma	-4.8	Turner 2018	Accretionary Wedg	Sediments	0.0
Goff 1998	Mexico	Gas	2.9	Bouvier 2008	Lesser Antilles	Arc Magma	0.5	Turner 2018	Accretionary Wedg	Sediments	-2.2
Goff 1998	Mexico	Gas	2.3	Bouvier 2008	Lesser Antilles	Arc Magma	1.5	Turner 2018	Accretionary Wedg	Sediments	-18.1
Goff 1998	Mexico	Gas	3.7	Bouvier 2008	Lesser Antilles	Arc Magma	1.1	Turner 2018	Accretionary Wedg	Sediments	-3.5
Goff 1998	Mexico	Gas	4.2	Bouvier 2008	Lesser Antilles	Arc Magma	0.8	Turner 2018	Accretionary Wedg	Sediments	-17.8
Goff 1998	Mexico	Gas	2.3	Bouvier 2008	Lesser Antilles	Arc Magma	2.1	Turner 2018	Accretionary Wedg	Sediments	-24.3
Goff 1998	Mexico	Gas	5.1	Bouvier 2008	Lesser Antilles	Arc Magma	2.8	Turner 2018	Accretionary Wedg	Sediments	-9.0
Goff 1998	Mexico	Gas	3.8	Bouvier 2008	Lesser Antilles	Arc Magma	3.3	Turner 2018	Accretionary Wedg	Sediments	-16.8
Goff 1998	Mexico	Gas	3.1	Bouvier 2008	Lesser Antilles	Arc Magma	-7.3	Turner 2018	Accretionary Wedg	Sediments	-8.8
Goff 1998	Mexico	Gas	3.5	Bouvier 2008	Lesser Antilles	Arc Magma	-8.2	Turner 2018	Accretionary Wedg	Sediments	-15.6
Goff 1998	Mexico	Gas	3.3	Bouvier 2008	Lesser Antilles	Arc Magma	-4.5	Turner 2018	Accretionary Wedg	Sediments	-13.8
Goff 1998	Mexico	Gas	3.2	Bouvier 2008	Lesser Antilles	Arc Magma	1.9	Turner 2018	Accretionary Wedg	Sediments	17.0
Goff 1998	Mexico	Gas	5.0	Bouvier 2008	Lesser Antilles	Arc Magma	1.7	Turner 2018	Accretionary Wedg	Sediments	0.8
Goff 1998	Mexico	Gas	5.4	Bouvier 2008	Lesser Antilles	Arc Magma	-2.1	Turner 2018	Accretionary Wedg	Sediments	-13.0
Goff 1998	Mexico	Gas	4.9	Bouvier 2008	Lesser Antilles	Arc Magma	3.1	Turner 2018	Accretionary Wedg	Sediments	-16.3
Goff 1998	Mexico	Gas	3.2	Bouvier 2008	Lesser Antilles	Arc Magma	2.9	Turner 2018	Accretionary Wedg	Sediments	7.2
Goff 1998	Mexico	Gas	3.4	Bouvier 2008	Lesser Antilles	Arc Magma	3.0	Turner 2018	Accretionary Wedg	Sediments	-13.2
Goff 1998	Mexico	Gas	3.4	Bouvier 2008	Lesser Antilles	Arc Magma	-1.9	Turner 2018	Accretionary Wedg	Sediments	-15.2
Goff 1998	Mexico	Gas	3.2	Bouvier 2008	Lesser Antilles	Arc Magma	5.5	Turner 2018	Accretionary Wedg	Sediments	-17.5
Goff 1998	Mexico	Gas	4.0	Bouvier 2008	Lesser Antilles	Arc Magma	4.9	Turner 2018	Accretionary Wedg	Sediments	2.9
Goff 1998	Mexico	Gas	2.9	Bouvier 2008	Lesser Antilles	Arc Magma	-4.9	Turner 2018	Accretionary Wedg	Sediments	0.4
Goff 1998	Mexico	Gas	3.2	Bouvier 2008	Lesser Antilles	Arc Magma	3.7	Turner 2018	Accretionary Wedg	Sediments	-11.4
Goff 1998	Mexico	Gas	3.5	Bouvier 2008	Lesser Antilles	Arc Magma	3.0	Turner 2018	Accretionary Wedg	Sediments	-17.3
Goff 1998	Mexico	Gas	3.3	Bouvier 2008	Lesser Antilles	Arc Magma	2.7	Turner 2018	Accretionary Wedg	Sediments	-20.4
Goff 1998	Mexico	Gas	3.4	Bouvier 2008	Lesser Antilles	Arc Magma	4.4	Turner 2018	Accretionary Wedg	Sediments	-15.7
Goff 1998	Mexico	Gas	2.8	Bouvier 2008	Lesser Antilles	Arc Magma	4.6	Turner 2018	Accretionary Wedg	Sediments	-23.9
Goff 1998	Mexico	Gas	2.3	Bouvier 2008	Lesser Antilles	Arc Magma	-3.3	Turner 2018	Accretionary Wedg	Sediments	-23.1
Goff 1998	Mexico	Gas	2.7	Bouvier 2008	Lesser Antilles	Arc Magma	-1.6	Turner 2018	Accretionary Wedg	Sediments	-10.6
Goff 1998	Mexico	Gas	2.1	Bouvier 2008	Lesser Antilles	Arc Magma	1.8	Turner 2018	Accretionary Wedg	Sediments	-10.3
Mather 2008	Central America	Gas	5.6	Bouvier 2008	Lesser Antilles	Arc Magma	2.3	Wang 2008	Accretionary Wedg	Sediments	-35.7
Mather 2008	Central America	Gas	5.4	Ueda 1984	Ryukyu Arc	Arc Magma	4.0	Wang 2008	Accretionary Wedg	Sediments	-32.6
Mather 2008	Central America	Gas	6.8	Ueda 1984	Ryukyu Arc	Arc Magma	4.0	Wang 2008	Accretionary Wedg	Sediments	-31.3
Mather 2008	Central America	Gas	6.6	De Hoog 2001	Indonesia	Arc Magma	4.1	Wang 2008	Accretionary Wedg	Sediments	-30.4
Mather 2008	Central America	Gas	10.9	De Hoog 2001	Indonesia	Arc Magma	4.5	Wang 2008	Accretionary Wedg	Sediments	-22.1
Mather 2008	Central America	Gas	6.5	De Hoog 2001	Indonesia	Arc Magma	3.4	Wang 2008	Accretionary Wedg	Sediments	-19.2
Mather 2008	Central America	Gas	4.9	De Hoog 2001	Indonesia	Arc Magma	5.2	Wang 2008	Accretionary Wedg	Sediments	-12.9
Mather 2008	Central America	Gas	7.1	De Hoog 2001	Indonesia	Arc Magma	4.8	Wang 2008	Accretionary Wedg	Sediments	-9.3
Mather 2008	Central America	Gas	7.1	De Hoog 2001	Indonesia	Arc Magma	4.2	Wang 2008	Accretionary Wedg	Sediments	-7.1
Mather 2008	Central America	Gas	7.9	De Hoog 2001	Indonesia	Arc Magma	5.8	Wang 2008	Accretionary Wedg	Sediments	-6.5
Mather 2008	Central America	Gas	7.4	De Hoog 2001	Indonesia	Arc Magma	3.5	Wang 2008	Accretionary Wedg	Sediments	-5.9
Mather 2008	Central America	Gas	7.3	De Hoog 2001	Indonesia	Arc Magma	2.5	Wang 2008	Accretionary Wedg	Sediments	-5.0
Mather 2008	Central America	Gas	5.8	De Hoog 2001	Indonesia	Arc Magma	4.4	Wang 2008	Accretionary Wedg	Sediments	-3.9
Mather 2008	Central America	Gas	5.7	De Hoog 2001	Indonesia	Arc Magma	2.0	Wang 2008	Accretionary Wedg	Sediments	-3.8
Mather 2008	Central America	Gas	6.0	De Hoog 2001	Indonesia	Arc Magma	5.2	Wang 2008	Accretionary Wedg	Sediments	-1.1
Mather 2008	Central America	Gas	5.5	De Hoog 2001	Indonesia	Arc Magma	28.0	Wang 2008	Accretionary Wedg	Sediments	0.5
Mather 2008	Central America	Gas	8.5	De Hoog 2001	Indonesia	Arc Magma	20.0	Wang 2008	Accretionary Wedg	Sediments	0.7
Mather 2008	Central America	Gas	5.5	De Hoog 2001	Indonesia	Arc Magma	6.0	Wang 2008	Accretionary Wedg	Sediments	2.0
Mather 2008	Central America	Gas	6.2	De Hoog 2001	Indonesia	Arc Magma	6.8	Wang 2008	Accretionary Wedg	Sediments	2.9
Mather 2008	Central America	Gas	6.2	De Hoog 2001	Indonesia	Arc Magma	4.3	Wang 2008	Accretionary Wedg	Sediments	5.6
Mather 2008	Central America	Gas	5.8	De Hoog 2001	Indonesia	Arc Magma	1.7	Wang 2008	Accretionary Wedg	Sediments	7.2
Mather 2008	Central America	Gas	6.1	De Hoog 2001	Indonesia	Arc Magma	3.8	Wang 2008	Accretionary Wedg	Sediments	8.4
Mather 2008	Central America	Gas	6.8	De Hoog 2001	Indonesia	Arc Magma	7.8	Wang 2008	Accretionary Wedg	Sediments	10.3
Mather 2008	Central America	Gas	7.5	De Hoog 2001	Indonesia	Arc Magma	6.8	Wang 2008	Accretionary Wedg	Sediments	11.9
Mather 2008	Central America	Gas	5.9	De Hoog 2001	Indonesia	Arc Magma	4.9	Wang 2008	Accretionary Wedg	Sediments	13.9
Mather 2008	Central America	Gas	5.9	De Hoog 2001	Indonesia	Arc Magma	6.0	Wang 2008	Accretionary Wedg	Sediments	16.0
Mather 2008	Central America	Gas	6.3	De Hoog 2001	Indonesia	Arc Magma	5.9	Wang 2008	Accretionary Wedg	Sediments	17.4
Mather 2008	Central America	Gas	6.0	De Hoog 2001	Indonesia	Arc Magma	4.7	Wang 2008	Accretionary Wedg	Sediments	20.1
Mather 2008	Central America	Gas	6.6	Gurenko 2018	Kamchatka	Arc Magma	6.7	Wang 2008	Accretionary Wedg	Sediments	22.5
Mather 2008	Central America	Gas	7.5	Gurenko 2018	Kamchatka	Arc Magma	6.9	Wang 2008	Accretionary Wedg	Sediments	24.1
Mather 2008	Central America	Gas	6.2	Gurenko 2018	Kamchatka	Arc Magma	10.1	Wang 2008	Accretionary Wedg	Sediments	32.7
Mather 2008	Central America	Gas	5.0	Gurenko 2018	Kamchatka	Arc Magma	6.7	Wang 2008	Accretionary Wedg	Sediments	-27.9
Mather 2008	Central America	Gas	6.3	Gurenko 2018	Kamchatka	Arc Magma	4.2	Wang 2008	Accretionary Wedg	Sediments	-25.3
Mather 2008	Central America	Gas	7.8	Gurenko 2018	Kamchatka	Arc Magma	7.0	Wang 2008	Accretionary Wedg	Sediments	-23.3
Mather 2008	Central America	Gas	5.0	Gurenko 2018	Kamchatka	Arc Magma	5.5	Wang 2008	Accretionary Wedg	Sediments	-21.6
Mather 2008	Central America	Gas	4.9	Gurenko 2018	Kamchatka	Arc Magma	-1.6	Wang 2008	Accretionary Wedg	Sediments	-15.8
Mather 2008	Central America	Gas	10.0	Gurenko 2018	Kamchatka	Arc Magma	6.6	Wang 2008	Accretionary Wedg	Sediments	-14.7
Mather 2008	Central America	Gas	4.6	Gurenko 2018	Kamchatka	Arc Magma	7.6	Wang 2008	Accretionary Wedg	Sediments	-13.7
Mather 2008	Central America	Gas	5.0	Gurenko 2018	Kamchatka	Arc Magma	6.1	Wang 2008	Accretionary Wedg	Sediments	-11.7
Mather 2008	Central America	Gas	5.0	Gurenko 2018	Kamchatka	Arc Magma	3.7	Wang 2008	Accretionary Wedg	Sediments	-11.4
Mather 2008	Central America	Gas	4.7	Gurenko 2018	Kamchatka	Arc Magma	4.4	Wang 2008	Accretionary Wedg	Sediments	-10.0
Mather 2008	Central America	Gas	4.9	Gurenko 2018	Kamchatka	Arc Magma	12.3	Wang 2008	Accretionary Wedg	Sediments	-9.1
Mather 2008	Central America	Gas	5.5	Gurenko 2018	Kamchatka	Arc Magma	6.9	Wang 2008	Accretionary Wedg	Sediments	-5.0
Mather 2008	Central America	Gas	6.5	Ueda 1984	Japan	Arc Magma	4.8	Wang 2008	Accretionary Wedg	Sediments	-4.2
Mather 2008	Central America	Gas	6.9	Ueda 1984	Japan	Arc Magma	4.2	Wang 2008	Accretionary Wedg	Sediments	-1.1
Mather 2008	Central America	Gas	7.2	Ueda 1984	Japan	Arc Magma	5.0	Wang 2008	Accretionary Wedg	Sediments	3.6
Mather 2008	Central America	Gas	4.9	Ueda 1984	Japan	Arc Magma	0.0	Wang 2008	Accretionary Wedg	Sediments	4.1
Mather 2008	Central America	Gas	4.7	Ueda 1984	Japan	Arc Magma	8.6	Wang 2008	Accretionary Wedg	Sediments	7.6
Mather 2008	Central America	Gas	8.1	Ueda 1984	Japan	Arc Magma	1.9	Wang 2008	Accretionary Wedg	Sediments	10.5
Mather 2008	Central America	Gas	5.9	Ueda 1984	Japan	Arc Magma	4.1	Wang 2008	Accretionary Wedg	Sediments	15.5
Mather 2008	Central America	Gas	6.8	Ueda 1984	Japan	Arc Magma	4.7	Wang 2008	Accretionary Wedg	Sediments	18.7
Mather 2008	Central America	Gas	8.0	Ueda 1984	Japan	Arc Magma	4.4	Wang 2008	Accretionary Wedg	Sediments	22.6
Mather 2008	Central America	Gas	6.9	Ueda 1984	Japan	Arc Magma	5.9	Wang 2008	Accretionary Wedg	Sediments	36.1
Mather 2008	Central America	Gas	5.4	Ueda 1984	Japan	Arc Magma	3.6	Wang 2008	Accretionary Wedg	Sediments	53.5
Mather 2008	Central America	Gas	5.3	Ueda 1984	Izu-Mariana	Arc Magma	5.3	Wang 2008	Accretionary Wedg	Sediments	-18.0
Mather 2008	Central America	Gas	11.6	Ueda 1984	Izu-Mariana	Arc Magma	2.7	Wang 2008	Accretionary Wedg	Sediments	-15.5
Mather 2008	Central America	Gas	9.5	Ueda 1984	Izu-Mariana	Arc Magma	5.6	Wang 2008	Accretionary Wedg	Sediments	-13.0
Mather 2008	Central America	Gas	6.2	Ueda 1984	Japan	Arc Magma	0.7	Wang 2008	Accretionary Wedg	Sediments	11.3
Mather 2008	Central America	Gas	7.0	Ueda 1984	Japan	Arc Magma	1.9	Wang 2008	Accretionary Wedg	Sediments	13.2
Mather 2008	Central America	Gas	6.3	Ueda 1984	Japan	Arc Magma	2.3	Wang 2008	Accretionary Wedg	Sediments	16.1
Mather 2008	Central America	Gas	6.9	Sasaki 1979	Japan, Granitoid	Intrusive	1.2	Wang 2008	Accretionary Wedg	Sediments	-34.2
Mather 2008	Central America	Gas	7.8	Sasaki 1979	Japan, Granitoid	Intrusive	4.4	Wang 2008	Accretionary Wedg	Sediments	-33.6
Mather 2008	Central America	Gas	7.7	Sasaki 1979	Japan, Granitoid	Intrusive	8.3	Wang 2008	Accretionary Wedg	Sediments	-30.4
Mather 2008	Central America	Gas	7.0	Sasaki 1979	Japan, Granitoid	Intrusive	4.8	Wang 2008	Accretionary Wedg	Sediments	-27.5

Citation	Location	Type	δ³⁴S (‰)
Mather 2008	Central America	Gas	6.5
Mather 2008	Central America	Gas	5.6
Mather 2008	Central America	Gas	7.6
Mather 2008	Central America	Gas	8.0
Mather 2008	Central America	Gas	7.0
Mather 2008	Central America	Gas	6.8
Mather 2008	Central America	Gas	11.7
Mather 2008	Central America	Gas	5.8
Mather 2008	Central America	Gas	6.9
Mather 2008	Central America	Gas	7.9
Mather 2008	Central America	Gas	8.7
Mather 2008	Central America	Gas	6.7
Mather 2008	Central America	Gas	10.3
Menyailov 1986	Central America	Gas	4.2
Menyailov 1986	Central America	Gas	6.8
Menyailov 1986	Central America	Gas	6.8
Giggenbach 1982	New Zealand	Gas	3.0
Giggenbach 1982	New Zealand	Gas	5.0
Giggenbach 1982	New Zealand	Gas	-2.0
Giggenbach 1982	New Zealand	Gas	6.0
Giggenbach 1982	New Zealand	Gas	4.0
Giggenbach 1982	New Zealand	Gas	4.4
Giggenbach 1982	New Zealand	Gas	2.9
Giggenbach 1982	New Zealand	Gas	3.6
Giggenbach 1982	New Zealand	Gas	3.0
Giggenbach 1982	New Zealand	Gas	4.0
Taran 2002	Mexico	Gas	3.6
Taran 2002	Mexico	Gas	2.9
Taran 2002	Mexico	Gas	3.8
de Moor 2013	Central America	Gas	5.1
de Moor 2013	Central America	Gas	4.3
de Moor 2013	Central America	Gas	4.5
de Moor 2013	Central America	Gas	5.1
de Moor 2013	Central America	Gas	5.4
de Moor 2013	Central America	Gas	4.7
de Moor 2013	Central America	Gas	4.8
Taran 1995	Kurils	Gas	2.9
Taran 1995	Kurils	Gas	5.9
Taran 1995	Kurils	Gas	3.6
Taran 1995	Kurils	Gas	6.4
Taran 2001	Mexico	Gas	3.6
Taran 2001	Mexico	Gas	2.9
Taran 2001	Mexico	Gas	3.8
Poorter 1991	Indonesia	Gas	5.5
Poorter 1991	Indonesia	Gas	4.9
Poorter 1991	Indonesia	Gas	1.6
Poorter 1991	Indonesia	Gas	2.2
Taran 1992	Kamchatka	Gas	6.8
Taran 1992	Kamchatka	Gas	7.5
Taran 1992	Kamchatka	Gas	8.8
Kasasaku 1999	Japan	Gas	5.2
Kasasaku 1999	Japan	Gas	8.4
Kasasaku 1999	Japan	Gas	7.4
Kasasaku 1999	Japan	Gas	5.6
Kasasaku 1999	Japan	Gas	4.7
Kasasaku 1999	Japan	Gas	3.2
Kasasaku 1999	Japan	Gas	4.4
Mizutani 1986	Japan	Gas	3.5
Mizutani 1986	Japan	Gas	3.2
Mizutani 1986	Japan	Gas	4.9
Mizutani 1986	Japan	Gas	3.0
Mizutani 1986	Japan	Gas	5.0
Mizutani 1986	Japan	Gas	5.7
Mizutani 1986	Japan	Gas	7.9
Mizutani 1986	Japan	Gas	4.9
Mizutani 1986	Japan	Gas	4.6
Mizutani 1986	Japan	Gas	4.5
Mizutani 1986	Japan	Gas	-0.1
Mizutani 1986	Japan	Gas	3.0
Mizutani 1986	Japan	Gas	4.7
Ohba 2008	Japan	Gas	4.4
Ohba 2008	Japan	Gas	5.7
Shinohara 1993	Japan	Gas	10.6
Shinohara 1993	Japan	Gas	10.3
Shinohara 1993	Japan	Gas	9.8
Shinohara 1993	Japan	Gas	10.1
Shinohara 1993	Japan	Gas	10.9
Shinohara 1993	Japan	Gas	9.7
Shinohara 1993	Japan	Gas	6.0
Shinohara 1993	Japan	Gas	13.2
Shinohara 1993	Japan	Gas	13.5
Sakai 1977	Japan	Gas	12.1
Sakai 1977	Japan	Gas	11.7
Sakai 1977	Japan	Gas	12.5
Sakai 1977	Japan	Gas	4.5
Sakai 1977	Japan	Gas	5.6
Sakai 1977	Japan	Gas	6.9
Sakai 1977	Japan	Gas	2.2
Sakai 1977	Japan	Gas	4.5
Sakai 1977	Japan	Gas	4.4
Taran 1997	Kamchatka	Gas	5.4
Taran 1997	Kamchatka	Gas	7.3

Citation	Location	Type	δ³⁴S (‰)
Sasaki 1979	Japan, Granitoid	Intrusive	3.9
Sasaki 1979	Japan, Granitoid	Intrusive	6.3
Sasaki 1979	Japan, Granitoid	Intrusive	6.0
Sasaki 1979	Japan, Granitoid	Intrusive	9.1
Sasaki 1979	Japan, Granitoid	Intrusive	5.7
Sasaki 1979	Japan, Granitoid	Intrusive	4.7
Sasaki 1979	Japan, Granitoid	Intrusive	0.5
Sasaki 1979	Japan, Granitoid	Intrusive	2.5
Sasaki 1979	Japan, Granitoid	Intrusive	1.0
Sasaki 1979	Japan, Granitoid	Intrusive	2.3
Sasaki 1979	Japan, Granitoid	Intrusive	2.2
Sasaki 1979	Japan, Granitoid	Intrusive	2.7
Sasaki 1979	Japan, Granitoid	Intrusive	4.3
Sasaki 1979	Japan, Granitoid	Intrusive	6.7
Ishihara 1989	Sierra Nevada, Gra	Intrusive	1.6
Ishihara 1989	Sierra Nevada, Gra	Intrusive	4.0
Ishihara 1989	Sierra Nevada, Gra	Intrusive	3.6
Ishihara 1989	Sierra Nevada, Gra	Intrusive	2.3
Ishihara 1989	Sierra Nevada, Gra	Intrusive	2.9
Lee 2018	Sierra Nevada, Pyr	Intrusive	0.5
Lee 2018	Sierra Nevada, Pyr	Intrusive	1.2
Lee 2018	Sierra Nevada, Pyr	Intrusive	1.7
Lee 2018	Sierra Nevada, Pyr	Intrusive	1.0
Lee 2018	Sierra Nevada, Pyr	Intrusive	0.4
Lee 2018	Sierra Nevada, Pyr	Intrusive	-0.1
Lee 2018	Sierra Nevada, Pyr	Intrusive	2.2
Lee 2018	Sierra Nevada, Pyr	Intrusive	4.5
Lee 2018	Sierra Nevada, Pyr	Intrusive	3.2
Lee 2018	Sierra Nevada, Pyr	Intrusive	2.0
Lee 2018	Sierra Nevada, Pyr	Intrusive	2.8

Citation	Location	Type	δ³⁴S (‰)
Wang 2008	Accretionary Wedg Sediments		-25.6
Wang 2008	Accretionary Wedg Sediments		-25.4
Wang 2008	Accretionary Wedg Sediments		-23.4
Wang 2008	Accretionary Wedg Sediments		-23.0
Wang 2008	Accretionary Wedg Sediments		-19.9
Wang 2008	Accretionary Wedg Sediments		-17.9
Wang 2008	Accretionary Wedg Sediments		-16.2
Wang 2008	Accretionary Wedg Sediments		-15.6
Wang 2008	Accretionary Wedg Sediments		-14.0
Wang 2008	Accretionary Wedg Sediments		-10.4
Wang 2008	Accretionary Wedg Sediments		-7.8
Wang 2008	Accretionary Wedg Sediments		-7.4
Wang 2008	Accretionary Wedg Sediments		-6.9
Wang 2008	Accretionary Wedg Sediments		-5.3
Wang 2008	Accretionary Wedg Sediments		-3.1
Wang 2008	Accretionary Wedg Sediments		-2.9
Wang 2008	Accretionary Wedg Sediments		-2.7
Wang 2008	Accretionary Wedg Sediments		4.6
Wang 2008	Accretionary Wedg Sediments		6.2
Wang 2008	Accretionary Wedg Sediments		12.6
Wang 2008	Accretionary Wedg Sediments		21.0
Wang 2008	Accretionary Wedg Sediments		23.8
Wang 2008	Accretionary Wedg Sediments		-35.6
Wang 2008	Accretionary Wedg Sediments		-32.6
Wang 2008	Accretionary Wedg Sediments		-31.6
Wang 2008	Accretionary Wedg Sediments		-30.1
Wang 2008	Accretionary Wedg Sediments		-22.6
Wang 2008	Accretionary Wedg Sediments		-19.4
Wang 2008	Accretionary Wedg Sediments		-12.8
Wang 2008	Accretionary Wedg Sediments		-9.9
Wang 2008	Accretionary Wedg Sediments		-7.1
Wang 2008	Accretionary Wedg Sediments		-6.5
Wang 2008	Accretionary Wedg Sediments		-5.8
Wang 2008	Accretionary Wedg Sediments		-5.1
Wang 2008	Accretionary Wedg Sediments		-4.4
Wang 2008	Accretionary Wedg Sediments		-3.9
Wang 2008	Accretionary Wedg Sediments		-1.5
Wang 2008	Accretionary Wedg Sediments		0.6
Wang 2008	Accretionary Wedg Sediments		0.6
Wang 2008	Accretionary Wedg Sediments		0.6
Wang 2008	Accretionary Wedg Sediments		0.8
Wang 2008	Accretionary Wedg Sediments		1.8
Wang 2008	Accretionary Wedg Sediments		2.8
Wang 2008	Accretionary Wedg Sediments		5.5
Wang 2008	Accretionary Wedg Sediments		7.0
Wang 2008	Accretionary Wedg Sediments		8.2
Wang 2008	Accretionary Wedg Sediments		10.3
Wang 2008	Accretionary Wedg Sediments		12.0
Wang 2008	Accretionary Wedg Sediments		15.9
Wang 2008	Accretionary Wedg Sediments		17.3
Wang 2008	Accretionary Wedg Sediments		17.3
Wang 2008	Accretionary Wedg Sediments		19.5
Wang 2008	Accretionary Wedg Sediments		22.4
Wang 2008	Accretionary Wedg Sediments		23.7
Wang 2008	Accretionary Wedg Sediments		32.3
Wang 2008	Accretionary Wedg Sediments		-35.1
Wang 2008	Accretionary Wedg Sediments		-28.6
Wang 2008	Accretionary Wedg Sediments		-28.6
Wang 2008	Accretionary Wedg Sediments		-28.1
Wang 2008	Accretionary Wedg Sediments		-23.3
Wang 2008	Accretionary Wedg Sediments		-22.1
Wang 2008	Accretionary Wedg Sediments		-19.6
Wang 2008	Accretionary Wedg Sediments		-19.6
Wang 2008	Accretionary Wedg Sediments		-16.7
Wang 2008	Accretionary Wedg Sediments		-16.0
Wang 2008	Accretionary Wedg Sediments		-15.8
Wang 2008	Accretionary Wedg Sediments		-12.0
Wang 2008	Accretionary Wedg Sediments		-10.9
Wang 2008	Accretionary Wedg Sediments		-10.2
Wang 2008	Accretionary Wedg Sediments		-9.3
Wang 2008	Accretionary Wedg Sediments		-4.1
Wang 2008	Accretionary Wedg Sediments		-3.2
Wang 2008	Accretionary Wedg Sediments		-0.6
Wang 2008	Accretionary Wedg Sediments		2.7
Wang 2008	Accretionary Wedg Sediments		3.8
Wang 2008	Accretionary Wedg Sediments		4.4
Wang 2008	Accretionary Wedg Sediments		4.6
Wang 2008	Accretionary Wedg Sediments		5.6
Wang 2008	Accretionary Wedg Sediments		5.6
Wang 2008	Accretionary Wedg Sediments		5.9
Wang 2008	Accretionary Wedg Sediments		7.9
Wang 2008	Accretionary Wedg Sediments		13.3
Wang 2008	Accretionary Wedg Sediments		14.1
Wang 2008	Accretionary Wedg Sediments		14.2
Wang 2008	Accretionary Wedg Sediments		14.7
Wang 2008	Accretionary Wedg Sediments		16.6
Wang 2008	Accretionary Wedg Sediments		16.8
Wang 2008	Accretionary Wedg Sediments		21.3
Wang 2008	Accretionary Wedg Sediments		28.1
Wang 2008	Accretionary Wedg Sediments		28.6
Wang 2008	Accretionary Wedg Sediments		-32.3
Wang 2008	Accretionary Wedg Sediments		-31.0
Wang 2008	Accretionary Wedg Sediments		-25.0
Wang 2008	Accretionary Wedg Sediments		-23.0
Wang 2008	Accretionary Wedg Sediments		-21.8
Wang 2008	Accretionary Wedg Sediments		-15.1
Wang 2008	Accretionary Wedg Sediments		-8.2
Wang 2008	Accretionary Wedg Sediments		9.1
Wang 2008	Accretionary Wedg Sediments		30.8

Citation	Location	Type	δ³⁴S (‰)	Citation	Location	Type	δ³⁴S (‰)	Citation	Location	Type	δ³⁴S (‰)
Alt 1992	Mariana Basin	Sediments	12.0	Alford 2011	Gabbro	AOC	4.7	Alt 2013	Low Temperature S	Serpentinite	-16.8
Canfield 2009	Sedimentary Pyrite	Sediments	-8.1	Alford 2011	Gabbro	AOC	8.7	Alt 2013	Low Temperature S	Serpentinite	-8.6
Canfield 2009	Sedimentary Pyrite	Sediments	-17.4	Alford 2011	Gabbro	AOC	1.2	Alt 2013	Low Temperature S	Serpentinite	-20.2
Canfield 2009	Sedimentary Pyrite	Sediments	-16.0	Alford 2011	Gabbro	AOC	16.1	Alt 2013	Low Temperature S	Serpentinite	9.0
Canfield 2009	Sedimentary Pyrite	Sediments	-30.0	Alford 2011	Gabbro	AOC	6.4	Alt 2013	High Temperature S	Serpentinite	8.0
Canfield 2009	Sedimentary Pyrite	Sediments	-13.0	Alford 2011	Gabbro	AOC	9.6	Alt 2013	High Temperature S	Serpentinite	7.4
Canfield 2009	Sedimentary Pyrite	Sediments	-23.4	Alford 2011	Gabbro	AOC	7.0	Alt 2013	High Temperature S	Serpentinite	5.7
Canfield 2009	Sedimentary Pyrite	Sediments	0.3	Alford 2011	Gabbro	AOC	0.2	Alt 2013	High Temperature S	Serpentinite	-5.8
Canfield 2009	Sedimentary Pyrite	Sediments	-28.5	Alford 2011	Gabbro	AOC	8.1	Alt 2013	High Temperature S	Serpentinite	4.6
Canfield 2009	Sedimentary Pyrite	Sediments	-35.0	Alford 2011	Gabbro	AOC	5.9	Alt 2013	Exhumed Serp. (H	Serpentinite	10.7
Canfield 2009	Sedimentary Pyrite	Sediments	-42.0	Alford 2011	Gabbro	AOC	-1.4	Alt 2013	Exhumed Serp. (H	Serpentinite	5.5
Canfield 2009	Sedimentary Pyrite	Sediments	-14.0	Alford 2011	Gabbro	AOC	2.0	Alt 2013	Low Temperature S	Serpentinite	4.4
Canfield 2009	Sedimentary Pyrite	Sediments	-12.5	Alford 2011	Gabbro	AOC	0.9	Alt 2013	Low Temperature S	Serpentinite	1.5
Canfield 2009	Sedimentary Pyrite	Sediments	-22.0	Alford 2011	Gabbro	AOC	-0.5	Alt 2013	Low Temperature S	Serpentinite	-8.5
Canfield 2009	Sedimentary Pyrite	Sediments	-9.5	Alford 2011	Gabbro	AOC	-1.5	Alt 2013	Low Temperature S	Serpentinite	-8.5
Canfield 2009	Sedimentary Pyrite	Sediments	-20.0	Alford 2011	Gabbro	AOC	4.8	Alt 2013	Low Temperature S	Serpentinite	15.1
Canfield 2009	Sedimentary Pyrite	Sediments	-10.0	Alford 2011	Gabbro	AOC	5.2	Alt 2013	High Temperature S	Serpentinite	6.9
Canfield 2009	Sedimentary Pyrite	Sediments	-30.0	Alford 2011	Gabbro	AOC	2.1	Alt 2013	High Temperature S	Serpentinite	11.1
Canfield 2009	Sedimentary Pyrite	Sediments	-5.0	Alt 1991	Gabbro	AOC	0.9	Alt 2013	High Temperature S	Serpentinite	4.5
Canfield 2009	Sedimentary Pyrite	Sediments	-35.0	Alt 1991	Gabbro	AOC	3.2	Alt 2013	High Temperature S	Serpentinite	9.0
Canfield 2009	Sedimentary Pyrite	Sediments	-17.0	Alt 1991	Gabbro	AOC	1.8	Alt 2013	High Temperature S	Serpentinite	4.4
Canfield 2009	Sedimentary Pyrite	Sediments	-24.0	Alt 1991	Gabbro	AOC	-3.3	Alt 2013	Exhumed Serp. (H	Serpentinite	9.3
Canfield 2009	Sedimentary Pyrite	Sediments	-21.0	Alt 1991	Gabbro	AOC	0.0	Alt 2013	Exhumed Serp. (H	Serpentinite	5.0
Canfield 2009	Sedimentary Pyrite	Sediments	-12.0	Alt 1991	Gabbro	AOC	1.0	Alt 2013	Exhumed Serp. (H	Serpentinite	1.2
Canfield 2009	Sedimentary Pyrite	Sediments	-38.3	Alt 1991	Gabbro	AOC	-2.2	Alt 2012a	Exhumed Serp. (H	Serpentinite	-2.8
Canfield 2009	Sedimentary Pyrite	Sediments	-31.0	Alt 1991	Gabbro	AOC	0.5	Alt 2012a	Exhumed Serp. (H	Serpentinite	9.7
Canfield 2009	Sedimentary Pyrite	Sediments	-31.0	Alt 1991	Gabbro	AOC	0.5	Alt 2012a	Exhumed Serp. (H	Serpentinite	8.7
Canfield 2009	Sedimentary Pyrite	Sediments	-22.9	Alt 1991	Gabbro	AOC	1.4	Alt 2012a	Exhumed Serp. (H	Serpentinite	5.6
Canfield 2009	Sedimentary Pyrite	Sediments	-46.0	Alt 1991	Gabbro	AOC	0.6	Alt 2012a	Exhumed Serp. (H	Serpentinite	4.9
Canfield 2009	Sedimentary Pyrite	Sediments	-37.4	Walters 2019	Gabbro Sulfides (I	AOC	2.5	Alt 2012a	Exhumed Serp. (H	Serpentinite	7.3
Canfield 2009	Sedimentary Pyrite	Sediments	-43.5	Alt 1989	Dike Sulfides, East	AOC	1.4	Alt 2012a	Exhumed Serp. (H	Serpentinite	-7.0
Canfield 2009	Sedimentary Pyrite	Sediments	-35.9	Alt 1989	Dike Sulfides, East	AOC	-0.2	Alt 2012a	Exhumed Serp. (H	Serpentinite	-3.5
Canfield 2009	Sedimentary Pyrite	Sediments	-38.3	Alt 1989	Dike Sulfides, East	AOC	1.4	Alt 2012a	Exhumed Serp. (H	Serpentinite	2.7
Canfield 2009	Sedimentary Pyrite	Sediments	-34.6	Alt 1989	Dike Sulfides, East	AOC	-0.3	Alt 2012a	Exhumed Serp. (H	Serpentinite	6.2
Canfield 2009	Sedimentary Pyrite	Sediments	-37.9	Alt 1989	Dike Sulfides, East	AOC	0.7	Alt 2012b	Exhumed Serp. (H	Serpentinite	14.3
Canfield 2009	Sedimentary Pyrite	Sediments	-24.7	Alt 1989	Dike Sulfides, East	AOC	-0.3	Alt 2012b	Exhumed Serp. (H	Serpentinite	11.5
Canfield 2009	Sedimentary Pyrite	Sediments	-28.9	Alt 1989	Dike Sulfides, East	AOC	-0.1	Alt 2012b	Exhumed Serp. (H	Serpentinite	9.6
Canfield 2009	Sedimentary Pyrite	Sediments	-40.3	Alt 1989	Dike Sulfides, East	AOC	0.4	Alt 2012b	Exhumed Serp. (H	Serpentinite	7.8
Canfield 2009	Sedimentary Pyrite	Sediments	-43.0	Alt 1989	Dike Sulfides, East	AOC	0.0	Schwarzenbach 20	Exhumed Serp. (H	Serpentinite	-8.5
Canfield 2009	Sedimentary Pyrite	Sediments	-30.2	Alt 1989	Dike Sulfides, East	AOC	-1.0	Schwarzenbach 20	Exhumed Serp. (H	Serpentinite	-11.6
Canfield 2009	Sedimentary Pyrite	Sediments	-31.8	Alt 1989	Dike Sulfides, East	AOC	3.4	Schwarzenbach 20	Exhumed Serp. (H	Serpentinite	12.9
Canfield 2009	Sedimentary Pyrite	Sediments	5.0	Alt 1989	Dike Sulfides, East	AOC	2.7	Schwarzenbach 20	Exhumed Serp. (H	Serpentinite	3.0
Canfield 2009	Sedimentary Pyrite	Sediments	-20.0	Alt 1989	Dike Sulfides, East	AOC	2.3	Schwarzenbach 20	Exhumed Serp. (H	Serpentinite	20.0
Canfield 2009	Sedimentary Pyrite	Sediments	-18.0	Alt 1989	Dike Sulfides, East	AOC	1.1	Schwarzenbach 20	Exhumed Serp. (H	Serpentinite	19.5
Canfield 2009	Sedimentary Pyrite	Sediments	-34.0	Alt 1989	Dike Sulfides, East	AOC	1.1	Li 2020	Exhumed Serp. (H	Serpentinite	3.6
Canfield 2009	Sedimentary Pyrite	Sediments	-18.0	Alt 1989	Dike Sulfides, East	AOC	0.1	Li 2020	Exhumed Serp. (H	Serpentinite	12.0
Canfield 2009	Sedimentary Pyrite	Sediments	-23.0	Alt 1989	Dike Sulfides, East	AOC	-0.3	Li 2020	Exhumed Serp. (H	Serpentinite	5.1
Canfield 2009	Sedimentary Pyrite	Sediments	-28.0	Alt 1989	Dike Sulfides, East	AOC	1.7	Schwarzenbach 20	Exhumed Serp. (H	Serpentinite	16.2
Canfield 2009	Sedimentary Pyrite	Sediments	-40.6	Alt 1989	Dike Sulfides, East	AOC	0.0	Schwarzenbach 20	Exhumed Serp. (H	Serpentinite	15.7
Canfield 2009	Sedimentary Pyrite	Sediments	-36.0	Alt 1989	Dike Sulfides, East	AOC	0.0	Schwarzenbach 20	Exhumed Serp. (H	Serpentinite	20.8
Canfield 2009	Sedimentary Pyrite	Sediments	-42.0	Alt 1989	Dike Sulfides, East	AOC	-0.1	Schwarzenbach 20	Exhumed Serp. (H	Serpentinite	19
Canfield 2009	Sedimentary Pyrite	Sediments	-20.0	Alt 1989	Dike Sulfides, East	AOC	3.1	Schwarzenbach 20	Exhumed Serp. (H	Serpentinite	20.1
Canfield 2009	Sedimentary Pyrite	Sediments	-27.7	Alt 1989	Dike Sulfides, East	AOC	2.6	Schwarzenbach 20	Exhumed Serp. (H	Serpentinite	18.1
Canfield 2009	Sedimentary Pyrite	Sediments	-50.4	Alt 1989	Dike Sulfides, East	AOC	0.5	Crossley 2018	Exhumed Serp. Su	Serpentinite	7.23
Canfield 2009	Sedimentary Pyrite	Sediments	-41.6	Alt 1989	Dike Sulfides, East	AOC	0.4	Crossley 2018	Exhumed Serp. Su	Serpentinite	9.3
Canfield 2009	Sedimentary Pyrite	Sediments	-48.3	Alt 1989	Dike Sulfides, East	AOC	-0.5	Crossley 2018	Exhumed Serp. Su	Serpentinite	8.8
Canfield 2009	Sedimentary Pyrite	Sediments	-53.7	Alt 1989	Dike Sulfides, East	AOC	0.5	Crossley 2018	Exhumed Serp. Su	Serpentinite	4.3
Canfield 2009	Sedimentary Pyrite	Sediments	-36.9	Alt 1989	Dike Sulfides, East	AOC	0.2	Crossley 2018	Exhumed Serp. Su	Serpentinite	7.6
Canfield 2009	Sedimentary Pyrite	Sediments	-50.4	Alt 1989	Dike Sulfides, East	AOC	0.2	Crossley 2018	Exhumed Serp. Su	Serpentinite	5.4
Canfield 2009	Sedimentary Pyrite	Sediments	2.0	Alt 1989	Dike Sulfides, East	AOC	0.4	Crossley 2018	Exhumed Serp. Su	Serpentinite	6.3
Canfield 2009	Sedimentary Pyrite	Sediments	3.8	Alt 1989	Dike Sulfides, East	AOC	1.3	Crossley 2018	Exhumed Serp. Su	Serpentinite	6.7
Canfield 2009	Sedimentary Pyrite	Sediments	-33.0	Alt 1989	Dike Sulfides, East	AOC	0.0	Crossley 2018	Exhumed Serp. Su	Serpentinite	5.9
Canfield 2009	Sedimentary Pyrite	Sediments	-41.0	Alt 1989	Dike Sulfides, East	AOC	0.0	Crossley 2018	Exhumed Serp. Su	Serpentinite	8.9
Canfield 2009	Sedimentary Pyrite	Sediments	-46.0	Alt 1989	Dike Sulfides, East	AOC	-4.9	Crossley 2018	Exhumed Serp. Su	Serpentinite	10.4
Canfield 2009	Sedimentary Pyrite	Sediments	-51.0	Alt 1989	Dike Sulfides, East	AOC	2.0	Crossley 2018	Exhumed Serp. Su	Serpentinite	6.8
Canfield 2009	Sedimentary Pyrite	Sediments	-7.0	Alt 1989	Dike Sulfides, East	AOC	0.2	Crossley 2018	Exhumed Serp. Su	Serpentinite	6.2
Canfield 2009	Sedimentary Pyrite	Sediments	-19.0	Alt 1989	Transition Zone Su	AOC	1.8	Crossley 2018	Exhumed Serp. Su	Serpentinite	8.7
Canfield 2009	Sedimentary Pyrite	Sediments	-37.2	Alt 1989	Transition Zone Su	AOC	3.1	Crossley 2018	Exhumed Serp. Su	Serpentinite	8.8
Canfield 2009	Sedimentary Pyrite	Sediments	-48.1	Alt 1989	Transition Zone Su	AOC	1.2	Crossley 2018	Exhumed Serp. Su	Serpentinite	9.4
Canfield 2009	Sedimentary Pyrite	Sediments	-32.9	Alt 1989	Transition Zone Su	AOC	2.9	Crossley 2018	Exhumed Serp. Su	Serpentinite	8.8
Canfield 2009	Sedimentary Pyrite	Sediments	-47.7	Alt 1989	Transition Zone Su	AOC	3.4	Crossley 2018	Exhumed Serp. Su	Serpentinite	5.0
Canfield 2009	Sedimentary Pyrite	Sediments	-46.3	Alt 1989	Transition Zone Su	AOC	4.2	Crossley 2018	Exhumed Serp. Su	Serpentinite	4.4
Canfield 2009	Sedimentary Pyrite	Sediments	-49.0	Alt 1989	Transition Zone Su	AOC	2.8	Crossley 2018	Exhumed Serp. Su	Serpentinite	8.0
Canfield 2009	Sedimentary Pyrite	Sediments	-41.8	Alt 1989	Transition Zone Su	AOC	2.9	Crossley 2018	Exhumed Serp. Su	Serpentinite	5.5
Canfield 2009	Sedimentary Pyrite	Sediments	-48.8	Alt 1989	Transition Zone Su	AOC	4.7	Crossley 2018	Exhumed Serp. Su	Serpentinite	7.9
Canfield 2009	Sedimentary Pyrite	Sediments	-37.6	Alt 1989	Transition Zone Su	AOC	0.2	Crossley 2018	Exhumed Serp. Su	Serpentinite	9.2
Canfield 2009	Sedimentary Pyrite	Sediments	-48.3	Alt 1989	Transition Zone Su	AOC	3.1	Crossley 2018	Exhumed Serp. Su	Serpentinite	3.9
Canfield 2009	Sedimentary Pyrite	Sediments	-40.3	Alt 1989	Transition Zone Su	AOC	2.5	Crossley 2018	Exhumed Serp. Su	Serpentinite	7.3
Canfield 2009	Sedimentary Pyrite	Sediments	-49.3	Alt 1989	Transition Zone Su	AOC	4.2	Crossley 2018	Exhumed Serp. Su	Serpentinite	8.4
Canfield 2009	Sedimentary Pyrite	Sediments	-2.8	Alt 1989	Transition Zone Su	AOC	1.4	Crossley 2018	Exhumed Serp. Su	Serpentinite	8.2
Canfield 2009	Sedimentary Pyrite	Sediments	-37.1	Alt 1989	Transition Zone Su	AOC	1.1	Crossley 2018	Exhumed Serp. Su	Serpentinite	7.9
Canfield 2009	Sedimentary Pyrite	Sediments	-37.0	Alt 1989	Transition Zone Su	AOC	4.0	Crossley 2018	Exhumed Serp. Su	Serpentinite	5.5
Canfield 2009	Sedimentary Pyrite	Sediments	-48.0	Alt 1989	Transition Zone Su	AOC	3.4	Crossley 2018	Exhumed Serp. Su	Serpentinite	8.8
Canfield 2009	Sedimentary Pyrite	Sediments	-29.4	Alt 1989	Transition Zone Su	AOC	4.0	Crossley 2018	Exhumed Serp. Su	Serpentinite	6.5
Canfield 2009	Sedimentary Pyrite	Sediments	-32.1	Alt 1989	Transition Zone Su	AOC	2.3	Crossley 2018	Exhumed Serp. Su	Serpentinite	7.5
Canfield 2009	Sedimentary Pyrite	Sediments	-15.0	Alt 1989	Transition Zone Su	AOC	2.7	Crossley 2018	Exhumed Serp. Su	Serpentinite	7.6
Canfield 2009	Sedimentary Pyrite	Sediments	-25.0	Alt 1989	Transition Zone Su	AOC	2.5	Crossley 2018	Exhumed Serp. Su	Serpentinite	1.8
Canfield 2009	Sedimentary Pyrite	Sediments	-26.5	Alt 1989	Transition Zone Su	AOC	4.7	Crossley 2018	Exhumed Serp. Su	Serpentinite	6.5
Canfield 2009	Sedimentary Pyrite	Sediments	-37.0	Alt 1989	Transition Zone Su	AOC	3.8	Crossley 2018	Exhumed Serp. Su	Serpentinite	8.4
Canfield 2009	Sedimentary Pyrite	Sediments	-35.0	Alt 1989	Transition Zone Su	AOC	3.1	Crossley 2018	Exhumed Serp. Su	Serpentinite	7.8
Canfield 2009	Sedimentary Pyrite	Sediments	-5.5	Alt 1989	Transition Zone Su	AOC	1.1	Crossley 2018	Exhumed Serp. Su	Serpentinite	6.0
Canfield 2009	Sedimentary Pyrite	Sediments	-23.8	Alt 1989	Transition Zone Su	AOC	3.1	Crossley 2018	Exhumed Serp. Su	Serpentinite	5.2
Canfield 2009	Sedimentary Pyrite	Sediments	-24.0	Alt 1989	Transition Zone Su	AOC	3.8	Crossley 2018	Exhumed Serp. Su	Serpentinite	5.9
Canfield 2009	Sedimentary Pyrite	Sediments	-28.0	Alt 1989	Transition Zone Su	AOC	4.6	Crossley 2018	Exhumed Serp. Su	Serpentinite	5.0
Canfield 2009	Sedimentary Pyrite	Sediments	-20.0	Alt 1989	Pillow Sulfides, Ea	AOC	-0.7	Crossley 2018	Exhumed Serp. Su	Serpentinite	3.3
Canfield 2009	Sedimentary Pyrite	Sediments	-40.0	Alt 1989	Pillow Sulfides, Ea	AOC	-1.0	Crossley 2018	Exhumed Serp. Su	Serpentinite	5.9
Canfield 2009	Sedimentary Pyrite	Sediments	-13.8	Alt 1989	Pillow Sulfides, Ea	AOC	-1.9	Crossley 2018	Exhumed Serp. Su	Serpentinite	7.4
Canfield 2009	Sedimentary Pyrite	Sediments	-28.0	Alt 1989	Anhydrite, Eastern	AOC	21.5	Crossley 2018	Exhumed Serp. Su	Serpentinite	3.1
Canfield 2009	Sedimentary Pyrite	Sediments	-20.8	Alt 1989	Anhydrite, Eastern	AOC	20.4	Crossley 2018	Exhumed Serp. Su	Serpentinite	3.0
Canfield 2009	Sedimentary Pyrite	Sediments	-18.6	Alt 1989	Anhydrite, Eastern	AOC	21.9	Crossley 2018	Exhumed Serp. Su	Serpentinite	6.9
Canfield 2009	Sedimentary Pyrite	Sediments	-31.7	Alt 1989	Anhydrite, Eastern	AOC	21.4	Crossley 2018	Exhumed Serp. Su	Serpentinite	12.7
Canfield 2009	Sedimentary Pyrite	Sediments	-11.0	Teagle 1998	Anhydrite, Eastern	AOC	18.9	Crossley 2018	Exhumed Serp. Su	Serpentinite	15.1
Canfield 2009	Sedimentary Pyrite	Sediments	-43.6	Teagle 1998	Anhydrite, Eastern	AOC	35.9	Crossley 2018	Exhumed Serp. Su	Serpentinite	10.3
Canfield 2009	Sedimentary Pyrite	Sediments	-20.8	Teagle 1998	Anhydrite, Eastern	AOC	21.9	Crossley 2018	Exhumed Serp. Su	Serpentinite	8.1
Canfield 2009	Sedimentary Pyrite	Sediments	-36.4	Teagle 1998	Anhydrite, Eastern	AOC	21.4	Crossley 2018	Exhumed Serp. Su	Serpentinite	7.8
Canfield 2009	Sedimentary Pyrite	Sediments	-33.7	Teagle 1998	Anhydrite, Eastern	AOC	21.5	Crossley 2018	Exhumed Serp. Su	Serpentinite	11.2
Canfield 2009	Sedimentary Pyrite	Sediments	-45.1	Teagle 1998	Anhydrite, Eastern	AOC	21.3	Crossley 2018	Exhumed Serp. Su	Serpentinite	10.5
Canfield 2009	Sedimentary Pyrite	Sediments	-48.7	Teagle 1998	Anhydrite, Eastern	AOC	21.2	Crossley 2018	Exhumed Serp. Su	Serpentinite	7.3
Canfield 2009	Sedimentary Pyrite	Sediments	-49.3	Teagle 1998	Anhydrite, Eastern	AOC	20.4	Crossley 2018	Exhumed Serp. Su	Serpentinite	10.2
Canfield 2009	Sedimentary Pyrite	Sediments	-49.3	Teagle 1998	Anhydrite, Eastern	AOC	4.0	Crossley 2018	Exhumed Serp. Su	Serpentinite	4.0
Canfield 2009	Sedimentary Pyrite	Sediments	-49.6	Teagle 1998	Anhydrite, Eastern	AOC	11.2	Crossley 2018	Exhumed Serp. Su	Serpentinite	4.5
Canfield 2009	Sedimentary Pyrite	Sediments	-33.3	Teagle 1998	Anhydrite, Eastern	AOC	11.9	Crossley 2018	Exhumed Serp. Su	Serpentinite	4.3
Canfield 2009	Sedimentary Pyrite	Sediments	-39.1	Alt 2011	Lavas, Cocos Plate	AOC	-4.0	Crossley 2018	Exhumed Serp. Su	Serpentinite	5.1

Table S11. (continued)

Citation	Location	Type	δ³⁴S (‰)
Canfield 2009	Sedimentary Pyrite	Sediments	-41.2
Canfield 2009	Sedimentary Pyrite	Sediments	-22.8
Canfield 2009	Sedimentary Pyrite	Sediments	-33.8
Canfield 2009	Sedimentary Pyrite	Sediments	-35.7
Canfield 2009	Sedimentary Pyrite	Sediments	-28.8
Canfield 2009	Sedimentary Pyrite	Sediments	-19.8
Canfield 2009	Sedimentary Pyrite	Sediments	-19.8
Canfield 2009	Sedimentary Pyrite	Sediments	-23.4
Canfield 2009	Sedimentary Pyrite	Sediments	-32.3
Li 2020	Metasediments (Hi	Sediments	-7.9
Li 2020	Metasediments (Hi	Sediments	-12.0

Citation	Location	Type	δ³⁴S (‰)
Alt 2011	Lavas, Cocos Plate	AOC	-2.3
Alt 2011	Lavas, Cocos Plate	AOC	-18.0
Alt 2011	Lavas, Cocos Plate	AOC	-2.5
Alt 2011	Lavas, Cocos Plate	AOC	-6.2
Alt 2011	Lavas, Cocos Plate	AOC	-2.5
Alt 2011	Lavas, Cocos Plate	AOC	-1.3
Alt 2011	Lavas, Cocos Plate	AOC	-0.2
Alt 2011	Lavas, Cocos Plate	AOC	0.8
Alt 2011	Lavas, Cocos Plate	AOC	-1.4
Alt 2011	Lavas, Cocos Plate	AOC	-1.5
Alt 2011	Lavas, Cocos Plate	AOC	-1.9
Alt 2011	Lavas, Cocos Plate	AOC	-2.2
Alt 2011	Lavas, Cocos Plate	AOC	-0.7
Alt 2011	Lavas, Cocos Plate	AOC	-7.9
Alt 2011	Lavas, Cocos Plate	AOC	-4.6
Alt 2011	Lavas, Cocos Plate	AOC	-2.3
Alt 2011	Lavas, Cocos Plate	AOC	-1.2
Alt 2011	Lavas, Cocos Plate	AOC	-6.2
Alt 2011	Lavas, Cocos Plate	AOC	-3.7
Alt 2011	Lavas, Cocos Plate	AOC	-3.7
Alt 2011	Lavas, Cocos Plate	AOC	-3.6
Alt 2011	Lavas, Cocos Plate	AOC	-3.6
Alt 2011	Lavas, Cocos Plate	AOC	-3.6
Alt 2011	Lavas, Cocos Plate	AOC	-3.6
Alt 2011	Lavas, Cocos Plate	AOC	-1.4
Alt 2011	Lavas, Cocos Plate	AOC	0.3
Alt 2011	Lavas, Cocos Plate	AOC	40.0
Alt 2011	Lavas, Cocos Plate	AOC	-1.1
Alt 2011	Lavas, Cocos Plate	AOC	1.6
Alt 2011	Lavas, Cocos Plate	AOC	1.2
Alt 2011	Lavas, Cocos Plate	AOC	-4.5
Alt 2011	Lavas, Cocos Plate	AOC	-0.8
Alt 2011	Lavas, Cocos Plate	AOC	-2.9
Alt 2011	Lavas, Cocos Plate	AOC	-3.0
Alt 2011	Lavas, Cocos Plate	AOC	-2.9
Alt 2011	Lavas, Cocos Plate	AOC	-6.9
Alt 2011	Lavas, Cocos Plate	AOC	-19.7
Alt 2011	Lavas, Cocos Plate	AOC	-2.0
Alt 2011	Lavas, Cocos Plate	AOC	-10.9
Alt 2011	Lavas, Cocos Plate	AOC	-5.3
Alt 2011	Lavas, Cocos Plate	AOC	0.5
Alt 2011	Lavas, Cocos Plate	AOC	1.7
Alt 2011	Lavas, Cocos Plate	AOC	-0.3
Alt 2011	Lavas, Cocos Plate	AOC	0.2
Ono 2012	Lavas, Juan de Fuc	AOC	-5.1
Ono 2012	Lavas, Juan de Fuc	AOC	-1.8
Ono 2012	Lavas, Juan de Fuc	AOC	-0.1
Ono 2012	Lavas, Juan de Fuc	AOC	-0.1
Ono 2012	Lavas, Juan de Fuc	AOC	1.0
Ono 2012	Lavas, Juan de Fuc	AOC	0.2
Ono 2012	Lavas, Juan de Fuc	AOC	-2.1
Ono 2012	Lavas, Juan de Fuc	AOC	-2.7
Ono 2012	Lavas, Juan de Fuc	AOC	-0.8
Ono 2012	Lavas, Juan de Fuc	AOC	-1.7
Ono 2012	Lavas, Juan de Fuc	AOC	-4.1
Ono 2012	Lavas, Juan de Fuc	AOC	-10.0
Ono 2012	Lavas, Juan de Fuc	AOC	-1.0
Ono 2012	Lavas, Juan de Fuc	AOC	-5.7
Ono 2012	Lavas, Juan de Fuc	AOC	-9.3
Ono 2012	Lavas, Juan de Fuc	AOC	-13.7
Ono 2012	Lavas, Juan de Fuc	AOC	-2.7
Ono 2012	Lavas, Juan de Fuc	AOC	-2.9
Ono 2012	Lavas, Juan de Fuc	AOC	-3.5
Ono 2012	Lavas, Juan de Fuc	AOC	-4.4
Ono 2012	Lavas, Juan de Fuc	AOC	-0.5
Ono 2012	Lavas, Juan de Fuc	AOC	-0.9
Ono 2012	Lavas, Juan de Fuc	AOC	-9.6
Ono 2012	Lavas, Juan de Fuc	AOC	-5.1
Ono 2012	Lavas, Juan de Fuc	AOC	-0.7
Ono 2012	Lavas, Juan de Fuc	AOC	-0.9
Ono 2012	Lavas, Juan de Fuc	AOC	0.0
Ono 2012	Lavas, Juan de Fuc	AOC	0.0
Ono 2012	Lavas, Juan de Fuc	AOC	-2.1
Ono 2012	Lavas, Juan de Fuc	AOC	-3.4
Ono 2012	Lavas, Juan de Fuc	AOC	-5.2
Ono 2012	Lavas, Juan de Fuc	AOC	-1.5
Ono 2012	Lavas, Juan de Fuc	AOC	-1.2
Ono 2012	Lavas, Juan de Fuc	AOC	-0.9
Ono 2012	Lavas, Juan de Fuc	AOC	-1.4
Ono 2012	Lavas, Juan de Fuc	AOC	-1.6
Ono 2012	Lavas, Juan de Fuc	AOC	-4.2
Ono 2012	Lavas, Juan de Fuc	AOC	0.1
Ono 2012	Lavas, Juan de Fuc	AOC	-1.7
Ono 2012	Lavas, Juan de Fuc	AOC	-1.5
Rouxel 2008	Lavas, Pacific Plate	AOC	-12.0
Rouxel 2008	Lavas, Pacific Plate	AOC	-12.7
Rouxel 2008	Lavas, Pacific Plate	AOC	-0.8
Rouxel 2008	Lavas, Pacific Plate	AOC	-2.1
Rouxel 2008	Lavas, Pacific Plate	AOC	-15.8
Rouxel 2008	Lavas, Pacific Plate	AOC	-7.7
Rouxel 2008	Lavas, Pacific Plate	AOC	-13.3
Rouxel 2008	Lavas, Pacific Plate	AOC	-4.9
Rouxel 2008	Lavas, Pacific Plate	AOC	-5.5
Rouxel 2008	Lavas, Pacific Plate	AOC	-12.9
Rouxel 2008	Lavas, Pacific Plate	AOC	-14.0
Rouxel 2008	Lavas, Pacific Plate	AOC	0.9
Rouxel 2008	Lavas, Pacific Plate	AOC	-5.0
Rouxel 2008	Lavas, Pacific Plate	AOC	-6.8
Barker 2010	Sheeted Dykes, Pit	AOC	-0.6
Barker 2010	Sheeted Dykes, Pit	AOC	1.4
Barker 2010	Sheeted Dykes, Pit	AOC	1.2
Barker 2010	Sheeted Dykes, Pit	AOC	-1.1
Barker 2010	Sheeted Dykes, Pit	AOC	2.5
Barker 2010	Sheeted Dykes, Pit	AOC	0.8
Barker 2010	Sheeted Dykes, Pit	AOC	1.3
Barker 2010	Sheeted Dykes, Pit	AOC	1.3
Barker 2010	Sheeted Dykes, Pit	AOC	1.6
Barker 2010	Sheeted Dykes, Pit	AOC	2.3
Barker 2010	Sheeted Dykes, Pit	AOC	2.3
Barker 2010	Sheeted Dykes, Pit	AOC	2.6
Barker 2010	Sheeted Dykes, Pit	AOC	1.5
Barker 2010	Sheeted Dykes, Pit	AOC	0.3
Barker 2010	Sheeted Dykes, Pit	AOC	1.2
Barker 2010	Sheeted Dykes, Pit	AOC	3
Barker 2010	Sheeted Dykes, Pit	AOC	3.1
Barker 2010	Sheeted Dykes, Pit	AOC	2.6
Li 2020	Metabasites (High	AOC	3.6
Li 2020	Metabasites (High	AOC	-4.4
Li 2020	Metabasites (High	AOC	-6.1
Li 2020	Metabasites (High	AOC	-7.2
Alt 2012	Metabasites (High	AOC	0.0
Lee 2018	Metabasites (High	AOC	0.0
Lee 2018	Metabasites (High	AOC	1.0
Lee 2018	Metabasites (High	AOC	-2.9
Lee 2018	Metabasites (High	AOC	-1.4
Lee 2018	Metabasites (High	AOC	2.5
Lee 2018	Metabasites (High	AOC	-1.7
Lee 2018	Metabasites (High	AOC	-1.1
Lee 2018	Metabasites (High	AOC	2.5
Schwarzenbach 20	Metabasites (High	AOC	17.1
Schwarzenbach 20	Metabasites (High	AOC	19.7
Schwarzenbach 20	Metabasites (High	AOC	18.8
Schwarzenbach 20	Metabasites (High	AOC	17.5
Schwarzenbach 20	Metabasites (High	AOC	12.9
Schwarzenbach 20	Metabasites (High	AOC	-1.53

Citation	Location	Type	δ³⁴S (‰)
Crossley 2018	Exhumed Serp. Su	Serpentinite	5.1
Crossley 2018	Exhumed Serp. Su	Serpentinite	5.0
Alt 2006	Conical Seamount,	Serpentinite	8.1
Alt 2006	Conical Seamount,	Serpentinite	20.5
Alt 2006	Conical Seamount,	Serpentinite	11.2
Alt 2006	Conical Seamount,	Serpentinite	9.3
Alt 2006	Conical Seamount,	Serpentinite	13.7
Alt 2006	Conical Seamount,	Serpentinite	14.0
Alt 2006	Conical Seamount,	Serpentinite	3.8
Alt 2006	Conical Seamount,	Serpentinite	6.6
Alt 2006	Conical Seamount,	Serpentinite	6.8
Alt 2006	Conical Seamount,	Serpentinite	5.8
Alt 2006	Conical Seamount,	Serpentinite	13.3
Alt 2006	Conical Seamount,	Serpentinite	-1.5
Alt 2006	Conical Seamount,	Serpentinite	14.0
Alt 2006	Conical Seamount,	Serpentinite	9.5
Alt 2006	Conical Seamount,	Serpentinite	8.2
Alt 2006	Conical Seamount,	Serpentinite	-2.6
Alt 2006	Conical Seamount,	Serpentinite	9.7
Alt 2006	Conical Seamount,	Serpentinite	11.7
Walters 2019	Model Estimate	Slab	-11.0
Walters 2019	Model Estimate	Slab	8.0
Li 2020	Model Estimate	Slab	-2.5
Chaussidon 1991	East Pacific Rise	MORB	0.0
Chaussidon 1991	East Pacific Rise	MORB	1.3
Chaussidon 1991	East Pacific Rise	MORB	1.0
Chaussidon 1991	East Pacific Rise	MORB	0.8
Chaussidon 1991	East Pacific Rise	MORB	1.1
Kanehira 1973	Mid Atlantic Ridge	MORB	1.6
Kanehira 1973	Mid Atlantic Ridge	MORB	1.2
Sakai 1984	Famous	MORB	-0.3
Sakai 1984	Galapagos	MORB	0.5
Sakai 1984	Juan de Fuca	MORB	0.4
Sakai 1984	Pacific Antarctica r	MORB	-0.6
Alt 1993	unkown	MORB	0.4

Table S11 Full Citations

Alford, S.E., Alt, J.C., Shanks, W.C., 2011. Sulfur geochemistry and microbial sulfate reduction during low-temperature alteration of uplifted lower oceanic crust: Insights from ODP Hole 735B. Chem. Geol. 286, 185–195. https://doi.org/10.1016/j.chemgeo.2011.05.005

Alt, J.C., Anderson, T.F., 1991. Mineralogy and Isotopic Composition of Sulfur in Layer 3 Gabbros from The Indian Ocean, Hole 735B. Proc. Ocean Drill. Program, Sci. Results 118, 113–125.

Alt, J.C., Anderson, T.F., Bonnell, L., 1989. The geochemistry of sulfur in a 1.3 km section of hydrothermally altered oceanic crust, DSDP Hole 504B. Geochim. Cosmochim. Acta 53, 1011–1023. https://doi.org/10.1016/0016-7037(89)90206-8

Alt, J.C., Burdett, J.W., 1992. Sulfur in Pacific deep-sea sediments (Leg 129) and implications for cycling of sediment in subduction zones. Proc., Sci. results, ODP, Leg 129, old Pacific crust 129, 283–291. https://doi.org/10.2973/odp.proc.sr.129.125.1992

Alt, J.C., Garrido, C.J., Shanks III, W.C., Turchyn, A., Padrón-Navarta, J.A., López Sánchez-Vizcaíno, V., Gómez Pugnaire, M.T., Marchesi, C., 2012a. Recycling of water, carbon, and sulfur during subduction of serpentinites: a stable isotope study of Cerro del Almirez, Spain. Earth Planet. Sci. Lett. 327–328, 50–60. https://doi.org/10.1016/j.epsl.2012.01.029

Alt, J.C., Iii, W.C.S., Crispini, L., Gaggero, L., Schwarzenbach, E.M., Früh-green, G.L., Bernasconi, S.M., 2012b. Uptake of carbon and sulfur during sea floor serpentinization and the effects of subduction metamorphism in Ligurian peridotites. Chem. Geol. 322–323, 268–277. https://doi.org/10.1016/j.chemgeo.2012.07.009

Alt, J.C., Schwarzenbach, E.M., Früh-Green, G.L., Shanks, W.C., Bernasconi, S.M., Garrido, C.J., Crispini, L., Gaggero, L., Padrón-Navarta, J.A., Marchesi, C., 2013. The role of serpentinites in cycling of carbon and sulfur: Seafloor serpentinization and subduction metamorphism. Lithos 178, 40–54. https://doi.org/10.1016/j.lithos.2012.12.006

Alt, J.C., Shanks, W.C., 2006. Stable isotope compositions of serpentinite seamounts in the Mariana forearc: Serpentinization processes, fluid sources and sulfur metasomatism. Earth Planet. Sci. Lett. 242, 272–285. https://doi.org/10.1016/j.epsl.2005.11.063

Alt, J.C., Shanks, W.C., Jackson, M.C., 1993. Cycling of sulfur in subduction zones: The geochemistry of sulfur in the Mariana Island Arc and back-arc trough. Earth Planet. Sci.Lett. 119, 477–494. https://doi.org/10.1016/0012-821X(93)90057-G

Barker, A.K., Coogan, L.A., and Gillis, K.M., 2010. Insights into the behaviour of sulphur in mid-ocean ridge axial hydrothermal systems from the composition of the sheeted dyke complex at Pito Deep. Chem. Geol. 275, 105–115. https://doi.org/10.1016/j.chemgeo.2010.05.003

Bénard, A., Klimm, K., Woodland, A.B., Arculus, R.J., Wilke, M., Botcharnikov, R.E., Shimizu, N., Nebel, O., Rivard, C., Ionov, D.A., 2018. Oxidising agents in sub-arc mantle melts link slab devolatilisation and arc magmas. Nat. Commun. 9. https://doi.org/10.1038/s41467-018-05804-

Bouvier, A.S., Métrich, N., Deloule, E., 2008. Slab-derived fluids in the magma sources of St. Vincent (lesser antilles arc): Volatile and light element imprints. J. Petrol. 49, 1427–1448. https://doi.org/10.1093/petrology/egn031

Canfield, D.E., Farquhar, J., 2009. Animal evolution, bioturbation, and the sulfate concentration of the oceans. Proc. Natl. Acad. Sci. U. S. A. 106, 8123–8127. https://doi.org/10.1073/pnas.0902037106

Chaussidon, M., Sheppard, S.M.F., Michard, A., Recherches, C. De, Vandoeuvre-les-nancy, F., 1991. Hydrogen, sulphur and neodymium isotope variations in the mantle beneath the EPR at 12°50'N. Stable Isot. Geochemistry A Tribut. to Samuel Epstein 15, 325–337.

Crossley, R.J., Evans, K.A., Jeon, H., Kilburn, M.R., 2018. Insights into sulfur cycling at subduction zones from in-situ isotopic analysis of sulfides in high-pressure serpentinites and 'hybrid' samples from Alpine Corsica. Chem. Geol. 493, 359–378. https://doi.org/10.1016/j.chemgeo.2018.06.014

De Hoog, J.C.M., Mason, P.R.D., Van Bergen, M.J., 2001. Sulfur and chalcophile elements in subduction zones: Constraints from a laser ablation ICP-MS study of melt inclusions from Galunggung volcano, Indonesia. Geochim. Cosmochim. Acta 65, 3147–3164. https://doi.org/10.1016/S0016-7037(01)00634-2

De Moor, J.M., Fischer, T.P., Sharp, Z.D., King, P.L., Wilke, M., Botcharnikov, R.E., Cottrell, E., Zelenski, M., Marty, B., Klimm, K., Rivard, C., Ayalew, D., Ramirez, C., Kelley, K.A., 2013. Sulfur degassing at Erta Ale (Ethiopia) and Masaya (Nicaragua) volcanoes: Implications for degassing processes and oxygen fugacities of basaltic systems. Geochemistry, Geophys. Geosystems 14, 4076–4108. https://doi.org/10.1002/ggge.20255

Giggenbach, W., 1982. The chemical and isotopic composition of gas discharges from New Zealand andesitic volcanoes. Bull. Volcanol. 45, 253–255. https://doi.org/10.1007/BF02597739

Goff, F., Janik, C.J., Delgado, H., Werner, C., Counce, D., Stimac, J.A., Siebe, C., Love, S.P., Williams, S.N., Fischer, T., Johnson, L., 1998. Geochemical surveillance of magmatic volatiles at Popocatepetl volcano, Mexico. Bull. Geol. Soc. Am. 110, 695–710. https://doi.org/10.1130/0016-7606(1998)110<0695:GSOMVA>2.3.CO;2

Gurenko, A.A., Belousov, A.B., Kamenetsky, V.S., Zelenski, M.E., 2018. Origin of volatiles emitted by Plinian mafic eruptions of the Chikurachki volcano, Kurile arc, Russia: Trace element, boron and sulphur isotope constraints. Chem. Geol. 478, 131–147. https://doi.org/10.1016/j.chemgeo.2017.10.009

Ishihara, S., Sasaki, A., 1989. Sulfur isotopic ratios of the magnetite-series and ilmenite-series granitoids of the Sierra Nevada batholith—a reconnaissance study. Geology 17, 788–791.

Kanehira, K., Yui, S., Sakai, H., Sasaki, A., 1973. Sulphide globules and sulphur isotope ratios in the abyssal tholeiite from the Mid-Atlantic Ridge near 30° N latitude. Geochem. J. 7, 89–96.

Kasasaku, K., Minari, T., Mukai, H., Murano, K., 1999. Stable Sulfur Isotope Ratios of the Gases from Mt. Sakurajima and Satsuma-Iwojima Volcanoes. Nippon Kagaku Kaishi 479–486. https://doi.org/10.1246/nikkashi.1999.479

Lee, C.T.A., Erdman, M., Yang, W., Ingram, L., Chin, E.J., DePaolo, D.J., 2018. Sulfur isotopic compositions of deep arc cumulates. Earth Planet. Sci. Lett. 500, 76–85. https://doi.org/10.1016/j.epsl.2018.08.017

Li, J.L., Schwarzenbach, E.M., John, T., Ague, J.J., Huang, F., Gao, J., Klemd, R., Whitehouse, M.J., Wang, X.S., 2020. Uncovering and quantifying the subduction zone sulfur cycle from the slab perspective. Nat. Commun. 11, 1–12. https://doi.org/10.1038/s41467-019-14110-4

Mather, T.A., Pyle, D.M., Heaton, T.H.E., 2008. Investigation of the use of filter packs to measure the sulphur isotopic composition of volcanic sulphur dioxide and the sulphur and oxygen isotopic composition of volcanic sulphate aerosol. Atmos. Environ. 42, 4611–4618. https://doi.org/10.1016/j.atmosenv.2008.01.052

Menyailov, A., Nikitina, P., Shapar, V.N., Pilipenko, V.P., 1986. Temperature Increase and Chemical Change of Fumarolic Gases at Momotombo Volcano, Nicaragua, in 1982-1985: Are These Indicators of Possible Eruption? J. Geophys. Res. 91, 199–214.

Mizutani, Y., Hayashi, S., Sugiura, T., 1986. Chemical and isotopic compositions of fumarolic gases from Kuju-Iwoyama, Kyushu, Japan. Geochem. J. 20, 273–285.

Ohba, T., Nogami, K., Hirabayashi, J.I., Mori, T., 2008. Isotopic fractionation of SO2 and H2S gases during the absorption by KOH solution, with the application to volcanic gas monitoring at Miyakejima Island, Japan. Geochem. J. 42, 119–131. https://doi.org/10.2343/geochemj.42.119

Ono, S., Keller, N.S., Rouxel, O., Alt, J.C., 2012. Sulfur-33 constraints on the origin of secondary pyrite in altered oceanic basement. Geochim. Cosmochim. Acta 87, 323–340. https://doi.org/10.1016/j.gca.2012.04.016

Poorter, R.P.E., Varekamp, J.C., Poreda, R.J., Van Bergen, M.J., Kreulen, R., 1991. Chemical and isotopic compositions of volcanic gases from the east Sunda and Banda arcs, Indonesia. Geochim. Cosmochim. Acta 55, 3795–3807. https://doi.org/10.1016/0016-7037(91)90075-G

Rouxel, O., Ono, S., Alt, J., Rumble, D., Ludden, J., 2008. Sulfur isotope evidence for microbial sulfate reduction in altered oceanic basalts at ODP Site 801. Earth Planet. Sci. Lett. 268, 110–123. https://doi.org/10.1016/j.epsl.2008.01.010

Sakai, H., Des Marais, D.J., Ueda, A., Moore, J.G., 1984. Concentrations and isotope ratios of carbon, nitrogen and sulfur in ocean-floor basalts. Geochim. Cosmochim. Acta 48, 2433–2411.

Sakai, H., Matsubaya, O., 1977. Stable isotopic studies of japanese geothermal systems. Geothermics 5, 97–124. https://doi.org/10.1016/0375-6505(77)90014-1

Sasaki, A., Ishihara, S., 1979. Sulfur isotopic composition of the magnetite-series and ilmenite-series granitoids in Japan. Contrib. to Mineral. Petrol. 68, 107–115.

Schwarzenbach, E.M., Früh-Green, G.L., Bernasconi, S.M., Alt, J.C., Shanks, W.C., Gaggero, L., Crispini, L., 2012. Sulfur geochemistry of peridotite-hosted hydrothermal systems: Comparing the Ligurian ophiolites with oceanic serpentinites. Geochim. Cosmochim. Acta 91, 283–305. https://doi.org/10.1016/j.gca.2012.05.021

Schwarzenbach, E.M., Caddick, M.J., Petroff, M., Gill, B.C., Cooperdock, E. H., Barnes, J., 2018. Sulphur and carbon cycling in the subduction zone mélange. Scientific Reports, 8, 15517. https://doi.org/10.1038/s41598-018-33610-9.

Shinohara, H., Giggenbach, W.F., Kazahaya, K., Hedenquist, J.W., 1993. Geochemistry of volcanic gases and hot springs of Satsuma-Iwojima, Japan: Following Matsuo. Geochem. J. 27, 271–285. https://doi.org/10.2343/geochemj.27.271

Taran, Y., Gavilanes, J.C., Cortés, A., 2002. Chemical and isotopic composition of fumarolic gases and the SO2 flux from Volcán de Colima, México, between the 1994 and 1998 eruptions. J. Volcanol. Geotherm. Res. 117, 105–119. https://doi.org/10.1016/S0377-0273(02)00239-1

Taran, Y.A., Bernard, A., Gavilanes, J.C., Lunezheva, E., Cortés, A., Armienta, M.A., 2001. Chemistry and mineralogy of high-temperature gas discharges from Colima volcano, Mexico. Implications for magmatic gas-atmosphere interaction. J. Volcanol. Geotherm. Res. 108, 245–264. https://doi.org/10.1016/S0377-0273(00)00289-4

Taran, Y.A., Connor, C.N., Shapar, V.N., Ovsyannikov, A.A., Bilichenko, A.A., 1997. Fumarolic activity of Avachinsky and Koryaksky volcanoes, Kamchatka, from 1993 to 1994. Bull. Volcanol. 58, 441–448.

Taran, Y.A., Hedenquist, J.W., Korzhinsky, M.A., Tkachenko, S., Shmulovich, K.I., 1995. Geochemistry of magmatic gases from Kudryavy volcano, Iturup, Kuril Islands. Geochim. Cosmochim. Acta 59, 1749–1761. https://doi.org/10.1016/0016-7037(95)00079-F

Teagle, D.A.H., Alt, J.C., Halliday, A.N., 1998. Tracing the chemical evolution of fluids during hydrothermal recharge: Constraints from anhydrite recovered in ODP Hole 504B. Earth and Planetary Science Letters.

Turner, S.C., 2018. Tracking Sulfur Diagenesis in Methane Rich Marine Sediments on the Cascadia Margin: Comparing Sulfur Isotopes of Bulk Sediment and Chromium Reducible Sulfur. University of New Hampshire.

Ueda, A., Sakai, H., 1984. Sulfur isotope study of Quaternary volcanic rocks from the Japanese Islands Arc. Geochim. Cosmochim. Acta 48, 1837–1848. https://doi.org/10.1016/0016-7037(84)90037-1

Walters, J.B., Cruz-Uribe, A.M., Marschall, H.R., 2019. Isotopic Compositions of Sulfides in Exhumed High-Pressure Terranes: Implications for Sulfur Cycling in Subduction Zones. Geochemistry, Geophys. Geosystems 20, 3347–3374. https://doi.org/10.1029/2019GC008374

Wang, J., Chen, Q., Wei, Q., Wang, X., Li, Q., Gao, Y., 2008. Authigenic Pyrites and Their Stable Sulfur Isotopes in Sediments From IODP 311 on Cascadia Margin , Northeastern Pacific. ICGH2008.

Williams, S.N., Sturchio, N.C., Calvache V., M.L., Mendez F., R., Londoño C., A., García P., N., 1990. Sulfur dioxide from Nevado del Ruiz volcano, Colombia: total flux and isotopic constraints on its origin. J. Volcanol. Geotherm. Res. 42, 53–68. https://doi.org/10.1016/0377-0273(90)90069-R

Table S12. Values used to calculate the $\delta^{34}S$ in the subducting slab at Lassen. See supplementary discussion for details and references.

Section	Lithology	Thickness (m)	S (ppm)	$\delta^{34}S$ (‰)
Sediment	Sediment	1,500	6,063 ± 2448	-11.1
	Upper Volcanic (Red Halo)	81	180 ± 70	-1.8
	Upper Volcanic (Dark Gray)	219	460 ± 340	-1.8
	Lower Volcanic	300	620 ± 320	-1.9
	Pyrite Veins	0.003	360,000	-2.5
	Transition Zone (Mineralized)	20	9,740 ± 6,900	3
	Transition Zone (Transition)	180	3,150 ± 4,300	3
	Transition Zone (Pyrite Veins)	0.19	360,000	3.2
AOC	Upper Dikes (dark gray)	415	660 ± 320	0.6
	Upper Dikes (light gray)	85	410 ± 240	0.6
	Upper Dikes (Pyrite Veins)	0.009	360,000	0
	Anhydrite	0.21	236,000	21
	Lower dikes (dark gray)	450	660 ± 340	2
	Lower dikes (light gray)	50	240 ± 360	2.3
	Lower Dikes (pyrite veins)	0.005	360,000	0.9
	Plutonic Section (Altered Gabbro)	500	230 ± 190	0.4
	Plutonic Section (Gabbro)	4,700	620 ± 180	0.1
Lithosphere	Hydrated Lithosphere	2,000	150 ± 50	4.9

Table S13. Compilation of mid ocean ridge basalt data from literature shown in Figure S3.

fO2(ΔQFM)	Citation	S(ppm)	Dy(ppm)	Sr(ppm)	Nd(ppm)	Citation	S(ppm)	Dy(ppm)	Sr(ppm)	Nd(ppm)	Citation	S34/32S	Citation	δ34S(‰)	Citation
-0.11	[1]	1466.6	6.3	92.4	10.4	[2]	965.0	3.4	110.9	4.7	[2]	0.08	[3]	0	[6]
-0.10	[1]	1238.3	6.9	117.5	12.1	[2]	920.5	3.3	105.7	4.6	[2]	0.09	[3]	1.3	[6]
-0.25	[1]	1012.0	4.3	87.6	5.7	[2]	941.6	3.4	107.3	4.9	[2]	0.06	[4]	1	[6]
-0.21	[1]	1242.8	6.8	117.6	11.7	[2]	950.5	3.3	108.4	4.7	[2]	0.03	[4]	0.8	[6]
-0.33	[1]	1176.8	5.4	98.7	9.4	[2]	930.8	3.4	106.0	4.5	[2]	0.04	[4]	1.1	[6]
0.01	[1]	1200.8	5.6	123.7	10.6	[2]	933.2	3.3	104.4	4.4	[2]	0.02	[4]	1.6	[7]
-0.07	[1]	1237.5	5.8	140.9	11.5	[2]	998.0	3.0	81.6	6.1	[2]	0.05	[4]	1.2	[7]
-0.13	[1]	1319.9	6.9	137.1	13.6	[2]	995.6	3.6	105.3	7.8	[2]	0.04	[4]	-0.3	[8]
-0.15	[1]	1195.5	5.9	132.7	11.5	[2]	985.4	3.5	105.2	7.5	[2]	0.07	[4]	0.5	[8]
-0.17	[1]	1180.3	5.9	129.8	11.3	[2]	1006.2	4.0	93.1	7.2	[2]	0.06	[4]	-0.63	[8]
0.02	[1]	1119.2	4.9	128.4	9.0	[2]	1067.2	4.7	99.5	9.2	[2]	0.06	[4]	0.4	[9]
-0.26	[1]	1262.3	6.0	138.2	12.1	[2]	1065.7	3.7	107.5	8.0	[2]	0.07	[4]		
-0.21	[1]	1124.7	5.3	152.4	11.1	[2]	1036.8	3.3	123.7	8.3	[2]	0.03	[4]		
-0.06	[1]	1213.8	5.7	130.8	11.9	[2]	987.2	3.3	119.9	8.4	[2]	0.02	[5]		
0.30	[1]	1054.4	5.3	112.3	11.8	[2]	1054.5	4.0	98.1	8.2	[2]				
0.00	[1]	963.7	4.0	126.0	9.8	[2]	1064.3	3.7	96.6	8.5	[2]				
0.12	[1]	1095.1	6.0	85.5	10.5	[2]	1072.7	4.1	94.5	7.7	[2]				
-0.13	[1]	933.7	4.3	141.6	11.0	[2]	1146.7	4.5	79.3	7.7	[2]				
-0.21	[1]	981.9	4.6	121.0	10.0	[2]	1044.0	4.1	76.5	7.2	[2]				
-0.14	[1]	961.6	3.8	105.3	8.4	[2]	912.0	3.4	93.0	6.6	[2]				
-0.12	[1]	1040.3	4.6	125.3	9.6	[2]	1116.2	3.7	99.5	7.3	[2]				
-0.30	[1]	1081.0	4.2	126.5	10.0	[2]	1120.0	3.7	98.1	7.5	[2]				
0.05	[1]	959.7	3.8	246.4	12.9	[2]	1130.5	4.4	97.5	9.6	[2]				
0.10	[1]	997.2	3.9	253.8	13.6	[2]	1139.7	4.1	98.1	9.1	[2]				
-0.25	[1]	950.8	4.0	257.3	13.7	[2]	1008.5	3.7	85.3	7.0	[2]				
-0.33	[1]	1409.9	7.1	141.6	14.2	[2]	1104.7	4.2	88.3	7.7	[2]				
-0.35	[1]	953.5	3.8	242.9	12.7	[2]	1378.5	6.8	121.4	13.3	[2]				
-0.44	[1]	1087.3	4.8	135.5	10.2	[2]	1136.5	4.8	133.2	9.4	[2]				
-0.17	[1]	1030.8	4.4	357.8	18.6	[2]	1143.2	5.0	134.5	9.2	[2]				
-0.31	[1]	955.0	3.9	247.5	13.4	[2]	1134.3	4.9	135.2	9.8	[2]				
-0.44	[1]	965.0	2.7	55.7	3.0	[2]	1129.0	5.0	137.7	9.9	[2]				
-0.40	[1]	1009.4	2.9	137.4	5.0	[2]	1135.2	5.0	136.5	9.9	[2]				
-0.31	[1]	1201.2	5.1	137.0	9.4	[2]	1171.8	4.6	100.6	10.1	[2]				
-0.33	[1]	1350.6	4.6	108.6	8.9	[2]	994.6	3.7	98.6	8.1	[2]				
-0.18	[1]	1312.8	4.6	110.5	9.3	[2]	910.4	3.2	100.5	6.8	[2]				
-0.31	[1]	1154.5	4.3	79.8	6.2	[2]	955.1	3.4	81.9	5.2	[2]				
-0.21	[1]	1177.2	4.3	81.5	6.0	[2]	957.4	3.0	82.3	4.7	[2]				
-0.24	[1]	878.4	2.4	56.3	2.9	[2]	963.8	3.0	83.2	5.0	[2]				
-0.18	[1]	1056.5	3.9	76.1	4.9	[2]	1120.6	5.2	123.4	9.5	[2]				
-0.32	[1]	1264.8	5.4	91.8	7.2	[2]	1503.1	6.6	84.2	11.7	[2]				
-0.12	[1]	1169.8	4.8	99.7	6.8	[2]	913.8	3.7	85.1	5.3	[2]				
-0.19	[1]	1194.0	4.8	100.9	6.8	[2]	928.3	3.7	85.0	5.3	[2]				
-0.21	[1]	1197.0	4.9	99.5	6.7	[2]	917.7	3.7	84.8	5.3	[2]				
-0.30	[1]	1222.2	4.8	99.7	6.9	[2]	1418.9	6.9	81.3	12.3	[2]				
0.07	[1]	1203.8	4.8	98.9	6.7	[2]	1400.4	6.8	80.7	12.1	[2]				
-0.14	[1]	1289.5	4.9	98.4	6.6	[2]	1080.6	4.1	114.5	7.0	[2]				
-0.36	[1]	1145.8	5.6	127.6	9.5	[2]	1125.4	4.1	115.8	7.0	[2]				
-0.22	[1]	1286.6	6.7	125.3	12.0	[2]	1165.0	4.2	115.5	7.2	[2]				
-0.30	[1]	1296.3	6.2	121.9	11.9	[2]	1137.0	4.0	110.6	6.9	[2]				
-0.29	[1]	1221.3	6.0	118.1	10.7	[2]	958.6	3.4	78.7	5.0	[2]				
-0.24	[1]	893.8	3.2	76.5	4.1	[2]	924.4	3.5	80.6	5.3	[2]				
-0.07	[1]	1261.0	6.1	118.4	10.1	[2]	1016.4	3.4	79.1	5.3	[2]				
-0.19	[1]	1227.6	6.3	122.3	10.6	[2]	972.4	3.4	79.7	5.1	[2]				
-0.22	[1]	1244.6	6.0	119.8	10.3	[2]	1424.6	7.1	83.9	11.7	[2]				
-0.23	[1]	1121.8	5.4	123.7	9.6	[2]	977.8	3.6	78.9	5.1	[2]				
-0.01	[1]	1140.2	5.7	123.8	9.7	[2]	972.8	3.4	79.8	5.3	[2]				
-0.04	[1]	1200.8	5.8	135.4	11.6	[2]	928.4	3.4	77.5	5.0	[2]				
0.04	[1]	1246.8	6.1	139.4	12.3	[2]	609.2	5.4	316.2	24.3	[2]				
-0.01	[1]	1216.0	5.9	136.9	11.7	[2]	720.6	3.9	100.9	8.0	[2]				
-0.07	[1]	1246.0	6.0	138.0	11.9	[2]	644.7	4.7	372.3	23.6	[2]				
-0.07	[1]	1201.5	6.1	137.9	11.9	[2]	695.4	4.8	382.0	24.0	[2]				
-0.09	[1]	1142.4	4.0	116.4	6.9	[2]	892.7	4.4	181.4	12.0	[2]				
-0.04	[1]	1127.4	4.1	116.1	7.1	[2]	1132.6	6.2	273.4	22.3	[2]				
-0.01	[1]	1210.8	4.2	118.4	9.4	[2]	1158.7	6.0	291.2	22.9	[2]				
-0.06	[1]	1093.5	4.2	111.8	10.0	[2]	1119.8	5.7	301.9	23.3	[2]				
0.02	[1]	1142.0	4.2	113.0	9.9	[2]	1110.2	5.9	296.3	23.3	[2]				
0.00	[1]	1105.0	4.2	111.7	9.7	[2]	1101.2	5.8	272.9	22.6	[2]				
-0.08	[1]	1126.4	4.1	111.6	9.5	[2]	1097.6	5.9	277.9	22.7	[2]				
-0.12	[1]	1219.2	3.8	111.3	8.5	[2]	1122.6	5.9	304.5	23.8	[2]				
0.07	[1]	1084.8	3.8	103.6	8.4	[2]	1103.8	6.0	275.4	23.3	[2]				
-0.23	[1]	1083.8	3.8	105.3	8.3	[2]	1190.2	5.8	295.2	23.3	[2]				
-0.09	[1]	1120.2	3.6	104.6	8.1	[2]	1084.5	5.3	115.9	9.9	[2]				
-0.16	[1]	1190.2	5.0	113.7	8.8	[2]	1276.4	7.0	164.9	15.9	[2]				
-0.30	[1]	1194.7	5.1	115.7	8.8	[2]	1179.8	5.3	174.2	12.3	[2]				
-0.42	[1]	1241.3	6.3	132.7	12.4	[2]	1167.8	5.6	144.5	12.4	[2]				
-0.71	[1]	1194.6	6.0	134.2	11.6	[2]	1113.8	5.6	186.6	13.3	[2]				
-0.22	[1]	1251.8	6.1	127.5	11.7	[2]	1093.0	5.8	147.5	12.1	[2]				
-0.43	[1]	1224.4	5.7	130.0	10.9	[2]	969.3	3.6	49.1	3.8	[2]				
-0.43	[1]	1159.6	5.9	132.2	11.4	[2]	1170.2	5.7	61.1	7.6	[2]				
0.02	[1]	1233.2	5.1	82.1	7.4	[2]	664.7	2.6	33.1	2.0	[2]				
-0.18	[1]	1086.7	4.0	106.1	5.9	[2]	1150.8	5.6	61.5	7.3	[2]				
-0.18	[1]	1057.0	5.7	143.6	11.0	[2]	976.6	3.9	106.1	6.9	[2]				
-0.33	[1]	926.2	5.9	256.3	25.0	[2]	978.6	3.9	107.1	6.5	[2]				
-0.13	[1]	928.2	5.4	238.5	23.8	[2]	1062.7	3.9	99.1	7.0	[2]				
0.02	[1]	871.8	5.4	246.9	23.8	[2]	943.4	4.0	108.2	6.9	[2]				
-0.09	[1]	1077.8	2.9	59.6	3.5	[2]	1074.4	5.0	97.0	8.4	[2]				
-0.42	[1]	1007.2	5.6	253.1	23.8	[2]	1158.6	4.9	95.9	8.3	[2]				
-0.19	[1]	1114.6	3.2	60.7	3.2	[2]	1103.4	5.0	96.4	8.3	[2]				
-0.42	[1]	1111.0	4.0	61.0	4.5	[2]	1090.2	4.9	97.5	8.4	[2]				
-0.24	[1]	1062.4	3.1	105.4	4.1	[2]	1199.4	5.5	114.8	12.1	[2]				
-0.37	[1]	1549.8	5.7	128.0	10.4	[2]	1166.6	5.6	113.6	11.7	[2]				
-0.30	[1]	1530.4	6.9	113.1	12.7	[2]	852.4	3.3	136.6	7.3	[2]				
-0.19	[1]	1250.0	5.2	131.5	10.0	[2]	1040.0	4.3	135.9	9.9	[2]				
-0.13	[1]	1428.2	5.8	103.1	10.2	[2]	1020.2	4.4	138.5	10.2	[2]				
-0.11	[1]	1565.0	7.2	109.3	12.9	[2]	995.4	4.6	137.6	10.1	[2]				
-0.38	[1]	1126.2	4.7	87.3	6.2	[2]	859.4	3.2	135.4	7.4	[2]				
-0.25	[1]	1166.2	4.8	89.9	6.6	[2]	906.6	3.3	132.8	7.0	[2]				
-0.25	[1]	1180.6	4.6	88.6	6.3	[2]	1152.2	4.3	180.9	14.1	[2]				
-0.23	[1]	1351.2	5.9	96.2	8.7	[2]	1093.8	4.7	144.2	10.7	[2]				
-0.17	[1]	1074.0	4.7	166.3	9.7	[2]	1011.4	4.0	143.9	10.8	[2]				
-0.20	[1]	1221.0	6.0	123.7	11.3	[2]	1141.8	4.6	143.4	10.9	[2]				
-0.51	[1]	1054.8	4.5	76.8	6.4	[2]	1123.8	4.5	144.6	10.6	[2]				
-0.15	[1]	1275.8	5.2	97.6	7.7	[2]	1430.7	6.9	132.8	13.6	[2]				
		1364.4	5.8	95.2	9.0	[2]	1481.3	6.7	131.0	13.2	[2]				
		1112.6	4.9	120.9	8.3	[2]	1207.8	9.4	138.2	20.6	[2]				
		913.8	3.4	109.7	4.6	[2]	1482.8	7.3	128.1	14.6	[2]				
		955.4	3.5	110.1	4.7	[2]	1337.0	7.0	137.3	13.9	[2]				
		905.8	3.2	109.4	4.4	[2]	1213.3	4.9	141.4	9.7	[2]				
		1183.5	5.3	87.5	8.0	[2]	1575.3	7.8	120.3	14.7	[2]				
		1192.5	5.2	89.1	8.6	[2]	1559.3	8.0	121.7	14.9	[2]				
		1180.3	5.2	89.2	8.6	[2]	1696.2	8.3	120.9	15.3	[2]				
		1183.0	4.4	127.2	8.2	[2]	1569.8	8.1	122.1	15.1	[2]				

[1] Zhang, H.L., Cottrell, E., Solheid, P.A., Kelley, K.A., and Hirschmann, M.M., 2018, Determination of Fe3+/ΣFe of XANES basaltic glass standards by Mössbauer spectroscopy and its application to the oxidation state of iron in MORB: Chemical Geology, v. 479, p. 166–175, https://d

[2] Jenner, F.E., O'Neil, H. St. C., Analysis of 60 elements in 616 ocean floor basaltic glasses: Geochemistry, Geophysics, Geosystems, https://doi.org/10.1029/2011GC004009.

[3] Lerner, A.H., 2020, The depths and locations of magma reservoirs and their consequences for the behavior of sulfur and volcanic degassing: University of Oregon, ProQuest Dissertations Publishing 28022240.

[4] Wallace, P.J., and Carmichael, I.S.E., 1994, Speciation in submarine basaltic glasses as determined by measurements of SKα X-ray wavelength shifts: American Mineralogist, v. 79, p. 161–167.

[5] Jugo,P.J., Wilke, M., and Botcharnikov, R.E., 2010, Sulfur K-edge XANES analysis of natural and synthetic basaltic glasses: Implications for S speciation and S content as functions of oxygen fugacity: Geochimica et Cosmochimica Acta, v. 74, p. 5926–5938, https://doi.org/10.1016

[6] Chaussidon, M., Sheppard, S.M.F., Michard, A., Recherches, C.De., and Vandoeuvre-les-nancy, F., 1991, Hydrogen, sulphur and neodymium isotope variations in the mantle beneath the EPR at 12°50'N: Stable Isotope Geochemistry: A Tribute to Samuel Epstein, v. 15, p. 325–33?

[7] Kanehira, K., Yui, S., Sakai, H., and Sasaki, A., 1973, Sulphide globules and sulphur isotope ratios in the abyssal tholeiite from the Mid-Atlantic Ridge near 30°N latitude: Geochemical Journal, v. 7, p. 89–96.

[8] Sakai, H., DesMarais, D.J., Ueda, A., and Moore, J.G., 1984, Concentrations and isotope ratios of carbon, nitrogen and sulfur in ocean-floor basalts: Geochimica et Cosmochimica Acta, v. 48, p. 2433–2411.

[9] Alt, J.C., Shanks, W.C., and Jackson, M.C., 1993, Cycling of sulfur in subduction zones: The geochemistry of sulfur in the Mariana Island Arc and back-arc trough: Earth and Planetary Science Letters, v. 119, p. 477–494, https://doi.org/10.1016/0012-821X(93)90057-G.

Table S14. Sampling locations used for each
Lassen cinder cone.

Cinder Cone	Lattitude	Longitude
BBL	40.584311	-121.617219
BORG	40.659719	-121.239039
BRM	40.574569	-121.588161
BPPC	40.328761	-121.913489
BAS-44	40.630911	-121.344839
BRVB	40.530200	-121.075469

CHAPTER III SUPPLEMENTARY INFORMATION AND FIGURES

Appendix B Supplementary Figures
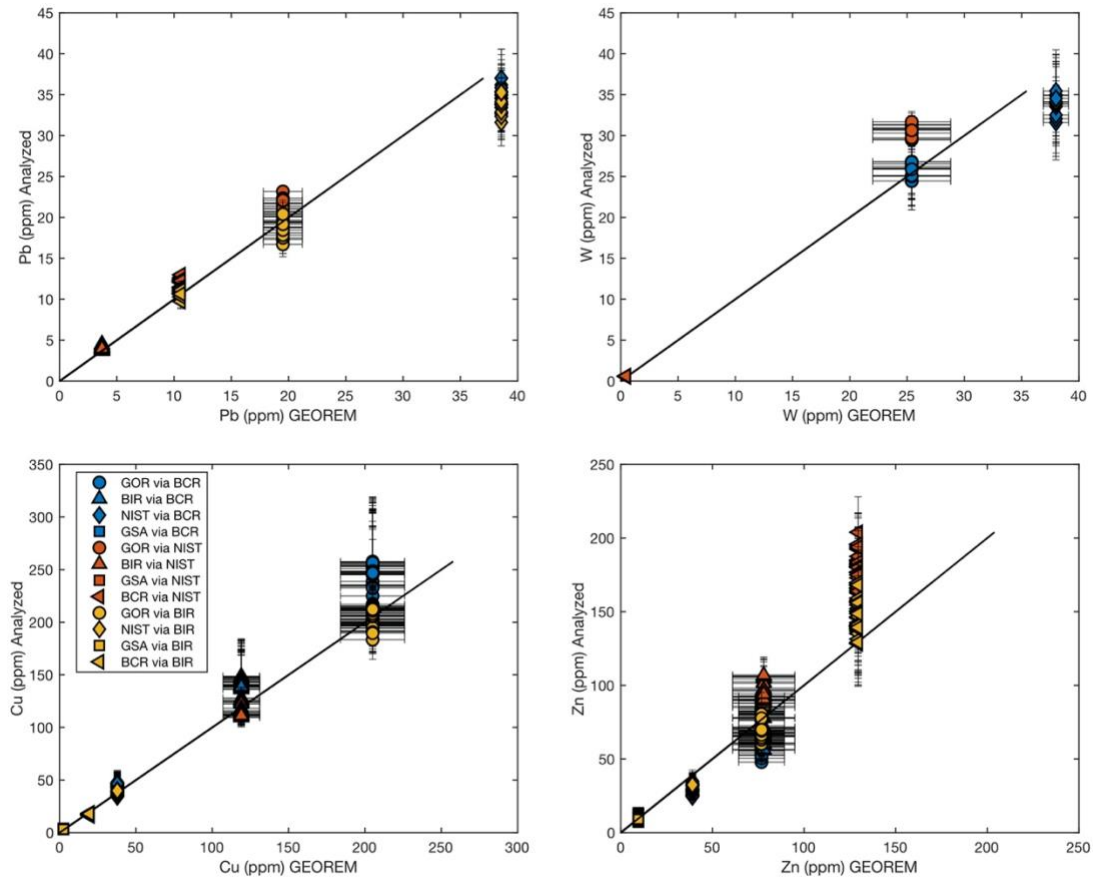
Figure S1. Analyzed concentrations of metals in glass standards via LA-ICPMS plotted against reference value (GEOREM, Jochum et al., 2007). Each symbol shape represents a distinct measured standard, and each symbol color represents a reference standard. 1:1 line shown for comparison.
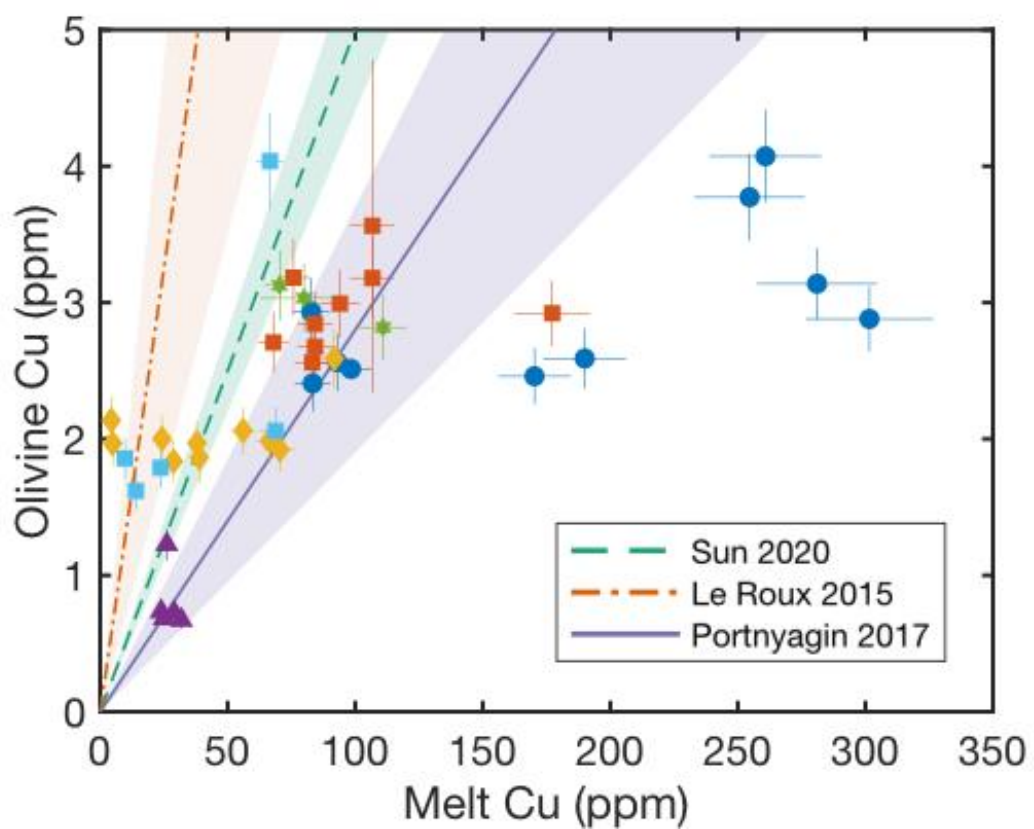
Figure S2. Analyzed Cu concentrations in melt inclusion and olivine hosts. Each symbol represents analysis on one melt inclusion. Error bars represent standard error. Olivine-Melt partitioning relationships from Sun et al. (2020), Le Roux et al. (2015), and Portnyagin et al. (2017) shown for comparison. Shaded regions beneath each line represent the reported one standard deviation for each partition coefficient.
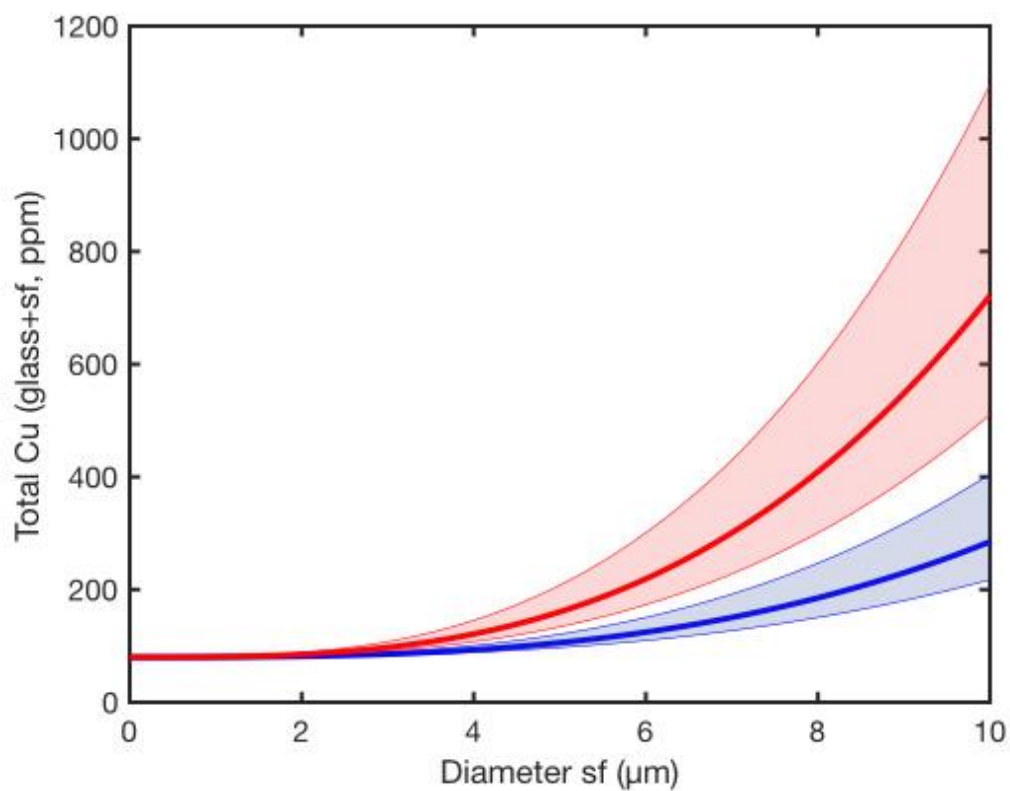
Figure S3. Calculated total Cu in a combined sulfide and silicate melt inclusion, plotted as a function of sulfide (sf) diameter. Thick lines show calculated Cu assuming a 70 µm diameter inclusion, and shaded regions show ± 10 µm diameter. Red line shows sulfide liquid (DCu = 1659; Kiseeva 2015) and blue line shows monosulfide solid solution (DCu = 531; Li and Audetat 2021) calculated assuming 1100 °C, and silicate melt containing 8 wt. % FeO, 80 ppm Cu, and 100 ppm Ni.
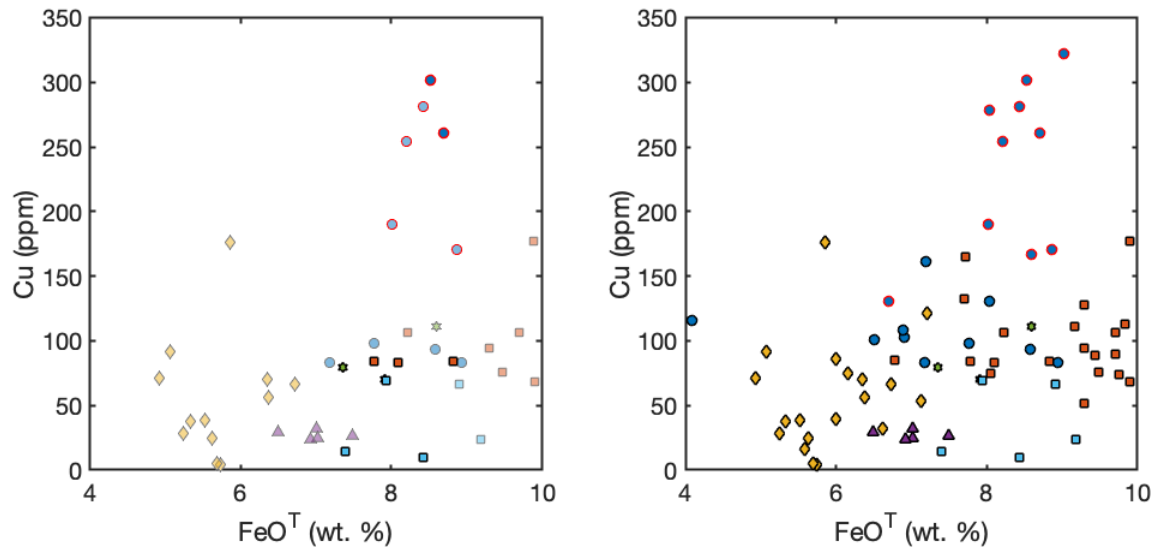
Figure S4. Analyzed melt inclusion compositions from each cinder cone. Symbols with red outlines show those that are affected by crustal assimilation and screened from primary magma calculations. Right panel shows melt inclusions with available petrographic data, where light symbols are inclusions that do not contain a sulfide, and dark symbols are inclusions that contain a sulfide.
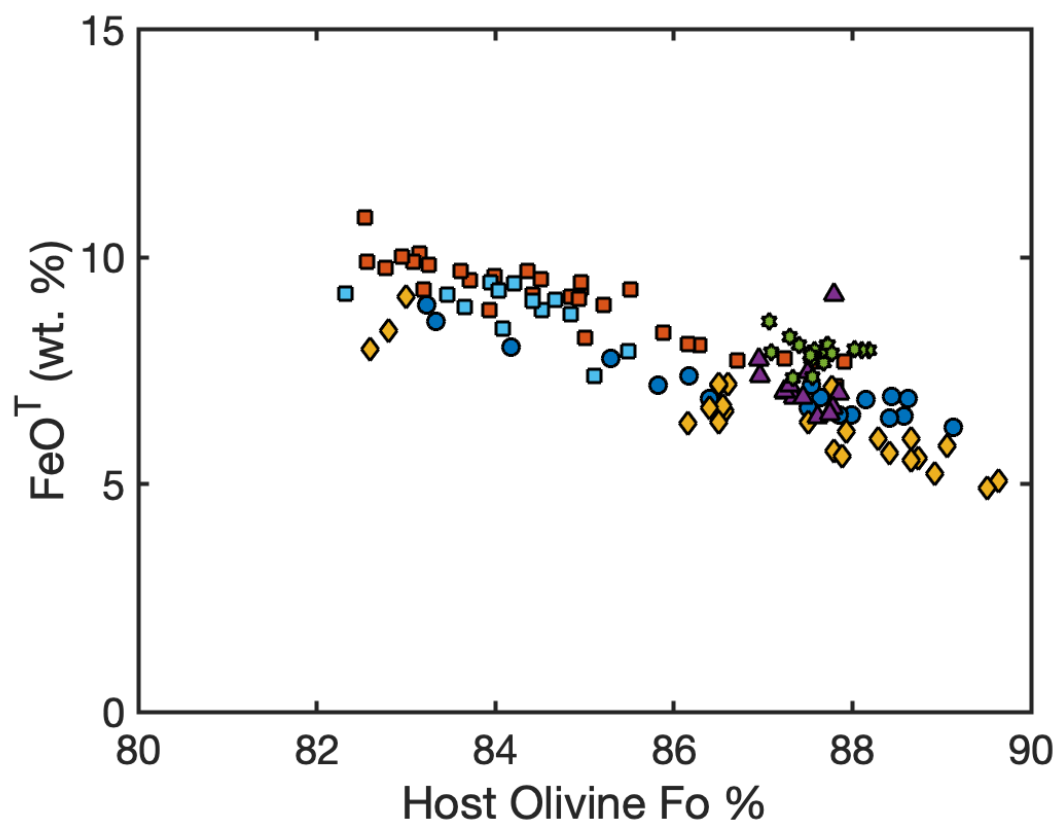
Figure S5. Analyzed melt inclusion compositions from each cinder cone plotted against host olivine forsterite content.
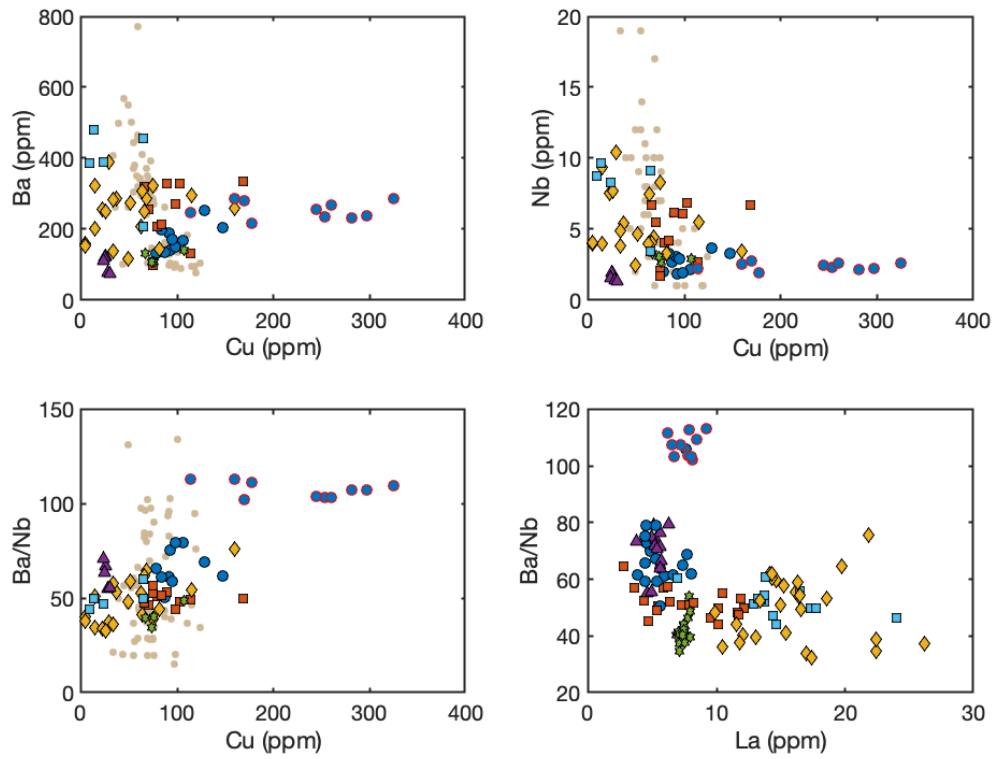
Figure S6. PEC-corrected melt inclusion compositions from each cinder cone. Symbols with red outlines show those affected by crustal assimilation and screened from primary magma calculations. Beige symbols show primitive (MgO > 8 wt. %) Lassen whole rock compositions.
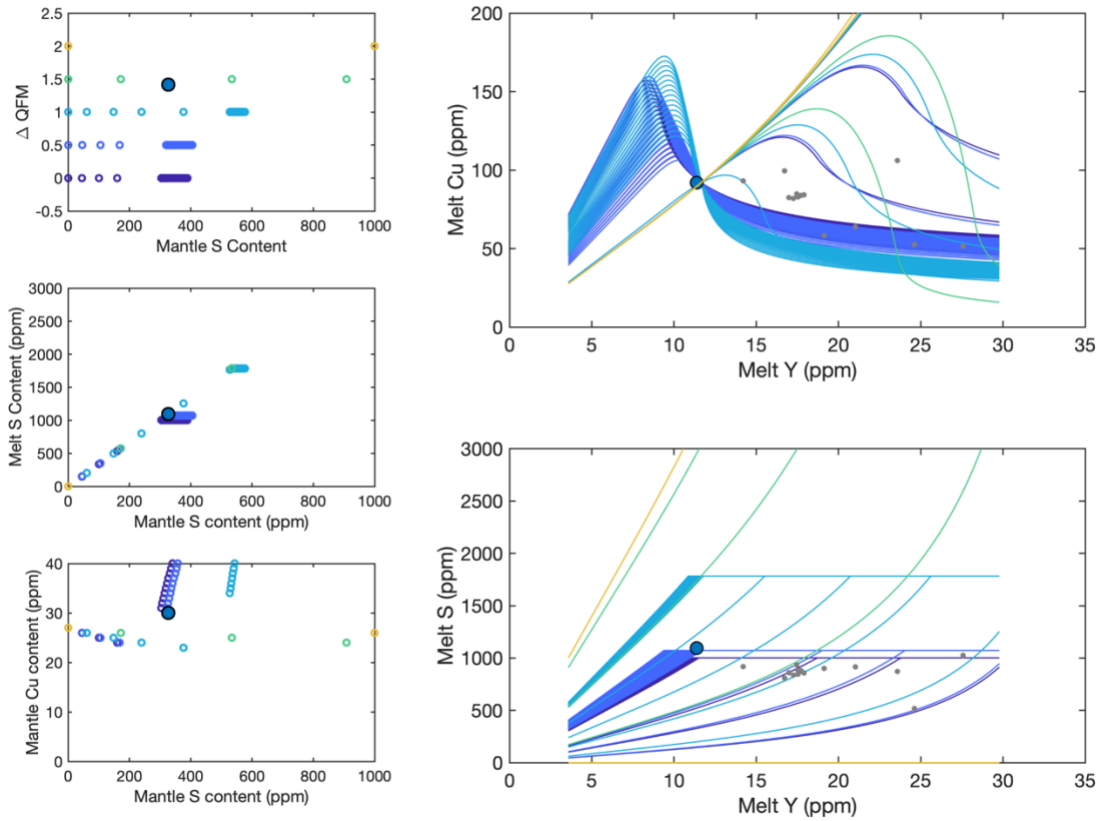
Figure S7. Mantle melting models at variable mantle f_{O_2} (QFM to QFM + 2 in increments of 0.5 log units) and variable initial mantle Cu content (1 to 40 ppm in incremements of 1 ppm). Only models that can reproduce the estimated primary melt Cu and Y contents of cinder cone BORG are shown. (Left) External constraints on mantle melting conditions for cinder cone BORG shown in filled symbols. Parameters used for each model shown in open symbols, where each data point corresponds to one model curve in the right panel. (Right) Primary melt compositions of cinder cone BORG (filled symbol) compared to modeled melt compositions during near aggregate fractional melting. Primitive MORB glasses shown in comparison in gray circles (Jenner et al., 2012). See main text for details.
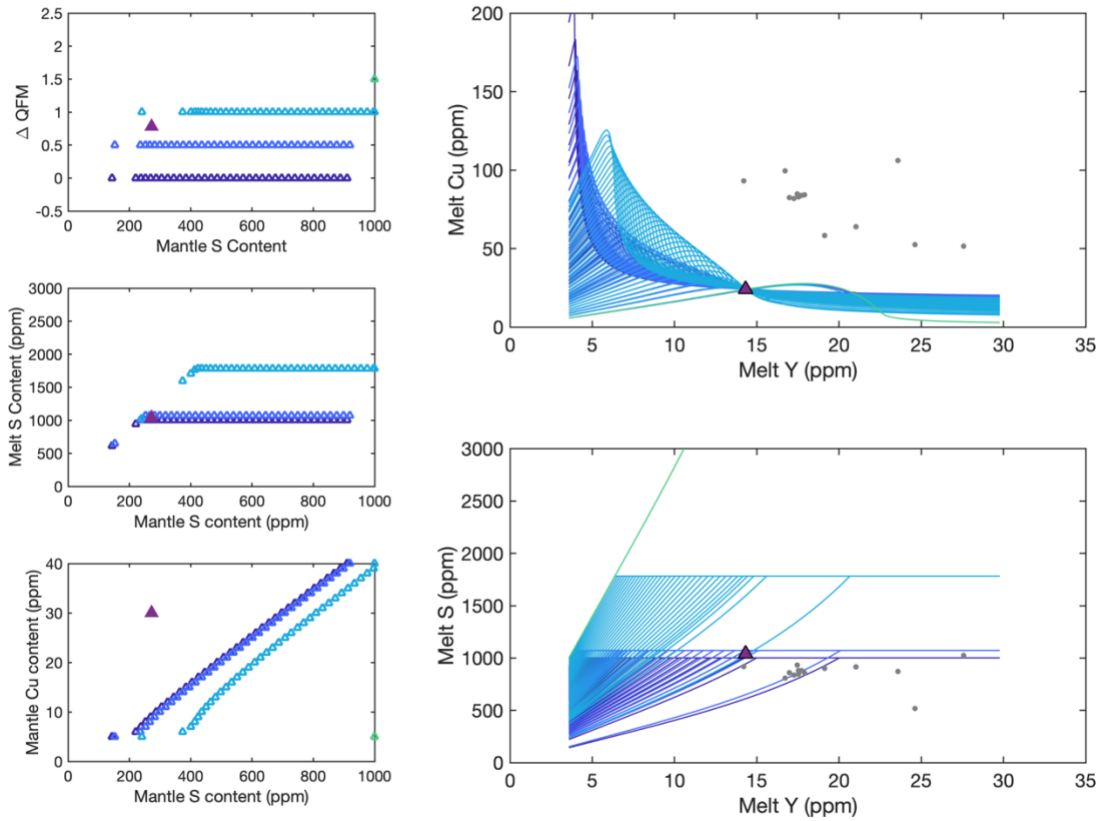
Figure S8. Mantle melting models at variable mantle fO_2 (QFM to QFM + 2 in increments of 0.5 log units) and variable initial mantle Cu content (1 to 40 ppm in incremements of 1 ppm). Only models that can reproduce the estimated primary melt Cu and Y contents of cinder cone BPPC are shown. (Left) External constraints on mantle melting conditions for cinder cone BPPC shown in filled symbols. Parameters used for each model shown in open symbols, where each data point corresponds to one model curve in the right panel. (Right) Primary melt compositions of cinder cone BPPC (filled symbol) compared to modeled melt compositions during near aggregate fractional melting. Primitive MORB glasses shown in comparison in gray circles (Jenner et al., 2012). See main text for details.
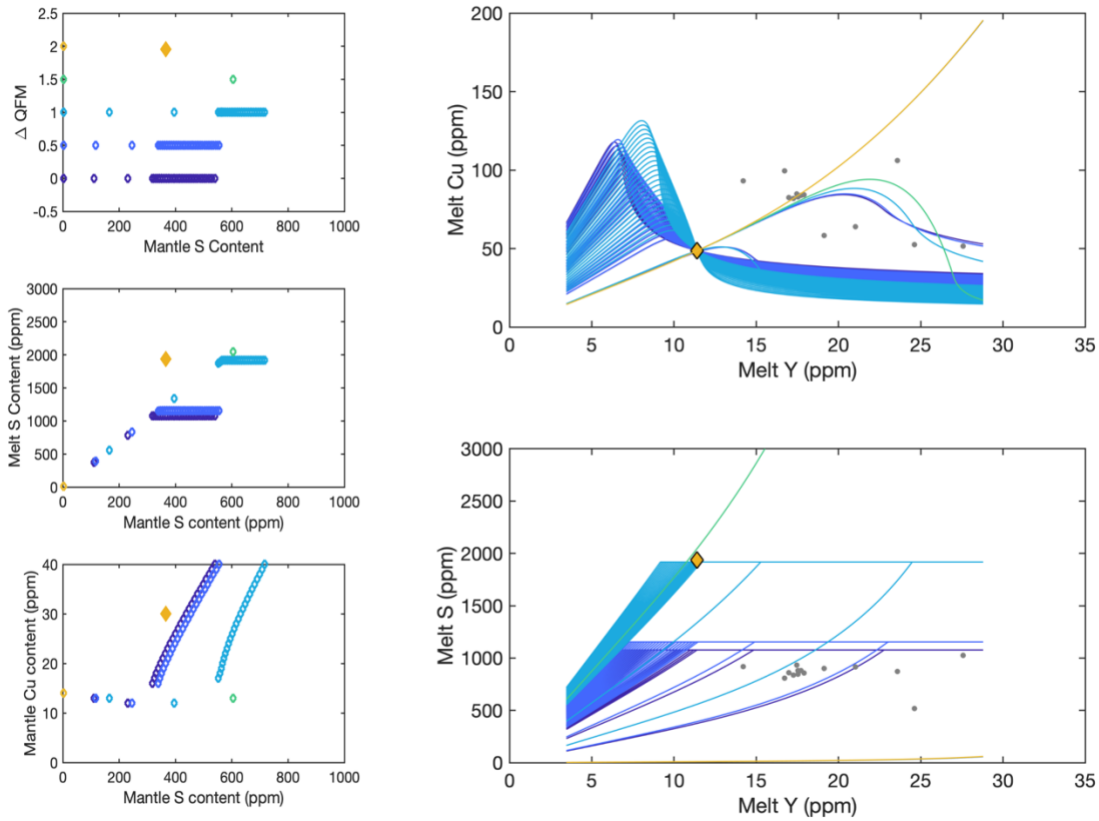
Figure S9. Mantle melting models at variable mantle fO_2 (QFM to QFM + 2 in increments of 0.5 log units) and variable initial mantle Cu content (1 to 40 ppm in incremements of 1 ppm). Only models that can reproduce the estimated primary melt Cu and Y contents of cinder cone BRM are shown. (Left) External constraints on mantle melting conditions for cinder cone BRM shown in filled symbols. Parameters used for each model shown in open symbols, where each data point corresponds to one model curve in the right panel. (Right) Primary melt compositions of cinder cone BRM (filled symbol) compared to modeled melt compositions during near aggregate fractional melting. Primitive MORB glasses shown in comparison in gray circles (Jenner et al., 2012). See main text for details.
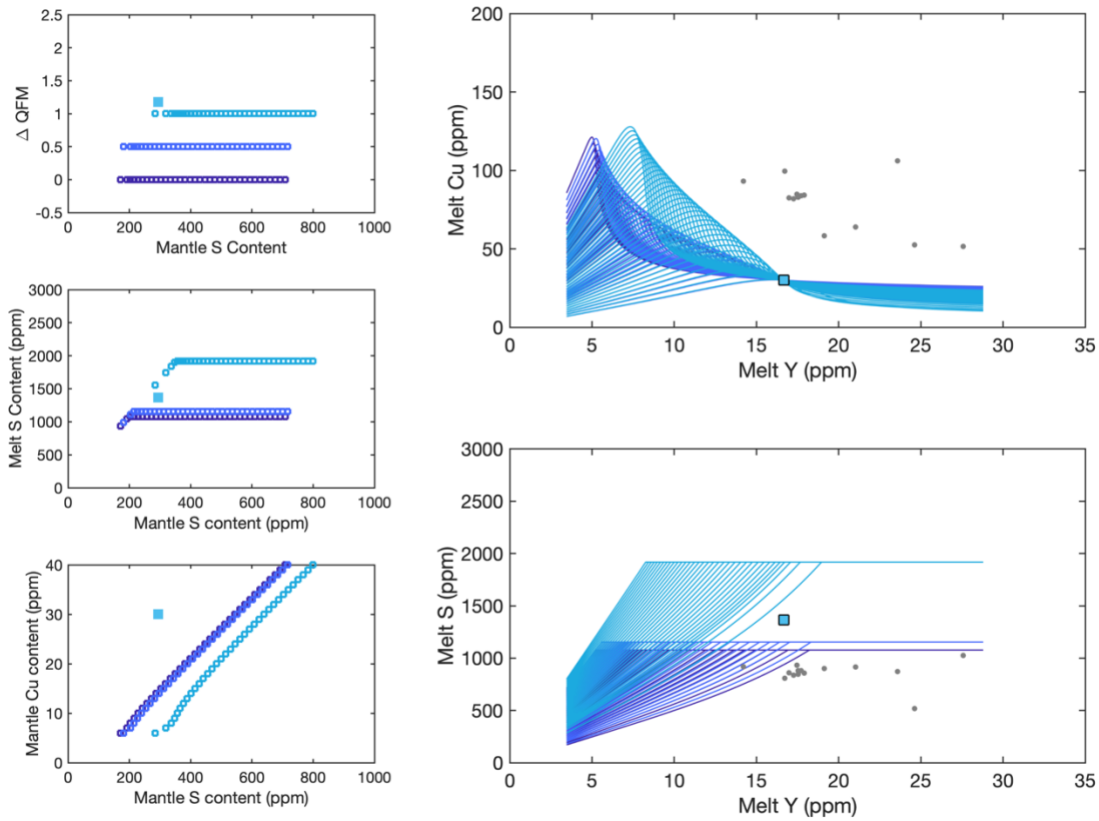
Figure S10. Mantle melting models at variable mantle fO_2 (QFM to QFM + 2 in increments of 0.5 log units) and variable initial mantle Cu content (1 to 40 ppm in incremements of 1 ppm). Only models that can reproduce the estimated primary melt Cu and Y contents of cinder cone BRVB are shown. (Left) External constraints on mantle melting conditions for cinder cone BRVB shown in filled symbols. Parameters used for each model shown in open symbols, where each data point corresponds to one model curve in the right panel. (Right) Primary melt compositions of cinder cone BRVB (filled symbol) compared to modeled melt compositions during near aggregate fractional melting. Primitive MORB glasses shown in comparison in gray circles (Jenner et al., 2012). See main text for details.
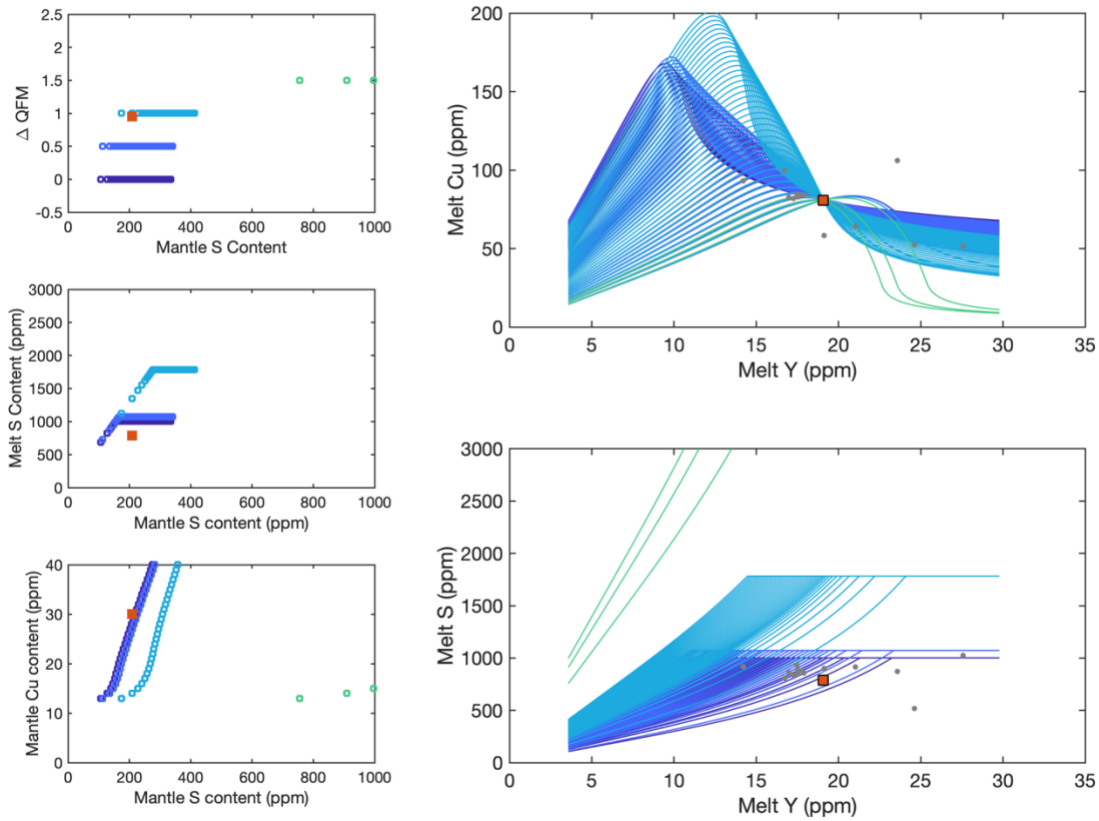
Figure S11. Mantle melting models at variable mantle fO_2 (QFM to QFM + 2 in increments of 0.5 log units) and variable initial mantle Cu content (1 to 40 ppm in incremements of 1 ppm). Only models that can reproduce the estimated primary melt Cu and Y contents of cinder cone BBL are shown. (Left) External constraints on mantle melting conditions for cinder cone BBL shown in filled symbols. Parameters used for each model shown in open symbols, where each data point corresponds to one model curve in the right panel. (Right) Primary melt compositions of cinder cone BBL (filled symbol) compared to modeled melt compositions during near aggregate fractional melting. Primitive MORB glasses shown in comparison in gray circles (Jenner et al., 2012). See main text for details.
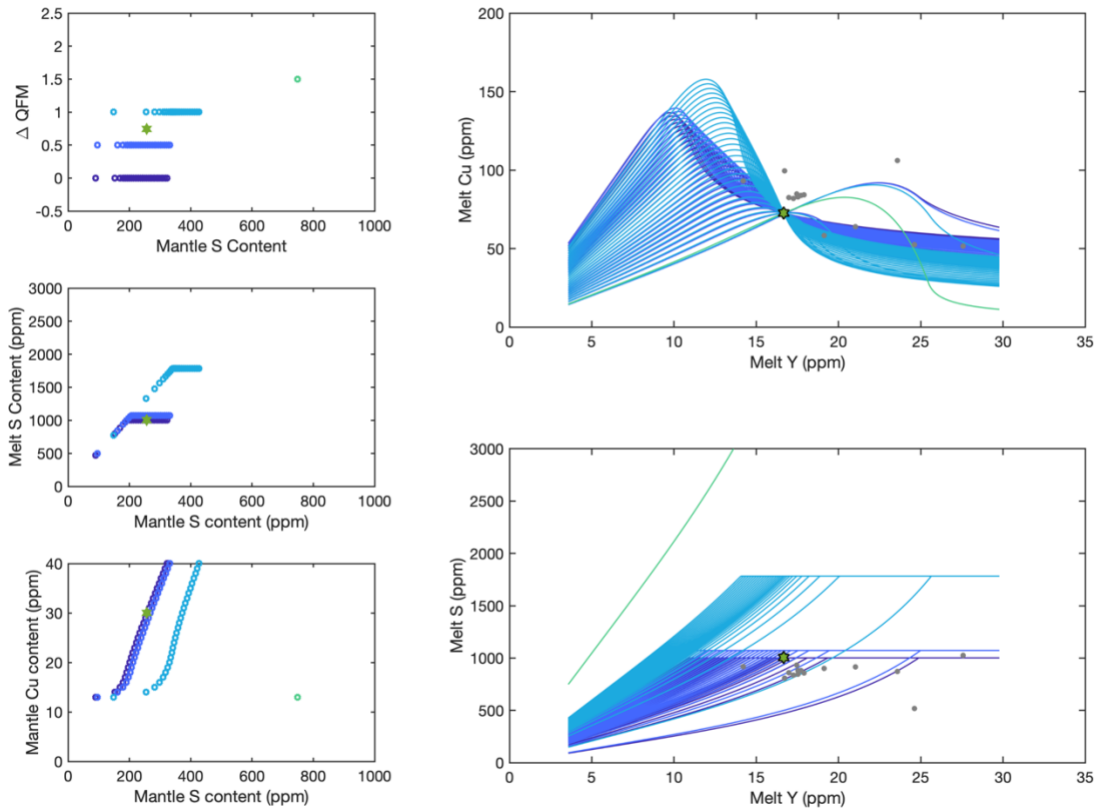
Figure S12. Mantle melting models at variable mantle fO_2 (QFM to QFM + 2 in increments of 0.5 log units) and variable initial mantle Cu content (1 to 40 ppm in incremements of 1 ppm). Only models that can reproduce the estimated primary melt Cu and Y contents of cinder cone BAS-44 are shown. (Left) External constraints on mantle melting conditions for cinder cone BAS-44 shown in filled symbols. Parameters used for each model shown in open symbols, where each data point corresponds to one model curve in the right panel. (Right) Primary melt compositions of cinder cone BAS-44 (filled symbol) compared to modeled melt compositions during near aggregate fractional melting. Primitive MORB glasses shown in comparison in gray circles (Jenner et al., 2012). See main text for details.

Table S1. Analyzed Major element and trace element melt inclusion data. Major elements values and standard deviation calculated from the average of 3-5 analysis spots. H2O uncertainty represents propagated error calculated with standard deviation of 2-4 sample thickness and absorbance peak height measurements. Trace elements measured via LA-ICPMS. Uncertainty represents standard error including uncertainty in calibration standard. Major elements, S, Cl, and H2O reported in wt. %. Trace elements reported in ppm.

| Cinder Cone	Tephra Sample	Inclusion	Minimum Inclusion Width (µm)	Maximum Inclusion Width (µm)	Vapor bubble?	Vapor bubble Diameter* (µm)	Oxide in MI?	Sulfide in MI?	Date Analyzed EPMA	SiO2	1 s.d.	TiO2	1 s.d.	Al2O3	1 s.d.	FeOT	1 s.d.
BAS-44	BAS-44-2	1	54	58	yes	12	no	no	7/31/18	48.47	0.26	0.84	0.04	17.63	0.06	7.85	0.16
BAS-44	BAS-44-2	10	36	40	yes	8	no	yes	7/31/18	48.14	0.52	1.01	0.04	18.25	0.06	8.31	0.21
BAS-44	BAS-44-2	2	52	91	yes	19	yes	yes	7/31/18	48.34	1.65	1.01	0.03	17.58	0.16	7.14	0.31
BAS-44	BAS-44-2	4	84	86	yes	22	yes	yes	7/23/18	48.86	0.41	1.04	0.03	18.26	0.29	7.15	0.45
BAS-44	BAS-44-2	5	55	66	yes	14	no	yes	7/23/18	47.49	2.34	0.98	0.01	17.63	0.12	7.61	0.19
BAS-44	BAS-44-2	6	62	98	yes	19	yes	yes	7/23/18	47.58	0.23	1.02	0.07	18.45	0.82	7.68	0.46
BAS-44	BAS-44-2	7a	36	66	no	n.r.	no	no	7/23/18	49.86	0.83	0.94	0.07	16.89	0.20	8.45	0.21
BAS-44	BAS-44-2	7b	46	58	no	n.r.	no	no	7/23/18	48.32	2.08	0.99	0.02	16.80	0.12	8.39	0.21
BBL	BBL-5	11	137	163	yes	29	yes	n.r.	6/12/17	47.97	0.04	1.22	0.00	17.00	0.16	9.90	0.05
BBL	BBL-5	14	106	109	yes	23	n.r.	n.r.	6/12/17	48.41	0.31	1.68	0.05	16.14	0.21	9.40	0.07
BBL	BBL-5	15	54	61	n.r.	n.r.	n.r.	n.r.	6/12/17	48.66	0.14	1.50	0.03	15.71	0.07	10.48	0.10
BBL	BBL-5	17	47	66	yes	12	n.r.	n.r.	6/12/17	48.10	0.17	1.09	0.03	18.34	0.18	7.46	0.14
BBL	BBL-5	18	51	65	n.r.	n.r.	n.r.	n.r.	6/12/17	48.75	0.16	1.49	0.02	16.07	0.29	9.77	0.15
BBL	BBL-5	19	103	87	yes	17	n.r.	n.r.	6/12/17	47.71	0.05	1.15	0.03	18.37	0.14	7.71	0.10
BBL	BBL-5	20	57	87	yes	19	n.r.	n.r.	6/12/17	47.97	0.24	1.29	0.03	17.64	0.63	9.51	0.10
BBL	BBL-5	21A	50	61	yes	11	n.r.	n.r.	6/12/17	48.18	0.41	1.44	0.04	17.23	0.56	8.98	0.06
BBL	BBL-5	21B	29	36	n.r.	n.r.	n.r.	n.r.	6/12/17	48.44	0.20	1.49	0.01	17.66	0.41	9.22	0.11
BBL	BBL-5	22	55	76	yes	10	yes	yes	6/12/17	48.11	0.24	1.15	0.04	18.00	0.43	7.93	0.15
BBL	BBL-5	23	112	72	n.r.	15	n.r.	n.r.	6/12/17	48.06	0.15	1.33	0.02	17.23	0.27	8.85	0.06
BBL	BBL-5	30	43	54	n.r.	10	n.r.	n.r.	6/12/17	49.12	0.25	1.17	0.04	17.17	0.15	9.03	0.10
BBL	BBL-5	31	88	88	yes	21	no	yes	7/31/18	49.96	0.89	1.23	0.05	15.94	0.17	8.56	0.22
BBL	BBL-5	32	46	68	no	n.r.	no	no	7/31/18	49.93	0.68	1.27	0.10	16.76	0.40	9.23	0.30
BBL	BBL-5	33	50	73	yes	15	no	no	7/23/18	49.22	0.83	1.29	0.03	16.75	0.12	9.61	0.42
BBL	BBL-5	34	66	70	yes	n.r.	no	yes	7/31/18	51.67	1.88	1.12	0.02	15.42	0.08	9.14	0.19
BBL	BBL-5	43	84	99	no	n.r.	no	no	11/14/19	49.59	0.31	1.25	0.04	16.66	0.31	9.49	0.42
BBL	BBL-5	44	46	50	no	n.r.	yes	yes	11/14/19	48.50	0.39	0.98	0.04	18.78	0.36	7.93	0.39
BBL	BBL-5	46	57	68	yes	17	yes	no	11/14/19	48.84	0.37	1.18	0.00	17.54	0.11	7.96	0.18
BBL	BBL-5	47	156	199	yes	30	yes	yes	11/14/19	49.02	0.27	0.94	0.02	18.90	0.50	7.71	0.18
BBL	BBL-5	49	87	124	yes	23	no	no	11/14/19	49.42	0.27	1.17	0.03	18.14	0.09	9.70	0.21
BBL	BBL-5	3	41	58	yes	7	n.r.	n.r.	6/12/17	48.13	0.37	1.14	0.06	18.53	0.35	7.20	0.13
BBL	BBL-5	4	62	79	yes	15	no	yes	6/12/17	48.53	0.61	1.20	0.09	18.94	0.42	7.01	0.33
BBL	BBL-5	5	44	52	n.r.	n.r.	n.r.	n.r.	6/12/17	48.59	0.51	1.39	0.03	16.13	0.40	11.50	0.29
BBL	BBL-5	6	97	105	yes	23	n.r.	n.r.	6/12/17	48.58	0.46	1.37	0.02	16.41	0.20	9.39	0.14
BBL	BBL-5	7	44	69	n.r.	n.r.	n.r.	n.r.	6/12/17	47.64	0.39	1.13	0.04	18.03	0.21	7.42	0.04
BORG	BORG-1	2	148	199	yes	50	n.r.	n.r.	6/5/17	47.68	0.38	0.77	0.00	20.18	0.29	8.72	0.05
BORG	BORG-1	3	84	117	yes	21	n.r.	n.r.	6/5/17	48.28	0.15	0.91	0.04	20.89	0.23	7.77	0.13
BORG	BORG-1	8	207	226	yes	61	n.r.	yes	6/5/17	47.35	0.46	0.73	0.03	20.83	0.24	8.15	0.06
BORG	BORG-1	9	154	174	yes	41	yes	n.r.	6/5/17	49.05	0.71	0.91	0.02	20.43	0.28	5.97	0.09
BORG	BORG-1	10	182	292	yes	73	n.r.	n.r.	6/5/17	49.86	0.28	0.90	0.03	20.13	0.69	7.60	0.10
BORG	BORG-1	11	87	94	yes	25	n.r.	n.r.	6/5/17	50.59	0.11	0.90	0.02	22.45	0.22	6.71	0.15
BORG	BORG-1	12	80	92	yes	36	n.r.	n.r.	6/5/17	49.70	0.33	0.85	0.04	20.27	0.42	8.49	0.11
BORG	BORG-1	14	108	127	yes	34	n.r.	n.r.	6/5/17	48.67	0.61	0.75	0.03	19.96	0.21	6.74	0.18
BORG	BORG-1	15	105	128	yes	32	n.r.	n.r.	6/5/17	50.62	0.29	0.98	0.03	19.43	0.63	9.08	0.11
BORG	BORG-1	19	101	127	yes	25	n.r.	n.r.	6/5/17	49.65	1.24	0.91	0.01	21.84	1.64	4.09	0.13
BORG	BORG-1	20	103	131	n.r.	n.r.	n.r.	n.r.	6/5/17	48.81	0.23	0.99	0.01	20.90	0.70	7.90	0.16
BORG	BORG-1	21	166	179	yes	41	n.r.	n.r.	6/5/17	48.03	0.73	0.80	0.02	21.21	0.66	6.69	0.32
BORG	BORG-1	22	113	142	yes	33	n.r.	n.r.	6/5/17	47.25	0.16	0.91	0.04	19.62	0.20	8.23	0.07
BORG	BORG-1	23	132	139	n.r.	n.r.	n.r.	n.r.	6/5/17	48.13	1.38	0.84	0.05	20.30	2.61	8.20	1.03
BORG	BORG-1	24	159	178	yes	40	n.r.	n.r.	6/5/17	48.67	0.18	0.83	0.02	19.77	0.52	7.87	0.13
BORG	BORG-1	25	91	145	yes	39	n.r.	n.r.	6/5/17	49.16	0.02	0.78	0.04	19.83	0.27	7.11	0.04
BORG	BORG-1	31	117	142	yes	n.r.	no	no	11/14/19	48.87	0.45	0.96	0.01	18.13	0.22	8.51	0.36
BORG	BORG-1	35	79	105	yes	30	yes	no	7/31/18	49.11	1.56	0.81	0.03	17.97	0.06	7.75	0.40
BORG	BORG-1	37	154	175	yes	43	no	no	7/23/18	47.87	0.92	0.80	0.01	17.80	0.17	8.17	0.42
BORG	BORG-1	38	119	156	yes	n.r.	no	yes	7/25/18	48.49	1.52	0.87	0.01	17.91	0.13	8.11	0.20
BORG	BORG-1	40	108	106	yes	12	no	no	11/14/19	48.46	0.19	0.85	0.07	18.68	0.84	8.19	0.50
BORG	BORG-1	42	92	157	yes	33	no	no	11/14/19	47.95	0.38	0.80	0.02	17.91	0.20	7.34	0.17
BORG	BORG-1	43	156	182	yes	36	no	no	11/14/19	48.95	0.18	0.85	0.01	18.20	0.22	8.10	0.37
BORG	BORG-1	44	120	124	yes	37	no	no	11/14/19	48.99	0.30	0.85	0.01	18.86	0.09	7.53	0.20
BORG	BORG-1	45	73	103	yes	26	no	no	11/14/19	48.39	0.19	0.95	0.04	18.72	0.97	8.58	0.40
BORG	MM-L17-BORG-1	1	80	95	yes	23	no	no	11/14/19	48.47	0.37	0.68	0.02	18.31	0.11	6.85	0.41
BPPC	MM-L17-BPPC-4	13	68	80	yes	21	no	no	11/14/19	49.61	0.42	0.77	0.02	17.03	0.43	7.23	0.31
BPPC	MM-L17-BPPC-4	14	59	72	yes	14	no	no	11/14/19	50.45	0.50	0.79	0.04	17.78	0.24	6.83	0.16
BPPC	MM-L17-BPPC-4	15	81	91	yes	19	yes	no	11/14/19	50.25	0.38	0.73	0.01	16.74	0.11	6.65	0.35
BPPC	MM-L17-BPPC-4	2	69	73	yes	n.r.	yes	no	7/31/18	48.73	1.53	0.77	0.01	17.45	0.12	6.13	0.10
BPPC	MM-L17-BPPC-4	3	72	81	yes	21	no	yes	7/23/18	50.50	1.35	0.80	0.02	16.52	0.01	7.02	0.13
BPPC	MM-L17-BPPC-4	4	68	92	yes	17	yes	no	7/31/18	48.99	0.31	0.83	0.00	17.48	0.36	6.56	0.27
BPPC	MM-L17-BPPC-4	5	50	59	yes	12	no	no	7/31/18	50.06	1.61	0.78	0.02	17.67	0.21	6.75	0.16
BRM	BRM-1	14	34	48	yes	21	n.r.	n.r.	6/5/17	49.46	1.06	n.a.		20.25	n.a.	5.89	n.a.
BRM	BRM-1	16	80	120	yes	44	yes	n.r.	6/5/17	50.46	0.18	1.07	0.03	19.27	0.54	5.90	0.02
BRM	BRM-1	17	64	109	yes	32	n.r.	n.r.	6/5/17	50.05	0.42	0.98	0.01	18.95	0.58	5.83	0.07
BRM	BRM-1	18	37	52	yes	22	n.r.	n.r.	6/5/17	47.82	0.28	1.14	0.04	19.50	0.74	5.74	0.12
BRM	BRM-1	19	51	81	yes	25	n.r.	n.r.	6/5/17	49.99	0.15	1.04	0.03	19.77	0.28	6.99	0.06
BRM	BRM-1	22	57	63	yes	23	n.r.	n.r.	6/5/17	49.85	0.63	1.03	0.01	19.48	0.28	6.00	0.25
BRM	BRM-1	23	n.r.	n.r.	n.r.	n.r.	n.r.	n.r.	6/5/17	48.72	0.21	1.15	0.03	18.43	0.31	4.51	0.02
BRM	BRM-1	24	58	70	yes	19	n.r.	n.r.	6/5/17	55.52	0.37	1.97	0.08	14.40	0.16	6.67	0.03
BRM	BRM-1	25	66	88	yes	26	yes	no	6/5/17	48.90	0.20	1.05	0.05	20.01	0.36	3.68	0.40
BRM	BRM-1	30	87	126	yes	32	no	no	7/31/18	51.28	1.40	0.84	0.00	18.24	0.13	6.07	0.25
BRM	BRM-1	34	57	83	yes	25	yes	no	7/23/18	49.52	0.67	1.00	0.01	20.07	0.30	6.25	0.23
BRM	BRM-1	35	44	55	no	n.r.	yes	no	7/23/18	48.22	0.02	0.98	0.01	19.34	0.04	5.24	0.21
BRM	BRM-1	36	43	48	yes	17	yes	no	7/31/18	51.28	1.48	1.06	0.01	19.58	0.08	4.59	0.01
BRM	BRM-1	39	39	90	yes	15	yes	no	7/31/18	51.14	1.41	0.97	0.04	18.66	0.16	5.96	0.41
BRM	BRM-1	40	33	47	yes	16	yes	no	7/23/18	49.54	0.40	1.04	0.01	20.01	0.12	5.63	0.07
BRM	BRM-1	41	56	104	yes	26	yes	no	7/31/18	49.16	0.83	0.85	0.02	18.68	0.22	5.47	0.04
BRM	BRM-1	2	55	62	yes	21	yes	n.r.	6/5/17	50.23	0.03	1.03	0.04	19.97	0.29	5.46	0.16
BRM	BRM-1	3	81	103	yes	33	yes	n.r.	6/5/17	50.41	0.34	1.03	0.02	19.94	0.47	5.74	0.13
BRM	BRM-1	5	49	72	yes	19	yes	n.r.	6/5/17	48.92	0.51	1.17	0.03	19.90	0.62	5.41	0.09
BRM	BRM-1	6	42	54	yes	20	n.r.	n.r.	6/5/17	48.37	0.31	1.04	0.03	20.29	1.14	6.91	0.25
BRM	BRM-1	7	45	67	n.r.	n.r.	n.r.	n.r.	6/5/17	49.79	0.72	1.17	0.11	20.03	1.02	6.49	0.59
BRM	BRM-1	8	50	68	yes	20	n.r.	n.r.	6/5/17	49.12	0.19	1.21	0.02	20.76	0.39	5.79	0.22
BRM	MM-L17-BRM-2	1	71	89	yes	28	yes	no	7/23/18	48.63	0.53	0.82	0.04	20.04	0.10	4.90	0.04
BRM	MM-L17-BRM-2	10	70	84	yes	30	yes	no	7/23/18	48.61	1.40	1.21	0.12	20.64	0.07	5.48	0.27
BRM	MM-L17-BRM-2	13	65	112	yes	33	n.r.	n.r.	7/23/18	48.87	1.07	1.13	0.08	20.24	0.06	5.22	0.07
BRM	MM-L17-BRM-2	14	43	64	yes	18	yes	no	7/23/18	49.26	1.81	0.85	0.02	19.96	0.08	5.33	0.16
BRM	MM-L17-BRM-2	16	38	52	n.r.	n.r.	n.r.	n.r.	7/23/18	48.42	0.76	0.87	0.08	19.75	0.32	4.91	0.24
BRM	MM-L17-BRM-2	17	44	81	yes	20	yes	n.r.	7/23/18	48.87	1.11	0.85	0.01	20.42	0.21	5.30	0.22
BRM	MM-L17-BRM-2	18	80	87	yes	32	yes	no	7/23/18	50.10	0.76	0.96	0.04	20.68	0.09	5.36	0.16
BRM	MM-L17-BRM-2	24	77	133	yes	41	no	no	11/14/19	49.55	0.36	1.00	0.03	19.60	0.17	6.61	0.28
BRM	MM-L17-BRM-2	25	70	144	yes	38	no	no	11/14/19	48.86	0.25	1.08	0.04	20.48	0.37	5.49	0.14
BRM	MM-L17-BRM-2	26	81	109	yes	41	yes	no	11/14/19	49.27	0.33	1.07	0.03	21.26	0.34	5.18	0.23
BRM	MM-L17-BRM-2	29	71	100	yes	34	yes	no	11/14/19	49.98	0.43	0.87	0.02	20.46	0.17	4.83	0.42
BRM	MM-L17-BRM-2	31	92	115	yes	36	no	no	11/14/19	49.30	0.17	0.85	0.02	19.98	0.49	5.20	0.37
BRM	MM-L17-BRM-2	32	68	82	yes	92	no	no	11/14/19	49.15	0.08	0.89	0.03	20.71	0.85	5.60	0.12
BRM	MM-L17-BRM-2	8	76	288	yes	50	yes	no	7/23/18	46.63	1.12	1.11	0.00	20.18	0.19	5.61	0.13
BRVB	MM-L17-BRVB-2	10	80	83	yes	n.r.	yes	no	11/14/19	48.59	0.32	1.36	0.02	17.02	0.55	8.89	0.28
BRVB	MM-L17-BRVB-2	2	72	70	yes	15	no	yes	11/14/19	49.48	0.19	1.19	0.02	17.25	0.30	7.64	0.04
BRVB	MM-L17-BRVB-2	4	55	66	yes	19	no	yes	11/14/19	48.27	0.52	1.49	0.01	19.09	0.26	8.32	0.11
BRVB	MM-L17-BRVB-2	6	55	62	yes	n.r.	no	yes	11/14/19	48.97	0.51	0.97	0.02	18.57	0.38	7.26	0.32
BRVB	MM-L17-BRVB-2	7	21	61	yes	70	no	no	11/14/19	47.72	0.57	1.49	0.01	18.52	0.22	8.72	0.47

Cinder Cone	Tephra Sample	Inclusion	MnO	1 s.d.	MgO	1 s.d.	CaO	1 s.d.	Na₂O	1 s.d.	K₂O	1 s.d.	P₂O₅	1 s.d.	S	1 s.d.	Cl	1 s.d.	H₂O	1 s.d.	Olivine Host Fo %
BAS-44	BAS-44-2	1	0.12	0.02	7.94	0.05	11.61	0.08	2.64	0.08	0.25	0.03	0.14	0.02	0.12	0.01	0.03	0.00	0.76	0.01	87.09
BAS-44	BAS-44-2	10	0.15	0.01	7.16	0.21	10.83	0.05	2.87	0.13	0.41	0.04	0.19	0.00	0.03	0.00	0.04	0.00	n. a.	n. a.	87.70
BAS-44	BAS-44-2	2	0.14	0.01	7.82	0.08	11.17	0.14	2.93	0.12	0.28	0.03	0.18	0.02	0.13	0.01	0.04	0.00	1.44	0.09	87.55
BAS-44	BAS-44-2	4	0.13	0.01	6.84	0.90	11.42	0.34	2.91	0.41	0.28	0.04	0.20	0.04	0.12	0.00	0.04	0.00	1.14	0.03	87.33
BAS-44	BAS-44-2	5	0.12	0.01	7.57	0.18	11.31	0.13	2.78	0.12	0.28	0.02	0.17	0.00	0.12	0.00	0.04	0.00	1.27	0.01	87.09
BAS-44	BAS-44-2	6	0.14	0.02	7.43	1.13	11.41	0.10	3.12	0.28	0.30	0.01	0.17	0.02	0.12	0.01	0.05	0.00	1.25	0.03	87.68
BAS-44	BAS-44-2	7a	0.16	0.00	7.77	0.10	10.79	0.10	2.76	0.13	0.34	0.03	0.16	0.04	0.11	0.01	0.04	0.00	0.51	0.72	87.06
BAS-44	BAS-44-2	7b	0.15	0.01	7.66	0.04	10.64	0.12	2.87	0.17	0.36	0.02	0.17	0.01	0.11	0.00	0.04	0.00	n. a.	n. a.	86.70
BBL	BBL-5	11	0.18	0.01	6.56	0.02	9.23	0.01	3.58	0.09	0.72	0.00	0.28	0.02	0.10	0.00	0.03	0.00	n. a.	n. a.	82.37
BBL	BBL-5	14	0.15	0.01	6.60	0.02	8.30	0.69	4.35	0.09	0.83	0.01	0.34	0.02	0.10	0.00	0.03	0.00	n. a.	n. a.	82.77
BBL	BBL-5	15	0.18	0.02	6.67	0.19	8.29	0.79	3.82	0.10	0.65	0.06	0.31	0.02	0.11	0.00	0.03	0.00	n. a.	n. a.	82.53
BBL	BBL-5	17	0.12	0.01	6.73	0.07	10.97	0.12	3.29	0.06	0.33	0.02	0.14	0.00	0.09	0.00	0.02	0.00	n. a.	n. a.	87.91
BBL	BBL-5	18	0.18	0.00	6.75	0.05	8.76	0.05	3.88	0.14	0.76	0.02	0.30	0.01	0.10	0.00	0.03	0.00	n. a.	n. a.	83.16
BBL	BBL-5	19	0.13	0.01	6.95	0.01	9.86	0.81	3.22	0.13	0.33	0.00	0.19	0.02	0.08	0.00	0.02	0.00	n. a.	n. a.	86.28
BBL	BBL-5	20	0.16	0.01	6.52	0.03	9.13	0.70	3.46	0.16	0.64	0.03	0.29	0.02	0.09	0.00	0.03	0.00	n. a.	n. a.	83.25
BBL	BBL-5	21A	0.15	0.02	6.82	0.32	8.99	0.84	3.78	0.09	0.61	0.01	0.28	0.02	0.09	0.00	0.02	0.00	n. a.	n. a.	84.96
BBL	BBL-5	21B	0.15	0.01	6.69	0.34	9.25	0.64	3.81	0.18	0.60	0.01	0.31	0.02	0.09	0.00	0.03	0.00	n. a.	n. a.	84.96
BBL	BBL-5	22	0.12	0.01	6.21	0.36	11.08	0.08	3.12	0.01	0.30	0.00	0.15	0.00	0.09	0.00	0.02	0.01	n. a.	n. a.	86.42
BBL	BBL-5	23	0.15	0.02	6.71	0.04	9.95	0.08	3.45	0.05	0.50	0.02	0.22	0.01	0.10	0.00	0.02	0.00	n. a.	n. a.	84.42
BBL	BBL-5	30	0.17	0.01	6.25	0.07	9.54	0.18	3.41	0.14	0.73	0.05	0.31	0.03	0.12	0.01	0.05	0.00	n. a.	n. a.	85.51
BBL	BBL-5	31	0.16	0.01	6.76	0.08	9.95	0.18	3.49	0.08	0.55	0.04	0.22	0.02	0.12	0.01	0.04	0.00	1.15	0.03	83.94
BBL	BBL-5	32	0.17	0.02	5.49	0.52	9.81	0.05	3.62	0.26	0.62	0.03	0.28	0.02	0.13	0.01	0.04	0.00	1.24	0.11	83.71
BBL	BBL-5	33	0.17	0.01	6.03	0.15	9.21	0.17	3.70	0.21	0.72	0.10	0.33	0.03	0.15	0.01	0.04	0.00	1.23	0.11	83.08
BBL	BBL-5	34	0.16	0.02	6.32	0.15	10.35	0.14	3.39	0.19	0.47	0.02	0.21	0.01	0.12	0.00	0.03	0.00	1.21	0.03	83.57
BBL	BBL-5	43	0.19	0.00	7.12	0.04	8.81	0.07	3.56	0.27	0.79	0.04	0.28	0.02	0.11	0.00	0.04	0.00	0.97	0.00	83.61
BBL	BBL-5	44	0.14	0.00	7.26	0.06	11.03	0.13	2.78	0.10	0.28	0.00	0.11	0.01	0.09	0.00	0.02	0.00	1.02	0.08	86.16
BBL	BBL-5	46	0.17	0.00	7.03	0.00	9.77	0.06	3.26	0.29	0.64	0.02	0.25	0.00	0.10	0.00	0.03	0.00	1.17	0.00	85.01
BBL	BBL-5	47	0.14	0.00	7.74	0.00	11.25	0.02	2.99	0.23	0.26	0.02	0.10	0.02	0.09	0.00	0.02	0.01	1.03	0.06	87.24
BBL	BBL-5	49	0.18	0.00	6.06	0.20	9.55	0.08	3.38	0.19	0.77	0.02	0.28	0.01	0.10	0.00	0.03	0.00	0.64	0.01	82.56
BBL	BBL-5	3	0.13	0.01	6.17	0.15	10.97	0.76	3.23	0.04	0.27	0.01	0.16	0.03	0.09	0.00	0.01	0.00	n. a.	n. a.	87.10
BBL	BBL-5	4	0.13	0.02	5.35	0.61	11.58	0.09	3.29	0.38	0.31	0.04	0.15	0.01	0.08	0.00	0.02	0.00	n. a.	n. a.	87.08
BBL	BBL-5	5	0.18	0.04	6.16	0.11	8.25	0.77	3.72	0.14	0.79	0.04	0.30	0.03	0.10	0.00	0.03	0.00	n. a.	n. a.	80.43
BBL	BBL-5	6	0.16	0.02	5.94	0.13	10.24	0.09	3.75	0.02	0.52	0.02	0.23	0.01	0.10	0.00	0.02	0.00	n. a.	n. a.	84.37
BBL	BBL-5	7	0.13	0.01	7.02	0.20	11.30	0.03	3.10	0.08	0.23	0.02	0.12	0.00	0.09	0.00	0.01	0.00	n. a.	n. a.	87.59
BORG	BORG-1	2	0.14	0.01	6.59	0.07	9.15	0.76	3.57	0.09	0.51	0.02	0.08	0.02	0.10	0.00	0.05	0.00	n. a.	n. a.	83.38
BORG	BORG-1	3	0.12	0.01	5.50	0.31	9.63	0.79	4.07	0.08	0.54	0.02	0.08	0.02	0.09	0.00	0.05	0.00	n. a.	n. a.	83.72
BORG	BORG-1	8	0.15	0.02	6.71	0.08	8.91	0.71	4.02	0.12	0.53	0.02	0.13	0.02	0.12	0.00	0.04	0.00	n. a.	n. a.	84.19
BORG	BORG-1	9	0.09	0.01	5.39	0.07	11.91	0.18	3.54	0.03	0.62	0.04	0.11	0.01	0.12	0.00	0.07	0.01	n. a.	n. a.	88.29
BORG	BORG-1	10	0.14	0.02	5.23	0.40	9.71	0.04	4.35	0.31	0.63	0.03	0.11	0.00	0.09	0.00	0.04	0.00	n. a.	n. a.	83.88
BORG	BORG-1	11	0.10	0.01	3.15	0.05	10.29	0.02	5.11	0.16	0.63	0.03	0.11	0.01	0.14	0.00	0.04	0.00	n. a.	n. a.	85.18
BORG	BORG-1	12	0.13	0.00	5.52	0.47	8.73	0.71	4.34	0.24	0.57	0.02	0.11	0.02	0.12	0.00	0.04	0.00	n. a.	n. a.	84.25
BORG	BORG-1	14	0.11	0.01	6.50	0.37	10.97	0.08	3.19	0.07	0.51	0.02	0.07	0.00	0.10	0.00	0.05	0.00	n. a.	n. a.	87.64
BORG	BORG-1	15	0.13	0.01	6.11	0.44	8.90	0.28	4.51	0.17	0.59	0.04	0.12	0.02	0.13	0.01	0.05	0.00	n. a.	n. a.	81.93
BORG	BORG-1	19	0.13	0.01	7.82	0.32	10.01	0.32	4.49	0.40	0.60	0.03	0.08	0.01	0.10	0.00	0.05	0.00	n. a.	n. a.	85.72
BORG	BORG-1	20	0.13	0.01	4.78	0.09	9.27	0.12	4.66	0.04	0.56	0.01	0.11	0.01	0.12	0.00	0.04	0.00	n. a.	n. a.	85.75
BORG	BORG-1	21	0.10	0.02	5.57	0.63	10.45	0.03	3.53	0.15	0.56	0.05	0.08	0.01	0.09	0.00	0.04	0.00	n. a.	n. a.	86.41
BORG	BORG-1	22	0.11	0.02	6.01	0.14	11.46	0.11	3.31	0.17	0.58	0.02	0.11	0.02	0.11	0.00	0.06	0.00	n. a.	n. a.	88.57
BORG	BORG-1	23	0.12	0.02	6.47	3.46	9.51	1.08	3.98	0.44	0.56	0.05	0.09	0.01	0.09	0.01	0.05	0.01	n. a.	n. a.	83.33
BORG	BORG-1	24	0.13	0.01	6.87	0.26	9.27	0.09	3.79	0.19	0.56	0.02	0.10	0.00	0.09	0.00	0.04	0.00	n. a.	n. a.	84.18
BORG	BORG-1	25	0.12	0.00	6.82	0.21	11.36	0.09	2.95	0.02	0.50	0.02	0.07	0.00	0.10	0.00	0.06	0.00	n. a.	n. a.	87.54
BORG	BORG-1	31	0.15	0.00	7.02	0.06	8.45	0.03	2.84	0.14	0.63	0.04	0.15	0.01	0.15	0.00	0.06	0.00	2.46	0.09	83.97
BORG	BORG-1	35	0.13	0.00	5.56	0.23	8.87	0.01	3.39	0.12	0.55	0.07	0.16	0.02	0.18	0.00	0.05	0.00	n. a.	n. a.	83.29
BORG	BORG-1	37	0.13	0.02	6.21	0.36	8.70	0.02	3.37	0.22	0.51	0.03	0.16	0.01	0.17	0.01	0.05	0.00	2.94	0.06	82.75
BORG	BORG-1	38	0.14	0.01	6.75	0.09	8.83	0.11	3.19	0.17	0.53	0.01	0.14	0.00	0.17	0.00	0.05	0.00	3.02	0.00	84.23
BORG	BORG-1	40	0.14	0.01	6.10	1.18	9.15	0.10	2.99	0.36	0.59	0.07	0.12	0.00	0.12	0.01	0.06	0.00	2.72	0.03	83.33
BORG	BORG-1	42	0.13	0.00	7.19	0.10	9.42	0.09	3.00	0.16	0.54	0.05	0.10	0.01	0.11	0.00	0.05	0.00	2.89	0.39	85.29
BORG	BORG-1	43	0.14	0.01	7.27	0.03	8.52	0.01	3.15	0.27	0.51	0.01	0.11	0.01	0.15	0.00	0.06	0.00	1.67	0.01	83.98
BORG	BORG-1	44	0.14	0.01	3.75	0.01	9.48	0.04	3.47	0.06	0.57	0.02	0.10	0.00	0.15	0.00	0.05	0.00	2.98	0.02	82.70
BORG	BORG-1	45	0.15	0.00	5.98	1.18	8.96	0.06	3.39	0.33	0.57	0.05	0.12	0.02	0.12	0.01	0.05	0.00	0.82	1.43	83.23
BORG	MM-L17-BORG-1	6	0.13	0.01	6.86	0.20	10.93	0.08	2.46	0.14	0.51	0.05	0.08	0.01	0.14	0.00	0.06	0.00	2.60	0.05	85.82
BPPC	MM-L17-BPPC-4	13	0.14	0.00	7.94	0.00	10.79	0.04	2.51	0.13	0.35	0.03	0.09	0.01	0.10	0.00	0.04	0.00	2.23	0.12	87.50
BPPC	MM-L17-BPPC-4	14	0.14	0.01	7.04	0.18	11.06	0.07	2.54	0.35	0.35	0.01	0.08	0.01	0.12	0.01	0.04	0.00	2.23	0.07	87.24
BPPC	MM-L17-BPPC-4	15	0.14	0.01	7.53	0.15	11.03	0.08	2.44	0.17	0.31	0.01	0.09	0.01	0.10	0.00	0.04	0.00	1.87	0.10	87.35
BPPC	MM-L17-BPPC-4	2	0.12	0.01	6.28	0.28	11.84	0.13	2.56	0.03	0.25	0.01	0.11	0.01	0.11	0.00	0.06	0.00	n. a.	n. a.	87.60
BPPC	MM-L17-BPPC-4	3	0.14	0.01	7.43	0.20	11.07	0.10	2.56	0.04	0.33	0.01	0.12	0.01	0.10	0.01	0.05	0.00	2.67	0.01	87.31
BPPC	MM-L17-BPPC-4	4	0.14	0.01	6.72	0.30	11.03	0.09	2.73	0.10	0.33	0.01	0.13	0.01	0.12	0.00	0.06	0.00	2.35	0.05	87.77
BPPC	MM-L17-BPPC-4	5	0.14	0.02	5.76	0.12	11.89	0.09	2.65	0.09	0.27	0.04	0.09	0.01	0.12	0.01	0.07	0.00	1.34	n. a.	87.86
BRM	BRM-1	14	0.08	n. a.	4.29	n. a.	11.18	n. a.	4.39	n. a.	0.76	n. a.	0.26	n. a.	0.24	n. a.	0.34	n. a.	n. a.	n. a.	88.45
BRM	BRM-1	16	0.08	0.01	4.79	0.04	10.31	0.09	4.64	0.15	0.70	0.02	0.22	0.01	0.18	0.00	0.27	0.00	n. a.	n. a.	88.34
BRM	BRM-1	17	0.08	0.01	5.46	0.19	9.85	0.08	4.69	0.19	0.64	0.03	0.19	0.01	0.17	0.00	0.25	0.00	n. a.	n. a.	88.29
BRM	BRM-1	18	0.09	0.01	5.28	0.05	10.31	0.10	4.30	0.23	0.98	0.04	0.31	0.00	0.21	0.00	0.27	0.00	n. a.	n. a.	88.93
BRM	BRM-1	19	0.09	0.02	4.66	0.03	8.54	0.72	4.36	0.12	0.89	0.06	0.23	0.02	0.14	0.00	0.25	0.01	n. a.	n. a.	86.61
BRM	BRM-1	22	0.09	0.00	3.97	0.39	10.50	0.05	5.27	0.21	0.62	0.07	0.21	0.02	0.19	0.00	0.29	0.00	n. a.	n. a.	87.93
BRM	BRM-1	23	0.10	0.00	7.51	0.11	9.55	0.86	4.58	0.19	0.86	0.02	0.30	0.03	0.17	0.00	0.23	0.00	n. a.	n. a.	86.70
BRM	BRM-1	24	0.09	0.02	3.78	0.08	7.21	0.02	4.37	0.04	1.81	0.04	0.48	0.01	0.05	0.00	0.36	0.01	n. a.	n. a.	86.39
BRM	BRM-1	25	0.09	0.02	6.45	0.34	10.68	0.04	4.85	0.01	0.64	0.04	0.24	0.01	0.21	0.01	0.32	0.00	n. a.	n. a.	86.16
BRM	BRM-1	30	0.10	0.02	4.94	0.33	8.82	0.06	3.95	0.09	0.67	0.05	0.20	0.02	0.19	0.00	0.30	0.00	3.13	0.06	86.16
BRM	BRM-1	34	0.09	0.01	4.12	0.15	10.83	0.14	4.50	0.16	0.80	0.04	0.26	0.02	0.27	0.00	0.33	0.00	2.36	0.19	87.51
BRM	BRM-1	35	0.07	0.01	4.63	0.21	10.31	0.06	4.32	0.09	0.78	0.00	0.28	0.01	0.26	0.00	0.35	0.00	n. a.	n. a.	88.61
BRM	BRM-1	36	0.06	0.02	4.39	0.01	11.11	0.02	4.08	0.38	0.81	0.00	0.30	0.03	0.26	0.00	0.41	0.00	0.58	0.00	88.40
BRM	BRM-1	39	0.09	0.01	4.08	0.15	9.98	0.06	4.05	0.11	0.81	0.02	0.27	0.02	0.22	0.01	0.41	0.01	3.85	0.05	88.17
BRM	BRM-1	40	0.07	0.02	3.93	0.36	10.84	0.19	3.89	0.07	0.82	0.02	0.31	0.01	0.27	0.00	0.34	0.00	n. a.	n. a.	87.62
BRM	BRM-1	41	0.08	0.02	5.11	0.21	11.13	0.19	3.42	0.23	0.57	0.05	0.19	0.01	0.23	0.01	0.32	0.01	2.05	0.06	87.79
BRM	BRM-1	2	0.07	0.02	3.55	0.24	11.62	0.90	4.32	0.02	0.63	0.03	0.22	0.02	0.18	0.00	0.27	0.00	n. a.	n. a.	89.02
BRM	BRM-1	3	0.08	0.00	4.49	0.03	10.35	0.07	4.74	0.08	0.71	0.01	0.21	0.01	0.17	0.00	0.27	0.01	n. a.	n. a.	87.64
BRM	BRM-1	5	0.07	0.01	4.42	0.12	10.84	0.04	4.62	0.09	0.78	0.02	0.28	0.01	0.20	0.00	0.31	0.00	n. a.	n. a.	88.74
BRM	BRM-1	6	0.07	0.02	3.88	0.43	10.86	0.86	4.21	0.18	0.60	0.03	0.24	0.03	0.17	0.00	0.27	0.00	n. a.	n. a.	87.77
BRM	BRM-1	7	0.11	0.02	3.61	0.90	10.79	0.33	4.51	0.46	0.79	0.08	0.27	0.01	0.17	0.00	0.27	0.01	n. a.	n. a.	86.57
BRM	BRM-1	8	0.07	0.01	2.82	0.36	9.89	0.68	5.07	0.07	0.98	0.14	0.27	0.02	0.23	0.01	0.33	0.00	n. a.	n. a.	88.66
BRM	MM-L17-BRM-2	1	0.07	0.01	5.17	0.05	11.50	0.05	4.06	0.18	0.56	0.04	0.19	0.01	0.24	0.01	0.38	0.00	0.98	0.00	89.64
BRM	MM-L17-BRM-2	10	0.08	0.01	3.42	0.02	10.85	0.07	4.50	0.23	0.86	0.02	0.31	0.04	0.30	0.00	0.26	0.00	0.89	0.03	87.27
BRM	MM-L17-BRM-2	13	0.09	0.01	4.74	0.06	10.92	0.15	4.63	0.16	0.83	0.04	0.37	0.02	0.29	0.00	0.34	0.00	n. a.	n. a.	88.62
BRM	MM-L17-BRM-2	14	0.07	0.01	4.63	0.03	11.37	0.08	4.30	0.01	0.69	0.02	0.20	0.02	0.24	0.00	0.30	0.00	0.89	0.01	88.40
BRM	MM-L17-BRM-2	16	0.09	0.03	3.93	0.07	11.25	0.02	3.94	0.21	0.59	0.03	0.25	0.01	0.25	0.00	0.27	0.00	2.43	0.11	89.04
BRM	MM-L17-BRM-2	17	0.09	0.02	4.57	0.12	12.14	0.11	3.84	0.43	0.55	0.03	0.21	0.02	0.20	0.01	0.29	0.00	0.70	0.04	88.98
BRM	MM-L17-BRM-2	18	0.09	0.02	3.42	0.25	10.77	0.17	4.19	0.15	0.83	0.06	0.23	0.03	0.19	0.00	0.26	0.00	0.71	0.03	88.65
BRM	MM-L17-BRM-2	24	0.10	0.01	5.27	0.08	10.58	0.03	3.87	0.31	0.92	0.04	0.26	0.00	0.23	0.01	0.24	0.00	1.25	0.01	86.55
BRM	MM-L17-BRM-2	25	0.08	0.01	5.05	0.10	10.82	0.04	4.02	0.13	0.81	0.04	0.27	0.01	0.25	0.00	0.33	0.01	0.66	0.04	87.89
BRM	MM-L17-BRM-2	26	0.08	0.00	4.88	0.07	10.98	0.06	4.25	0.16	0.87	0.09	0.28	0.00	0.35	0.01	0.87	0.02	0.82	0.02	88.92
BRM	MM-L17-BRM-2	29	0.07	0.00	5.00	0.03	11.40	0.03	4.05	0.24	0.72	0.01	0.18	0.01	0.22	0.00	0.28	0.00	0.33	0.01	89.51
BRM	MM-L17-BRM-2	31	0.08	0.00	5.53	0.20	11.60	0.04	3.67	0.26	0.56	0.03	0.17	0.01	0.23	0.00	0.28	0.00	0.34	0.00	90.49
BRM	MM-L17-BRM-2	32	0.09	0.01	4.94	0.08	11.93	0.05	3.80	0.09	0.58	0.03	0.20	0.01	0.22	0.00	0.27	0.00	0.84	0.05	88.42
BRM	MM-L17-BRM-2	8	0.08	0.00	4.79	0.00	11.29	0.03	4.33	0.22	0.75	0.10	0.33	0.03	0.38	0.01	0.37	0.00	4.30	0.11	89.06
BRVB	MM-L17-BRVB-2	10	0.15	0.00	6.95	0.06	9.41	0.02	2.90	0.23	1.02	0.03	0.28	0.00	0.17	0.00	0.05	0.00	1.97	0.01	83.46
BRVB	MM-L17-BRVB-2	2	0.13	0.01	6.97	0.16	10.20	0.11	2.57	0.05	0.57	0.02	0.15	0.00	0.17	0.01	0.02	0.00	0.61	1.06	85.50
BRVB	MM-L17-BRVB-2	4	0.15	0.01	5.73	0.05	10.67	0.03	3.54	0.10	0.97	0.03	0.33	0.01	0.13	0.00	0.05	0.00	0.32	0.01	84.09
BRVB	MM-L17-BRVB-2	6	0.14	0.00	7.61	0.03	10.98	0.01	3.01	0.09	0.36	0.03	0.16	0.00	0.13	0.00	0.03	0.00	0.73	0.06	85.11
BRVB	MM-L17-BRVB-2	7	0.15	0.00	5.92	0.10	10.06	0.14	3.57	0.18	1.12	0.02	0.33	0.01	0.20	0.01	0.07	0.00	1.92	0.05	83.66

Cinder Cone	Tephra Sample	Inclusion	Li	s.e.	B	s.e.	Sc	s.e.	V	s.e.	Rb	s.e.	Sr	s.e.	Y	s.e.	Zr	s.e.	Nb	s.e.
BAS-44	BAS-44-2	1	n.a.	n.a.	n.a.	n.a.	n.a.	n.a.	n.a.	n.a.	n.a.	n.a.	n.a.	n.a.	n.a.	n.a.	n.a.	n.a.	n.a.	n.a.
BAS-44	BAS-44-2	10	n.a.	n.a.	n.a.	n.a.	n.a.	n.a.	n.a.	n.a.	n.a.	n.a.	n.a.	n.a.	n.a.	n.a.	n.a.	n.a.	n.a.	n.a.
BAS-44	BAS-44-2	2	n.a.	n.a.	n.a.	n.a.	30.36	3.01	196.85	27.52	n.a.	n.a.	401.19	10.74	18.36	1.08	75.81	5.61	2.84	0.22
BAS-44	BAS-44-2	4	n.a.	n.a.	n.a.	n.a.	31.88	3.20	222.42	6.65	n.a.	n.a.	430.87	5.60	18.76	1.06	79.88	4.43	3.33	0.25
BAS-44	BAS-44-2	5	n.a.	n.a.	n.a.	n.a.	37.58	3.70	214.50	4.05	n.a.	n.a.	445.71	2.82	21.10	1.14	83.85	4.59	3.46	0.28
BAS-44	BAS-44-2	6	n.a.	n.a.	n.a.	n.a.	n.a.	n.a.	n.a.	n.a.	n.a.	n.a.	n.a.	n.a.	n.a.	n.a.	n.a.	n.a.	n.a.	n.a.
BAS-44	BAS-44-2	7a	n.a.	n.a.	n.a.	n.a.	35.90	3.59	210.63	4.48	n.a.	n.a.	432.60	6.00	19.92	1.08	81.45	4.47	2.97	0.24
BAS-44	BAS-44-2	7b	n.a.	n.a.	n.a.	n.a.	n.a.	n.a.	n.a.	n.a.	n.a.	n.a.	n.a.	n.a.	n.a.	n.a.	n.a.	n.a.	n.a.	n.a.
BBL	BBL-5	11	10.87	1.59	3.71	1.38	35.77	1.47	212.51	11.13	11.71	0.25	405.10	6.29	18.50	1.60	101.53	7.47	5.76	0.55
BBL	BBL-5	14	8.41	1.18	3.02	1.16	42.48	1.69	255.53	13.57	13.27	0.35	305.18	8.62	30.87	2.29	137.78	10.36	6.43	0.66
BBL	BBL-5	15	10.47	1.52	4.95	1.86	51.28	2.73	311.08	17.22	12.92	0.37	363.62	8.58	30.19	2.46	133.86	11.47	6.45	0.64
BBL	BBL-5	17	9.65	1.40	2.26	0.99	55.25	2.31	339.21	18.52	6.72	0.28	432.46	10.74	33.97	2.62	106.60	8.31	2.66	0.34
BBL	BBL-5	18	10.21	1.46	3.05	1.20	44.73	1.83	230.41	12.18	12.17	0.22	326.15	5.58	25.13	2.31	123.99	9.40	6.44	0.62
BBL	BBL-5	19	7.30	1.04	0.37	0.38	31.38	1.39	205.76	11.30	4.51	0.22	265.44	5.30	21.22	1.60	75.49	5.60	2.45	0.27
BBL	BBL-5	20	11.70	1.90	4.40	1.70	47.80	2.60	301.70	16.40	13.40	0.30	460.30	9.90	23.80	2.30	123.00	10.80	6.50	0.70
BBL	BBL-5	21A	9.80	1.72	3.62	1.48	46.21	2.89	341.21	18.26	12.35	0.56	382.44	10.32	24.75	2.96	109.26	11.38	5.89	0.61
BBL	BBL-5	21B	9.32	1.53	3.63	1.43	44.90	2.42	299.84	15.22	10.57	0.31	324.96	17.00	23.79	2.72	120.69	12.86	5.89	0.58
BBL	BBL-5	22	n.a.	n.a.	n.a.	n.a.	n.a.	n.a.	n.a.	n.a.	n.a.	n.a.	n.a.	n.a.	n.a.	n.a.	n.a.	n.a.	n.a.	n.a.
BBL	BBL-5	23	10.48	1.58	2.80	1.07	40.95	1.84	293.40	18.25	8.20	0.20	313.52	6.23	24.44	1.85	91.60	6.91	4.11	0.41
BBL	BBL-5	30	15.16	2.36	4.51	2.39	41.03	1.70	194.72	3.61	12.68	0.28	403.72	9.49	28.21	2.47	122.37	15.20	6.44	0.82
BBL	BBL-5	31	n.a.	n.a.	n.a.	n.a.	39.65	3.89	228.75	4.69	n.a.	n.a.	290.43	4.18	25.95	1.46	94.76	5.92	4.29	0.34
BBL	BBL-5	32	n.a.	n.a.	n.a.	n.a.	38.17	3.75	199.68	3.72	n.a.	n.a.	329.01	2.52	24.67	1.34	107.08	5.81	5.90	0.45
BBL	BBL-5	33	n.a.	n.a.	n.a.	n.a.	39.74	3.90	220.76	4.54	n.a.	n.a.	344.96	2.81	27.22	1.52	125.64	7.10	7.04	0.54
BBL	BBL-5	34	n.a.	n.a.	n.a.	n.a.	n.a.	n.a.	n.a.	n.a.	n.a.	n.a.	n.a.	n.a.	n.a.	n.a.	n.a.	n.a.	n.a.	n.a.
BBL	BBL-5	43	n.a.	n.a.	n.a.	n.a.	38.02	3.73	199.67	2.17	n.a.	n.a.	342.09	6.44	24.01	1.31	118.48	6.42	7.06	0.53
BBL	BBL-5	44	n.a.	n.a.	n.a.	n.a.	31.37	3.12	202.12	3.72	n.a.	n.a.	267.48	3.31	20.87	1.19	64.72	3.62	2.26	0.17
BBL	BBL-5	46	n.a.	n.a.	n.a.	n.a.	37.00	3.62	219.52	6.26	n.a.	n.a.	352.83	6.06	23.39	1.29	109.60	5.92	6.64	0.51
BBL	BBL-5	47	n.a.	n.a.	n.a.	n.a.	35.99	3.54	204.01	2.64	n.a.	n.a.	262.59	1.59	20.36	1.08	62.32	3.29	1.91	0.15
BBL	BBL-5	49	n.a.	n.a.	n.a.	n.a.	35.52	3.56	218.75	3.89	n.a.	n.a.	416.17	2.70	22.65	1.20	117.96	6.27	6.91	0.52
BBL	BBL-5	3	n.a.	n.a.	n.a.	n.a.	n.a.	n.a.	n.a.	n.a.	n.a.	n.a.	n.a.	n.a.	n.a.	n.a.	n.a.	n.a.	n.a.	n.a.
BBL	BBL-5	4	n.a.	n.a.	n.a.	n.a.	n.a.	n.a.	n.a.	n.a.	n.a.	n.a.	n.a.	n.a.	n.a.	n.a.	n.a.	n.a.	n.a.	n.a.
BBL	BBL-5	5	n.a.	n.a.	n.a.	n.a.	n.a.	n.a.	n.a.	n.a.	n.a.	n.a.	n.a.	n.a.	n.a.	n.a.	n.a.	n.a.	n.a.	n.a.
BBL	BBL-5	6	10.75	1.58	2.72	1.11	42.99	1.68	271.14	16.02	7.97	0.23	317.15	4.86	24.30	1.94	100.95	7.69	4.42	0.43
BBL	BBL-5	7	11.40	1.70	2.40	1.40	50.80	2.20	375.60	19.50	4.30	0.20	362.90	7.70	27.80	2.60	92.00	8.50	3.10	0.50
BORG	BORG-1	2	n.a.	n.a.	n.a.	n.a.	n.a.	n.a.	n.a.	n.a.	n.a.	n.a.	n.a.	n.a.	n.a.	n.a.	n.a.	n.a.	n.a.	n.a.
BORG	BORG-1	3	n.a.	n.a.	n.a.	n.a.	n.a.	n.a.	n.a.	n.a.	n.a.	n.a.	n.a.	n.a.	n.a.	n.a.	n.a.	n.a.	n.a.	n.a.
BORG	BORG-1	8	n.a.	n.a.	n.a.	n.a.	n.a.	n.a.	n.a.	n.a.	n.a.	n.a.	n.a.	n.a.	n.a.	n.a.	n.a.	n.a.	n.a.	n.a.
BORG	BORG-1	9	n.a.	n.a.	n.a.	n.a.	n.a.	n.a.	n.a.	n.a.	n.a.	n.a.	n.a.	n.a.	n.a.	n.a.	n.a.	n.a.	n.a.	n.a.
BORG	BORG-1	10	n.a.	n.a.	n.a.	n.a.	n.a.	n.a.	n.a.	n.a.	n.a.	n.a.	n.a.	n.a.	n.a.	n.a.	n.a.	n.a.	n.a.	n.a.
BORG	BORG-1	11	6.80	1.00	4.70	1.80	33.40	1.60	261.20	13.90	9.30	0.40	715.70	14.50	14.90	1.20	61.40	4.60	2.50	0.30
BORG	BORG-1	12	6.32	1.06	5.74	2.26	39.20	2.03	278.90	14.47	9.01	0.21	760.81	16.13	17.40	1.40	70.48	5.55	2.64	0.27
BORG	BORG-1	14	6.99	1.01	2.68	1.07	35.18	1.52	268.70	17.48	4.97	0.10	487.96	7.94	12.97	1.00	53.39	4.05	2.07	0.20
BORG	BORG-1	15	8.00	1.10	6.70	2.50	30.20	1.70	254.30	14.90	9.40	0.40	604.20	10.80	12.70	1.00	61.80	5.10	2.60	0.30
BORG	BORG-1	19	7.40	1.10	3.80	1.40	25.30	1.60	253.20	14.50	5.10	0.10	533.60	10.70	14.40	1.10	51.90	4.00	2.30	0.20
BORG	BORG-1	20	7.20	1.00	4.90	1.80	30.70	1.40	243.80	15.60	8.10	0.20	640.40	9.40	12.40	1.10	53.10	4.00	2.50	0.30
BORG	BORG-1	21	5.47	0.78	2.65	1.03	32.09	1.93	252.48	14.38	4.99	0.18	508.41	8.71	12.43	0.94	51.19	3.86	2.07	0.20
BORG	BORG-1	22	6.58	0.98	4.19	1.65	37.54	1.49	271.57	15.43	6.22	0.12	467.93	8.20	14.11	1.15	69.47	5.35	3.06	0.31
BORG	BORG-1	23	n.a.	n.a.	n.a.	n.a.	n.a.	n.a.	n.a.	n.a.	n.a.	n.a.	n.a.	n.a.	n.a.	n.a.	n.a.	n.a.	n.a.	n.a.
BORG	BORG-1	24	8.35	1.20	4.17	1.91	38.55	1.94	307.75	15.89	8.15	0.29	664.56	16.76	17.22	1.53	72.45	6.09	3.73	0.37
BORG	BORG-1	25	11.42	1.82	4.20	1.74	53.92	2.40	429.98	21.93	8.13	0.30	694.96	26.80	18.44	1.39	83.54	6.63	3.61	0.41
BORG	BORG-1	31	n.a.	n.a.	n.a.	n.a.	29.21	2.87	205.34	3.61	n.a.	n.a.	547.31	4.19	13.07	0.69	62.69	3.34	2.75	0.21
BORG	BORG-1	35	n.a.	n.a.	n.a.	n.a.	28.21	2.79	219.27	22.59	n.a.	n.a.	611.22	5.18	13.35	0.72	56.64	3.04	2.56	0.19
BORG	BORG-1	37	n.a.	n.a.	n.a.	n.a.	26.64	2.63	218.22	22.45	n.a.	n.a.	598.21	3.57	13.56	0.74	56.93	3.22	2.59	0.20
BORG	BORG-1	38	n.a.	n.a.	n.a.	n.a.	27.59	2.72	187.59	3.70	n.a.	n.a.	575.75	7.31	13.09	0.73	50.41	2.83	2.24	0.17
BORG	BORG-1	40	n.a.	n.a.	n.a.	n.a.	29.65	2.92	211.16	2.77	n.a.	n.a.	502.63	8.38	13.32	0.78	58.11	3.36	3.11	0.24
BORG	BORG-1	42	n.a.	n.a.	n.a.	n.a.	29.85	2.93	215.68	2.53	n.a.	n.a.	509.03	5.63	13.08	0.71	55.86	2.99	2.98	0.23
BORG	BORG-1	43	n.a.	n.a.	n.a.	n.a.	26.47	2.59	184.92	1.91	n.a.	n.a.	547.75	5.25	12.92	0.68	52.17	2.79	2.15	0.16
BORG	BORG-1	44	n.a.	n.a.	n.a.	n.a.	32.20	3.16	229.18	3.52	n.a.	n.a.	594.34	16.29	15.35	0.84	56.69	3.03	2.07	0.18
BORG	BORG-1	45	n.a.	n.a.	n.a.	n.a.	27.96	2.91	223.05	2.49	n.a.	n.a.	504.38	7.09	13.53	0.94	57.99	3.22	3.24	0.24
BPPC	MM-L17-BORG-1	1	n.a.	n.a.	n.a.	n.a.	31.42	3.13	109.89	1.38	n.a.	n.a.	450.79	4.11	12.14	0.79	50.46	2.71	2.09	0.17
BPPC	MM-L17-BPPC-4	13	n.a.	n.a.	n.a.	n.a.	34.39	3.39	229.41	23.55	n.a.	n.a.	423.71	4.50	15.66	0.83	59.40	3.21	1.83	0.14
BPPC	MM-L17-BPPC-4	14	n.a.	n.a.	n.a.	n.a.	32.89	3.37	253.51	26.24	n.a.	n.a.	463.15	8.03	15.42	1.07	57.27	3.56	1.93	0.16
BPPC	MM-L17-BPPC-4	15	n.a.	n.a.	n.a.	n.a.	33.15	3.26	222.63	23.28	n.a.	n.a.	463.74	10.34	15.33	0.86	55.68	3.23	1.59	0.14
BPPC	MM-L17-BPPC-4	2	n.a.	n.a.	n.a.	n.a.	33.52	3.31	218.58	3.91	n.a.	n.a.	459.54	12.21	16.27	0.90	54.42	3.14	1.47	0.12
BPPC	MM-L17-BPPC-4	3	n.a.	n.a.	n.a.	n.a.	n.a.	n.a.	n.a.	n.a.	n.a.	n.a.	n.a.	n.a.	n.a.	n.a.	n.a.	n.a.	n.a.	n.a.
BPPC	MM-L17-BPPC-4	4	n.a.	n.a.	n.a.	n.a.	n.a.	n.a.	n.a.	n.a.	n.a.	n.a.	n.a.	n.a.	n.a.	n.a.	n.a.	n.a.	n.a.	n.a.
BPPC	MM-L17-BPPC-4	5	n.a.	n.a.	n.a.	n.a.	38.80	3.85	226.76	5.22	n.a.	n.a.	522.41	4.84	17.80	0.99	57.90	3.12	1.42	0.12
BRM	BRM-1	14	n.a.	n.a.	n.a.	n.a.	n.a.	n.a.	n.a.	n.a.	n.a.	n.a.	n.a.	n.a.	n.a.	n.a.	n.a.	n.a.	n.a.	n.a.
BRM	BRM-1	16	n.a.	n.a.	n.a.	n.a.	n.a.	n.a.	n.a.	n.a.	n.a.	n.a.	n.a.	n.a.	n.a.	n.a.	n.a.	n.a.	n.a.	n.a.
BRM	BRM-1	17	7.67	1.12	4.55	1.70	31.70	1.86	292.84	14.68	10.11	0.45	1720.19	42.82	16.75	1.40	119.26	9.18	5.83	0.58
BRM	BRM-1	18	n.a.	n.a.	n.a.	n.a.	n.a.	n.a.	n.a.	n.a.	n.a.	n.a.	n.a.	n.a.	n.a.	n.a.	n.a.	n.a.	n.a.	n.a.
BRM	BRM-1	19	5.35	1.22	4.17	1.71	28.18	1.56	224.81	14.42	15.29	0.03	1362.67	48.84	13.41	1.10	115.34	9.59	5.74	0.58
BRM	BRM-1	22	9.18	1.53	3.01	1.26	30.87	1.63	345.69	22.65	8.95	0.28	2135.02	55.18	14.21	1.11	126.25	9.36	4.86	0.53
BRM	BRM-1	23	n.a.	n.a.	n.a.	n.a.	n.a.	n.a.	n.a.	n.a.	n.a.	n.a.	n.a.	n.a.	n.a.	n.a.	n.a.	n.a.	n.a.	n.a.
BRM	BRM-1	24	18.60	2.80	8.00	3.00	30.00	1.60	350.00	17.50	23.00	0.40	734.40	18.10	20.70	1.80	175.50	13.10	12.80	1.30
BRM	BRM-1	25	8.80	1.30	3.00	1.20	32.00	1.50	250.50	17.60	7.60	0.20	1595.40	28.70	13.10	1.00	104.50	7.80	4.30	0.50
BRM	BRM-1	30	n.a.	n.a.	n.a.	n.a.	23.43	2.30	177.33	3.86	n.a.	n.a.	1160.96	8.58	12.80	0.71	90.89	4.92	4.28	0.33
BRM	BRM-1	34	n.a.	n.a.	n.a.	n.a.	24.94	2.48	196.18	5.11	n.a.	n.a.	1364.11	19.99	13.85	0.77	106.60	5.77	5.06	0.39
BRM	BRM-1	35	n.a.	n.a.	n.a.	n.a.	n.a.	n.a.	n.a.	n.a.	n.a.	n.a.	n.a.	n.a.	n.a.	n.a.	n.a.	n.a.	n.a.	n.a.
BRM	BRM-1	36	n.a.	n.a.	n.a.	n.a.	n.a.	n.a.	n.a.	n.a.	n.a.	n.a.	n.a.	n.a.	n.a.	n.a.	n.a.	n.a.	n.a.	n.a.
BRM	BRM-1	39	n.a.	n.a.	n.a.	n.a.	n.a.	n.a.	n.a.	n.a.	n.a.	n.a.	n.a.	n.a.	n.a.	n.a.	n.a.	n.a.	n.a.	n.a.
BRM	BRM-1	40	n.a.	n.a.	n.a.	n.a.	n.a.	n.a.	n.a.	n.a.	n.a.	n.a.	n.a.	n.a.	n.a.	n.a.	n.a.	n.a.	n.a.	n.a.
BRM	BRM-1	41	n.a.	n.a.	n.a.	n.a.	25.39	2.49	200.59	3.63	n.a.	n.a.	1173.64	10.26	12.18	0.65	80.92	4.37	4.24	0.33
BRM	BRM-1	2	n.a.	n.a.	n.a.	n.a.	n.a.	n.a.	n.a.	n.a.	n.a.	n.a.	n.a.	n.a.	n.a.	n.a.	n.a.	n.a.	n.a.	n.a.
BRM	BRM-1	3	n.a.	n.a.	n.a.	n.a.	n.a.	n.a.	n.a.	n.a.	n.a.	n.a.	n.a.	n.a.	n.a.	n.a.	n.a.	n.a.	n.a.	n.a.
BRM	BRM-1	5	12.03	2.27	1.75	0.76	31.16	1.98	308.97	17.08	16.28	0.34	2099.54	100.51	16.31	1.36	145.21	11.93	10.46	1.19
BRM	BRM-1	6	8.00	1.50	1.50	1.50	22.80	1.70	195.00	12.10	5.70	0.10	878.30	41.20	8.30	0.80	61.60	5.20	2.60	0.40
BRM	BRM-1	7	12.50	1.90	2.50	1.10	33.90	2.20	358.20	25.00	16.00	0.70	2243.10	149.90	19.80	1.70	162.80	16.00	11.20	1.30
BRM	BRM-1	8	8.50	1.70	6.40	3.10	40.40	2.00	318.20	17.50	16.60	0.80	2086.80	17.40	13.70	1.50	133.70	9.50	9.50	0.90
BRM	MM-L17-BRM-2	1	n.a.	n.a.	n.a.	n.a.	26.33	2.61	211.45	4.06	n.a.	n.a.	1251.65	7.90	11.92	0.69	80.05	4.47	3.64	0.28
BRM	MM-L17-BRM-2	10	n.a.	n.a.	n.a.	n.a.	n.a.	n.a.	n.a.	n.a.	n.a.	n.a.	n.a.	n.a.	n.a.	n.a.	n.a.	n.a.	n.a.	n.a.
BRM	MM-L17-BRM-2	13	n.a.	n.a.	n.a.	n.a.	n.a.	n.a.	n.a.	n.a.	n.a.	n.a.	n.a.	n.a.	n.a.	n.a.	n.a.	n.a.	n.a.	n.a.
BRM	MM-L17-BRM-2	14	n.a.	n.a.	n.a.	n.a.	n.a.	n.a.	n.a.	n.a.	n.a.	n.a.	n.a.	n.a.	n.a.	n.a.	n.a.	n.a.	n.a.	n.a.
BRM	MM-L17-BRM-2	16	n.a.	n.a.	n.a.	n.a.	n.a.	n.a.	n.a.	n.a.	n.a.	n.a.	n.a.	n.a.	n.a.	n.a.	n.a.	n.a.	n.a.	n.a.
BRM	MM-L17-BRM-2	17	n.a.	n.a.	n.a.	n.a.	n.a.	n.a.	n.a.	n.a.	n.a.	n.a.	n.a.	n.a.	n.a.	n.a.	n.a.	n.a.	n.a.	n.a.
BRM	MM-L17-BRM-2	18	n.a.	n.a.	n.a.	n.a.	24.65	2.42	198.88	3.57	n.a.	n.a.	1250.41	13.12	14.23	0.77	96.59	5.23	5.57	0.43
BRM	MM-L17-BRM-2	24	n.a.	n.a.	n.a.	n.a.	26.88	2.63	188.35	2.08	n.a.	n.a.	1158.90	10.80	12.77	0.69	98.46	5.20	7.72	0.59
BRM	MM-L17-BRM-2	25	n.a.	n.a.	n.a.	n.a.	22.87	2.26	194.46	2.37	n.a.	n.a.	1431.35	19.97	12.21	0.67	108.07	5.92	8.13	0.61
BRM	MM-L17-BRM-2	26	n.a.	n.a.	n.a.	n.a.	22.09	2.21	184.30	1.92	n.a.	n.a.	1557.82	11.04	12.63	0.69	113.05	6.23	8.56	0.65
BRM	MM-L17-BRM-2	29	n.a.	n.a.	n.a.	n.a.	23.80	2.47	202.09	4.08	n.a.	n.a.	1304.03	14.65	13.11	0.71	91.04	4.89	4.45	0.35
BRM	MM-L17-BRM-2	31	n.a.	n.a.	n.a.	n.a.	26.75	2.66	199.29	2.55	n.a.	n.a.	1181.07	13.93	11.43	0.64	74.60	4.34	4.28	0.34
BRM	MM-L17-BRM-2	32	n.a.	n.a.	n.a.	n.a.	25.44	2.51	217.09	3.75	n.a.	n.a.	1227.00	13.73	11.42	0.68	80.79	4.39	4.42	0.37
BRM	MM-L17-BRM-2	8	n.a.	n.a.	n.a.	n.a.	22.93	2.25	171.43	3.35	n.a.	n.a.	1545.02	27.30	12.90	0.70	140.42	7.58	3.74	0.29
BRVB	MM-L17-BRVB-2	10	n.a.	n.a.	n.a.	n.a.	29.22	2.86	276.19	25.91	n.a.	n.a.	462.66	4.65	18.96	1.01	105.84	5.63	8.26	0.63
BRVB	MM-L17-BRVB-2	2	n.a.	n.a.	n.a.	n.a.	36.51	3.60	276.10	28.40	n.a.	n.a.	383.35	4.74	24.99	1.39	88.91	5.14	3.63	0.28
BRVB	MM-L17-BRVB-2	4	n.a.	n.a.	n.a.	n.a.	31.48	3.10	242.94	2.49	n.a.	n.a.	514.31	3.64	21.59	1.17	120.06	6.39	9.11	0.69
BRVB	MM-L17-BRVB-2	6	n.a.	n.a.	n.a.	n.a.	28.83	2.85	292.18	30.48	n.a.	n.a.	591.87	9.60	22.98	1.27	129.06	7.72	10.02	0.80
BRVB	MM-L17-BRVB-2	7	n.a.	n.a.	n.a.	n.a.	35.37	3.51	308.06	31.68	n.a.	n.a.	573.24	5.59	24.19	1.33	134.90	7.47	9.38	0.77

Table S1. (continued)

Cinder Cone	Tephra Sample	Inclusion	Ba	s.e.	La	s.e.	Ce	s.e.	Nd	s.e.	Sm	s.e.	Dy	s.e.	Yb	s.e.	Pb	s.e.	Cu	s.e.	Zn	s.e.	Mo	s.e.	Sn	s.e.	W	s.e.
BAS-44	BAS-44-2	1	n.a.	n.a.	n.a.	n.a.	n.a.	n.a.	n.a.	n.a.	n.a.	n.a.	n.a.	n.a.	n.a.	n.a.	n.a.	n.a.	n.a.	n.a.	n.a.	n.a.	n.a.	n.a.	n.a.	n.a.	n.a.	n.a.
BAS-44	BAS-44-2	10	n.a.	n.a.	n.a.	n.a.	n.a.	n.a.	n.a.	n.a.	n.a.	n.a.	n.a.	n.a.	n.a.	n.a.	n.a.	n.a.	n.a.	n.a.	n.a.	n.a.	n.a.	n.a.	n.a.	n.a.	n.a.	n.a.
BAS-44	BAS-44-2	2	114.47	1.91	7.88	0.20	21.08	0.57	12.95	0.30	2.95	0.08	3.40	0.15	2.40	0.15	2.26	0.09	n.a.	n.a.	n.a.	n.a.	n.a.	n.a.	0.13	n.a.	0.09	0.09
BAS-44	BAS-44-2	4	115.24	2.68	6.78	0.19	21.20	0.67	13.08	0.35	3.43	0.15	3.48	0.19	2.33	0.19	1.91	0.03	79.92	17.18	84.76	19.73	1.05	0.18	n.a.	n.a.	0.09	0.09
BAS-44	BAS-44-2	5	136.41	2.37	8.35	0.18	21.93	0.43	13.35	0.30	3.31	0.10	3.78	0.15	2.22	0.15	2.08	0.07	70.36	5.91	69.75	15.30	0.36	0.04	1.55	0.12	0.07	0.01
BAS-44	BAS-44-2	6	n.a.	n.a.	n.a.	n.a.	n.a.	n.a.	n.a.	n.a.	n.a.	n.a.	n.a.	n.a.	n.a.	n.a.	n.a.	n.a.	n.a.	n.a.	n.a.	n.a.	n.a.	n.a.	n.a.	n.a.	n.a.	n.a.
BAS-44	BAS-44-2	7a	144.20	3.42	8.27	0.15	20.99	0.55	12.79	0.46	3.30	0.19	3.64	0.14	2.29	0.14	2.72	0.08	110.90	9.20	77.84	17.26	0.52	0.06	1.27	0.08	0.14	0.01
BAS-44	BAS-44-2	7b	n.a.	n.a.	n.a.	n.a.	n.a.	n.a.	n.a.	n.a.	n.a.	n.a.	n.a.	n.a.	n.a.	n.a.	n.a.	n.a.	n.a.	n.a.	n.a.	n.a.	n.a.	n.a.	n.a.	n.a.	n.a.	n.a.
BBL	BBL-5	11	314.82	5.14	10.96	0.22	27.95	0.62	15.67	0.34	3.75	0.21	3.02	0.21	2.43	0.13	3.83	0.19	85.39	7.47	110.92	2.82	0.50	0.06	0.80	0.14	n.a.	n.a.
BBL	BBL-5	14	336.73	8.65	12.36	0.36	30.10	0.78	18.58	0.65	4.26	0.11	5.93	0.45	3.30	0.33	3.69	0.14	73.45	10.36	76.79	2.61	0.52	0.07	1.32	0.26	n.a.	n.a.
BBL	BBL-5	15	336.91	10.41	12.67	0.30	30.82	0.60	19.53	0.51	4.44	0.14	5.61	0.23	3.60	0.41	3.68	0.21	120.95	11.47	110.49	3.06	0.73	0.11	1.13	0.23	n.a.	n.a.
BBL	BBL-5	17	190.65	5.51	6.69	0.32	19.13	0.86	15.50	0.54	3.94	0.39	5.96	0.54	3.59	0.24	2.00	0.19	164.94	8.31	97.41	4.46	0.17	0.14	1.46	0.36	n.a.	n.a.
BBL	BBL-5	18	329.36	6.39	11.94	0.46	30.87	0.82	18.74	0.59	5.30	0.54	4.91	0.25	2.62	0.22	3.70	0.24	69.44	9.40	90.67	3.52	0.80	0.13	1.00	0.20	n.a.	n.a.
BBL	BBL-5	19	125.48	2.45	5.40	0.08	13.61	0.43	9.59	0.45	2.72	0.21	3.84	0.15	1.96	0.17	1.33	0.07	75.00	5.60	69.73	2.75	0.36	0.06	0.63	0.12	n.a.	n.a.
BBL	BBL-5	20	350.00	13.10	12.30	0.40	32.20	0.70	18.80	0.90	3.90	0.30	3.90	0.40	2.40	0.30	5.40	0.40	113.10	10.80	143.30	3.50	0.70	0.20	16.00	6.70	n.a.	n.a.
BBL	BBL-5	21A	310.63	11.30	12.49	0.53	28.92	0.57	17.12	0.69	3.67	0.33	4.96	0.39	3.25	0.22	4.29	0.26	127.60	11.38	118.60	7.32	0.93	0.15	1.18	0.23	n.a.	n.a.
BBL	BBL-5	21B	288.08	12.92	10.70	0.58	30.59	0.67	15.29	2.02	4.51	0.24	5.37	0.38	2.86	0.40	3.72	0.24	88.76	12.86	124.23	4.45	0.62	0.12	1.06	0.20	n.a.	n.a.
BBL	BBL-5	22	n.a.	n.a.	n.a.	n.a.	n.a.	n.a.	n.a.	n.a.	n.a.	n.a.	n.a.	n.a.	n.a.	n.a.	n.a.	n.a.	n.a.	n.a.	n.a.	n.a.	n.a.	n.a.	n.a.	n.a.	n.a.	n.a.
BBL	BBL-5	23	219.71	4.36	8.19	0.18	23.36	1.33	14.08	0.42	3.25	0.12	3.50	0.30	2.03	0.24	2.96	0.11	111.50	6.91	102.12	3.54	0.53	0.10	0.95	0.18	n.a.	n.a.
BBL	BBL-5	30	339.03	9.11	13.42	0.56	35.16	0.81	16.76	1.51	5.03	0.40	6.59	0.45	3.94	0.14	4.63	0.31	93.99	7.82	83.07	18.17	0.77	0.04	1.42	0.08	0.19	0.01
BBL	BBL-5	31	218.93	4.20	8.35	0.17	20.99	0.56	13.53	0.53	2.95	0.40	4.43	0.16	3.02	0.16	3.12	0.07	84.18	6.96	75.17	16.54	0.67	0.04	1.50	0.09	0.12	0.01
BBL	BBL-5	32	273.97	5.73	10.28	0.20	25.13	0.44	15.82	0.40	4.08	0.11	4.48	0.11	2.82	0.11	3.71	0.11	75.78	6.46	81.00	17.73	0.64	0.04	1.40	0.13	0.21	0.02
BBL	BBL-5	33	349.28	5.99	12.75	0.24	30.31	0.60	18.55	0.44	4.33	0.13	4.65	0.20	2.92	0.20	4.61	0.10	177.23	14.82	79.06	17.41	0.87	0.06	1.71	0.10	0.21	0.02
BBL	BBL-5	34	n.a.	n.a.	n.a.	n.a.	n.a.	n.a.	n.a.	n.a.	n.a.	n.a.	n.a.	n.a.	n.a.	n.a.	n.a.	n.a.	n.a.	n.a.	n.a.	n.a.	n.a.	n.a.	n.a.	n.a.	n.a.	n.a.
BBL	BBL-5	43	341.20	5.68	12.04	0.27	29.94	0.49	17.97	0.25	4.24	0.13	4.70	0.14	2.93	0.14	4.90	0.14	106.71	8.79	83.08	18.52	1.00	0.06	1.55	0.11	0.17	0.03
BBL	BBL-5	44	118.57	2.60	4.79	0.10	12.55	0.28	8.27	0.35	2.37	0.14	3.62	0.14	2.07	0.14	1.41	0.11	83.14	6.89	69.85	15.54	0.35	0.04	1.32	0.11	0.05	0.01
BBL	BBL-5	46	292.18	5.40	10.96	0.18	26.31	0.43	15.72	0.23	4.08	0.09	3.94	0.13	2.99	0.13	4.11	0.09	106.73	8.75	84.74	18.91	0.78	0.05	1.68	0.09	0.19	0.02
BBL	BBL-5	47	108.41	2.62	4.04	0.08	10.83	0.35	8.58	0.21	2.26	0.09	3.53	0.15	2.33	0.15	1.46	0.06	84.26	6.97	67.72	15.09	0.22	0.04	1.08	0.09	0.05	0.01
BBL	BBL-5	49	329.50	6.60	12.14	0.24	30.06	0.51	17.28	0.53	4.18	0.08	4.20	0.13	2.59	0.13	4.59	0.16	67.91	5.87	98.84	22.12	0.82	0.06	2.91	0.37	0.23	0.01
BBL	BBL-5	3	n.a.	n.a.	n.a.	n.a.	n.a.	n.a.	n.a.	n.a.	n.a.	n.a.	n.a.	n.a.	n.a.	n.a.	n.a.	n.a.	n.a.	n.a.	n.a.	n.a.	n.a.	n.a.	n.a.	n.a.	n.a.	n.a.
BBL	BBL-5	4	n.a.	n.a.	n.a.	n.a.	n.a.	n.a.	n.a.	n.a.	n.a.	n.a.	n.a.	n.a.	n.a.	n.a.	n.a.	n.a.	n.a.	n.a.	n.a.	n.a.	n.a.	n.a.	n.a.	n.a.	n.a.	n.a.
BBL	BBL-5	5	n.a.	n.a.	n.a.	n.a.	n.a.	n.a.	n.a.	n.a.	n.a.	n.a.	n.a.	n.a.	n.a.	n.a.	n.a.	n.a.	n.a.	n.a.	n.a.	n.a.	n.a.	n.a.	n.a.	n.a.	n.a.	n.a.
BBL	BBL-5	6	228.55	4.47	8.77	0.23	23.54	0.73	13.66	0.50	3.44	0.31	4.23	0.20	2.19	0.14	2.94	0.15	90.02	7.69	104.14	2.75	0.49	0.07	0.87	0.16	n.a.	n.a.
BBL	BBL-5	7	151.90	5.40	6.20	0.40	16.80	0.40	11.50	0.70	2.40	0.50	5.20	0.90	3.60	0.40	1.60	0.20	132.30	8.50	127.00	3.90	n.a.	n.a.	0.80	0.20	n.a.	n.a.
BORG	BORG-1	2	n.a.	n.a.	n.a.	n.a.	n.a.	n.a.	n.a.	n.a.	n.a.	n.a.	n.a.	n.a.	n.a.	n.a.	n.a.	n.a.	n.a.	n.a.	n.a.	n.a.	n.a.	n.a.	n.a.	n.a.	n.a.	n.a.
BORG	BORG-1	3	n.a.	n.a.	n.a.	n.a.	n.a.	n.a.	n.a.	n.a.	n.a.	n.a.	n.a.	n.a.	n.a.	n.a.	n.a.	n.a.	n.a.	n.a.	n.a.	n.a.	n.a.	n.a.	n.a.	n.a.	n.a.	n.a.
BORG	BORG-1	8	n.a.	n.a.	n.a.	n.a.	n.a.	n.a.	n.a.	n.a.	n.a.	n.a.	n.a.	n.a.	n.a.	n.a.	n.a.	n.a.	n.a.	n.a.	n.a.	n.a.	n.a.	n.a.	n.a.	n.a.	n.a.	n.a.
BORG	BORG-1	9	n.a.	n.a.	n.a.	n.a.	n.a.	n.a.	n.a.	n.a.	n.a.	n.a.	n.a.	n.a.	n.a.	n.a.	n.a.	n.a.	n.a.	n.a.	n.a.	n.a.	n.a.	n.a.	n.a.	n.a.	n.a.	n.a.
BORG	BORG-1	10	n.a.	n.a.	n.a.	n.a.	n.a.	n.a.	n.a.	n.a.	n.a.	n.a.	n.a.	n.a.	n.a.	n.a.	n.a.	n.a.	n.a.	n.a.	n.a.	n.a.	n.a.	n.a.	n.a.	n.a.	n.a.	n.a.
BORG	BORG-1	11	282.10	5.70	9.00	0.20	18.70	0.90	11.20	0.20	2.70	0.30	3.20	0.20	1.30	0.50	4.60	0.20	130.50	4.60	78.80	2.40	0.60	0.10	0.50	0.10	n.a.	n.a.
BORG	BORG-1	12	298.27	8.78	9.66	0.39	20.27	0.36	11.78	0.99	2.19	0.14	2.71	0.21	2.15	0.49	4.64	0.24	167.24	5.55	104.71	3.18	0.15	0.16	0.47	0.10	n.a.	n.a.
BORG	BORG-1	14	156.17	3.55	4.91	0.09	13.01	0.48	7.69	0.23	2.06	0.09	2.26	0.11	1.04	0.10	2.46	0.18	103.15	4.05	71.83	2.69	0.33	0.09	0.48	0.10	n.a.	n.a.
BORG	BORG-1	15	284.50	4.80	8.40	0.20	20.90	0.70	12.40	0.20	2.30	0.30	2.60	0.10	1.10	0.10	5.30	0.30	322.00	5.10	121.90	3.90	0.30	0.00	0.60	0.10	n.a.	n.a.
BORG	BORG-1	19	182.00	3.40	5.80	0.10	14.70	0.50	9.20	0.40	2.30	0.10	2.70	0.20	1.20	0.20	3.10	0.10	116.10	4.00	80.40	3.50	0.40	0.10	0.50	0.10	n.a.	n.a.
BORG	BORG-1	20	258.10	4.50	7.40	0.20	17.80	0.60	10.90	0.20	2.60	0.20	2.30	0.20	1.00	0.10	4.40	0.40	278.70	4.00	92.40	2.80	0.40	0.00	0.70	0.10	n.a.	n.a.
BORG	BORG-1	21	164.02	4.81	5.02	0.21	12.82	0.31	8.20	0.21	1.83	0.11	2.37	0.14	1.06	0.09	2.15	0.08	108.06	3.86	77.33	3.68	0.34	0.09	0.45	0.09	n.a.	n.a.
BORG	BORG-1	22	154.61	3.02	6.46	0.09	16.57	0.58	10.37	0.29	2.51	0.31	2.90	0.18	1.77	0.07	2.52	0.11	100.86	5.35	65.22	1.61	0.32	0.04	0.55	0.10	n.a.	n.a.
BORG	BORG-1	23	n.a.	n.a.	n.a.	n.a.	n.a.	n.a.	n.a.	n.a.	n.a.	n.a.	n.a.	n.a.	n.a.	n.a.	n.a.	n.a.	n.a.	n.a.	n.a.	n.a.	n.a.	n.a.	n.a.	n.a.	n.a.	n.a.
BORG	BORG-1	24	257.07	7.84	7.81	0.27	18.88	0.25	12.13	0.48	2.26	0.60	2.94	0.26	3.81	0.29	3.28	0.15	130.90	6.09	102.23	3.83	0.63	0.14	0.63	0.12	n.a.	n.a.
BORG	BORG-1	25	222.97	7.81	8.86	0.24	23.08	0.40	12.88	1.40	4.14	0.29	3.37	0.23	2.28	0.23	3.42	0.22	161.54	6.63	114.27	2.76	0.66	0.16	0.63	0.13	n.a.	n.a.
BORG	BORG-1	31	281.14	5.56	8.09	0.13	18.35	0.34	11.52	0.17	2.61	0.11	2.68	0.07	1.48	0.07	4.69	0.12	170.26	14.23	86.38	19.24	0.54	0.03	0.89	0.06	0.08	0.01
BORG	BORG-1	35	265.06	4.65	8.08	0.15	18.04	0.29	11.47	0.30	2.68	0.10	2.60	0.11	1.43	0.11	4.95	0.11	254.62	21.58	81.67	17.91	0.47	0.03	1.08	0.07	0.10	0.01
BORG	BORG-1	37	267.76	4.36	8.09	0.15	18.57	0.32	11.43	0.20	2.84	0.12	2.51	0.07	1.53	0.07	4.42	0.23	260.83	21.91	88.37	19.40	0.55	0.04	1.10	0.06	0.11	0.01
BORG	BORG-1	38	240.11	3.86	7.32	0.13	16.26	0.29	10.49	0.19	2.55	0.08	2.50	0.07	1.39	0.07	4.18	0.03	301.58	24.92	74.69	16.40	0.44	0.03	1.07	0.06	0.11	0.01
BORG	BORG-1	40	190.20	3.75	6.06	0.11	14.30	0.37	8.67	0.43	2.54	0.09	2.56	0.08	1.36	0.08	2.86	0.06	93.02	8.29	85.05	19.00	0.40	0.03	1.18	0.09	0.10	0.01
BORG	BORG-1	42	176.15	3.49	5.57	0.08	13.55	0.20	8.70	0.13	2.32	0.05	2.53	0.06	1.37	0.06	2.58	0.05	98.34	8.10	74.83	16.74	0.45	0.03	1.03	0.07	0.07	0.00
BORG	BORG-1	43	230.41	3.76	6.51	0.12	15.05	0.22	9.45	0.23	2.51	0.05	2.43	0.05	1.34	0.05	4.30	0.10	281.05	23.53	90.77	20.20	0.46	0.03	1.07	0.06	0.09	0.00
BORG	BORG-1	44	231.19	4.45	6.64	0.15	15.04	0.24	10.40	0.15	2.66	0.18	2.89	0.12	1.58	0.12	4.08	0.11	189.97	16.27	90.62	20.18	0.46	0.04	1.09	0.09	0.08	0.00
BORG	MM-L17-BORG-1	45	198.88	5.31	6.62	0.14	16.02	0.32	10.73	0.34	2.96	0.15	2.44	0.08	1.49	0.08	3.01	0.09	83.31	7.06	96.55	21.63	0.53	0.05	0.97	0.07	0.07	0.01
BPPC	MM-L17-BPPC-4	1	137.56	2.43	4.68	0.17	11.39	0.27	7.74	0.31	2.02	0.12	2.53	0.11	1.64	0.11	2.12	0.05	82.74	7.18	0.00	0.00	0.41	0.04	0.98	0.06	0.05	0.02
BPPC	MM-L17-BPPC-4	13	122.10	1.88	5.75	0.09	14.26	0.21	8.95	0.16	2.27	0.11	3.01	0.09	1.75	0.09	2.16	0.10	26.14	2.14	69.95	15.62	0.45	0.03	1.00	0.07	0.08	0.01
BPPC	MM-L17-BPPC-4	14	122.75	2.07	5.76	0.13	14.98	0.31	9.16	0.16	2.63	0.18	3.29	0.12	1.93	0.12	2.13	0.06	25.03	2.06	62.02	13.81	0.32	0.04	1.04	0.11	0.08	0.02
BPPC	MM-L17-BPPC-4	15	112.46	2.22	5.48	0.12	13.80	0.34	8.37	0.14	2.37	0.14	3.07	0.11	2.04	0.11	1.77	0.36	23.90	2.29	69.24	15.49	0.31	0.03	0.82	0.10	0.09	0.02
BPPC	MM-L17-BPPC-4	2	81.10	1.64	4.89	0.10	12.91	0.24	8.18	0.28	2.27	0.15	2.93	0.13	1.60	0.13	1.69	0.03	29.04	2.42	53.86	11.78	0.29	0.03	1.04	0.07	0.14	0.02
BPPC	MM-L17-BPPC-4	3	n.a.	n.a.	n.a.	n.a.	n.a.	n.a.	n.a.	n.a.	n.a.	n.a.	n.a.	n.a.	n.a.	n.a.	n.a.	n.a.	n.a.	n.a.	64.97	14.28	n.a.	n.a.	n.a.	n.a.	n.a.	n.a.
BPPC	MM-L17-BPPC-4	5	78.58	1.77	5.26	0.11	14.38	0.31	9.07	0.38	2.24	0.07	2.99	0.10	2.05	0.10	2.11	0.10	31.87	2.76	93.94	21.18	0.21	0.03	1.13	0.11	n.a.	n.a.
BRM	BRM-1	14	n.a.	n.a.	n.a.	n.a.	n.a.	n.a.	n.a.	n.a.	n.a.	n.a.	n.a.	n.a.	n.a.	n.a.	n.a.	n.a.	n.a.	n.a.	n.a.	n.a.	n.a.	n.a.	n.a.	n.a.	n.a.	n.a.
BRM	BRM-1	16	n.a.	n.a.	n.a.	n.a.	n.a.	n.a.	n.a.	n.a.	n.a.	n.a.	n.a.	n.a.	n.a.	n.a.	n.a.	n.a.	n.a.	n.a.	n.a.	n.a.	n.a.	n.a.	n.a.	n.a.	n.a.	n.a.
BRM	BRM-1	17	310.15	9.89	20.12	0.33	45.64	0.90	20.04	1.19	3.07	0.17	3.03	0.46	1.13	0.08	5.57	0.23	39.71	9.18	83.86	2.63	0.04	0.09	1.12	0.21	n.a.	n.a.
BRM	BRM-1	18	n.a.	n.a.	n.a.	n.a.	n.a.	n.a.	n.a.	n.a.	n.a.	n.a.	n.a.	n.a.	n.a.	n.a.	n.a.	n.a.	n.a.	n.a.	n.a.	n.a.	n.a.	n.a.	n.a.	n.a.	n.a.	n.a.
BRM	BRM-1	19	311.71	12.26	17.44	0.70	39.10	1.49	20.73	0.91	4.33	0.30	2.80	0.32	1.05	0.23	6.86	0.51	121.49	9.59	70.20	3.72	0.66	0.10	0.66	0.14	n.a.	n.a.
BRM	BRM-1	22	313.30	12.85	21.78	0.69	48.73	2.54	23.72	1.69	4.17	0.35	2.32	0.16	0.35	0.48	5.53	0.37	74.79	9.36	90.57	5.98	0.57	0.10	0.76	0.15	n.a.	n.a.
BRM	BRM-1	23	n.a.	n.a.	n.a.	n.a.	n.a.	n.a.	n.a.	n.a.	n.a.	n.a.	n.a.	n.a.	n.a.	n.a.	n.a.	n.a.	n.a.	n.a.	n.a.	n.a.	n.a.	n.a.	n.a.	n.a.	n.a.	n.a.
BRM	BRM-1	24	574.00	15.50	29.70	0.50	65.70	1.00	34.70	0.90	6.00	0.30	4.30	0.20	2.30	0.10	9.80	0.40	n.a.	n.a.	80.10	4.30	n.a.	n.a.	0.90	0.20	n.a.	n.a.
BRM	BRM-1	25	219.20	6.50	16.30	0.20	40.70	1.20	19.70	0.60	4.90	0.50	2.70	0.30	0.70	0.10	4.40	0.30	15.40	7.80	106.30	2.60	0.40	0.10	0.90	0.20	n.a.	n.a.
BRM	BRM-1	30	264.99	4.46	15.28	0.27	34.94	0.56	18.57	0.32	3.33	0.09	2.38	0.05	1.33	0.04	5.16	0.09	70.48	5.88	61.37	14.33	0.53	0.03	1.44	0.10	0.18	0.02
BRM	BRM-1	34	297.93	5.12	17.72	0.34	40.28	0.82	21.46	0.46	3.49	0.10	2.80	0.11	1.61	0.10	6.34	0.14	56.01	4.74	55.45	12.42	0.57	0.06	1.44	0.10	0.31	0.03
BRM	BRM-1	35	n.a.	n.a.	n.a.	n.a.	n.a.	n.a.	n.a.	n.a.	n.a.	n.a.	n.a.	n.a.	n.a.	n.a.	n.a.	n.a.	n.a.	n.a.	n.a.	n.a.	n.a.	n.a.	n.a.	n.a.	n.a.	n.a.
BRM	BRM-1	36	n.a.	n.a.	n.a.	n.a.	n.a.	n.a.	n.a.	n.a.	n.a.	n.a.	n.a.	n.a.	n.a.	n.a.	n.a.	n.a.	n.a.	n.a.	n.a.	n.a.	n.a.	n.a.	n.a.	n.a.	n.a.	n.a.
BRM	BRM-1	39	n.a.	n.a.	n.a.	n.a.	n.a.	n.a.	n.a.	n.a.	n.a.	n.a.	n.a.	n.a.	n.a.	n.a.	n.a.	n.a.	n.a.	n.a.	n.a.	n.a.	n.a.	n.a.	n.a.	n.a.	n.a.	n.a.
BRM	BRM-1	40	n.a.	n.a.	n.a.	n.a.	n.a.	n.a.	n.a.	n.a.	n.a.	n.a.	n.a.	n.a.	n.a.	n.a.	n.a.	n.a.	n.a.	n.a.	n.a.	n.a.	n.a.	n.a.	n.a.	n.a.	n.a.	n.a.
BRM	BRM-1	41	170.26	2.77	13.05	0.23	30.61	0.57	16.53	0.29	3.21	0.18	2.42	0.08	1.32	0.06	3.49	0.06	4.36	0.37	51.41	11.28	0.41	0.03	1.02	0.07	0.07	0.00
BRM	BRM-1	2	n.a.	n.a.	n.a.	n.a.	n.a.	n.a.	n.a.	n.a.	n.a.	n.a.	n.a.	n.a.	n.a.	n.a.	n.a.	n.a.	n.a.	n.a.	n.a.	n.a.	n.a.	n.a.	n.a.	n.a.	n.a.	n.a.
BRM	BRM-1	3	n.a.	n.a.	n.a.	n.a.	n.a.	n.a.	n.a.	n.a.	n.a.	n.a.	n.a.	n.a.	n.a.	n.a.	n.a.	n.a.	n.a.	n.a.	n.a.	n.a.	n.a.	n.a.	n.a.	n.a.	n.a.	n.a.
BRM	BRM-1	5	360.84	19.99	25.10	1.50	60.16	3.06	26.43	1.09	4.71	0.78	2.55	0.37	1.62	0.14	6.56	0.44	16.52	11.93	84.28	3.02	0.68	0.11	1.02	0.20	n.a.	n.a.
BRM	BRM-1	6	125.20	6.80	10.70	0.70	26.30	1.20	12.30	0.70	3.00	0.30	1.40	0.20	1.80	0.40	3.10	0.50	53.20	5.20	62.02	13.81	0.32	0.08	1.40	0.00	n.a.	n.a.
BRM	BRM-1	7	419.30	22.10	28.30	1.90	63.70	3.80	27.10	1.50	4.20	0.30	4.10	0.20	1.90	0.20	7.20	0.40	31.90	16.00	94.00	2.60	0.60	0.10	1.40	0.30	n.a.	n.a.
BRM	BRM-1	8	369.20	12.80	25.80	0.60	59.40	1.60	30.00	1.60	4.70	0.50	4.30	0.40	1.30	0.10	6.80	0.30	24.00	4.70	0.70	0.20	1.40	0.30	n.a.	n.a.	n.a.	n.a.
BRM	MM-L17-BRM-2	1	160.83	2.92	12.94	0.27	31.34	0.52	16.18	0.35	3.05	0.12	2.49	0.06	1.49	0.06	4.21	0.25	91.73	7.77	44.66	10.00	n.a.	0.85	1.63	0.19	0.15	0.01
BRM	MM-L17-BRM-2	10	n.a.	n.a.	n.a.	n.a.	n.a.	n.a.	n.a.	n.a.	n.a.	n.a.	n.a.	n.a.	n.a.	n.a.	n.a.	n.a.	n.a.	n.a.	n.a.	n.a.	n.a.	n.a.	n.a.	n.a.	n.a.	n.a.
BRM	MM-L17-BRM-2	13	n.a.	n.a.	n.a.	n.a.	n.a.	n.a.	n.a.	n.a.	n.a.	n.a.	n.a.	n.a.	n.a.	n.a.	n.a.	n.a.	n.a.	n.a.	n.a.	n.a.	n.a.	n.a.	n.a.	n.a.	n.a.	n.a.
BRM	MM-L17-BRM-2	14	n.a.	n.a.	n.a.	n.a.	n.a.	n.a.	n.a.	n.a.	n.a.	n.a.	n.a.	n.a.	n.a.	n.a.	n.a.	n.a.	n.a.	n.a.	n.a.	n.a.	n.a.	n.a.	n.a.	n.a.	n.a.	n.a.
BRM	MM-L17-BRM-2	16	n.a.	n.a.	n.a.	n.a.	n.a.	n.a.	n.a.	n.a.	n.a.	n.a.	n.a.	n.a.	n.a.	n.a.	n.a.	n.a.	n.a.	n.a.	n.a.	n.a.	n.a.	n.a.	n.a.	n.a.	n.a.	n.a.
BRM	MM-L17-BRM-2	17	n.a.	n.a.	n.a.	n.a.	n.a.	n.a.	n.a.	n.a.	n.a.	n.a.	n.a.	n.a.	n.a.	n.a.	n.a.	n.a.	n.a.	n.a.	n.a.	n.a.	n.a.	n.a.	n.a.	n.a.	n.a.	n.a.
BRM	MM-L17-BRM-2	18	322.58	6.31	17.46	0.37	40.23	0.74	19.75	0.41	3.68	0.13	2.79	0.09	1.75	0.09	6.49	0.09	38.86	3.36	52.74	11.54	0.57	0.04	1.24	0.08	0.27	0.02
BRM	MM-L17-BRM-2	24	318.52	5.40	15.97	0.30	38.01	0.61	19.10	0.40	3.61	0.11	2.50	0.06	1.55	0.11	6.65	0.42	66.41	5.42	65.11	14.51	0.78	0.05	1.47	0.06	0.20	0.01
BRM	MM-L17-BRM-2	25	273.93	4.76	18.32	0.33	43.89	0.76	22.08	0.33	3.86	0.08	2.60	0.06	1.23	0.06	5.26	0.10	24.24	2.00	58.79	13.16	0.65	0.05	1.30	0.10	0.19	0.01
BRM	MM-L17-BRM-2	26	277.89	4.75	19.35	0.31	46.07	0.74	22.91	0.36	4.00	0.07	2.51	0.08	1.19	0.11	5.21	0.09	28.73	2.62	44.99	11.33	n.a.	0.30	1.34	0.08	0.19	0.02
BRM	MM-L17-BRM-2	29	233.81	4.47	15.25	0.25	36.31	0.69	18.24	0.36	3.59	0.15	2.41	0.06	1.38	0.04	4.95	0.08	71.16	5.87	48.39	10.80	0.61	0.08	1.43	0.09	0.18	0.01
BRM	MM-L17-BRM-2	31	153.97	2.45	11.82	0.37	29.67	0.43	15.22	0.28	3.01	0.18	2.23	0.11	1.24	0.11	3.50	0.16	37.98	3.16	53.97	12.05	0.48	0.03	1.26	0.12	0.10	0.01
BRM	MM-L17-BRM-2	32	166.20	3.06	12.96	0.21	31.78	0.49	15.94	0.37	3.12	0.07	2.07	0.08	1.38	0.10	3.45	0.08	4.92	0.43	53.47	11.94	0.40	0.06	0.96	0.05	0.12	0.01
BRM	MM-L17-BRM-2	8	283.10	7.45	24.04	0.65	60.37	1.62	30.86	0.88	5.35	0.13	2.84	0.10	1.11	0.10	5.58	0.15	176.05	15.76	60.37	13.50	0.78	0.05	3.24	0.26	0.09	0.01
BRVB	MM-L17-BRVB-2	10	388.98	6.94	14.39	0.23	34.60	0.59	19.77	0.49	4.14	0.16	3.86	0.07	2.14	0.07	4.30	0.09	23.69	1.96	95.85	20.17	0.90	0.06	1.55	0.09	0.26	0.01
BRVB	MM-L17-BRVB-2	2	218.90	3.84	7.32	0.12	17.71	0.29	12.38	0.25	3.51	0.13	4.46	0.10	2.89	0.10	3.45	0.08	68.80	6.09	76.99	17.19	0.38	0.04	1.44	0.09	0.09	0.01
BRVB	MM-L17-BRVB-2	4	402.25	6.27	15.27	0.24	36.57	0.53	21.80	0.44	4.73	0.22	3.86	0.14	2.18	0.09	3.96	0.07	9.73	0.98	90.49	21.52	0.87	0.14	1.70	0.10	0.32	0.02
BRVB	MM-L17-BRVB-2	6	498.79	13.85	18.00	0.46	43.73	1.52	25.86	0.63	6.17	0.45	4.31	0.21	2.21	0.21	4.64	0.17	14.02	1.22	91.95	20.53	1.25	0.10	1.83	0.14	0.27	0.01
BRVB	MM-L17-BRVB-2	7	467.12	8.76	18.24	0.48	40.15	0.61	25.14	0.67	5.00	0.29	4.81	0.21	2.73	0.21	5.64	0.29	66.57	5.44	101.29	22.77	1.10	0.06	2.75	0.20	0.44	0.04

n. a. = not analyzed
n.r. = not recorded
*many bubble diameters reported here have been measured on intersected inclusions and are a minimum value

Table S2. Corrected major element and trace element melt inclusion data. Major element compositions and trace element concentrations have been corrected for post entrapment crystallization and Fe-Mg reequlibration. Major elements, S, Cl, and H2O reported in wt. %. Trace elements reported in ppm.

Cinder Cone	Tephra Sample	Melt Incl	SiO$_2$	TiO$_2$	Al$_2$O$_3$	FeO^T	MnO	MgO	CaO	Na$_2$O	K$_2$O	P$_2$O$_5$	S	Cl	H$_2$O
BAS-44	BAS-44-2	1	49.16	0.83	17.39	8.94	0.12	8.97	11.45	2.60	0.25	0.14	0.12	0.03	0.77
BAS-44	BAS-44-2	10	48.79	0.97	17.53	9.08	0.14	9.68	10.40	2.76	0.39	0.18	0.03	0.04	n. a.
BAS-44	BAS-44-2	2	49.06	0.97	16.96	9.09	0.13	9.57	10.78	2.83	0.27	0.17	0.12	0.04	1.47
BAS-44	BAS-44-2	4	49.19	0.98	17.23	9.02	0.12	9.33	10.77	2.75	0.26	0.19	0.11	0.04	1.16
BAS-44	BAS-44-2	5	48.84	0.97	17.49	8.98	0.12	9.01	11.22	2.76	0.28	0.17	0.12	0.04	1.31
BAS-44	BAS-44-2	6	48.11	0.98	17.72	9.04	0.13	9.44	10.96	3.00	0.29	0.16	0.12	0.04	1.27
BAS-44	BAS-44-2	7a	50.31	0.92	16.54	8.95	0.16	9.22	10.57	2.70	0.33	0.16	0.10	0.04	n. a.
BAS-44	BAS-44-2	7b	49.76	1.00	16.92	8.99	0.15	8.89	10.71	2.89	0.36	0.17	0.10	0.04	n. a.
BBL	BBL-5	11	49.52	1.22	17.32	10.15	0.20	7.51	9.37	3.67	0.71	0.31	0.10	0.03	n. a.
BBL	BBL-5	14	49.98	1.72	16.25	10.10	0.20	7.82	8.38	4.44	0.81	0.30	0.10	0.03	n. a.
BBL	BBL-5	15	50.58	1.54	16.17	10.18	0.21	7.84	8.55	3.91	0.72	0.31	0.11	0.03	n. a.
BBL	BBL-5	17	48.02	0.97	16.07	10.51	0.09	11.43	9.66	2.90	0.26	0.09	0.08	0.02	n. a.
BBL	BBL-5	18	50.02	1.50	16.15	10.22	0.20	8.07	8.83	3.91	0.80	0.30	0.10	0.03	n. a.
BBL	BBL-5	19	48.55	1.03	17.23	10.36	0.09	10.00	9.27	3.00	0.28	0.19	0.08	0.02	n. a.
BBL	BBL-5	20	49.34	1.30	17.61	10.10	0.20	7.93	9.11	3.50	0.60	0.30	0.09	0.03	n. a.
BBL	BBL-5	21A	49.24	1.36	16.68	10.26	0.10	9.08	8.73	3.68	0.58	0.29	0.09	0.02	n. a.
BBL	BBL-5	21B	48.87	1.44	16.94	10.26	0.19	9.00	8.81	3.64	0.57	0.29	0.09	0.03	n. a.
BBL	BBL-5	22	48.57	1.10	16.47	10.39	0.09	10.02	10.16	2.84	0.27	0.09	0.08	0.02	n. a.
BBL	BBL-5	23	49.20	1.27	16.83	10.22	0.10	8.59	9.78	3.33	0.49	0.20	0.09	0.02	n. a.
BBL	BBL-5	3	48.32	0.98	16.48	10.41	0.09	10.63	9.80	2.85	0.27	0.18	0.08	0.01	n. a.
BBL	BBL-5	30	49.57	1.12	16.11	10.38	0.19	9.61	8.90	3.18	0.66	0.28	0.11	0.04	n. a.
BBL	BBL-5	31	50.72	1.16	15.43	10.20	0.19	8.51	9.61	3.40	0.58	0.19	0.12	0.04	1.10
BBL	BBL-5	32	50.43	1.24	15.99	10.18	0.19	8.36	9.33	3.43	0.57	0.29	0.13	0.03	1.16
BBL	BBL-5	33	50.22	1.27	16.38	10.23	0.20	8.06	9.02	3.63	0.69	0.29	0.14	0.04	1.19
BBL	BBL-5	34	51.74	1.05	14.70	10.18	0.19	8.39	9.83	3.25	0.48	0.19	0.12	0.03	1.15
BBL	BBL-5	4	48.29	1.04	16.38	10.40	0.09	10.54	10.06	2.86	0.26	0.09	0.07	0.01	n. a.
BBL	BBL-5	43	50.24	1.18	16.43	10.25	0.20	8.66	8.66	3.54	0.79	0.30	0.11	0.04	0.94
BBL	BBL-5	44	48.36	0.92	17.37	10.35	0.09	9.79	10.16	2.59	0.28	0.09	0.09	0.02	0.94
BBL	BBL-5	46	49.32	1.14	16.62	10.31	0.19	9.12	9.31	3.13	0.57	0.28	0.09	0.03	1.09
BBL	BBL-5	47	48.04	0.80	16.87	10.40	0.09	10.68	10.08	2.68	0.27	0.09	0.08	0.02	0.92
BBL	BBL-5	49	49.60	1.17	17.66	10.06	0.20	7.55	9.37	3.32	0.78	0.29	0.10	0.03	0.62
BBL	BBL-5	5	50.69	1.48	17.03	10.02	0.21	6.82	8.67	3.91	0.85	0.32	0.11	0.04	n. a.
BBL	BBL-5	6	49.61	1.36	15.88	10.19	0.19	8.54	9.88	3.68	0.48	0.19	0.10	0.02	n. a.
BBL	BBL-5	7	47.99	0.99	16.23	10.45	0.09	11.00	10.19	2.79	0.18	0.09	0.08	0.01	n. a.
BORG	BORG-1	10	49.71	0.86	19.18	8.85	0.13	7.03	9.25	4.15	0.60	0.10	0.09	0.04	n. a.
BORG	BORG-1	11	48.86	0.78	19.45	8.97	0.09	7.70	8.92	4.43	0.55	0.10	0.13	0.04	n. a.
BORG	BORG-1	12	49.78	0.82	19.55	8.91	0.13	7.40	8.42	4.18	0.55	0.11	0.11	0.04	n. a.
BORG	BORG-1	14	48.52	0.69	18.28	9.24	0.10	9.53	10.05	2.92	0.47	0.06	0.09	0.05	n. a.
BORG	BORG-1	15	50.42	0.98	19.41	8.61	0.13	6.16	8.89	4.51	0.59	0.12	0.13	0.05	n. a.
BORG	BORG-1	19	48.14	0.83	19.94	9.01	0.12	7.95	9.14	4.10	0.55	0.07	0.10	0.05	n. a.
BORG	BORG-1	2	48.97	0.79	20.81	8.75	0.14	6.66	9.44	3.68	0.53	0.08	0.10	0.05	n. a.
BORG	BORG-1	20	48.68	0.91	19.30	9.13	0.12	8.22	8.56	4.30	0.52	0.10	0.12	0.04	n. a.
BORG	BORG-1	21	48.22	0.74	19.67	9.11	0.09	8.49	9.69	3.27	0.52	0.07	0.09	0.04	n. a.
BORG	BORG-1	22	47.74	0.82	17.68	9.33	0.10	10.24	10.33	2.98	0.52	0.10	0.10	0.06	n. a.

Table S2. (continued)

Cinder Cone	Tephra Sample	Melt Incl	SiO_2	TiO_2	Al_2O_3	FeO^T	MnO	MgO	CaO	Na_2O	K_2O	P_2O_5	S	Cl	H_2O
BORG	BORG-1	23	48.82	0.85	20.51	8.73	0.12	6.55	9.61	4.02	0.57	0.09	0.09	0.05	n. a.
BORG	BORG-1	24	49.35	0.83	19.78	8.87	0.13	7.18	9.28	3.79	0.56	0.10	0.09	0.04	n. a.
BORG	BORG-1	25	48.57	0.72	18.19	9.22	0.11	9.40	10.42	2.71	0.46	0.06	0.10	0.05	n. a.
BORG	BORG-1	3	48.77	0.89	20.40	8.86	0.12	6.84	9.40	3.97	0.53	0.08	0.09	0.05	n. a.
BORG	BORG-1	31	50.94	1.00	18.89	8.88	0.16	7.34	8.80	2.96	0.66	0.16	0.15	0.06	2.56
BORG	BORG-1	35	51.37	0.82	18.24	8.96	0.13	7.09	9.00	3.44	0.56	0.16	0.17	0.05	n. a.
BORG	BORG-1	37	50.92	0.85	18.90	8.79	0.14	6.66	9.24	3.58	0.54	0.17	0.17	0.05	3.12
BORG	BORG-1	38	50.69	0.90	18.49	8.96	0.14	7.49	9.12	3.29	0.55	0.14	0.18	0.05	3.12
BORG	BORG-1	40	50.58	0.88	19.27	8.82	0.14	6.87	9.44	3.08	0.61	0.12	0.12	0.06	2.81
BORG	BORG-1	42	50.17	0.82	18.32	9.04	0.13	8.01	9.63	3.07	0.55	0.10	0.11	0.05	2.96
BORG	BORG-1	43	50.94	0.89	19.00	8.78	0.15	7.20	8.89	3.29	0.53	0.11	0.15	0.06	1.74
BORG	BORG-1	44	51.25	0.84	18.69	8.76	0.14	6.62	9.39	3.44	0.57	0.10	0.14	0.05	2.95
BORG	BORG-1	45	50.47	0.99	19.48	8.60	0.16	6.56	9.32	3.53	0.59	0.13	0.12	0.05	0.85
BORG	BORG-1	8	48.24	0.73	20.96	8.94	0.15	7.14	8.97	4.05	0.53	0.13	0.12	0.04	n. a.
BORG	BORG-1	9	48.08	0.79	17.66	9.28	0.08	9.97	10.29	3.06	0.54	0.10	0.11	0.06	n. a.
BORG	MM-L17-BORG-1	1	49.90	0.67	18.12	9.03	0.13	8.13	10.82	2.43	0.50	0.08	0.13	0.05	2.57
BPPC	MM-L17-BPPC-4	13	51.31	0.79	17.49	7.58	0.14	8.43	11.08	2.58	0.36	0.09	0.10	0.04	2.26
BPPC	MM-L17-BPPC-4	14	51.34	0.79	17.74	7.57	0.14	8.26	11.04	2.53	0.35	0.08	0.11	0.04	2.24
BPPC	MM-L17-BPPC-4	15	51.95	0.74	17.03	7.56	0.14	8.33	11.22	2.48	0.32	0.09	0.10	0.04	1.91
BPPC	MM-L17-BPPC-4	2	50.84	0.77	17.44	7.57	0.12	8.33	11.84	2.56	0.25	0.11	0.11	0.06	n. a.
BPPC	MM-L17-BPPC-4	3	52.66	0.86	17.72	7.22	0.15	6.13	11.87	2.75	0.35	0.13	0.10	0.05	2.69
BPPC	MM-L17-BPPC-4	4	50.90	0.83	17.49	7.63	0.10	8.65	11.04	2.73	0.33	0.13	0.11	0.06	2.41
BPPC	MM-L17-BPPC-4	5	51.22	0.76	17.16	7.54	0.14	8.52	11.55	2.57	0.26	0.09	0.11	0.07	1.37
BRM	BRM-1	14	49.25	0.98	18.66	7.49	0.07	7.72	10.30	4.05	0.70	0.24	0.22	0.31	n. a.
BRM	BRM-1	16	50.37	0.99	17.91	7.54	0.07	7.94	9.58	4.31	0.65	0.20	0.16	0.25	n. a.
BRM	BRM-1	17	50.47	0.93	18.02	7.54	0.08	7.96	9.37	4.46	0.61	0.18	0.16	0.24	n. a.
BRM	BRM-1	18	48.85	1.09	18.61	7.59	0.09	8.17	9.84	4.10	0.94	0.30	0.19	0.25	n. a.
BRM	BRM-1	19	50.94	1.01	19.26	7.51	0.09	7.15	8.32	4.25	0.87	0.22	0.14	0.24	n. a.
BRM	BRM-1	2	49.87	0.92	17.86	7.57	0.06	8.30	10.39	3.86	0.56	0.20	0.16	0.24	n. a.
BRM	BRM-1	22	49.99	0.96	18.12	7.49	0.08	7.48	9.77	4.90	0.58	0.20	0.17	0.26	n. a.
BRM	BRM-1	23	50.25	1.20	19.23	7.22	0.10	5.63	9.97	4.78	0.90	0.31	0.18	0.23	n. a.
BRM	BRM-1	24	56.73	1.96	14.31	7.19	0.09	5.55	7.16	4.34	1.80	0.48	0.05	0.35	n. a.
BRM	BRM-1	25	48.96	0.99	18.87	7.49	0.08	7.63	10.07	4.57	0.60	0.23	0.19	0.30	n. a.
BRM	BRM-1	3	50.22	0.96	18.57	7.47	0.07	7.39	9.64	4.41	0.66	0.20	0.16	0.25	n. a.
BRM	BRM-1	30	52.59	0.82	17.80	7.65	0.10	7.27	8.61	3.85	0.65	0.20	0.18	0.29	3.05
BRM	BRM-1	34	49.57	0.94	18.80	7.50	0.08	7.21	10.14	4.21	0.75	0.24	0.25	0.31	2.21
BRM	BRM-1	35	49.56	0.93	18.33	7.61	0.07	8.08	9.77	4.09	0.74	0.26	0.24	0.32	n. a.
BRM	BRM-1	36	50.63	0.96	17.68	7.48	0.05	7.90	10.03	3.68	0.73	0.27	0.23	0.36	0.52
BRM	BRM-1	39	51.40	0.89	17.15	7.71	0.08	8.39	9.17	3.72	0.74	0.25	0.20	0.29	3.54
BRM	BRM-1	40	50.03	0.97	18.75	7.46	0.07	7.31	10.16	3.64	0.77	0.29	0.25	0.31	n. a.
BRM	BRM-1	41	50.56	0.83	18.15	7.52	0.08	7.48	10.81	3.32	0.55	0.19	0.22	0.30	1.99
BRM	BRM-1	5	49.17	1.08	18.35	7.60	0.06	8.04	10.00	4.26	0.72	0.26	0.18	0.28	n. a.
BRM	BRM-1	6	49.23	0.99	19.40	7.45	0.07	7.23	10.38	4.03	0.57	0.23	0.16	0.25	n. a.
BRM	BRM-1	7	49.97	1.11	18.93	7.42	0.10	6.60	10.20	4.26	0.75	0.26	0.16	0.26	n. a.
BRM	BRM-1	8	49.37	1.09	18.69	7.56	0.06	8.15	8.90	4.56	0.88	0.24	0.20	0.29	n. a.
BRM	MM-L17-BRM-2	1	48.96	0.76	18.46	7.54	0.06	8.64	10.60	3.74	0.52	0.17	0.21	0.34	0.90
BRM	MM-L17-BRM-2	10	49.23	1.14	19.36	7.36	0.08	6.83	10.18	4.22	0.81	0.29	0.27	0.24	0.83
BRM	MM-L17-BRM-2	13	48.82	1.04	18.70	7.51	0.08	7.80	10.09	4.28	0.77	0.34	0.26	0.31	n. a.
BRM	MM-L17-BRM-2	14	49.46	0.79	18.61	7.50	0.07	7.65	10.60	4.01	0.64	0.19	0.22	0.27	0.83
BRM	MM-L17-BRM-2	16	49.56	0.80	18.22	7.63	0.08	8.45	10.38	3.63	0.54	0.23	0.22	0.24	2.24
BRM	MM-L17-BRM-2	17	48.96	0.78	18.85	7.47	0.08	7.93	11.21	3.54	0.52	0.19	0.18	0.26	0.65
BRM	MM-L17-BRM-2	18	49.99	0.86	18.62	7.52	0.08	8.10	9.70	3.77	0.75	0.21	0.16	0.23	0.64
BRM	MM-L17-BRM-2	24	50.01	0.98	19.25	7.33	0.10	6.51	10.39	3.80	0.90	0.26	0.23	0.23	1.23
BRM	MM-L17-BRM-2	25	49.14	1.02	19.44	7.41	0.08	7.26	10.27	3.82	0.77	0.26	0.23	0.31	0.63
BRM	MM-L17-BRM-2	26	48.65	0.97	19.34	7.48	0.07	8.03	9.99	3.87	0.79	0.26	0.24	0.32	0.79
BRM	MM-L17-BRM-2	29	49.37	0.78	18.37	7.60	0.06	8.70	10.23	3.64	0.65	0.16	0.19	0.24	0.30
BRM	MM-L17-BRM-2	31	49.20	0.77	18.18	7.40	0.07	9.36	10.55	3.34	0.51	0.16	0.21	0.25	0.31
BRM	MM-L17-BRM-2	32	48.91	0.83	19.25	7.53	0.08	7.61	11.09	3.53	0.54	0.19	0.20	0.25	0.78
BRM	MM-L17-BRM-2	8	47.67	1.05	19.07	7.52	0.08	8.11	10.67	4.09	0.71	0.31	0.36	0.35	4.06
BRVB	MM-L17-BRVB-2	10	50.18	1.40	17.54	9.18	0.15	7.28	9.70	2.99	1.05	0.29	0.17	0.05	2.03
BRVB	MM-L17-BRVB-2	2	50.56	1.17	16.94	9.29	0.13	8.49	10.02	2.52	0.56	0.15	0.16	0.02	0.60
BRVB	MM-L17-BRVB-2	4	48.47	1.45	18.57	9.02	0.15	7.09	10.38	3.44	0.94	0.32	0.12	0.05	0.31
BRVB	MM-L17-BRVB-2	6	49.22	0.95	18.21	9.20	0.14	7.89	10.77	2.95	0.35	0.16	0.12	0.03	0.72
BRVB	MM-L17-BRVB-2	7	48.51	1.48	18.42	9.13	0.15	7.06	10.00	3.55	1.11	0.33	0.20	0.07	1.91

171

Table S2. (continued)

Cinder Cone	Tephra Sample	Melt Incl	% olivine	Fo Olivine	Li	B	Sc	V	Rb	Sr	Y	Zr	Nb	Sn	Ba
BAS-44	BAS-44-2	1	3.4	87.1	n. a.	n. a.	n. a.	n. a.	n. a.	n. a.	n. a.	n. a.	n. a.	n. a.	n. a.
BAS-44	BAS-44-2	10	6.7	87.7	n. a.	n. a.	n. a.	n. a.	n. a.	n. a.	n. a.	n. a.	n. a.	n. a.	n. a.
BAS-44	BAS-44-2	2	6.3	87.5	n. a.	n. a.	28.34	183.72	n. a.	374.44	17.13	70.75	2.65	23.46	106.84
BAS-44	BAS-44-2	4	8.3	87.3	n. a.	n. a.	29.19	203.69	n. a.	394.59	17.18	73.15	3.05	1.15	105.53
BAS-44	BAS-44-2	5	4.4	87.1	n. a.	n. a.	35.75	204.07	n. a.	424.04	20.08	79.77	3.29	1.48	129.78
BAS-44	BAS-44-2	6	6.3	87.7	n. a.	n. a.	n. a.	n. a.	n. a.	n. a.	n. a.	n. a.	n. a.	n. a.	n. a.
BAS-44	BAS-44-2	7a	3.8	87.1	n. a.	n. a.	34.54	202.67	n. a.	416.25	19.16	78.37	2.85	1.22	138.75
BAS-44	BAS-44-2	7b	2.8	86.7	n. a.	n. a.	n. a.	n. a.	n. a.	n. a.	n. a.	n. a.	n. a.	n. a.	n. a.
BBL	BBL-5	11	1.6	82.4	10.70	3.65	35.22	209.24	11.53	398.86	18.21	99.96	5.67	0.79	309.97
BBL	BBL-5	14	2.9	82.8	8.16	2.93	41.24	248.06	12.88	296.26	29.96	133.76	6.24	1.28	326.88
BBL	BBL-5	15	1.1	82.5	10.39	4.92	50.92	308.91	12.83	361.09	29.98	132.93	6.41	1.12	334.56
BBL	BBL-5	17	16.6	87.9	8.21	1.92	46.98	288.38	5.71	367.66	28.88	90.62	2.26	1.24	162.08
BBL	BBL-5	18	3.0	83.2	9.91	2.96	43.41	223.63	11.81	316.55	24.39	120.34	6.25	0.97	319.68
BBL	BBL-5	19	10.6	86.3	6.55	0.33	28.14	184.52	4.05	238.04	19.03	67.70	2.20	0.57	112.53
BBL	BBL-5	20	3.4	83.3	11.32	4.26	46.24	291.86	12.96	445.28	23.02	118.99	6.29	15.48	338.58
BBL	BBL-5	21A	6.6	85.0	9.18	3.39	43.28	319.54	11.57	358.14	23.18	102.32	5.52	1.11	290.90
BBL	BBL-5	21B	6.7	85.0	8.71	3.39	41.94	280.08	9.87	303.55	22.23	112.73	5.50	0.99	269.09
BBL	BBL-5	22	12.7	86.4	n. a.	n. a.	n. a.	n. a.	n. a.	n. a.	n. a.	n. a.	n. a.	n. a.	n. a.
BBL	BBL-5	23	5.6	84.4	9.88	2.64	38.63	276.78	7.73	295.77	23.05	86.41	3.88	0.89	207.27
BBL	BBL-5	3	15.6	87.1	n. a.	n. a.	n. a.	n. a.	n. a.	n. a.	n. a.	n. a.	n. a.	n. a.	n. a.
BBL	BBL-5	30	9.7	85.5	13.78	4.10	37.29	317.54	11.53	366.92	25.64	111.21	5.85	0.99	308.12
BBL	BBL-5	31	5.8	83.9	n. a.	n. a.	37.31	215.27	n. a.	273.31	24.42	89.18	4.04	1.41	206.03
BBL	BBL-5	32	7.8	83.7	n. a.	n. a.	35.35	184.93	n. a.	304.70	22.84	99.17	5.46	1.30	253.72
BBL	BBL-5	33	5.1	83.1	n. a.	n. a.	37.85	210.22	n. a.	328.49	25.92	119.64	6.70	1.63	332.60
BBL	BBL-5	34	6.3	83.6	n. a.	n. a.	n. a.	n. a.	n. a.	n. a.	n. a.	n. a.	n. a.	n. a.	n. a.
BBL	BBL-5	4	18.2	87.1	n. a.	n. a.	n. a.	n. a.	n. a.	n. a.	n. a.	n. a.	n. a.	n. a.	n. a.
BBL	BBL-5	43	3.7	83.6	n. a.	n. a.	36.61	192.25	n. a.	329.39	23.12	114.08	6.80	1.49	328.53
BBL	BBL-5	44	9.6	86.2	n. a.	n. a.	28.37	182.78	n. a.	241.88	18.87	58.52	2.04	1.19	107.22
BBL	BBL-5	46	8.0	85.0	n. a.	n. a.	34.04	201.95	n. a.	324.58	21.51	100.82	6.11	1.54	268.79
BBL	BBL-5	47	11.9	87.2	n. a.	n. a.	31.79	180.21	n. a.	231.95	17.98	55.05	1.68	0.96	95.76
BBL	BBL-5	49	3.6	82.6	n. a.	n. a.	34.28	211.12	n. a.	401.66	21.86	113.84	6.67	2.81	318.01
BBL	BBL-5	5	1.8	80.4	n. a.	n. a.	n. a.	n. a.	n. a.	n. a.	n. a.	n. a.	n. a.	n. a.	n. a.
BBL	BBL-5	6	6.8	84.4	10.06	2.54	40.21	253.63	7.45	296.67	22.73	94.43	4.14	0.81	213.79
BBL	BBL-5	7	14.3	87.6	9.85	2.07	43.90	324.55	3.72	313.57	24.02	79.50	2.68	0.69	131.25
BORG	BORG-1	10	5.7	83.9	n. a.	n. a.	n. a.	n. a.	n. a.	n. a.	n. a.	n. a.	n. a.	n. a.	n. a.
BORG	BORG-1	11	14.0	85.2	5.92	4.09	29.09	227.48	8.10	623.31	12.98	53.47	2.18	0.44	245.69
BORG	BORG-1	12	4.7	84.2	6.02	5.48	37.39	265.97	8.59	725.55	16.59	67.21	2.52	0.45	284.44
BORG	BORG-1	14	10.6	87.6	6.26	2.40	31.51	240.67	4.45	437.05	11.62	47.82	1.86	0.43	139.88
BORG	BORG-1	15	0.4	81.9	8.06	6.75	30.41	256.08	9.47	608.44	12.79	62.23	2.62	0.60	286.50
BORG	BORG-1	19	7.3	85.7	6.75	3.47	32.31	231.13	4.66	487.08	13.14	47.38	2.10	0.46	166.13
BORG	BORG-1	2	0.5	83.4	n. a.	n. a.	n. a.	n. a.	n. a.	n. a.	n. a.	n. a.	n. a.	n. a.	n. a.
BORG	BORG-1	20	9.6	85.7	6.55	4.46	27.93	221.80	7.37	582.60	11.28	48.31	2.27	0.64	234.81
BORG	BORG-1	21	9.9	86.4	4.94	2.40	28.99	228.13	4.51	459.39	11.23	46.25	1.87	0.40	148.20
BORG	BORG-1	22	14.2	88.6	5.69	3.63	32.50	235.15	5.38	405.17	12.22	60.15	2.65	0.48	133.87

Table S2. (continued)

Cinder Cone	Tephra Sample	Melt Incl	% olivine	Fo Olivine	Li	B	Sc	V	Rb	Sr	Y	Zr	Nb	Sn	Ba
BORG	BORG-1	23	0.5	83.3	n. a.	n. a.	n. a.	n. a.	n. a.	n. a.	n. a.	n. a.	n. a.	n. a.	n. a.
BORG	BORG-1	24	1.6	84.2	8.19	4.09	37.79	301.66	7.99	651.41	16.88	71.02	3.66	0.62	251.98
BORG	BORG-1	25	9.2	87.5	10.38	3.82	48.98	390.65	7.39	631.40	16.76	75.90	3.28	0.58	202.58
BORG	BORG-1	3	4.2	83.7	n. a.	n. a.	n. a.	n. a.	n. a.	n. a.	n. a.	n. a.	n. a.	n. a.	n. a.
BORG	BORG-1	31	0.1	84.0	n. a.	n. a.	29.17	205.02	n. a.	546.46	13.05	62.59	2.74	0.89	280.70
BORG	BORG-1	35	3.9	83.3	n. a.	n. a.	27.06	210.36	n. a.	586.38	12.80	54.34	2.45	1.04	254.29
BORG	BORG-1	37	0.2	82.7	n. a.	n. a.	26.53	217.39	n. a.	595.94	13.51	56.71	2.58	1.09	266.74
BORG	BORG-1	38	1.6	84.2	n. a.	n. a.	27.13	184.46	n. a.	566.15	12.87	49.57	2.20	1.05	236.11
BORG	BORG-1	40	1.5	83.3	n. a.	n. a.	29.20	207.99	n. a.	495.10	13.12	57.24	3.07	1.16	187.35
BORG	BORG-1	42	2.8	85.3	n. a.	n. a.	28.88	208.67	n. a.	492.49	12.65	54.04	2.88	0.99	170.43
BORG	BORG-1	43	0.4	84.0	n. a.	n. a.	26.52	185.27	n. a.	548.80	12.95	52.27	2.15	1.07	230.85
BORG	BORG-1	44	7.1	82.7	n. a.	n. a.	30.06	213.98	n. a.	554.92	14.33	52.93	1.94	1.02	215.86
BORG	BORG-1	45	0.3	83.2	n. a.	n. a.	27.91	222.67	n. a.	503.53	13.51	57.89	3.23	0.96	198.54
BORG	BORG-1	8	1.5	84.2	n. a.	n. a.	n. a.	n. a.	n. a.	n. a.	n. a.	n. a.	n. a.	n. a.	n. a.
BORG	BORG-1	9	16.0	88.3	n. a.	n. a.	n. a.	n. a.	n. a.	n. a.	n. a.	n. a.	n. a.	n. a.	n. a.
BORG	MM-L17-BORG-1	1	5.0	85.8	n. a.	n. a.	29.73	103.97	n. a.	426.52	11.48	47.75	1.98	0.92	130.15
BPPC	MM-L17-BPPC-4	13	0.7	87.5	n. a.	n. a.	34.20	229.41	n. a.	421.32	15.57	59.07	1.82	0.99	121.41
BPPC	MM-L17-BPPC-4	14	3.1	87.2	n. a.	n. a.	31.87	253.51	n. a.	448.67	14.94	55.48	1.87	1.01	118.92
BPPC	MM-L17-BPPC-4	15	2.1	87.3	n. a.	n. a.	32.41	222.63	n. a.	453.50	14.99	54.45	1.56	0.80	109.98
BPPC	MM-L17-BPPC-4	2	5.5	87.6	n. a.	n. a.	31.71	218.58	n. a.	434.70	15.39	51.47	1.39	0.99	76.72
BPPC	MM-L17-BPPC-4	3	3.5	87.3	n. a.	n. a.	n. a.	n. a.	n. a.	n. a.	n. a.	n. a.	n. a.	n. a.	n. a.
BPPC	MM-L17-BPPC-4	4	4.8	87.8	n. a.	n. a.	n. a.	n. a.	n. a.	n. a.	n. a.	n. a.	n. a.	n. a.	n. a.
BPPC	MM-L17-BPPC-4	5	6.8	87.9	n. a.	n. a.	36.28	226.76	n. a.	488.46	16.65	54.14	1.32	1.06	73.47
BRM	BRM-1	14	9.9	88.4	n. a.	n. a.	n. a.	n. a.	n. a.	n. a.	n. a.	n. a.	n. a.	n. a.	n. a.
BRM	BRM-1	16	9.2	88.3	n. a.	n. a.	n. a.	n. a.	n. a.	n. a.	n. a.	n. a.	n. a.	n. a.	n. a.
BRM	BRM-1	17	7.6	88.3	7.09	4.20	29.31	270.76	9.35	1590.51	15.49	110.27	5.39	1.04	286.77
BRM	BRM-1	18	8.5	88.9	n. a.	n. a.	n. a.	n. a.	n. a.	n. a.	n. a.	n. a.	n. a.	n. a.	n. a.
BRM	BRM-1	19	5.8	86.6	5.06	3.94	26.65	212.64	14.46	1288.89	12.68	109.10	5.43	0.62	294.84
BRM	BRM-1	2	13.7	89.0	n. a.	n. a.	n. a.	n. a.	n. a.	n. a.	n. a.	n. a.	n. a.	n. a.	n. a.
BRM	BRM-1	22	9.7	87.9	8.33	2.73	28.02	313.76	8.12	1937.83	12.90	114.59	4.41	0.69	284.36
BRM	BRM-1	23	1.5	84.7	n. a.	n. a.	n. a.	n. a.	n. a.	n. a.	n. a.	n. a.	n. a.	n. a.	n. a.
BRM	BRM-1	24	4.0	86.7	17.87	7.69	28.83	336.35	22.10	705.76	19.89	168.65	12.30	1.25	551.61
BRM	BRM-1	25	7.4	88.4	8.07	2.75	29.35	229.72	6.97	1463.06	12.01	95.83	3.94	0.83	201.02
BRM	BRM-1	3	8.7	87.6	n. a.	n. a.	n. a.	n. a.	n. a.	n. a.	n. a.	n. a.	n. a.	n. a.	n. a.
BRM	BRM-1	30	6.6	86.2	n.d.	n.d.	21.88	165.62	0.00	1084.25	11.95	84.89	3.99	1.03	247.48
BRM	BRM-1	34	8.4	87.5	n.d.	n.d.	22.92	180.24	0.00	1253.28	12.73	97.94	4.65	1.32	273.72
BRM	BRM-1	35	10.4	88.6	n. a.	n. a.	n. a.	n. a.	n. a.	n. a.	n. a.	n. a.	n. a.	n. a.	n. a.
BRM	BRM-1	36	12.0	88.4	n. a.	n. a.	n. a.	n. a.	n. a.	n. a.	n. a.	n. a.	n. a.	n. a.	n. a.
BRM	BRM-1	39	11.8	88.2	n. a.	n. a.	n. a.	n. a.	n. a.	n. a.	n. a.	n. a.	n. a.	n. a.	n. a.
BRM	BRM-1	40	9.7	87.6	n. a.	n. a.	n. a.	n. a.	n. a.	n. a.	n. a.	n. a.	n. a.	n. a.	n. a.
BRM	BRM-1	41	7.3	87.8	n.d.	n.d.	23.53	185.93	0.00	1087.81	11.29	75.00	3.93	0.95	157.81
BRM	BRM-1	5	11.0	88.7	10.76	1.57	27.87	276.33	14.56	1877.70	14.59	129.87	9.36	0.91	322.72
BRM	BRM-1	6	7.8	87.8	7.41	1.39	21.12	180.64	5.28	813.61	7.69	57.06	2.41	0.46	115.98
BRM	BRM-1	7	7.7	86.6	11.57	2.31	31.39	331.65	14.81	2076.84	18.33	150.73	10.37	1.30	388.22
BRM	BRM-1	8	14.4	88.7	7.39	5.56	35.12	276.64	14.43	1814.25	15.13	116.24	8.26	1.22	320.98
BRM	MM-L17-BRM-2	1	11.3	89.6	n. a.	n. a.	23.41	188.00	n. a.	1112.82	10.60	71.17	3.23	1.45	142.99
BRM	MM-L17-BRM-2	10	9.8	87.3	n. a.	n. a.	n. a.	n. a.	n. a.	n. a.	n. a.	n. a.	n. a.	n. a.	n. a.
BRM	MM-L17-BRM-2	13	9.9	88.6	n. a.	n. a.	n. a.	n. a.	n. a.	n. a.	n. a.	n. a.	n. a.	n. a.	n. a.
BRM	MM-L17-BRM-2	14	9.6	88.4	n. a.	n. a.	n. a.	n. a.	n. a.	n. a.	n. a.	n. a.	n. a.	n. a.	n. a.
BRM	MM-L17-BRM-2	16	13.4	89.0	n. a.	n. a.	n. a.	n. a.	n. a.	n. a.	n. a.	n. a.	n. a.	n. a.	n. a.
BRM	MM-L17-BRM-2	17	10.5	89.0	n. a.	n. a.	n. a.	n. a.	n. a.	n. a.	n. a.	n. a.	n. a.	n. a.	n. a.
BRM	MM-L17-BRM-2	18	13.6	88.7	n. a.	n. a.	21.55	173.87	n. a.	1093.19	12.44	84.44	4.87	1.12	282.02
BRM	MM-L17-BRM-2	24	3.4	86.6	n. a.	n. a.	25.95	181.85	n. a.	1118.89	12.33	95.07	7.46	1.13	307.53
BRM	MM-L17-BRM-2	25	7.3	87.9	n. a.	n. a.	21.19	180.14	n. a.	1325.90	11.31	100.11	7.54	1.20	253.75
BRM	MM-L17-BRM-2	26	10.4	88.9	n. a.	n. a.	19.82	165.40	n. a.	1398.14	11.33	101.46	7.68	1.20	249.41
BRM	MM-L17-BRM-2	29	12.5	89.5	n. a.	n. a.	20.95	177.86	n. a.	1147.69	11.54	80.12	3.92	1.26	205.78
BRM	MM-L17-BRM-2	31	11.9	90.5	n. a.	n. a.	23.68	176.41	n. a.	1045.50	10.12	66.03	3.79	1.12	136.30
BRM	MM-L17-BRM-2	32	8.6	88.4	n. a.	n. a.	23.23	198.23	n. a.	1120.39	10.43	73.77	4.04	0.87	151.76
BRM	MM-L17-BRM-2	8	9.4	89.1	n. a.	n. a.	20.83	155.72	n. a.	1403.44	11.72	127.55	3.39	2.95	257.16
BRVB	MM-L17-BRVB-2	10	0.2	83.5	n. a.	n. a.	29.17	251.43	n. a.	461.76	18.92	105.64	8.24	1.53	388.23
BRVB	MM-L17-BRVB-2	2	5.2	85.5	n. a.	n. a.	34.53	261.08	n. a.	362.48	23.63	84.07	3.44	1.36	206.99
BRVB	MM-L17-BRVB-2	4	4.0	84.1	n. a.	n. a.	30.25	233.51	n. a.	494.35	20.75	115.40	8.76	1.63	386.63
BRVB	MM-L17-BRVB-2	6	3.1	85.1	n. a.	n. a.	27.80	281.74	n. a.	570.73	22.16	124.45	9.67	1.77	480.98
BRVB	MM-L17-BRVB-2	7	2.7	83.7	n. a.	n. a.	34.42	299.84	n. a.	557.94	23.54	131.30	9.13	2.68	454.66

Table S2. (continued)

Cinder Cone	Tephra Sample	Melt Incl	La	Ce	Nd	Sm	Dy	Yb	Pb	Cu	Zn	Mo	Sn	W
BAS-44	BAS-44-2	1	n.a.	n.a.	n.a.	n.a.	n.a.	n.a.	n.a.	n.a.	n.a.	n.a.	n.a.	n.a.
BAS-44	BAS-44-2	10	n.a.	n.a.	n.a.	n.a.	n.a.	n.a.	n.a.	n.a.	n.a.	n.a.	n.a.	n.a.
BAS-44	BAS-44-2	2	7.35	19.68	12.08	2.75	3.17	2.24	n.a.	75.48	n.a.	0.98	n.a.	n.a.
BAS-44	BAS-44-2	4	7.12	19.42	11.98	3.14	3.19	2.14	1.75	73.19	77.63	0.96	n.a.	0.08
BAS-44	BAS-44-2	5	7.94	20.86	12.71	3.15	3.60	2.11	1.98	66.94	66.36	0.34	1.48	0.07
BAS-44	BAS-44-2	6	n.a.	n.a.	n.a.	n.a.	n.a.	n.a.	n.a.	n.a.	n.a.	n.a.	n.a.	n.a.
BAS-44	BAS-44-2	7a	7.96	20.20	12.31	3.18	3.50	2.21	2.61	106.71	74.90	0.50	1.22	0.13
BAS-44	BAS-44-2	7b	n.a.	n.a.	n.a.	n.a.	n.a.	n.a.	n.a.	n.a.	n.a.	n.a.	n.a.	n.a.
BBL	BBL-5	11	10.79	27.52	15.43	3.69	2.97	2.39	3.77	84.07	109.21	0.49	0.79	n.a.
BBL	BBL-5	14	12.00	29.22	18.04	4.14	5.75	3.20	3.58	71.30	74.54	0.51	1.28	n.a.
BBL	BBL-5	15	12.58	30.60	19.40	4.41	5.57	3.57	3.65	120.11	109.72	0.73	1.12	n.a.
BBL	BBL-5	17	5.69	16.26	13.18	3.35	5.07	3.05	1.70	140.23	82.82	0.15	1.24	n.a.
BBL	BBL-5	18	11.59	29.96	18.19	5.14	4.76	2.54	3.59	67.40	88.00	0.78	0.97	n.a.
BBL	BBL-5	19	4.85	12.21	8.60	2.44	3.44	1.76	1.19	67.26	62.54	0.32	0.57	n.a.
BBL	BBL-5	20	11.90	31.15	18.19	3.77	3.77	2.32	5.22	109.41	138.62	0.68	15.48	n.a.
BBL	BBL-5	21A	11.70	27.08	16.03	3.44	4.65	3.04	4.02	119.49	111.07	0.87	1.11	n.a.
BBL	BBL-5	21B	9.99	28.57	14.28	4.21	5.02	2.67	3.47	82.91	116.04	0.57	0.99	n.a.
BBL	BBL-5	22	n.a.	n.a.	n.a.	n.a.	n.a.	n.a.	n.a.	n.a.	n.a.	n.a.	n.a.	n.a.
BBL	BBL-5	23	7.73	22.04	13.28	3.06	3.30	1.92	2.79	105.18	96.34	0.50	0.89	n.a.
BBL	BBL-5	3	n.a.	n.a.	n.a.	n.a.	n.a.	n.a.	n.a.	n.a.	n.a.	n.a.	n.a.	n.a.
BBL	BBL-5	30	12.20	31.95	15.23	4.57	5.99	3.58	4.21	89.23	78.87	0.73	1.35	0.18
BBL	BBL-5	31	7.85	19.75	12.73	2.78	4.17	2.84	2.94	79.22	70.74	0.63	1.41	0.11
BBL	BBL-5	32	9.52	23.27	14.65	3.78	4.15	2.61	3.44	70.18	75.01	0.59	1.30	0.19
BBL	BBL-5	33	12.14	28.86	17.66	4.12	4.43	2.78	4.39	168.76	75.28	0.83	1.63	0.20
BBL	BBL-5	34	n.a.	n.a.	n.a.	n.a.	n.a.	n.a.	n.a.	n.a.	n.a.	n.a.	n.a.	n.a.
BBL	BBL-5	4	n.a.	n.a.	n.a.	n.a.	n.a.	n.a.	n.a.	n.a.	n.a.	n.a.	n.a.	n.a.
BBL	BBL-5	43	11.59	28.83	17.30	4.08	4.53	2.82	4.72	102.75	79.99	0.97	1.49	0.16
BBL	BBL-5	44	4.33	11.35	7.48	2.15	3.27	1.87	1.28	75.18	63.17	0.31	1.19	0.05
BBL	BBL-5	46	10.09	24.20	14.46	3.75	3.63	2.75	3.78	98.18	77.96	0.72	1.54	0.18
BBL	BBL-5	47	3.57	9.57	7.58	2.06	3.12	2.06	1.29	74.43	59.82	0.20	0.96	0.04
BBL	BBL-5	49	11.72	29.01	16.68	4.03	4.05	2.50	4.43	65.54	95.39	0.80	2.81	0.22
BBL	BBL-5	5	n.a.	n.a.	n.a.	n.a.	n.a.	n.a.	n.a.	n.a.	n.a.	n.a.	n.a.	n.a.
BBL	BBL-5	6	8.21	22.02	12.78	3.22	3.95	2.05	2.75	84.21	97.42	0.46	0.81	n.a.
BBL	BBL-5	7	5.36	14.52	9.94	2.07	4.49	3.11	1.38	114.32	109.74	#VALUE!	0.69	n.a.
BORG	BORG-1	10	n.a.	n.a.	n.a.	n.a.	n.a.	n.a.	n.a.	n.a.	n.a.	n.a.	n.a.	n.a.
BORG	BORG-1	11	7.84	16.29	9.75	2.35	2.79	1.13	4.01	113.65	68.63	0.52	0.44	n.a.
BORG	BORG-1	12	9.21	19.33	11.23	2.09	2.58	2.05	4.43	159.49	99.85	0.15	0.45	n.a.
BORG	BORG-1	14	4.40	11.65	6.88	1.84	2.03	0.93	2.21	92.39	64.34	0.30	0.43	n.a.
BORG	BORG-1	15	8.46	21.05	12.49	2.32	2.62	1.11	5.34	324.26	122.76	0.30	0.60	n.a.
BORG	BORG-1	19	5.29	13.42	8.40	2.10	2.46	1.10	2.83	105.98	73.39	0.37	0.46	n.a.
BORG	BORG-1	2	n.a.	n.a.	n.a.	n.a.	n.a.	n.a.	n.a.	n.a.	n.a.	n.a.	n.a.	n.a.
BORG	BORG-1	20	6.73	16.19	9.92	2.37	2.09	0.91	4.00	253.55	84.06	0.36	0.64	n.a.
BORG	BORG-1	21	4.53	11.59	7.41	1.66	2.14	0.96	1.94	97.64	69.88	0.31	0.40	n.a.
BORG	BORG-1	22	5.59	14.35	8.98	2.17	2.51	1.54	2.18	87.33	56.48	0.28	0.48	n.a.

Table S2. (continued)

Cinder Cone	Tephra Sample	Melt Incl	La	Ce	Nd	Sm	Dy	Yb	Pb	Cu	Zn	Mo	Sn	W
BORG	BORG-1	23	n. a.	n. a.	n. a.	n. a.	n. a.	n. a.	n. a.	n. a.	n. a.	n. a.	n. a.	n. a.
BORG	BORG-1	24	7.66	18.51	11.89	2.21	2.88	1.77	3.21	128.31	100.20	0.25	0.62	n. a.
BORG	BORG-1	25	8.05	19.15	11.70	3.76	3.06	2.07	3.11	146.77	103.82	0.60	0.58	n. a.
BORG	BORG-1	3	n. a.	n. a.	n. a.	n. a.	n. a.	n. a.	n. a.	n. a.	n. a.	n. a.	n. a.	n. a.
BORG	BORG-1	31	8.08	18.33	11.50	2.60	2.68	1.48	4.68	169.99	86.25	0.54	0.89	0.08
BORG	BORG-1	35	7.76	17.31	11.00	2.57	2.50	1.37	4.40	244.27	78.35	0.45	1.04	0.10
BORG	BORG-1	37	8.06	18.50	11.38	2.83	2.50	1.53	4.40	259.84	88.03	0.55	1.09	0.11
BORG	BORG-1	38	7.19	15.99	10.31	2.51	2.46	1.37	4.11	296.55	73.44	0.43	1.05	0.10
BORG	BORG-1	40	5.97	14.08	8.54	2.50	2.52	1.34	2.82	91.63	83.77	0.40	1.16	0.10
BORG	BORG-1	42	5.39	13.11	8.42	2.25	2.45	1.33	2.49	95.15	72.40	0.44	0.99	0.07
BORG	BORG-1	43	6.53	15.08	9.47	2.52	2.43	1.34	4.30	281.59	90.94	0.46	1.07	0.09
BORG	BORG-1	44	6.20	14.04	9.71	2.49	2.70	1.47	3.81	177.37	84.61	0.43	1.02	0.08
BORG	BORG-1	45	6.60	15.99	10.71	2.96	2.44	1.48	3.00	83.17	96.39	0.53	0.96	0.07
BORG	BORG-1	8	n. a.	n. a.	n. a.	n. a.	n. a.	n. a.	n. a.	n. a.	n. a.	n. a.	n. a.	n. a.
BORG	BORG-1	9	n. a.	n. a.	n. a.	n. a.	n. a.	n. a.	n. a.	n. a.	n. a.	n. a.	n. a.	n. a.
BORG	MM-L17-BORG-1	1	4.43	10.78	7.32	1.91	2.40	1.55	2.01	78.29	n. a.	0.38	0.92	0.05
BPPC	MM-L17-BPPC-4	13	5.72	14.18	8.90	2.26	3.00	1.74	2.14	25.99	69.55	0.45	0.99	0.07
BPPC	MM-L17-BPPC-4	14	5.58	14.51	8.87	2.54	3.19	1.87	2.07	24.25	60.08	0.31	1.01	0.08
BPPC	MM-L17-BPPC-4	15	5.35	13.50	8.19	2.32	3.00	1.99	1.73	23.37	67.71	0.30	0.80	0.09
BPPC	MM-L17-BPPC-4	2	4.63	12.21	7.74	2.15	2.77	1.51	1.60	27.47	50.95	0.27	0.99	0.14
BPPC	MM-L17-BPPC-4	3	n. a.	n. a.	n. a.	n. a.	n. a.	n. a.	n. a.	n. a.	67.32	n. a.	n. a.	n. a.
BPPC	MM-L17-BPPC-4	4	n. a.	n. a.	n. a.	n. a.	n. a.	n. a.	n. a.	n. a.	56.08	n. a.	n. a.	n. a.
BPPC	MM-L17-BPPC-4	5	4.92	13.44	8.48	2.09	2.80	1.92	1.97	29.80	87.84	0.20	1.06	n. a.
BRM	BRM-1	14	n. a.	n. a.	n. a.	n. a.	n. a.	n. a.	n. a.	n. a.	n. a.	n. a.	n. a.	n. a.
BRM	BRM-1	16	n. a.	n. a.	n. a.	n. a.	n. a.	n. a.	n. a.	n. a.	n. a.	n. a.	n. a.	n. a.
BRM	BRM-1	17	18.61	42.20	18.53	2.84	2.80	1.05	5.15	36.71	77.54	0.04	1.04	n. a.
BRM	BRM-1	18	n. a.	n. a.	n. a.	n. a.	n. a.	n. a.	n. a.	n. a.	n. a.	n. a.	n. a.	n. a.
BRM	BRM-1	19	16.50	36.99	19.61	4.10	2.65	0.99	6.49	114.92	66.21	0.63	0.62	n. a.
BRM	BRM-1	2	n. a.	n. a.	n. a.	n. a.	n. a.	n. a.	n. a.	n. a.	n. a.	n. a.	n. a.	n. a.
BRM	BRM-1	22	19.77	44.23	21.53	3.79	2.11	0.31	5.02	67.88	82.20	0.52	0.69	n. a.
BRM	BRM-1	23	n. a.	n. a.	n. a.	n. a.	n. a.	n. a.	n. a.	n. a.	n. a.	n. a.	n. a.	n. a.
BRM	BRM-1	24	28.54	63.14	33.35	5.77	4.13	2.21	9.42	n. a.	n. a.	n. a.	n. a.	n. a.
BRM	BRM-1	25	14.95	37.32	18.07	4.49	2.48	0.64	4.04	14.12	97.48	0.37	0.83	n. a.
BRM	BRM-1	3	n. a.	n. a.	n. a.	n. a.	n. a.	n. a.	n. a.	n. a.	n. a.	n. a.	n. a.	n. a.
BRM	BRM-1	30	14.27	32.63	17.34	3.11	2.22	1.24	4.82	65.82	57.31	0.49	1.03	0.16
BRM	BRM-1	34	16.28	37.00	19.72	3.21	2.57	1.48	5.82	51.46	50.95	0.52	1.32	0.29
BRM	BRM-1	35	n. a.	n. a.	n. a.	n. a.	n. a.	n. a.	n. a.	n. a.	n. a.	n. a.	n. a.	n. a.
BRM	BRM-1	36	n. a.	n. a.	n. a.	n. a.	n. a.	n. a.	n. a.	n. a.	n. a.	n. a.	n. a.	n. a.
BRM	BRM-1	39	n. a.	n. a.	n. a.	n. a.	n. a.	n. a.	n. a.	n. a.	n. a.	n. a.	n. a.	n. a.
BRM	BRM-1	40	n. a.	n. a.	n. a.	n. a.	n. a.	n. a.	n. a.	n. a.	n. a.	n. a.	n. a.	n. a.
BRM	BRM-1	41	12.08	28.37	15.32	2.98	2.25	1.22	3.23	4.04	47.65	0.38	0.95	0.07
BRM	BRM-1	5	22.45	53.81	23.64	4.21	2.28	1.45	5.87	14.78	75.38	0.61	0.91	n. a.
BRM	BRM-1	6	9.91	24.36	11.39	2.78	1.30	1.30	2.87	49.28	198.89	0.37	0.46	n. a.
BRM	BRM-1	7	26.20	58.98	25.09	3.89	3.80	1.76	6.67	29.54	87.03	0.74	1.30	n. a.
BRM	BRM-1	8	22.43	51.64	26.08	4.09	2.09	1.13	5.91	74.94	78.85	0.61	1.22	n. a.
BRM	MM-L17-BRM-2	1	11.51	27.87	14.38	2.71	2.22	1.32	3.74	81.56	39.71	n. a.	1.45	0.13
BRM	MM-L17-BRM-2	10	n. a.	n. a.	n. a.	n. a.	n. a.	n. a.	n. a.	n. a.	n. a.	n. a.	n. a.	n. a.
BRM	MM-L17-BRM-2	13	n. a.	n. a.	n. a.	n. a.	n. a.	n. a.	n. a.	n. a.	n. a.	n. a.	n. a.	n. a.
BRM	MM-L17-BRM-2	14	n. a.	n. a.	n. a.	n. a.	n. a.	n. a.	n. a.	n. a.	n. a.	n. a.	n. a.	n. a.
BRM	MM-L17-BRM-2	17	n. a.	n. a.	n. a.	n. a.	n. a.	n. a.	n. a.	n. a.	n. a.	n. a.	n. a.	n. a.
BRM	MM-L17-BRM-2	18	15.27	35.17	17.27	3.21	2.44	1.53	5.68	33.97	46.11	0.50	1.12	0.23
BRM	MM-L17-BRM-2	24	15.42	36.70	18.44	3.49	2.42	1.23	4.88	64.11	62.87	0.75	1.13	0.19
BRM	MM-L17-BRM-2	25	16.97	40.66	20.45	3.58	2.41	1.14	4.87	22.45	54.46	0.61	1.20	0.18
BRM	MM-L17-BRM-2	26	17.37	41.35	20.56	3.59	2.29	1.06	4.68	25.78	40.38	n. a.	1.20	0.17
BRM	MM-L17-BRM-2	29	13.42	31.96	16.05	3.16	2.12	1.21	4.36	62.63	42.59	0.54	1.26	0.16
BRM	MM-L17-BRM-2	31	10.46	26.27	13.47	2.66	1.97	1.10	2.89	33.62	47.77	0.42	1.12	0.09
BRM	MM-L17-BRM-2	32	11.83	29.02	14.56	2.85	1.89	1.26	3.15	4.49	48.82	0.36	0.87	0.08
BRM	MM-L17-BRM-2	8	21.84	54.83	28.04	4.86	2.58	1.01	5.07	159.91	54.83	0.71	2.95	0.08
BRVB	MM-L17-BRVB-2	10	14.36	34.53	19.68	4.13	3.86	2.14	4.30	23.65	95.66	0.89	1.53	0.26
BRVB	MM-L17-BRVB-2	2	6.93	16.74	11.70	3.32	4.22	2.73	3.26	65.06	72.80	0.36	1.36	0.09
BRVB	MM-L17-BRVB-2	4	14.67	35.15	20.96	4.55	4.03	2.10	3.71	9.35	86.98	0.84	1.63	0.31
BRVB	MM-L17-BRVB-2	6	17.36	42.17	24.93	5.95	4.16	2.13	4.48	13.52	88.67	1.20	1.77	0.26
BRVB	MM-L17-BRVB-2	7	17.76	39.07	24.46	4.87	4.69	2.66	5.49	64.79	98.59	1.07	2.68	0.43

n. a. = not analyzed
n. d. = not detected

Table S3. Major element data for melt inclusion olivine hosts analyzed via EPMA. Values reported in wt. %. Values and standard deviation calculated from the average of 3-5 analysis spots. Cu measured via LA-ICPMS. Values Reported in ppm. Uncertainty represents standard error, including uncertainty in calibration standard.

Cinder Cone	Tephra Sample	Inclusion	Date Analyzed	SiO$_2$	1 s. d.	Al$_2$O$_3$	1 s. d.	FeO^T	1 s. d.	MnO	1 s. d.	MgO	1 s. d.	CaO	1 s. d.	Cu	1.s.d.
BAS-44	BAS-44-2	1	8/1/18	40.29	0.31	0.03	0.01	12.02	0.07	0.19	0.00	45.50	0.14	0.22	0.01	n. a.	n. a.
BAS-44	BAS-44-2	10	8/1/18	39.93	0.49	0.04	0.00	11.69	0.09	0.18	0.01	46.78	0.31	0.22	0.00	n. a.	n. a.
BAS-44	BAS-44-2	2	8/1/18	40.97	0.50	0.05	0.00	11.28	0.08	0.17	0.01	44.48	0.26	0.21	0.01	3.7	0.3
BAS-44	BAS-44-2	4	8/1/18	38.34	0.27	0.05	0.00	11.82	0.14	0.18	0.02	45.70	0.12	0.21	0.00	3.0	0.3
BAS-44	BAS-44-2	5	7/25/18	41.08	0.40	0.04	0.00	12.54	0.09	0.18	0.02	47.44	0.37	0.22	0.00	3.1	0.3
BAS-44	BAS-44-2	6	7/25/18	38.23	0.24	0.04	0.00	11.84	0.12	0.18	0.01	47.28	0.20	0.22	0.00	2.8	0.2
BAS-44	BAS-44-2	7a	7/25/18	40.26	0.63	0.04	0.00	12.33	0.22	0.18	0.00	46.57	0.44	0.22	0.00	n. a.	n. a.
BAS-44	BAS-44-2	7b	8/1/18	41.02	0.26	0.04	0.00	12.64	0.17	0.20	0.01	46.24	0.50	0.23	0.00	n. a.	n. a.
BBL	BBL-5	11	6/12/17	39.13	0.18	0.02	0.00	16.03	0.29	0.27	0.01	42.00	0.31	0.18	0.01	n. a.	n. a.
BBL	BBL-5	14	6/12/17	39.62	0.22	0.02	0.00	15.89	0.33	0.28	0.00	42.82	0.17	0.21	0.00	n. a.	n. a.
BBL	BBL-5	15	6/12/17	39.76	0.44	0.02	0.00	16.07	0.42	0.27	0.01	42.59	0.46	0.22	0.01	n. a.	n. a.
BBL	BBL-5	17	11/26/18	40.51	0.23	0.07	0.02	11.77	0.18	0.19	0.01	48.00	0.93	0.24	0.00	n. a.	n. a.
BBL	BBL-5	18	11/26/18	38.66	0.28	0.06	0.01	15.75	0.08	0.27	0.01	43.62	0.45	0.20	0.01	n. a.	n. a.
BBL	BBL-5	19	11/26/18	39.34	0.36	0.08	0.02	12.77	0.40	0.21	0.02	45.04	1.10	0.23	0.00	n. a.	n. a.
BBL	BBL-5	20	11/26/18	39.70	0.26	0.04	0.02	15.74	0.30	0.27	0.01	43.90	1.20	0.22	0.00	n. a.	n. a.
BBL	BBL-5	21A	11/26/18	39.36	0.21	0.05	0.01	14.12	0.16	0.24	0.01	44.76	0.32	0.24	0.00	n. a.	n. a.
BBL	BBL-5	21B	11/26/18	39.36	0.21	0.05	0.01	14.12	0.16	0.24	0.01	44.76	0.32	0.24	0.00	n. a.	n. a.
BBL	BBL-5	22	11/26/18	40.15	0.38	0.06	0.01	12.90	0.51	0.21	0.01	46.05	0.28	0.22	0.00	n. a.	n. a.
BBL	BBL-5	23	11/26/18	39.69	0.57	0.04	0.02	14.73	0.27	0.25	0.01	44.78	0.88	0.22	0.00	n. a.	n. a.
BBL	BBL-5	30	11/26/18	39.57	0.58	0.05	0.02	13.71	0.21	0.23	0.02	45.40	0.58	0.22	0.01	n. a.	n. a.
BBL	BBL-5	30b	8/1/18	38.80	0.07	0.03	0.00	15.57	0.14	0.24	0.02	43.25	0.24	0.20	0.01	3.0	0.2
BBL	BBL-5	31	8/1/18	39.52	0.55	0.04	0.00	14.70	0.12	0.24	0.01	43.08	0.63	0.23	0.00	2.8	0.2
BBL	BBL-5	32	8/1/18	39.21	0.22	0.04	0.00	14.62	0.10	0.23	0.01	42.15	0.55	0.23	0.00	3.2	0.3
BBL	BBL-5	33	7/25/18	38.26	0.66	0.02	0.00	15.68	0.24	0.25	0.01	43.20	0.33	0.22	0.01	2.9	0.2
BBL	BBL-5	34	8/1/18	40.60	0.64	0.03	0.00	14.91	0.27	0.25	0.01	42.55	0.56	0.23	0.01	n. a.	n. a.
BBL	BBL-5	43	2/12/20	39.75	0.15	n. a.	n. a.	15.49	0.82	n. a.	n. a.	44.35	0.62	n. a.	n. a.	3.56	1.22
BBL	BBL-5	44	2/12/20	40.11	0.10	n. a.	n. a.	13.19	0.18	n. a.	n. a.	46.07	0.51	n. a.	n. a.	2.56	0.21
BBL	BBL-5	46	2/12/20	39.75	0.07	n. a.	n. a.	14.16	0.06	n. a.	n. a.	45.04	0.23	n. a.	n. a.	3.18	0.31
BBL	BBL-5	47	2/12/20	40.17	0.06	n. a.	n. a.	12.21	0.10	n. a.	n. a.	46.83	0.21	n. a.	n. a.	2.68	0.22
BBL	BBL-5	49	2/12/20	39.61	0.06	n. a.	n. a.	16.41	0.14	n. a.	n. a.	43.57	0.15	n. a.	n. a.	2.71	0.22
BBL	BBL-5	3	11/26/18	40.63	0.45	0.07	0.02	12.41	0.66	0.19	0.00	46.99	0.64	0.23	0.00	n. a.	n. a.
BBL	BBL-5	4	11/26/18	40.25	0.14	0.06	0.03	12.38	0.30	0.20	0.01	46.81	0.25	0.22	0.00	n. a.	n. a.
BBL	BBL-5	5	11/26/18	38.82	0.35	0.03	0.02	18.12	0.55	0.32	0.01	41.76	0.73	0.22	0.00	n. a.	n. a.
BBL	BBL-5	6	11/26/18	40.40	0.24	0.07	0.02	14.96	0.31	0.24	0.00	45.29	0.75	0.23	0.00	n. a.	n. a.
BBL	BBL-5	7	6/12/17	40.15	0.19	0.05	0.00	11.41	0.39	0.18	0.01	45.19	0.58	0.22	0.00	n. a.	n. a.
BORG	BORG-1	2	6/5/17	40.09	0.37	0.03	0.01	15.72	0.11	0.21	0.01	44.24	1.23	0.15	0.01	n. a.	n. a.
BORG	BORG-1	3	6/5/17	40.65	0.41	0.03	0.00	15.31	0.27	0.20	0.01	44.15	0.23	0.15	0.00	n. a.	n. a.
BORG	BORG-1	8	6/5/17	40.20	0.32	0.03	0.00	14.86	0.31	0.20	0.01	44.38	0.41	0.14	0.01	n. a.	n. a.
BORG	BORG-1	9	6/5/17	40.63	0.34	0.03	0.00	10.90	0.25	0.15	0.01	46.09	0.60	0.16	0.00	n. a.	n. a.
BORG	BORG-1	10	6/5/17	41.23	0.18	0.02	0.00	15.25	0.19	0.21	0.00	44.51	0.25	0.14	0.01	n. a.	n. a.
BORG	BORG-1	11	6/5/17	40.93	0.36	0.02	0.01	14.21	0.92	0.19	0.01	45.79	0.12	0.14	0.01	n. a.	n. a.
BORG	BORG-1	12	6/5/17	40.77	0.35	0.03	0.00	14.65	0.68	0.20	0.01	43.93	0.63	0.14	0.01	n. a.	n. a.
BORG	BORG-1	13	6/5/17	41.72	0.19	0.02	0.01	14.36	1.11	0.19	0.01	46.36	1.39	0.15	0.01	n. a.	n. a.
BORG	BORG-1	14	6/5/17	40.40	0.31	0.03	0.00	11.62	0.28	0.16	0.00	46.22	0.21	0.15	0.00	n. a.	n. a.
BORG	BORG-1	15	6/5/17	40.53	0.31	0.02	0.00	17.13	0.33	0.22	0.01	43.56	0.44	0.13	0.00	n. a.	n. a.
BORG	BORG-1	18	6/5/17	39.24	0.52	0.02	0.01	15.36	0.82	0.21	0.01	43.12	0.85	0.14	0.00	n. a.	n. a.
BORG	BORG-1	19	6/5/17	40.57	0.22	0.02	0.01	13.45	1.11	0.19	0.01	45.29	0.30	0.15	0.00	n. a.	n. a.
BORG	BORG-1	20	6/5/17	40.25	0.28	0.03	0.01	13.24	1.87	0.19	0.02	44.66	1.05	0.14	0.01	n. a.	n. a.
BORG	BORG-1	21	6/5/17	38.72	1.29	0.03	0.00	12.59	0.24	0.17	0.01	44.88	1.08	0.14	0.02	n. a.	n. a.
BORG	BORG-1	22	6/5/17	40.16	0.34	0.02	0.00	10.71	0.36	0.16	0.00	46.57	0.31	0.16	0.00	n. a.	n. a.
BORG	BORG-1	23	6/5/17	39.65	0.52	0.03	0.01	15.45	0.24	0.21	0.01	43.34	0.49	0.13	0.01	n. a.	n. a.

Table S3. (continued)

Cinder Cone	Tephra Sample	Inclusion	Date Analyzed	SiO$_2$	1 s. d.	Al$_2$O$_3$	1 s. d.	FeO^T	1 s. d.	MnO	1 s. d.	MgO	1 s. d.	CaO	1 s. d.	Cu	1.s.d.
BORG	BORG-1	24	6/5/17	39.79	0.50	0.03	0.00	14.95	0.70	0.20	0.01	44.62	0.55	0.14	0.00	n. a.	n. a.
BORG	BORG-1	25	6/5/17	40.36	0.57	0.02	0.01	11.86	0.27	0.16	0.01	46.74	0.39	0.16	0.00	n. a.	n. a.
BORG	BORG-1	31	2/12/20	39.72	0.07	n. a.	n. a.	15.13	0.06	n. a.	n. a.	44.47	0.05	n. a.	n. a.	2.46	0.21
BORG	BORG-1	35	8/1/18	39.11	0.85	0.02	0.00	15.56	0.19	0.21	0.01	43.53	0.44	0.14	0.00	3.8	0.3
BORG	BORG-1	37	8/1/18	39.59	0.93	0.02	0.00	16.17	0.14	0.22	0.01	43.50	0.31	0.14	0.00	4.1	0.3
BORG	BORG-1	38	7/25/18	39.66	0.32	0.02	0.00	14.82	0.29	0.20	0.02	44.40	0.19	0.14	0.00	2.9	0.2
BORG	BORG-1	40	2/12/20	39.57	0.03	n. a.	n. a.	15.74	0.15	n. a.	n. a.	44.15	0.11	n. a.	n. a.	2.56	0.21
BORG	BORG-1	42	2/12/20	40.02	n. a.	n. a.	n. a.	14.05	n. a.	n. a.	n. a.	45.70	n. a.	n. a.	n. a.	n. a.	n. a.
BORG	BORG-1	43	2/12/20	39.60	0.22	n. a.	n. a.	15.19	0.10	n. a.	n. a.	44.67	0.06	n. a.	n. a.	3.14	0.26
BORG	BORG-1	44	2/12/20	38.04	2.94	n. a.	n. a.	16.15	0.17	n. a.	n. a.	43.32	0.88	n. a.	n. a.	2.59	0.22
BORG	BORG-1	45	2/12/20	39.44	0.37	n. a.	n. a.	15.79	0.36	n. a.	n. a.	43.96	0.29	n. a.	n. a.	2.41	0.21
BORG	MM-L17-BORG-1	1	2/12/20	40.17	0.26	n. a.	n. a.	13.53	0.45	n. a.	n. a.	45.92	0.81	n. a.	n. a.	2.93	0.25
BORG	MM-L17-BORG-1	2	2/12/20	40.30	0.17	n. a.	n. a.	13.06	1.47	n. a.	n. a.	46.41	1.35	n. a.	n. a.	n. a.	n. a.
BPPC	MM-L17-BPPC-4	13	2/12/20	40.60	0.09	n. a.	n. a.	12.10	0.11	n. a.	n. a.	47.50	0.14	n. a.	n. a.	1.23	0.12
BPPC	MM-L17-BPPC-4	14	2/12/20	39.78	1.02	n. a.	n. a.	12.24	0.15	n. a.	n. a.	46.93	0.32	n. a.	n. a.	0.68	0.06
BPPC	MM-L17-BPPC-4	15	2/12/20	40.62	0.06	n. a.	n. a.	12.22	0.10	n. a.	n. a.	47.34	0.15	n. a.	n. a.	0.74	0.06
BPPC	MM-L17-BPPC-4	2	7/25/18	40.67	0.43	0.03	0.00	11.44	0.12	0.18	0.01	45.37	0.29	0.20	0.00	0.7	0.1
BPPC	MM-L17-BPPC-4	3	8/1/18	40.53	0.56	0.03	0.00	11.76	0.16	0.18	0.01	45.41	0.42	0.20	0.00	0.76	0.06
BPPC	MM-L17-BPPC-4	4	8/1/18	40.37	0.92	0.03	0.01	11.56	0.11	0.19	0.00	46.54	0.39	0.20	0.01	0.7	0.1
BPPC	MM-L17-BPPC-4	5	8/1/18	38.53	1.61	0.03	0.00	11.34	0.19	0.18	0.01	46.02	0.79	0.20	0.01	0.7	0.1
BRM	BRM-1	14	11/26/18	41.10	0.40	0.02	0.01	11.46	0.13	0.16	0.01	49.22	1.01	0.11	0.00	n. a.	n. a.
BRM	BRM-1	16	11/26/18	41.24	0.44	0.02	0.01	11.59	0.30	0.17	0.00	49.26	0.25	0.10	0.00	n. a.	n. a.
BRM	BRM-1	17	11/26/18	40.87	0.36	0.03	0.01	11.45	0.36	0.16	0.01	48.44	0.40	0.11	0.00	n. a.	n. a.
BRM	BRM-1	18	11/26/18	40.93	0.70	0.02	0.01	10.95	0.07	0.15	0.01	49.35	0.75	0.11	0.00	n. a.	n. a.
BRM	BRM-1	19	11/26/18	40.74	0.42	0.07	0.02	13.21	1.13	0.20	0.02	47.93	1.18	0.12	0.01	n. a.	n. a.
BRM	BRM-1	22	11/26/18	41.53	6.44	0.07	0.02	11.74	3.43	0.17	0.41	48.01	6.93	0.10	0.32	n. a.	n. a.
BRM	BRM-1	23	11/26/18	39.88	0.68	0.07	0.02	14.80	0.91	0.21	0.02	46.07	1.04	0.12	0.02	n. a.	n. a.
BRM	BRM-1	24	11/26/18	40.38	0.28	0.07	0.02	12.93	0.37	0.19	0.01	47.25	1.16	0.12	0.00	n. a.	n. a.
BRM	BRM-1	25	11/26/18	40.67	0.35	0.07	0.02	11.49	0.07	0.16	0.01	49.07	0.47	0.10	0.00	n. a.	n. a.
BRM	BRM-1	30	8/1/18	40.01	0.68	0.00	0.00	13.01	0.30	0.17	0.00	45.40	0.14	0.06	0.01	1.92	0.16
BRM	BRM-1	34	7/25/18	40.47	0.47	0.01	0.00	12.23	0.13	0.17	0.01	48.05	0.43	0.10	0.00	2.06	0.17
BRM	BRM-1	35	7/25/18	39.04	0.26	n. a.	n. a.	10.77	0.12	0.16	0.00	47.03	0.15	0.08	0.01	n. a.	n. a.
BRM	BRM-1	36	8/1/18	40.30	0.39	0.01	0.00	10.72	0.05	0.15	0.02	45.84	0.38	0.11	0.00	n. a.	n. a.
BRM	BRM-1	39	8/1/18	41.24	0.27	0.01	0.00	10.97	0.07	0.15	0.01	45.88	0.26	0.11	0.00	n. a.	n. a.
BRM	BRM-1	40	7/25/18	40.33	0.49	0.01	0.00	11.66	0.06	0.16	0.01	46.27	0.34	0.11	0.00	n. a.	n. a.
BRM	BRM-1	41	8/1/18	40.81	0.40	0.01	0.00	10.82	0.25	0.16	0.01	43.65	0.13	0.12	0.00	2.1	0.2
BRM	BRM-1	2	11/26/18	41.25	0.07	0.07	0.02	10.81	0.21	0.16	0.00	49.15	0.36	0.12	0.00	n. a.	n. a.
BRM	BRM-1	3	11/26/18	40.45	0.45	0.07	0.02	12.15	0.36	0.18	0.01	48.33	1.45	0.14	0.01	n. a.	n. a.
BRM	BRM-1	5	11/26/18	40.88	0.33	0.07	0.02	11.07	0.85	0.16	0.02	48.91	1.01	0.10	0.00	n. a.	n. a.
BRM	BRM-1	6	11/26/18	40.95	0.35	0.07	0.02	11.96	1.45	0.18	0.02	48.16	0.60	0.11	0.01	n. a.	n. a.
BRM	BRM-1	7	11/26/18	39.71	0.16	0.07	0.02	13.14	0.76	0.21	0.01	47.51	0.75	0.08	0.04	n. a.	n. a.
BRM	BRM-1	8	11/26/18	41.02	0.33	0.07	0.02	11.33	0.02	0.16	0.00	49.68	0.72	0.11	0.00	n. a.	n. a.
BRM	MM-L17-BRM-2	1	8/1/18	40.20	0.85	n. a.	n. a.	9.76	0.23	0.14	0.01	47.40	0.38	0.12	0.01	2.6	0.2
BRM	MM-L17-BRM-2	10	7/25/18	39.43	0.41	0.01	0.00	12.01	0.04	0.16	0.01	46.18	0.11	0.11	0.00	n. a.	n. a.
BRM	MM-L17-BRM-2	13	7/25/18	39.10	0.82	0.00	0.00	10.81	0.14	0.13	0.01	47.25	0.34	0.10	0.00	n. a.	n. a.
BRM	MM-L17-BRM-2	14	7/25/18	39.02	0.13	0.00	0.00	10.79	0.28	0.13	0.01	46.13	0.43	0.11	0.00	n. a.	n. a.
BRM	MM-L17-BRM-2	16	8/1/18	41.36	0.40	n. a.	n. a.	10.30	0.03	0.14	0.01	46.92	0.13	0.10	0.00	n. a.	n. a.
BRM	MM-L17-BRM-2	17	7/25/18	39.47	0.46	0.00	0.00	10.51	0.39	0.14	0.00	47.64	0.28	0.11	0.01	n. a.	n. a.
BRM	MM-L17-BRM-2	18	7/25/18	39.54	0.44	0.00	0.00	10.71	0.10	0.14	0.00	46.96	0.30	0.10	0.00	1.9	0.2
BRM	MM-L17-BRM-2	24	2/12/20	41.44	0.19	n. a.	n. a.	12.71	0.30	n. a.	n. a.	45.90	0.20	n. a.	n. a.	1.99	0.16
BRM	MM-L17-BRM-2	25	2/12/20	40.38	0.18	n. a.	n. a.	11.61	0.65	n. a.	n. a.	47.25	0.73	n. a.	n. a.	2.00	0.17
BRM	MM-L17-BRM-2	26	2/12/20	41.47	0.06	n. a.	n. a.	10.40	0.17	n. a.	n. a.	46.82	0.11	n. a.	n. a.	1.84	0.16
BRM	MM-L17-BRM-2	29	2/12/20	41.92	0.33	n. a.	n. a.	9.87	0.09	n. a.	n. a.	47.24	0.27	n. a.	n. a.	1.97	0.16
BRM	MM-L17-BRM-2	31	2/12/20	41.05	0.09	n. a.	n. a.	9.30	0.04	n. a.	n. a.	49.68	0.13	n. a.	n. a.	1.97	0.16
BRM	MM-L17-BRM-2	32	2/12/20	41.77	0.20	n. a.	n. a.	10.85	0.43	n. a.	n. a.	46.47	0.36	n. a.	n. a.	1.6	0.1
BRM	MM-L17-BRM-2	8	7/25/18	38.91	0.11	0.00	0.00	10.32	0.08	0.13	0.00	47.13	0.34	0.09	0.01	1.6	0.1
BRVB	MM-L17-BRVB-2	10	2/12/20	39.68	0.12	n. a.	n. a.	15.61	0.12	n. a.	n. a.	44.19	0.12	n. a.	n. a.	1.79	0.15
BRVB	MM-L17-BRVB-2	2	2/12/20	39.96	0.04	n. a.	n. a.	13.81	0.23	n. a.	n. a.	45.67	0.03	n. a.	n. a.	2.06	0.17
BRVB	MM-L17-BRVB-2	4	2/12/20	39.79	0.04	n. a.	n. a.	15.11	0.17	n. a.	n. a.	44.81	0.02	n. a.	n. a.	1.86	0.15
BRVB	MM-L17-BRVB-2	6	2/12/20	39.99	0.04	n. a.	n. a.	14.16	0.12	n. a.	n. a.	45.42	0.09	n. a.	n. a.	1.62	0.14
BRVB	MM-L17-BRVB-2	7	2/12/20	41.12	0.40	n. a.	n. a.	15.45	0.20	n. a.	n. a.	44.36	0.44	n. a.	n. a.	4.04	0.35

n. a. = not analyzed

Appendix C Supplementary Figures
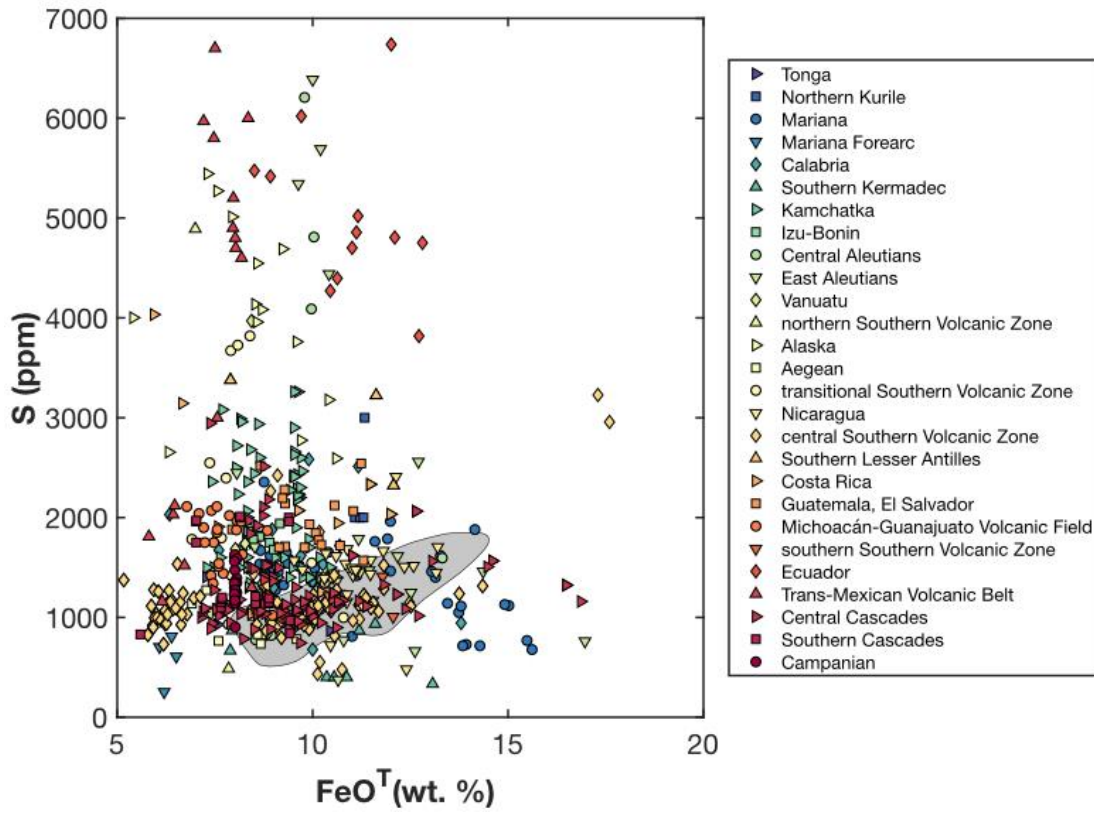
Figure S1. PEC-corrected compositions of compiled melt inclusions. Each symbol represents one melt inclusion. Each symbol type represents one subduction zone segment. MORB data shown in gray shaded region (Jenner et al., 2012).
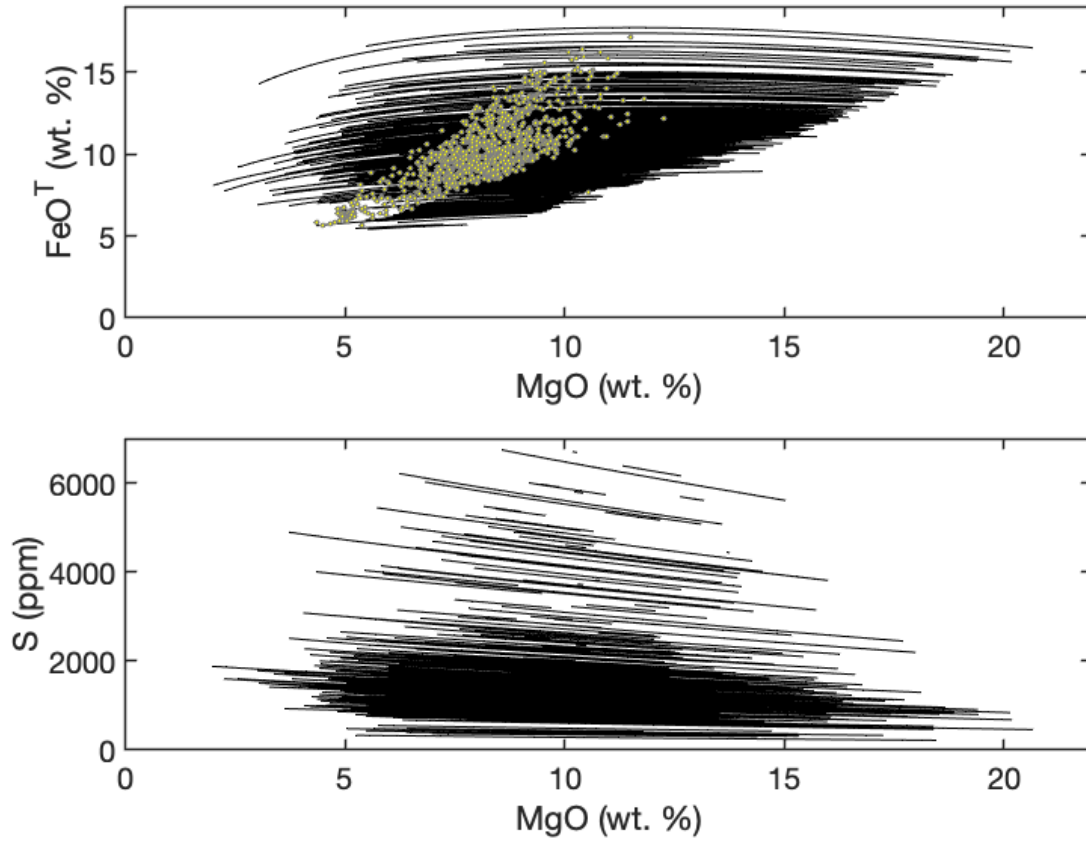
Figure S2. Reverse crystallization calculations for all inclusions within the global compilation. Black lines show reverse olivine crystallization paths. Yellow circles are arc primitive lavas for comparison (Schmidt and Jagoutz 2017).
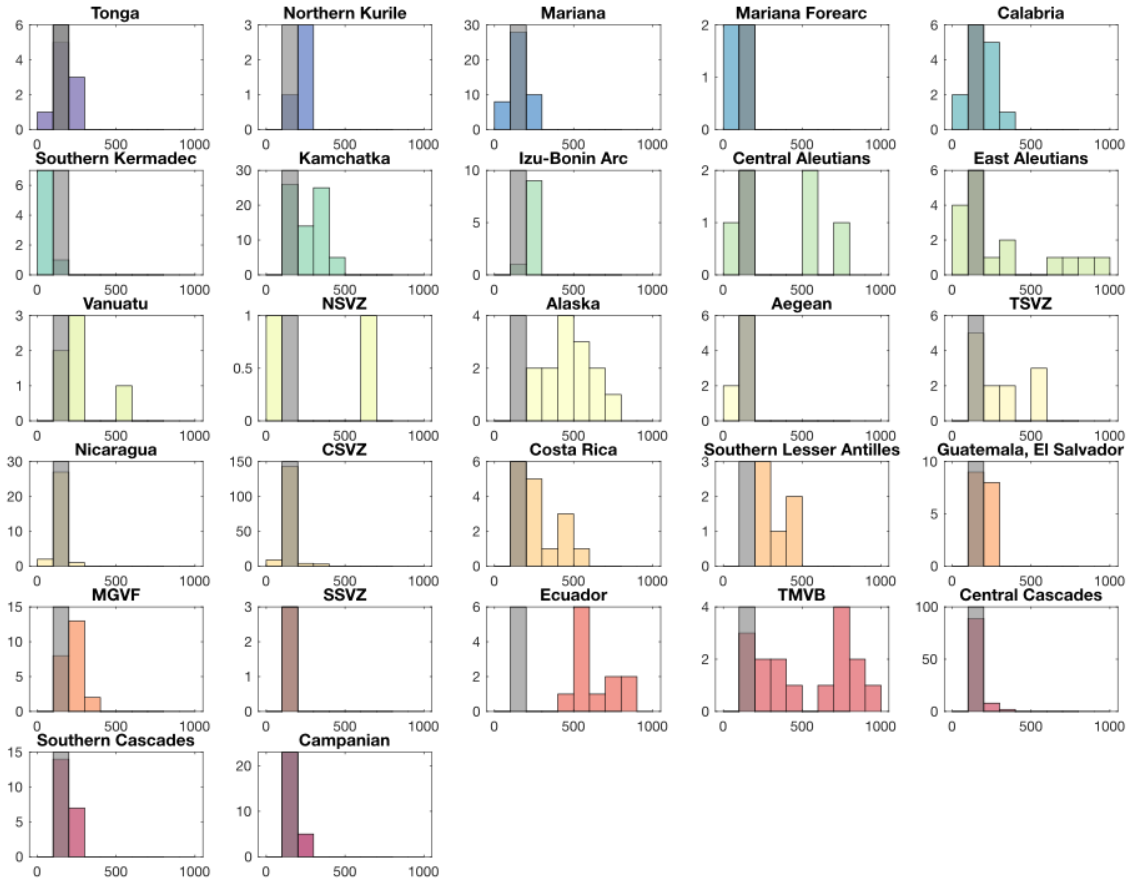
Figure S3. Minimum mantle sulfur content needed to generate primary magma sulfur concentrations for volcanoes within each arc, assuming melt fraction F = 0.15. Horizontal axis represents S content in ppm, and vertical axis represents number of inclusions. Gray bands show MORB source estimates for comparison (Ding and Dasgupta 2017, Saal et al., 2002).
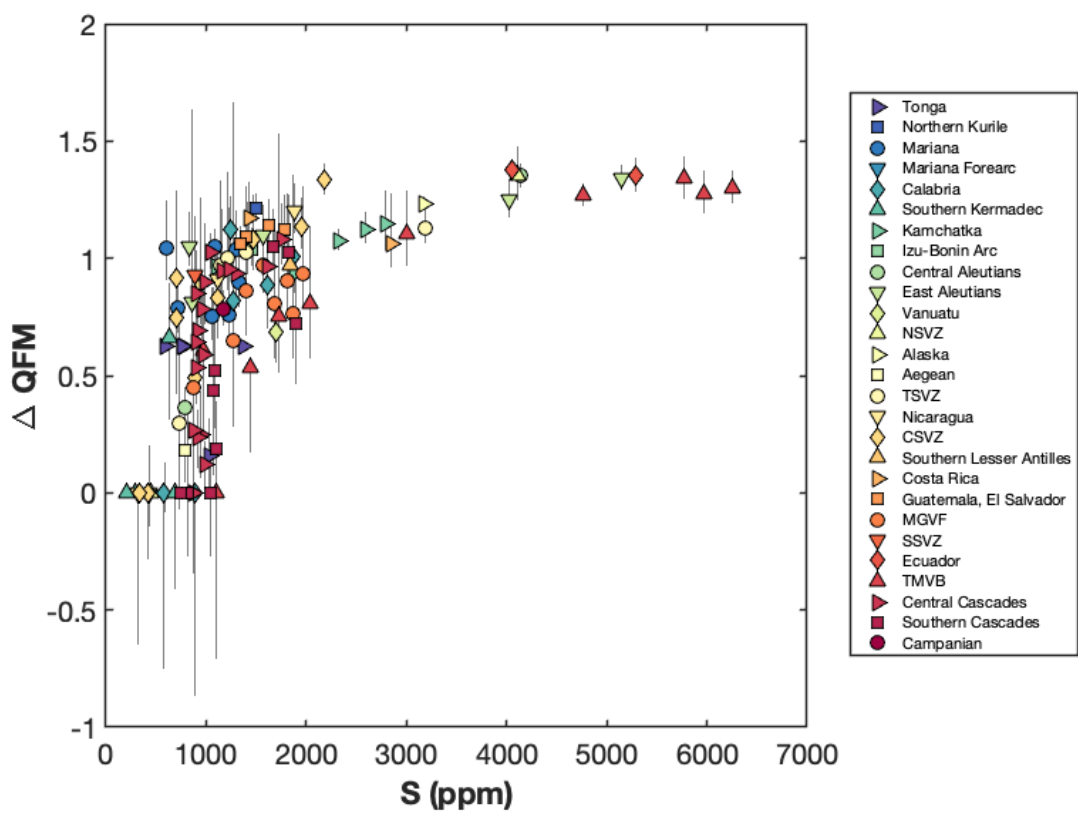
Figure S4. Calculated minimum f_{O_2} based on measured sulfur contents in melt inclusions, plotted as a function of average melt S for volcanoes from each arc segment. Error bars represent uncertainty for each volcano as described in the text.
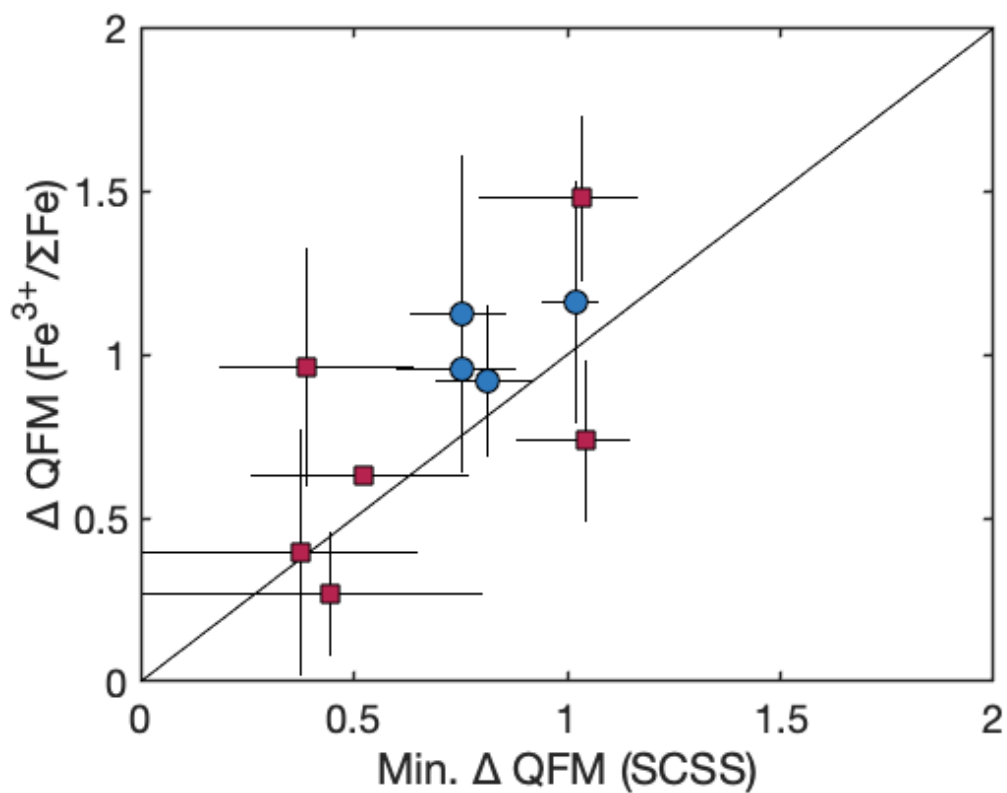
Figure S5. Average calculated minimum f_{O2} based on measured sulfur contents in melt inclusions, plotted as a function of f_{O2} calculated from measured $Fe^{3+}/\sum Fe$ using analyzed melt inclusion compositions at 400 MPa, 1150 °C. Red squares are inclusions from the southern Cascade arc (Muth and Wallace, 2021) and blue circles are inclusions from the Mariana arc (Brounce et al., 2014). Mariana arc $Fe^{3+}/\sum Fe$ values have been recalculated based on the updated calibration of Zhang et al. (2018).

REFERENCES CITED

Chapter II

Alt, J.C., Shanks, W.C., and Jackson, M.C., 1993, Cycling of sulfur in subduction zones: The geochemistry of sulfur in the Mariana Island Arc and back-arc trough: Earth and Planetary Science Letters, v. 119, p. 477–494, https://doi.org/10.1016/0012-821X(93)90057-G.

Alt, J.C., Garrido, C.J., Shanks III, W.C., Turchyn, A., Padrón-Navarto, J.A., Sánchez-Vizcaíno, V.L., Pugnaire, M.T.G., Marchesi, C., 2012, Recycling of water, carbon, and sulfur during subduction of serpentinites: A stable isotope study of Cerro del Almirez, Spain: Earth and Planetary Science Letters, v. 327-238, p. 50-60, https://doi.org/10.1016/j.epsl.2012.01.029.

Auer, S., Bindeman, I., Wallace, P., Ponomareva, V., and Portnyagin, M., 2009, The origin of hydrous, high-$\delta^{18}O$ voluminous volcanism: Diverse oxygen isotope values and high magmatic water contents within the volcanic record of Klyuchevskoy volcano, Kamchatka, Russia: Contributions to Mineralogy and Petrology, v. 157, p. 209–230, https://doi.org/10.1007/s00410-008-0330-0.

Ballhaus, C., Berry, R.F., and Green, D.H., 1991, High-pressure experimental calibration of the olivine-orthopyroxene-spinel oxygen geobarometer: implications for the oxidation state of the upper mantle: Contributions to Mineralogy and Petrology, v. 118, p. 109, https://doi.org/10.1007/BF00310615.

Bénard, A., Klimm, K., Woodland, A.B., Arculus, R.J., Wilke, M., Botcharnikov, R.E., Shimizu, N., Nebel, O., Rivard, C., and Ionov, D.A., 2018, Oxidising agents in sub-arc mantle melts link slab devolatilisation and arc magmas: Nature Communications, v. 9, https://doi.org/10.1038/s41467-018-05804-2.

Borg, L.E., Clynne, M.A., and Bullen, T.D., 1997, The variable role of slab-derived fluids in the generation of a suite of primitive calc-alkaline lavas from the Southernmost Cascades, California: Canadian Mineralogist, v. 35, p. 425–452.

Brounce, M.N., Kelley, K.A., and Cottrell, E., 2014, Variations in $Fe^{3+}/\Sigma Fe$ of Mariana Arc Basalts and Mantle Wedge fO_2: Journal of Petrology, v. 55, p. 2514–2536, https://doi.org/10.1093/petrology/egu065.

Clynne, M.A., and Borg, L.E., 1997, Olivine and chromian spinel in primitive calc-alkaline and tholeiitic lavas from the southernmost cascade range, California: A reflection of relative fertility of the source: Canadian Mineralogist, v. 35, p. 453–472.

Cottrell, E., Birner, S., Brounce, M., David, F., Waters, L.E., and Kelley, K.A., 2020, Oxygen Fugacity Across Tectonic Settings, *in* Neuville, D.R. and Moretti, R. eds., AGU Geophysical Monograph Redox: variables and mechanisms in magmatism and volcanism. https://doi.org/10.1002/essoar.10502445.1

Debret, B., and Sverjensky, D.A., 2017, Highly oxidising fluids generated during serpentinite breakdown in subduction zones: Scientific Reports, v. 7, p. 1–6, https://doi.org/10.1038/s41598-017-09626-y.

Ding, S., and Dasgupta, R., 2017, The fate of sulfide during decompression melting of peridotite – implications for sulfur inventory of the MORB-source depleted upper mantle: Earth and Planetary Science Letters, v. 459, p. 183–195, https://doi.org/10.1016/j.epsl.2016.11.020.

Evans, K.A., 2012, The redox budget of subduction zones: Earth-Science Reviews, v. 113, p. 11–32, https://doi.org/10.1016/j.earscirev.2012.03.003.

Evans, K.A., and Frost, B.R., 2021, Deserpentinization in Subduction Zones as a Source of Oxidation in Arcs: A Reality Check: Journal of Petrology, https://doi.org/10.1093/petrology/egab016.

Ghiorso, M.S., Hirschmann, M.M., Reiners, P.W., and Kress, V.C., 2002, The pMELTS: A revision of MELTS for improved calculation of phase relations and major element partitioning related to partial melting of the mantle to 3 GPa: Geochemistry, Geophysics, Geosystems, v. 3, p. 1–35, https://doi.org/10.1029/2001gc000217.

Jégo, S., and Dasgupta, R., 2014, The fate of sulfur during fluid-present melting of subducting basaltic crust at variable oxygen fugacity: Journal of Petrology, v. 55, p. 1019–1050, https://doi.org/10.1093/petrology/egu016.

Kelley, K.A., and Cottrell, E., 2009, Water and the Oxidation State of Subduction Zone Magmas: Science, v. 325, p. 605-607.

Klimm, K., Kohn, S.C., and Botcharnikov, R.E., 2012, The dissolution mechanism of sulphur in hydrous silicate melts. II: Solubility and speciation of sulphur in hydrous silicate melts as a function of fO_2: Chemical Geology, v. 322–323, p. 250–267, https://doi.org/10.1016/j.chemgeo.2012.04.028.

Lee, C-.T.A., Luffi, P., Le Roux, V., Dasgupta, R., Albaréde, F., and Leeman, W.P., 2010, The redox state of arc mantle using Zn/Fe systematics: Nature, v. 468, p. 681–685, https://doi.org/10.1038/nature09617.

Lee, C-.T.A., and Tang, M., 2020, How to make porphyry copper deposits: Earth and Planetary Science Letters, v. 529, https://doi.org/10.1016/j.epsl.2019.115868.

Matjuschkin, V., Blundy, J.D., and Brooker, R.A., 2016. The effect of pressure on sulphur speciation in mid- to deep-crustal arc magmas and implications for the formation of porphyry copper deposits. Contributions to Mineralogy and Petrology. 171.

Maurice, J., Bolfan-Casanova, N., Demouchy, S., Chauvigne, P., Schiavi, F., and Debret, B., 2020. The intrinsic nature of antigorite breakdown at 3 GPa: Experimental constraints on redox conditions of serpentinite dehydration in subduction zones. Contributions to Mineralogy and Petrology. 175.

Miyoshi, T., Sakai, H., and Chiba, H., 1984. Experimental study of sulfur isotope fractionation factors between sulfate and sulfide in high temperature melts. Geochemical Journal. 18, 75–84.

Nash, W.M., Smythe, D.J., and Wood, B.J., 2019. Compositional and temperature effects on sulfur speciation and solubility in silicate melts. Earth and Planetary Science Letters. 507, 187–198.

O'Neill, H.St.C., 2021. Comment on 'Compositional and temperature effects on sulfur speciation and solubility in silicate melts' by Nash et al. (Earth and Planetary Science Letters 507, 187–198, 2019). Earth and Planetary Science Letters. 560, 116843.

Richards, J.P., 2015. The oxidation state, and sulfur and Cu contents of arc magmas: Implications for metallogeny. Lithos. 233, 27–45.

Ruscitto, D.M., Wallace, P.J., Cooper, L.B., and Plank, T., 2012. Global variations in H_2O/Ce: 2. Relationships to arc magma geochemistry and volatile fluxes. Geochemistry, Geophysics, Geosystems. 13.

Saal, A.E., Hauri, E.H., Langmuir, C.H., Perfit, M.R., 2002. Vapour undersaturation in primitive mid-ocean-ridge basalt and the volatile content of Earth's upper mantle. Nature. 419.

Sisson, T.W., and Kelemen, P.B., 2018, Near-solidus melts of MORB + 4 wt% H_2O at 0.8–2.8 GPa applied to issues of subduction magmatism and continent formation. Contributions to Mineralogy and Petrology. 173, 1–23.

Syracuse, E.M., van Keken, P.E., Abers, G.A., Suetsugu, D., Bina, C., Inoue, T., Wiens, D., and Jellinek, M., 2010. The global range of subduction zone thermal models. Physics of the Earth and Planetary Interiors. 183, 73–90.

Tang, M., Erdmann, M., Eldridge, G., Lee, C-T.A., 2018. The redox "filter" beneath magamtic orogens and the formation of continental crust. Science Advances. 4.

Underwood, S.J., and Clynne, M.A., 2017. Oxygen isotope geochemistry of mafic phenocrysts in primitive mafic lavas from the southernmost Cascade Range, California. American Mineralogist. 102, 252–261.

Walowski, K.J., Wallace, P.J., Clynne, M.A., Rasmussen, D.J., and Weis, D., 2016. Slab melting and magma formation beneath the southern Cascade arc. Earth and Planetary Science Letters. 446, 100–112.

Walowski, K.J., Wallace, P.J., Hauri, E.H., Wada, I., and Clynne, M. A., 2015. Slab melting beneath the Cascade Arc driven by dehydration of altered oceanic peridotite. Nature Geoscience. 8, 404–409.

Walters, J.B., Cruz-Uribe, A.M., and Marschall, H.R., 2019. Isotopic Compositions of Sulfides in Exhumed High-Pressure Terranes: Implications for Sulfur Cycling in Subduction Zones. Geochemistry, Geophysics, Geosystems. 20, 3347–3374.

Chapter III

Alonso-Perez, R., Müntener, O., and Ulmer, P., 2009. Igneous garnet and amphibole fractionation in the roots of island arcs. Experimental constraints on andesitic liquids: Contributions to Mineralogy and Petrology. 157, 541–558.

Aster, E.M., Wallace, P.J., Moore, L.R., Watkins, J., Gazel, E., and Bodnar, R.J., 2016, Reconstructing CO_2 concentrations in basaltic melt inclusions using Raman analysis of vapor bubbles. Journal of Volcanology and Geothermal Research. 323,148–162.

Audétat, A., and Pettke, T., 2006. Evolution of a porphyry-Cu mineralized magma system at Santa Rita, New Mexico (USA). Journal of Petrology. 47, 2021–2046.

Audétat, A., Zhang, L., and Ni, H., 2018. Copper and Li diffusion in plagioclase, pyroxenes, olivine and apatite, and consequences for the composition of melt inclusions. Geochimica et Cosmochimica Acta. 243, 99–115.

Bali, E., Keppler, H., and Audétat, A., 2012. The mobility of W and Mo in subduction zone fluids and the Mo-W-Th-U systematics of island arc magmas. Earth and Planetary Science Letters. 351–352, 195–207.

Barber, N.D., Edmonds, M., Jenner, F., Audétat, A., and Williams, H., 2021. Amphibole Control on Copper Systematics in Arcs. Insights from the Analysis of Global Datasets: Geochimica et Cosmochimica Acta. 307, 192-211.

Berge, P.A., and Stauber, D.A., 1987. Seismic refraction study of upper crustal structure in the Lassen Peak area, northern California (USA). Journal of Geophysical Research, 92.

Blakely, R.J., Christiansen, R.L., Guffanti, M., Wells, R.E., Donnelly-Nolan, J.M., Muffler, L.J.P., Clynne, M.A., and Smith, J.G., 1997. Gravity anomalies, Quaternary vents, and Quaternary faults in the southern Cascade Range, Oregon and California: Implications for arc and backarc evolution. Journal of Geophysical Research. Solid Earth. 102, 22513–22527.

Blatter, D.L., Sisson, T.W., and Hankins, W. Ben, 2013. Crystallization of oxidized, moderately hydrous arc basalt at mid- to lower-crustal pressures: Implications for andesite genesis. Contributions to Mineralogy and Petrology, 166, 861–886.

Borg, L.E., Clynne, M.A., and Bullen, T.D., 1997. The variable role of slab-derived fluids in the generation of a suite of primitive calc-alkaline lavas from the Southernmost Cascades, California. Canadian Mineralogist, 35, 425–452.

Borg, L.E., Blichert-Toft, J., and Clynne, M.A., 2002. Ancient and modern subduction zone contributions to the mantle sources of lavas from the Lassen region of California inferred from Lu-Hf isotopic systematics. Journal of Petrology, 43, 705–723.

Brounce, M.N., Kelley, K.A., and Cottrell, E., 2014. Variations in $Fe^{3+}/\Sigma Fe$ of Mariana Arc Basalts and Mantle Wedge fO_2. Journal of Petrology. 55, 2514–2536.

Bullen, T.D., and Clynne, M.A., 1990. Trace element and isotopic constraints on magmatic evolution at Lassen volcanic center. Journal of Geophysical Research, 95.

Canil, D., and Fellows, S.A., 2017. Sulphide–sulphate stability and melting in subducted sediment and its role in arc mantle redox and chalcophile cycling in space and time. Earth and Planetary Science Letters. 470, 73–86.

Cao, M.J., Evans, N.J., Hollings, P., Cooke, D.R., McInnes, B.I.A., Qin, K.Z., and Li, G.M., 2018a. Phenocryst zonation in porphyry-related rocks of the Baguio District, Philippines. Evidence for magmatic and metallogenic processes. Journal of Petrology, 59, 825–848.

Cao, M., Hollings, P., Cooke, D.R., Evans, N.J., McInnes, B.I.A., Qin, K., Li, G., Sweet, G., and Baker, M., 2018b. Physicochemical processes in the magma chamber under the Black Mountain porphyry Cu-Au deposit, Philippines: Insights from mineral chemistry and implications for mineralization. Economic Geology, 113, 63–82.

Cecil, M.T., Rotberg, G.L., Ducea M.N., Saleeby, J.B., Gehrels, G.E., 2012. Magmatic growth and batholithic root development in the northern Sierra Nevada, California. Geosphere. 8 (3) 592-606.

Chambefort, I., Dilles, J.H., and Kent, A.J.R., 2008. Anhydrite-bearing andesite and dacite as a source for sulfur in magmatic-hydrothermal mineral deposits. Geology. 36, 719–722.

Chiaradia, M., 2013. Copper enrichment in arc magmas controlled by overriding plate thickness. Nature Geoscience. 7, 43–46.

Chiaradia, M., 2020. Gold endowments of porphyry deposits controlled by precipitation efficiency. Nature Communications. 11.

Cline, J.S., and Bodnar, R.J., 1991. Can economic porphyry copper mineralization be generated by a typical calc-alkaline melt? Journal of Geophysical Research. 96, 8113–8126.

Clynne, M.A., and Borg, L.E., 1997. Olivine and chromian spinel in primitive calc-alkaline and tholeiitic lavas from the southernmost cascade range, California: A reflection of relative fertility of the source. Canadian Mineralogist, 35, 453–472.

Clynne, M. A., Muffler, L. J. P., Siems, D. F., Taggart, J. E., Jr., and Bruggman, P., 2008. Major and EDXRF trace element chemical analyses of volcanic rocks from Lassen Volcanic National Park and vicinity, California. - U.S. Geol. Surv. Open-File Rept. 2008-1091. 1 - 10.

Core, D.P., Kesler, S.E., and Essene, E.J., 2006. Unusually Cu-rich magmas associated with giant porphyry copper deposits: Evidence from Bingham, Utah. Geology, 34, 41–44.

Danyushevsky, L. V., Della-Pasqua, F.N., and Sokolov, S., 2000. Re-equilibration of melt inclusions trapped by magnesian olivine phenocrysts from subduction-related magmas: Petrological implications. Contributions to Mineralogy and Petrology. 138, 68–83.

Danyushevsky, L.V., 2001. The effect of small amounts of H_2O on crystallisation of mid-ocean ridge and backarc basin magmas: Journal of Volcanology and Geothermal Research. 110 (3) 265-280.

Danyushevsky, L. V., and Plechov, P., 2011. Petrolog3: Integrated software for modeling crystallization processes. Geochemistry, Geophysics, Geosystems. 12.

De Hoog, J.C.M., Mason, P.R.D., and Van Bergen, M.J., 2001. Sulfur and chalcophile elements in subduction zones: Constraints from a laser ablation ICP-MS study of melt inclusions from Galunggung Volcano, Indonesia. Geochimica et Cosmochimica Acta. 65 (18) 3147–3164.

Dickinsin, W.R., 2008. Accretionary Mesozoic-Cenozoic expansion of the Cordilleran continental margin in California and adjacent Oregon. Geosphere. 4, 329–353.

Ding, S., and Dasgupta, R., 2017. The fate of sulfide during decompression melting of peridotite – implications for sulfur inventory of the MORB-source depleted upper mantle. Earth and Planetary Science Letters. 459, 183–195.

188

Du, J., and Audétat, A., 2020. Early sulfide saturation is not detrimental to porphyry Cu-Au formation. Geology. 48, 519–524.

Gaetani, H., O'Leary, J.A., Shimizu, N.B., Bucholz, C.R., Newville, M., 2012. Rapid reequilibration of H_2O and oxygen fugacity in olivine-hosted melt inclusions. Geology. 40 (10) 915-918.

Georgatou, A., Chiaradia, M., Rezeau, H., Wälle, M., 2018. Magmatic sulphides in Quaternary Ecuadorian arc magmas. Lithos 296–299, 580–599.

Ghiorso, M.S., Gualda, G.A.R., 2015. An H_2O–CO_2 mixed fluid saturation model compatible with rhyolite-MELTS. Contributions to Mineralology and Petrology. 169, 1–30.

Grondahl, C., and Zajacz, Z., 2017. Magmatic controls on the genesis of porphyry Cu–Mo–Au deposits: The Bingham Canyon example. Earth and Planetary Science Letters, 480, 53–65.

Gualda G.A.R., Ghiorso M.S., Lemons R.V., Carley T.L., 2012. Rhyolite-MELTS: A modified calibration of MELTS optimized for silica-rich, fluid-bearing magmatic systems. Journal of Petrology. 53, 875-890.

Guffanti, M., Clynne, M.A., Smith, J.G., Muffler, L.J.P., and Bullen, T.D., 1990. Late Cenozoic volcanism, subduction, and extension in the Lassen region of California, southern Cascade Range. Journal of Geophysical Research. 95.

Hamlyn, P.R., Keays, R.R., Cameron, W.E., Crawford, A.J., and Waldron, H.M., 1985. Precious metals in magnesian low-Ti lavas: Implications for metallogenesis and sulfur saturation in primary magmas. Geochimica et Cosmochimica Acta. 49, 1797–1811.

Hanson, B., Delano, J.W., and Lindstrom, D.J., 1996, High-precision analysis of hydrous rhyolitic glass inclusions in quartz phenocrysts using the electron microprobe and INAA: American Mineralogist, v. 81, p. 1249–1262, https://doi.org/10.2138/am-1996-9-1023.

Hollyday, A.E., Leiter, S.H., and Walowski, K.J., 2020. Pre-eruptive storage, evolution, and ascent timescales of a high-Mg basaltic andesite in the southern Cascade Arc. Contributions to Mineralogy and Petrology. 175, 1–21.

Hutchinson, M.C., and Dilles, J.H., 2019. Evidence for magmatic anhydrite in porphyry copper intrusions. Economic Geology. 114, 143–152.

Humphreys, J., Brounce, M., Walowski, K. In Review. Diffusive re-equilibration of water and oxygen fugacity in natural olivine hosted melt inclusions. Earth and Planetary Science Letters.

Iacovino K., Matthews S., Wieser P.E., Moore G.M., and Begue F. (in press) VESIcal Part I: An open-source thermodynamic model engine for mixed volatile (H_2O-CO_2) solubility in silicate melts, Earth and Space Sciences.

Iveson, A.A. et al., 2021. Deciphering variable mantle sources and hydrous inputs to arc magmas in Kamchatka. Earth and Planetary Science Letters. 562, 116848.

Jenner, F.E., O'Neill, H.St.C., Arculus, R.J., and Mavrogenes, J.A., 2010. The Magnetite Crisis in the Evolution of Arc-related Magmas and the Initial Concentration of Au , Ag and Cu. Journal of Petrology. 51.

Jenner, F.E., Arculus, R.J., Mavrogenes, J.A., Dyriw, N.J., Nebel, O., and Hauri, E.H., 2012. Chalcophile element systematics in volcanic glasses from the northwestern Lau Basin. Geochemistry, Geophysics, Geosystems, 13.

Jenner, F.E., O'Neil, H. St. C., 2012. Analysis of 60 elements in 616 ocean floor basaltic glasses. Geochemistry, Geophysics, Geosystems, 13.

Jenner, F.E., Hauri, E.H., Bullock, E.S., König, S., Arculus, R.J., Mavrogenes, J.A., Mikkelson, N., and Goddard, C., 2015. The competing effects of sulfide saturation versus degassing on the behavior of the chalcophile elements during the differentiation of hydrous melts. Geochemistry, Geophysics, Geosystems. 16, 1490–1507.

Jenner, F.E., 2017. Cumulate causes for the low contents of sulfide-loving elements in the continental crust. Nature Geoscience. 10, 524–529.

Jochum, K.P., Nohl, U. N., Herwig, K., Lammel, E., Stoll, B., Hofman, A. W., 2007. GeoReM: A New Geochemical Database for Reference Materials and Isotopic Standards. Geostandards and Geoanalytical Research. 29, 333-338.

John, D.A., Ayuso, R.A., Barton, M.D., Blakely, R.J., Bodnar, R.J., Dilles, J.H., Gray, Floyd, Graybeal, F.T., Mars, J.C., McPhee, D.K., Seal, R.R., Taylor, R.D., and Vikre, P.G., 2010. Porphyry copper deposit model, chap. B of Mineral deposit models for resource assessment: U.S. Geological Survey Scientific Investigations Report 2010–5070–B. 169.

Jugo, P.J., Wilke, M., and Botcharnikov, R.E., 2010, Sulfur K-edge XANES analysis of natural and synthetic basaltic glasses: Implications for S speciation and S content as function of oxygen fugacity. Geochimica et Cosmochimica Acta, 74, 5926–5938.

Kamenetsky, V.S., and Kamenetsky, M.B., 2010. Magmatic fluids immiscible with silicate melts: Examples from inclusions in phenocrysts and glasses, and implications for magma evolution and metal transport. Geofluids. 10, 293–311.

Keith, M., Haase, K.M., Klemd, R., Schwarz-Schampera, U., and Franke, H., 2017. Systematic variations in magmatic sulphide chemistry from mid-ocean ridges, back-arc basins and island arcs. Chemical Geology. 451, 67–77.

Kelley, K.A., and Cottrell, E., 2009. Water and the Oxidation State of Subduction Zone Magmas. Science. 325, 605–607.

Kiseeva, E.S., and Wood, B.J., 2015. The effects of composition and temperature on chalcophile and lithophile element partitioning into magmatic sulphides. Earth and Planetary Science Letters. 424, 280–294.

Kogiso, T., Tatsumi, Y., and Nakano, S., 1997. Trace element transport during dehydration processes in the subducted oceanic crust: 1. Experiments and implications for the origin of ocean island basalts. Earth and Planetary Science Letters. 148, 193–205.

König, S., Münker, C., Schuth, S., and Garbe-Schönberg, D., 2008. Mobility of tungsten in subduction zones. Earth and Planetary Science Letters, 274, 82–92.

König, S., Münker, C., Schuth, S., Luguet, A., Hoffmann, J.E., and Kuduon, J., 2010. Boninites as windows into trace element mobility in subduction zones. Geochimica et Cosmochimica Acta. 74, 684–704.

Korges, M., Weis, P., and Andersen, C., 2020. The role of incremental magma chamber growth on ore formation in porphyry copper systems. Earth and Planetary Science Letters, 552, 116584.

Krawczynski, M.J., Grove, T.L., and Behrens, H., 2012. Amphibole stability in primitive arc magmas: Effects of temperature, H_2O content, and oxygen fugacity. Contributions to Mineralogy and Petrology. 164, 317–339.

Laubier, M., Schiano, P., Doucelance, R., Ottolini, L., and Laporte, D., 2007. Olivine-hosted melt inclusions and melting processes beneath the FAMOUS zone (Mid-Atlantic Ridge). Chemical Geology, 240, 29–150.

Leath, J.M., 2019. Metals in subduction related magmatism: Insights from melt inclusions and assciated glass groundmass from the Southern Kermadec Arc, New Zealand. Master's Thesis, University of Wellington.

Lee, C-T.A., Luffi, P., Plank, T., Dalton, H., Leeman, W.P., 2009. Constraints on the depths and temperatures of basaltic magma generation on Earth and other terrestrial planets using new thermobarometers for mafic magmas. Earth and Planetary Science Letters. 279, 20–33.

Lee, C-T.A., Luffi, P., Chin, E.J., Bouchet, R., Dasgupta, R., Morton, D.M., Roux, V. Le, Yin, Q., and Jin, D., 2012. Copper Systematics in Arc Magmas and Implications for Crust-Mantle Differentiation. Science. 336, 64–68.

Lee, C-T.A., and Tang, M., 2020. How to make porphyry copper deposits: Earth and Planetary Science Letters. 529, 115868.

Li, Y., Audétat, A., Liu, Z., and Wang, F., 2021. Chalcophile element partitioning between Cu-rich sulfide phases and silicate melt and implications for the formation of Earth's continental crust. Geochimica et Cosmochimica Acta. 302, 61–82.

Li, Z., Chu, F., Zhu, J., Ding, Y., Zhu, Z., Liu, J., Wang, H., Li, X., Dong, Y., and Zhao, D., 2019. Magmatic sulfide formation and oxidative dissolution in the SW Okinawa Trough: A precursor to metal-bearing magmatic fluid. Geochimica et Cosmochimica Acta. 258, 138–155.

Liu, X., Xiong, X., Audétat, A., Li, Y., Song, M., Li, L., Sun, W., and Ding, X., 2014. Partitioning of copper between olivine, orthopyroxene, clinopyroxene, spinel, garnet and silicate melts at upper mantle conditions. Geochimica et Cosmochimica Acta. 125, 1-22.

Liu, K., Zhang, L., Guo, X., and Ni, H., 2021. Effects of sulfide composition and melt H_2O on sulfur content at sulfide saturation in basaltic melts. Chemical Geology. 559, 119913.

Lorand, J.P., and Luguet, A., 2016. Chalcophile and siderophile elements in mantle rocks: Trace elements controlled by trace minerals. Reviews in Mineralogy and Geochemistry. 81, 441–488.

Loucks, R.R., 2014. Distinctive composition of copper-ore-forming arc magmas. Australian Journal of Earth Sciences. 61, 5–16.

Lowenstern, J.B., Mahood, G.A., Rivers, M.L., and Sutton, S.R., 1991. Evidence for extreme partitioning of copper into a magmatic vapor phase. Scientific Reports. 296, 1405–1409.

Luhr, J.F., and Aranda-Gómez, J.J., 1997. Mexican peridotite xenoliths and tectonic terranes: Correlations among vent location, texture, temperature, pressure, and oxygen fugacity. Journal of Petrology. 38, 1075–1112.

Luhr, J.F., 2001. Glass inclusions and melt volatile contents at Parícutin volcano, Mexico. Contributions to Mineralogy and Petrology. 142, 261–283.

MacLennan, J., 2008. Concurrent mixing and cooling of melts under Iceland. Journal of Petrology. 49, 1931–1953.

Matjuschkin, V., Blundy, J.D., and Brooker, R.A., 2016. The effect of pressure on sulphur speciation in mid- to deep-crustal arc magmas and implications for the formation of porphyry copper deposits. Contributions to Mineralogy and Petrology. 171.

Mavrogenes, J. A., and O'Neil, H. St.C., 1999. The relative effects of pressure, temperature and oxygen fugacity on the solubility of sulfide in mafic magmas. Geochimica et Cosmochimica Acta. 63, (7-8), 1173-1180.

Menges, F., 2020, Spectragryph - optical spectroscopy software:Version 1.2.14.

Mironov, N.L., and Portnyagin, M. V., 2018. Coupling of redox conditions of mantle melting and copper and sulfur contents in primary magmas of the Tolbachinsky Dol (Kamchatka) and Juan de Fuca Ridge (Pacific Ocean). Petrology. 26, 145–166.

Moore, N.E., and DeBari, S.M., 2012. Mafic magmas from Mount Baker in the northern Cascade arc, Washington: Probes into mantle and crustal processes. Contributions to Mineralogy and Petrology. 163, 521–546.

Morgan, G.B., and London, D., 2005. Effect of current density on the electron microprobe analysis of alkali aluminosilicate glasses. American Mineralogist. 90, 1131–1138.

Morgan, G.B., and London, D., 1996. Optimizing the electron microprobe analysis of hydrous alkali aluminosilicate glasses. American Mineralogist. 81, 1176–1185.

Mullen, E.K., Weis, D., Marsh, N.B., and Martindale, M., 2017. Primitive arc magma diversity: New geochemical insights in the Cascade Arc. Chemical Geology. 448, 43–70.

Mungall, J.E., Su, S., 2005. Interfacial tension between magmatic sulfide and silicate liquids. Constraints on kinetics of sulfide liquation and sulfide migration through silicate rocks. Earth and Planetary Science Letters. 234, 135–149.

Müntener, O., and Ulmer, P., 2006. Experimentally derived high-pressure cumulates from hydrous arc magmas and consequences for the seismic velocity structure of lower arc crust. Geophysical Research Letters. 33, 1–5.

Muth, M.J., and Wallace, P.J., 2021, Slab-derived sulfate generates oxidized basaltic magmas in the southern Cascade arc (California, USA): Geology.

Nandedkar, R.H., Ulmer, P., and Müntener, O., 2014. Fractional crystallization of primitive, hydrous arc magmas: An experimental study at 0.7 GPa. Contributions to Mineralogy and Petrology. 167, 1–27.

Nash, W.M., Smythe, D.J., and Wood, B.J., 2019. Compositional and temperature effects on sulfur speciation and solubility in silicate melts. Earth and Planetary Science Letters. 507, 187–198.

Noll, P.D., Newsom, H.E., Leeman, W.P., and Ryan, J.G., 1996. The role of hydrothermal fluids in the production of subduction zone magmas: Evidence from siderophile and chalcophile trace elements and boron. Geochimica et Cosmochimica Acta. 60, 587–611.

O'Neill, H. St.C., 2021, Comment on 'Compositional and temperature effects on sulfur speciation and solubility in silicate melts" by Nash et al. (Earth and Planetary Science Letters 507, 187–198, 2019): Earth and Planetary Science Letters,.

Patten, C., Barnes, S.J., Mathez, E.A., 2012. Textural variations in morb sulfide droplets due to differences in crystallization history. Canadian Mineralogist. 50, 675–692.

Pearce, J.A., Peate, D.W., 1995. Tectonic implications of the composition of volcanic arc magmas. Annual Reviews in Earth Science. 23, 251-258.

Portnyagin, M. V., Mironov, N.L., and Nazarova, D.P., 2017. Copper partitioning between olivine and melt inclusions and its content in primitive island-arc magmas of Kamchatka. Petrology. 25, 419–432.

Portnyagin, M. V., Almeev, R., Matveev, S., Holtz, F., 2008. Experimental evidence for rapid water exchange between melt inclusions in olivine and host magma. Earth and Planetary Science Letters. 272, 541–552.

Rezeau, H., and Jagoutz, O., 2020. The importance of H_2O in arc magmas for the formation of porphyry Cu deposits. Ore Geology Reviews. 126.

Richards, J.P., 2015. The oxidation state, and sulfur and Cu contents of arc magmas: implications for metallogeny: Lithos. 233, 27–45.

Richards, J.P., 2009. Postsubduction porphyry Cu-Au and epithermal Au deposits: Products of remelting of subduction-modified lithosphere. Geology. 37, 247–250.

Le Roux, V., Dasgupta, R., and Lee, C-T.A., 2015. Recommended mineral-melt partition coefficients for FRTEs (Cu), Ga, and Ge during mantle melting. American Mineralogist. 100, 2533–2544.

Ruscitto, D.M., Wallace, P.J., Johnson, E.R., Kent, A.J.R., and Bindeman, I.N., 2010. Volatile contents of mafic magmas from cinder cones in the Central Oregon High Cascades: Implications for magma formation and mantle conditions in a hot arc. Earth and Planetary Science Letters. 298, 153–161.

Ruscitto, D.M., Wallace, P.J., Cooper, L.B., Plank, T., 2012. Global variations in H_2O/Ce: 2. Relationships to arc magma geochemistry and volatile fluxes. Geochemistry, Geophysical Geosystems. 13.

Saal, A.E., Hauri, E.H., Langmuir, C.H., and Perfit, M.R., 2002. Vapour undersaturation in primitive mid-ocean-ridge basalt and the volatile content of earth's upper mantle. Nature. 419, 451–455.

Salters, V.J.M., Stracke, A., 2004. Composition of the depleted mantle. Geochemistry, Geophys. Geosystems. 5.

Schiano, P., 2003. Primitive mantle magmas recorded as silicate melt inclusions in igneous minerals. Earth Science Reviews. 63, 121–144.

Sillitoe, R.H., 2010. Porphyry copper systems. Economic Geology. 105, 3–41.

Smythe, D.J., Wood, B.J., and Kiseeva, E.S., 2017. The S content of silicate melts at sulfide saturation: New experiments and a model incorporating the effects of sulfide composition. American Mineralogist. 102, 795–803.

Sobolev, A. V., and Shimizu, N., 1993. Ultra-depleted primary melt included in an olivine from the Mid-Atlantic Ridge. Nature. 363, 151–154.

Stolper, E., Newman, S. 1994. The role of water in the petrogenesis of Mariana trough magmas. Earth and Planetary Science Letters. 121, 293-325.

Sugawara, T., 2000. Empirical relationships between temperature, pressure, and MgO content in olivine and pyroxene saturated liquid. Journal of Geophysical Research: Solid Earth. 105, 8457–8472.

Sun, Z., Xiong, X., Wang, J., Liu, X., Li, L., Ruan, M., Zhang, L., and Takahashi, E., 2020. Sulfur abundance and heterogeneity in the MORB mantle estimated by copper partitioning and sulfur solubility modelling. Earth and Planetary Science Letters. 538.

Syracuse, E.M., van Keken, P.E., Abers, G.A., Suetsugu, D., Bina, C., Inoue, T., Wiens, D., and Jellinek, M., 2010. The global range of subduction zone thermal models. Physics of the Earth and Planetary Interiors. 183, 73–90.

Timm, C., De Ronde, C.E.J., Leybourne, M.I., Layton-Matthews, D., and Graham, I.J., 2012. Sources of chalcophile and siderophile elements in kermadec Arc Lavas. Economic Geology. 107, 1527–1538.

Toplis, M.J., 2005. The thermodynamics of iron and magnesium partitioning between olivine and liquid: Criteria for assessing and predicting equilibrium in natural and experimental systems. Contributions to Mineralogy and Petrology. 149, 22–39.

Turner, S.J., Langmuir, C.H., Dungan, M.A., and Escrig, S., 2017. The importance of mantle wedge heterogeneity to subduction zone magmatism and the origin of EM1. Earth and Planetary Science Letters. 472, 216–228.

Ulmer, P., Kaegi, R., and Müntener, O., 2018. Experimentally derived intermediate to silica-rich arc magmas by fractional and equilibrium crystallization at 1.0 GPa: An evaluation of phase relationships, compositions, liquid lines of descent and oxygen fugacity. Journal of Petrology. 59, 11–58.

Underwood, S.J., and Clynne, M.A., 2017. Oxygen isotope geochemistry of mafic phenocrysts in primitive mafic lavas from the southernmost Cascade Range, California. American Mineralogist. 102, 252–261.

Venugopal, S., Moune, S., Williams-Jones, G., Druitt, T., Vigouroux, N., Wilson, A., and Russell, J.K., 2020. Two distinct mantle sources beneath the Garibaldi Volcanic Belt: Insight from olivine-hosted melt inclusions. Chemical Geology. 532.

Valetich, M.J., Mavrogenes, J., Arculus, R., and Umino, S., 2019. Evolution of chalcophile elements in the magmas of the Bonin Islands. Chemical Geology. 508, 234–249.

Villiger, S., Ulmer, P., Muntener, O., Thompson, A.B., 2004. The The Liquid Line of Descent of Anhydrous, Mantle-Derived, Tholeiitic Liquids by Fractional and Equilibrium Crystallization- an Experimental Study at 1.0 GPa. Journal of Petrology. 45 (12) 2369-2388.

Wallace, P.J., and Edmonds, M., 2011. The sulfur budget in magmas: Evidence from melt inclusions, submarine glasses, and volcanic gas emissions, *in* Reviews in Mineralogy and Geochemistry. 73, 215–246.

Walowski, K.J., Wallace, P.J., Cashman, K. V., Marks, J.K., Clynne, M.A., and Ruprecht, P., 2019. Understanding melt evolution and eruption dynamics of the 1666 C.E. eruption of Cinder Cone, Lassen Volcanic National Park, California: Insights from olivine-hosted melt inclusions. Journal of Volcanology and Geothermal Research. 387, 106665.

Walowski, K.J., Wallace, P.J., Clynne, M.A., Rasmussen, D.J., and Weis, D., 2016. Slab melting and magma formation beneath the southern Cascade arc. Earth and Planetary Science Letters. 446, 100–112.

Walowski, K.J., Wallace, P.J., Hauri, E.H., Wada, I., and Clynne, M.A., 2015. Slab melting beneath the Cascade Arc driven by dehydration of altered oceanic peridotite. Nature Geoscience. 8, 404–408.

Walters, J.B., Cruz-Uribe, A.M., and Marschall, H.R., 2020. Sulfur loss from subducted altered oceanic crust and implications for mantle oxidation. Geochemical Perspectives Letters. 36–41.

Walters, J.B., Cruz-Uribe, A.M., Marschall, H.R., and Boucher, B., 2021. The role of sulfides in the chalcophile and siderophile element budget of the subducted oceanic crust. Geochimica et Cosmochimica Acta. 304, 191–215.

Wang, Z., Becker, H., 2015. Abundances of Ag and Cu in mantle peridotites and the implications for the behavior of chalcophile elements in the mantle. Geochimica Cosmochimica Acta. 160, 209–226.

Wang, Z., Park, J.W., Wang, X., Zou, Z., Kim, J., Zhang, P., and Li, M., 2019. Evolution of copper isotopes in arc systems: Insights from lavas and molten sulfur in Niuatahi volcano, Tonga rear arc. Geochimica et Cosmochimica Acta. 250, 18–33.

Waters, L.E., Cottrell, E., Coombs, M.L., and Kelley, K.A., 2020. Generation of Calc-Alkaline Magmas During Crystallization at High Oxygen Fugacity: An Experimental and Petrologic Study of Tephras from Buldir Volcano, Western Aleutian Arc, Alaska, USA. Journal of Petrology. 1–36.

Wieser, P.E., Jenner, F., Edmonds, M., Maclennan, J., and Kunz, B.E., 2020. Chalcophile elements track the fate of sulfur at Kīlauea Volcano, Hawai'i. Geochimica et Cosmochimica Acta. 282, 245–275.

Wilkinson, J.J., 2013. Triggers for the formation of porphyry ore deposits in magmatic arcs. Nature Geoscience. 6, 917–925.

Wilson, D.S., 2002, The Juan de Fuca plate and slab: Isochron structure and Cenozoic plate motions *in* The Cascaida Subduction Zone and Related Systems. 9.

Workman, R.K., and Hart, S.R., 2005. Major and trace element composition of the depleted MORB mantle (DMM). Earth and Planetary Science Letters. 231, 53–72.

Wysoczanski, R., and Tani, K., 2006, Spectroscopic FTIR imaging of water species in silicic volcanic glasses and melt inclusions: An example from the Izu-Bonin arc: Journal of Volcanology and Geothermal Research, v. 156, p. 302–314, https://doi.org/10.1016/j.jvolgeores.2006.03.024.

Zajacz, Z., Candela, P.A., Piccoli, P.M., Wälle, M., and Sanchez-Valle, C., 2012. Gold and copper in volatile saturated mafic to intermediate magmas: Solubilities, partitioning, and implications for ore deposit formation. Geochimica et Cosmochimica Acta. 91, 140–159.

Chapter IV

Ackerman, L., Walker, R.J., Puchtel, I.S., Pitcher, L., Jelínek, E., Strnad, L., 2009. Effects of melt percolation on highly siderophile elements and Os isotopes in subcontinental lithospheric mantle: A study of the upper mantle profile beneath Central Europe. Geochimica Cosmochimica Acta. 73, 2400–2414.

Aiuppa, A., Fischer, T.P., Plank, T., Bani, P., 2019. CO_2 flux emissions from the Earth's most actively degassing volcanoes, 2005–2015. Scientific Reports. 9, 2005–2015.

Alt, J.C., Shanks, W.C., Jackson, M.C., 1993. Cycling of sulfur in subduction zones: The geochemistry of sulfur in the Mariana Island Arc and back-arc trough. Earth and Planetary Science Letters. 119, 477–494.

Alt, J.C., 1995. Sulfur isotopic profile through the oceanic crust: sulfur mobility and seawater-crustal sulfur exchange during hydrothermal alteration. Geology. 23, 585–588.

Alt, J.C., Schwarzenbach, E.M., Früh-Green, G.L., Shanks, W.C., Bernasconi, S.M., Garrido, C.J., Crispini, L., Gaggero, L., Padrón-Navarta, J.A., Marchesi, C., 2013. The role of serpentinites in cycling of carbon and sulfur: Seafloor serpentinization and subduction metamorphism. Lithos. 178, 40-54.

Bachmann, O., Dungan, M.A., Bussy, F., 2005. Insights into shallow magmatic processes in large silicic magma bodies: The trace element record in the Fish Canyon magma body. Colorado. Contributions to Mineralogy and Petrology. 149. 338–349.

Barber, N.D., Edmonds, M., Jenner, F., Audétat, A., and Williams, H., 2021. Amphibole Control on Copper Systematics in Arcs: Insights from the Analysis of Global Datasets. Geochimica et Cosmochimica Acta. 307, 192-211.

Barnes, J.D., Sharp, Z.D., Fischer, T.P., Hilton, D.R., Carr, M.J., 2009. Chlorine isotope variations along the Central American volcanic front and back arc. Geochemistry, Geophys. Geosystems 10.

Bénard, A., Klimm, K., Woodland, A.B., Arculus, R.J., Wilke, M., Botcharnikov, R.E., Shimizu, N., Nebel, O., Rivard, C., Ionov, D.A., 2018. Oxidising agents in sub-arc mantle melts link slab devolatilisation and arc magmas. Nature Communications. 9, 3500.

Birner, S.K., Warren, J.M., Cottrell, E., Davis, F.A., Kelley, K.A., Falloon, T.J., 2017. Forearc peridotites from tonga record heterogeneous oxidation of the mantle following subduction initiation. Journal of Petrology. 58, 1755–1780.

Botcharnikov, R.E., Linnen, R.L., Wilke, M., Holtz, F., Jugo, P.J., Berndt, J., 2011. High gold concentrations in sulphide-bearing magma under oxidizing conditions. Nature Geoscience. 4, 112–115.

Brounce, M., Cottrell, E., Kelley, K.A., 2019. The redox budget of the Mariana subduction zone. Earth and Planetary Science Letters. 528.

Brounce, M.N., Kelley, K.A., Cottrell, E., 2014. Variations in $Fe^{3+}/\Sigma Fe$ of Mariana Arc Basalts and Mantle Wedge fO_2. Journal of Petrology. 55, 2514–2536.

Büchl, A., Brügmann, G., Batanova, V.G., Münker, C., Hofmann, A.W., 2002. Melt percolation monitored by Os isotopes and HSE abundances: A case study from the mantle section of the Troodos Ophiolite. Earth and Planetary Science Letters. 204, 385–402.

Burgisser, A., Scaillet, B., 2007. Redox evolution of a degassing magma rising to the surface. Nature 445. 194–197.

Callegaro, S., Geraki, K., Marzoli, A., de Min, A., Maneta, V., Baker, and D.R., 2020. The quintet completed: the partitioning of sulfur between nominally volatile-free minerals and silicate melts. American Mineralogist. 105, 697–707.

Canil, D., Fellows, S.A., 2017. Sulphide–sulphate stability and melting in subducted sediment and its role in arc mantle redox and chalcophile cycling in space and time. Earth and Planetary Science Letters. 470, 73–86.

Carroll, M.R., Rutherford, M.J., 1987. The stability of igneous anhydrite: Experimental results and implications for sulfur behavior in the 1982 El chichon trachyandesite and other evolved magmas. Journal of Petrology. 28, 781–801.

Carroll, M.R., Rutherford, M.J., 1988. Sulfur speciation in hydrous experimental glasses of varying oxidation state: results from measured wavelength shifts of sulfur X-rays. American Mineralogist. 73, 845–849.

Cottrell, E., Kelley, K.A., 2011. The oxidation state of Fe in MORB glasses and the oxygen fugacity of the upper mantle. Earth Planetary Science Letters. 305, 270–282.

Cottrell, E., Birner, S., Brounce, M., David, F., Waters, L.E., and Kelley, K.A., 2020, Oxygen Fugacity Across Tectonic Settings, *in* Neuville, D.R. and Moretti, R. eds., AGU Geophysical Monograph Redox: variables and mechanisms in magmatism and volcanism. https://doi.org/10.1002/essoar.10502445.1

Chambefort, I., Dilles, J.H., Kent, A.J.R., 2008. Anhydrite-bearing andesite and dacite as a source for sulfur in magmatic-hydrothermal mineral deposits. Geology. 36, 719–722.

Danyushevsky, L. V, Della, F.N., Sokolov, S., 2000. Re-equilibration of melt inclusions trapped by magnesian olivine phenocrysts from subduction-related magmas : petrological implications. Contributions to Mineralogy and Petrology. 138, 68–83.

Danyushevsky, L.V., 2001. The effect of small amounts of H_2O on crystallisation of mid-ocean ridge and backarc basin magmas: Journal of Volcanology and Geothermal Research. 110 (3) 265-280.

Danyushevsky, L. V., and Plechov, P., 2011. Petrolog3: Integrated software for modeling crystallization processes. Geochemistry, Geophysics, Geosystems. 12.

De Astis, G., Ventura, G., Vilardo, G., 2003. Geodynamic significance of the Aeolian volcanism (Southern Tyrrhenian Sea, Italy) in light of structural, seismological and geochemical data. Tectonics. 22, 1–17.

De Hoog, J. C.M., Taylor, B.E., Van Bergen, M.J., 2001. Sulfur isotope systematics of basaltic lavas from Indonesia: Implications for the sulfur cycle in subduction zones. Earth and Planetary Science Letters. 189, 237–252.

Debret, B., Andreani, M., Delacour, A., Rouméjon, S., Trcera, N., Williams, H., 2017. Assessing sulfur redox state and distribution in abyssal serpentinites using XANES spectroscopy. Earth and Planetary Science Letters. 466, 1–11.

Ding, S., Dasgupta, R., 2017. The fate of sulfide during decompression melting of peridotite – implications for sulfur inventory of the MORB-source depleted upper mantle. Earth and Planetary Science Letters. 459, 183–195.

Ding, S., Dasgupta, R., 2018. Sulfur inventory of ocean island basalt source regions constrained by modeling the fate of sulfide during decompression melting of a heterogeneous mantle. Journal of Petrology. 59, 1281–1308.

Evans, K.A., Tomkins, A.G., 2011. The relationship between subduction zone redox budget and arc magma fertility. Earth and Planetary Science Letters. 308, 401–409.

Evans, K.A., Frost, B.R., 2021. Deserpentinization in Subduction Zones as a Source of Oxidation in Arcs: A Reality Check. Journal of Petrology. 62, 3.

Ewart, A., Hawkesworth, C.J., 1987. The pleistocene-recent tonga-kermadec arc lavas: Interpretation of new isotopic and rare earth data in terms of a depleted mantle source model. Journal of Petrology. 28, 495–530.

Faccenna, C., Civetta, L., D'Antonio, M., Funiciello, F., Margheriti, L., Piromallo, C., 2005. Constraints on mantle circulation around the deforming Calabrian slab. Geophysical Research Letters. 32, 1–4.

Ferrando, S., Frezzotti, M.L., Dallai, L., Compagnoni, R., 2005. Multiphase solid inclusions in UHP rocks (Su-Lu, China): Remnants of supercritical silicate-rich aqueous fluids released during continental subduction. Chemical Geology. 223, 68–81.

Fiege, A., Holtz, F., Shimizu, N., Mandeville, C.W., Behrens, H., Knipping, J.L., 2014. Sulfur isotope fractionation between fluid and andesitic melt: An experimental study. Geochimica Cosmochimica Acta 142, 501–521.

Fortin, M.A., Riddle, J., Desjardins-Langlais, Y., Baker, D.R., 2015. The effect of water on the sulfur concentration at sulfide saturation (SCSS) in natural melts. Geochimica Cosmochimica Acta. 160, 100–116.

Gale, A., Dalton, C.A., Langmuir, C.H., Su, Y., Schilling, J.G., 2013. The mean composition of ocean ridge basalts. Geochemistry, Geophysics, Geosystems 14, 489–518.

Georgatou, A., Chiaradia, M., Rezeau, H., Wälle, M., 2018. Magmatic sulphides in Quaternary Ecuadorian arc magmas. Lithos. 296–299, 580–599.

Gómez Tuena, A., LaGatta, A.B., Langmuir, C.H., Goldstein, S.L., Fernando, O.G., Carrasco-Núñez, G., 2003. Temporal control of subduction magmatism in the eastern Trans-Mexican Volcanic Belt: Mantle sources, slab contributions, and crustal contamination. Geochemistry, Geophysics, Geosystems. 4.

Grove, T.L., Elkins-Tanton, L.T., Parman, S.W., Chatterjee, N., Müntener, O., Gaetani, G.A., 2003. Fractional crystallization and mantle-melting controls on calc-alkaline differentiation trends. Contributions to Mineralogy Petrology. 145, 515–533.

Gurenko, A.A., 2021. Origin of sulphur in relation to silicate-sulphide immiscibility in Tolbachik primitive arc magma (Kamchatka, Russia): Insights from sulphur and boron isotopes. Chemical Geology. 120244.

Heydolph, K., Hoernle, K., Hauff, F., Bogaard, P. van den, Portnyagin, M., Bindeman, I., Garbe-Schönberg, D., 2012. Along and across arc geochemical variations in NW Central America: Evidence for involvement of lithospheric pyroxenite. Geochimica Cosmochimica Acta. 84, 459–491.

Hochstaedter, A.G., Gill, J.B., Taylor, B., Ishizuka, O., Yuasa, M., Morita, S., 2000. Across-arc geochemical trends in the Izu-Bonin arc: Constraints on source composition and mantle melting. Journal of Geophysical Resarch Solid Earth 105, 495–512.

Hutchinson, M.C., Dilles, J.H., 2019. Evidence for magmatic anhydrite in porphyry copper intrusions. Economic Geology. 114, 143–152.

Iveson, A.A., Humphreys, M.C.S., Savov, I.P., Hoog, J.C.M. De, Turner, S.J., Churikova, T.G., Macpherson, C.G., Mather, T.A., Gordeychik, B.N., Tomanikova, L., Agostini, S., Hammond, K., Pyle, D.M., Cooper, G.F., 2021. Deciphering variable mantle sources and hydrous inputs to arc magmas in Kamchatka. Earth and Planetary Science Letters. 562, 116848.

Jégo, S., Dasgupta, R., 2014. The fate of sulfur during fluid-present melting of subducting basaltic crust at variable oxygen fugacity. Journal of Petrology. 55, 1019–1050.

Jenner, F.E., Arculus, R.J., Mavrogenes, J.A., Dyriw, N.J., Nebel, O., Hauri, E.H., 2012. Chalcophile element systematics in volcanic glasses from the northwestern Lau Basin. 13.

Jenner, F.E., O'Neil, H. St. C., 2012. Analysis of 60 elements in 616 ocean floor basaltic glasses. Geochemistry, Geophysics, Geosystems, 13.

Johnson, E.R., Wallace, P.J., Delgado Granados, H., Manea, V.C., Kent, A.J.R., Bindeman, I.N., Donegan, C.S., 2009. Subduction-related volatile recycling and magma generation beneath Central Mexico: Insights from melt inclusions, oxygen isotopes and geodynamic models. Journal of Petrology. 50, 1729–1764.

Johnson, E.R., Wallace, P.J., Cashman, K. V, Delgado, H., 2010. Degassing of volatiles H_2O, CO_2, S, Cl during ascent, crystallization, and eruption at mafic monogenetic volcanoes in central Mexico. Journal of Volcanology and Geothermal Research. 197, 225–238.

Jugo, P.J., Luth, R. W., Richards, J., 2005. An Experimental Study of the Sulfur Content in Basaltic Melts Saturated with Immiscible Sulfide or Sulfate Liquids at 1300 °C and 1.0 GPa. Journal of Petrology. 46 (4) 783-798.

Jugo, P.J., Wilke, M., Botcharnikov, R.E., 2010. Sulfur K-edge XANES analysis of natural and synthetic basaltic glasses: Implications for S speciation and S content as function of oxygen fugacity. Geochimica Cosmochimica Acta 74, 5926–5938.

Kagoshima, T., Sano, Y., Takahata, N., Maruoka, T., Fischer, T.P., 2015. Sulphur geodynamic cycle 7, 1–6.

Kamenetsky, V.S., and Kamenetsky, M.B., 2010. Magmatic fluids immiscible with silicate melts: Examples from inclusions in phenocrysts and glasses, and implications for magma evolution and metal transport. Geofluids. 10, 293–311.

Kamenetsky, V.S., Zelenski, M., Gurenko, A., Portnyagin, M., Ehrig, K., Kamenetsky, M., Churikova, T., Feig, S., 2017. Silicate-sulfide liquid immiscibility in modern arc basalt (Tolbachik volcano, Kamchatka): Part II. Composition, liquidus assemblage and fractionation of the silicate melt. Chemical Geology. 471, 92–110.

Keith, M., Haase, K.M., Klemd, R., Schwarz-Schampera, U., Franke, H., 2017. Systematic variations in magmatic sulphide chemistry from mid-ocean ridges, back-arc basins and island arcs. Chemical Geology. 451, 67–77.

Kelemen, P.B., Hanghøj, K., Greene, A.R., 2003. One View of the Geochemistry of Subduction-Related Magmatic Arcs, with an Emphasis on Primitive Andesite and Lower Crust. Treatise on Geochemistry 3–9, 2–70.

Kelley, K.A., Cottrell, E., 2009. Water and the Oxidation State of Subduction Zone Magmas. Science. 325 (80) 605–607.

Kelley, K.A., Cottrell, E., 2012. The influence of magmatic differentiation on the oxidation state of Fe in a basaltic arc magma. Earth and Planetary Science Letters. 329–330, 109–121.

Kent, A.J.R., Elliott, T.R., 2002. Melt inclusions from Marianas arc lavas: Implications for the composition and formation of island arc margins. Chemical Geology. 183, 263–286.

Lee, C.T.A., 2002. Platinum-group element geochemistry of peridotite xenoliths from the Sierra Nevada and the Basin and Range, California. Geochimica Cosmochimica Acta. 66, 3987–4005.

Lee, C.T.A., Luffi, P., Chin, E.J., Bouchet, R., Dasgupta, R., Morton, D.M., Le Roux, V., Yin, Q.Z., Jin, D., 2012. Copper systematics in arc magmas and implications for crust-mantle differentiation. Science. 336, 64–66.

Lee, C-.T.A., and Tang, M., 2020. How to make porphyry copper deposits. Earth and Planetary Science Letters. 529.

Leeman, W.P., Smith, D.R., Hildreth, W., Palacz, Z., Rogers, N., 1990. Compositional diversity of late Cenozoic basalts in a transect across the southern Washington Cascades: implications for subduction zone magmatism. Journal of Geophysical Research. 95.

Li, J.L., Schwarzenbach, E.M., John, T., Ague, J.J., Huang, F., Gao, J., Klemd, R., Whitehouse, M.J., Wang, X.S., 2020. Uncovering and quantifying the subduction zone sulfur cycle from the slab perspective. Nature Communications. 11, 1–12.

Liu, K., Zhang, L., Guo, X., Ni, H., 2021. Effects of sulfide composition and melt H_2O on sulfur content at sulfide saturation in basaltic melts. Chemical Geology. 559, 119913.

Lorand, J.P., Luguet, A., 2016. Chalcophile and siderophile elements in mantle rocks: Trace elements controlled by trace minerals. Reviews in Mineralogy and Geochemistry. 81, 441-488.

Matjuschkin, V., Blundy, J.D., and Brooker, R.A., 2016. The effect of pressure on sulphur speciation in mid- to deep-crustal arc magmas and implications for the formation of porphyry copper deposits. Contributions to Mineralogy and Petrology. 171.

Mungall, J.E., 2002. Roasting the mantle: Slab melting and the genesis of major Au and Au-rich Cu deposits. Geology. 30, 915–918.

Muth, M.J., Wallace, P.J., 2021. Slab-derived sulfate generates oxidized basaltic magmas in the southern Cascade arc (California, USA). Geology.

Muth, M.J., Rasumussen, D. J., Wallace, P.J., Andrys, J., Plank, T., Cottrell, E., in prep. Best practices for measurings sulfur in silicate glasses via EPMA. American Mineralogist.

Nash, W.M., Smythe, D.J., and Wood, B.J., 2019. Compositional and temperature effects on sulfur speciation and solubility in silicate melts. Earth and Planetary Science Letters. 507, 187–198.

Newton, R.C., Manning, C.E., 2005. Solubility of Anhydrite, CaSO4, in NaCl – H_2O Solutions at High Pressures and Temperatures : Applications to Fluid – Rock Interaction. Journal of Petrology. 46, 701–716.

Parman, S.W., Grove, T.L., 2004. Harzburgite melting with and without H_2O: Experimental data and predictive modeling. Journal of Geophysical Resarch Solid Earth 109, 1–20.

Pearce, J.A., Parkinson, I.J., 1993. Trace element models for mantle melting: Application to volcanic arc petrogenesis. Geological Society Special Publications. 76, 373–403.

Pearce, J.A., Peate, D.W., 1995. Tectonic implications of the composition of volcanic arc magmas. Annual Reviews in Earth Science. 23, 251-258.

Rasmussen, D.J., Plank, T.A., Wallace, P.J., Newcombe, M.E., Lowenstern, J.B., 2020. Vapor-bubble growth in olivine-hosted melt inclusions. American Mineralogist. 105, 1898–1919.

Rezeau, H., Jagoutz, O., 2020. The importance of H_2O in arc magmas for the formation of porphyry Cu deposits. Ore Geology Reviews. 126, 103744.

Richards, J.P., 2015. The oxidation state, and sulfur and Cu contents of arc magmas: Implications for metallogeny. Lithos 233, 27–45.

Richards, J.P., 2011. High Sr/Y arc magmas and porphyry Cu ± Mo ± Au deposits: Just add water. Economic Geology. 106, 1075–1081.

Richards, J.P., Kerrich, R., 2007. Special paper: Adakite-like rocks: Their diverse origins and questionable role in metallogenesis. Economic Geology. 102, 537–576.

Robidoux, P., Aiuppa, A., Rotolo, S.G., Rizzo, A.L., Hauri, E.H., Frezzotti, M.L., 2017. Volatile contents of mafic-to-intermediate magmas at San Cristóbal volcano in Nicaragua. Lithos. 272–273, 147–163.

Ruscitto, D.M., Wallace, P.J., Johnson, E.R., Kent, A.J.R., Bindeman, I.N., 2010. Volatile contents of mafic magmas from cinder cones in the Central Oregon High Cascades: Implications for magma formation and mantle conditions in a hot arc. Earth and Planetary Science Letters. 298, 153–161.

Ruscitto, D.M., Wallace, P.J., Cooper, L.B., Plank, T., 2012. Global variations in H_2O/Ce: 2. Relationships to arc magma geochemistry and volatile fluxes. Geochemistry, Geophysical Geosystems. 13.

Saal, A.E., Hauri, E.H., Langmuir, C.H., Perfit, M.R., 2002. Vapour undersaturation in primitive mid-ocean-ridge basalt and the volatile content of earth's upper mantle. Nature. 419, 451–455.

Scaillet, B., Pichavant, M., 2005. A model of sulphur solubility for hydrous mafic melts: Application to the determination of magmatic fluid compositions of Italian volcanoes. Annals of Geophysics. 48, 671–698.

Schiavi, F., Bolfan-Casanova, N., Buso, R., Laumonier, M., Laporte, D., Medjoubi, K., Venugopal, S., Gómez-Ulla, A., Cluzel, N., Hardiagon, M., 2020. Quantifying magmatic volatiles by Raman microtomography of glass inclusion-hosted bubbles. Geochemical Perspectives Letters. 16, 17–24.

Schmidt, M.W., Jagoutz, O., 2017. The global systematics of primitive arc melts. Geochemistry, Geophys. Geosystems. 18.

Shimizu, K., Saal, A.E., Myers, C.E., Nagle, A.N., Hauri, E.H., Forsyth, D.W., Kamenetsky, V.S., Niu, Y., 2016. Two-component mantle melting-mixing model for the generation of mid-ocean ridge basalts: Implications for the volatile content of the Pacific upper mantle. Geochimica Cosmochimica Acta. 176, 44–80.

Shinohara, H., 2008. Excess degassing from volcanoes and its role on eruptive and intrusive activity. Reviews in Geophysics. 46, 1–31.

Smythe, D.J., Wood, B.J., Kiseeva, E.S., 2017. The S content of silicate melts at sulfide saturation: New experiments and a model incorporating the effects of sulfide composition. American Mineralogist. 102, 795–803.

Spilliaert, N., Allard, P., Métrich, N., Sobolev, A. V., 2006. Melt inclusion record of the conditions of ascent, degassing, and extrusion of volatile-rich alkali basalt during the powerful 2002 flank eruption of Mount Etna (Italy). Journal of Geophysical Research. 111.

Sun, Z., Xiong, X., Wang, J., Liu, X., Li, L., Ruan, M., Zhang, L., Takahashi, E., 2020. Sulfur abundance and heterogeneity in the MORB mantle estimated by copper partitioning and sulfur solubility modelling. Earth and Planetary Science Letters. 538.

Syracuse, E.M., van Keken, P.E., Abers, G.A., Suetsugu, D., Bina, C., Inoue, T., Wiens, D., Jellinek, M., 2010. The global range of subduction zone thermal models. Physics of the Earth and Planetary Interiors. 183, 73–90.

Till, C.B., 2017. A review and update of mantle thermobarometry for primitive arc magmas. American Mineralogist. 102, 931-947.

Thomas, R.W., Wood, B.J., 2021. The chemical behaviour of chlorine in silicate melts. Geochimica Cosmochimica Acta. 294, 28–42.

Tomkins, A.G., Evans, K.A., 2015. Separate zones of sulfate and sulfide release from subducted mafic oceanic crust. Earth and Planetary Science Letters. 428, 73–83.

Toplis, M.J., 2005. The thermodynamics of iron and magnesium partitioning between olivine and liquid: Criteria for assessing and predicting equilibrium in natural and experimental systems. Contributions to Mineralogy and Petrology. 149, 22–39.

Turner, S.J., Langmuir, C.H., Dungan, M.A., Escrig, S., 2017. The importance of mantle wedge heterogeneity to subduction zone magmatism and the origin of EM1. Earth and Planetary Science Letters. 472, 216–228.

Ulmer, P., Kaegi, R., Müntener, O., 2018. Experimentally derived intermediate to silica-rich arc magmas by fractional and equilibrium crystallization at 1.0 GPa: An evaluation of phase relationships, compositions, liquid lines of descent and oxygen fugacity. Journal of Petrology. 59, 11–58.

Van den Bleeken, G., Koga, K.T., 2015. Experimentally determined distribution of fluorine and chlorine upon hydrous slab melting, and implications for F-Cl cycling through subduction zones. Geochimica Cosmochimica Acta. 171, 353–373.

Venugopal, S., Schiavi, F., Moune, S., Bolfan-Casanova, N., Druitt, T., Williams-Jones, G., 2020. Melt inclusion vapour bubbles: the hidden reservoir for major and volatile elements. Scientific Reports. 10, 1–14.

Vigouroux, N., Wallace, P.J., Kent, A.J.R., 2008. Volatiles in high-K magmas from the Western trans-Mexican volcanic belt: Evidence for fluid fluxing and extreme enrichment of the mantle wedge by subduction processes. Journal of Petrology. 49, 1589–1618.

Wang, Z., Becker, H., 2015. Abundances of Ag and Cu in mantle peridotites and the implications for the behavior of chalcophile elements in the mantle. Geochimica Cosmochimica Acta 160, 209–226.

Wallace, P.J., Carmichael, I.S.E., 1994. S speciation in submarine basaltic glasses as determined by measurements of SKα X-ray wavelength shifts. American Mineralogist. 79, 161–167.

Wallace, P.J., 2005. Volatiles in subduction zone magmas: Concentrations and fluxes based on melt inclusion and volcanic gas data. Journal of Volcanology Geothermal Research. 140, 217–240.

Wallace, P.J., Edmonds, M., 2011. The sulfur budget in magmas: Evidence from melt inclusions, submarine glasses, and volcanic gas emissions. Reviews in Mineralogy and Geochemistry. 73, 215–246.

Walowski, K.J., Wallace, P.J., Hauri, E.H., Wada, I., Clynne, M.A., 2015. Slab melting beneath the Cascade Arc driven by dehydration of altered oceanic peridotite. Nature Geoscience. 8, 404–408.

Walters, J.B., Cruz-Uribe, A.M., Marschall, H.R., 2019. Isotopic Compositions of Sulfides in Exhumed High-Pressure Terranes: Implications for Sulfur Cycling in Subduction Zones. Geochemistry, Geophysics Geosystems. 20, 3347–3374.

Walters, J.B., Cruz-Uribe, A.M., Marschall, H.R., 2020. Sulfur loss from subducted altered oceanic crust and implications for mantle oxidation. Geochemical Perspectives Letters. 36–41.

Webster, J.D., Vetere, F., Botcharnikov, R.E., Goldoff, B., McBirney, A., Doherty, A.L., 2015. Experimental and modeled chlorine solubilities in aluminosilicate melts at 1 to 7000 bars and 700 to 1250 °C: Applications to magmas of Augustine Volcano, Alaska. American Mineralogist. 100, 522–535.

Wieser, P.E., Jenner, F., Edmonds, M., Maclennan, J., and Kunz, B.E., 2020. Chalcophile elements track the fate of sulfur at Kīlauea Volcano, Hawai'i. Geochimica et Cosmochimica Acta. 282, 245–275.

Woodhead, J., Eggins, S., Gamble, J., 1993. High field strength and transition element systematics in island arc and back-arc basin basalts: evidence for multi-phase melt extraction and a depleted mantle wedge. Earth and Planetary Science Letters. 114, 491-504.

Yogodzinski, G.M., Brown, S.T., Kelemen, P.B., Vervoort, J.D., Portnyagin, M., Sims, K.W.W., Hoernle, K., Jicha, B.R., Werner, R., 2014. The role of subducted basalt in the source of Island Arc magmas: Evidence from seafloor lavas of the Western Aleutians. Journal of Petrology. 56, 441–492.

Zhang, H.L., Cottrell, E., Solheid, P.A., Kelley, K.A., Hirschmann, M.M., 2018. Determination of $Fe^{3+}/\Sigma Fe$ of XANES basaltic glass standards by Mössbauer spectroscopy and its application to the oxidation state of iron in MORB. Chemical Geology. 479, 166–175.